Stretching the Definition of a Lipid Bilayer: Elasticity's Role in Protein and Lipid Organization

Thesis by
Tristan Scott Ursell

In Partial Fulfillment of the Requirements
for the Degree of
Doctor of Philosophy

California Institute of Technology
Pasadena, California

2009

(Defended May 29th, 2009)

So long . . . and thanks for all the fish.

I suppose this is where I get to sum up my thoughts about the last six years, if that is even possible. No amount of elegant prose or deserved obsequious gratitude can properly express how much these years have meant to me, how much growth they have resulted in, nor how fondly I will look back on them. Clearly, there are a great many people to thank for encouraging me, challenging me and guiding me — but this is not the end of an intellectual journey, it is the beginning, and I know that many of the people I am about to mention will be characters in this continuing story. That fact truly fills me with optimism and excitement. In the same way that the rest of this thesis is meant to be a record of my scientific thought process and progress, so this brief section is really my own record of gratitude — to those whom I accidentally omit, please do not take any offense. The only way I can think to do this rationally is in some kind of chronological order, and maybe that will require some context that seems unnecessary.

First, my parents, Tim and Eva, and my sister Elisabeth, have always been in support of my endeavors for higher education. Most importantly, they stoked the fire of curiosity from a very young age. What other eight year old has his own laboratory and workshop, and is given free reign to play with all manner of equipment, electronics and chemicals? Countless hours were spent during my childhood 'experimenting', building, shocking and igniting (I almost burnt the house down twice), and learning about what makes things tick, usually quite literally, by taking apart everything I could get my hands on. Those early years were the training that would give me the adept hands and curious mind that have and will continue to fuel my passionate love of science. I only hope that someday I can provide the same environment.

I left high school thinking I was a hot shot, and I suppose by relative comparison I was, but during that first year of college, if I learned one thing, it is that I had (and have) a lot to learn. That time was no less important in my development as a scientist, and there are a few people I have to thank for guiding me during those years, and sharing in tribulations and triumphs of what now seems like a very short era. First, I want to thank Joe Schreier, not only for being an excellent friend and late night study / problem set partner, but also for teaching me a lot about what it means to form a good argument. I think our healthy competitive natures, mutually pushed each other to be the best physicists we could be. I also want to thank Stefan Delvoye broadening my musical horizons, and accompanying me on many a wacky adventure. I also had two great, unofficial academic advisors during that time. Peter Persans, in addition to teaching me a hell of a lot about physics, was a great friend and mentor. The many hours spent in his office chatting about physics, politics and life are amongst my best times in college. Likewise, Peter Kramer was a great teacher and mentor. Much of my mathematical prowess (dare I use that word) is due to his extraordinarily high standards of rigor and careful thinking, and the great care he took in seeing that I pushed myself to do my best. Lastly, I want to thank Alejandro Sela, who encouraged me

to study abroad and helped open my eyes to the value of understanding another culture. Rarely have I seen a professor with such calm, yet complete care for the well-roundedness of his students.

During my sophomore year, I heard about an undergraduate program that let students perform research at any one of NASA's national laboratories, and with gusto I applied for a fellowship at JPL in Pasadena, CA. That summer, I worked for Jeff Snyder in the thermoelectrics division at JPL. Words cannot express how awesome that first summer (2001) was, and how important a role it played in my future trajectory. There I was, a green, twenty-year-old kid, watching the Mars Rovers practice in rough terrain next to my building and eating at the same cafeteria where engineers and scientists mapped the exploration of the cosmos. Jeff was everything a budding scientist could ask for in a mentor: jovial, intelligent, curious, accepting of my lack of experience and knowledge, and always willing to teach. We also shared a mutual love of tinkering, and I spent many hours at his house helping him fix his scooter and lawn equipment. I think it was in his office in Building 272, scrawling out ideas and equations, that I learned how to properly use a piece of chalk. Additionally, Jeff and his wife Sossina Haile (a professor at Caltech), provided me with a family on the west coast — I even lived next door one summer in their neighbor's pool house. I came back to work with Jeff the following two summers and into my first year of graduate school, eventually culminating in my first two scientific publications.

Moving on, I remember that in my senior year of college, I had just finished mid-term exams and driven with friends down to Mardi Gras for a week of debaucherous fun. I was a few drinks into my first evening in New Orleans when I got a call from some guy named Rob Phillips at Caltech, informing me that I had been accepted! I quickly tried to pull myself together and hold a cogent conversation, needless to say, elated. After that call, the celebratory efforts were redoubled. While I had other acceptances, as it turns out, the choice to come to Caltech was easy. I arrived that fall, and was greeted by not only a demanding class schedule, but a great group of new graduate students with whom I developed a strong and lasting bond. Over the last six years we have shared many experiences, and all of them have been great friends, adventure mates, and taught me a thing or two about physics and life; among those good friends are: Deepak Kumar, Raviv Perahia, Vikram Deshpande, Waheb Bishara, Jen Dionne, Erin Koos and Mike Meyer. There are also a number of other friends who have been equally as supportive and instrumental in making my time at Caltech the personal success it was; together we grew as scientists and people, and their company has meant so much to me, in particular: Tristan Smith, Jenny Roizen, Hernan Garcia, Eric Peterson, and Anna Folinsky. In addition to these good friends, there have been two close companions who have shared in my daily life, listened to my rants, I to theirs, and who have been close confidants and provided immeasurable support: Jenn Stockdill and Amanda Dunn.

After a somewhat tumultuous first year, with my tail between my legs, Rob accepted me into his group and I quickly devoted myself to the task of figuring out what this field of 'biophysics' was all about. At the time, I was admittedly stigmatized against it, and I'll never forget that first year trying to figure out all the jargon of a new field: what on earth does 'assay' and 'aliquot', 'homolog'

and 'phenotype', and the alphabet soup of gene and protein names mean? Slowly but surely, I pieced things together. Throughout that time and the years to come, a number of fellow graduate students and post-docs were immensely helpful with experiments, in brainstorming, and often, even without realizing it, mentoring; among them special thanks goes to: Corinne Ladous, Paul Grayson, Dave Wu[1], Paul "Off-Color" Wiggins, Stephanie "You're so much like my brother" Johnson, Heun Jin "Master of Understatement" Lee, and the ever conscientious Maja Bialecka. Throughout my graduate career, a number of people have been immensely helpful in getting experiments to work, troubleshooting, and generating and vetting ideas, namely: Chris Gandhi[2], Fan Yang, Olaf Andersen, Sergei Sukharev, Sarah Keller, Rod MacKinnon, Daniel Schmidt,and Evan Evans. Finally, I have had the honor of working with excellent collaborators on nearly all of the projects discussed in this thesis. They have provided expert advice and guidance, with special thanks going to: Doug Rees[3], Bill Klug, Pierre Sens, Dan Reeves, Liz Haswell, Jennifer Lippincott-Schwartz and Jané Kondev.

I spent the summer of 2006 (part of 2007) at the Marine Biological Laboratory in Woods Hole, and I am not sure words describe how fantastic that summer was. I met so many great people there, and was given the opportunity to intensely work on a number of really interesting projects, which also entailed that I learn about microscopy, biochemistry, cell biology, and graffiti. Among those I have to thank for making those summers truly epic are: Ron Vale and Tim Mitchison, Dyche Mullins, Jen Gillette, Carolyn Ott, Eric Wieschaus, and all my classmates in the summer of 2006.

Outside of the Phillips Lab, I have many friends who have taught me a lot about the real meaning of diligence, intellectual honesty, philosophy of science, and most importantly creativity, while accompanying me on so many great adventures over the years: Mikie Olsen, Robert Sidney Cox III, Alexander Hamilton Farley, Matthew MacDougall, Robb Walters, Andrea Choe, Dylan Moon Morris, Peretz Partensky, Justin Bois, Hari Shroff, Doug Campbell, Ethan Garner, and Anselm Levskaya. I look forward to many more fun and goofy years with these great thinkers and shakers, and hopefully, together, we will change a few, less savory, aspects of the world around us.

My candidacy and thesis committees have also provided me with needed guidance and perspective, and to their credit they have accepted the daunting task of vetting the work in this thesis; much thanks goes to: Michael Roukes[4], Doug Rees, Michael Elowitz, Bill Klug[5], Scott "You need

[1] As a precocious first year, Dave uttered one of the truest statements I have yet heard about graduate school. One afternoon, during our first year, we were both toiling in the Steele lab, and he turned to me and said "Every step is a mountain."

[2] Special thanks goes to Chris for teaching me a lot about biochemistry and protein purification, at one point proclaiming "You know ... this is easy, it's just like cooking."

[3] A big thanks goes to Doug for opening his lab and his expertise, and offering his sage advice throughout my graduate career.

[4] I have always enjoyed my interactions with Michael, and I remember on one occasion during our very first bootcamp, we were talking and he said something that solidified my desire to stay in academia, "What I love most about being a professor is that every five years I get to reinvent myself."

[5] A man of consummate good nature.

it now." Fraser, and Kaushik Bhattacharya.

During the fateful summer of 2005, Rob invited a post-doc to come visit our lab for a month to conduct experiments on bacterial membranes. Occasionally in life, we meet someone, and within the first five minutes you know that you are going to be good friends. This was the case with KC Huang. He has been a great friend, thoughtful mentor, and a faithful ear. I have always valued our interactions, whether they centered on our mutual love of off-color humor or deep musings in physics, our dynamic has stimulated a wealth of good and devious ideas. I greet my upcoming tenure in his research group with the excitement that surrounds any worthy intellectual endeavor, and the calm of being in the company of a good friend.

Last, but certainly not least, I owe a huge debt of gratitude to my advisor Robert Brooks Phillips. First and foremost, his integrity and earnestness are an example to us all. He has a fitting quote for all occasions, and one of the strangest senses of humor I have yet encountered. I have been, and remain, impressed at his ability to sniff out weak points in theoretical and experimental work, and his tendency to give sound advice. His dedication to ensuring that the science that comes out of his lab is cogent, relevant, thorough, and thoughtful is something I will strive to employ in my future endeavors. While I think I was spread a bit thin in his lab, partially his fault and partially my own, I immensely appreciate his willingness to let me follow my nose, make my own mistakes, and pursue many of my own ideas. His knowledge of science history and its relevance to how we do science today is inspiring, and as I have come to realize, crucially important for understanding our motivations and our challenges as scientists. No advisor nor student is perfect, and I know that many days we frustrated each other to the point of *complete* exasperation[6], but I like to think that as much as he mentored me, and he did, we also taught each other to a degree. Rob's devotion to collaboration and his tireless efforts to expose us to new frontiers of research through the many great scientists, writers, and thinkers he has brought into our midst is one of the joys of my career thus far. I leave his lab with an education that was about far more than 'just' the science itself, and with a good friend and collaborator for many years to come.

Finally, in closing, I must say how privileged I feel. The ability to wake up each morning, albeit tired, but excited to go to work is rare from all that I gather. Sure, I have worked very hard, but really I would be nowhere were it not for the myriad opportunities with which I have been presented, and the many people who have invested in me.

Curiosity and intellectual honesty are the fundamental human virtues — practice them daily, fearlessly.

Tristan S. Ursell
May 2009
Pasadena, CA

[6]There are many choice quotes, but a recent one stands out; I asked Rob if I was the biggest pain in the ass student he has ever had, to which he responded, "The list of pains in my ass is long, but I am also a good psychological mirror so I have no doubt that it is better to give than receive, and I have given much pain."

Abstract

The Central Dogma forms the foundation of molecular biology couched in polymer language; all the key players are there — DNA, RNA, protein — or so it would seem. Yet one class of biologically synthesized molecules, crucial for life, is often over looked: lipids. These amphiphilic molecules exhibit a number of strange properties, integral to the cells ability to separate self from non-self in a chemically diverse environment. Lipids self-assemble into two-dimensional bi-layered fluids with aspect ratios of a thousand to one or more, capable of self-healing and bending into extraordinarily complex shapes. Within the cell, membranes allow for numerous chemically-distinct compartments, essential for metabolism, protein assembly, genome management, and cell division. With literally hundreds of different kinds of lipids and proteins interacting on a given membrane, we have much to learn about how membranes regulate the flow of materials into and out of cells. Clearly, molecular level detail is integral to our understanding of these systems, however, on the mesoscopic level membranes exhibit certain mechanical effects that serve to organize lipids and proteins, the study of which forms the bulk of this dissertation. We start by building an elastic model of bilayers, where embedded proteins deform the surrounding membrane and incur a free energy cost. This allows the mechanical attributes of the bilayer to influence the conformation of embedded proteins. We explore this connection in the context of mechanosensation in bacteria, as well as developing methods that allow bilayer mechanics to comment on the structure of classically voltage-gated ion channels. In addition to affecting conformational preferences, these same deformations have a finite length-scale that results in interactions between embedded proteins. Depending on the protein shape, these interactions can be attractive or repulsive, may exert torques on proteins, provide for a mechanism of shape-specific oligomerization, and importantly allow proteins to utilize the bilayer as a generic communicator of conformational information. The effects of these elastic interactions are discussed in the context of mean protein spacing, dimerization, conformational cooperativity, and likely pathways to multi-mer protein assembly, with the bacterial mechanosensitive channel MscL as a structural example. In subsequent chapters, bilayer elasticity is used to shed light on the large-scale organization of lipids themselves. Biological membranes likely have multiple fluid, lipid phases, where sequestration of saturated lipids and cholesterol form lipid domains. We found that formation of domains above a certain critical size induces morphological transitions to a ‘dimpled’ phase which turns on repulsive, elastic interactions that serve to spatially organize domains as well as severely inhibit domain coalescence. This provides a mechanism for the maintenance of lipid lateral heterogeneity on relatively short length-scales and long time scales. We further observed discrete transitions to a ‘budded’ domain morphology and developed a set of interpretive energetic transition rules between flat, dimpled and budded domains. We demonstrate that these morphologies and their attendant transitions lead to a unique form of domain-size-dependent transport in membranes. Further, we employ the mechanics of vesicles to model osmoregulation via channel proteins, and in the setting of conserved surface area and volume to develop a theoretical and experimental framework to study membrane adhesion in the context of the homophilic protein binding.

Contents

1 Lipid Bilayer Mechanics and Mechanosensation **13**

1.1 Introduction . . . 13

1.2 Statistical Mechanics of Mechanosensitive Channels . . . 14

1.2.1 Lipid Bilayer vs. Protein Internal Degrees of Freedom . . . 14

1.3 Bilayer Free Energy and Channel Gating . . . 18

1.3.1 The Case Study of MscL . . . 21

1.4 Bilayer Deformation, Free Energy and the Role of Tension . . . 23

1.4.1 Midplane Deformation . . . 24

1.4.2 Thickness Deformations . . . 27

1.4.3 Approximating Bilayer Deformation: The Variational Approach . . . 32

1.4.4 Variational Approach for Midplane Deformations . . . 33

1.4.5 Variational Approach for Membrane Thickness Deformations . . . 34

1.4.6 Distilling the Design Principles . . . 36

1.5 Experimental Considerations . . . 38

1.5.1 Other Experimental Clues . . . 41

1.6 Interaction between Transmembrane Proteins . . . 43

1.6.1 Enthalpic Interactions . . . 43

1.6.2 Entropic Interactions . . . 44

1.6.3 Protein Conformations Affected by Interaction . . . 45

1.6.4 Interaction and Protein Density in Biological Membranes . . . 46

1.7 Overview and Concluding Remarks . . . 46

1.8 Acknowledgments . . . 48

2 Bilayer-Mediated Protein Interactions **49**

2.1 Introduction . . . 49
2.2 Background . . . 49
2.3 Elastic Deformation Induced by Membrane Proteins . . . 51
2.4 Gating Behavior of Two Interacting Channels . . . 56
2.5 Interactions between Diffusing Proteins . . . 58
2.6 Further Discussion . . . 65
2.6.1 Comparison to Other Interactions . . . 65
2.6.2 Role of Elastic Boundary Conditions . . . 66
2.6.3 Effects of Spontaneous Curvature . . . 67
2.6.4 Implications of Bilayer Volume Conservation . . . 69
2.6.5 Experimental Examples of Bilayer Mediated Interactions . . . 72
2.7 Computational Methods . . . 73
2.8 Accession Number and Acknowledgments . . . 74
2.9 Summary of Bilayer-Mediated Interactions . . . 74
2.10 Non-Specific Interactions from Crowding . . . 74
2.10.1 Ideal Crowding Tension . . . 76
2.10.2 Slightly Non-Ideal Crowding Tension . . . 77
2.10.3 Proteins that Change Area . . . 79
2.10.4 Choosing an Ensemble . . . 80
2.10.5 Excluded Area Effects . . . 81
2.11 Crowding in a Lipid Domain . . . 83
2.12 Concluding Remarks . . . 86

3 Volumetric Flow in Protein Channels **89**

3.1 Not All Are for Ions . . . 89
3.2 Gating and Conductance Properties of MscL . . . 90
3.3 Modeling Hypo-Osmotic Shock . . . 93
3.4 Measuring Ensemble Channel Flow . . . 104
3.4.1 Bilayer Permeability and Proof of Concept . . . 110
3.4.2 Using Gain-of-Function Mutants . . . 112
3.4.3 Controlling for Channel Density . . . 116

3.5 Speculations . . . 117
3.5.1 Possible Effects of Temperature . . . 118
3.5.2 Interesting Possibilities . . . 119
3.6 Effects of Glass-Bilayer Binding in Electrophysiology . . . 120
3.6.1 The Zero Pressure Limit . . . 120
3.6.2 Patches Under Pressure . . . 121
3.6.3 Determining γ from Patch Curvature . . . 124
3.7 Concluding Remarks . . . 126

4 Organization and Morphology of Lipid Domains 129
4.1 Introduction . . . 129
4.2 Dilute Domain Interactions . . . 130
4.2.1 The Elastic Model and Morphological Transitions . . . 132
4.2.2 Elastic Interactions of Dimpled Domains . . . 137
4.2.3 Discussion of Dilute Domain Interactions . . . 141
4.2.4 Summary of Dilute Domain Interactions . . . 142
4.3 Dimpled Domain Organization and Budding . . . 142
4.3.1 Spatial Organization of Dimpled Domains . . . 144
4.3.2 The Budding Transition . . . 149
4.3.3 The 'Algebra' of Morphology . . . 154
4.3.4 Discussion of Domain Morphology . . . 161
4.3.5 Summary of Domain Organization and Morphology . . . 163
4.4 Detailed Analysis of Theory and Experiment . . . 163
4.4.1 Overview of Materials and Methods . . . 164
4.4.2 Calculating Membrane Curvature and Area . . . 165
4.4.3 Conservation of Domain Area . . . 167
4.4.4 The Small Gradient Limit . . . 168
4.4.5 Gaussian Curvature . . . 174
4.4.6 Equilibrium Domain Shapes . . . 176
4.4.7 Scaling and the Critical Exponent . . . 178
4.4.8 Divergence Theorem Solution for the Deformation Energy . . . 180
4.4.9 Spherical Domain Budding . . . 182

4.5 Vesicle Tension and Entropy . . . 185
4.5.1 Constructing a Thermal Ensemble . . . 186
4.5.2 The Equation of State . . . 187
4.5.3 Simulating Membrane Conformations . . . 196
4.6 The 1D Interaction Potential . . . 197
4.6.1 Interactions of Asymmetric Domains . . . 198
4.6.2 Effects of Domain Size Asymmetry . . . 201
4.6.3 Corrections from Size Asymmetry . . . 202
4.7 Coarse Control of Membrane Tension and Inducing Phase Separation . . . 206
4.8 Error Introduced by the Curved Vesicle Surface . . . 207
4.9 *In vitro* Selection and Representative Data . . . 211
4.10 Domain Tracking and Data Analysis . . . 213
4.10.1 The Fictitious Confining Potential . . . 219
4.10.2 The Geometric Derivation . . . 222
4.11 Plasma Membrane Domains . . . 224
4.11.1 Experimental Methods . . . 225
4.11.2 Plasma Membrane Domain Interactions . . . 225
4.12 Concluding Remarks . . . 228
4.13 Acknowledgments . . . 230

5 Membrane Adhesion by Homophilic Protein Binding 231

5.1 Introduction . . . 231
5.2 Physiology of L1 Binding . . . 231
5.3 The Adhered Vesicle Shape . . . 234
5.3.1 Shape Constraints . . . 235
5.3.2 Calculating Surface Area . . . 236
5.3.3 Calculating Volume . . . 237
5.3.4 Protein Conservation and Surface Energy . . . 238
5.3.5 Vesicle Bending Energy . . . 241
5.4 Free Energy of Adhesion . . . 243
5.4.1 Connection to Experiment . . . 244
5.5 Simulating Adhered Vesicle Shape . . . 244

5.5.1 Note on Linearity of Tension and Pressure . . . 246
5.6 Tether-Based Assay of Vesicle Adhesion . . . 246
5.6.1 Tethered Vesicle Area . . . 252
5.6.2 Tethered Vesicle Volume . . . 253
5.6.3 Bending Energy of a Tethered Vesicle . . . 253
5.6.4 Free Energy of Tethered Vesicle Adhesion . . . 254
5.6.5 Connection with Experiments . . . 254
5.7 Experimental Setup . . . 255
5.7.1 Controls and Vesicle-Vesicle Binding . . . 257
5.7.2 Azimuthally Symmetric Vesicle Adhesion . . . 259
5.7.3 Possible Extensions and Complications . . . 259
5.8 Concluding Remarks . . . 261

A Detailed Derivation of Bilayer Thickness Deformation **263**

B MscL Synthesis and Purification **269**

C Micropipette Preparation Protocol **277**

D Basics of 2D Phase Separation **281**
D.1 Background . . . 281
D.2 Derivation of the Cahn-Hilliard Equation . . . 281
D.2.1 Deriving a Natural Length and Time Scale . . . 283
D.3 Kinetics in Fourier Space . . . 284

E Electroformation of Giant Unilamellar Vesicles **287**

F Protocol for Giant Plasma Membrane Vesicles **293**

References **297**

Thesis Summary and Guide

"The most difficult subjects can be explained to the most slow-witted man if he has not formed any idea of them already; but the simplest thing cannot be made clear to the most intelligent man if he is firmly persuaded that he knows already, without a shadow of doubt, what is laid before him."
– Leo Tolstoy

In large part, the pursuit of science is one of simplification — break a complex system down to its most fundamental parts and attempt to understand the input-output relationship between them. This reductionist scheme has been immensely successful throughout chemistry, physics, and other scientific disciplines, forming the basis of our mechanistic theories that describe the world around us. In 1839, Theodor Schwann enunciated a startling and broadly impactful statement that would forever affect how we view the process of life:

> *"We have seen that all organisms are composed of essentially like parts, namely, of cells; that these cells are formed and grow in accordance with essentially the same laws; hence, that these processes must everywhere result from the operation of the same forces."*

Such revelations came on the heels of massive efforts to classify, categorize, and take stock of the myriad life forms found in incredibly diverse environments (*e.g.* Linnaeus' *Systema Naturae*, 1770 and *Species Plantarum*, 1764). Given the shear number of different organisms deriving their livelihood from diverse sources, it was likely hard to imagine that there were (non-supernatural) unifying principles that linked *every* organism on the planet. Likewise, as Erwin Schroedinger espoused in his book *What is Life?*, it was equally hard to imagine that the same basic, physical principles governing the relatively simple orbits of planets and electrons were responsible for the complexity inherent in life — surely new physical processes, forces and laws must be at work! Yet, in one of the most beautiful and amazing tales of science, the resounding answer seems to be that life is 'just' a bafflingly complex implementation of the same physical principles.

At the turn of the 20th century, we knew that to begin to understand life, we had to explain a few key processes: How was hereditary information maintained and passed on? Was there a material that held information in a form generic enough that all life could possess and manipulate it? What molecular structures were so modular that they could be locally produced and employed to perform all the metabolic and reproductive tasks of a cell? How could a cell separate self from non-self to regulate its internal chemical environment while still interacting with the external world? The discovery that DNA and RNA are the vehicles of genetic information and heredity; the identification of twenty indispensable amino acids that build all of the cell's machinery; and

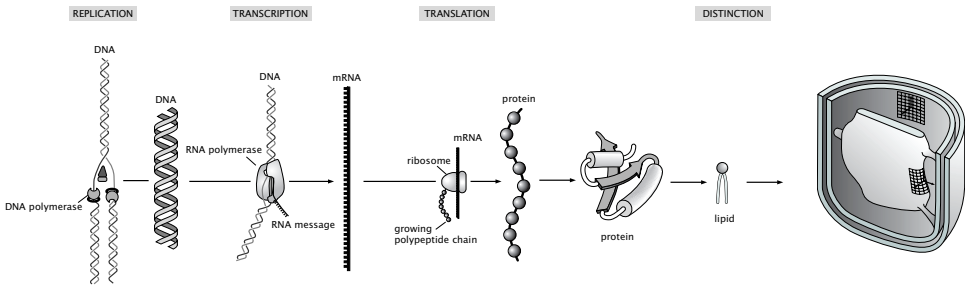

Figure 1: The Central Dogma of biology conceptually links the three major biological polymers: DNA, RNA and poly-peptides, to form the basis of our molecular understanding of life. Given the supremely important role of lipids, one might add the process of 'Distinction' to the list of fundamental biological mechanisms, whereby lipids are the molecules solely responsible for distinguishing self from non-self, allowing a cell to create and control its internal chemical environment. Modified from [1].

deciphering of the base-pair and codon alphabets that connect these three classes of molecules, seemed to provide the answers; enough so that Francis Crick, in 1958, enunciated The Central Dogma of biology, now held as a cornerstone in our understanding of life. Unfortunately, the Central Dogma orphans the last of these questions; though there is clearly another set of modular, biologically-synthesized molecules that are neither nucleic nor amino acids, whose exclusive role is to define the chemical boundary of the cell and compartmentalize its internal components. Thus one might rightly make an addition to the Central Dogma, as shown in Fig. 1.

Lipid molecules take on a number of unique and crucial roles in cellular physiology. The properties of a lipid bilayer, when compared to the macroscopic materials around which our intuitions are built, are supremely strange - it is a high aspect-ratio, self-organized, self-healing, highly bendable material, that is selectively permeable to a host different small molecules, formed of multiple fluid phases. The proteins embedded within it are responsible for regulating the flow of nutrients and wastes, orchestrating the cytoskeleton for motility, and receiving and transmitting signals via peptides, ions, sugars and other small molecules. This combination of properties allows membranes to take on a complex shapes, that compartmentalize cellular volume into a number of chemically distinct regions, ultimately separating self from non-self, and shown in Fig. 2. While the detailed, molecular properties of the bilayer, and its interactions with these proteins, are clearly important for forming a coherent mechanistic picture of these processes, the membrane can be viewed mesoscopically as a mechanical medium with its own unifying framework. In this thesis, we examine some of the generic mechanical interactions that enable the membrane to affect proteins within it, likely help to spatially organize proteins and lipids, and allow proteins to mechanically communicate with one another in the membrane. Viewed as a continuous material, a lipid bilayer has a bending and stretch stiffness, a well-defined thickness, and potentially multiple fluid phases that render continuum mechanics an informative tool for analyzing how lipids interact with other

lipids and proteins embedded in the bilayer. The topics explored in this thesis revolve around the membrane as a mechanical entity with a diverse set of lipid–lipid and lipid–protein interactions. In particular:

- Following previous work by others, we discuss the construction of a continuum mechanical model of bilayers that reduces the atomistic complexity of proteins to a set of boundary conditions at the protein–lipid interface, employed in the context of bacterial mechanosensation.
- We develop a set of experimental predictions that comment on the energetic interplay between ion channel structure and the mechanical properties of the bilayer, notably the scaling of gating voltage as a function of lateral tension, in hopes of elucidating mechanisms of conformational changes in ion channels.
- We construct a theory of deformation-mediated interactions that allow for shape-specific repulsive or attractive forces between embedded proteins, which simultaneously allow proximal embedded proteins to conformationally couple, in the absence of direct physical contact.
- We discuss potential models of omsoregulation in bacteria and their physical implications, and outline an experimental design for the ensemble measurement of the pressure-driven flux of osmolytes and water through certain 'non-ion' channels, notably concentrating on the bacterial channel MscL.
- We build a theory and report on experiments concerning the spatial organization, morphologies and qualitative kinetics of lipid domains in model, ternary membrane systems, with some discussion of possible biological relevance.
- We develop theory and discuss initial results of experiments that utilize conserved volume and surface area unilamellar vesicles to examine membrane adhesion mediated by homophilic protein binding.

The rest of this summary is a chapter-by-chapter guide that discusses the key results and outlines the theoretical and experimental tools used in each project.

Chapter 1: Protein-Bilayer Mechanics

This chapter serves as the background motivation and mathematical foundation for much of the thesis. Whether it is an analysis of mechanosensation, membrane-mediated protein interactions, lipid domain morphology or vesicle adhesion, these mechanical models incorporate energies calculated from an elastic model of membrane stretching and bending. Exactly how to formulate that model depends on the membrane geometry and degree of curvature. The chapter begins by discussing the biological context of mechanosensation and the likely influential role that lipids play in membrane protein function. Proteins that are embedded in the membrane impose boundary conditions at

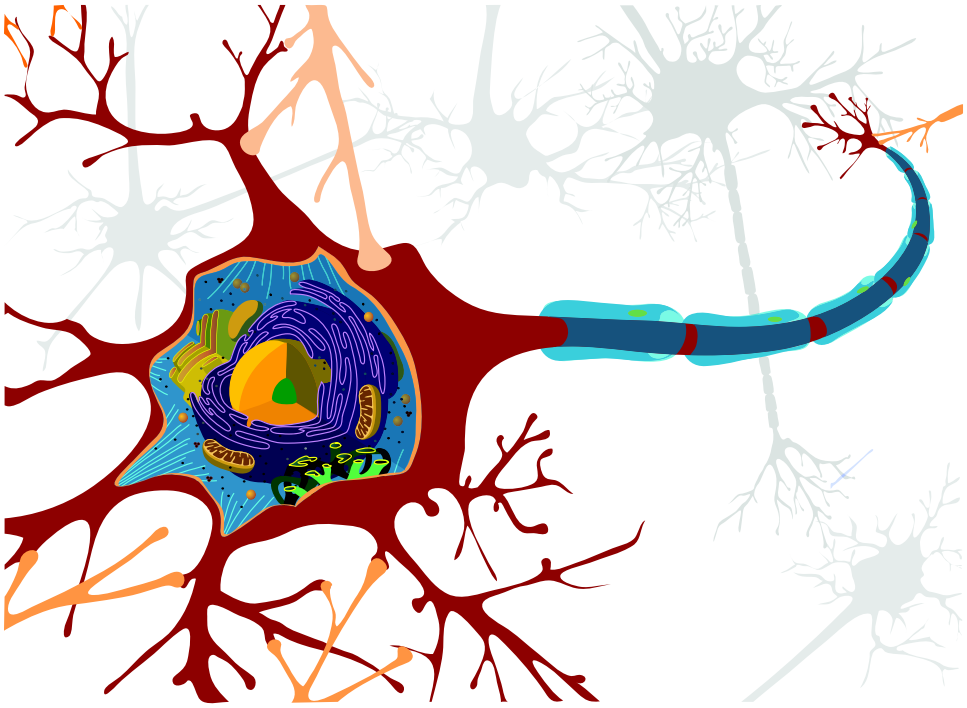

Figure 2: Schematic of the basic membrane structures found in a eukaryotic neuron. The diagram shows a number of membranous compartments that allow for chemically distinct regions in the cell, and give the cell the ability to separate self from non-self. These extremely intricate shapes can only be achieved with a material that self-heals and flows to relieve mechanical stress — two of the most important properties of lipid bilayers. Membrane structures shown in the diagram are: the plasma membrane, the rough and smooth endoplasmic reticulum, mitochondria, the Golgi apparatus, and the nuclear envelope. This figure adapted from a publicly released image under CCL licensor.

the protein-lipid interface, and can result in both midplane bending and thickness deformations. Following commonly used techniques, the energy cost of these deformations can be written as a functional of the deformation fields, and sections of this chapter derive those functionals as well as their analytic, two dimensional solutions. These deformation energies depend on some combination of the bilayer mechanical properties, like bending and stretch stiffness or bilayer thickness, all of which can be measured experimentally. We make refinements to these models in regards to how tension affects bilayer thickness deformations. We use the analytical results from this chapter to examine the way that deformation energies scale with bilayer mechanical properties, to understand which parameters are the strongest determinants of bilayer-protein interaction. Relevant to these energies, we discuss how one generates protein boundary conditions, useful in the elastic theory, from known atomistic structures, akin to Fig. 3. These results are put into context by examining recent experimental work in which channel gating properties were examined as lipid properties were systematically varied, either by changing membrane thickness or altering membrane properties through dopants.

The chapter finishes with an overview of our work on how mechanical attributes of the bilayer, like lateral tension or thickness, could be used as a reporter for the structural rearrangements in the gating of ion channels, in particular the potassium channel Kv1.2. While the structure of many ion channels is known, those structures are of either the closed or open state, and in fact, no ion channel has been definitively crystallized in both the open and closed state; hence the precise conformational rearrangements upon gating are unknown. That said, if the conformational change is accompanied by a change in the lipid-protein boundary conditions, a free energy cost is incurred that is accompanied by a mechanical signature in the gating properties. These concepts are also discussed in relation to the topic of membrane dopants that affect classically non-mechanosensitive ion channel function.

Finally, we qualitatively discuss the level of crowding in real biological membranes with relevance to the potential roles that crowding or explicit bilayer-mediated interactions might be playing in membrane protein function.

Chapter 2: Bilayer-Mediated Protein Interactions

Building on the analysis of Chapter 1, this chapter explores the origin and consequences of bilayer-mediated protein-protein interactions. In the same way that ionic solutions act as a medium of interaction between two charged bodies, embedded proteins that alter bilayer thickness or bend the bilayer midplane disturb the surrounding lipids with a characteristic decay length — usually on on the order of a nanometer or tens of nanometers, respectively. In crowded biological membranes, this means that proteins can 'sense' each other through the membrane. This sensing takes the form of an energetic interaction, such that two membrane proteins in proximity, relative to the elastic decay length, exert a number of different forces on each other. The simplest of these forces seeks to spatially organize the proteins by either attraction or repulsion, as shown in Fig. 4.

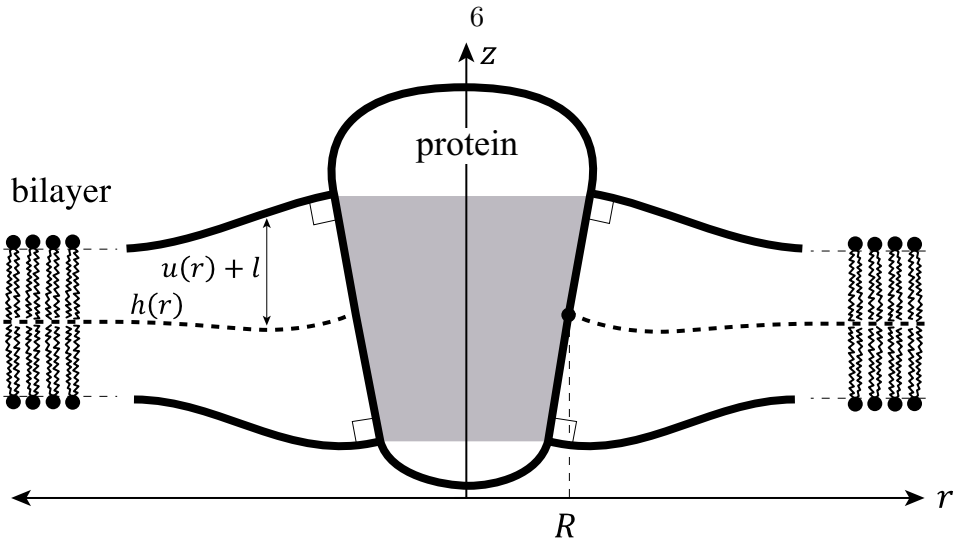

Figure 3: A schematic showing the different ways that a conical protein can deform the surrounding bilayer. An embedded protein of radius R can bend the bilayer midplane and/or change the bilayer thickness. If these deformations are large enough, the free energy difference between the deformed and undeformed state of the bilayer is comparable to energetic driving forces from tension or membrane potential. Here the unperturbed bilayer thickness is l, the leaflet deformation field is $u(r)$, and the midplane deformation field is $h(r)$.

The form of these potentials depends on the type of deformation and the shape of the proteins that are interacting. If two conformations of a protein present different shapes to the membrane, elastic interactions with other nearby proteins will shift the equilibrium probability of finding that protein in any particular conformation. We use the mechanosensitive channel of large conductance (MscL) as a case study to examine the implications of these bilayer mediated elastic interactions on protein conformational statistics and clustering. The deformations around MscL cost energy on the order of $10\,k_BT$ and extend $\sim 3\,\text{nm}$ from the protein edge, as such elastic forces induce cooperative gating, and we propose experiments to measure these effects. Additionally, since elastic interactions couple to protein conformation, we find that conformational changes can severely alter the average separation between proteins, effectively leading to a membrane-mediated dimerization or oligomerization. We discuss the implications of elastic interactions on cooperative conformational changes and the spatial organization of membrane proteins into functional groups. We examine the implications of bilayer volume conservation and boundary conditions at the protein-lipid interface in detail. In the final section of the chapter, we discuss different membrane crowding scenarios that result in non-specific interactions between membrane proteins, to produce a crowding tension and protein-induced depletion forces.

Chapter 3: Volumetric Flow in Protein Channels

Continuing the theme of using MscL as a model protein, this chapter lays the foundation for experi-

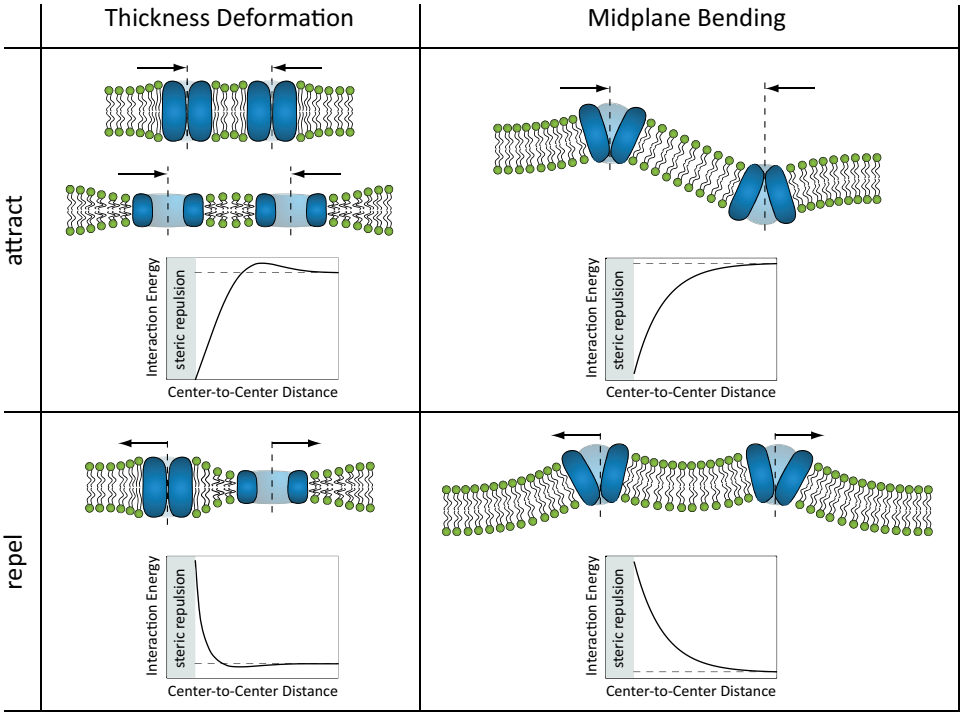

Figure 4: A graphical table showing the mostly attractive or mostly repulsive potentials resulting from bilayer deformations. For proteins that deform membrane thickness, like attracts like, whereas the opposite is true for proteins that deform the bilayer midplane. The thickness changing proteins have the approximate, relative dimensions of MscL in its closed and open states, demonstrating the qualitatively different interactions that arise from having two distinct conformations. Below a certain center-to-center spacing steric repulsion of the protein cores dominates.

ments that measure the volumetric flux of large-pore channels, as a function of pressure drop across the membrane[7], and uses models of volume change in vesicles to report on the aspects of the dose-response curve that depend on mechanical interactions between lipids and proteins. Many channels are clearly meant to pass electrical current in the form of ions, often in a highly selective manner, where the pore only admits ions of a certain kind. In many physiological settings, transmembrane potentials are the driving force that gate the channel, and when open, these same transmembrane potentials drive ions through the channel pore in an Ohmic fashion. Given this scenario, electrophysiology is a sensible tool for understanding the mechanism and function of voltage-gated channels. However, for channels whose physiological driving force is lateral tension, generated by pressure gradients across the membrane, it seems more sensible to query their flow properties, than their electrical properties. These channels likely span a wide range of volumetric conductances; for instance, aquaporins conduct water in single file, while aquaglyceroporins conduct larger uncharged solutes, and a channel like MscL has a relatively large pore area, able to accommodate ~ 40 water molecules in cross-section. For a pore size only an order of magnitude larger than the discrete water molecules passing through it, a central question is whether this behaves like a classic low Reynolds number fluid, a granular flow, or has new flow characteristics? Additionally, we will discuss how thermal fluctuations might play an important role in volumetric conductance.

We start the chapter by developing a physical model of osmotic shock that accounts for membrane permeation, bilayer elasticity, and utilizes different models of channel flow through a switchable channel. We make estimates of the flow through the MscL pore in the laminar flow and diffusive transport regimes, and discuss the relevance of granular flow at this scale. We discuss in detail the reconstitution of MscL into giant unilamellar vesicles as a vehicle for studying the ensemble flow characteristics of the channel, as well as lipid-dependent gating characteristics. The proposed set of experiments use micropipette aspiration and video microscopy to track volume changes of vesicles over time as a function of the pressure gradient, as shown in Fig. 5. We discuss a number of experimental challenges and their proposed solutions, including the use of gain-of-function MscL mutants to reduce the high tensions required to gate the channel, and an experimental calibration for channel density.

Chapter 4: Organization and Morphology of Lipid Domains

This chapter is a first attempt to acknowledge membrane heterogeneity by examining a two phase model membrane system, meant to mimic the formation of 'lipid rafts' in cellular membranes. This chapter is one of the longest in the thesis, and as such has been laid out in a pedagogical fashion, examining many aspects of the mechanical theory of domain morphology, experimental techniques, and data processing.

Once lipid domains have formed and grown to a certain size, it becomes reasonable to discuss the morphology and morphological transitions of these domains. We discuss how the competing forces

[7]This work began with a series of stimulating conversations with Evan Evans.

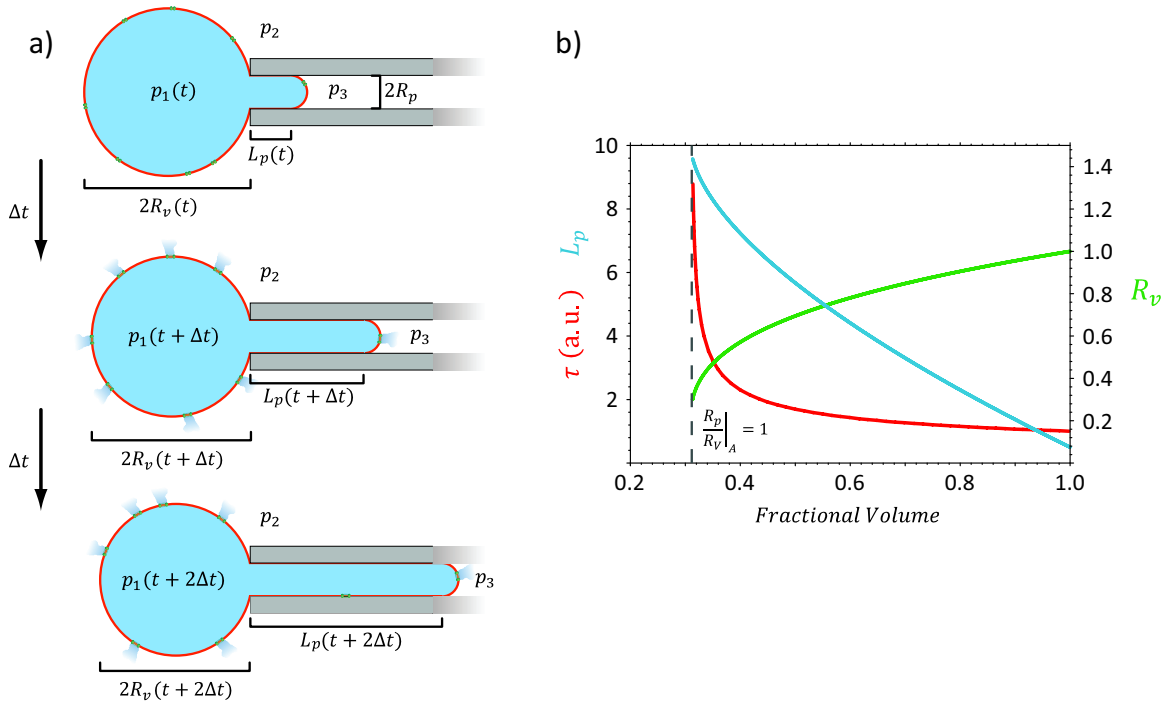

Figure 5: General experimental design for MscL volumetric flux experiments. a) A schematic showing how the aspirated shape of a large vesicle (orange), held by a pipette (gray), evolves over time as water is driven through the membrane-embedded efflux channels (green) by the pressure gradients $p_1 - p_3$ and $p_1 - p_2$. Over time the outer vesicle radius (R_v) shrinks, while the in-pipette length (L_p) geometrically amplifies the change in volume due to channel efflux. Shown here are the exact shapes for $\Delta V/\Delta t = -V_o/10$, where V_o is the vesicle volume in the first frame. b) In cases where the additional area from membrane stretch can be neglected, the outer vesicle radius and in-pipette length can be written as a function of the fractional volume; these plots show this in arbitrary units for the vesicle in (a).

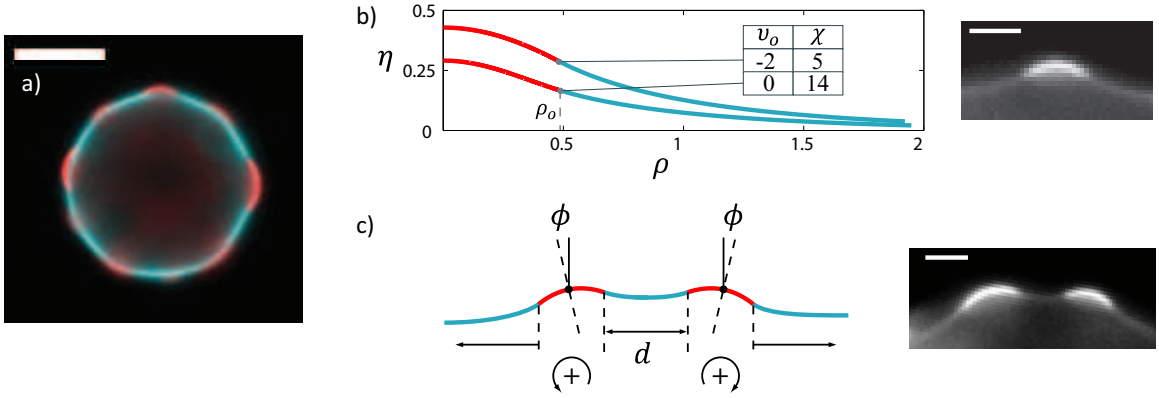

Figure 6: Morphologies and interaction of lipid domains. a) A two-color phase-separated vesicle with conserved surface area and volume shows spatially ordered, dimpled lipid domains on its surface. Scale bar 10 μm. b) Theoretical predictions for the shape of dimpled domains in dimensionless coordinates with line tension (χ) and spontaneous curvature (υ_o) as indicated, and corresponding epi-fluorescence view of a dimpled domain on the surface of a vesicle. c) Schematic of two domains interacting elastically, and the corresponding epi-fluorescence view of dimpled domains interacting on the surface of a vesicle. Scale bars in (b) and (c) are 3 μm.

of tension, line tension and bending stiffness yield dimpled and budded domains in an idealized flat surface metric. The tension ensemble used in this theoretical analysis is discussed in the context of our experimental system of conserved surface area and volume, giant unilamellar vesicles. The chapter then moves into a detailed discussion of the experimental, three component system used to visualize these domain morphologies. The mechanical buckling transition that yields dimpled domains results in elastically mediated interactions between the domains that tend to spatially organize them and significantly slow coalescence kinetics. We derive a 1D model, and discuss other's work on a 2D model, that describes pairwise interactions quantitatively, with representative data shown in the chapter. Beyond this dilute limit, the radial and angular distributions of domains that densely populate their parent vesicle exhibit properties that are a mix of the organizational principles of solid and liquid phases. In certain cases, the domains on these vesicles also undergo size-selective budding transitions, and we appeal to a simplified model of their morphology to understand this phenomena, as well as the transitions between dimpled and budded domains.

The chapter finishes with experimental work showing that interacting domains exist in real biological membranes under certain conditions. By inducing large scale membrane blebbing in RAW macrophages, we show that membranes with a multitude of lipid and protein species exhibit phase separation and domain organization akin to that observed in the model vesicle system.

Chapter 5: Membrane Adhesion by Homophilic Protein Binding

When trying to understand how cells stick together to form epithelia or connective nerve tissues,

certain proteins play a crucial role in mediating close-contact adhesion between cells. A common adhesion mechanism is to have a protein that is firmly rooted in the bilayer and simultaneously has an extra-cellular (often repeated) domain that engages in homophilic binding. The strength of this binding, its potential for cooperativity, and its relation to known disease phenotypes remains unclear. This chapter develops a dual-pronged theory and reports initial results on membrane adhesion, mediated by the membrane-anchored homophilic binding protein L1. The first theoretical model applies to a passive substrate adhesion assay; giant unilamellar vesicles are doped at a controlled level with special nickel-containing lipids onto which variants of L1 chelate. These vesicles containing L1 settle onto a glass substrate with a known density of L1 already adhered to the glass. With the vesicle volume and surface area constrained, and the membrane having a known bending modulus, adhesion of the vesicle to the surface yields a predictable deformation of the vesicle shape that, across many measurements, can be used as a reporter for both the adhesion strength and level of binding cooperativity, as shown in Fig. 7. In a similar assay, these same vesicles can additionally be doped with biotin-conjugated lipids. Beads coated with strepavidin will bind to the membrane, and a laser tweezer can be used to apply force to the beads to deform the adhered vesicle, with the force of deformation directly related to the easily measurable vesicle geometric properties and the adhesion strength. The limitations of these assays, imposed by optical resolution, force resolution, and material properties, are discussed.

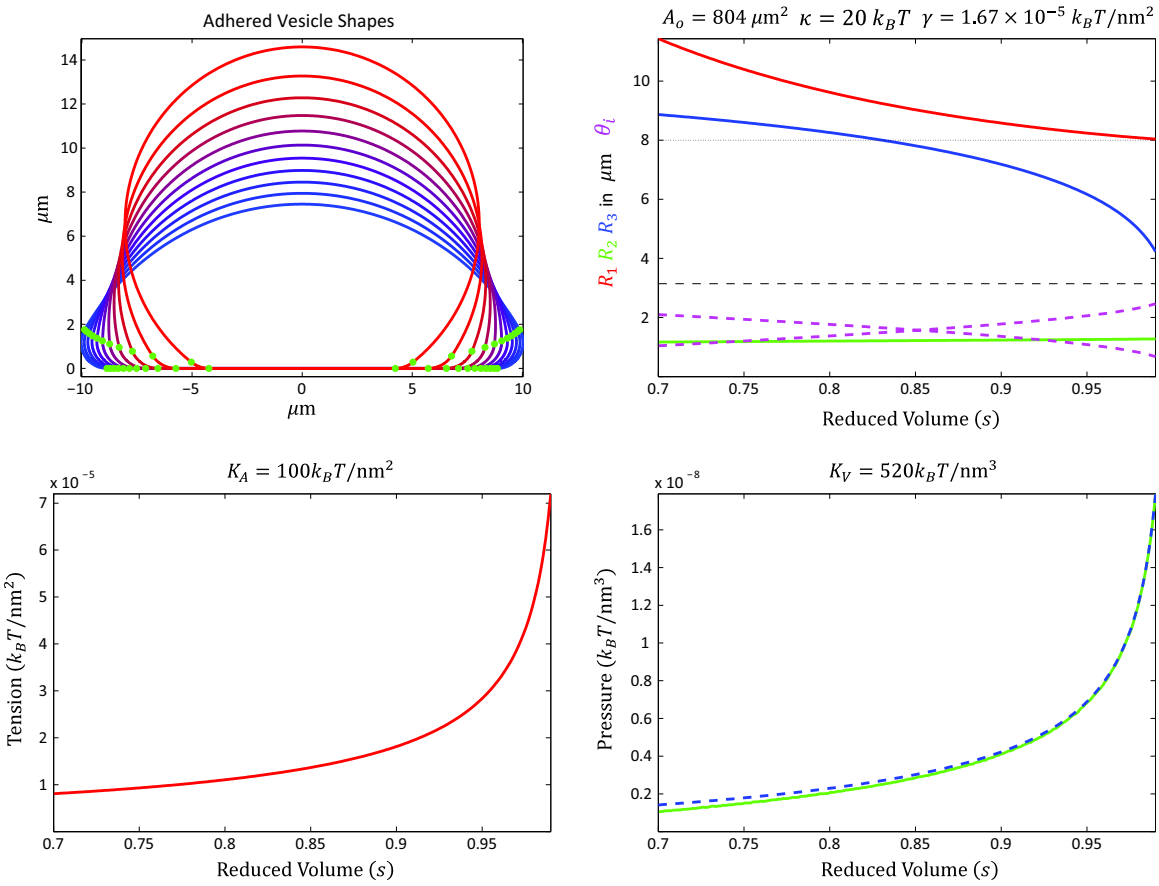

Figure 7: Shapes and intrinsic properties of substrate-adhered vesicles. a) Adhered vesicle shapes for different values of reduced volume from 0.7 to 0.99; the green dots indicate boundaries between the flat, toroidal, and spherical basis shapes in each deformed vesicle. The vesicle radius of curvature is R_1, the transition (toroidal) zone radius of curvature is R_2, and the adhesion zone radius is R_3. b) Radii of curvature and angles (as indicated by colors) characterizing the vesicle shape as a function of reduced volume, for the membrane parameters in the graph title. The upper dashed line defines the vesicle radius at a reduced volume of 1.0; the lower dashed line is the sum of the two angles, which always equals π. c) Membrane tension as a function of the reduced volume, with the indicated stretch modulus. d) Outward pressure gradient across the membrane as a function of reduced volume, using the bulk modulus for water. The dashed blue line is the approximation from the Laplace-Young relation $\Delta p = 2\tau/R_1$.

Chapter 1

Lipid Bilayer Mechanics and Mechanosensation

"All models are wrong, some are useful." – George Box

1.1 Introduction

Cells interact with each other and with their external environment. These interactions are enabled by transmembrane proteins — machines that have evolved to allow cells to detect and respond to changes in their environment. These proteins detect external cues, such as an increase in ligand concentration or the presence of forces or voltage, and transiently alter the permeability of the cell membrane allowing ions, water, or even larger molecules to cross, as well as triggering receptors for signaling [2, 3]. The passage of these ions (or molecules) and the triggering of receptors then leads to a series of downstream events within the cell, enabling a response to these environmental cues.

Mechanical forces and their corresponding deformations constitute one of the most important classes of external cues. Mechanosensation is a widespread phenomenon in a host of different single-celled and multicellular organisms [4, 5, 6, 7, 8, 9]. In bacteria, experimental evidence suggests that mechanosensation arises to detect and regulate the response to changes in the osmotic environment [10, 11, 12]. More generally, the issue of cell shape and its attendant deformation is important not only in the context of osmotic stress and the management of physical stresses to which membranes are subjected [13], but also arises in context of remodeling of the cell and organelle membranes during cell division [14, 15].

In multicellular organisms, mechanosensation is important in a variety of ways. One intriguing class of mechanosensors is linked to motility. For example, in nematodes like the much studied *C. elegans*, mechanosensation permits the worm to decide which way to move and may have a role in detecting body curvature, thus telling the worm when to change its wave-like shape [6]. Similarly, flies have hair bristles that respond to touch [16], while the mechanosensitive lateral-line organelles in zebrafish provide the means for detecting directional water movement in a way very similar to the workings of our inner ear [6]. In each of these cases, genetics has led to the identification of a variety of genes implicated in the ability of the organism to respond to some form of mechanical stimulus. Parallel insights have been obtained in plants (*Arabidopsis* in particular), with the identification of a collection of novel proteins that also appear to be mechanosensitive [17].

Mechanosensitive ion channels are a class of membrane proteins that have recently garnered

significant interest. Genetic, biochemical and structural studies all conspire to make this a particularly opportune time to demand a more quantitative picture of the function of these channels. In particular, there is a growing list of success stories in which the structures of channels associated with mechanosensation have been found in both closed and open states [11, 18, 19, 20]. In addition, functional studies that probe how gating depends upon membrane tension or external forces are beginning to make it possible to dissect the various contributions to the energetics of channel gating [21, 22, 23, 24].

As a result of these studies, a number of ideas have been proposed to explain the different ways in which external force can couple to membrane-protein conformation. Two modes of action that have been hypothesized for channels are: i) cases in which physical, polypeptide linkers pull on some part of the protein resulting in gating, ii) cases in which tension in the surrounding bilayer forces the channel to open. The aim of this chapter is to show how statistical mechanics and simple models of bilayer elasticity can be used to glean insights into this second class of mechanosensors, as well as play the role of a structural reporter.

The remainder of this chapter is built in four main sections. In the next section, we describe how statistical mechanics can be used to analyze the probability that a two-state mechanosensitive channel is open. This discussion will include an analysis of how the external load (*i.e.* the tension) can be included in the statistical mechanical treatment of these problems. The next section considers the elastic deformations imposed on a bilayer by the presence of a transmembrane protein, and shows how these deformations result in a mechanosensitive channel acting as a bistable switch (*i.e.* a protein with two stable conformations). In the subsequent section, we discuss experimental considerations that will help form a tighter connection between theory and experimental techniques, with specific reference to way in which bilayer mechanics might be used to better understand structural changes during channel gating. Finally, we examine the way multiple channels in a membrane might interact through the intervening lipid bilayer and how these interactions can alter the conformational statistics of individual channels.

1.2 Statistical Mechanics of Mechanosensitive Channels

To begin, we review the application of statistical mechanics to a simple two-state mechanosensitive channel. This analysis will serve as the starting point for our subsequent, more detailed analysis which explores how bilayer elasticity can contribute to the energetics of the closed and open states of a channel.

1.2.1 Lipid Bilayer vs. Protein Internal Degrees of Freedom

One convenient scheme for characterizing the state of ion channels is to invoke the state variable σ, which is defined by $\sigma = 0$ if the channel is closed and $\sigma = 1$ if the channel is open. Our aim is to compute the open probability p_{open} which, in terms of our state variable σ, can be

written as $\langle\sigma\rangle$, where $\langle\cdots\rangle$ denotes an average. When $\langle\sigma\rangle \approx 0$, this means that the probability of finding the channel open is low. Similarly, when $\langle\sigma\rangle \approx 1$, this means that it is almost certain that we will find the channel open. To evaluate these probabilities we need to invoke the Boltzmann distribution, which tells us that the probability of finding the system in a state with energy $E(\sigma)$ is $p(\sigma) = e^{-\beta E(\sigma)}/Z$, where Z is the partition function defined by $Z = \sum_\sigma e^{-\beta E(\sigma)}$, $\beta = 1/k_B T$, k_B is Boltzmann's constant, and $T \simeq 300K$.

On the level of a single channel, we introduce ϵ_{closed} and ϵ_{open} for the energies of the closed and open states, respectively. These energies contain contributions from deformations of the surrounding lipid bilayer as well as internal protein energetics; however, they do not contain the tension-dependent driving force which we will address separately. The state variables can be used to write the channel energy (in the absence of tension) as

$$E(\sigma) = (1-\sigma)\epsilon_{closed} + \sigma\epsilon_{open}. \tag{1.1}$$

With these energies in hand, we can assign weights to the different states, where the probability that the channel is open is given by $\langle\sigma\rangle$ and can be computed as $\langle\sigma\rangle = \sum_{\sigma=0}^{1} \sigma p(\sigma)$, where $p(\sigma)$ is the probability of finding the channel in state σ. To compute these probabilities, we invoke the Boltzmann distribution, and evaluate the partition function given by

$$Z = \sum_{\sigma=0}^{1} e^{-\beta E(\sigma)} = e^{-\beta\epsilon_{closed}} + e^{-\beta\epsilon_{open}}. \tag{1.2}$$

As a result, we see that the open probability can be written as

$$\langle\sigma\rangle = \frac{e^{-\beta\epsilon_{open}}}{e^{-\beta\epsilon_{closed}} + e^{-\beta\epsilon_{open}}} = \frac{1}{1 + e^{\beta(\epsilon_{open} - \epsilon_{closed})}}. \tag{1.3}$$

This expression is relatively sterile in the absence of some term that tunes the energies of the open and closed states to reflect the impact of external driving forces. In fact, one of the most remarkable features of ion channels is that the probability of being in different states can be tuned by external factors such as ligand concentration, the application of a voltage, or application of tension in the surrounding membrane. In general, this formalism can account for any of these driving forces, but we will restrict our attention to the important case of mechanosensitive channels, where the key driving forces are mechanical. In this case, gating occurs when the energy balance between the open and closed states is altered by membrane tension.

To give the origin of membrane tension a physical meaning, we introduce the notion of a "loading device," which we define as the external agent acting on a lipid bilayer to alter its tension. As depicted by hanging weights on the bilayer in Fig. 1.1, we can make a toy model of how changes in bilayer geometry are coupled to the energy of this loading device. The point of introducing this hypothetical situation is to enforce the idea that, in our statistical mechanical treatment of this problem, the loading device is an important part of the overall free energy budget of the system.

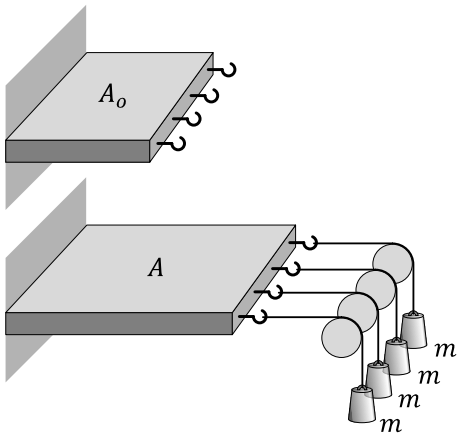

Figure 1.1: Energy of the loading device for membrane deformation. This figure compares the unloaded and loaded membrane and shows how membrane deformation results in a *lowering* of the potential energy of the loading device. In this hypothetical experiment, the tension (force per unit edge length) in the membrane is given by $\tau = mg/\Delta l$ where Δl is the distance between two consecutive hooks, and g is the acceleration due to gravity.

As a result, when we write down the partition function for a problem involving a channel and a deformable membrane, we have to account for the internal protein energetics, the deformation energy of the lipid bilayer, and the energy associated with the loading device itself. In particular, we note that an increase in the membrane area will lead to a lowering of the weights depicted in Fig. 1.1 and a corresponding decrease in the energy of the loading device. Of course, the application of tension in real membranes is not performed by hanging weights, but through techniques such as micropipette aspiration [25, 26]. Nevertheless, the concept of hanging weights brings the importance of the energy of the loading device into sharp focus.

For the case of tension-activated ion channels, the open probability, $\langle\sigma\rangle$, is dictated by a competition between the energetic advantage associated with reduction in the energy of the loading device and the energetic cost of the open state due to both the internal protein energetics and the energetics of membrane deformation. Following up on the idea of Fig. 1.1, but now with special reference to the case of a mechanosensitive ion channel, Fig. 1.2 shows how the opening of the channel results in a reduction of the energy of the loading device.

The total area of the bilayer is constant (to within a few percent), and as a result, when the channel opens and the radius gets larger the weights in our hypothetical loading device are lowered by some amount, which lowers the potential energy. The greater the weights, the larger the change in potential energy. The notion of weights is a simple representation of externally applied forces on the membrane. If we imagine a finite membrane with fixed area as shown in Fig. 1.2, when the channel opens, the outer radius will change as $\Delta R_{out} = (R/R_{out})\Delta R$, where R is the closed channel radius, ΔR is the change in channel radius upon opening, R_{out} is the outer radius of the membrane when the channel is closed, and ΔR_{out} is the increase in the outer radius of the membrane when

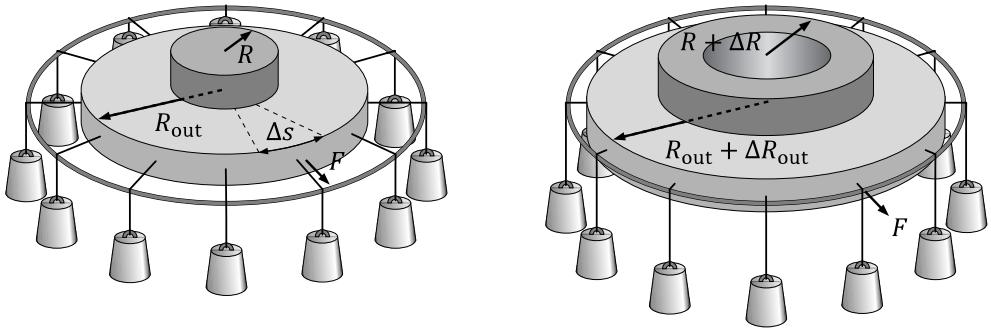

Figure 1.2: Schematic of how channel opening results in a relaxation in the loading device. For simplicity, we represent the loading device as a set of weights attached to the membrane far from the channel. When the channel opens, these weights are lowered, and the potential energy of the loading device is decreased.

the channel opens. We are interested in evaluating the change in potential energy of the loading device (*i.e.* the dropping of the weights) as a result of channel opening. To do so, we compute the work associated with the force F, which is most conveniently parameterized through a force per unit length (the tension, τ) acting through the distance ΔR_{out} as shown in Fig. 1.2. This results in

$$\Delta G_{\text{tens}} = \underbrace{\tau \Delta s}_{\text{force on arc}} \times \underbrace{\frac{R}{R_{out}} \Delta R}_{\text{displacement of arc}} \times \underbrace{\frac{2\pi R_{out}}{\Delta s}}_{\text{number of arcs}} . \tag{1.4}$$

where ΔG represents a change in free energy. We have introduced the variable Δs for the increment of arc length such that $\tau = F/\Delta s$. Given these definitions, we see that the change in the energy of the loading device is given by

$$\Delta G_{\text{tens}} = -\tau 2\pi R \Delta R. \tag{1.5}$$

In light of our insights into the energy of the loading device, we introduce the energy as a function of the applied tension τ, which is given by

$$E(\sigma, \tau) = (1 - \sigma)\epsilon_{closed} + \sigma \epsilon_{open} - \sigma \tau \Delta A. \tag{1.6}$$

The term $-\sigma\tau\Delta A$ favors the open state and reflects the fact that the energy of the loading device is lowered in the open state. In fact, this term reveals that any increase in protein area is energetically favored when membrane tension is present, which could imply hidden mechanosensitivity in other classes of ion channels and receptors — a subject we will discuss later in Section 1.5.

To compute the open probability of the channel in the presence of applied tension, we need to once again evaluate the partition function $Z = \sum_\sigma e^{-\beta E(\sigma)}$. Using the energy given in eqn. 1.6, we find

$$Z = e^{-\beta \epsilon_{closed}} + e^{-\beta(\epsilon_{open} - \tau \Delta A)}. \tag{1.7}$$

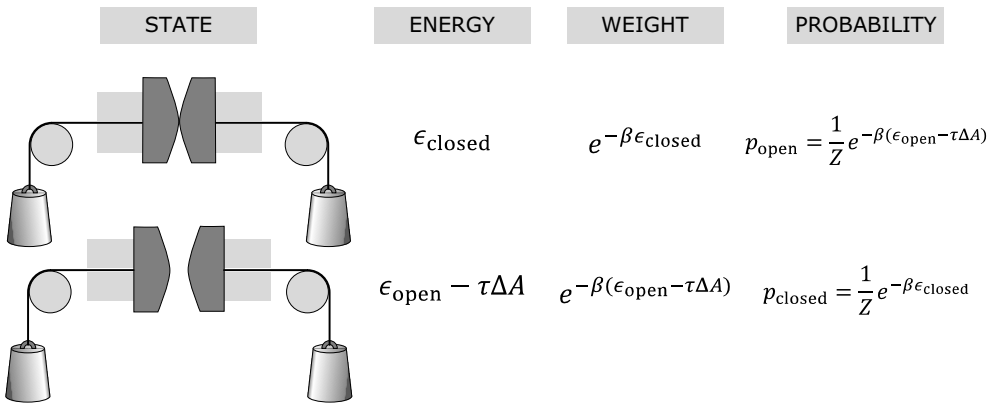

Figure 1.3: States, weights and corresponding probabilities for a two-state mechanosensitive channel under load.

This permits us to write down the open probability directly as

$$p_{open} = \frac{1}{1 + e^{\beta(\epsilon_{open} - \epsilon_{closed} - \tau\Delta A)}}. \tag{1.8}$$

The corresponding states, weights, and probabilities for a channel under applied tension are shown in Fig. 1.3. The open probability of a mechanosensitive channel is shown in Fig. 1.4 as an increasing function of the applied tension.

To understand how a particular channel is going to behave under a driving force, we need to know two things. First, we need to understand the channel's intrinsic preference for each of its two states, which is encoded by ϵ_{closed} and ϵ_{open}. Second, we need to understand how the external driving force alters the relative energies of these different states. With these two quantitative measurements in hand, statistical mechanics allows us to compute the behavior of the channel under a range of driving forces. To make further progress, we need to examine the microscopic origins of ϵ_{closed} and ϵ_{open}. Intriguing recent experiments suggest that these energies are driven in large measure by membrane deformations.

1.3 Bilayer Free Energy and Channel Gating

The abstract formalism of the previous section leaves us poised to examine mechanosensation to the extent that we can understand the physical origins of ϵ_{closed} and ϵ_{open}. The main idea is to show how simple models of the elastic properties of lipid bilayers can be used to determine the bilayer's contribution to ϵ_{closed} and ϵ_{open}. One of the key clues that hints at the importance of membrane deformation in dictating channel gating is the data shown in Fig. 1.5a. In particular, this plot shows how the open probability depends upon the lipid carbon tail length. This data strongly

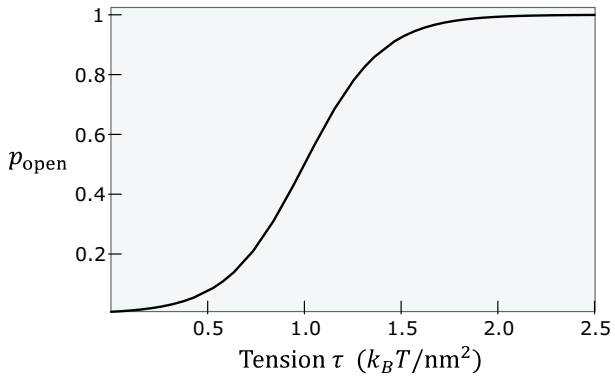

Figure 1.4: Ion channel open probability as a function of applied tension. The plot shows $p_{open} = \langle\sigma\rangle$ as a function of the applied tension τ. The parameters used in the plot for a model mechanosensitive channel are $\epsilon_{open} - \epsilon_{closed} = 10\,k_BT$ and $\Delta A = 10\,\text{nm}^2$. The critical tension is $1.0\,k_BT/\text{nm}^2$, corresponding to $p_{open} = 1/2$. For reference, the tension can be rewritten as $1\ \text{pN/nm} \simeq 0.25\,k_BT/\text{nm}^2$.

suggests that the energetics of the surrounding membrane is an important part of the overall free energy budget of channel gating (also see [27] and the informative review [28]).

The parameters ϵ_{closed} and ϵ_{open} can each depend on some combination of the energetics of protein conformation, membrane deformation, and hydration energy. Our strategy is to use the tools of continuum mechanics to calculate how the deformation of lipids surrounding a protein and the applied tension work in concert to affect the channel's preference for a particular state [29, 30, 31, 32]. Unfortunately, relatively little is known about how the internal rearrangements of the protein and the hydration energy of the channel pore contribute to the overall free energy balance [33, 34]. This ignorance is in part due to a lack of general rules that tell us how internal rearrangements translate into changes in protein energy. Further, the lack of crystal structures in the open and closed states of many channel proteins means we cannot be sure where each residue moves, which are exposed to the surrounding lipids and which are facing the hydrated internal pore. It is also difficult for molecular dynamics to comment on the energies associated with the internal movements of the protein [35, 36, 37, 38] because the all-atom energies of these simulations are very large in comparison to the changes in free energy, and hence it is difficult to distill relatively small free energy changes in the background of large energy fluctuations. To complicate the issue further, it is also possible that the internal movements of the protein yield relatively small free energy changes between the two states, but may provide various kinetic hurdles in the form of energy barriers, which affect the transition *rate* from one state to another.

It is reasonable on the scale of a single membrane protein to ask whether a bilayer composed of discrete lipid molecules can be approximated as a continuum material. We argue heuristically that, given the relative diffusion coefficients of membrane proteins ($D \sim 0.1 - 1\mu\text{m}^2/s$) [39, 40, 41] and lipids ($D \sim 10\mu\text{m}^2/s$) [42], in the time it takes a transmembrane protein to diffuse one lipid diameter, many lipids will have exchanged places near the protein, in a sense averaging out the

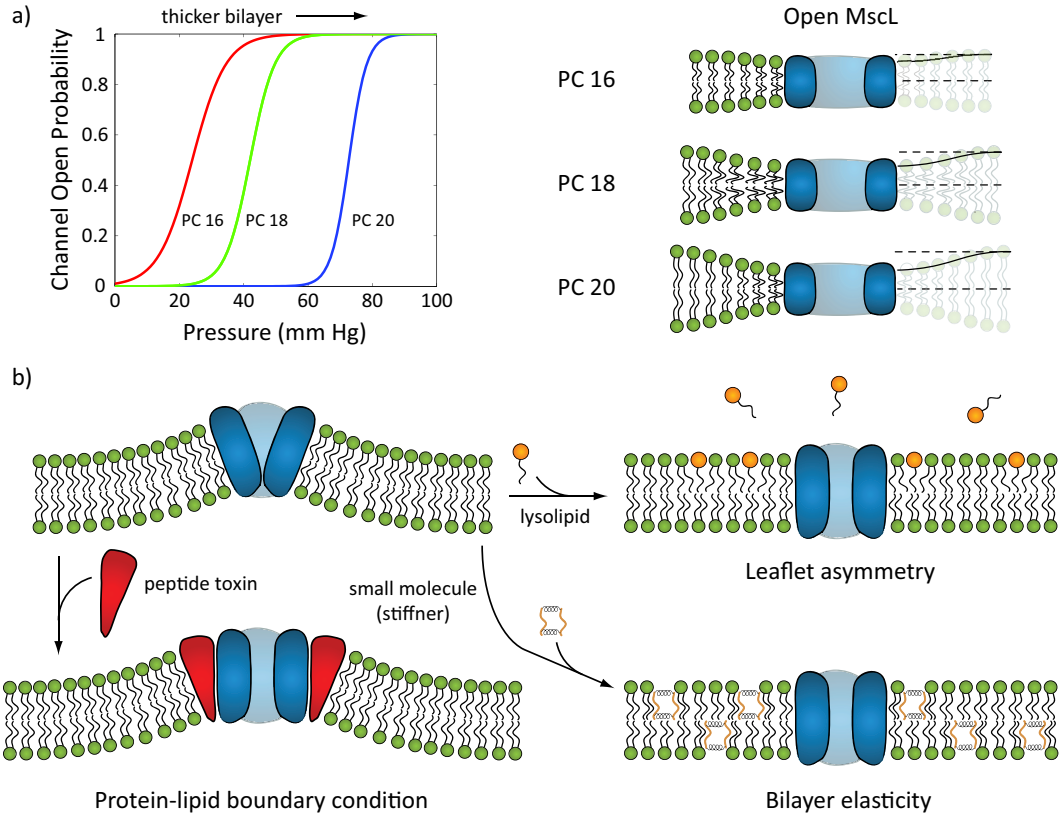

Figure 1.5: Effects of bilayer thickness and small molecules on open channel probability. a) MscL open probability as a function of pipette pressure in lipids with different tail lengths. The curves are an empirical fit to patch-clamp data from [22]. The diagrams on the right show how different tail lengths imply a different hydrophobic mismatch as a result of the boundary conditions at the proteinlipid interface. PC16, PC18 and PC20 are phospholipid bilayers with acyl chain lengths of 16, 18 and 20 carbons, respectively. b) Membrane doping and membrane protein function. The diagrams show hypothetical mechanisms whereby the insertion of amphiphilic molecules can alter the membrane–protein interaction. For example, the asymmetrical insertion of lysolipids in the membrane produces a torque on the protein. The introduction of toxins can alter the boundary conditions between the protein and the surrounding lipids. Finally, small molecules can stiffen the membrane. In principle, all these effects could alter the bilayer's contribution to channel gating.

discreteness of the lipid molecules. Additionally, the transition time for protein conformational change ($\sim 5\,\mu s$) [43] is slow compared to lipid diffusion. Hence, we argue the bilayer can be approximated as a continuous material in equilibrium with well-defined elastic properties [44]. Further, we choose to formulate our analysis in the language of continuum mechanics, rather than lateral pressure profiles [45].

Approximating the membrane as a continuum material [46, 29, 30, 31, 44, 47, 32], we will concentrate our analysis on how the mechanical properties and deformations of lipids affect the energy balance of the protein, and how tension can play the role of a driving force for gating the channel. In particular, the mechanosensitive channel of large conductance (MscL) is one of the best characterized mechanosensitive channels. Additionally, a combination of X-ray crystallography and electron paramagnetic resonance studies have yielded insights into the structures of both the closed and open states of MscL [11, 48, 19]. One of the outcomes of this structural analysis is the idea that the structure can be roughly approximated as a cylinder, making it amenable to mechanical modeling. MscL exemplifies many of the characteristics one might call "design principles" for a mechanosensitive channel [47, 32], such as change in hydrophobic thickness, a change in radius, and sensitivity to membrane curvature. In the next few sections, we will lay the foundation for a continuum mechanical understanding of how lipid deformations and tension work together to give a switchable channel.

1.3.1 The Case Study of MscL

In the prokaryotic setting, the physiological purpose of MscL is thought to be an emergency relief valve under conditions of hypoosmotic shock [10, 11, 12], where the osmotic pressure difference between the inside of a cell and the environment translates into increased membrane tension. The channel responds by gating and non-selectively releasing osmolytes to the environment until the internal and external pressures are equilibrated [21, 49]. This presents us with (at least) two key questions. First, what gives MscL its ability to "sense" tension in the membrane? Second, what role is the lipid bilayer playing in the gating transition?

We argue that the answers to these questions are found in the properties of a lipid bilayer and the geometrical features of the channel as revealed in Table 1.1. In particular, the bilayer has four key elastic properties that give it the ability to transduce tension and resist deformation by a transmembrane protein. The most striking elastic feature is the in-plane fluidity of the bilayer, which, in the absence of cytoskeletal interactions, results in equalization of tension throughout the membrane. This means that any in-plane stress (*i.e.* tension) on the membrane is felt everywhere equally. Hence, in the case of MscL, an increase in tension is applied uniformly to the outer edge of the protein, essentially trying to "pull" the channel open. We argue it is this "pulling" which constitutes the driving force for channel gating. However, this driving force is competing with the energetic cost to gate the channel due to internal conformational changes within the protein and deformations of the surrounding lipid.

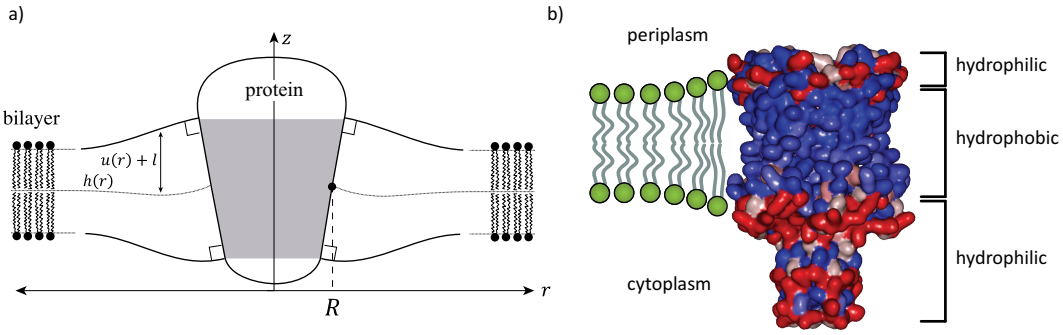

Figure 1.6: Continuum view of bilayer deformation and hydrophobic mismatch. a) A schematic representation of how a conical protein with a hydrophobic region, shown in gray, can both locally alter membrane thickness, characterized by the function $u(r)$, and induce bilayer midplane curvature, characterized by the function $h(r)$. b) Space filled view of the closed-state structure of the mechanosensitive channel of large conductance (MscL). Hydrophobic residues have been colored blue and hydrophilic resides red, clearly showing the region of the protein that aligns itself with the bilayer's hydrophobic core. On the left, lipids are schematically shown extending their length to match the hydrophobic thickness of the protein.

Three other properties give the membrane the ability to store energy elastically upon deformation. First, each leaflet of the membrane resists changes in the angle between adjacent lipid molecules, leading to bending stiffness of the membrane [46, 29, 30, 31, 44, 32]. Second, the membrane has a preferred spacing of the lipid molecules in-plane and will resist any changes in this spacing due to external tension [30, 26]. Third, the membrane has a well-defined equilibrium hydrophobic thickness, which, when given an embedded protein of a different hydrophobic thickness, leads to energetically costly 'hydrophobic mismatch' [30, 31, 44, 47, 32]. These concepts are demonstrated schematically for a protein that alters bilayer thickness and induces midplane curvature, and more specifically the bilayer thickness deformations induced by the closed MscL channel, in Fig. 1.6.

The competition between the driving force and the energetic cost to gate the channel hints at a set of design principles that dictate how the channel behaves as a bistable switch. If we neglect the molecular details of MscL, its conformational change can be characterized by a set of simple changes in geometrical parameters. In particular, in our coarse-grained description we will think of the gating transition as being accompanied by changes in height, radius and protein angle, all of which couple to various modes of membrane deformation as shown in Fig. 1.7. The central question becomes, is deformation of the lipids surrounding the protein a major player in gating energetics? Indeed, experiments have already suggested that the gating characteristics are intimately linked to the hydrophobic mismatch between the protein and bilayer as was shown in Fig. 1.5 [22, 27, 28]. It is the goal of the following sections to build up a theoretical framework for understanding the various kinds of bilayer deformation around a transmembrane protein and to describe how these

Parameter:	Value:	Source:
Closed height	~ 3.8 nm	[11]
Closed radius	~ 2.5 nm	[11]
Open height	~ 2.5 nm	[19]
Open radius	~ 3.5 nm	[19]
Measured ΔA^*	$\sim 7 - 20\,\mathrm{nm}^2$	[50, 21, 23]
Measured ΔG^*	$\sim 20 - 50\,k_BT$	[50, 21, 23]
Calculated ΔG^* (at critical tension)	$\sim 55\,k_BT$	this work
Critical Tension*	$\sim 2.5\,k_BT/\mathrm{nm}^2$	[23]
Lytic Tension*	$\sim 3.5\,k_BT/\mathrm{nm}^2$	[26]
Bending Modulus (κ_b)	$\sim 20\,k_BT$	[51, 26]
Area Stretch Modulus (K_A)	$\sim 60\,k_BT/\mathrm{nm}^2$	[26]
Leaflet Thickness (l)	~ 1.75 nm	[26]

Table 1.1: MscL geometrical and bilayer elastic parameters. $^{(*)}$ These parameters depend on the elastic properties of the bilayer, in particular the bilayer bending modulus (κ_b), the bilayer area stretch modulus (K_A), and the leaflet hydrophobic thickness (l).

deformations contribute to the overall free energy budget associated with the gating of MscL (and probably other channels as well).

1.4 Bilayer Deformation, Free Energy and the Role of Tension

To investigate the contribution of membrane deformation to channel gating in mechanosensitive channels, we put our ignorance of the internal protein energetics aside and focus on the response of the membrane. The point of this analysis is to see how large the membrane contributions are to the free energy of channel gating, and to examine how they compare to the measured values. A mechanosensitive channel must resist the driving force due to tension to exhibit the properties of a bistable switch. As we will demonstrate in this section, deformation of the surrounding lipids can provide this resistance, and almost certainly does in the case of MscL, given our knowledge of the open and closed structures and the body of experimental data describing the interactions between lipids and MscL [21, 22, 52].

The deformations that a transmembrane protein induces can be most broadly split into two main classes: those that deform the midplane of the bilayer, and those that deform the bilayer leaflet thickness. If the deformation is not too severe, these two types of deformation are independent of one another [32]. Figure 1.7 shows these two classes of deformation and the simple model idealizations implied by elastic descriptions. The basic structure of the models we consider are those in which the contributions of deformation to the overall free energy are obtained by computing local bending

and thickness deformation, and then summing over the contributions from all the area elements making up the bilayer.

1.4.1 Midplane Deformation

Deformation of the midplane of the bilayer involves a cost to bend the midplane from its flat, equilibrium position [46, 44, 32]. We use the function $h(\mathbf{r})$ to denote this change in height of the bilayer midplane as a function of the position $\mathbf{r}$ as shown in Fig. 1.7. The energy cost associated with bending the membrane away from its flat configuration can be written as

$$G_{\text{bend}}^{(\text{mid})} = \frac{\kappa_b}{2} \int \left(\nabla^2 h(\mathbf{r}) - c_o^b \right)^2 \mathrm{d}^2\mathbf{r}, \tag{1.9}$$

where the bilayer bending modulus $\kappa_b \simeq 20\, k_B T$ [51, 26] and c_o^b is the bilayer spontaneous curvature. Throughout this chapter the gradient operator is defined by $\nabla = (\partial/\partial x, \partial/\partial y)$, and the Laplacian operator by $\nabla^2 = \partial^2/\partial x^2 + \partial^2/\partial y^2$, in Cartesian coordinates. In general, bilayers with symmetric leaflet compositions have zero midplane spontaneous curvature, although we will discuss the origins of spontaneous curvature and quote the relevant energetic contribution later in this chapter. Tension also plays a role in the energetics of midplane deformation because any bend in the midplane results in a reduction in the projected area of the membrane, which couples directly to an increase in the energy of the loading device, resulting in a contribution to the free energy of the form

$$G_{\text{ten}}^{(\text{mid})} = \frac{\tau}{2} \int (\nabla h(\mathbf{r}))^2 \mathrm{d}^2\mathbf{r}, \tag{1.10}$$

where the tension, τ, ranges from zero up to the nominal membrane lytic tension of $\sim 3.5\, k_B T/\text{nm}^2$ [26][1]. In general, the elastic parameters we use are representative of a typical phosphatidylcholine (PC) lipid. Thus the total energy expended to deform the midplane over an area A is

$$G^{(\text{mid})} = \int_A \left(\frac{\tau}{2} (\nabla h(\mathbf{r}))^2 + \frac{\kappa_b}{2} (\nabla^2 h(\mathbf{r}))^2 \right) \mathrm{d}^2\mathbf{r}. \tag{1.11}$$

The logic behind this kind of analysis is to find the free energy minimizing function $h(\mathbf{r})$. One way to carry out this minimization is by solving a partial differential equation that is generated by formally minimizing the free energy, the details of which are discussed in the second half of chap. 4. An alternative (and approximate) scheme to be explored later in this section is to make a guess for the functional form of $h(\mathbf{r})$ and to minimize with respect to some small set of parameters. This approach is called a variational method and can be quite useful for developing intuition.

In the midplane-deforming model, the protein can dictate the slope of the membrane at the protein-lipid interface which, in addition to the protein radius, will determine the deformation energy. The length scale over which the membrane returns to its unperturbed state is given by

[1] The lytic tension of a bilayer is technically a stochastic quantity [53], however, we quote the lytic tension as the tension at which bilayer lysis is a rapid, spontaneous process.

$\lambda_\tau = \sqrt{\kappa_b/\tau}$ and the energy for this type of deformation is

$$G^{(\text{mid})}(R,\tau) = \pi\kappa_b\theta^2\frac{R}{\lambda_\tau}\cdot\frac{K_0(R/\lambda_\tau)}{K_1(R/\lambda_\tau)}, \tag{1.12}$$

where R is the radius of the protein, θ is the slope of the membrane at the protein-lipid interface as shown in Fig. 1.7, and K_i are modified Bessel functions of the second kind of order i [54, 32]. Given a protein with a particular radius and fixed boundary slope, an increase in tension will make any deformation *more* costly. Hence, for midplane deformation, increased tension prefers a flatter membrane and/or smaller protein radius. To get a feel for the energy scale of this deformation several examples for different parameter values are summarized in Table 1.2.

With the contribution to the free energy difference arising from midplane deformation in hand, we can now explore the competition between applied tension and the energetics of membrane deformation in dictating channel gating. The key to understanding the interplay between tension and deformation energetics lies in the scaling of these two effects with protein radius. The midplane deformation energy scales roughly linearly with the radius of the protein and is unfavorable. On the other hand, the term proportional to the applied tension scales as the square of the protein radius and favors the open state. If we fix the membrane slope, then the energy of a midplane deforming protein as a function of protein radius and tension is

$$G(R,\tau) \simeq G^{(\text{mid})}(R,\tau) - \tau\pi R^2. \tag{1.13}$$

As tension increases, the potential energy of the loading device eventually overcomes the deformation energy and a larger protein radius and/or more cylindrical protein shape is the preferred state. Indeed, midplane deformations have been hypothesized to be an important functional mechanism of MscL [54]. One of the uncertainties that accompanies a model of this type is the fact that there is some function that connects the slope of the membrane at the protein-lipid interface (θ) with the current radius of the channel, that is, there is some unknown function $\theta(R)$ [55]. Future experiments will be necessary to further clarify this point. If we make the simplest approximation that $\theta(R) =$ constant and look at two reasonable values of $\theta = 0.6$ and $\theta = 0.8$ [54], using eqn. 1.13 and the parameters in Table 1.1, we find the rather small critical tensions $\sim 0.004\,k_BT/\text{nm}^2$ and $\sim 0.06\,k_BT/\text{nm}^2$, respectively, compared to the known critical tension of MscL at $\sim 2.5\,k_BT/\text{nm}^2$ [23, 34]. Though we have shown that midplane deformations are capable of endowing a channel protein with bistability, the scale of the critical tension and the free energy difference between conformations indicates that, at least for MscL, an additional kind of deformation might be important as well.

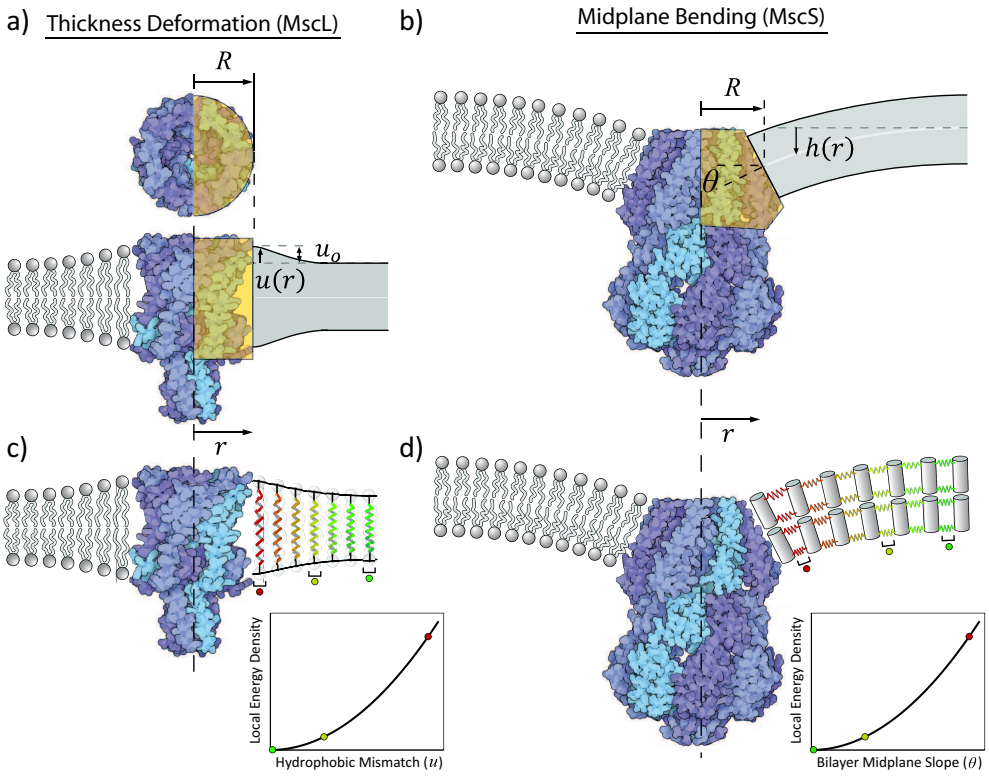

Figure 1.7: Elastic idealizations of deformations and protein-lipid boundary conditions. a) Atomic-level structure [11] and an elastic idealization of the mechanosensitive channel of large conductance (MscL) as a rigid cylinder of radius R with hydrophobic mismatch at the proteinlipid interface, u_o, and the bilayer thickness deformation described by the function $u(r)$. For $r \gg \lambda_k$ the membrane thickness is at its equilibrium value. b) Atomic-level structure [18] and an elastic idealization of the mechanosensitive channel of small conductance (MscS) as a protein that deforms the membrane midplane by an angle θ at the protein lipid interface, causing a midplane height deformation described by the function $h(r)$. For $r \gg \lambda_\tau$ the bilayer midplane is flat. c) Membrane distortion and corresponding free energy of deformation per unit area of membrane surrounding MscL. d) Membrane distortion and corresponding free energy of deformation per unit area of membrane surrounding MscS. In (c) and (d) the elastic response of the lipids is captured with springs, and the color coding indicates the local strain energy density at different distances from the proteins.

Fixed Parameters:	Dynamic Parameter:	Free Energy Difference:
$R = 3$ nm, $\theta = 0.5$	$\tau = 0 \rightarrow 2\,k_BT/\text{nm}^2$	$10\,k_BT$
$R = 3$ nm, $\tau = 2\,k_BT/\text{nm}^2$	$\theta = 0 \rightarrow 0.5$	$10\,k_BT$
$R = 3$ nm, $\tau = 2\,k_BT/\text{nm}^2$	$\theta = 0 \rightarrow 0.8$	$26\,k_BT$
$\theta = 0.5$, $\tau = 2\,k_BT/\text{nm}^2$	$R = 3 \rightarrow 6$ nm	$14\,k_BT$
$\theta = 0.8$, $\tau = 2.5\,k_BT/\text{nm}^2$	$R = 2.5 \rightarrow 3.5$ nm	$13\,k_BT$

Table 1.2: Typical free energies for midplane deformation. The first row indicates how tension leads to an increase in deformation energy. The second and third rows show the sensitivity to the boundary slope. The fourth row indicates how protein radius changes deformation energy. The last row is a comparison with the known radius change and critical tension of MscL.

1.4.2 Thickness Deformations

We have examined how protein conformation can alter midplane bending of the surrounding lipid bilayer and how this deformation energy penalizes the open state by virtue of its larger radius. A second major class of deformations are those that bend and compress a single leaflet of the membrane [29, 56, 31, 32] and can be thought of as imposing a local thickness on the lipid bilayer that is different from its equilibrium value, as illustrated in Fig. 1.7. This kind of deformation relies on the fact that most proteins are rigid in comparison to the flexibility of a lipid molecule. Hence, when trying to match the hydrophobic region of the protein to the hydrophobic core of the bilayer, it is the lipid that will undergo the vast majority of the deformation. For the calculations considered here, we assume that leaflet deformations are symmetric: whatever happens to the top leaflet is mirrored in the bottom leaflet. The deformation is measured as the deviation of the equilibrium position of the lipid head-groups by the function $u(\mathbf{r})$ at each position $\mathbf{r}$ on the membrane as was introduced schematically in Fig. 1.7. The bending energy takes the form

$$G_{\text{bend}}^{(\text{leaf})} = \frac{\kappa_b}{4}\int(\nabla^2 u(\mathbf{r}) - c_o^l)^2 \text{d}^2\mathbf{r}, \tag{1.14}$$

where $\kappa_b \simeq 20\,k_BT$ is the bending modulus of a bilayer [51, 26], equal to approximately twice the bending modulus of a leaflet, and the spontaneous curvature of the leaflet, c_o^l, characterizes the leaflet's natural tendency for a curved state at a hydrophobic-hydrophilic interface [30]. For many bilayer forming lipids, such as phosphatidylcholines, the spontaneous curvature is small [57], however, for many other lipids this is not the case, and it behooves us to briefly digress to discuss the origin of monolayer spontaneous curvature.

Monolayer spontaneous curvature can be an important contribution to the free energy budget of thickness deformations, explored in some detail in Section 2.6.3. The origin of monolayer spontaneous curvature is asymmetry in the rotationally averaged shape of individual lipid molecules [57]. The volume explored by individual lipids can be thought of as a truncated cone, as shown in Fig. 1.8. If this truncated cone uses more area in the head group region than in the tail region,

monolayers of that lipid tend to curve towards the tail group. If the truncated cone uses more area in the tail region, than in the head group region, the monolayer tends to curve towards the head group. The desire of the monolayer to adopt these curved states has been explored through the use of so-called hexagonal phases of lipid monolayers, a topic elegantly reviewed in [58]. Using these ideas, we can construct a simple parameter that characterizes a lipid's tendency to form monolayers of a particular spontaneous curvature. Given the lipid length l and effective volume v, along with the previously mentioned head group and acyl chain effective areas, a_{top} and a_{bott}, respectively, we define the shape parameter

$$S = \frac{v}{a_{\text{top}} l}, \tag{1.15}$$

where values greater than one generally correspond to lipids with negative monolayer spontaneous curvature, and values less than one generally correspond to lipids with positive monolayer spontaneous curvature, as shown schematically in Fig. 1.8. Additionally, one can estimate the spontaneous curvature itself from the shape factor by straightforward geometric analysis to find

$$c_o^l = \frac{2}{l}(1 - S). \tag{1.16}$$

Some lipids, notably lyso-PC lipids, have such a high degree of spontaneous curvature that they cannot form bilayers, and in fact tend to break up bilayers if introduced at a level above a certain critical concentration. Having built intuition for the origins of monolayer spontaneous curvature, let us return to calculating the thickness deformation energy.

In addition to bending, matching the hydrophobic regions of the protein and bilayer necessarily means the bilayer will change in thickness, giving rise to a bilayer energy penalty of the form

$$G_{\text{comp}}^{(\text{leaf})} = \frac{K_A}{2} \int \left(\frac{u(\mathbf{r})}{l} \right)^2 \mathrm{d}^2\mathbf{r}, \tag{1.17}$$

where $l \simeq 1.75\,\text{nm}$ is the leaflet hydrophobic thickness, and due to membrane volume conservation, the bilayer area stretch modulus, $K_A \simeq 60\,k_BT/\text{nm}^2$, is associated with this deformation [26]. Yet another contribution to the free energy of deformation in those cases where the membrane thickness is perturbed is a local change in the area per lipid as the bilayer thickness varies around the protein. Membrane volume conservation arises because the membrane is roughly forty times more resistant to volume change than area change [60, 61][2]. As a result, if a transmembrane protein locally thins the bilayer, lipid area locally increases in a way that conserves volume. Similarly, if the protein locally thickens the bilayer, the area per lipid will locally decrease. This implies that the area change near the protein is proportional to the compression $u(\mathbf{r})$, and the work done on the bilayer is the integrated area change multiplied by tension

$$G_{\text{ten}}^{(\text{leaf})} = \tau \int \frac{u(\mathbf{r})}{l} \mathrm{d}^2\mathbf{r}, \tag{1.18}$$

[2]This topic is discussed in detail in Section 2.6.4.

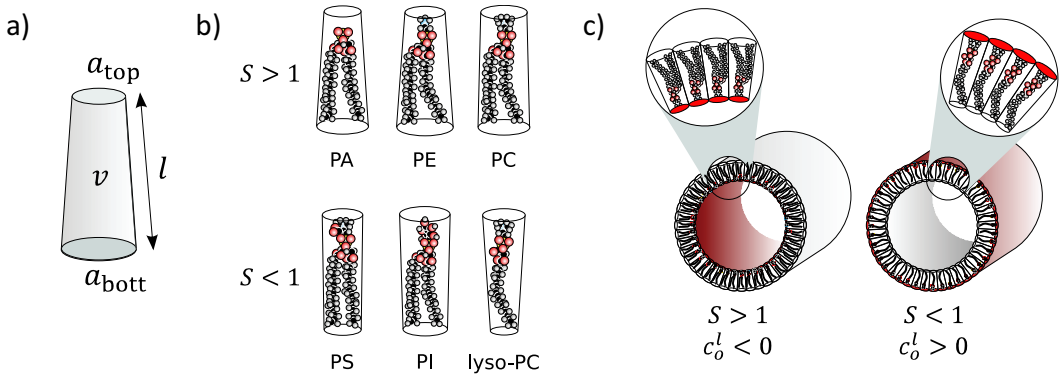

Figure 1.8: Lipid shape as a determinant of monolayer spontaneous curvature. a) Lipid shape can be approximated as a truncated cylinder with a certain length, upper and lower area, and effective volume. These features can be used to estimate the shape factor of the lipid, which is related to the monolayer spontaneous curvature. b) Approximate shapes and shape factors for some common lipid types: PA is phosphatidic acid, PE is phosphatidylethanolamine, PC is phosphatidylcholine, PS is phosphatidylserine, PI is phosphatidylinositol, and lyso-PC is a single chain phosphatidylcholine. c) Diagram showing how lipids with shape factors greater than one and less than one, organize into the hexagonal phase. Measurements of the lattice constant in the hexagonal phase have been used to measure the spontaneous curvature of monolayers. Parts of this figure adapted from [59].

where τ is the externally applied bilayer tension. Hence, u less than zero corresponds to a reduction in the energy of the loading device. All of these contributions can be added up to yield the free energy cost associated with thickness variations of the two leaflets that can be written as

$$G^{(\text{leaf})} = \int_A \left(\frac{K_A}{2} \left(\frac{u}{l} \right)^2 + \frac{\tau u}{l} + \frac{\kappa_b}{2} \left(\nabla^2 u \right)^2 \right) \mathrm{d}^2\mathbf{r}. \tag{1.19}$$

In elastic models of this type, the protein dictates the degree of hydrophobic height mismatch, $u(R) = u_o$, and the angle at which the leaflet contacts the protein at the interface between the protein and the surrounding lipids, as shown schematically in Fig. 1.6. Far from the protein, we expect the bilayer to be flat and slightly thinner in accordance with the applied tension, *i.e.* $|\nabla u(\infty)| = 0$ and $u(\infty) = -\tau l / K_A$, respectively. In the case of a cylindrical protein we make the further simplifying assumption that the angle is zero (*i.e.* $|\nabla u(R)| = 0$) [29], however non-zero values are of interest as they allow monolayer spontaneous curvature and monolayer Gaussian curvature to influence energetics, a topic discussed further in section 2.6.3. The hydrophobic mismatch itself depends on membrane properties; changes in membrane thickness are linearly related to the hydrophobic mismatch by $u_o = d/2 - l$, where d is the hydrophobic thickness of the protein. Unlike midplane deformation, the length scale at which the leaflet returns to its

unperturbed state, λ_k, depends only on fixed elastic parameters of the membrane given by

$$\lambda_k = \left(\frac{l^2\kappa_b}{K_A}\right)^{\frac{1}{4}} \simeq 1\,\text{nm}. \tag{1.20}$$

The deformation energy due to thickness variation in the surrounding lipids induced by the protein can be written in a simple form when the radius of the protein is larger than λ_k (which is the case for MscL) as

$$G^{(\text{leaf})}(R,\tau) = \pi\kappa_b\left(\frac{u_o}{\lambda_k} + \frac{\tau}{K_A}\frac{l}{\lambda_k}\right)^2\left(1+\sqrt{2}\frac{R}{\lambda_k}\right). \tag{1.21}$$

The deformation energy scales linearly with protein radius and depends quadratically on the hydrophobic mismatch, u_o [32], making the overall deformation energy particularly sensitive to the hydrophobic mismatch, and hence leaflet thickness l[3]. The deformation energy is fairly insensitive to changes in stretch stiffness, K_A (*i.e.* most terms in the energy are sublinear), and generally insensitive to changes in the bending modulus since $G \propto \kappa_b^{1/4}$. Additionally, given the actual values of the elastic parameters, one finds that the leaflet free energy scales roughly *linearly* with tension, due to the very small value of τ/K_A. Like midplane deformation, we see that thickness deformation prefers a smaller protein radius. On the other hand, in the midplane case, tension always increases the deformation energy around a channel while in the case of lipid bilayer thickness variations, the tension can either increase or decrease the deformation energy depending on the sign of the hydrophobic mismatch. In fact, since the hydrophobic mismatch can be either positive or negative (*i.e.* the protein can be thicker or thinner than the bilayer), tension will increase the deformation energy around a protein that is thicker than the membrane (*e.g.* the closed state of MscL) and decrease the deformation energy around a protein that is thinner than the membrane (*e.g.* the open state).

One of the nice outcomes of this simple thickness variation elastic theory is that the total free energy as a function of protein radius can be written in the simple form

$$G(R,\tau) = G^{(\text{leaf})}(R,\tau) - \tau\pi R^2, \tag{1.22}$$

which is reminiscent of classical nucleation theory and results in free energy profiles as shown in Fig. 1.9. At zero tension, the deformation clearly prefers a smaller protein radius, limited only by the steric constraints of the protein structure, which means that there is a certain minimum radius that the protein can adopt. As the tension increases, the quadratic dependence of the driving force on radius will eventually overcome the linear dependence of the deformation energy, leading to a preference for the open state (corresponding to larger R). We introduce a "hard wall" potential at the open radius which provides a severe energy penalty for radii larger than the open state radius

[3]The concept of hydrophobic mismatch is valid when the hydrophobic regions of the protein and the bilayer strongly interact, however, this concept has its limits based on the chemistry between the lipids and the transmembrane region of the protein [62, 63, 64], and eventually this condition will be broken if the mismatch is too large [32].

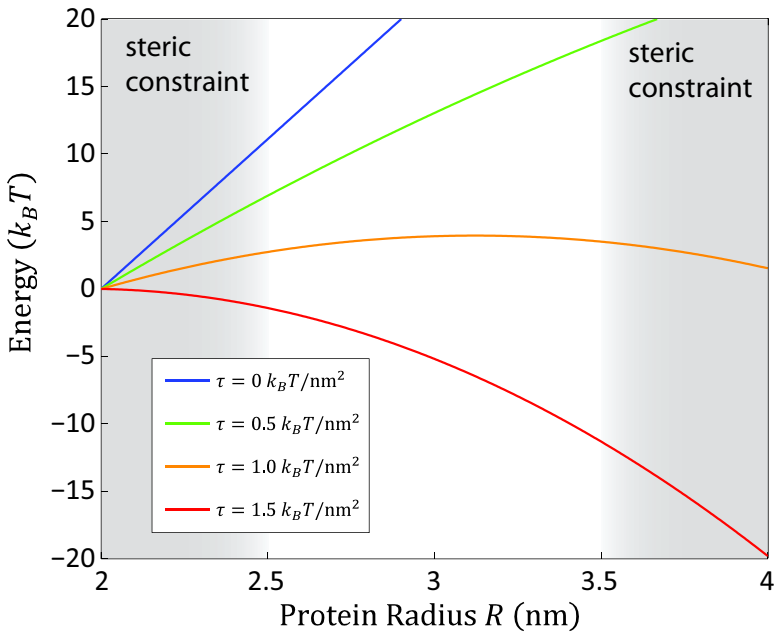

Figure 1.9: Thickness deformation and tension induced energy of a MscL-like channel. Competition between the cost of deforming the lipid surrounding a protein and the benefit of opening a pore under tension leads to a bistable switch. At zero tension, the cost of deformation favors a small protein radius, limited only by the steric constraints of the protein. As tension increases, the benefit to opening a pore is comparable to the energetic cost to deform the lipids surrounding the protein, and a larger protein radius is now possible. At high tension, the potential energy of the loading device far outweighs the deformation cost and a larger protein radius is favored, again limited by the steric constraints of the protein.

and argue that this approximation captures the idea that opening the channel any further would lead to some degree of energetically costly denaturation. This model also captures the correct scale for the critical gating tension which is on the order of $1\,k_BT/\text{nm}^2$.

It is of interest to compare the energy scale implied by this elastic model to measured values. The free energy change of MscL gating was measured to be $\simeq 51\,k_BT$ using native bacterial membranes [23, 34]. If one uses the independently measured geometrical properties of the channel, contained in Table 1.1, and elastic properties of pure bilayers (in the text) to calculate the free energy of the closed and open states, their difference is approximately $55\,k_BT$ at the critical tension of $2.5\,k_BT/\text{nm}^2$. Though very encouraging, this close correspondence depends sensitively upon the choice of hydrophobic mismatch, as dictated by the channel structure and bilayer thickness. It is worth noting that, like the midplane bending case, compression deformation also is accompanied by a constraint which relates the hydrophobic mismatch of the channel to the radius (*i.e.* $u_o(R)$). In calculating the free energy change of MscL above, we only made use of the end points of this function at $u_o(R_{closed})$ and $u_o(R_{open})$.

1.4.3 Approximating Bilayer Deformation: The Variational Approach

In previous sections, we performed cursory derivations of the energy functionals which govern membrane shape for both midplane and membrane thickness deformations. In order to extract meaning from these energies, we had to minimize the free energy functionals of eqns. 1.11 and 1.19 with respect to membrane shape. To solve the full problem, the conventional scheme (used to obtain the earlier quoted results) is to use the calculus of variations to derive a corresponding partial differential equation in the unknown deformation fields $h(\mathbf{r})$ and $u(\mathbf{r})$[4]. A useful and intuitive alternative is to adopt a variational approach in which we guess a family of solutions (called 'trial functions') that depend upon a small set of parameters and then minimize the deformation energy with respect to those parameters.

For simplicity, we will showcase this method for one-dimensional membranes which amounts to the approximation that the protein radius is larger than the natural length-scale of deformation, schematized in Fig. 1.10. We will use the variational approach to find an approximation for the functions $h(\mathbf{r})$ and $u(\mathbf{r})$ with their related energies, and in the process derive the natural length-scale of deformations in both cases. Picking a 'good' trial function is intimately related to the success of the variational approach. The choice of the trial function is often dictated by what we know about the character of the solution. In this case, we know that in the near-field the protein is locally disturbing the bilayer by inducing bending or hydrophobic mismatch. In the far-field, these disturbances should decay back to a flat bilayer. Keeping in mind that most of the energy cost is stored in the local disturbance around the protein, we want a trial function that has locally varying character around the protein and then a simple decay far from the protein. Such a trial function (call it $f(x)$) could be constructed using a local disturbance, $g(x)$, within a decaying envelope

$$f(x) = g(x)e^{-x/\lambda}. \tag{1.23}$$

The constant λ is an as-yet undetermined natural length scale of deformation and will emerge from the minimization process itself. Further, this choice of an exponential envelope essentially guarantees that the membrane returns to its unperturbed state far from the protein.

As a practical tool for calculation, our choice of $g(x)$ should have enough parameters to reproduce the given boundary conditions. In addition, we want to choose $g(x)$ such that the free energy is a simple function of these parameters. The power of the variational approach is that once we have written the energy in terms of these variational parameters, the best version of $f(x)$ is, by definition, the one that minimizes the energy. Thus, for instance, if the trial function has two free parameters a and b, $f(x; a, b)$, finding the best trial function amounts to solving a system of algebraic equations defined by

$$\frac{\partial}{\partial a}G[f(x; a, b)] = 0 \quad \text{and} \quad \frac{\partial}{\partial b}G[f(x; a, b)] = 0, \tag{1.24}$$

[4]A detailed derivation of the thickness deformation and deformation energy are found in Appendix A.

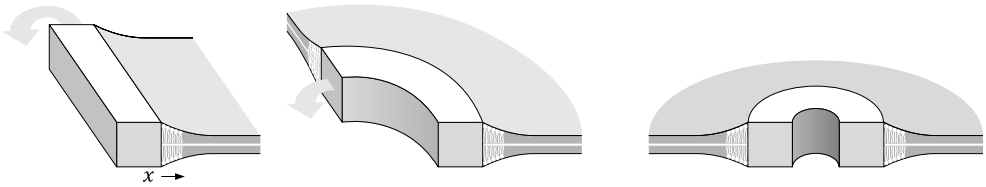

Figure 1.10: Protein-induced line tension. Deformation of the membrane around an ion channel can be described using a line tension. This line tension is obtained by solving for a one-dimensional deformation energy per unit length and then imposing that energy around the circumference of the channel. The diagrams above show the sequential wrapping of this one-dimensional line tension around a cylindrical channel.

where the brackets indicate the energy, G, is calculated using the trial function f. This variational strategy can also be used as the basis of numerical approaches in which the membrane deformation is represented using finite elements, for example. In this case, the trial functions permit us to determine the energy to an arbitrary degree of accuracy. Our strategy in the remainder of this section is to use the simplicity of the variational approach to find approximate energies for the midplane and thickness deformations imposed by membrane proteins.

1.4.4 Variational Approach for Midplane Deformations

Our goal is to obtain an approximate expression for the one-dimensional energy due to midplane bending given by

$$G^{(\mathrm{mid})} = 2\pi R \int_0^\infty \left(\frac{\tau}{2} \left(\frac{\mathrm{d}}{\mathrm{d}x} h(x) \right)^2 + \frac{\kappa_b}{2} \left(\frac{\mathrm{d}^2}{\mathrm{d}x^2} h(x) \right)^2 \right) \mathrm{d}x. \tag{1.25}$$

The presence of the $2\pi R$ in this expression is due to the fact that we are computing the energy per unit length for a deformed bilayer, as shown in Fig. 1.10, and must then multiply by the length (the circumference) of deformed material.

The strategy employed in the variational approach is to plug the trial function into the free energy functional and compute the resulting energy, which depends upon the parameters in the trial function. Our trial function has the form

$$h(x) = g(x) e^{-\left(\frac{x}{\lambda}\right)}. \tag{1.26}$$

The choice of $g(x)$ can be made based upon the boundary conditions. In particular, at the boundary of the protein, we require that

$$\frac{\mathrm{d}}{\mathrm{d}x} h(x)|_{x=0} = \theta, \tag{1.27}$$

which tells us that we can make the choice $g(x) =$ constant. Applying this boundary condition

yields the functional form

$$h(x) = -\theta\lambda e^{-\left(\frac{x}{\lambda}\right)}, \tag{1.28}$$

where the only remaining undetermined parameter is the length scale, λ. This trial function can be plugged into eqn. 1.25 and the integral is easily evaluated to yield the free energy

$$G^{(\text{mid})}(\lambda) = \frac{\pi}{2} R\theta^2 \left(\tau\lambda + \frac{\kappa_b}{\lambda}\right). \tag{1.29}$$

The next step in the variational strategy is to minimize the free energy with respect to λ,

$$\frac{\partial}{\partial\lambda} G^{(\text{mid})}(\lambda) = 0 \quad \rightarrow \quad \lambda = \sqrt{\frac{\kappa_b}{\tau}}, \tag{1.30}$$

which upon substitution yields

$$G^{(\text{mid})} = \theta^2 \pi \kappa_b \frac{R}{\lambda} = \theta^2 \pi R \sqrt{\kappa_b \tau}. \tag{1.31}$$

This is precisely the asymptotic ($(R/\lambda_\tau) \gg 1$) form of eqn. 1.12 for midplane bending energy, and our minimization correctly defines the natural length-scale of midplane deformation. Though it should be noted that given a nominal protein size of a few nanometers and nominal values of tension in membranes [26, 13], rarely is this an applicable regime for midplane deformations.

1.4.5 Variational Approach for Membrane Thickness Deformations

A similar analysis can be made for the one-dimensional deformations induced by hydrophobic mismatch. In this case, the free energy functional in the absence of tension can be written as

$$G^{(\text{leaf})} = 2\pi R \int_0^\infty \left(\frac{K_A}{2} \left(\frac{u(x)}{l} \right)^2 + \frac{\kappa_b}{2} \left(\frac{\mathrm{d}^2}{\mathrm{d}x^2} u(x) \right)^2 \right) \mathrm{d}x. \tag{1.32}$$

We adopt the same functional form for the trial function, namely,

$$u(x) = g(x) e^{-\left(\frac{x}{\lambda}\right)}. \tag{1.33}$$

In this case, we specify two boundary conditions in the near-field; there is a hydrophobic mismatch which demands

$$u(R) = u_o, \tag{1.34}$$

and the leaflet has a particular slope at the membrane interface, which we will set to zero,

$$\frac{\mathrm{d}}{\mathrm{d}x} u(x)|_{x=0} = 0. \tag{1.35}$$

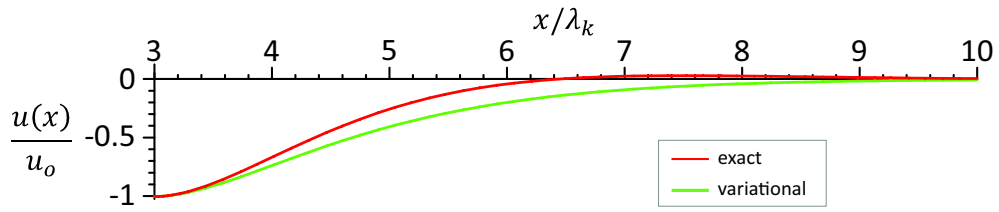

Figure 1.11: Comparison of the exact and variational solutions for the thickness deformations around a protein. The variational approach generates an approximation to $u(x)$ which is close to the exact solution. The protein radius is $R/\lambda = 3$.

In order to accommodate these two boundary conditions, $g(x)$ must have two free parameters. As a result, we pick the simplest function which has two degrees of freedom, namely a line, and hence set $g(x) = ax/\lambda + b$, where a and b are constants. Applying the two near-field boundary conditions constrains the trial function to the form

$$u(x) = u_o \left(1 + \frac{x}{\lambda}\right) e^{-\left(\frac{x}{\lambda}\right)}, \tag{1.36}$$

where λ is a free parameter with respect to which the energy must be minimized. Using this trial function, the free energy can be written as a simple expression of the form

$$G^{(\text{leaf})}(\lambda) = \pi \kappa_b u_o^2 R \left(\frac{5}{4}\frac{K_A}{\kappa_b l^2}\lambda + \frac{1}{4\lambda^3}\right). \tag{1.37}$$

Minimizing the energy with respect to λ gives

$$\frac{\partial}{\partial \lambda} G^{(\text{leaf})}(\lambda) = 0 \quad \rightarrow \quad \lambda = \left(\frac{3}{5}\right)^{\frac{1}{4}} \left(\frac{\kappa_b l^2}{K_A}\right)^{\frac{1}{4}} \tag{1.38}$$

which upon substitution gives the membrane thickness energy

$$G^{(\text{leaf})} = \left(\frac{5}{3}\right)^{\frac{3}{4}} \left(\frac{K_A}{\kappa_b l^2}\right)^{\frac{3}{4}} \pi \kappa_b u_o^2 R. \tag{1.39}$$

Again, the variational approach has reproduced the correct asymptotic form of the energy with a small multiplicative error (see eqn. 1.21); the exact asymptotic result has $\sqrt{2}$ instead of $\left(\frac{5}{3}\right)^{\frac{3}{4}}$, introducing an error of $\sim 4\%$.

Finally, there are many forms of $u(x)$ which yield roughly the same *energy*, but how does the exact deformation *shape* compare with our minimized trial function? Here too, the variational approach gives a trial function that nearly matches the exact result as shown in Fig. 1.11.

1.4.6 Distilling the Design Principles

Having explored how midplane bending, thickness variation and area change are coupled to tension and the geometric features of the MscL channel, can we distill general rules for what makes a membrane protein mechanosensitive? One simple statement is that under tension an increase in protein area is always favored, regardless of bilayer elastic properties, because an increase in area lowers the potential energy of the loading device. Conversely, both midplane and thickness deformations prefer a smaller channel, because a larger radius results in a larger annulus of deformed lipid and hence a larger free energy penalty (except in the case where the spontaneous curvature favors a larger radius [32]). With the area change preferring a larger radius and deformation preferring a smaller radius, we have the necessary energetic competition that ultimately leads to bistability. This also means the sign of the free energy change due to deformation (midplane or thickness) must be positive. Hence, the channel is going from a closed state with less deformed lipid surrounding it, to an open state with more deformed lipid surrounding it. The contributions to the free energy budget of a mechanosensitive protein, like MscL, due to channel-area change and membrane deformations are shown in Fig. 1.12. The basic point of this picture is to show how various contributions to the free energy scale with the radius (R) and the elastic parameters.

Midplane deformation is the deformation which depends most simply on membrane properties, since it is only linked to the bending modulus. Additionally, its tension dependence is such that the cost of the deformation always increases with tension and angle, hence we know that tension in addition to preferring a larger protein, also wants a more cylindrical protein in the case of midplane bending. This allows us, within the limitations of our theory, to put an upper bound on the cost of midplane deformations. Taking the lytic tension as an upper bound, a nominal bending modulus of $20\,k_BT$, and $\theta = 0.6$ as a reasonable value of the membrane slope [54], the maximum energetic cost of deformations for a protein of radius R (in nm) is $\simeq R \times 9\,k_BT/\text{nm}$, or in other words, a midplane deformation induced line tension of $\sim 1.5\,k_BT/\text{nm}$.

Thickness deformation depends on all the elastic parameters; bending modulus, area stretch modulus, and membrane thickness. The tension dependence of thickness deformation energy is also more complex, though a general principle does emerge. We know that tension can increase or decrease the overall thickness deformation energy, but the general principle is that it always prefers the protein to have the same hydrophobic thickness as the bilayer, though the bilayer thickness is itself decreased as tension increases. The other important feature to note is that a decrease in the thickness of a transmembrane protein is always accompanied by an increase in the area of the membrane surrounding the protein due to volume conservation of the membrane. This change in membrane area is *indistinguishable* from a change in protein area. Indeed for MscL, the measured area change is probably a mix of a change in the areal footprint of the protein, and a local increase in the membrane area surrounding the protein, together giving the measured value of $\sim 20\,\text{nm}^2$. An estimate of the upper bound of leaflet deformations is made by assuming the maximum $u_o = 0.5\,\text{nm}$, then the maximum change in free energy for a protein of radius R (in nm) is $\simeq R \times 22\,k_BT/\text{nm}$

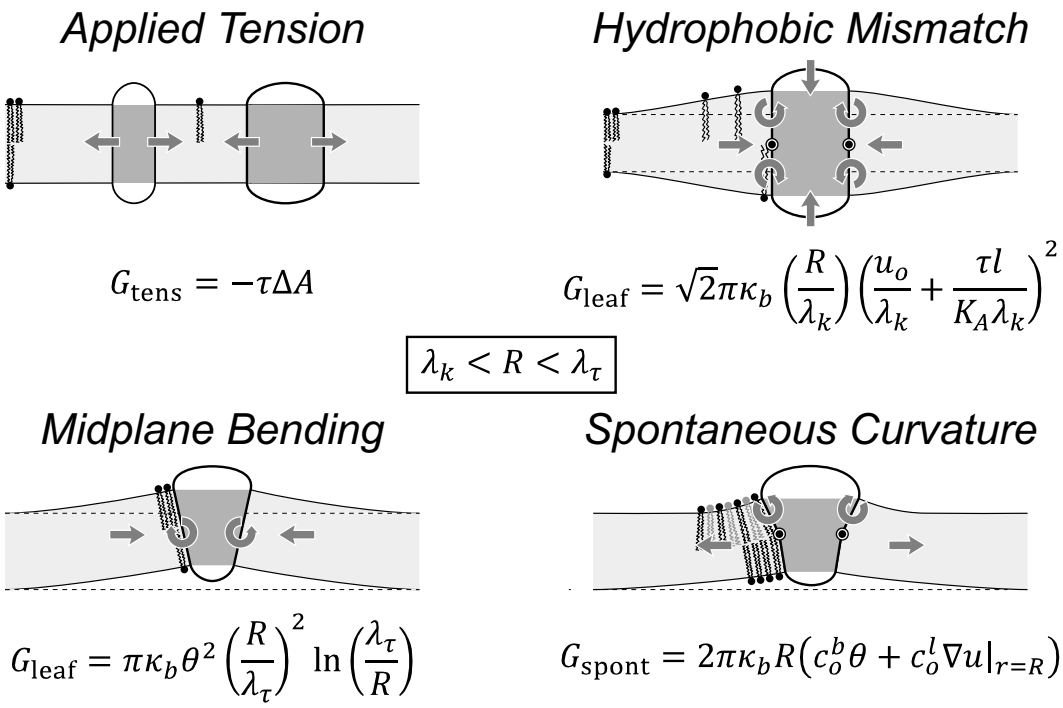

Figure 1.12: Contributions to the deformation free energy. This figure shows how the different modes of deformation contribute to the overall free energy budget of the membrane-protein system. The energies are written in the limit where $\lambda_k < R < \lambda_\tau$ to show their dominant scaling with the relevant parameters. For the sake of simplicity, we did not address how spontaneous curvature factors into the free energy budget. However, a thorough discussion of both midplane and leaflet spontaneous curvature energy contributions are found in [32]. The arrows indicate the forces and torques felt by the protein due to lipid deformations.

at zero tension with the given elastic parameters (see Table 1.1). This corresponds to a thickness deformation induced line tension of $\sim 3.5\, k_B T/\text{nm}$. This illustrates that while both midplane and thickness deformations are important factors in determining the preferred protein conformation, thickness deformations are generally associated with a higher energy scale.

1.5 Experimental Considerations

Much of our knowledge of the function of mechanosensitive channels, including MscL, comes from detailed electrophysiology studies where gating of the channel is monitored by sharp differences in the ion flux through a membrane patch [10, 21, 49, 22, 23, 34]. A small voltage ($\sim$ 50mV) is applied across a patch of membrane at the tip of a micropipette. As a function of pressure difference, channel opening events are recorded as stochastic changes in patch current by an ammeter with picoamp (pA) sensitivity. This truly amazing single-molecule spectroscopy technique allows the experimenter to adjust the voltage as well as the pressure difference across the membrane as shown in Fig. 1.14. The pressure difference across the membrane translates into a lateral membrane tension (via the Laplace-Young relation [65]), responsible for gating the mechanosensitive channel. However, there are two serious problems with this method when probing the mechanisms of mechanosensitive channels.

Arguably, the most serious problem is that often *pressure difference* (J/m^3) across the membrane is taken to be the input variable of prime importance, when in fact *tension* (J/m^2) is the membrane parameter which governs mechanosensitive gating. Pressure difference is linearly related to tension via the radius of curvature of the membrane, hence in principle the fix is straightforward - image the membrane patch (see Fig. 1.14). While certainly not impossible [21, 50], the membrane patch can be difficult to image due to its small size and the fact that it is inside the micropipette. A recent study [50] demonstrated the importance of measuring tension in lieu of pressure difference. It was shown that using the standard methods for creating "identical" micropipettes, the measured characteristics of a channel varied significantly. However, when the membrane patch was imaged and tension used as the principal input variable, the same data collapsed to within a few percent of each other, as shown in Fig. 3.3. In general, if one could perfectly control the size and shape of the micropipette tip used for contacting and sealing the membrane patch, all measurements would be related by a single constant (the radius of curvature). However, variations in micropipette shape and size, as well as variations in how the membrane contacts and adheres to the pipette[5] tip all lead to potentially large variations in the perceived gating characteristics of the channel. Additionally, it is difficult to compare the wealth of quantitative data coming from electrophysiology studies to theoretical models when pressure difference, instead of tension, is used as the principal input variable. Tension is routinely measured in micropipette aspiration experiments [26], and in fact, single-channel electrophysiology recordings are possible in such a setup [25] using ion channels

[5] Glass–bilayer adhesion, specifically in the context of electrophysiology, is discussed in detail in Section 3.6.

with conductances *lower* than MscL. Hence, this technique might provide a useful way to apply known membrane tension to reconstituted MscL channels in well characterized membranes, a topic discussed further in Chapter 3.

With tension being used as the variable of prime importance, electrophysiology is poised to put the continuum mechanical view to the test, elucidating the role of lipids in ion channel function. In particular, the elastic properties of many lipids have been measured [26], enabling a careful examination of the dependence of gating energy on lipid carbon chain length. The simple continuum view we set forth here predicts a quadratic dependence of the lipid thickness deformation energy on hydrophobic mismatch, which is directly linked to carbon chain length. This, of course, has implications for both the function of various transmembrane proteins, and comments meaningfully on the ability of bilayer thickness to segregate proteins in biological membranes.

A second class of intriguing experiments concerns the mechanosensitivity of other ion channels and receptors, generally regarded not to be mechanosensitive [66, 67]. This is both interesting from a functional standpoint, in an effort to understand the full physiological effects of these proteins, and as a tool for understanding structural features such as the motions of transmembrane helices. Performing a similar experiment where lipid carbon chain length is varied around a voltage-gated ion channel (for example) could reveal hidden mechanosensitivity, and energetic analysis from such an experiment could comment on the degree of height and area change during the gating transition. Indeed by comparing the known electrostatic gating energy of $\sim 15 k_B T$ for common voltage-gated ion channels, contributions to the gating energy from membrane deformation can be estimated, and used in two ways [68]. First, one can use such estimates to predict the shift in the gating voltage of these channels as a function of bilayer mechanical attributes like leaflet thickness or tension, as shown in Fig. 1.13. Second, the way in which these predicted changes in gating voltage scale with various mechanical properties, can serve as a indicator of which deformation modes are dominant during gating, and hence might indicate relevant structural changes in the protein upon gating. Such analysis has been performed in detail [68], and the results for a typical voltage-gated ion channel are shown in Fig. 1.13.

The second problem facing a complete understanding of the function of mechanosensitive channels is that for many such channels volumetric flow, and not ion flux, is the relevant physiological parameter[6]. Hence, ion flux is used as a surrogate measurable in place of the true physiological output of the channel. One could argue that ion flux is proportional to volumetric flow, however this assumes that the way ions flow through the channel pore is identical to the way water flows through the pore. Experiments have elucidated the roughly Ohmic nature of mechanosensitive channels [22, 75] at low voltage ($\lesssim 80$mV), however we know essentially nothing about how a pressure gradient across the membrane translates into a volumetric flow. Even the simplest continuum approximation (Hagen-Poiseuille flow) would predict a non-linear function relating the area of the

[6]The mechanosensitive bacterial channel MscS [12, 69, 18] is another example. Although, there are also mechanosensitive channels that appear to be highly ion selective, such as the bacterial mechanosensitive ion channel MscK [70] and the K2P family of mammalian mechanosensitive channels [71, 72, 73, 74].

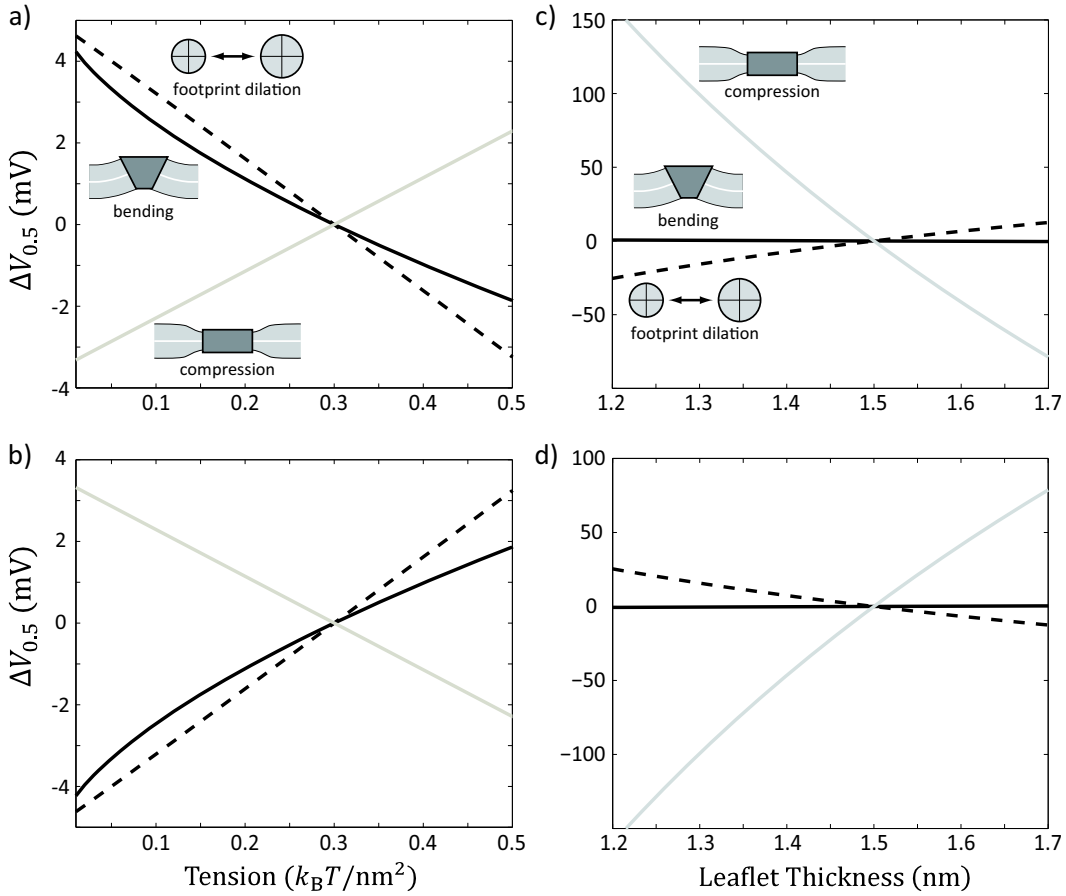

Figure 1.13: Mechanosensitivity as a structural reporter. These plots apply to the expected shifts in gating voltage of the *Shaker* family protein Kv1.2. In all plots the solid gray lines represent thickness deformations, the dotted gray lines represent protein area dilation, and the solid black lines represent midplane bending deformations. a) Shift in gating voltage as a function of tension, assuming the closed channel deforms the membrane. b) Shift in gating voltage as a function of tension, assuming the open channel deforms the membrane. c) Shift in gating voltage as a function of leaflet thickness, assuming the closed channel deforms the membrane. d) Shift in gating voltage as a function of leaflet thickness, assuming the open state deforms the membrane. This figure adapted from [68].

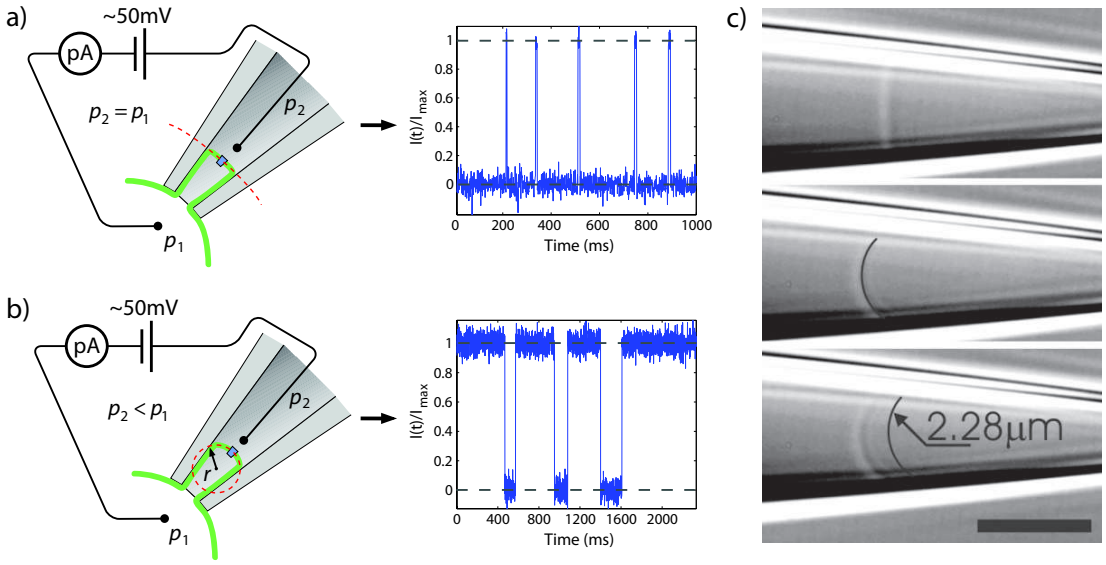

Figure 1.14: Measurement of tension vs. pressure difference in an electrophysiological experiment. A channel protein (small blue rectangle) is embedded in a membrane patch (green). A potential of order 50mV is applied across the sealed membrane patch, and channel opening events are measured by an ammeter (circle) with picoamp (pA) sensitivity. a) At low pressure difference, the tension in the patch is low, the mechanosensitive channel is in the closed conformation, and the patch has a large radius of curvature. The plot to the right shows normalized channel current as a function of time for a simulated channel; the open state has low occupation at low tension. b) At high pressure difference, the tension in the patch is high, the mechanosensitive channel will occupy the open state, and the radius of curvature (r) is on the order of microns. The plot to the right shows the open state has high occupation at high tension. c) Optical micrograph of vertically oriented membrane patch at low (top) and high (middle and bottom) pressure differences, illustrating the decrease in the radius of curvature with increase pressure difference (from [50]). The scale bar is 5μm.

channel pore to the volumetric flow, in contrast to the linear relationship between ion flux and channel pore area as predicted by Ohm's Law [76]. It would be of considerable physical and physiological interest to expand our understanding of fluid flow at the molecular level, by measuring the relationship between pressure gradient and volumetric flow through a large-pore channel like MscL. This topic will be discussed in detail in Chapter 3.

1.5.1 Other Experimental Clues

In addition to aforementioned analysis of MscL, other avenues of research have shown interesting links between the function of membrane proteins and the lipid environment. One such avenue is the effects of membrane doping (by toxins, lipids or cholesterol) on channel activity, as schematically

shown in Fig. 1.5b. Certain lipid species and other membrane components are clearly required for proper protein function [77, 78], but studies using toxins support the idea that the membrane is also a generic mechanical medium with which proteins interact. Rather than having evolved to target a specific channel, some toxins impair the function of multiple membrane proteins, and some small molecules, such as capsaicin [79], and peptide toxins, like those found in spider venom [80], target membrane channels across many species. These broad-ranging effects favor a mechanism that targets a generic property of membrane proteins. It has therefore been proposed that these toxins affect the interactions with the membrane itself. But can these toxins be understood in terms of a coarse-grained membrane model?

As discussed earlier, many studies have shown that bilayer thickness, bending stiffness and monolayer spontaneous curvature can affect the function of embedded proteins [81, 28]. Indeed, although the role of certain proteins (such as mechanosensitive channels) is to respond to membrane mechanical stress, in principle this stress can alter the function of any membrane protein. For example, the dimerization kinetics of the channel-forming peptide gramicidin A can be controlled by externally applied membrane tension, resulting in membrane thinning and decreasing the hydrophobic mismatch between the membrane and the gramicidin dimer [25]. Furthermore, using gramicidin A enantiomers as sensors for membrane mechanical properties, the small molecule capsaicin has been shown to indirectly target and trigger the pain receptor TRPV1 by decreasing the bending modulus of lipid bilayers in a concentration-dependent manner, that is, not with a certain fixed stoichiometric relation between toxin and channel, but progressively by altering the membranes bending stiffness [79]. Conversely, voltage-dependent sodium channels are inactivated by capsaicin with no significant change to the conductance properties of the channels, but by an alteration of the gating voltage itself, suggesting that even channels that are not mechanically gated may still be subject to the effects of membrane mechanics through alterations of membrane properties [82, 67, 83]. In addition, it seems that some peptide toxins target multiple types of stretch–activated cation channels, not by changing membrane properties *per se* but by changing the effective boundary conditions at or near the protein-lipid interface [80]. This is yet another generic method by which membrane mechanics can couple to protein function, as indicated in Fig. 1.5b. In particular, it seems that either enantiomer of a peptide toxin is localized in the membrane close to the channel and shifts its dose-response curve. Altogether, these experiments show that the entire range of membrane mechanical properties, as well as alteration of protein-lipid boundary conditions, can be utilized to affect channel function. If the changes such membrane dopants cause to bilayer mechanical properties can be carefully quantitated, future experiment may be able to utilize these methods to get a better understanding of the role of lipids in membrane protein function.

1.6 Interaction between Transmembrane Proteins

One intriguing consequence of the deformations induced in membranes by ion channels is that channels will interact. These interactions can lead to cooperativity in the gating of neighboring channels and can also induce spatial ordering of the proteins. These interactions can be thought of as arising from two different effects: those of *elastic* origin and those of *thermal* origin. The elastic forces are purely an enthalpic effect coming from a minimization of the deformation energy around two proteins separated by a given distance. The thermal forces are entropically driven by the thermal fluctuations of the membrane and are analogous to Van der Waals forces. Though we briefly discuss these forces here, Chapter 2 is devoted to an in depth analysis of bilayer mediated interactions.

1.6.1 Enthalpic Interactions

As discussed above, proteins which change the membrane thickness or bend the membrane midplane produce deformations which extend anywhere from a few nanometers (thickness) up to tens of nanometers (midplane) from the protein edge. As two proteins approach each other, their respective deformation fields overlap resulting in a deformation profile between them that is different than either of them produce separately. In this case, the total deformation energy of the system is dependent on the separation between the two proteins and results in an interaction potential that is dependent upon the conformation of the proteins. These forces arise purely from the mechanical attributes of the deformed membrane and have no entropic component. We know that midplane and thickness deformations are independent, and hence there are distinct interactions due to midplane and thickness deformations.

Pairwise interactions due to midplane deformation using eqn. 1.11 have previously been calculated for a variety of membrane curvature environments and protein shapes at zero tension [84]. Using a bilayer bending modulus of $\sim 100\,k_BT$, attractive interactions of order $\sim 1-5\,k_BT$ were found when the proteins were separated by 1 - 2 protein radii (which we estimate to be 5 - 10 nm measured center-to-center for a typical transmembrane protein). If we adjust the energy scale to be consistent with a phosphatidylcholine bilayer bending modulus of $\sim 20\,k_BT$ this lowers the interaction energetics to $\sim 0.5-3\,k_BT$. These interactions tend to be long-ranged with a power-law decay of $1/r^4$ [85]. Simple pairwise interaction will be inadequate to describe the nature of interactions between more than two proteins. This arises because one protein can shield other proteins from feeling the deformation of a neighboring protein, and hence interactions are not (in general) pairwise additive. Apart from direct numerical simulation, there are few analytical (*i.e.* theoretical) tools which allow one to study how many interacting proteins in close proximity behave as a group [44]. In the presence of positive membrane tension, these interactions take on a distinctly different form, having a finite interaction length scale given by λ_τ, where proteins that curve the membrane in the same direction tend to repel and proteins that curve the membrane in opposite directions

tend to attract, as shown in Fig. 1.15.

Like midplane deformations, the thickness deformation fields extending from the edges of two proteins will overlap and interact as the proteins come into close proximity [86, 56, 87]. We provided evidence that lipids likely influence the function of MscL through thickness deformations and once again we will appeal to MscL as a case study for interacting membrane proteins. The short-range nature of thickness deformations (essentially exponential decay) means there is no power-law asymptotic formula for their interaction, though these interactions were numerically explored for all possible conformations of two MscL proteins as shown in Fig. 1.15. As we saw with single proteins, the energetic scale of thickness interactions is generally higher than with midplane deformations, and can vary greatly depending on the hydrophobic mismatch. The leaflet interactions between two MscL proteins are appreciable when they are within several nanometers of each other, and ranged from $\sim 2 - 25\, k_B T$ depending on the protein conformations and the tension in the membrane. This kind of short-ranged interaction might play an important role in membrane protein function [88, 89, 90], given the nominal density of transmembrane proteins in biological membranes leads to spacings on the order of $10 - 100$ nm [91].

Additionally, the interactions due to thickness variations can be either attractive or repulsive depending on the shape of the proteins. The general principle that emerges is that 'like' proteins attract and 'unlike' proteins repel (in contrast to electrostatics) as shown in Fig. 1.15 [87]. Proteins whose hydrophobic mismatch has the same sign (*i.e.* both are taller or both are shorter than the membrane) lead to net attractive interactions; proteins with opposite signs of hydrophobic mismatch lead to repulsive interactions. As discussed later in this chapter, and in detail in Chapter 2, we can show that these conformation-dependent interactions communicate state information between two proteins, leading to cooperative channel gating.

1.6.2 Entropic Interactions

A second class of forces between membrane proteins arise due to membrane fluctuations. Like most entropic forces, the thermal interactions between transmembrane proteins are fairly weak, on the order of a few $k_B T$. Two fluctuation-induced forces have been studied in some detail in the literature; a long-ranged Casimir force due to the surface fluctuations of the membrane [85, 92], and a very short-ranged depletion force due to the excluded volume of lipid molecules between two membrane proteins [93].

The Casimir force between two membrane proteins arises because the available spectrum of fluctuations of the membrane-midplane depend on the distance between two proteins. Entropically, the membrane-protein system seeks to maximize the number of available modes of fluctuation and hence an energetic potential exists between two transmembrane proteins in a fluctuating, thermally active membrane. Through a series of elegant calculations, this force was shown to have a $1/r^4$ asymptotic form, where r is the center-to-center distance between two cylindrical proteins [85, 92]. If we presume that this potential is approximately correct for small separations ($r \simeq 2R$), this

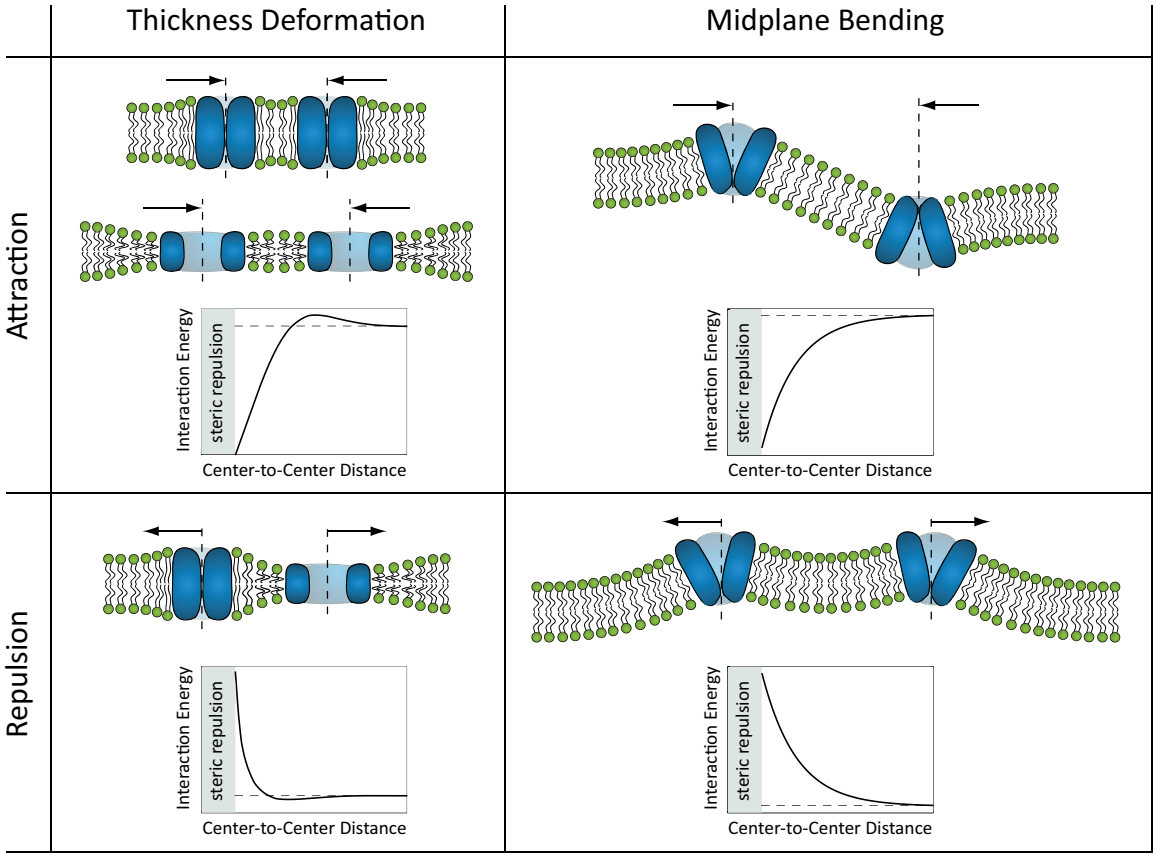

Figure 1.15: Trends in bilayer mediated protein-protein interactions. In thickness deformations, proteins that either both thicken or both thin the membrane tend to attract (upper left), while proteins repel each other if one thickens and one thins the bilayer (lower left). In midplane deformations, proteins that bend the bilayer in the same direction tend to repel each other (lower right), while proteins that bend the bilayer in opposite directions tend to attract each other (upper right).

implies an attractive potential with an energy scale of $\sim 1\, k_B T$.

Lateral density fluctuations of lipids in the membrane also lead to entropic forces between proteins. Using Monte Carlo simulations, these entropic depletion forces (also called 'excluded volume forces') between cylindrical proteins were shown to be appreciable only when the proteins' edges were within ~ 1 lipid molecular diameter [93]. For cylindrical proteins, with diameters on the order of $\sim 1-2\,\text{nm}$, direct edge contact resulted in a favorable interaction with an energy scale of $\sim 2\, k_B T$.

1.6.3 Protein Conformations Affected by Interaction

As noted above, the elastic interactions between ion channels, such as MscL, depend on protein conformation. In earlier sections, we established that the equilibrium conformations of the channel are entirely determined by the free energy difference between the two states. As a result, elastic

interactions which change the energy of a two-channel system will affect the probability that we measure any one channel in the open state [87]. In fact, electrophysiology (see Fig. 1.14) is well suited to such measurements where the total amount of time spent in the open state divided by the total measurement time *is* the open probability.

The free energy difference between the open and closed states of a single channel is roughly $50\,k_BT$ [23], which implies the energy scale for two channels is roughly $100\,k_BT$. In Chapter 2 we show that two MscL channels in proximity have interactions on an energy scale of roughly $\sim 20\,k_BT$ as shown in Fig. 2.3. Two open channels have a strong, favorable interaction that can significantly alter the open probability of a given channel relative to the isolated channel value as shown in Fig. 2.3. Such interactions also affect channel 'sensitivity', defined by the derivative of the p_{open} curve with respect to tension [87], which quantifies how responsive the channel is to changes in the driving force, in this case tension. The full-width at half maximum of this peaked function is a measure of the range of tension over which the channel has an appreciable response. In general, the area under the sensitivity curve is equal to one, hence increases in sensitivity are always accompanied by decreases in range of response, as demonstrated by the effects of the beneficial open-open interaction on channel statistics. The critical gating tension and sensitivity are essentially the key properties which define the transition to the open state, and are analogs to the properties which define the transition of *any* two-state ion channel. Hence, the elastic interactions can affect channel function on a fundamental level.

1.6.4 Interaction and Protein Density in Biological Membranes

Recent proteomic and lipidomic approaches have made it possible to survey the protein and lipid content of biological membranes, revealing a crowded and heterogeneous bilayer. Whether we consider a synaptic vesicle [94], bacteria or red blood cells [91, 95], the conclusion is the same, that biological membranes are as much protein as they are lipid, with typical protein-to-lipid mass ratios of approximately 60–to–40 [91, 95]. There are many ways to estimate the mean spacing between membrane proteins, and while the details change from one cell type to another, the message is always the same: biological membranes are crowded. The mean center-to-center spacing between proteins is estimated at about 10 nm (comparable to the distance between proteins in the cytoplasm [96, 97]), strongly indicating that these proteins might be able to influence each other through the intervening membrane.

1.7 Overview and Concluding Remarks

The goal of this chapter is to take stock of the role of lipid bilayer deformations in membrane protein function, using mechanosensation as a case study. More precisely, we have argued that the lipid bilayer is not a passive bystander in the energetics of channel gating. As a result, by tuning membrane properties it is possible to alter channel function. We have emphasized two broad

classes of membrane deformation that are induced by the presence of a transmembrane protein: i) deformation and bending of the midplane of the lipid bilayer, ii) variations in the thickness of the lipid bilayer that are induced by hydrophobic mismatch. As a result of these deformations, there is a free energy cost to changing the radius of a channel since the open state implies a larger annulus of deformed material and hence a higher free energy. This deformation energy competes with the energetic relaxation of the loading device.

One of the key reasons for performing theoretical analyses like those described here is that they permit us to sharpen the questions that can be asked about a given biological problem. This sharpness is ultimately most meaningful if it is translated into precise experimental predictions. The theoretical results described here suggest a variety of experimental predictions.

- *Dependence of gating tension on hydrophobic mismatch.* Previous work has already shown that lipid bilayer tail lengths can alter channel gating by changing the hydrophobic mismatch. To more precisely examine this relationship, careful measurements of the membrane tension need to be made, as opposed to pipette pressures, to elucidate the energetics underlying gating. Alternatively, mutagenesis could be used to explore the same effect by changing the hydrophobic thickness of the protein.

- *Hidden mechanosensitivity in other classes of channels and receptors.* The results described here have been applied to the case study of MscL, and we briefly touched upon Kv1.2. However, we argue that any transmembrane protein that varies its radius or hydrophobic thickness upon conformational change will exhibit mechanosensitivity. Furthermore, the way tension affects the function of these proteins might help elucidate the classes of structural changes that occur during their conformational change.

- *Cooperative gating of channels.* As a result of the elastic deformations induced in the lipid bilayer by mechanosensitive channels, nearby channels can communicate their conformational state, resulting in cooperative gating. This cooperativity should be observable in electrophysiology experiments as a change in the critical tension and channel sensitivity with an increase in channel density.

Shortcomings of the Theory. Obviously, the use of simple ideas from elasticity theory to capture the complex process of mechanosensation provides a caricature of the real process. One signature of the shortcomings of this kind of approach is the fact that single amino acid substitutions can completely alter the properties of certain proteins [33, 98]. This serves as a warning of the pitfalls of models that ignore atomic-level details and their impact on biological function. A second class of complaint that can be registered against the models described here is that we have ignored material heterogeneity. In particular, biological membranes are built up of a broad range of different lipids and are riddled with membrane proteins. As a result, it is not clear if an elastic description like that described here is appropriate, and if it is, how to select the relevant material parameters.

Regardless of the difficulties highlighted above, it is clear that the emergence of an increasing number of structures of ion channels coupled with functional studies of these proteins has raised the bar for what should be expected of theoretical models of channel function.

1.8 Acknowledgments

We are grateful to a number of people who have given us both guidance and amusement in thinking about these problems, as well as insightful comments: Doug Rees, Olaf Anderson, Fred Sachs, Evan Evans, Cathy Morris, Sergei Sukharev, Mathew Turner, Eduardo Perozo, Nily Dan, Fyl Pincus, and Liz Haswell. Much of this chapter was taken from a series of papers [87, 68, 99] written with excellent collaborators and friends Jane Kondev, Paul Wiggins, Daniel Reeves, and Pierre Sens.

Chapter 2

Bilayer-Mediated Protein Interactions

"Happy is he who has discovered the causes of things and has cast beneath his feet all fears, unavoidable fate, and the din of the devouring Underworld." – Virgil

2.1 Introduction

Biological membranes are elastic media in which the presence of a transmembrane protein leads to local bilayer deformation. The energetics of deformation allow two membrane proteins in close proximity to influence each other's equilibrium conformation via their local deformations, and spatially organize the proteins based on their geometry. We use the mechanosensitive channel of large conductance (MscL) as a case study to examine the implications of bilayer-mediated elastic interactions on protein conformational statistics and clustering. The deformations around MscL cost energy on the order of $10\,k_BT$ and extend $\sim 3\,\text{nm}$ from the protein edge, as such elastic forces induce cooperative gating and we propose experiments to measure these effects. Additionally, since elastic interactions are coupled to protein conformation, we find that conformational changes can severely alter the average separation between two proteins. This has important implications for how conformational changes organize membrane proteins into functional groups within membranes[1]. Additionally, we will discuss potential non-specific interactions between proteins due membrane crowding.

2.2 Background

Biological membranes are active participants in the function and spatial organization of membrane proteins [100, 63, 28]. At the simplest level, the membrane positions proteins into a two-dimensional space, where they are often laterally organized into groups. These groups can serve specific purposes on the cell surface and within organelles, such as sensing, adhesion and transport [101, 102, 103, 104, 105, 106]. Electrostatic and van der Waals forces help drive lateral organization [85], however there is an additional class of purely bilayer-mediated elastic forces that can facilitate the formation of complexes of membrane proteins.

[1]Much of this chapter is adapted from [87]. The author would also like to thank Eric Peterson and KC Huang for being excellent and continuing collaborators on this project.

Conformational changes of membrane proteins result from a wide range of environmental factors including temperature, pH, ligand and small molecule binding, phosphorylation, membrane voltage, and membrane tension. Likewise, conformational state is often tightly coupled with function (*e.g.* for ion channels) [10, 2, 3]. In this work, we demonstrate how elastic interactions can communicate information about protein conformation from one neighboring protein to another coupling their conformational state. Additionally, we find that these interactions lead to spatial organization within the bilayer that is strongly dependent on protein conformation.

We suggest that elastic forces play a role in the function and spatial organization of many membrane proteins across many cell types, given the generically high areal density of membrane proteins [91] and the strength of these interactions. We use the mechanosensitive channel of large conductance (MscL) from *E. coli* as the model protein for this study. MscL is a transmembrane homo-pentamer found in the plasma membrane of *E. coli* (and many other bacteria) serving as an emergency relief valve under hypo-osmotic shock [10, 11, 12]. As membrane tension increases, this non-selective ion channel changes conformation from a closed state to an open state, releasing osmolytes [21, 49]. Though several substates have been identified in this gating transition, the relatively short dwell-times in these substates as compared to the fully open or fully closed states, allow us to approximate the protein as a simple two-state system [21, 23]. Crystal and electron-paramagnetic-resonance structures suggest the bilayer-spanning region is nearly cylindrical in both the open and closed conformations [11, 48, 19], making MscL particularly amenable to mechanical modeling. Electrophysiology of reconstituted channels allows measurement of the state of one or more of these proteins with excellent temporal and number resolution. Therefore, theoretical predictions for how elastic interactions change the gating behavior of a MscL protein can be readily tested using electrophysiology and other experimental techniques.

Following earlier work, we use continuum mechanics to break down the deformation caused by a cylindrical transmembrane protein into a term penalizing changes in bilayer thickness and a term penalizing bending of a bilayer leaflet [29, 86, 56, 31, 32], and we introduce a third term that preserves bilayer volume under deformation [62]. Due to its structural symmetry, MscL can be characterized by its radius and bilayer-spanning thickness in its two conformations (*i.e.* open and closed), neglecting any specific molecular detail (see Fig. 2.2). As these geometric parameters change with conformation, the bilayer-mediated interaction between two channels is altered. Using the interaction potentials in each combination of conformations, we explore how both the single-channel and interacting energetics affect the spatial and conformational behavior of two channels.

In the first section we cover the physical principles behind bilayer deformation due to the presence of membrane proteins. In the second section we explore the differences in gating behavior of two MscL proteins when held at a fixed separation. In the third section we explore the conformational and spatial behavior of diffusing MscL proteins as a function of areal density. Finally, in the fourth section we discuss the relevance of these forces as compared to other classes of bilayer-mediated forces and support our hypotheses with results from previous experiments.

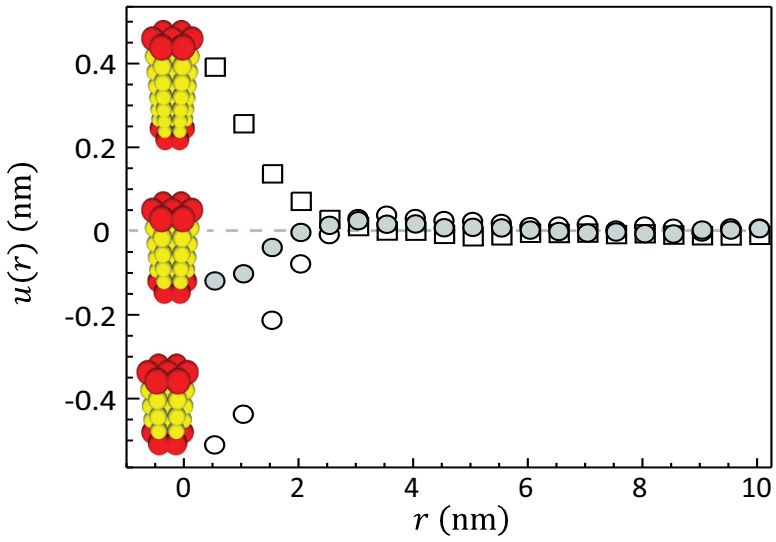

Figure 2.1: Bilayer thickness deformations in molecular dynamics. This plots shows the normalized thickness variations for coarse-grained proteins with both positive and negative hydrophobic mismatch in a coarse-grained lipid bilayer. This figure adapted from [108].

2.3 Elastic Deformation Induced by Membrane Proteins

The bilayer is composed of discrete lipid molecules whose lateral diffusion ($D \sim 10\,\mu\text{m}^2/s$) [42] is faster than the diffusion of transmembrane proteins ($D \sim 0.1 - 1\mu\text{m}^2/s$) [39, 40, 41]. In the time it takes a transmembrane protein to diffuse one lipid diameter, many lipids will have exchanged places near the protein to average out the discreteness of the lipid molecules. Additionally, the transition time for protein conformational change ($\sim 5\,\mu s$) [43] is slow compared to lipid diffusion. Hence, we argue the bilayer can be approximated as a continuous material in equilibrium with well-defined elastic properties [44]. A number of recent coarse-grained molecular dynamics simulations [107, 108, 109] show that the deformation profiles around cylindrical proteins with either positive or negative hydrophobic mismatch are well approximated by the continuum deformation profiles we derive in this section, as demonstrated in Fig. 2.1, and hence the energies calculated with continuum mechanics serve as good estimates. Further, we choose to formulate our analysis in the language of continuum mechanics, rather than lateral pressure profiles [45]. In particular, each leaflet of the bilayer resists changes in the angle between adjacent lipid molecules, leading to bending stiffness of the bilayer [29, 46]. Likewise, the bilayer has a preferred spacing of the lipid molecules in-plane and will resist any changes in this spacing due to external tension [26]. Finally, experiments suggest that the volume per lipid is conserved [60, 61] such that changes in bilayer thickness are accompanied by changes in lipid spacing [63, 44].

Transmembrane proteins can compress and bend a bilayer leaflet via at least two mechanisms. The protein can force the bilayer to adopt a new thickness, matching the hydrophobic region of the protein to the hydrophobic core of the bilayer. Additionally, a non-cylindrical protein can induce

a slope in the leaflet at the protein-lipid interface [31, 30].

For transmembrane proteins like MscL, that can be approximated as cylindrical, symmetry dictates that the deformation energy of the bilayer is twice the deformation energy of one leaflet. Presuming the protein does not deform the bilayer too severely, we can write the bending and compression (thickness change) energies in a form analogous to Hooke's law, and account for external tension with a term analogous to PV work. We denote the deformation of the leaflet by the function $u(\mathbf{r})$, which measures the deviation of the lipid head-group from its unperturbed height as a function of the position $\mathbf{r}$ (see Fig. 2.2). In all the calculations that follow the physical parameters chosen are representative of a typical phosphocholine (PC) lipid bilayer and the number of lipids in this model bilayer is fixed. The energy penalizing compression of the bilayer is

$$G_{\text{comp}} = \frac{K_A}{2} \int \left(\frac{u(\mathbf{r})}{l} \right)^2 \mathrm{d}^2\mathbf{r}, \tag{2.1}$$

where K_A is the bilayer area stretch modulus ($\sim 58\, k_BT/\text{nm}^2$, k_BT is the thermal energy unit, with $T = 300\, K$) and l is the unperturbed leaflet thickness ($\sim 1.75\,\text{nm}$) [26]. The bending energy of a leaflet is

$$G_{\text{bend}} = \frac{\kappa_b}{4} \int (\nabla^2 u(\mathbf{r}) - c_o)^2 \mathrm{d}^2\mathbf{r}, \tag{2.2}$$

where κ_b ($\sim 14\, k_BT$) is the bilayer bending modulus, c_o is the spontaneous curvature of the leaflet [44, 26, 51], and $\nabla^2 = \partial^2/\partial x^2 + \partial^2/\partial y^2$ is the Laplacian operator.

Coupling external tension to bilayer deformations is more subtle than the previous two energetic contributions. We note that the bilayer is roughly forty times more resistant to volume change than area change [60, 61], hence if a transmembrane protein locally thins the bilayer, lipids will expand in the area near the protein to conserve volume. Likewise, if the protein locally thickens the bilayer, lipids near the protein will condense (see Fig. 2.2). Therefore, the area change near the protein is proportional to the compression $u(\mathbf{r})$, and the work done on the bilayer is the integrated area change multiplied by tension

$$G_{\text{ten}} = \tau \int \frac{u(\mathbf{r})}{l} \mathrm{d}^2\mathbf{r}, \tag{2.3}$$

where τ is the externally applied bilayer tension [56, 62]. Slightly below bilayer rupture, and near the expected regime of MscL gating, $\tau \simeq 2.6\, k_BT/\text{nm}^2$ [21, 26]. In total, the bilayer deformation energy is

$$G = \frac{1}{2} \int \left(K_A \left(\frac{u}{l} + \frac{\tau}{K_A} \right)^2 + \kappa_b \left(\nabla^2 u - c_o \right)^2 \right) \mathrm{d}^2\mathbf{r}, \tag{2.4}$$

where we have made use of the constant bilayer area to elucidate the interplay between tension and compression. Specifically, we added a constant proportional to membrane area and τ^2, which is identically zero when calculating differences in free energy.

To obtain the length and energy scales of these deformations, we non-dimensionalize the bilayer deformation energy, G. We scale both the position $\mathbf{r}$ and displacement $u(\mathbf{r})$ by $\lambda = (\kappa_b l^2/K_A)^{1/4} \simeq$

1 nm, the natural length scale of deformation, to give the new variables $\boldsymbol{\rho}$ and $\eta(\boldsymbol{\rho})$ respectively, where $\boldsymbol{\rho} = \mathbf{r}/\lambda$ and $\eta(\boldsymbol{\rho}) = u(\mathbf{r})/\lambda$. Then G can be written as

$$G = \frac{\kappa_b}{2} \int \left((\eta + \chi)^2 + \left(\nabla^2 \eta - \nu_o \right)^2 \right) \mathrm{d}^2 \boldsymbol{\rho}, \tag{2.5}$$

where $\nu_o = \lambda c_o$ is the dimensionless spontaneous curvature and $\chi = \tau l / K_A \lambda$ is the dimensionless tension, which is $\simeq 0.09$ in the regime of MscL gating. The energy scale is set by the bending modulus, κ_b.

Using the standard Euler-Lagrange equation from the calculus of variations [110], the functional for the deformation energy can be translated into the partial differential equation[2]

$$\nabla^4 \eta + \eta + \chi = 0. \tag{2.6}$$

The deformation profile $u(\mathbf{r})$ that solves this partial differential equation depends on four boundary conditions. In the far-field, we expect the bilayer to be flat and slightly thinner in accordance with the applied tension, *i.e.* $|\nabla u(\infty)| = 0$ and $u(\infty) = -\tau l / K_A$, respectively. At the protein-lipid interface ($\mathbf{r} = r_o$) the hydrophobic regions of the protein and the bilayer must be matched, *i.e.* $u(r_o) = u_o$ (see Fig. 2.2), where u_o is one-half the mismatch between the hydrophobic region of the protein and the hydrophobic core of the bilayer. Finally, the slope of the bilayer at the protein-lipid interface is set to zero (*i.e.* $|\nabla u(r_o)| = 0$). The motivation for this last boundary condition is subtle and will be examined in more detail in the Discussion.

To understand how the deformation energy scales with hydrophobic mismatch (u_o), protein size (r_o), and tension (τ), we solve eqn. 2.6 analytically for a single cylindrical protein. The deformation energy is

$$G_{\text{single}} = \pi \kappa_b \int_{\rho_o}^{\infty} \left((\eta + \chi)^2 + \left(\nabla^2 \eta - \nu_o \right)^2 \right) \rho \mathrm{d}\rho, \tag{2.7}$$

where $\rho_o = r_o/\lambda$ is the dimensionless radius of the protein. The leaflet deformation around a single protein is a linear combination of zeroth order modified Bessel functions of the second kind (K_0) [31, 32]. For proteins such as MscL with a radius larger than λ (*i.e.* 1 nm) the deformation energy is well-approximated by

$$G_{\text{single}} = \pi \kappa_b \left(\frac{u_o}{\lambda} + \frac{\tau}{K_A} \frac{l}{\lambda} \right)^2 \left(1 + \sqrt{2} \frac{r_o}{\lambda} \right). \tag{2.8}$$

The deformation energy scales linearly with protein radius and depends quadratically on the *combination* of hydrophobic mismatch (u_o) and tension (τ). This makes the overall deformation energy particularly sensitive to the hydrophobic mismatch, and hence leaflet thickness l. The deformation energy is fairly insensitive to changes in K_A (*i.e.* most terms in the energy are sublinear), and

[2] With no loss of generality, the equation that governs deformation can also be written in the parameter free form $\nabla^4 \eta + \eta = 0$, with all parametric sensitivity absorbed into the boundary conditions.

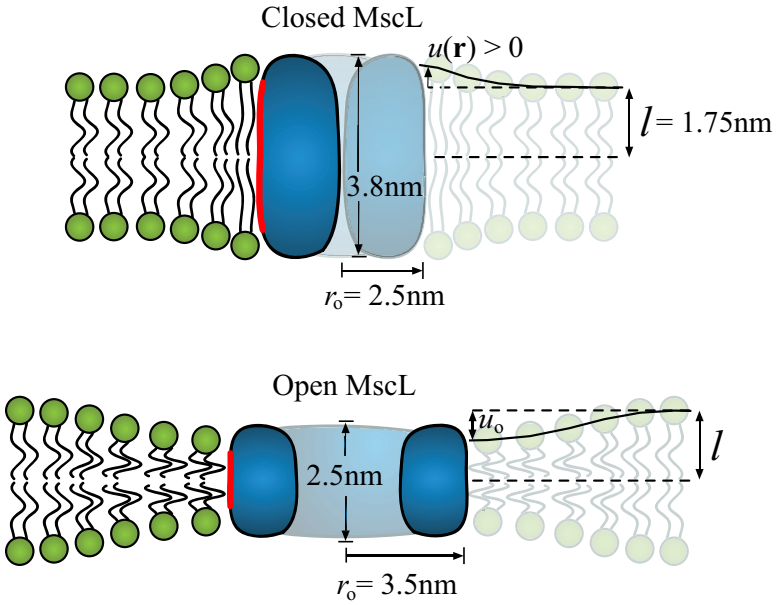

Figure 2.2: Schematic of bilayer deformations due to MscL. Mismatch between the hydrophobic regions of the lipid bilayer and an integral membrane protein gives rise to bending and compression deformations in each leaflet of the bilayer. The largest deformations occur at the protein-lipid interface, and over the scale of a few nanometers the bilayer returns to its unperturbed state. MscL is shown schematically at zero tension in its closed and open states with relevant dimensions. The red region of the protein indicates the hydrophobic zone. The hydrophobic mismatch at the protein-lipid interface is denoted by u_o. The deformation profile, denoted by $u(\mathbf{r})$, is measured with reference to the unperturbed leaflet thickness (l) from the protein center at $\mathbf{r} = 0$.

generally insensitive to changes in the bending modulus since $G \propto \kappa_b^{1/4}$.

Using our standard elastic bilayer parameters and the dimensions of a MscL channel (see Fig. 2.2), the change in deformation energy between the closed and open states is $\Delta G_{\text{single}} \simeq 50\, k_B T$. The measured value for the free energy change of gating a MscL protein, including internal changes of the protein and deformation of surrounding lipids is $\simeq 51\, k_B T$ [23]. This close correspondence does not indicate that bilayer deformation accounts for all of the free energy change of gating [33], but does suggest that it is a major contributor.

The gating energy of two channels in close proximity is a complex function of their conformations and the distance between them. As two proteins come within a few nanometers of each other (*i.e.* a few λ), the deformations which extend from their respective protein-lipid interfaces begin to overlap and interact. The bilayer adopts a new shape (*i.e.* a new $u(\mathbf{r})$), distinct from the deformation around two independent proteins, and hence the total deformation energy changes as well. This is the physical origin of the elastic interaction between two bilayer-deforming proteins [86, 56].

Each protein imposes its own local boundary conditions on the bilayer, that vary with conformation, hence the deformation around a pair of proteins is a function of their individual conformation and the distance between them. A MscL protein has two distinct conformations, hence there can be pairwise interactions between two closed channels, an open and a closed channel, or two open channels (see Fig. 2.3). Tension also affects the deformations. The hydrophobic mismatch can be either positive or negative (*i.e.* the protein can be thicker or thinner than the bilayer), thus tension will strengthen the interaction of proteins that are thicker than the bilayer (*e.g.* the closed-closed interaction of two MscL proteins) and weaken the interaction of proteins that are thinner than the bilayer (*e.g.* the open-open interaction). This effect is demonstrated in Fig. 2.3. The interactions due to leaflet deformations have been explored before [86, 56], but our model elucidates the role that these interactions can play in communicating conformational information between proteins. Additionally, in our model, tension can play an important role in determining the overall deformation energy around a protein.

In a one-dimensional model, the interaction potentials can be solved for analytically. For two identical proteins in close proximity (*e.g.* closed-closed and open-open interactions), the approximate shape of the potential is linearly attractive $\kappa_b(u_o/\lambda)^2(d/2\lambda - \sqrt{2})$. Between two dissimilar proteins in close proximity (*e.g.* open-closed interaction) the potential is approximately $\kappa_b(u_o/\lambda)^2\pi^4/4(d/\lambda)^3$, where in both cases d is measured from the edges of the proteins. This illustrates the general principle that two similar proteins attractively interact, while two dissimilar proteins tend to repel each other. This one-dimensional model helps build intuition for what governs the strength of elastic interactions. Whether the interaction is attractive or repulsive, the strength of the interaction is dominated by its quadratic dependence on the combination of hydrophobic mismatch and tension-induced thinning. Hence, interactions between proteins that deform the membrane more severely are simultaneously more sensitive to tension. These effects are demonstrated in Fig. 2.3 where the closed-closed interaction, which has less hydrophobic mismatch,

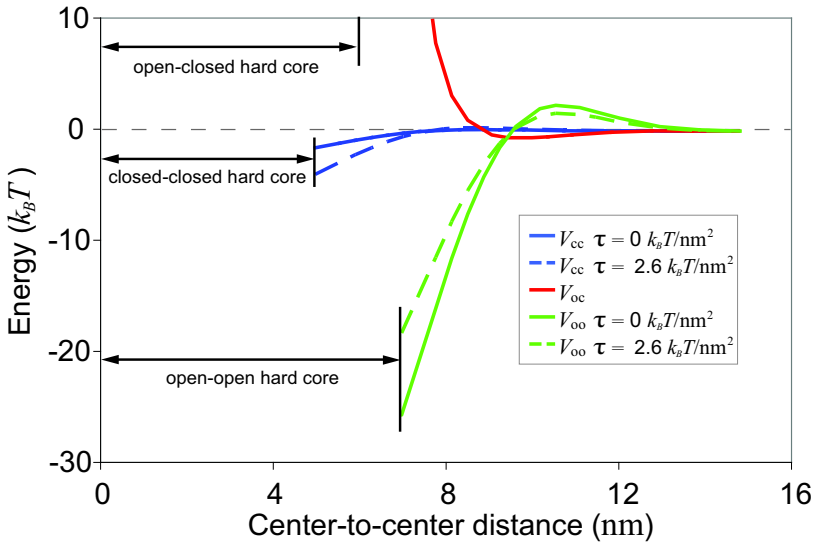

Figure 2.3: Elastic potentials between two MscL proteins. To minimize deformation energy, two transmembrane proteins exert elastic forces on each other. MscL has three distinct interaction potentials between its two distinct conformations. External tension weakens the interaction between two open channels (V_{oo}) and strengthens the interaction between two closed channels (V_{cc}), but has almost no effect on the interaction between an open and closed channel (V_{oc}). The open-open and closed-closed interactions are both more strongly attracting than the open-closed interaction, indicating that elastic potentials favor interactions between channels in the same state. The 'hard core' distance is where the proteins' edges are in contact.

is both weaker and less sensitive to tension than the open-open interaction. In a two-dimensional bilayer, the geometry and boundary conditions of the two proteins makes it difficult to solve for the interaction analytically, thus numerical techniques were used (see Materials and Methods).

This theoretical framework provides a strong foundation for understanding how protein geometries and lipid properties give rise to elastic interactions. With this, we can investigate how elastic forces change the conformational statistics of a two-state protein population.

2.4 Gating Behavior of Two Interacting Channels

To probe the range of separations over which elastic interactions affect the gating of two MscL proteins, we need to account for the non-interacting energetics of gating a single channel in addition to the interactions between two channels. The non-interacting energy is the sum of three effects. First, there is some energetic cost to deform the surrounding membrane, which we already calculated as ΔG_{single}. Second, there is some cost to change the protein's internal conformation, independent of the membrane. Together, these first two effects are the gating energy $\Delta G_{\text{gate}} \simeq 51\, k_BT$ for MscL

[23]. Finally, there is an energetic mechanism that overcomes these costs and opens the channel as tension increases. This mechanism is provided by the bilayer tension working in concert with the conformational area change of the protein ($\Delta A \simeq 20\,\mathrm{nm}^2$ for MscL [23]). Given the experimentally determined values for ΔG_{gate} and the area change during gating, the critical tension, defined by $\Delta G_{\mathrm{gate}} = \tau_c \Delta A$, is $\tau_c = 2.6\, k_B T/\mathrm{nm}^2$.

In our thermodynamic treatment we need to keep track of the conformations of each protein in a population in a way that allows us to tabulate the non-interacting and interacting contributions to the free energy. To this end, we assign a state variable, s_i, to each channel indicating the conformational state of a protein, where $s_i = 0$ indicates that the ith channel is closed and $s_i = 1$ indicates that the ith channel is open. The non-interacting energy for two channels is then

$$H_{\mathrm{non}}(s_1, s_2; \tau) = (\Delta G_{\mathrm{gate}} - \tau \Delta A)\,(s_1 + s_2). \tag{2.9}$$

If both channels are closed ($s_1 = s_2 = 0$) the free energy is defined to be zero. If one channel is open and the other closed ($s_1 = 1, s_2 = 0$ or $s_1 = 0, s_2 = 1$) this counts as the cost to gate one channel working against the benefit at a particular tension to opening the channel. Likewise, this counts twice if both channels are open ($s_1 = s_2 = 1$). We will measure all energies that follow in units of $k_B T$ ($\simeq 4.14 \times 10^{-21} J$).

As we alluded to earlier, the interacting component of the free energy between two channels is a function of their states (s_1 and s_2), their edge separation (d), and the tension. Using a numerical relaxation technique to minimize the functional in eqn. 2.5 (see Materials and Methods), we calculated the interaction potentials $H_{\mathrm{int}}(s_1, s_2, d; \tau)$ for a range of tensions and separation distances (see Fig. 2.3). The total energy, $H_{\mathrm{non}} + H_{\mathrm{int}}$, is used to derive the Boltzmann weight for the three possible configurations of the two-channel system,

$$z(s_1, s_2) = e^{-(H_{\mathrm{non}}(s_1,s_2;\tau) + H_{\mathrm{int}}(s_1,s_2,d;\tau))}. \tag{2.10}$$

The probability that the system has two closed channels is

$$P_0 = \frac{z(0,0)}{Z}, \tag{2.11}$$

where the partition function Z is the sum of the Boltzmann weights for all possible two-channel configurations,

$$Z = \sum_{s_1, s_2 = 0}^{1} z(s_1, s_2) = z(0,0) + 2z(0,1) + z(1,1). \tag{2.12}$$

Likewise, the probabilities for the system to have exactly one or two open channels are

$$P_1 = \frac{2z(0,1)}{Z} \quad \text{and} \quad P_2 = \frac{z(1,1)}{Z}, \tag{2.13}$$

respectively. Finally, the probability for any one channel in this two channel system to be open is

$$P_{\text{open}}(\tau, d) = \frac{z(0,1) + z(1,1)}{Z}. \tag{2.14}$$

If the distance between two channels is much greater than λ, they will behave independently. As the channels get closer ($d \lesssim 5\lambda$) they begin to interact and their conformational statistics are altered. P_{open} as a function of tension for certain fixed separations is shown in Fig. 2.4. The open-open interaction is the most energetically favorable for most separations, hence the transition to the open state generally shifts to lower tensions as the distance between the two proteins is decreased. Though the edge spacing can be small, even fractions of the width of a lipid molecule, the two-dimensional nature of the interaction means that the majority of the interaction is mediated by lipids in the intervening region between the two proteins. Thus, a continuum model is still applicable, albeit less accurate, for very small protein separations.

Interactions also affect channel 'sensitivity', defined as the derivative of P_{open} with respect to tension, which quantifies how responsive the channel is to changes in tension. The full-width at half maximum of this peaked function is a measure of the range of tension over which the channel has an appreciable response. The area under the sensitivity curve is equal to 1, hence increases in sensitivity are always accompanied by decreases in range of response, as demonstrated by the effects of the beneficial open-open interaction on channel statistics (see Fig. 2.4).

In summary, we find that elastic interactions between two proteins have significant effects when the protein edges are closer than $\sim 5\,\text{nm}$. At these separations the elastic interactions alter the critical gating tension and change the tension sensitivity of the channel (see Fig. 2.4). The critical gating tension and sensitivity are the key properties which define the transition to the open state, and are analogs to the properties that define the transition of *any* two-state membrane protein. Hence, we have shown that elastic interactions can affect protein function at a fundamental level.

2.5 Interactions between Diffusing Proteins

With an understanding of how two proteins will interact at a fixed distance, we now study the conformational statistics of two freely-diffusing MscL proteins allowed to interact via their elastic potentials. In biological membranes, transmembrane proteins that are not rigidly attached to any cytoskeletal elements are often free to diffuse throughout the membrane and interact with various lipid species as well as other membrane proteins. On average, the biological areal density of such proteins is high enough ($\sim 10^3 - 10^4\,\mu\text{m}^{-2}$ [91]) that elastic interactions should alter the conformational statistics and average protein separations.

We expect that if two MscL proteins are diffusing and interacting, the open probability will be a function of their areal density as well as the tension. It then follows that for a given areal density, elastic interactions will couple conformational changes to the average separation between

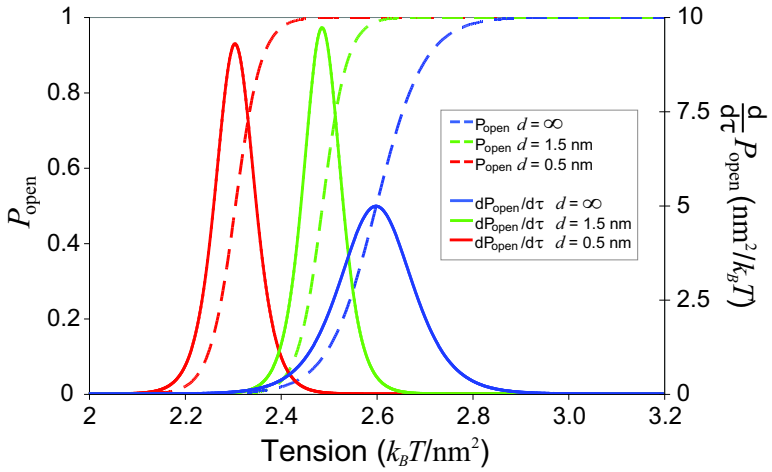

Figure 2.4: Conformational statistics of interacting MscL proteins. Interactions between neighboring channels lead to shifts in the probability that a channel will be in the open state (dashed lines). The sensitivity and range of response to tension, $dP_{open}/d\tau$, are also affected by bilayer deformations (solid lines). P_{open} and $dP_{open}/d\tau$ are shown for separations of 0.5 nm (red) and 1.5 nm (green) with reference to non-interacting channels at $d = \infty$ (blue). Interactions shift the critical gating tension for the closest separation by $\sim 12\%$. Additionally, the peak sensitivity is increased by $\sim 90\%$ from $\sim 5\text{nm}^2/k_BT$ to $\sim 9.5\text{nm}^2/k_BT$, indicating a Hill coefficient of ~ 2.

the proteins. To calculate the open probability of two diffusing MscL proteins, the Boltzmann weight for these proteins to be in the conformations s_1 and s_2 must be summed at every possible position, giving

$$\langle z(s_1, s_2)\rangle = e^{-H_{\rm non}} \int\int e^{-H_{\rm int}} \mathrm{d}^2\mathbf{r}_1 \mathrm{d}^2\mathbf{r}_2, \tag{2.15}$$

where $\langle \ldots \rangle$ indicates a sum over all positions. The distance between the proteins is measured center-to-center as $|\mathbf{r}_1 - \mathbf{r}_2|$ and only the absolute distance between the two proteins determines their interaction, hence we can rewrite the integrand as a function of $r = |\mathbf{r}_1 - \mathbf{r}_2|$. We then change the form of the integrand to

$$e^{-H_{\rm int}(s_1,s_2,r;\tau)} = 1 + f_{12}(r), \tag{2.16}$$

which allows us to separate the interacting effects from the non-interacting effects (the function f_{12} is often called the Mayer-f function) [111]. Thus, the position-averaged Boltzmann weights are

$$\langle z(s_1, s_2)\rangle = e^{-H_{\rm non}} \left(1 + \frac{2\pi}{A}\int_0^\infty f_{12}(r) r \mathrm{d}r\right), \tag{2.17}$$

where A is the total area occupied by the two proteins. Following our previous calculations, the probability that any one channel is open in this two-channel system is

$$P_{\rm open}(\tau, \alpha) = \frac{\langle z(0,1)\rangle + \langle z(1,1)\rangle}{\langle Z\rangle}, \tag{2.18}$$

where α is the protein areal density (*i.e.* $\alpha = 2/A$) and $\langle Z\rangle = \sum_{s_1,s_2} \langle z(s_1, s_2)\rangle$.

In Fig. 2.5a, we plot $P_{\rm open}(\tau, \alpha)$ over a wide range of areal density, from the area of $\sim$ 100 lipids up to areas on the whole-cell scale. The more beneficial open-open interaction tends to shift the transition to the open state to lower tensions, with the most pronounced effect when the two proteins are most tightly confined. For the estimated biological membrane protein density of $\sim 10^3 - 10^4\,\mu\mathrm{m}^{-2}$ (or $\sim 10 - 30\,\mathrm{nm}$ spacing) [91], the gating tension is decreased by $\sim$ 13%, the sensitivity is increased by $\sim$ 85% and the range of response is decreased by $\sim$ 55%. For the *in vivo* expression of MscL of $\sim 1 - 10\,\mu\mathrm{m}^{-2}$ [112] the gating tension is reduced by $\sim$ 7%, the sensitivity is increased by $\sim$ 70% and the range of response is decreased by $\sim$ 40%. These changes in gating behavior are accessible to electrophysiological experiments where MscL proteins can be reconstituted at a known areal density ($\sim 0.1 - 10\,\mu\mathrm{m}^{-2}$), and the open probability can be measured as a function of tension.

In addition to lowering the critical tension and augmenting channel sensitivity, the conformational states of channels are tightly coupled by their interaction. The probability that exactly one channel is open (P_1) decreases dramatically as areal density increases. For tensions above the critical tension, interacting channels ($\sim 10^3\,\mu\mathrm{m}^{-2}$) are nearly three orders of magnitude less likely to gate as single channels than their non-interacting counterparts ($\sim 10^{-3}\,\mu\mathrm{m}^{-2}$), as shown in Fig. 2.5b. Additionally, the tension at which it is more likely to have *both* channels open, rather

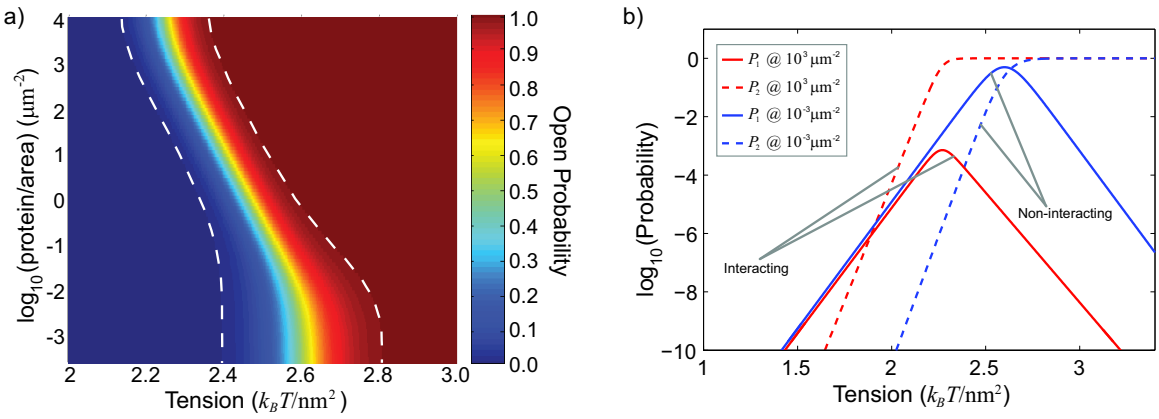

Figure 2.5: Elastic interactions lower the critical gating tension and couple conformation changes. Two MscL proteins in a square box of area A diffuse and interact via their elastic potentials. a) At low areal density, the response to tension is the same as an independent channel. As the areal density increases, the more beneficial open-open interaction (see Fig. 2.3) shifts the open probability to lower tensions and decreases the range of response (dashed lines) while increasing the peak sensitivity, indicating that areal density can alter functional characteristics of a transmembrane protein. b) The probability for exactly one channel to be open (P_1 - solid lines) is shown at a low (blue) and high (red) areal density. For tensions past the critical tension, interacting channels are $\sim$ 1000 times less likely to gate individually. The probability for both channels to be open simultaneously (P_2 - dashed lines) is shown for low (blue) and high (red) areal density. The tension at which two simultaneously open channels are favored is significantly lower for interacting channels. Together these facts signify a tight coupling of the conformational changes for two interacting channels.

than a single channel, is significantly lower for interacting channels, signaling that gating is a tightly coupled process. In addition to altering the open probability of two channels, the favorable open-open interaction provides an energetic barrier to leaving the open-open state. Based on a simple Arrhenius argument, the average open lifetime of two channels that are both open and interacting will be orders of magnitude longer than two open but noninteracting channels.

Having shown conformational coupling over a range of areal densities, it is reasonable to expect that elastic interactions will affect the separation between two proteins. We ask, how do interactions affect the average separation between proteins? How often will we find the two proteins separated by a distance small enough that we can consider them 'dimerized'?

From eqns. 2.15 and 2.16 it follows that the Boltzmann weight for the two proteins to be separated by a distance r is

$$z(s_1, s_2, r) = e^{-H_{\rm non}} \frac{2\pi}{A}(1 + f_{12})r. \tag{2.19}$$

The probability that the proteins are separated by a distance r, regardless of their conformation, is

$$P(r) = \frac{Z(r)}{\langle Z \rangle} = \frac{\sum_{s_1,s_2} z(s_1, s_2, r)}{\langle Z \rangle}, \tag{2.20}$$

from which we calculate the average separation

$$\begin{aligned} \langle r \rangle &= \frac{1}{\langle Z \rangle} \int Z(r) r \mathrm{d}r \\ &= \frac{1}{\langle Z \rangle} \sum_{s_1,s_2} e^{-H_{\rm non}} \left(\delta \frac{\pi}{6} \sqrt{A} + \frac{2\pi}{A} \int_0^\infty f_{12} r^2 \mathrm{d}r \right). \end{aligned} \tag{2.21}$$

This equation is valid as long as the area does not confine the proteins so severely that they are sterically forced to interact. The constant δ is an order-one quantity that is defined by the entropic component of average separation on a surface $\mathcal{S}$, given by $\int \int_{\mathcal{S}(A)} |\mathbf{r}_1 - \mathbf{r}_2| \frac{\mathrm{d}^2\mathbf{r}_1}{A} \frac{\mathrm{d}^2\mathbf{r}_2}{A} = \delta \frac{\pi}{6} \sqrt{A}$, and depends on the actual shape of the surface. For a square box, $\delta \simeq 1$, and for a circle, $\delta \simeq \sqrt{2}$. The average separation of two MscL proteins as a function of tension is plotted for various areal densities in Fig. 2.6. For certain densities, elastic interactions couple the conformational change from the closed to open state with a decrease in the average separation by more than two orders of magnitude. Our estimates of biological membranes yield fairly high membrane-protein densities ($\sim 10^3 - 10^4\,\mu\mathrm{m}^{-2}$) [91] which corresponds to the more highly confined conditions on the Figs. 2.5, 2.6 and 2.7. In the native *E. coli* plasma membrane, MscL, with a copy number of ~ 5 [112], is present at a density of $\sim 1 - 10\,\mu\mathrm{m}^{-2}$, which means that even membrane proteins expressed at a low level are subject to the effects of elastic interactions.

To quantify the effects of interaction on the spatial organization of two channels, we define a 'dimerized' state by the maximum separation below which two channels will favorably interact with an energy greater than $k_B T$ (*i.e.* $H_{\rm int}(s_1, s_2, \tau, r) < -1$). This defines a critical separation, $r_c(s_1, s_2, \tau)$, which depends on the conformations of each protein and the tension. The probability

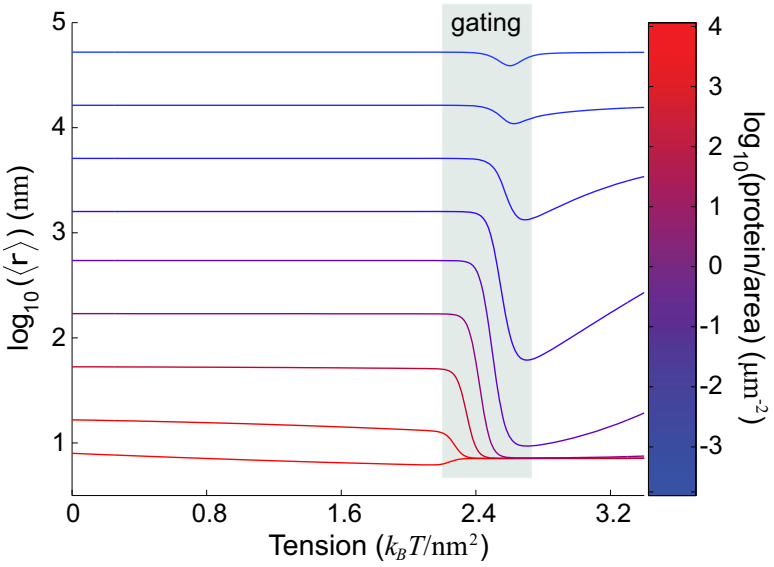

Figure 2.6: Average separation between proteins drops significantly due to elastic interactions. The average separation between two diffusing MscL proteins in a box of area A is plotted as a function of tension for a range of areal densities, each shown as a different line color. The grey region roughly indicates when gating is occurring. At low areal density (most blue) the conformational change does not draw the proteins significantly closer together. As the areal density increases, the conformational change is able to draw the proteins up to $\sim$ 100 times closer than they would otherwise be. At the highest areal density (most red) the steric constraint of available area intrinsically positions the proteins close to one another regardless of their conformation. The average separation begins to increase again as higher tension weakens the open-open interaction.

that the two proteins are found with a separation less than or equal to r_c is

$$P_{\text{dimer}}(\tau,\alpha) = \frac{1}{\langle Z\rangle}\sum_{s_1,s_2} e^{-H_{\text{non}}}\left(\frac{\pi r_c^2}{A} + \frac{2\pi}{A}\int_0^{r_c} f_{12} r \mathrm{d}r\right). \tag{2.22}$$

This 'dimerization probability' is plotted as a function of tension and areal density in Fig. 2.7.

At low tension and high areal density, the channels are closed and near enough that the closed-closed interaction can dimerize them a fraction of the time. Keeping the areal density high, increasing tension strengthens the closed-closed interaction and the dimerization probability increases until tension switches the channels to the open state, where the significantly stronger open-open interaction dimerizes them essentially 100 percent of the time. When the areal density decreases to moderate levels, as denoted by the white dashed lines in Fig. 2.7, the dimerization is strongly correlated with the conformational change to the open state. The zero tension separation between the two proteins for this one-to-one correlation is $\sim$ 40 nm to $\sim$ 2 μm. Finally, when the areal density is very low, entropy dominates, and neither the closed-closed, nor the open-open interaction is strong

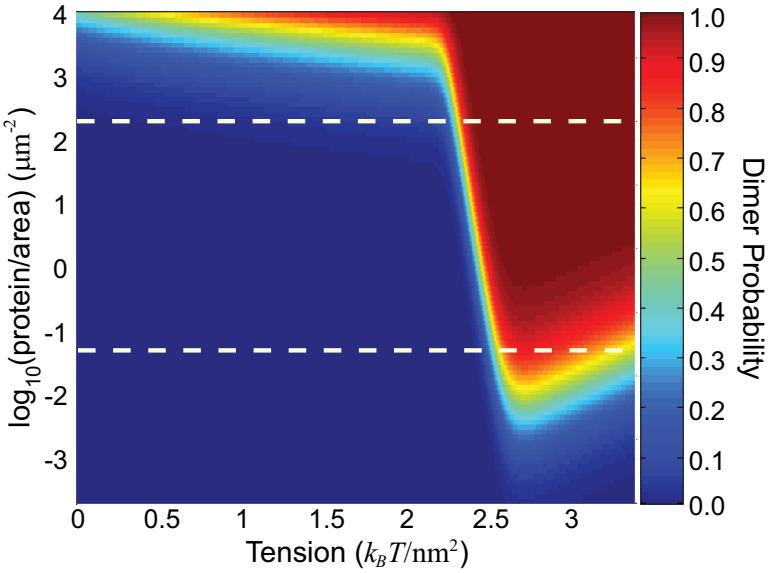

Figure 2.7: Elastic interactions tightly couple conformational change with protein dimerization. Diffusing MscL proteins are considered dimerized when they are close enough that they attract with an energy greater than k_BT. At high areal density, the net attractive closed-closed interaction is sufficient to dimerize the two channels part of the time. As the areal density decreases, the closed-closed interaction is not strong enough to dimerize the two channels — now dimerization only happens at higher tensions after both channels have switched to the open conformation. As the areal density decreases further, the open-open interaction is no longer strong enough to overcome entropy. This loss of dimerization is amplified by the fact that the open-open interaction is weaker at higher tensions (see Fig. 2.3). The white dashed lines roughly indicate the range of areal densities for which dimerization probability and open channel probability are equal to each other (see Fig. 2.5).

enough to dimerize the channels. Understanding the onset and stability of dimers is an important first step in understanding the formation of larger oligomers of membrane proteins. As the areal density of membrane proteins increases, clusters of more than two proteins become favorable and are energetically stabilized by their multi-body interactions. For a rigorous theoretical treatment of these multi-body interactions we refer the interested reader to [113, 114, 115].

In summary, we have shown that over a broad range, areal density plays a non-trivial role in allowing two channels to communicate conformational information. This communication can lead to large changes in the average separation between two proteins and the probability that they will be found together in a dimerized state. This may have implications for how conformational changes of transmembrane proteins in biological membranes are able to facilitate the formation of functional groups of specific proteins.

2.6 Further Discussion

In this section, we will perform a brief survey of other bilayer-mediated forces between proteins and make a comparison of their relative length and energy scales. We will also address some of the finer details of our model and how boundary conditions can affect deformation energy around a protein. Finally, we will suggest experiments using MscL to observe the predicted changes in conformational statistics, as well as provide evidence from previous experiments that leaflet interactions lead to significant changes in conformational statistics.

2.6.1 Comparison to Other Interactions

There are at least two other classes of purely bilayer-mediated forces between membrane proteins. The first is a different type of bilayer deformation that bends the mid-plane of the bilayer. This arises from transmembrane proteins with a conical shape that impose a bilayer slope at the protein-lipid interface [30, 84]. If the protein does not deform the bilayer too severely, the mid-plane deformation energy of a bilayer is

$$G_{\rm mid} = \int \left(\frac{\tau}{2} (\nabla h(\mathbf{r}))^2 + \frac{\kappa_b}{2} (\nabla^2 h(\mathbf{r}))^2 \right) \mathrm{d}^2\mathbf{r}, \tag{2.23}$$

where $h(\mathbf{r})$ is the deviation of the height of the mid-plane from a flat configuration [32, 46]. These kinds of interactions have been calculated for a variety of bilayer curvature environments and protein shapes at zero [84, 116] and positive [117] tension. Using a bilayer bending modulus of $\sim 100\, k_B T$, attractive interactions of order $\sim 1-5\, k_B T$ were found when the proteins were separated by $1-2$ protein radii (which we estimate to be $5-10\,$nm measured center-to-center for a typical transmembrane protein). If we adjust the energy scale to be consistent with a PC bilayer bending modulus of $\sim 14\, k_B T$ this lowers the interaction energetics to $\sim 0.4-2\, k_B T$. Hence, although the length scale of appreciable interaction for mid-plane deformation is longer than for leaflet deformation, the interaction energies from leaflet deformation can be 10 times greater depending on protein geometry. The deformation fields $h(\mathbf{r})$ and $u(\mathbf{r})$ exert their effects independent of one another [32], suggesting that while energetically weaker than leaflet deformation, mid-plane deformation probably also contributes to the spatial organization and conformational communication between transmembrane proteins. However, for the resting tension of many biological membranes [13], the interaction due to midplane deformation has a length-scale ($\sqrt{\kappa_b/\tau} \simeq 50\,$nm) longer than the nominal spacing of proteins ($\simeq 10-30\,$nm [91]). Thus, one protein can shield other proteins from feeling the deformation of a neighboring protein, and hence interactions are not (in general) pairwise additive. In fact, this is a general feature for both leaflet and midplane elastic interactions — they can be shielded by the presence of other proteins, and non-specific protein interactions can couple to conformation and position within the membrane in the same manner as the specific interactions we have explored in the previous sections.

The second class of bilayer-mediated forces is a product of the thermal fluctuations of the bilayer.

There is a small thermal force due to the excluded volume between two proteins, calculated via Monte Carlo methods to have a favorable $\sim 2\,k_BT$ interaction [93]. This force only exists when the proteins are separated by a fraction of the width of a lipid molecule. There is also a long-range thermal force, due to the surface fluctuations of the bilayer, which tends to drive two rigid proteins closer together [85, 92]. This force is proportional to $1/r^4$ and is generally attractive. Estimates using this power law indicate that the interaction is $\sim 1\,k_BT$ when the center-to-center separation is roughly 2 protein radii. Though elegant, the derivation of this force is only valid in the far-field, thus how this force might contribute to conformational communication between proteins in close proximity is not entirely clear.

To gauge the overall importance of leaflet interactions, the virial coefficient used in eqn. 2.17,

$$C_V = 2\pi \int_0^\infty f_{12}(r) r \mathrm{d}r, \tag{2.24}$$

quantifies how the combination of length and energy scales leads to a deviation from non-interacting behavior; it is *exponentially* sensitive to the energy but only *quadratically* sensitive to the length-scale. One can interpret the virial coefficient as the area per particle that makes the competing effects of entropy and interaction equivalent. Using this measure, we estimated the virial coefficients for all of these bilayer-mediated forces and found that leaflet deformations, while having a short length scale, actually lead to the most significant deviation from non-interacting behavior, due to their high energy scale. We estimate the virial coefficients from leaflet interactions to be $\sim 10^4 - 10^6\,\mathrm{nm}^2$, while mid-plane bending interactions are $\sim 10^3\,\mathrm{nm}^2$, and the thermal forces $\sim 10^2\,\mathrm{nm}^2$.

2.6.2 Role of Elastic Boundary Conditions

Examining our elastic model in greater detail, we have assumed that the slope of the leaflet at the protein-lipid interface is zero, which eliminates any dependence on the spontaneous and Gaussian curvatures of the leaflet. In a more general continuum-mechanical theory, the slope would be left as a free parameter with respect to which the energy could be minimized [31]. We examined this possibility and found that, at most, the energy was reduced by a factor of two. Spontaneous curvature couples to the slope of the leaflet at the protein-lipid interface, however the spontaneous curvature of bilayer forming lipids, such as phosphocholines, is small [57]. In addition, for proteins whose radius is larger than λ, if we assume the modulus associated with Gaussian curvature is of the same magnitude as the mean curvature modulus (κ_b) [118], the Gaussian contribution to the deformation energy is a second-order effect. We also examined the possibility of a term proportional to $(\nabla u)^2$; using the interfacial tension ($\sim 5\,k_BT/\mathrm{nm}^2$) as a modulus for this term, these effects were also second-order. Finally, we imposed the 'strong hydrophobic matching' condition at the protein-lipid interface, assuming that the interaction of lipids with the hydrophobic zone of the protein is very favorable. Relaxing this condition would result in a decrease in the magnitude of the hydrophobic matching condition, u_o, and hence an overall decrease in energetics [32].

There are also experimental and mechanical reasons to believe the boundary slope on a cylindrical protein is small. The membrane protein gramicidin was used to comment on this so-called 'contact angle' problem of lipid-protein boundary conditions [29, 119]. It was found that indeed the slope was nearly zero. From a mechanical standpoint, if the lipids are incompressible, a positive boundary slope that deviates significantly from zero would correspond to the creation of an energetically costly void at the protein-lipid interface when the protein is shorter than the bilayer. Conversely, lipid would have to penetrate the core of the protein to produce a negative slope when the protein is taller than the bilayer, again a very costly proposition.

We examined a roughly cylindrical protein and demonstrated the interesting effects elastic interactions would have in such cases. However, the scope of possible effects increases when non-cylindrical proteins are considered. Most notably, non-cylindrical cross-sections allow for orientational degrees of freedom in the interaction, hence such proteins do not just attract or repel each other, but would have preferred orientations in the membrane with respect to each other. Efforts are underway to understand the nature of these shape-dependent interactions, specifically what torques proteins exert on each other, how to encode specificity of interaction through shape, what effects monomer shape has on the assembly of oligomeric membrane proteins.

2.6.3 Effects of Spontaneous Curvature

While there are good reasons to believe that the slope of the bilayer deformation profile is small at the cylindrical protein-bilayer interface, as discussed in the previous section, it behooves to have a better understanding of how energetics and membrane conformation change as we relax this condition. For simplicity, we will examine this in the one dimensional setting, which is a valid framework when the protein radius is larger than the elastic decay length (as it is for MscL). Written in one dimension, the free energy of bilayer thickness deformation is

$$G = \pi\kappa_b\rho_o \int_{\rho_o}^{\infty} \left((\eta + \chi)^2 + \left(\eta'' - \nu_o\right)^2 \right) \mathrm{d}\rho \tag{2.25}$$

akin to eqn. 2.5. Solving the resulting Euler-Lagrange equation, subject to the boundary conditions $\eta(\rho)|_{\rho=\rho_o} = \eta_o$ and $\eta'(\rho)|_{\rho=\rho_o} = \epsilon$, gives the one dimensional thickness deformation profile,

$$\eta(\rho) = e^{-\frac{\rho-\rho_o}{\sqrt{2}}} \left((\eta_o + \chi)\cos\left(\frac{\rho-\rho_o}{\sqrt{2}}\right) + (\eta_o + \chi + \epsilon\sqrt{2})\sin\left(\frac{\rho-\rho_o}{\sqrt{2}}\right)\right) - \chi, \tag{2.26}$$

which can then be substituted into this functional to find the deformation energy, where we leave the boundary slope, ϵ, as a free parameter. The resulting deformation energy, with spontaneous curvature included is

$$G = \sqrt{2}\pi\kappa_b\rho_o \left((\eta_o + \chi)^2 + \epsilon(\epsilon + \sqrt{2}(\eta_o + \chi + \nu_o)) \right). \tag{2.27}$$

Note that if the boundary slope is set to zero, the deformation energy does not depend on the spontaneous curvature. Minimizing this free energy with respect to the boundary slope, that is $\partial G/\partial\epsilon = 0$, gives the an equation for the minimum energy boundary slope, which can be solved to find

$$\epsilon_{\min} = -\frac{1}{\sqrt{2}}\left(\eta_o + \chi + \nu_o\right). \tag{2.28}$$

This can then be substituted into the free energy of eqn. 2.27, to find the boundary slope minimized deformation energy

$$G_{\min} = \sqrt{2}\pi\kappa_b\rho_o\left((\eta_o+\chi)^2 - \frac{1}{2}(\eta_o+\chi+\nu_o)^2\right). \tag{2.29}$$

In the absence of spontaneous curvature, we see that the slope-minimized deformation energy is precisely one half the deformation energy calculated when setting the boundary slope equal to zero. For the moment, let us presume that the dimensionless spontaneous curvature is small, and hence the contribution to the deformation free energy from spontaneous curvature is approximately linear and of the form

$$G_{\text{spc}} \simeq -\sqrt{2}\pi\kappa_b\rho_o\nu_o(\eta_o+\chi). \tag{2.30}$$

Measurements of the spontaneous curvature in the HII phase of lipid monolayers [58] vary with bilayer composition, but a good approximate value for bilayer forming lipids is $\nu_o \simeq 0.1$. Recall that we assume the deformation is weak, that is $(\eta_o + \chi)$ is small, and hence the elastic energy terms that include spontaneous curvature and those that do not, are both of the same order of magnitude. Hence, if the monolayer slope at the protein-bilayer interface is allowed to freely vary, we expect the monolayer spontaneous curvature to further reduce the thickness deformation energy by an amount comparable to the magnitude of the spontaneous curvature independent deformation energy. Taken together, allowing the slope to vary, and possibly including monolayer spontaneous curvature, both reduce the severity of the deformation profile, and hence we expect that they reduce the magnitude of the bilayer mediated elastic interactions between proteins.

We can also use this one dimensional analysis to comment on whether the low gradient limit ($|\nabla\eta| < 1$) is valid. Using eqn. 2.26 for the thickness deformation profile, the position of the maximum monolayer slope is given by

$$\frac{\partial^2\eta}{\partial\rho^2} = 0, \tag{2.31}$$

which can be solved to find

$$\rho_{\max} = \rho_o + \sqrt{2}\tan^{-1}\left(\frac{\eta_o+\chi+\sqrt{2}\epsilon}{\eta_o+\chi}\right). \tag{2.32}$$

In the scenario where $\epsilon = 0$, the deformation profile's maximum slope is at $\rho_{\max} = \rho_o + \frac{\pi}{2\sqrt{2}}$, which

when substituted into $\partial\eta/\partial\rho$, gives the maximum slope

$$\left|\frac{\partial\eta}{\partial\rho}\right|_{\max} = |\eta_o + \chi| e^{-\frac{\pi}{4}}. \tag{2.33}$$

Even with the large hydrophobic mismatch of MscL, $|\eta_o + \chi| \leq 0.6$, the maximum boundary slope is only $\left|\frac{\partial\eta}{\partial\rho}\right|_{\max} \simeq 0.27$, indicating that our approximation is likely valid when $\epsilon = 0$. In the scenario where the energy is minimized with respect to the boundary slope, the position of the maximum slope is given by

$$\rho_{\max} = \rho_o - \sqrt{2}\tan^{-1}\left(\frac{\nu_o}{\eta_o + \chi}\right), \tag{2.34}$$

where it should noted that if $\nu_o/(\eta_o + \chi) > 0$, the maximum monolayer slope occurs at the protein-lipid interface, that is $\rho_{\max} = \rho_o$; alternatively stated, this equation is not valid for $\nu_o/(\eta_o + \chi) > 0$. However, if $\nu_o/(\eta_o + \chi) < 0$, this can be substituted into $\partial\eta/\partial\rho$ to find a general expression for the maximum monolayer slope,

$$\left|\frac{\partial\eta}{\partial\rho}\right|_{\max} = \sqrt{\frac{(\eta_o + \chi)^2 + \nu_o^2}{2}} \cdot e^{\tan^{-1}\left(\frac{\nu_o}{\eta_o + \chi}\right)}. \tag{2.35}$$

If the spontaneous curvature is zero, then $\rho_{\max} = \rho_o$, and the maximum slope is

$$\left|\frac{\partial\eta}{\partial\rho}\right|_{\max} = \frac{|\eta_o + \chi|}{\sqrt{2}}, \tag{2.36}$$

where using the upper bound $|\eta_o + \chi| \leq 0.6$, this gives the maximum profile slope $\left|\frac{\partial\eta}{\partial\rho}\right|_{\max} = 0.42$. Finally, evaluating the maximum slope for the estimated value of spontaneous curvature $\nu_o \simeq 0.1$ and the upper bound hydrophobic mismatch of MscL, we find $\left|\frac{\partial\eta}{\partial\rho}\right|_{\max} = 0.49$ if $\nu_o/(\eta_o + \chi) > 0$, and $\left|\frac{\partial\eta}{\partial\rho}\right|_{\max} = 0.36$, if $\nu_o/(\eta_o + \chi) < 0$. While these last three results have slightly higher maximum slopes than the $\epsilon = 0$ case, they still suggest that we are within reasonable bounds to calculate the thickness deformation energy using a low gradient approximation.

2.6.4 Implications of Bilayer Volume Conservation

When examining the mechanics of bilayer deformations around a channel, we considered the bilayer to be a volume preserving material. In the first part of this section, we quantitatively show that this is the case, using values of the isothermal compressibility of bilayers [60, 61], the area stretch modulus, and bilayer thickness [26]. Imagine we compress the bilayer thickness by an amount u and ask the question — given the elastic parameters, does the bilayer preserve volume and hence change area, or does the area remain relatively constant at the cost of changing volume? If volume is preserved, the area change of the membrane will be proportional to the compression u. Indeed, this was the model espoused throughout this work, but we can be more explicit as to why it is a good approximation.

Consider a patch of membrane with undeformed area A_o and undeformed volume V_o. We write the change in patch area as

$$\Delta A = A_o - A, \tag{2.37}$$

and the change in patch volume as

$$\Delta V = A(l + u) - A_o l. \tag{2.38}$$

Treating the bilayer as a linear elastic material, the energy in both area changing and volume changing deformation modes is a quadratic function of the strain in both modes, written as

$$G_{\text{vol}} = \frac{B}{2}\left(\frac{\Delta V}{V_o}\right)^2 V_o + \frac{K_A}{2}\left(\frac{\Delta A}{A_o}\right)^2 A_o, \tag{2.39}$$

where $K_A \simeq 60\, k_B T/\text{nm}^2$ is the area stretch modulus [26] and $B \simeq 2\,\text{GPa}$ is the bulk modulus of a typical bilayer known from previous measurements [60, 61]. Equation 2.39 can be rearranged into a dimensionless form, written as

$$G_{\text{vol}} = \frac{K_A A_o}{2}\left[f\left(\frac{\Delta V}{V_o}\right)^2 + \left(\frac{\Delta A}{A_o}\right)^2\right], \tag{2.40}$$

where the dimensionless material constant $f = \frac{Bl}{K_A}$ is a relative measure of the area compressibility and volume compressibility – if this value is greater than one, area change is the preferred mode of deformation, if the values is less than one, volume change is the preferred mode of deformation. With the aforementioned values of the elastic constants $f \simeq 40$. Using eqn. 2.37 and 2.38, we can rewrite the patch deformation free energy as a function of patch area

$$G_{\text{vol}} = \frac{K_A A_o}{2}\left[f\left(\frac{A}{A_o}(1+\mu) - 1\right)^2 + \left(\frac{A}{A_o} - 1\right)^2\right] \tag{2.41}$$

where the dimensionless constant $\mu = u/l$ is simply a normalized value of the compression. This free energy is then minimized with respect to the only variable, the patch area A, to find

$$\left(\frac{A}{A_o}\right)_{\text{min}} = \frac{f(1+\mu)+1}{f(1+\mu)^2+1} \tag{2.42}$$

In this same notation, the areal strain is written as

$$\frac{\Delta A}{A_o} = \left(\frac{A}{A_o}\right)_{\text{min}} - 1 \tag{2.43}$$

and the volumetric strain is written as

$$\frac{\Delta V}{V_o} = \left(\frac{A}{A_o}\right)_{\text{min}} (1+\mu) - 1. \tag{2.44}$$

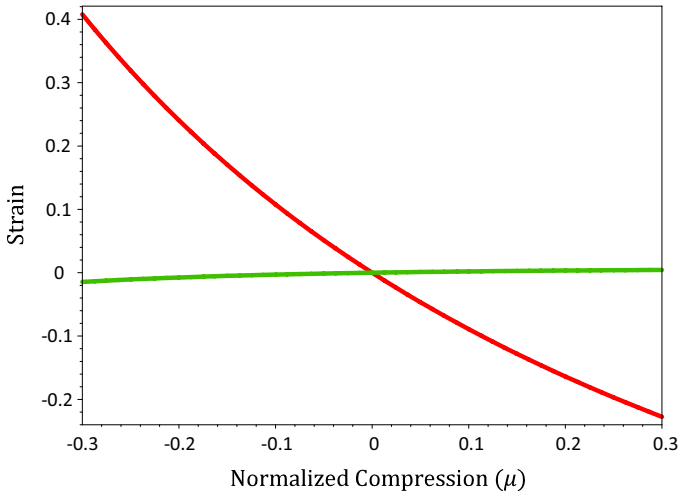

Figure 2.8: Comparison of areal and volumetric strain. Upon compressing a bilayer patch by an amount μ, the bilayer both changes volume and area, however the bilayer thickness, stretch modulus, and bulk modulus conspire to conserve volume and allow the membrane to change area, as shown by the relatively small volumetric strain (green) and the relatively large areal strain (red).

Finally, we are in a position to quantitatively comment on the way area and volume of a bilayer patch change with compression μ. It is likely that MscL represents a protein whose structural change is accompanied by a severe change in membrane thickness. As we showed earlier, the anticipated compression in the open state is $\mu \simeq 0.3$, and hence we plot the areal and volumetric strain over a range of $-0.3 < \mu < 0.3$, as shown in Fig. 2.8, demonstrating that under bilayer compression, volume is conserved and area is not.

The fact that bilayer is generally volume conserving has implications for our understanding of mechanosensation in general. Up until now, we modeled single channel gating statistics by the equation

$$P_{\text{open}} = \frac{1}{1 + e^{(\Delta G_{\text{mem}} + \Delta G_{\text{prot}} - \tau \Delta A)}} \tag{2.45}$$

where here ΔA refers to the change in channel area upon gating, ΔG_{mem} is the component of the free energy change from membrane deformation, and ΔG_{prot} is the component from internal changes in the protein itself. However, operating under the assumption of volume conservation, we derived the bilayer deformation free energy

$$G_{\text{single}} = \pi \kappa_b \left(\frac{u_o}{\lambda} + \frac{\tau}{K_A} \frac{l}{\lambda} \right)^2 \left(1 + \sqrt{2} \frac{r_o}{\lambda} \right) \tag{2.46}$$

in eqn. 2.8. Expanding the term in parentheses we find both a linear and quadratic term in bilayer tension. Considering that $l/\lambda = O(1)$ and $\tau/K_A \ll 1$, only the linear term is important for our energetic analysis. The linear term can be interpreted as the component of the free energy that is

due to the area change of the *lipids* surrounding the protein, and not the protein itself. Consider the free energy change for a cylindrical protein whose hydrophobic mismatch has an initial value $u_o^{(i)}$ and final value $u_o^{(f)}$ and, for simplicity, whose radius is constant. In addition to the expected term that is quadratic in u_o/λ, there is a term linear in the tension, given by

$$\Delta G_{\text{linear}} = \tau \cdot \underbrace{2\pi \frac{\kappa_b l}{K_A \lambda^2} \left(1 + \sqrt{2}\frac{r_o}{\lambda}\right) \left(u_o^{(f)} - u_o^{(i)}\right)}_{\text{lipid area change}}, \tag{2.47}$$

that corresponds to the area change of the lipids surrounding the protein. Thus the perceived area change during an experiment is partly composed of a change in the area of the protein, and partly composed of a change in the area of the lipids surrounding the protein. This means that changing bilayer thickness changes both the tension independent contribution to the gating free energy, and adds a tension dependent contribution that depends on the bilayer thickness relative to the change in hydrophobic thickness of the protein. Hence we would expect that changing bilayer thickness changes not only the nominal gating tension of the channel, but also adjusts the sensitivity to tension upon gating, that is, the slope of the P_{open} curve. Indeed, the experiments by Perozo *et al.* [22] showed both of these effects, a decrease in gating tension and corresponding decrease in channel sensitivity. The change in sensitivity, and hence change in total gating area, was somewhat unexpected because the open state conductance properties and hence open state area were identical regardless of bilayer thickness — alternatively stated — if open state structure is essentially the same, why would the perceived area change with lipid thickness? The simple argument presented here qualitatively explains these results, however, experiments that measure the membrane tension itself (as opposed to the trans-patch pressure), as well as more precise information about channel structure, would be needed to make a quantitative comparison with this theoretical insight.

2.6.5 Experimental Examples of Bilayer Mediated Interactions

Measuring the changes in conformational statistics of two MscL proteins held at a fixed separation would allow for quantitative verification of our predictions. Electrophysiology is a common tool used to probe the conformation of ion channels, and is routinely used to measure the open probability of a single MscL protein *in vitro* [21, 23, 22]. Cysteine point mutations on the outer edges of two MscL proteins [48] could be covalently linked [120, 121, 122, 123] by a polymer with a specific length ($\sim 0.5 - 10\,\text{nm}$) to control the separation distance [124, 125]. Linking stoichiometry could be controlled genetically [126] to ensure one channel interacts with only one other channel.

Similar experiments have been performed using gramicidin A channels [88]. The conducting form of gramicidin A is a cylindrical transmembrane protein which, like MscL, tends to compress the surrounding bilayer [29, 44, 127] and hence have a beneficial interaction. Electrophysiology of polypeptide-linked gramicidin channels [88] qualitatively supports our hypothesis that the beneficial interaction of the deformed lipids around two gramicidin channels significantly increases the

lifetime of the conducting state [128]. As another example, recent FRET studies showed that oligomerization of rhodopsin is driven by precisely these kinds of elastic interactions, and exhibits a marked dependence on the severity of the deformation as modulated by bilayer thickness [90]. Additionally, recent experimental work has shown that the bacterial potassium channel KscA exhibits coupled gating and spatial clustering in artificial membranes [89].

In summary, we have demonstrated that leaflet deformations are one of the key mechanisms of bilayer-mediated protein-protein interactions. We provided support for our choice of boundary conditions at the protein-lipid interface, and suggested that extensions of our model for non-cylindrical shape have exciting possibilities for the specificity of elastic interaction. Finally, we suggested how one might measure the predicted changes in conformational statistics and drew an analogy to previous gramicidin channel experiments.

2.7 Computational Methods

To compute the pairwise elastic potentials in Fig. 2.3, we discretize the bilayer height, $\eta(\rho)$, and minimize the deformation energy in eqn. 2.5 using a preconditioned conjugate gradient approach. A separate minimization with the aforementioned boundary conditions, including the zero-slope boundary condition, was computed for each combination of channel configurations, protein-protein separation, and bilayer tension. Except in the regions of the bilayer nearby a protein at position (x_o, y_o), we use a Cartesian grid with spacing $dx = dy = 0.1\lambda = 0.093\,\text{nm}$. However, since deformations in the bilayer are largest at the circular membrane-protein interface, we interpolate between a polar grid at the interface at $\mathbf{r} = r_o$ and a Cartesian grid along the square $\mathcal{S}$ defined by $|x - x_o| < \Delta, |y - y_o| < \Delta$, where Δ is chosen to be an integral multiple of dx. This interpolation ensures an accurate estimate of the elastic deformation energy of a single protein and preserves the symmetry of the protein in its immediate vicinity.

The lines connecting the grid points along $\mathcal{S}$ define n_θ angular grid points θ_i $(i = 1, \ldots, n_\theta)$, and $n_r + 1$ grid points within the interpolation region are defined by the polar coordinates $(r_{ij}, \theta_i) = (r_o + \delta r_i j/n_r, \theta_i)$, where r_o is the radius of the protein and the distance from the center of the protein to $\mathcal{S}$ along θ_i is $r_o + \delta r_i$ (*e.g.*, for $\theta_i = 0$, $\delta r_i = \Delta - r_o$; for $\theta_i = \pi/4$, $\delta r_i = \Delta\sqrt{2} - r_o$. For a protein in the open or closed configuration, Δ was chosen such that $n_\theta = 320$ or 224, respectively.

The deformation energy determined using this numerical relaxation method is converged with respect to dx, Δ and the overall dimensions of the bilayer ($18.5\,\text{nm} \times 37.1\,\text{nm}$), and reproduces the analytic results for a single protein given by eqn. 2.8. The elastic potentials were determined over the relevant range of channel separations from 0 to $\sim 8\,\text{nm}$ (measured from protein edge to protein edge), and for a range of bilayer tensions from 0 to $3.4\,k_BT/\text{nm}^2$.

2.8 Accession Number and Acknowledgments

The primary accession numbers (in parentheses) from the Protein Data Bank (http://www.pdb.org) are: mechanosensitive channel of large conductance (2OAR; formerly 1MSL), gramicidin A ion channel (1GRM), bacterial potassium ion channel KscA (1F6G), and bovine rhodopsin (1GZM).

We would like to thank Doug Rees, Olaf Andersen, Pierre Sens, Sergei Sukharev, Nily Dan, Jennifer Stockdill, and Ned Wingreen for their thoughtful comments on this work, Chris Gandhi for his input into possible experiments, Ben Freund for useful discussion.

2.9 Summary of Bilayer-Mediated Interactions

In the first part of this chapter, we described the important role of an elastic bilayer in the function of, and communication between, membrane proteins. The interplay between the length scale of interaction (a few nanometers) and the energetics of interaction (on the order of $10k_BT$) mean elastic interactions are relevant over a wide range of areal densities; from protein separations on the order of nanometers up to a micron or more. Transmembrane proteins can communicate information about their conformational state via the deformations they cause in the surrounding bilayer. We demonstrated with a model protein, the tension-sensitive channel MscL, how deformations lead to elastic forces and result in cooperative channel gating. Additionally, we found that elastic interactions strongly correlate conformational changes to changes in spatial organization, aggregating two channels even at low areal densities, and hence bringing them together over very large distances relative to their size.

The elastic theory presented here can be easily expanded to include more complex deformation effects (such as spontaneous curvature) and protein shapes, and is applicable to any protein which causes thickness deformation in the membrane. Our calculations for the conformational statistics, average separation, and dimerization are insensitive to the actual stimulus triggering the conformational change. Hence, we suggest that elastic interactions are likely to play a role in the function and organization of many membrane proteins which respond to environmental stimuli by forming functional groups of multiple membrane proteins. Recent work suggests chemotactic receptors in *E. coli* function by precisely this kind of spatially clustered and conformationally coupled modality [129].

2.10 Non-Specific Interactions from Crowding

In this section we explore how protein crowding and phase separation [130] affect the way that proteins laterally organize. Our previous discussions in this chapter focused on specific interactions between proteins that are mediated by bilayer mechanics. In a mechanism similar to how crowding in the cytosolic environment affects chemical reactions and equilibria [131, 132], we hypothesize that there may be important effects from protein and lipid crowding in a membrane environment,

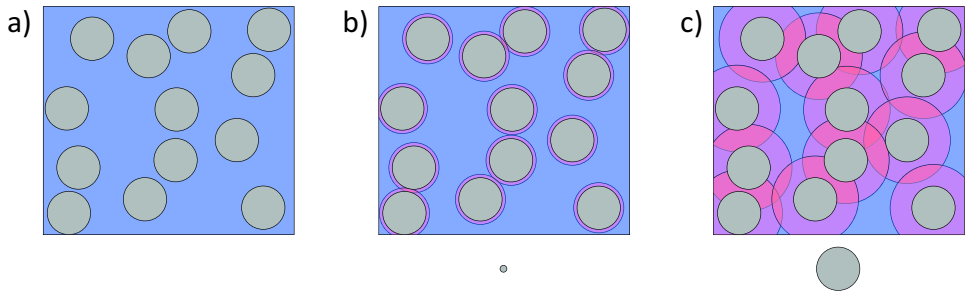

Figure 2.9: Depictions of crowding and depletion zones in two dimensions. a) A crowded arrangement of discs (gray) in a finite area (blue). b) The same discs as in (a), now with small red zones around each disc showing the excluded zone for the particle shown just under the box. The relative sizes here reflect the different between the area of lipids and nominal membrane proteins. c) The same discs as in (a), now with red zones around each disc showing the excluded zone for the particle shown just under the box. The relative sizes here reflect crowding of membrane proteins by membrane proteins. The red zones indicate regions where another crowding particle cannot enter, and in regions where red zones overlap, other crowding particles are completely excluded.

as shown schematically in Fig. 2.9, where the density of proteins is such that neighboring proteins are generally within a few nanometers of each other [91]. In fact, during the composition of this thesis, new and interesting research on the effects of membrane protein crowding was published [133], and advocated for a more systematic look at the effects of crowding in membranes. We will discuss in detail the effects of 'ideal' crowding, that is, crowding from a dilute 'gas' of proteins, as well as some approximate schemes for handling weakly non-ideal crowding. As we show in the following few subsections, the statistical mechanical ensemble one chooses significantly affects how crowding tension in the membrane exerts its effect.

First, consider what general forces are at work that give a lipid bilayer its coarse structure. Hydration energy of the lipid tails, though arguably due to the reduction in entropy of water when in contact with those tails [134], is essentially an enthalpic effect that causes lipids to aggregate. The smectic nature of the liquid crystal is due to its amphiphilic qualities, but again is generally an enthalpic effect [57]. Once the lipids have aggregated into a smectic liquid crystal, the tails themselves entropically explore space similar to a worm like chain polymer [57], and hence push against the surrounding tails to gain volume in which to wander around. The result is a competition between this tail entropy, which prefers more area per lipid, and the hydration forces, that assemble a membrane into a structure with minimum surface free energy, and a well defined area per lipid molecule. From this energetic competition the membrane is able to support lateral tension. We discuss the course structure of a bilayer to build intuition for why lipids do not simply form a molecular gas when in an aqueous solution, and by way of contrast to the two dimensional gas of

membranes we are about to discuss, that exist in the bilayer itself.

2.10.1 Ideal Crowding Tension

Consider a nearly spherical vesicle[3] with total area A and a dilute (ideal) solution of N membrane proteins embedded within it. The proteins' sampling of configuration space includes the entire metric area of the membrane, which we denote as A, as opposed to some flat plane projection of that metric area. The partition function is then

$$Z = A^N, \tag{2.48}$$

where we have neglected the factor of $1/N!$, because it does not affect our calculations. Then the free energy due to entropy is

$$G_{\text{ideal}} = -Nk_BT\ln(A). \tag{2.49}$$

The spectrum of thermal undulations on a membrane is heavily weighted towards wavelengths much longer than the size of a typical protein, and on the length scale of a protein, the bilayer is exceptionally flat due to the bending stiffness (see Section 4.5 for details). Considering that the proteins can explore the metric area of the membrane, flattening of these long wavelength thermal fluctuations does not make more area available to the proteins; only a change in the area per lipid adds configurational area. Thus an appropriate description of the bilayer is a linear elastic material, where the metric area of the lipid bilayer at zero lateral tension is A_o and with an areal strain the area becomes $A = A_o(1+\phi)$, where ϕ is the areal strain. In the ideal limit, the area taken up by proteins is negligible compared to the total membrane area, and hence this equation for A is valid. When stretched, the membrane elastically stores energy

$$G_{\text{stretch}} = A_o\int_0^{\phi}\tau(\phi')\mathrm{d}\phi' = A_o\frac{K_A}{2}\phi^2, \tag{2.50}$$

resulting in the total free energy for the vesicle with dilutely embedded proteins

$$G = G_{\text{ideal}} + G_{\text{stretch}} = -Nk_BT\ln(A_o(1+\phi)) + A_o\frac{K_A}{2}\phi^2. \tag{2.51}$$

The equilibrium value of areal strain is found by solving

$$\frac{\partial G}{\partial \phi} = 0 \tag{2.52}$$

for ϕ, yielding

$$\phi = \frac{1}{2}\left(\sqrt{1+\frac{4}{\delta}} - 1\right) \simeq \frac{1}{\delta}, \tag{2.53}$$

[3] We assume that the vesicle has some amount of free area, but that the shape is roughly that of a sphere.

where $\delta = K_A A_o / N k_B T$ is a dimensionless measure of stretch energy compared to thermal entropic energy. In the dilute limit, where $\delta \to \infty$, the crowding tension on the bilayer is independent of bilayer properties, and is given by

$$\tau_c = k_B T \frac{N}{A_o} = k_B T c. \tag{2.54}$$

Note that this tension is always positive, meaning it pulls on the bilayer in an attempt to make more configurational area available to the diffusing proteins. In the dilute solution for typical values of the stretch modulus in phospholipid bilayers (*e.g.* $K_A \simeq 60\, k_B T/\mathrm{nm}^2$), $\delta \gg 1$.

2.10.2 Slightly Non-Ideal Crowding Tension

Keeping the same physical picture and ensemble, where the number of lipids and proteins is fixed, we now consider a more crowded vesicle where the area available to each protein to wander around is actually reduced by the presence of the other proteins. The area of the lipids in such a vesicle is

$$A_\ell = A_o(1 + \phi), \tag{2.55}$$

where A_o is the unstressed area of the *lipids*. The total area of the proteins is then simply $A_\mathrm{p} = N\alpha$, where α is the area per protein, such that the total area of the vesicle is $A_\mathrm{tot} = A_\ell + A_\mathrm{p}$. Then the available area for any one protein to wander around is

$$A_\mathrm{ent} = A_\mathrm{tot} - N\frac{\alpha}{p_\mathrm{max}} = A_\ell - N\alpha\left(p_\mathrm{max}^{-1} - 1\right) = A_\ell\left(1 - \frac{N\alpha}{A_\ell}\left(p_\mathrm{max}^{-1} - 1\right)\right), \tag{2.56}$$

the constant $p_\mathrm{max} = \pi\sqrt{3}/6 \simeq 0.907$ is the maximum 2D packing fraction for discs. Effectively, this is subtracting from the total area of the vesicle N hexagonal unit cells of area α/p_max, to give a more accurate measure of the area in which any one protein can wander. From this equation, we can see that the ideal gas assumption is indeed the dilute limit $N\alpha/A_\ell \ll 1$. Then the partition function of this system is

$$Z = \left(A_\ell - N\alpha\left(p_\mathrm{max}^{-1} - 1\right)\right)^N. \tag{2.57}$$

This partition function is the popular approximation [135] that leads to the equation of state for a 2D hard disc gas

$$\tau_c = k_B T \frac{c}{1 - \frac{c}{c_\mathrm{max}}}, \tag{2.58}$$

when the derivative is taken with respect to A_tot, but we are asserting that proteins are incompressible, and it is only A_ℓ that can change. The parameter $c_\mathrm{max} = p_\mathrm{max}/\alpha$ is the maximum packing concentration of discs in 2D. Then the entropic component of the free energy is

$$G_\mathrm{non\text{-}ideal} = -N k_B T \ln\left(A_\ell - N\alpha\left(p_\mathrm{max}^{-1} - 1\right)\right). \tag{2.59}$$

Like before, the elastic energy stored in the bilayer is

$$G_{\text{stretch}} = A_o \frac{K_A}{2}\phi^2, \tag{2.60}$$

so that the total free energy is

$$G = G_{\text{ideal}} + G_{\text{stretch}} = -Nk_BT \ln\left(A_o(1+\phi) - N\alpha\left(p_{\max}^{-1} - 1\right)\right) + A_o\frac{K_A}{2}\phi^2. \tag{2.61}$$

Again we solve $\partial G/\partial\phi = 0$ to find the entropic areal strain

$$\phi = \frac{1}{2}\left[\sqrt{(\epsilon-1)^2 + \frac{4}{\delta}} + \epsilon - 1\right], \tag{2.62}$$

where the new constant,

$$\epsilon = \frac{N\alpha}{A_o}\left(p_{\max}^{-1} - 1\right), \tag{2.63}$$

is the ratio of the total close-packed interstitial area to the total area of unstressed lipids, and δ is defined immediately after eqn. 2.53. The value $\epsilon = 1$ signifies that all available lipid is packed into the interstitial sits of the hexagonal protein crystal. The value of ϵ is generally between 0 and 1, however, values greater than 1 are possible, simply corresponding to the case where all protein is in a close-packed disc crystal and there is stressed lipid in the interstitial area. For a situation where the proteins are nearly close-packed, and hence $\epsilon \simeq 1$, $\phi \simeq \delta^{-1/2}$. Generally, this equation of state does a good job of accounting for the first few terms of the real Virial expansion of the non-ideal hard disc gas, and contains a singularity in the right place (*i.e.* when the packing fraction reaches $p_{\max}$), however, the order of the singularity is not correct [135].

Examining δ we find it is a constant, $K_A a_o/k_BT \sim 35$, connected to the stretch stiffness per lipid (a_o is the unstressed area per lipid), multiplied by the molar ratio of lipid to protein, N_ℓ/N. If the area per protein is $10\,\text{nm}^2$ and each protein is occupying twice as much area as the minimum unit cell ($\alpha/p_{\max}$), then the lipid associated with each protein uses $\sim 12\,\text{nm}^2$, or ~ 20 lipids. Using these values, the molar ratio of lipid to protein is twenty, and then the $\delta \simeq 700$, $\epsilon \simeq 0.09$, $\phi = 0.0016$, and $\tau_c = 0.09\,k_BT/\text{nm}^2$.

Let us estimate what this means for the crowding tension felt by lipids in the bilayer. If the proteins are fairly densely packed (only 25% more area than the minimum unit cell) then for a $10\,\text{nm}^2$ protein, the area of lipid is $\sim 3.8\,\text{nm}^2$ or about 6 lipids per protein. Then $\delta \simeq 220$, $\epsilon \simeq 0.27$, $\phi \simeq 0.0062$, and $\tau_c \simeq 0.36\,k_BT/\text{nm}^2$. Already this suggests some interesting possibilities for lipids in the bilayer, if there are organizational principles in membranes that are dependent on the lateral tension felt by lipids, this protein induced crowding tension may be important. Additionally, this means that in a protein dense membrane, there will be a chemical potential benefit for lipids to join the bilayer, distinct from the aforementioned hydrophobic effects. This crowding tension is felt by the lipids, but the overall effect on embedded proteins remains unclear, although we will explore

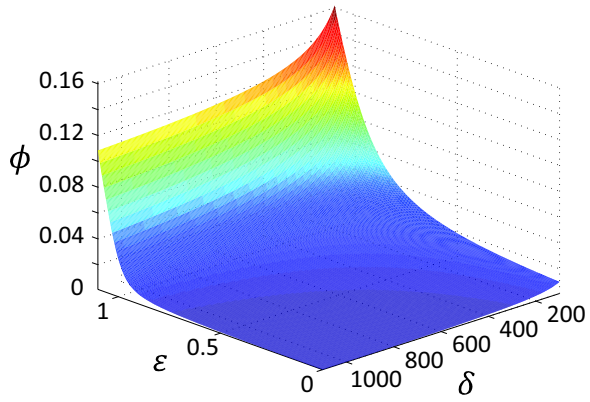

Figure 2.10: Plot showing the effects of material constants and protein concentration on the osmotic areal strain in the bilayer. This plots show how the areal strain (ϕ) in the slightly non-ideal crowding tension model depends on the dimensionless material constant δ, and the dimensionless protein area occupancy ϵ. Multiply ϕ by $\sim 60\, k_B T/\text{nm}^2$ to get the corresponding osmotic lateral tension.

two physical scenarios below.

2.10.3 Proteins that Change Area

Given the analysis of Section 2.10.1, we question what overall osmotic tension is felt by an embedded membrane protein, and more specifically, we ask what happens if a protein changes area? As an initial inquiry, and to build intuition, we will simply assume that there are $N-1$ crowding proteins with area α and one area-changing protein with area α_c. Recall that in both of the previous cases, the area available for proteins to explore was the *bilayer* area. Given the rather small areal strains that we would expect from the previous analysis, let us assume the area per lipid is constant, then the canonical partition function is

$$Z = A_o^N, \tag{2.64}$$

where A_o is the area of the bilayer. So long as the number of proteins and lipids remains constant in the system, a change in protein area, represented by a change in α_c, does not change the metric area of the bilayer. Thus, to lowest order, the net crowding tension felt by embedded proteins is zero. Alternatively said, as far as an area-changing protein is concerned, the positive tension on the membrane due to expansion of the protein gas is exactly balanced by the negative osmotic tension of those same crowding proteins, as schematically shown in Fig. 2.11b.

In this problem, the ensemble we choose plays a critical role. One example of an ensemble where the area changing protein *does* feel a crowding tension, is when the total area of the vesicle is held constant, and the protein area α_c is allowed to change, necessitating that more lipid be added. In

this case, the partition function would be

$$Z = (A_o + \alpha_{\mathrm{c}}^{(o)} - \alpha_{\mathrm{c}})^N, \tag{2.65}$$

where $\alpha_{\mathrm{c}}^{(o)} - \alpha_{\mathrm{c}}$ is the area of lipid added as the initial protein area, $\alpha_{\mathrm{c}}^{(o)}$, changes. Then the free energy is

$$G = -Nk_BT\ln(A_o + \alpha_{\mathrm{c}}^{(o)} - \alpha_{\mathrm{c}}), \tag{2.66}$$

and the crowding tension would be

$$\tau_c = -k_BT\frac{N}{A_o}\cdot\underbrace{\frac{1}{1-\frac{\alpha_{\mathrm{c}}^{(o)}-\alpha_{\mathrm{c}}}{A_o}}}_{\simeq 1} = -k_BTc, \tag{2.67}$$

where the approximation indicated by the bracket is valid for any sufficiently large system. Thus we see that this ensemble generates a net compressive tension, or alternatively, this could be viewed as the tension felt by an external membrane reservoir. In other words, the current ensemble becomes relevant if there is a reservoir of lipid from which lipids can be added to the vesicle to hold the area constant during the area change of the protein. The current physical scenario is similar to a conserved volume container with gas, where if one of the gas particles changes size, that change in volume *is* available to the configurational volume of the other molecules. However, in a bilayer, the medium in which the particles are diffusing is essentially incompressible, thus a change in protein size translates to a change in 'container' size. From the perspective of crowding tensions that affect protein conformations, this is a dubious physical picture (as discussed in the following section) because it holds the total vesicle area constant, when in reality, on the time scales for protein conformational area changes (on the order of microseconds [43]), we want to hold the total number of lipids and proteins constant.

2.10.4 Choosing an Ensemble

While there are myriad scenarios where the choice of ensemble has little effect on the overall thermodynamics of a system, this does not seem to be one them. Due to the fact that we are calculating the configurational entropy of proteins within a certain available area, and that area depends on the ensemble we choose, the ensemble plays a key role in the physical interpretation of crowding tension. Additionally, the time scale of interest affects what ensemble is reasonable. For instance, consider a large vesicle that encloses machinery capable of producing new lipids over time - part of what one might call a simple model of a cell. Simultaneously, this vesicle has some population of membrane proteins that can change their areal footprint. If the time required to produce and incorporate a group of lipids, whose area is comparable to the area change of the protein, is much longer than the time scale of the protein conformational change, it seems reasonable that the right ensemble to choose is one of fixed protein and lipid number, as we did above.

In fact, we can estimate and compare these time scales, at least in the microbial setting. For instance, consider the nominal dimensions of an *E. coli* bacterium (a pill of length $\sim 2\,\mu$m and radius $\sim 0.5\,\mu$m), whose area corresponds to approximately 10^7 lipids per leaflet[4], with the area per lipid $\sim 0.6\,\text{nm}^2$ [136]. Under the best, and hence fastest, growth conditions, the bacterium will divide approximately every $\sim 1200\,s$ (20 minutes), meaning that, at their fastest, lipids must be incorporated at a rate of approximately one lipid per $100\,\mu s$. On the other hand, the well studied channel protein MscL has a gating time scale of $\sim 5\,\mu s$ [43], and for this particular channel, a rather large change in area upon gating of $O(10\,\text{nm}^2) = O(10\,\text{lipids})$ [21, 50, 19]. Thus on the time scale of protein conformational change, the area of the lipids added, as compared to the area change of the protein, is small. Hence, it seems that the appropriate ensemble for studying the effects of crowding on channel gating, even for proteins whose area change is a tenth of MscL, is the fixed particle number ensemble, in which the *net* crowding tension on the channel is zero (in the ideal limit), as shown in Fig. 2.11. It should be noted that this equilibrium world view may be inaccurate in the fast-paced setting of a dividing cell.

If on the other hand, we are concerned with the behavior of this system on much longer time scales, the fixed particle number ensemble is likely not appropriate. While it is difficult to know the 'right' ensemble in the various contexts relevant to a cell, we can make a general and interesting comment, rooted in a basic understanding of configurational entropy. A simple calculation of configurational entropy shows that the maximum degree of entropy is reached when half of the available sites for a protein to occupy are filled. This suggests that, at least from an entropic perspective, there is an energetic driving force that prefers the area taken up by lipids and the area taken up by proteins in the membrane, to be equal. With no claims of causality, it is interesting to note that cellular measurements of the relative areas of lipid and protein are approximately one to one in various biological membranes [91], in line with this notion of maximizing the configurational entropy.

An interesting result of the fixed particle number ensemble in the ideal limit is that regardless of dimensionality, particles immersed in an incompressible medium (like water or a bilayer) experience zero net osmotic forces per unit length (2D) or area (3D). This is not to say that there are no effects from crowding; indeed an excluded area force exists, as we will show in the next section.

2.10.5 Excluded Area Effects

This section does not present any new work, and indeed, excluded volume forces have been a topic of intense research interest for decades [137]. In the context of lipid bilayers, there has been some work exploring the effects of excluded area forces, due to the depletion of lipids between proteins [93], however our discussion here is more centered on excluded area forces arising from a population of crowding proteins. This calculation is included for the sake of completeness in the context of

[4]This assumes the leaflet is made up entirely of lipids, but considering the mass ratio of protein and lipid in many membranes is roughly one to one [91], this is correct within a factor of two.

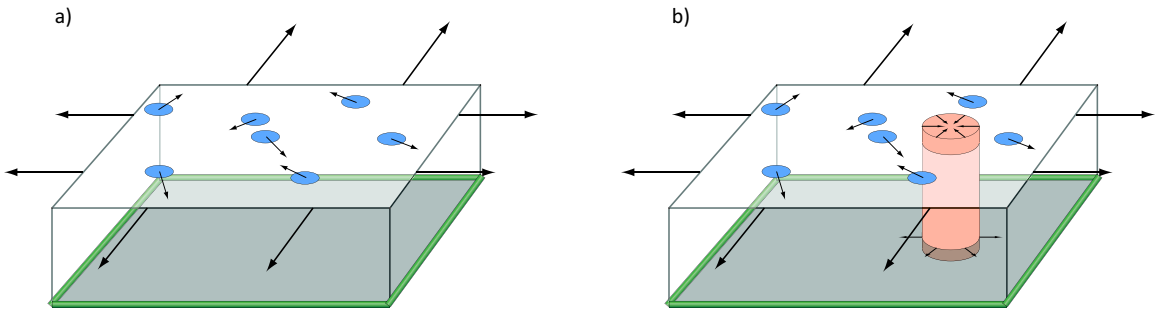

Figure 2.11: Schematic showing how protein expansion tension couples to the bilayer equation of state. a) The upper layer represents the protein configurational space, while the lower layer is a bilayer. Proteins, shown as blue circles, thermally wander around in the upper layer and exert an expansive tension on the boundary as shown by the arrows. Demanding that the area of the upper and lower layers be equal, is equivalent to saying that the proteins remain in the bilayer; then the expansive tension couples directly to the elastic equation of state of the bilayer below. b) Upon insertion of an area changing element, it is clear that the crowding proteins in the upper layer exert a compressive tension on this element, while those same proteins couple to the equation of state in the lower bilayer, causing an equal and opposite expansive tension. Thus there is zero net tension on the area changing element.

discussing crowding effects. While it might seem that the previous calculations of crowding tension affect how we think of excluded area forces, the following calculations demonstrate that these forces remain intact.

Consider a box of area A with N diffusing particles of radius R and two blocks a distance D apart, as shown in Fig. 2.12. Choosing either the fixed particle or fixed area ensemble does not affect this situation because no particles are changing size and the particle numbers are being conserved. The distance between the blocks does not affect how much area is available to the blocks, hence we need not consider the conformational entropy of the blocks. However, the area available to each diffusing particle is

$$A_{\text{ent}} = A - N\alpha p_{\text{max}}^{-1} - \Theta(2R - D)D\ell \tag{2.68}$$

where ℓ is the length of the blocks, $\alpha = \pi R^2$ is the area of the diffusing particles, and Θ is the Heaviside function. The partition function is then

$$Z = \left(A - N\alpha p_{\text{max}}^{-1} - \Theta(2R - D)D\ell\right)^N, \tag{2.69}$$

and the free energy is

$$G = -Nk_BT \ln\left(A - N\alpha p_{\text{max}}^{-1} - \Theta(2R - D)D\ell\right). \tag{2.70}$$

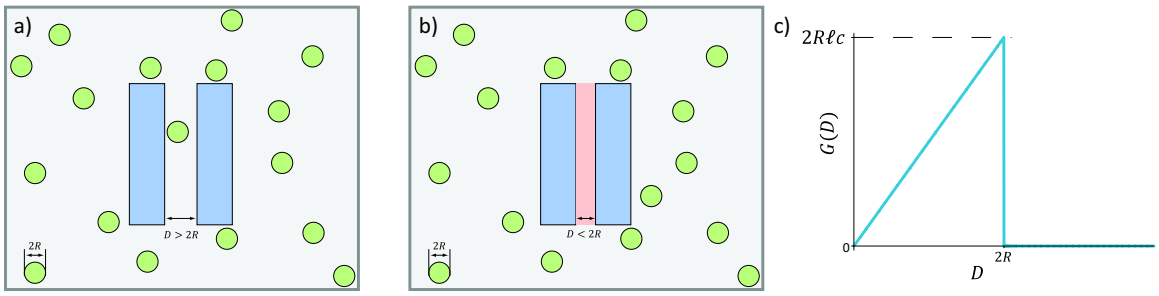

Figure 2.12: Depictions of origin of excluded area forces. Particles of radius R (green) interact with two larger blocks (blue) in a 2D plane. a) If the distance D between the blocks is greater than $2R$ there is no net change in area available to the crowding particles, and hence no excluded area force. b) When the distance between the blocks is less than $2R$, there is an excluded zone between the blocks, shown in red, that will entropically cause the blocks to attract. c) Potential between the blocks in the dilute limit as a function of separation distance D in units of k_BT.

For simplicity, let us assume the ideal limit, which amounts to letting $\alpha \to 0$, and the potential between the two blocks is then

$$G(D) = -Nk_BT\left[\ln(A) + \ln\left(1 - \Theta(2R - D)\frac{D\ell}{A}\right)\right]. \tag{2.71}$$

For any sufficiently large system $\frac{D\ell}{A} \ll 1$, and we can zero the potential to find

$$G(D) = k_BTc \cdot \Theta(2R - D)D\ell. \tag{2.72}$$

Thus the same analysis we used previously shows that excluded area forces exist, with an initial energy barrier of $2R\ell c\, k_BT$ at $D = 2R$, and an attractive force below that of $F = -c\ell\, k_BT$. To make a rough estimate, let us assume these 'blocks' are proteins with length $\ell = 10\,\text{nm}$, and there is a concentration of crowding proteins of $c = 0.001\,\text{nm}^2$, then the depletion force is on the very relevant scale of $F = 1\,\text{pN}$.

2.11 Crowding in a Lipid Domain

As a transition to the next chapter, which will discuss phase separation and formation of lipid domains, we take a look at how proteins with a hydrophobic mismatch that is better suited to a lipid domain, energetically segregate themselves into a domain. This has relevance to both the specific interactions we discussed, in that the hydrophobic mismatch considered here is the same mechanical effect we discussed earlier. Likewise, the osmotic tension of proteins in a domain will be an important effect, and hence this section serves to demonstrate one particular union between specific mechanical and non-specific entropic effects.

Consider a domain whose lipids occupy an area A_{D} and proteins with fixed area α. Due to the membrane thickness difference between the domain and the surrounding membrane, there is an energy cost per unit boundary length γ around the domain [130, 138]. We assume that due to the difference in membrane deformation around the protein outside and inside the domain, there is a fixed energy benefit $-\mu$ for the protein to enter the domain — this can be calculated from membrane mechanics and is generally related to the difference of the squares of the hydrophobic mismatch in the two lipid regions and the protein in question, although strictly speaking there are contributions from the size of the protein, relative to the size of the lipid domain. Given these assumptions, we see that the free energy for N proteins to enter a domain at $T = 0$ is

$$G = 2\sqrt{\pi}\gamma\left[\sqrt{A_{\mathrm{D}} + N\alpha} - \sqrt{A_{\mathrm{D}}}\right] - N\mu, \tag{2.73}$$

where the first terms accounts for the change in unfavorable lipid domain boundary length upon entry of a protein, and the second term is the elastic benefit of a protein entering a domain. We define the dimensionless constant[5]

$$\chi = \frac{\gamma\alpha}{\mu\sqrt{A_{\mathrm{D}}}}, \tag{2.74}$$

which can be interpreted as the ratio of the compressive tension on the domain from the unfavorable boundary, to effective tension on the protein when entering the domain. We also define the dimensionless protein concentration as

$$\eta = \frac{N\alpha}{A_{\mathrm{D}}}. \tag{2.75}$$

For a domain that contains proteins, this parameter measures the area taken up by proteins relative to the area taken up by lipids within the lipid phase boundary. Finally, a natural energy scale can be defined, such that the energy is normalized by

$$G_o = \beta\frac{\mu A_{\mathrm{D}}}{\alpha}, \tag{2.76}$$

where $\beta = 1/k_B T$, yielding the dimensionless energy

$$G = G_o\left[2\sqrt{\pi}\chi\left(\sqrt{1+\eta} - 1\right) - \eta\right]. \tag{2.77}$$

Recall that the maximum packing density is $p_{\max}$, hence the maximum dimensionless particle number is $\eta_{\max} = \left(p_{\max}^{-1} - 1\right)^{-1} \simeq 9.74$. This energy function has a number of interesting features. Upon examination, one finds that the energy decreases with increasing protein concentration as long as $\chi < \pi^{-\frac{1}{2}}$, up to $\eta_{\max}$. For values of χ greater than this critical value, there is an energy barrier for proteins to join the domain. For a given domain size and line tension around the phase boundary, this means that proteins that are too large (α) and/or proteins whose chemical potential from hydrophobic mismatch (μ) is too small will be energetically inhibited from joining the domain, up

[5] We apologize for the redundancy in parameter naming, but there are only so many Greek and Latin letters.

to a point. Above this critical value, the maximum of the energy barrier is located at $\chi = \pi^{-\frac{1}{2}}$, and hence if the dimensionless protein concentration in the domain is greater than this value, the free energy change for other proteins to join the domain again becomes negative. Hence, this has the appearance of nucleation a problem, with a twist. If the domain size is large, and the protein size is small, and/or the chemical potential is very favorable, any addition of protein is energetically beneficial. Although, above the critical value of χ, there is a critical protein concentration, below which addition of the proteins to the domain is inhibited. Generically, this means that larger domains are more promiscuous than smaller domains, about which proteins are energetically favored to enter. Thus, the values of the parameter χ determine a domain's ability to segregate proteins by hydrophobic mismatch, with higher values of chemical potential μ corresponding to stronger enrichment of the corresponding protein in the domain.

To include the effects of entropy in the ideal limit[6], we define the fixed concentration of protein outside the domain as c_o and the concentration of protein inside the domain is

$$c = \frac{N}{A_{\rm D} + N\alpha} = \frac{1}{\alpha} \cdot \frac{1}{\frac{1}{\eta} + 1} \simeq \frac{\eta}{\alpha} = \frac{N}{A_{\rm D}}, \tag{2.78}$$

where to get analytical answers, we have taken the limit of low protein concentration, $\eta \to 0$, such that the entropic component of the chemical potential for a protein to enter the domain is

$$\mu_{\rm c}(n) = k_B T \ln\left(\frac{c}{c_o}\right) = k_B T \ln\left(\frac{n}{c_o A_{\rm D}}\right), \tag{2.79}$$

where n is the integration variable for the number of proteins, as shown below. Making use of this result from the statistical mechanics of an ideal gas, allows us to skip the laborious spatial integrals that pertain to the position of each protein in the system. The free energy contribution from entropy is then

$$G_{\rm c} = \beta \sum_{n=1}^{N} \mu_{\rm c}(n) = \ln\left[\frac{N!}{(c_o A_{\rm D})^N}\right]. \tag{2.80}$$

Then the total free energy is

$$G_{\rm tot} = G_o\left[2\sqrt{\pi}\chi\left(\sqrt{1+\eta} - 1\right) - \eta\right] + \ln\left[\frac{N!}{(c_o A_{\rm D})^N}\right], \tag{2.81}$$

and the mode concentration of proteins in the domain, in the limit of low protein concentration and large domain area, is found by solving $\partial G_{\rm tot}/\partial N = 0$, to give

$$\frac{N}{A_{\rm D}} \simeq c_o e^{\beta\mu\left(1-\chi\sqrt{\pi}\right)} = c_o e^{\beta\left(\mu - \gamma\alpha\sqrt{\frac{\pi}{A_{\rm D}}}\right)}, \tag{2.82}$$

[6]It is a relatively straightforward extension to include non-ideal terms in the entropy.

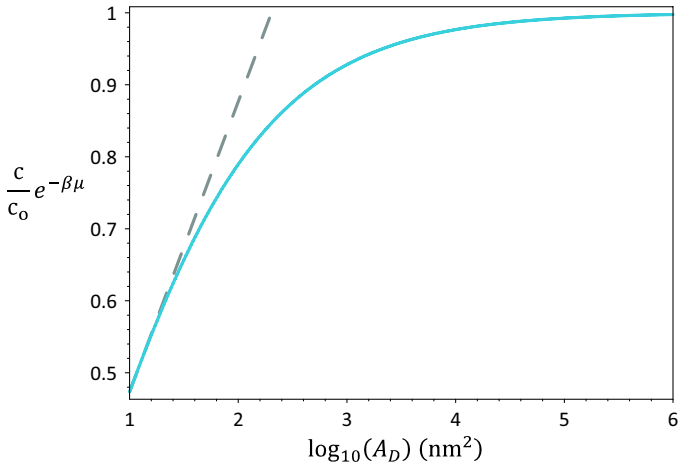

Figure 2.13: Normalized concentration enrichment as a function of the domain area for $\alpha = 10\,\mathrm{nm}^2$ and $\gamma = 0.4\,k_BT/\mathrm{nm}$. Note that as the domain area grows, the concentration enrichment increases, but the rate of that increase drops past a certain domain area, as indicated by the dashed line.

and further

$$\frac{c}{c_o} = e^{\beta\left(\mu - \gamma\alpha\sqrt{\frac{\pi}{A_\mathrm{D}}}\right)}, \tag{2.83}$$

with $c \simeq N/A_\mathrm{D}$. As domain area grows larger, and the marginal cost in line tension for adding a new protein shrinks, and we approach the maximum enrichment factor

$$\frac{c}{c_o} = e^{\beta\mu}. \tag{2.84}$$

Figure 2.13 plots the concentration enrichment, normalized by this maximum enrichment, as a function of the initial lipid domain size. More work remains to better understand how the mechanics of a phase separated bilayer, and the hydrophobic mismatch of an embedded protein work in concert to segregate specific proteins into domains, but this section serves as good launching point.

2.12 Concluding Remarks

This chapter was about interactions between proteins. In the first few sections we showed that the deformations of the lipid bilayer due to thickness mismatch encode specific information about protein state, and not only allow proteins to exert specific forces of attraction or repulsion on each other, but also imbue a protein dense membrane with a generic form of protein cooperativity and communication. Work is ongoing to understand how protein shape, that is deviations from a cylindrical shape, affect these interactions, as well as what relevance they might have to the way proteins in real biomembranes assemble and interact (*e.g.* chemotatic receptors in bacteria [129, 139]). We then discussed a set of non-specific, and more generic interactions between membrane

proteins that arise from crowding in the membrane. We calculated an approximation for the depletion force due to crowding, finding it has a relevant scale of around one pico-Newton. We found that likely on the time scales of protein conformational changes, the appropriate choice of ensemble for crowding is fixed particle number, and thus likely there is a corresponding zero net crowding tension. On the other hand, crowding likely serves as an energetic bias that prefers the addition of lipids, and might even be at work setting the coarse lipid-protein areal ratio in membranes. Lastly, we combined a subset of this information to begin to understand how lipid domains might be able to both specifically select and enrich the concentration of certain proteins within their borders. All of these projects are ongoing, and we hope that the varied stories each of these physical effects tell will come to some convergence in our future work.

Chapter 3

Volumetric Flow in Protein Channels

"*A scientist prizes what he does not understand at least as much as what he does.*" – Unknown

3.1 Not All Are for Ions

As a cell grows and eventually divides, a host of processes are in play to manage cell size and partition internal components. Broadly speaking, the genome must be replicated and partitioned, new membrane and cell wall (where applicable) must be synthesized, and throughout the process of continual growth, cell and organelle volume must be managed in accordance with the rate of production of lipids, cell wall material, and internal components [15, 14]. Permeation of water through the membrane is a passive process [140], which when driven by osmotic gradients can serve as a mechanism for volume management. Though beyond that, cells have a number of membrane channels whose main purpose is to move water and osmolytes [141], for instance the well know protein family of aquaporins [142, 143] and aquaglyceroporins [144, 145] is found in nearly all organisms. In some cases, the channel activity is coupled to membrane tension [71, 73], indicating that transmembrane pressure may be the basal physiological regulator of their conformational state. In particular, bacteria [69, 11, 18, 24] and, by homology, certain plants species [17] have developed a set of membrane tension sensitive channels that, by virtue of their ability to rescue microbes from osmotic shock or regulate organelle morphology in plants, respectively, are ostensibly involved in volume management. In both the microbe and plant cases (and aquaporins as well), absence or mutations of these channels has serious deleterious effects on the organism under certain physiological conditions. Yet, despite their clearly important role in cellular physiology, there are two aspects of these channels that are relatively unexplored. First, as we have discussed at length in Chapters 1 and 2 of this thesis, details of the mechanical interaction between lipids and these channels remain largely at a hypothetical stage, where in Chapter 1 we discussed the possible effects of lipid mechanics on channel function. The second set of questions, which we will explore in more detail in this chapter, revolve around the volumetric flow properties of these channels in a physical sense. More specifically, the manner in which water osmolytes move through the channel pore present us with fertile ground for experimentation. A few well-formed questions have motivated our thinking on this topic, in particular: What is the relationship between pressure gradient, pore size and flow through the channel? Does the flow follow 'typical' low Reynolds number properties

of a small pipe? Does the flow exhibit any effects from the fact that the pore is only an order of magnitude larger (or less) than the size of the particles passing through it? Do thermal fluctuations of the water and solute molecules affect the flow properties of the channel?

A huge amount of experimental effort has been expended to understand the gating properties [21, 22, 50, 49] and structure [11, 18, 146, 19] of the microbial channels, as well as propose possible functions *in vivo* [147, 148, 149]. In these explorations, electrophysiology has been an indispensable tool in measuring the conformational states of channels (*i.e.* conducting or non-conducting states) as well as probing what physiological factors cause these changes in conformation [21, 50] (*e.g.* transmembrane voltage, tension, or ligand concentration). In accordance with their proposed function as regulators of volume and/or pressure (depending the physical viewpoint), and the fact that the membrane is essentially impermeable on time scales of channel gating [43], these channels must be sensitive to the pressure acting on the membrane. Indeed, in a system where the enclosed volume and membrane surface area are conserved on time scales relevant to volume flux through these channels, membrane tension is a reporter of pressure and enclosed volume. In particular, the Laplace-Young relation [65] relates the mean curvature of a surface to the pressure drop across it and surface tension on it (in the absence of bending). Using this relationship, many important material properties of membranes have been gleaned through the use of micropipette aspiration [140, 26, 150].

In this chapter we perform a series of calculations aimed at estimating channel flow properties and constraining the range of parameters that might be seen in experiments that attempt to measure those properties. On the experimental side, we will discuss at length how to measure the ensemble flow properties of the bacterial mechanosensitive channel of large conductance (MscL), using both wild-type and mutant forms, to gain a better understanding of both the lipid-related gating behavior and the nanoscopic flow across a membrane. Additionally, we will present preliminary experimental results on pressure-driven water flux across a bilayer, as a proof of concept of the proposed volumetric channel flow measurement.

3.2 Gating and Conductance Properties of MscL

In their varied environments, microbes are subject to a number of different mechanical forces, and must be able to compensate for potentially large differences in the external osmotic pressure, as schematically shown in Fig. 3.1. In particular, it was observed that bacteria could survive high degrees of hypo-osmotic shock by selectively releasing ions and other uncharged osmolytes rapidly after osmotic down shock [148, 149]. Much of this osmolyte transport was traced back to a large pore channel in the inner bacterial membrane, composed of five monomers, each 125 residues in length and about 15 kD in mass [11], that seemed to be sensitive to pressure gradients and/or membrane tension [147, 151]. Given the now standard tools of bacterial molecular biology and protein purification, such a channel is a good place to begin studying volume and osmolyte

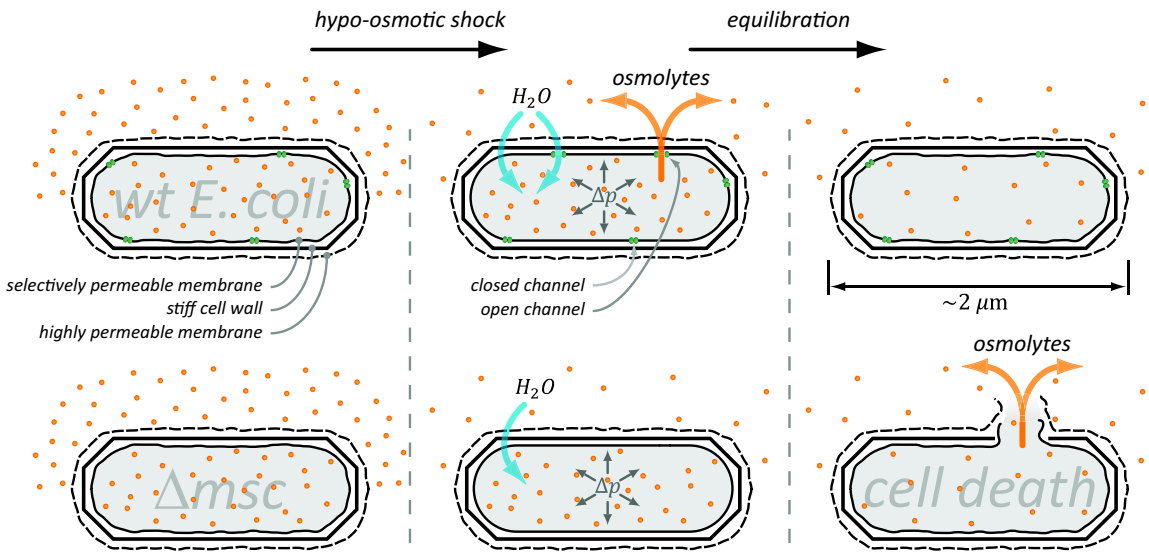

Figure 3.1: Hypo-osmotic shock in *E. coli*. Schematic showing how bacteria cope with rapid reduction in the external, absolute osmotic pressure. First row: cells initially in equilibrium with the surrounding osmotic pressure are subject to hypo-osmotic shock. Water rapidly permeates across the membrane increasing cell volume and raising membrane tension. At some critical tension, mechanosensitive channels open, increasing the influx of water, but also allowing the cell to jettison some portion of its internal osmolytes, thereby returning to equilibrium with the external osmotic pressure. Second row: upon hypo-osmotic shock, cells that lack mechanosensitive channels increase in volume, membrane tension increases, and without alleviation of the internal osmotic pressure and corresponding membrane tension, the membrane ruptures resulting in cell death.

movement on the scale of a single cell.

The low copy-number [112] ($\sim$ 10 per cell) bacterial channel MscL is an excellent target for studying how water and osmolytes move across a membrane when a pressure gradient, and corresponding membrane tension, are present. It has been conclusively shown that membrane tension is the key physical parameter that regulates the gating of this channel [21, 50]. The channel does not exhibit any strong ion selectivity, again suggesting that its purpose is not to move ions, *per se*, but to allow flow of water and/or osmolytes. In the microbial setting, the pressure gradient across the inner membrane couples to the radius of curvature of the membrane to produce a lateral tension on the membrane surface. At relatively low membrane tension the channel adopts a closed, non-conducting conformation, while at tensions near the rupture tension of a typical bilayer, the channel transitions to an open state, and spends relatively little time in sub-conducting states [21, 50, 49]. For this reason, we can reasonably approximate the channel, mechanically coupled to the membrane, as a two-state system whose equilibrium probability for being in either state is influenced by the bilayer tension. As we will show in the following subsections, experimental techniques are available to quantitatively control the tension on giant unilamellar vesicles in such

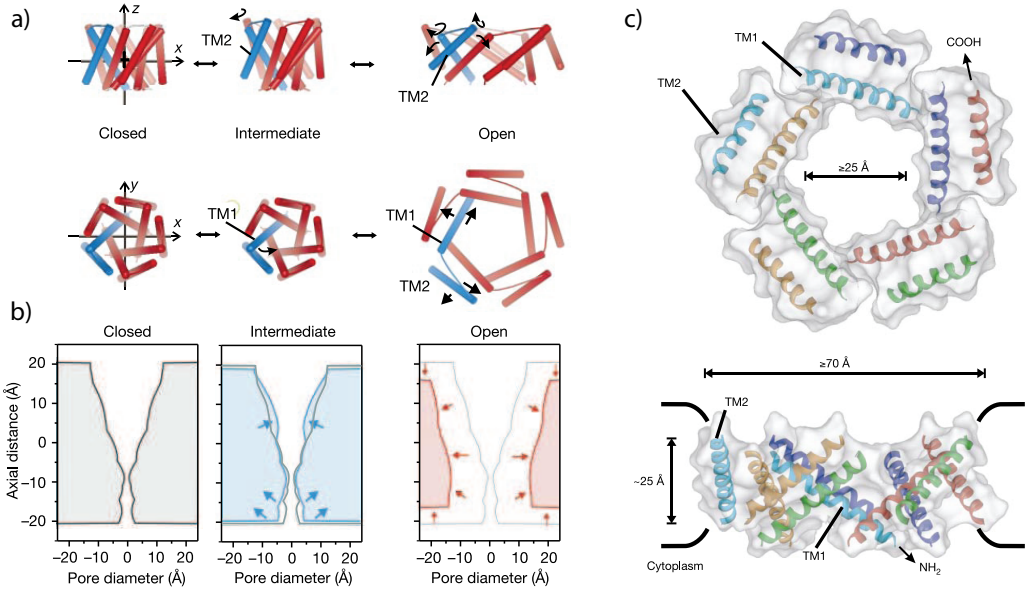

Figure 3.2: Schematics showing the hypothetical structural transitions of MscL. a) Side and top views of the transmembrane α-helices (TM1 and TM2) as they transition from the closed to proposed open state, in an iris-like mechanism. b) View of the pore cross-section during the same three stages of the closed to open transition, showing that the pore gets wider and shorter going from closed to open. c) Detailed view, with dimensions, of the orientation and resultant pore size of the transmembrane α-helices in the open state as measured from electron paramagnetic resonance. Figure adapted from [19].

a way that we can control which channel conformation dominates.

In the open state, the channel pore is relatively large [146, 19, 75], approximately 3 nm in diameter (as compared to the pore sizes of channels that conduct single chains of water [145] or ions [78, 152]) and ~ 2.5 nm in length [49, 146, 19], as schematically shown in Fig. 3.2. With a pore of this size conducting ~ 4nS[1], the electrical conductance is $\sim 10 - 100$ times larger than typical ion channels [153], and in fact is so large that even small proteins can pass through [75, 154]. If our goal is to construct an experiment capable of measuring the water and osmolyte flux through a channel, the large size of this channel's pore makes it a good target for studying how a variety of osmolytes, with different sizes and hydration shells (*e.g.* glycerol, sugars, urea, amino acids and small peptides) affect channel flow [148, 149]. Similarly, the large pore means that the flux per channel will be relatively high, in comparison to the aforementioned water transport channels, and thus we expect the contribution to the volume change of a vesicle or cell from each channel to be relatively high.

Additionally, this particular channel has the advantage that it does not exhibit significant

[1]By comparison a copper wire with these dimensions would conduct a whopping 170mS, or 40 million times more current!

transitions to, nor latency in, non-conducting states [49], like those seen in other mechanosensitive channels [24]. This feature will prove crucial to our experimental construction, since it means that for a given tension, the equilibrium probability that the channel is in the open state remains constant in time, or put another way, the channel is a well behaved two-state system (closed and open). This gives us confidence that the behavior of the channel is described well by the relatively simple dose-response curve shown in Fig. 3.3. The free energy difference between the open and closed states has three main contributions, as were discussed earlier in Chapter 1. The increase in channel area couples to membrane tension to give a free energy contribution of the form $-\tau\Delta A$, while the change in the deformation of the surrounding membrane and internal structure of the protein give contributions ΔG_{mem} and ΔG_{prot}, respectively. Measurements of the area change upon gating span a range from $6.5 - 7\,\text{nm}^2$ [21, 50] up to $\sim 20\,\text{nm}^2$ [23]. The free energy difference coming from membrane deformation has already been discussed in detail in Chapter 1. In contrast, relatively little is known about the free energy component coming from rearrangements of the protein's internal structure or hydration of the pore [34, 98], although this contribution will be discussed in later sections of this chapter. Measurements of the free energy of channel gating, in different lipid bilayer compositions, range from $\sim 15 - 20\,k_BT$ [21, 50] up to $\sim 50\,k_BT$ [23], and we will use $20\,k_BT$ as the typical value. Together, these contributions yield the open state probability as a function of tension given by

$$P_o(\tau) = \frac{1}{1 + e^{(\Delta G_{\text{mem}} + \Delta G_{\text{prot}} - \tau\Delta A)/k_BT}}. \tag{3.1}$$

Though we do not know the precise molecular origins of the protein free energy ΔG_{prot}, we do know that its contribution can be made to favor the open state via single point mutation of residues lining the channel pore; the use of such mutants will be discussed later in this chapter. With these facts in mind, we are now in a position to (conceptually) build an experiment, using MscL, that measures the ensemble volumetric flow through a protein pore, though first we will build intuition for how bilayers with and without volumetric channels respond to osmotic shock.

3.3 Modeling Hypo-Osmotic Shock

The following few subsections discuss the volumetric measurement, and its theoretical background, in detail. We begin with a series of thought experiments that will help us understand how osmolarity, elasticity, pressure, volume, and permeation relate to one another to establish the behavior of an osmotically shocked vesicle. To begin, we consider a large membrane sphere composed of a single bilayer of lipids that contains the channel protein MscL at a molar ratio, m, with the surrounding lipid, where $m \ll 1$.[2] This so-called 'giant unilamellar vesicle' (GUV) has some initial radius R_o,

[2] In later parts of this chapter and accompanying appendices, we discuss how to create such vesicular structures as well as reconstitute channels into them. Molar ratio is used because this is an unambiguous measure of the relative protein and lipid content, as opposed to mass ratio.

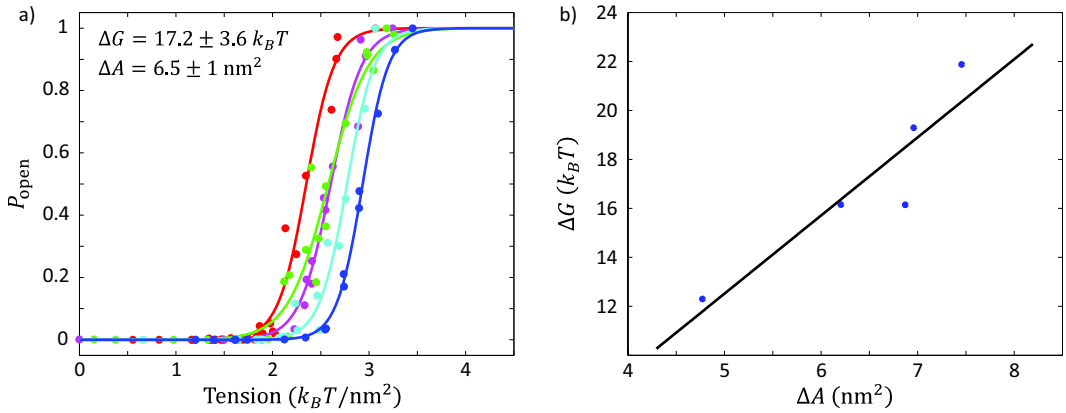

Figure 3.3: Experimental dose response curves of MscL under tension. a) Five different traces of MscL channel activity as a function of membrane tension in an electrophysiological bilayer patch composed of a 1:1 molar mixture of PE:PC lipids, as measured using the Laplace-Young relation. The mean free energy of transition, $\Delta G_{\mathrm{mem}} + \Delta G_{\mathrm{prot}}$, and mean area change of the channel, ΔA, are shown on the graph. Plotted as a function of pressure gradient across the patch, these curves do not line up nearly as well [50]. These traces represent some of the lower measured values for both gating parameters, ΔG and ΔA, which are highly correlated as shown in (b) for each of the five traces and [23]. Raw data kindly provided by P. Blount [50], and reprocessed by the author.

that specifies the volume V_o and surface area A_o. At the onset, we presume the concentration of osmolytes inside and outside the vesicle is equilibrated such that the resting membrane tension is close to zero; or in other words, the pressure gradient across the membrane is zero. Assuming the osmolytes are dilute, we can use the ideal gas approximation (in this setting often referred to as the 'ideal solution' approximation) to calculate the absolute osmotic pressure outside the vesicle as

$$p_1^{(O)} = \alpha_1 \bar{c}_1 k_B T, \tag{3.2}$$

and the absolute osmotic pressure inside the vesicle as

$$p_2^{(O)} = \alpha_2 \bar{c}_2 k_B T, \tag{3.3}$$

where $\bar{c}_i$ is the number concentration per unit volume of solute molecules in the two regions, proportional to the molarity, α_i is the van 't Hoff coefficient which relates molarity to osmolarity, k_B is Boltzmann's constant ($1.38 \times 10^{-23}\,J/\mathrm{K}$), and T is the temperature ($\simeq 300\,\mathrm{K}$). To consider mixed osmolytes, one simply uses the sum of osmolarities of the individual components, $\sum_i \alpha_i \bar{c}_i$, according to Raoult's Law, analogous to the law of partial pressures. For ease of notation, we refer to the concentration of osmolytes as $c_i = \alpha_i \bar{c}_i$. With the external volume much larger than the volume enclosed by the vesicle, we presume the external, absolute osmotic pressure remains constant, unless we as the experimentalists cause a change in external osmolarity. Then the osmotic

pressure gradient across the membrane is $\Delta p^{(O)} = (\alpha_1 \bar{c}_1 - \alpha_2 \bar{c}_2) k_B T = (c_1 - c_2) k_B T$, where every 44 mOsm difference in osmolyte concentration corresponds to approximately one atmosphere of pressure. In the experiments we propose below, the internal osmolyte is sucrose, with a van 't Hoff coefficient of $\alpha_1 \simeq 1.12$, and the external osmolyte is glucose, with a van 't Hoff coefficient of $\alpha_2 \simeq 1.06$ [155][3].

The Laplace-Young Law [65] allows us to easily calculate the membrane tension for a spherical vesicle with a pressure gradient. As a two-dimensional fluid, the bilayer does not accumulate shear stress, and hence any tension that exists on the membrane is equal everywhere. Then the energy of this spherical vesicle has three contributions, coming from bending of the bilayer into a spherical shape, tension on the bilayer surface, and PV work of the volume enclosed by the membrane. The bending energy of a sphere is proportional to bending stiffness of the membrane, $\kappa_b \simeq 20 k_B T$ [26, 51], and is calculated using the area and constant mean curvature of a sphere, to find $E_{\text{bend}} = 8\pi\kappa_b \simeq 500\, k_B T$ [57]. Since the bending contributes a constant energy for any size spherical vesicle, it has no effect on the overall vesicle size. The remaining free energy of the spherical vesicle as a function of vesicle radius, R, is written as

$$E = \tau 4\pi R^2 - \Delta p \frac{4\pi}{3} R^3. \tag{3.4}$$

Solving for the sphere radius with minimum energy, $\partial E / \partial R = 0$, gives the tension on the vesicle surface (τ) as a function of radius and pressure gradient, $\tau = \Delta p R / 2$.

With these facts in mind, let us conduct two thought experiments. First, consider what happens to such a vesicle under conditions of hypo-osmotic shock, where the external concentration of osmolytes drops sharply, to produce a relatively large inward pressure gradient. In the *absence* of membrane volumetric channels, there are two mechanisms by which the pressure can equilibrate. First, water can permeate across the membrane into the vesicle in an attempt to equilibrate the internal and external osmolyte concentrations, thus increasing the enclosed volume. Second, the sugar molecules (or other relevant osmolytes) themselves could permeate across the membrane (in the opposite direction) to equilibrate the internal and external osmolyte concentrations, accompanied by a relatively minor reduction in volume. In fact, both of these mechanisms happen simultaneously, however the *rate* at which they happen is significantly different. Early experiments in membrane physiology show that the ratio of the permeation rate of water to the permeation rate of sugars is 100,000 to 1, and several orders of magnitude larger for the relative permeation rate of charged species [1][4]. The result is that if no channels are present in the bilayer, the vesicle volume swells and the membrane stretches.

As we will suggest later in this chapter using preliminary experimental results, and has been suggested by others [140, 156], water permeation across the membrane has an approximately linear

[3] The van 't Hoff coefficients for sucrose and glucose are constant for solute concentrations up to ~ 1 M.

[4] Although, *in vivo*, bacteria have a number of transporters responsible for the active pumping of osmolytes [141].

response to a pressure gradient, of the form

$$\frac{\mathrm{d}V}{\mathrm{d}t} = c_p \Delta p A, \tag{3.5}$$

where this volume flux is the total water volume entering the vesicle through the bilayer per unit time due to permeation, and c_p is the lipid-specific permeation coefficient, with values from preliminary experiments in the lipid DOPC of $c_p \simeq 2 \times 10^{-6}\,\mu\mathrm{m}^3/\mathrm{pN}\cdot\mathrm{s}$, in good agreement with previous measurements [140]. This simple relationship merely states that the volume flux across each unit area of membrane is proportional to the pressure gradient. Given our previous statements about the very slow relative rate of permeation of osmolytes across the membrane, water permeation is, by far, the dominant mechanism by which vesicle volume changes in the absence of channels.

The pressure gradient driving water across the membrane is the sum of contributions from the osmotic concentration gradient, which tries to move water inward, and membrane stretch as the vesicle volume increases (analogous to the pressure generated inside a balloon as it is inflated), which tries to move water outward. First, let us tackle the contribution from the concentration gradient. The concentration of osmolytes inside the vesicle is simply $c_1 = n_o/V$ where n_o is the number of osmolytes enclosed at $t = 0$, and we will write this number as $n_o = c_1^{(o)} V_o$ where $c_1^{(o)}$ is the initial internal concentration of osmolytes at $t = 0$. Then as a function of vesicle volume, the osmotic pressure gradient is

$$\Delta p^{(O)} = c_1^{(o)} k_B T \frac{1}{w}\left(w\frac{V_o}{V} - 1\right), \tag{3.6}$$

where the dimensionless parameter $w = c_1^{(o)}/c_2$ is the ratio of the concentration of osmolytes inside and outside the vesicle, respectively, upon osmotic shock at $t = 0$. This quantifies the degree of hypo-osmotic shock, with higher values corresponding to initially larger osmotic differences. To calculate the second contribution to the pressure gradient, membrane elasticity must be taken into account. Given that the number of lipids in the vesicle is conserved, the increase in vesicle volume must be accompanied by membrane stretch, and hence a positive areal strain, ϕ, given by

$$\phi = \frac{A}{A_o} - 1, \tag{3.7}$$

which can be written as a function of the volume using $A = (6\sqrt{\pi}V)^{2/3}$,

$$\phi = \left(\frac{V}{V_o}\right)^{\frac{2}{3}} - 1. \tag{3.8}$$

In modes of pure stretch, the bilayer behaves like a standard linear elastic material [26, 57], such that the areal strain and tension are linearly related through the lipid-specific stretch modulus, by $\tau = K_A \phi$, with $K_A \simeq 60\,k_B T/\mathrm{nm}^2$ for a typical phosphocholine bilayer [26]. Relating these two equations to the Laplace-Young relation for a sphere, we see that membrane stretch produces a

pressure gradient in the opposite direction as the concentration gradient, given by

$$\Delta p^{(s)} = -\frac{2K_A}{R_o}\left(\frac{V_o}{V}\right)^{\frac{1}{3}}\left(\left(\frac{V}{V_o}\right)^{\frac{2}{3}} - 1\right). \tag{3.9}$$

Then the volume change of the vesicle as a function of time is given by the differential equation

$$\frac{\mathrm{d}V}{\mathrm{d}t} = c_p\left(6\sqrt{\pi}V\right)^{2/3}\left(\Delta p^{(O)} + \Delta p^{(s)}\right). \tag{3.10}$$

With this equation in hand, we can now estimate how much of an osmotic down shock a vesicle without channels can withstand, and how exactly this threshold down shock relates to material parameters and vesicle size. Let us assume temporarily that the membrane can stretch indefinitely, then equilibrium corresponds to zero pressure gradient, given by

$$\left(\frac{V}{V_o}\right)\Delta p = 0 = k_B T\frac{c_1^{(o)}}{w}\left(w - \frac{V}{V_o}\right) - \frac{2K_A}{R_o}\left(\frac{V}{V_o}\right)^{2/3}\left(\left(\frac{V}{V_o}\right)^{2/3} - 1\right), \tag{3.11}$$

which can be simplified to

$$\frac{\rho}{w}\left(w - \frac{V}{V_o}\right) - \left(\frac{V}{V_o}\right)^{2/3}\left(\left(\frac{V}{V_o}\right)^{2/3} - 1\right) = 0, \tag{3.12}$$

where the dimensionless constant $\rho = k_B T c_1^{(o)} R_o/2K_A$ is the ratio of the pressure scales set by the internal osmotic pressure and membrane stretch. For a typical phosphocholine bilayer vesicle at room temperature, with initial radius $R_o = 10\,\mu$m and internal osmolyte concentration of 300 mOsm (equivalent to the concentration of osmolytes in healthy *E. coli* [157]), $\rho \simeq 18$, or with a radius $R_o = 1\,\mu$m, closer to the size of a bacterium, $\rho \simeq 1.8$. While the fluid properties of bilayers allow them to bend into fantastically contorted shapes, bilayers cannot withstand high degrees of lateral stress, and tend to rupture for areal strains of only a few percent [26]. With this in mind, we employ the approximation $(V/V_o) - 1 \ll 1$ in eqn. 3.12 to find a simple expression for the equilibrium volume increase of a vesicle without channels under conditions of hypo-osmotic shock,

$$\left.\frac{V}{V_o}\right|_{t\to\infty} = \frac{(3\rho+2)w}{3\rho+2w}. \tag{3.13}$$

Finally, the equilibrium areal strain on a bilayer after osmotic down shock is

$$\phi = \left(\left(\frac{V}{V_o}\right)^{2/3} - 1\right) = \left(\left(\frac{(3\rho+2)w}{3\rho+2w}\right)^{2/3} - 1\right), \tag{3.14}$$

and knowing the rupture tension of a typical bilayer, we can bound the value of osmotic shock, w, that the vesicle can withstand in the absence of volume conducting channels. Assuming a maximum areal strain of $\sim 10\%$ can be sustained (and in many cases this is a high estimate), this puts an

upper bound on the hypo-osmotic shock a vesicle lacking volumetric channels can withstand, at the relatively low values of $w \simeq 1.16$ or $w \simeq 1.23$, for $R_o = 10\,\mu$m and $\rho = 18$ or $R_o = 1\,\mu$m and $\rho = 1.8$, respectively. For reference, these values of w correspond to a reduction of ~ 40 mOsm and ~ 55 mOsm respectively, from the 300 mOsm concentration in a typical bacterium [157], assuming the bacterium (or vesicle) is initially in osmotic equilibrium with its surroundings.

Moving forward, let us consider the same scenario, except now the bilayer contains volumetric conducting channels. This introduces two distinct, new processes. First, upon channel opening, the pressure gradient will drive volume through the channel pores into the vesicle. Second, the open pore acts as a diffusion channel for the movements of osmolytes down the concentration gradient, and out of the vesicle, where the exit of these osmolytes causes a small reduction in volume. To make this model tractable, we must simplify certain physical processes. The first assumption is that the internal and external concentrations of osmolytes are well mixed on time scales relevant to osmotic shock. In our current picture, this corresponds to the time required for the root-mean-square deviation of an osmolyte's position to traverse one vesicle radius, set by the diffusion coefficient of the osmolytes, the dimensionality, and vesicle size. Then the time scale of concentration equilibration is

$$t_{\text{eq}} = \frac{R_o^2}{6D} \tag{3.15}$$

in three dimensions. Given that the diffusion coefficient of sucrose in water at 25C (for instance) is $D \simeq 600\,\mu\text{m}^2/s$ [155], the concentration equilibration time scale is ~ 25 ms for a $10\,\mu$m vesicle or about $\sim 300\,\mu s$ for an *E. coli* size vesicle of radius $1\,\mu$m. As we will see in the forthcoming model, when the channels are open, the dynamics governing vesicle volume and osmolyte concentration are slow in comparison to this time scale, hence this is probably a reasonable approximation.

The second, more offending assumption is that the volume flux through the pore into the vesicle is independent of the flux of osmolytes through the pore, down the concentration gradient, and out of the vesicle. While this assumption might be invalidated by specific charge-based effects or interactions with the channel pore, we speculate that this approximation is reasonable in the scenario where the drift velocity of the water and osmolytes through the channel pore, due to the pressure and concentration gradients, respectively, is slow in comparison to their root-mean-square velocity through the pore from diffusion. For instance, given the pore length and diffusion coefficient of water ($\sim 3000\,\mu\text{m}^2/s$ [140]), the root-mean-square velocity through the channel pore is on the order of a $1\,\text{m}/s$. Using the same diffusion coefficient and considering one atmosphere of pressure driving water through the pore, for example, the drift velocity is only of order $0.01\,\text{m}/s$, hence this might be a reasonable approximation.

Like the previous thought experiment, the initial hypo-osmotic shock still produces a large inward pressure gradient that causes water to permeate into the vesicle. However, as the tension on the vesicle surface rises past a critical tension, the volumetric channels adopt the open conformation. If the pore of the channel is large enough to conduct water, but cannot conduct larger osmolytes, channel gating merely serves as a tension sensitive, discontinuous increase in the water

permeation coefficient of the bilayer, since there is still essentially no exchange of osmolytes across the membrane. Conversely, if the channel pore is large enough to pass osmolytes of various sizes, then for a sufficiently high density of channels in the bilayer, gating corresponds to a large, discontinuous increase in the permeation of *osmolytes*, as well as water. Thus as water permeates across the membrane and through the channels' pores into the vesicle, driven by the osmotic pressure gradient, osmolytes diffuse out through the channel pore driven by the concentration gradient. Already this suggests a basic design principle for channels that regulate osmotic pressure. If the flow of water through the channel pore is fast relative to the flow of osmolytes, channel gating only accelerates the onset of membrane rupture. On the other hand, if the flow of water through the channel pore is relatively slow, osmolytes can flow out equilibrating the osmotic pressure, before the influx of volume causes membrane rupture.

Let us again begin with the differential equation describing the vesicle volume, however now there are two new terms, one to account for the flow of water into the vesicle through the channel pore, and the second term to account for the removal of volume form the vesicle as osmolytes leave, giving the equation

$$\frac{\mathrm{d}V}{\mathrm{d}t} = c_p A \Delta p + N P_o(\tau) F_c(A_c, L, \eta, \Delta p) + V_{\text{osm}} \frac{\mathrm{d}n}{\mathrm{d}t}, \tag{3.16}$$

where N is the total number of channels, $P_o(\tau)$ is the open channel probability, and V_{osm} is the volume of each osmolyte. The time scale for conformational changes of the protein, on the order of a few microseconds [43], is much faster than any of the other processes involved with osmoregulation, and hence the actual protein dynamics are irrelevant to this model. The per channel flow rate, $F_c(A_c, L, \eta, \Delta p)$, is technically an unknown function of the pressure gradient across the pore (Δp), the pore area (A_c), pore length (L), and fluid viscosity (η). In fact, it is this flow that we eventually want to measure in our experiment, as a function of pressure gradient.

For the purposes of our model here, *a priori*, there are (at least) three reasonable classes of models to employ. First, is that of low Reynolds number, Hagen–Poiseuille flow through a pipe of area A_c and length L [153, 158], given by

$$F_c = \Delta p \frac{A_c^2}{8\pi\eta L}. \tag{3.17}$$

Physically speaking, models of laminar flow, like this, have the interesting property of time reversal symmetry, which means that the flow rate through the pore is independent of the direction of flow [158]. Hence the orientation of the channel in the bilayer has no effect on its flow properties, because the way that fluid moves through the pore does not depend on the direction of flow. Let us estimate the magnitude of flow predicted by this model. The open pore area of MscL is $A_c \simeq 7\,\mathrm{nm}^2$, the pore length is $L \simeq 2.5\,\mathrm{nm}$ and the viscosity of water at room temperature is $\eta \simeq 0.001\,\mathrm{N\,s/m}^2$. Notice that if we divide F_c by the channel area and pressure gradient, we arrive at what can be thought of as the permeation coefficient of the channel; in comparison to the flux of water across a pure bilayer, a MscL channel permeates water at a rate $\sim 10^4$ times faster (in this model). More concretely,

with one atmosphere of pressure across the pore, this model predicts a flow of $\sim 0.08\,\mu\text{m}^3/s$, or $\sim 10^6 - 10^7$ pore volumes per second.

Another possible model is that of granular flow, relevant in systems where particle and pore size are comparable and friction and/or dissipation are important dynamical parameters, as they are at low Reynolds number. Considering that the diameter of a water molecule is $\sim 0.4\,\text{nm}$, then the pore is only ~ 9 water molecules in diameter, and the entire pore can hold only about ~ 600 water molecules. Under these circumstances, one might rightly ask if a laminar flow approximation, like Hagen–Poiseuille flow, is valid. The physics of granular flow is an area of active research [159, 160, 161], and a few qualitative features are broadly acknowledged, namely a dependence on the ratio of the pore diameter to the particle diameter (even for values much larger than unity), the fact that the pressure (in most cases due to gravity) does not affect the flow rate through the pore, and a very different scaling of flux with pore area, $A_c^{3/4}$ [162], as opposed to A_c^2 for laminar flow or A_c as in the following diffuse transport model.

Unfortunately, no large scale molecular dynamics simulations have been undertaken to assess how volume moves through pores as large as the MscL pore. However, a few important facts have been garnered simulating the pressure driven flow of water through a model aquaglyceroporin channel [163]. These simulations show two important features; first that the flux through the channel is approximately linear with pressure gradient, and second that the permeation coefficient is not strongly dependent on the direction of flow, as shown in Fig. 3.4. Considering that a single file chain of water passes through the pore, let us assume that the pore has a diameter of one water molecule, and then the permeation coefficient of the pore is $\sim 0.008\,\mu\text{m}^3/\text{pN}s$, about 4000 times more permeable than a pure bilayer. The resulting flow rate is in agreement with the order of magnitude of channel flow found in cellular swelling experiments [142]. The scaling of the flux with pore area and length is still unknown, however the following paragraph attempts to estimate this scaling in the regime of diffuse transport.

The third model is the only one of these models that expressly accounts for the effects of temperature and diffusion, and pleasingly also depends on both the size of the pore and the size of molecules passing through it. At low Reynolds number the relevant equation of motion for a particle immersed in a fluid is Aristotelian, where the velocity (not acceleration) is proportional to the force through a mobility coefficient, $\mu F = v$ [111]. The Einstein relation, $D = \mu k_B T$, connects the diffusion of a particle to is mobility and temperature, such that we can write the equation of motion as $v = \frac{D}{k_B T} F$. Then consider that the pressure gradient across the pore can be easily translated into a force per molecule if we know the cross-sectional area of the molecule, by $F = \Delta p a$, where a is the area per molecule. Then the volumetric flux through the channel pore is

$$F_c = \Delta p \cdot A_c a \frac{D}{k_B T}. \tag{3.18}$$

Being a small, uncharged molecule, for all reasonable osmolyte concentrations, water is the major molecule passing through the pore, and hence its diffusion coefficient and cross-sectional area are

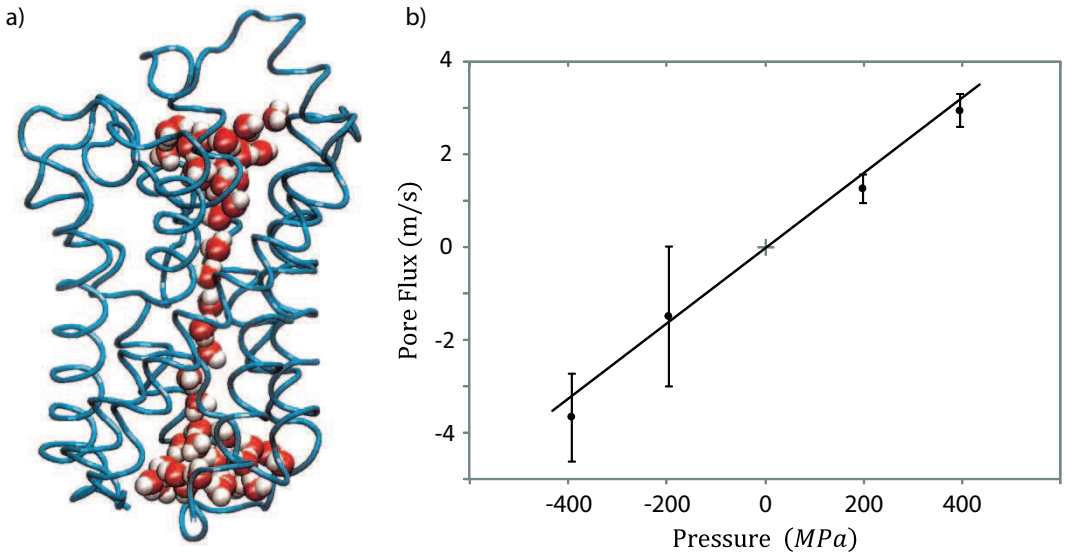

Figure 3.4: Molecular dynamics of aquaglyceroporin channel flow. a) Depiction of a single chain of water molecules in the pore of the aquaporin family protein GlpF as they are driven through by a pressure gradient. b) Flux of water per unit area per unit time as a function applied pressure gradient as simulated by all-atom molecular dynamics. The slope of this line is the pore permeation coefficient equal to $\sim 0.008\,\mu\mathrm{m}^3/\mathrm{pN}s$. Figure adapted from [163].

of interest. The diffusion coefficient of water is $D \simeq 3000\,\mu\mathrm{m}^2/s$ [140] and the cross-sectional area of a water molecule is $a \simeq 0.12\,\mathrm{nm}^2$. Under the same conditions we used in the laminar flow example, the channel would conduct a very similar value of $\sim 0.06\,\mu\mathrm{m}^3/s$, although this similarity is coincidental since the scaling with pore size is quite different. Compared to the flux through aquaglycerporin, as calculated through molecular dynamics [163], this method estimates the water permeation of the MscL pore is $\sim 0.09\,\mu\mathrm{m}^3/\mathrm{pN}s$, or about tens times more permeable per unit pore area. This is a reasonable model if the drift velocity of water molecules through the channel pore is slow in comparison to their root-mean-square velocity, which as we showed earlier, is the case for even the highest pressures encountered in the setting of osmoregulation.

Given that both the simulations of aquaglyceroporin and our own estimates of the diffuse transport of water through the pore predict a linear scaling with pressure gradient, let us invoke a constitutive model of pore flux, linear in both pore area and pressure gradient with permeation coefficient c_{pore}, such that the volume change of the vesicle is

$$\frac{\mathrm{d}V}{\mathrm{d}t} = \left(c_p A + N P_o(\tau) A_c c_{\mathrm{pore}}\right) \Delta p + V_{\mathrm{osm}} \frac{\mathrm{d}n}{\mathrm{d}t}. \tag{3.19}$$

The osmolyte volume, V_{osm}, is calculated using the effective hydrodynamic radius from the mobility, which includes coordinated waters around the osmolyte [134]; for example, $V_{\mathrm{osm}} = 0.20\,\mathrm{nm}^3$ for sucrose, which is the relevant osmolyte in our *in vitro* experiments.

Having discussed possible mechanisms by which channels conduct water, let us consider how channels regulate the effects of osmotic shock. In addition to its volumetric conductance, an open channel allows the passage of osmolytes across the membrane, hence changing the number of osmolytes enclosed by the vesicle. The osmolar concentration gradient causes a flux of osmolytes out of the vesicle, where Fick's Law for the flux of osmolytes through the cylindrical channel pore is given by

$$J_c = -D_o A_c \cdot \frac{\Delta c}{\Delta x} = -D_o A_c \cdot \frac{c_1 - c_2}{L}, \tag{3.20}$$

where D_o is the osmolyte diffusion coefficient, with $D_o \simeq 600\,\mu\text{m}^2/s$ for sucrose in water at 25C [155], and this is presumed to be a reasonable estimate of the diffusion coefficient for all osmolytes of interest[5]. That said, the structure of bacterial mechanosensitive channels (both MscL and MscS [11, 18]) have cytoplasmic domains that are proposed to be molecular sieves, only allowing the passage of certain osmolytes. Which osmolytes those are is still unknown, but if this speculative function of these domains is correct, it means that the osmolyte flux through the channel is not as simple as Fick's Law, because the concentration gradient that matters is then only the gradient of the osmolytes that can pass through the sieve. Rearranging this equation we see that the osmolyte flux is proportional to the osmotic pressure

$$J_c = -\frac{D_o A_c}{L k_B T} \cdot \Delta p^{(O)}. \tag{3.21}$$

Again, using the Einstein relation, $D_o = \mu_o k_B T$ [111], we find that within the limits of this approximation, the *osmotic* conductivity of a large pore channel is $\mu_o A_c / L$, a result completely analogous to the formula for electrical conductivity. Using this relationship, the total flux of osmolytes out of the vesicle is the product of this per-channel flux and the mean number of open channels. If the total number of channels in the vesicle is N, then the mean number of open channels, N_o, is simply

$$N_o = N P_o(\tau), \tag{3.22}$$

where, as shown in eqn. 3.14, τ is a function of the relative volume increase V/V_o. Thus the total flux of osmolytes out of the vesicle is

$$\frac{\mathrm{d}n}{\mathrm{d}t} = -N P_o \frac{D_o A_c}{L k_B T} \cdot \Delta p^{(O)}, \tag{3.23}$$

where we have made use of the continuity equation $N_o J_c - \mathrm{d}n/\mathrm{d}t = 0$. We now have two coupled, first order differential equations that describe the movement of volume, in terms of vesicle size, and the movement of osmolytes. Notice that the osmotic pressure, which appears in both equations, can be written as a function of the normalized volume, V/V_o, normalized number of osmolytes

[5] Accounting for osmolytes with differing diffusion coefficients is a straightforward extension of this equation.

n/n_o, and osmotic down shock, w, by

$$\Delta p^{(O)} = c_1^{(o)} k_B T \frac{1}{w}\left(w\frac{n}{n_o}\frac{V_o}{V} - 1\right). \tag{3.24}$$

Already we can see that the conditions of equilibrium, when $\dot{n} = \dot{V} = 0$, differ from a vesicle lacking channels; in this case equilibrium demands both $\Delta p^{(O)} = 0$ and $\Delta p = 0$. This has a number of significant implications. Unlike a vesicle lacking channels, vesicles with channels equilibrate their internal osmolarity with the external osmolarity and given sufficient time will return to their original volume after osmotic shock, and hence return to their original state of (nearly) zero tension.

To demonstrate the concepts laid out in this thought experiment, we will numerically solve this set of equations to demonstrate their behavior in a few different regimes. After some lengthy algebraic manipulation, the differential equation for the volume change can be written as

$$\begin{aligned}\frac{\mathrm{d}}{\mathrm{d}t}\left(\frac{V}{V_o}\right) = \frac{2K_A}{V_o R_o}\left(\frac{V_o}{V}\right)\left[4\pi R_o^2 c_p\left(\frac{V}{V_o}\right)^{\frac{2}{3}} + NP_o A_c c_{\mathrm{pore}}\right]\cdot \\ \left[\frac{\rho}{w}\left(w\frac{n}{n_o} - \frac{V}{V_o}\right) - \left(\frac{V}{V_o}\right)^{\frac{2}{3}}\left(\left(\frac{V}{V_o}\right)^{\frac{2}{3}} - 1\right)\right] + c_1^{(o)} V_{\mathrm{osm}}\frac{\mathrm{d}}{\mathrm{d}t}\left(\frac{n}{n_o}\right)\end{aligned} \tag{3.25}$$

where the initial condition is $V/V_o|_{t=0} = 1$. With similar algebraic manipulation, the equation for the relative number of osmolytes in the vesicle can be written as

$$\frac{\mathrm{d}}{\mathrm{d}t}\left(\frac{n}{n_o}\right) = -NP_o \cdot \frac{D_o A_c}{L V_o}\cdot\frac{1}{w}\left(w\frac{n}{n_o}\frac{V_o}{V} - 1\right), \tag{3.26}$$

where the initial conditions is $n/n_o|_{t=0} = 1$.

In Fig. 3.5, we numerically explore the behavior of an *E. coli* size vesicle with $R_o = 1\,\mu$m under differing degrees of osmotic shock, two different channel densities, and using both the calculated permeation rate of the MscL from eqn. 3.18 and the 'measured' permeation rate of aquaglyceroporin applied to the MscL pore. This analysis shows a number of interesting effects and unique time scales for swelling and equilibration. Qualitatively, we can map out how such a vesicle will behave under different conditions. Consider first the following scenario: upon osmotic shock, the vesicle swells and tension increases. If the osmotic shock is relatively low, the vesicle swells slowly, the tension does not rise enough to trigger channel opening, and we are essentially in the regime where the presence of the channels, at any molar concentration, does not matter (*e.g.* see Fig. 3.5 for $w = 1.05$). Next, consider the contrasting scenario, where the osmotic shock is relatively high, the vesicle rapidly swells, the tension rises, and upon reaching the gating tension of the channel, osmolytes begin to flow out of the vesicle at a rate determined by the product of channel osmolyte conductivity and channel density. Concomitantly, volume rushes into the vesicle through the channels and, depending on the degree of osmotic shock, for a sufficient density of channels the internal osmolyte concentration decreases rapidly enough so that the tension / areal strain peaks below the value for

bilayer rupture (*e.g.* see Fig. 3.5 for $w \leq 2$). Then the tension gradually drops, the channels begin to close, and the vesicle volume slowly returns to its initial state. These are necessary steps for proper osmoregulation. Finally, again consider high osmotic shock, but where the channel density is too low, or the flux of water through the pore into the vesicle is high relative to the flux of osmolytes through the pore out of the vesicle, the tension will rise to the point of rupture (*e.g.* see Fig. 3.5 for $w \geq 10$ for all but the last column).

While we acknowledge that our analysis is fairly simplistic, built on simple models of the various physical processes involved, one might also see this as making the model robust in a certain sense. The bottom line of this preliminary analysis is multi-faceted. First, at the ostensible *in vivo* channel density (~ 10 per cell [112] or 10 per $R_o = 1\,\mu$m vesicle), this model indicates that large changes in the volumetric conductance of the channel (by an order of magnitude) have relatively little effect on the maximum degree of osmotic shock that can be tolerated, and that maximum degree, on the surface, seems incommensurate with the degrees of osmotic down shock that cells are known to be able to withstand in experiment. Specifically, for the set of parameters meant to mimic bacterial conditions, in Fig. 3.5(a–c)(low flow) and (g–i)(high flow), the maximum change in osmolyte concentration that does not rupture the membrane is ~ 150 mOsm (and in terms of this model, that is likely a high estimate). Whereas experiments show that bacteria can withstand reductions of ~ 500 mOsm [17, 164]. In a similar manner, increasing channel density (in our model) by an order of magnitude does not rectify this apparent discrepancy, as shown in Fig. 3.5(d–f), but does raise the maximum osmotic down shock to ~ 250 mOsm.

There are a number of possible explanations of these results. One possibility is that the bacterial membrane permeates water much more slowly than *in vitro* bilayers. Another, possibility is that the bacterial membrane is much stiffer than purified bilayers. The author speculates that the cell wall acts to stiffen the effective stretch modulus of the inner membrane, thereby allowing the cell to osmoregulate even with large degrees of down shock, as shown in Fig. 3.5(j–ℓ), but this remains to be seen through further modeling and experimentation.

3.4 Measuring Ensemble Channel Flow

Now that we have built some intuition for how channel density, qualitative channel flow characteristics, and osmotic shock affect the state of tension and volume of a free vesicle we are in a position to design an experiment that will actually measure the volumetric flow through a channel under certain assumptions. The experiment begins with a vesicle containing reconstituted MscL channels, with a surface area to volume ratio larger than that of a sphere, that is, a vesicle with extra area. The vesicle contains sucrose inside at a controlled osmolarity, and glucose in the solution outside, at the same osmolarity. The slight density difference between the sucrose solution inside and glucose solution outside [155], sediments the vesicle to the bottom of the microscope chamber in which the experiment will take place, allowing it to be easily viewed. The membrane is fluorescently labeled

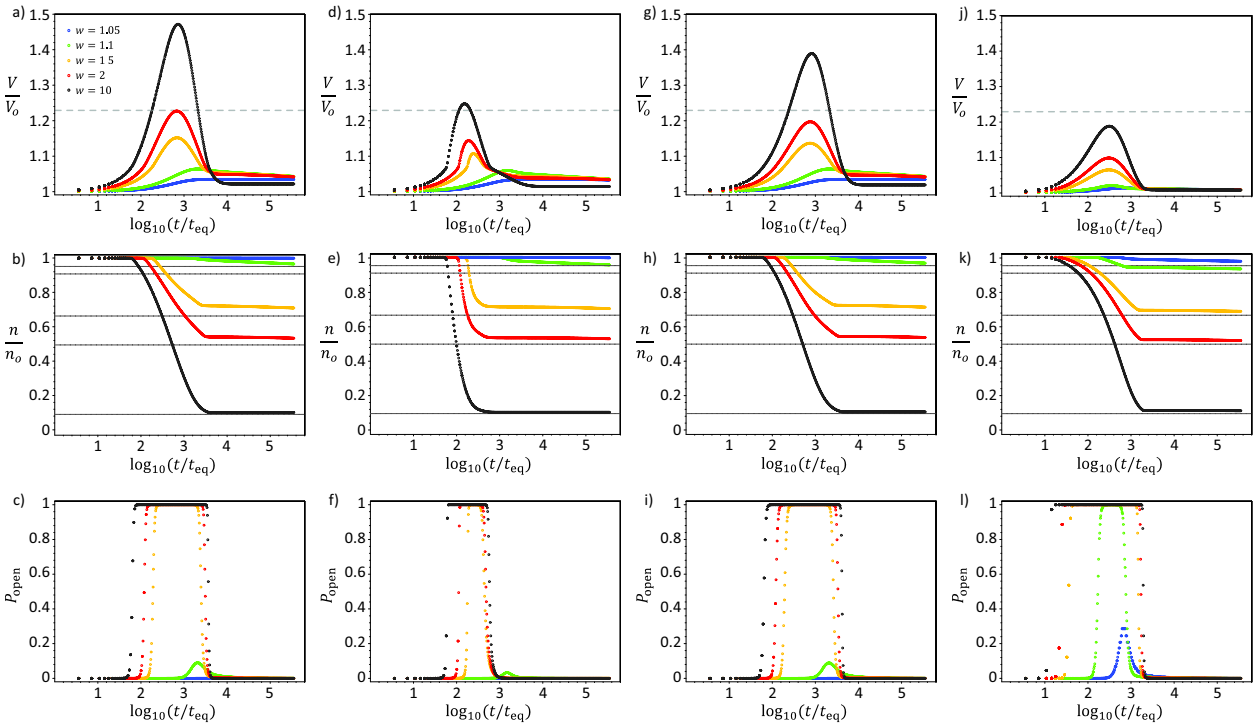

Figure 3.5: Numerical solutions for the behavior of a vesicle with volumetric channels under hypo-osmotic shock. In all plots the pore area is $A_c = 7\,\text{nm}^2$, the pore length is $L = 2.5\,\text{nm}$, the free energy of gating is $\Delta G = 20\,k_BT$, the vesicle radius is $R_o = 1\,\mu\text{m}$ (approximately the size of an *E. coli* bacterium), the initial internal osmolyte concentration is $c_1^{(o)} = 300\,\text{mOsm}$ which is the measured absolute osmotic concentration in *E. coli* [157], and the degree of osmotic shock w is listed in the legend; all other parameters are indicated in the text. The gray lines in the plots of relative osmolyte number (n/n_o) are the asymptotic values, given by $1/w$. As discussed in this section, a relative volume increase of $V/V_o \simeq 1.23$ is the maximum areal strain that a membrane vesicle of this size can withstand before rupture; this level is indicated by the gray dashed lines in the plots of V/V_o. a-c) The relative volume, relative number of osmolytes and ensemble channel open probability, respectively, for a vesicle with a molar ratio of channel protein to lipid of $1{:}10^6$, estimated to be the *in vivo* ratio [112]. In these plots the channel flow follows the diffuse model of eqn. 3.18. d-f) The relative volume, relative number of osmolytes and ensemble channel open probability, respectively, for a vesicle with a molar ratio of protein to lipid of $1{:}10^5$, ten times higher than the *in vivo* estimate. Notice that even with elevated protein levels, osmoregulation is still compromised. g-i) The relative volume, relative number of osmolytes and ensemble channel open probability, respectively, for a vesicle with estimated *in vivo* molar ratio of channel protein to lipid of $1{:}10^6$, but a flow rate set by the permeation coefficient of aquaporin as measured by molecular dynamics [163]. Notice that changing the pore permeation coefficient by a factor of ten has only a minor effect on the osmoregulation, as compared to (a-c). j-ℓ) The relative volume, relative number of osmolytes and ensemble channel open probability, respectively, for a vesicle with a molar ratio of protein to lipid of $1{:}10^6$, and channel flow following the diffuse model of eqn. 3.18, but with the membrane stretch modulus five times higher than a typical bilayer, that is $K_A = 300\,k_BT/\text{nm}^2$, as a speculative estimate to approximate stiffness of the surrounding cell wall in an actual bacterium.

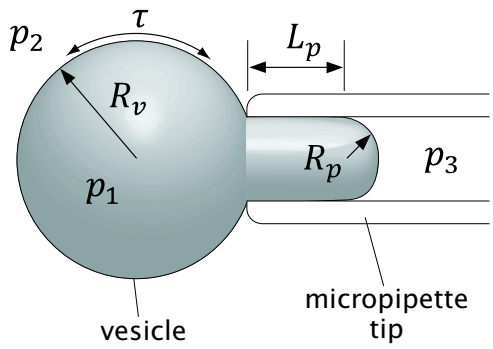

Figure 3.6: Schematic of aspirated vesicle shape. The shape of an aspirated vesicle is characterized by a large outer portion with radius R_v, a cylindrical portion in the pipette of length L_p and radius R_p with a hemispherical cap of radius R_p. Knowing the pressure gradient $p_2 - p_3$, one can calculate the internal pressure of the vesicle, p_1, and the membrane tension τ. Figure adapted from [1].

with a small mole fraction of rhodamine head-group labeled lipid (usually 0.5%), which is used to visualize the vesicle in epi-fluorescence.

In the equatorial plane of the vesicle, we approach with a glass micropipette, pre-coated with bovine serum albumin, so as to prevent the bilayer sticking to the glass. The solution inside the pipette is the same as the solution outside the vesicle. In the far field, the pressure drop across the pipette tip is controlled by the height of a water bath and it has been adjusted so that there is zero pressure drop across the pipette tip at the height of the equatorial plane of the vesicle. As we get close to the vesicle surface, the height of the water bath is lowered, creating a small suction pressure, of only a few tens of Pascals, at the pipette tip. Presuming the tip is close enough to the target vesicle, the vesicle enters the tip forming the aspirated shape shown in Fig. 3.6. The bending energy difference between this aspirated shape and the nominally spherical shape before aspiration is miniscule in comparison to the energy of stretching the membrane and performing PV work with the pipette.

This shape is characterized by three main geometric features: an outer vesicle radius R_v, an in-pipette length L_p, and a pipette radius R_p. Additionally, three pressures exist in the three volumetric regions. In the pipette is the lowest pressure, p_3, set by the far-field water bath; in the vesicle is the highest pressure, p_1; and in the region outside the vesicle is atmospheric pressure p_2. Because the pipette has been coated with a blocking agent that prevents membrane sticking to the pipette, there is a slip boundary condition inside the pipette, and thus the tension on the membrane is equal in all regions. We can calculate this tension by again employing the Laplace-Young relation. The pressure drop across the outer vesicle is $(p_1 - p_2)$ and hence the tension is

$$\tau = \frac{1}{2}(p_1 - p_2)R_v, \tag{3.27}$$

and the pressure drop across the inner spherical region is $(p_1 - p_3)$ and hence the tension is also

given by

$$\tau = \frac{1}{2}(p_1 - p_3)R_p. \tag{3.28}$$

This gives us two equations and two unknowns, namely the tension τ and the internal pressure p_1. Solving this system of equations leads to the well-known approximation for vesicle tension [26]

$$\tau = \frac{p_2 - p_3}{2}\frac{R_p}{1 - \frac{R_p}{R_v}}, \tag{3.29}$$

and internal pressure is calculated using

$$\tau = \frac{1}{2}(p_1 - p_2)R_v, \tag{3.30}$$

to find

$$p_1 - p_2 = (p_2 - p_3)\frac{R_p/R_v}{1 - \frac{R_p}{R_v}}. \tag{3.31}$$

Typical experimental values for the ratio R_p/R_v range from ~ 0 to $\sim 1/2$, and thus the factor on the right hand side of this equation is, at most, order unity. Typical values of the pressure gradient, $(p_2 - p_3)$, are set by the relative height of the water bath, equivalent to a few inches of water (1 inch water at STP $= 249.0\,Pa$), thus the pressure gradient across the membrane is on the order of a kilo-Pascal or less. Another important feature to notice is that these equations are monotonic in the variable R_p/R_v which means that as the vesicle progressively deforms and enters the pipette, tension and pressure always rise, as shown in Fig. 3.7.

Clearly, to make a measurement of channel volumetric flux, we must be able to measure some kind of volume change. One of the results from our earlier calculation is that a pressure gradient across a membrane of a few kilo-Pascals, fractions of an atmosphere, has essentially no effect on osmolyte concentrations in the volume enclosed by a pure bilayer vesicle if the absolute, but balanced, osmotic pressure is multiple atmospheres. This suggests that the easiest way to conduct this experiment is with an internal and external osmolyte concentration of a few hundred milli-osmolar, equivalent to a few atmospheres of absolute osmotic pressure. Under these circumstances, the pressure gradients $p_1 - p_2$ and $p_1 - p_3$ will not cause any significant water permeation across the membrane.

The volume and surface area of an aspirated vesicle are calculated using the geometry of the aspirated shape, where the total vesicle volume is

$$V = \frac{2}{3}\pi R_p^3\left[2\left(\frac{R_v}{R_p}\right)^3 + \frac{3}{2}\frac{L_p}{R_p} + 1\right], \tag{3.32}$$

and the total vesicle area is

$$A = \pi R_p^2\left[4\left(\frac{R_v}{R_p}\right)^2 + 2\frac{L_p}{R_p} + 1\right], \tag{3.33}$$

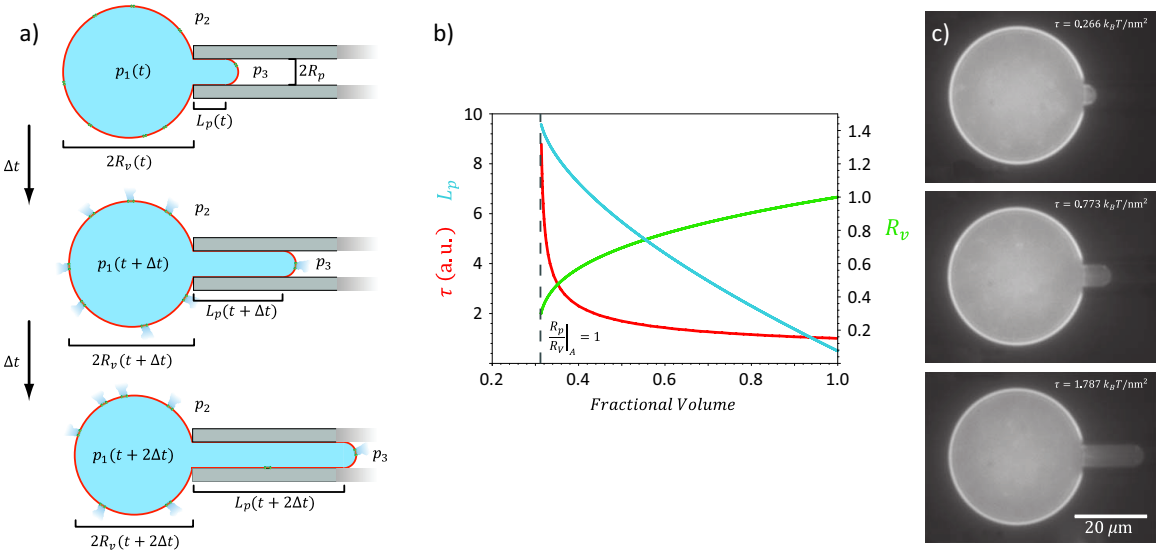

Figure 3.7: General experimental design for MscL volumetric flux experiments. a) A schematic showing how the aspirated shape of a large vesicle (orange), held by a pipette (gray), evolves over time as water and osmolytes are driven through the membrane-embedded efflux channels (green) by the pressure gradients $p_1 - p_3$ and $p_1 - p_2$. Over time the outer vesicle radius (R_v) shrinks, while the in-pipette length (L_p) geometrically amplifies the change in volume due to channel efflux. Shown here are the exact shapes of a vesicle for $\Delta V/\Delta t = -V_o/10$, where V_o is the vesicle volume in the first frame. b) In cases where the additional area from membrane stretch can be neglected, the outer vesicle radius and in-pipette length can be written as a function of the fractional volume, that is, the current volume normalized by the volume at $t = 0$; these plots show this in arbitrary units for the vesicle in (a). c) Fluorescence images of an actual vesicle at varying levels of membrane tension, as indicated on the images.

both written in terms of the dimensionless shape measures, L_p/R_p and R_v/R_p, which are the relevant independent shape variables considering that R_p is a geometric parameter fixed by the pipette; or in other words, these are the parameters one measures during an experiment. Thus measuring volume and area of an aspirated vesicle is reduced to measuring a few geometric parameters, which can be easily tracked in time through video microscopy. This system of equations can be solved for the values of these geometric parameters, which we will use later in this section, however the results are rather lengthy to write out explicitly.

Let us presume that the aspirated vesicle has some concentration of channels, such that there are N channels in the bilayer. Then the flux of water and osmolytes out of the aspirated vesicle is given by the product of the number of open channels subject to a particular pressure gradient across the two relevant patches of membrane

$$\frac{\mathrm{d}V}{\mathrm{d}t} = -NP_o(\tau)\left[\frac{\pi(4R_v^2 - R_p^2)}{A}F_c(p_1 - p_2) + \frac{2\pi R_p^2}{A}F_c(p_1 - p_3)\right], \tag{3.34}$$

or in a slightly simplified form[6]

$$\frac{\mathrm{d}V}{\mathrm{d}t} = -\frac{N}{A}P_o(\tau)\pi R_p^2\left[(4(R_v/R_p)^2 - 1)F_c(p_1 - p_2) + 2F_c(p_1 - p_3)\right]. \tag{3.35}$$

As indicated in the two equations above, the two relevant patches of membrane are the outer vesicle region, and the spherical patch of membrane inside the pipette. The cylindrical patch of membrane presumably has the same density of channels, but as it pressed up against the glass pipette, and is in force balance, there is no water flux through the channels in this region.

Qualitatively, the course of events of the experiment will go as follows. The vesicle is initially aspirated, tension is at a low level, relative to the gating tension of the channels. Even at this low tension, channels sporadically open and release volume, the geometric parameters change, and the vesicle tension and internal pressure incrementally increase. As this process continues, tension rises until the gating tension is reached and then volume begins to rapidly exit the vesicle, regulated by the channel density, their pressure dependent flow rate, and the area of membrane across which the pressure gradient acts, which is ever decreasing. At some point the vesicle will lose enough volume that it either pops or is sucked into the pipette. One advantage of such a setup is that each experiment samples a range of pressure gradients across the membrane. The setup just described is the simplest, because it fixes the pressure drop across the pipette $p_2 - p_3$. There are also other ways one could conduct the experiment, namely, if software is written to track vesicle shape in real time, the tension and internal pressure can be calculated, and a feedback to the pressure mechanism could be used such that the tension or internal pressure is held constant even as the vesicle shape evolves. In such experiments, the vesicle volume and geometric parameters, R_v/R_p and L_p/R_p, as

[6]Equation 3.35 can be further simplified if the vesicle volume and area are such that $R_v/R_p > 1$, such that the area in the outer vesicle is much larger than the area in the spherical region inside the pipette; under these circumstances, the second term on the right hand side of eqn. 3.35 can be ignored.

a function of time are the basal measurements.

As we did in the previous section, where osmotic shock of a free vesicle was examined, this equation can be numerically simulated if we write the tension (τ), internal pressure (p_1), area (A) and outer vesicle radius (R_v) as a function of the enclosed volume (V), using eqns. 3.29, 3.31, 3.33 and 3.32, respectively. To perform this simulation we must again appeal to a presumptive model of channel flow, and for consistency with the previous calculation, we will again assume that the volumetric flux through the channel is linear in the pore area and pressure gradient, given by eqn. 3.18, with the permeability calculated from the diffusion coefficient of water. We performed these simulations under two generic conditions that correspond roughly to energetic properties of two mutants of MscL, namely the relatively difficult to gate wild-type protein, and a gain-of-function point mutant with lower gating free energy, as shown in Fig. 3.8. The advantages to using the gain of function mutant are two-fold, as discussed in Section 3.4.2. The idea is that mutants can be to answer both of our motivating questions. Independent of the lipid-protein interactions, the gain-of-function mutant can be used to measure the volumetric flow properties of the channel, as shown in Fig. 3.8(c and d); this experiment is of significant interest in and of itself, but is also necessary to measure ensemble channel gating properties. With that information in hand[7], the gain-of-function mutant can be used to measure the dose-response curve (*i.e.* P_{open} vs. τ), as simulated in Fig. 3.8(e and f).

3.4.1 Bilayer Permeability and Proof of Concept

In an effort to put the conceptual layout of the experiment discussed in the previous section on a firm footing, we performed a series of membrane permeation experiments that serve as a proof of concept for our ability to track detailed vesicle shape, membrane tension and internal pressure through time. The advantage to conducting these preliminary experiments is two-fold: first we could move forward with detailed experimental design and software development without having to first streamline protein purification and reconstitution; second, given our analysis of osmotic shock in previous sections we expect that membrane permeation results in a slow change in volume, relative to vesicles that have volumetric channels at a reasonable molar fraction, and hence we can assess the temporal sensitivity of our experimental setup. Additionally, corroborating our measurement of pressure-driven permeation in a standard phosphocholine bilayer to values determined by others [140, 156], serves as a reality check that our setup is working properly.

The protocol for measuring membrane permeability is exactly the same as the protocol for measuring channel volumetric flux, except, of course, there were no channels in the bilayer. One other important difference between the two experimental setups was that to actually enable water to permeate through the bilayer, the osmotic gradient had to be balanced and the absolute osmotic pressure had to be very low, in this case we simply set the internal and external absolute osmotic pressure to zero (*i.e.* the internal and external sugar concentrations were zero). Results from

[7]This is not meant to be flippant, we are sure many unique challenges lie in wait for us during these experiments.

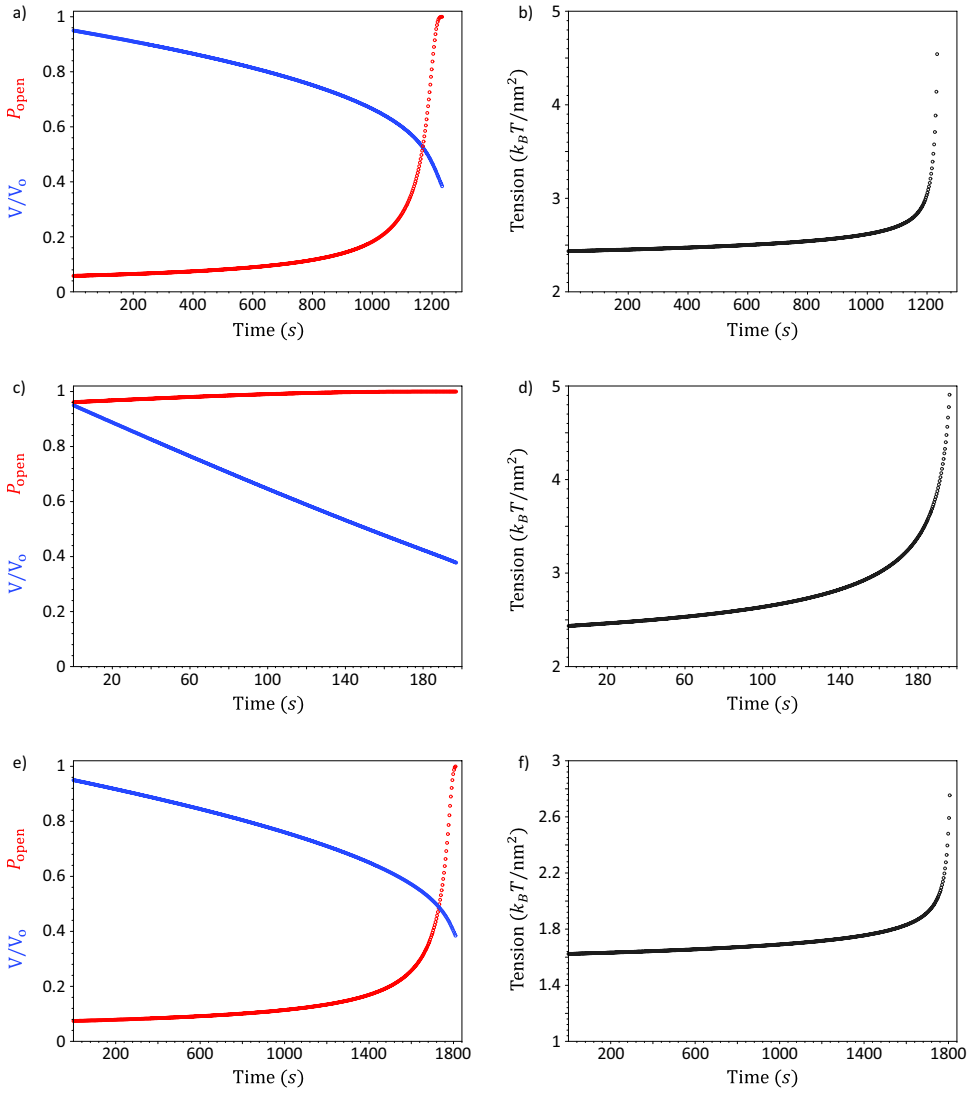

Figure 3.8: Simulating a measurement of ensemble channel flux via GUV aspiration. In all plots the protein to lipid ratio is $1:5\times10^4$, the channel pore area is $A_c = 7\,\mathrm{nm}^2$, the pipette radius is $R_p = 5\,\mu\mathrm{m}$, the initial vesicle radius is $R_o = 20\,\mu\mathrm{m}$, the initial volume is 95% the volume of a sphere with radius R_o (*i.e.* $0.95V_o$), and the constitutive flow model employed is 3.18. a) The channel open probability and normalized volume V/V_o as a function time for the wild-type channel. b) The membrane tension as a function of time for the same physical scenario as (a). In (a) and (b) the pressure gradient is $p_2 - p_3 = 3000\,\mathrm{Pa}$. c) The channel open probability and normalized volume V/V_o as a function time for the gain-of-function mutant channel ($\Delta G = 14\,k_BT$). d) The membrane tension as a function of time for the same physical scenario as (c). In (c) and (d) the pressure gradient is $p_2 - p_3 = 3000\,\mathrm{Pa}$. Notice that using the mutant at this pressure gradient linearizes the vesicle volume flux, because $P_o \simeq 1$, and speeds up the experiment by an order of magnitude. e) The channel open probability and normalized volume V/V_o as a function time for the mutant channel. f) The membrane tension as a function of time for the same physical scenario as (e). In (e) and (f) the pressure gradient is $p_2 - p_3 = 2000\,\mathrm{Pa}$, lowering the membrane tension considerably, and lengthening the experiment by an order of magnitude as compared to (c) and (d).

these preliminary experiments are very encouraging (see Fig. 3.9); under optimal conditions we can measure changes in vesicle volume of a percent or less, measure changes in internal pressure of $\sim 25\,\mathrm{Pa}$, and measure changes in membrane tension as small as $\sim 0.01\,k_BT/\mathrm{nm}^2$, all of which suggest that we have adequate sensitivity to measure the volumetric flux through channels.

From these experiments we were able to calculate the water permeation rate and hence water permeation coefficient of a typical phosphocholine bilayer (DOPC), as shown in Fig. 3.9. Equally encouraging as determining that we have more than sufficient sensitivity to perform the proposed measurement, the value of the permeation coefficient we measure, while somewhat variable due to issues of image quality, is in good quantitative agreement with previous measurements; Olbrich and coworkers [140] measured a permeation coefficient in DOPC of $1.9 \times 10^{-6}\mu\mathrm{m}^3/\mathrm{pN}s$ and we measured a tension-independent value for the permeation coefficient of $1.9 \pm 1.5 \times 10^{-6}\mu\mathrm{m}^3/\mathrm{pN}s$.

3.4.2 Using Gain-of-Function Mutants

While the experiment, discussed above is relatively simple in concept there are two complications that should be discussed, and for which we have likely found a solution by using mutant forms of MscL that gate at significantly lower tensions. The first issue is that rupture of a bilayer, caused by tension, does not exhibit the same properties as failure in macroscopic materials. In previous sections, we stated that an areal strain greater than $\sim 10\%$ results in membrane rupture, and indeed this is a good upper bound value for the tensile strain of a typical bilayer. Although, unlike a macroscopic material (*e.g.* latex, steel, etc.), whose tensile strength has a well defined value; the rupture, and hence rupture tension, of a bilayer is a stochastic process sensitive to thermal fluctuations. More precisely, rupture of a bilayer is caused by the nucleation of membrane holes. Above a critical size a hole will grow rapidly causing catastrophic failure of membrane integrity [53], similar to the popping of a balloon, where the kinetics of hole nucleation depend on thermal fluctuations and membrane properties.

We can briefly outline this failure mechanism to understand how the rate of failure depends on membrane tension. When a hole is created in a bilayer, the hydrophobic core of the membrane is exposed to water, and lipids will leave their normal positions to partially cover the core. The combined exposure of the hydrophobic core and the deformation of lipids that try to cover the core, cost a certain energy per unit length. This line tension was measured in a series of experiments where giant unilamellar vesicles where electroporated during pipette aspiration, in a manner similar to the experiments discussed here. The line tension was found to be $\gamma \simeq 2.5\,k_BT/\mathrm{nm}$ for a typical phosphocholine bilayer (without cholesterol)[165]. If the membrane is subject to a tension τ, the creation of a hole of radius r will have an elastic free energy

$$G_{\mathrm{hole}} = 2\pi r\gamma - \pi r^2\tau. \tag{3.36}$$

This equation always has a minimum at $r = 0$, and there is a barrier between this stable state and

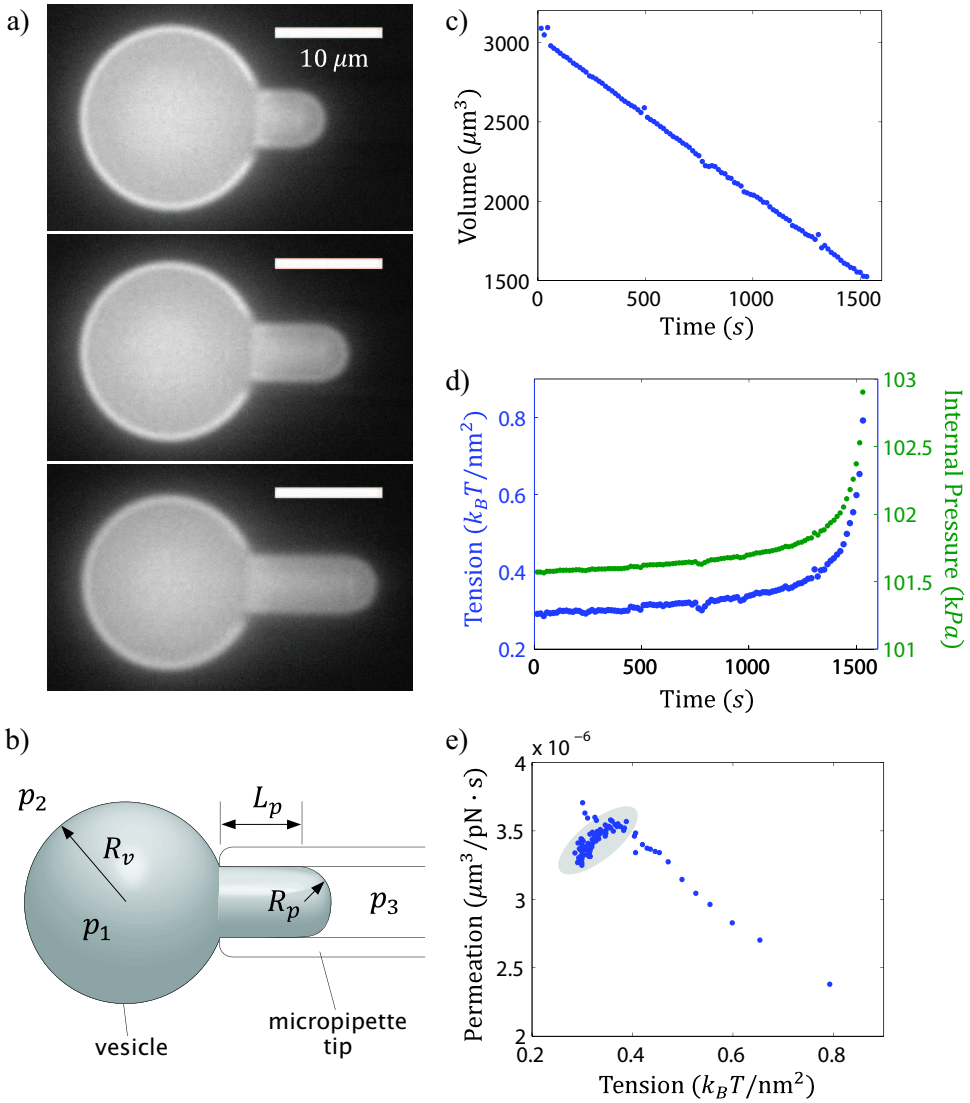

Figure 3.9: Proof of concept by measuring bilayer water permeability. a) Three fluorescent images of an aspirated giant unilamellar vesicle, as water permeates through the bilayer decreasing the enclosed volume. b) Schematic of an aspirated vesicle showing the important shape characteristics and pressures required to calculate volume, area, and tension as a function of vesicle shape. c) Volume of the aspirated vesicle in (a) as a function of time at constant pressure gradient $p_2 - p_3$. d) Calculated membrane tension and internal pressure as a function of time as vesicle volume decreases. e) The bilayer permeation coefficient as a function of the calculated membrane tension. For the approximately linear regime of tension in (d), the permeation coefficient increases slightly, as indicated by the gray ellipse, but has an approximately constant value of $3.5 \times 10^{-6} \mu\text{m}^3/\text{pN}s$. The average permeation coefficient measured over a number vesicles ($n = 16$) was $1.9 \pm 1.5 \times 10^{-6} \mu\text{m}^3/\text{pN}s$, in good quantitative agreement with previous measurements [140].

hole nucleation that leads to membrane failure, where the critical size for hole nucleation is $r_c = \gamma/\tau$ and the barrier height for the rupture transition is $G_{\rm barr} = \pi\gamma^2/\tau$. We can estimate the maximum tension that can be stably applied to a vesicle by saying that the barrier to hole nucleation must be much greater than k_BT, for instance $G_{\rm barr} \sim 10\,k_BT$, which happens when $\tau = \pi\gamma^2/10\,k_BT$. For the value of line tension quoted above, this yields a nominal maximum stable tension of $\sim 2\,k_BT/{\rm nm}^2$ which is in line with our previous estimates. The point of this little exercise is to show that membrane failure is actually a stochastic process, whose rate, $k_{\rm hole} \propto e^{-G_{\rm barr}}$, increases rapidly with τ. Thus if we are forced to subject the bilayer to high membrane tensions, like those estimated in bacteria and measured *in vitro* to gate the MscL channel, we are already tempting stochastic fate to rupture the membrane. If we can use lower tensions to gate the channel, the chances that the membrane will rupture during an experiment decrease exponentially.

The second issue concerns the requirement that we know the detailed dose-response curve of channel opening. In eqn. 3.1 and borne out in Fig. 3.3, we saw that the gating tension of MscL was $\sim 2 - 3\,k_BT/{\rm nm}^2$, again close to the expected rupture tension of a membrane. Our analysis of vesicle shape shows that pressures and/or reduction in volume required to achieve this tension are relatively high, and hence to actually relate the volume flux of the channel to the reduction in volume of the vesicle would require detailed knowledge of $P_o(\tau)$. It is then a bittersweet fact that the dose-response curve changes with lipid type [22] and even shows variability within the same bilayer composition, as shown in Fig. 3.3. One way around this complication is to employ a mutant channel whose gating tension is easily achieved, such that past some relatively low value of membrane tension, we can be sure that the probability that any one channel is open is essentially unity. In other words, we seek a mutant form of the channel for which it is easy to force the function $P_o \simeq 1$ for some value of τ much less than the rupture tension, and hence the detailed nature of the dose-response becomes irrelevant.

Thankfully, mutational studies of MscL have shown that by changing the hydration energy of the channel pore, the free energy of gating related to channel structure, $\Delta G_{\rm prot}$, can be reduced [34, 33] (or augmented [98]). Specifically, examining the hydrophobicity of residues lining the channel pore that become hydrated upon channel opening, one finds a number of them have a high degree of hydrophobicity, as measured by standard hydropathy [166]. The mutant form of the channel we will use[8] has a single point mutation at the 23rd residue from the C-terminus, changing a hydrophobic valine (hydropathy 4.2 [166]) to either of two hydrophilic residues, threonine (hydropathy -0.7 [166]) or aspartic acid (hydropathy -3.5 [166]), at the narrowest point of the channel pore, as shown in Fig. 3.10. In practice, the latter mutant opens too easily and hence is generally toxic to the bacteria at expressions levels required for purification of the channel.

Using measured values of the hydration energy of amino acids, in this case free energies of transfer from octanol to water [167], the free energy of transfer of valine is $0.77\,k_BT$ per molecule,

[8] Kindly constructed and donated, with a poly-histidine purification tag, for the purposes of this research by S. Sukharev, University of Maryland.

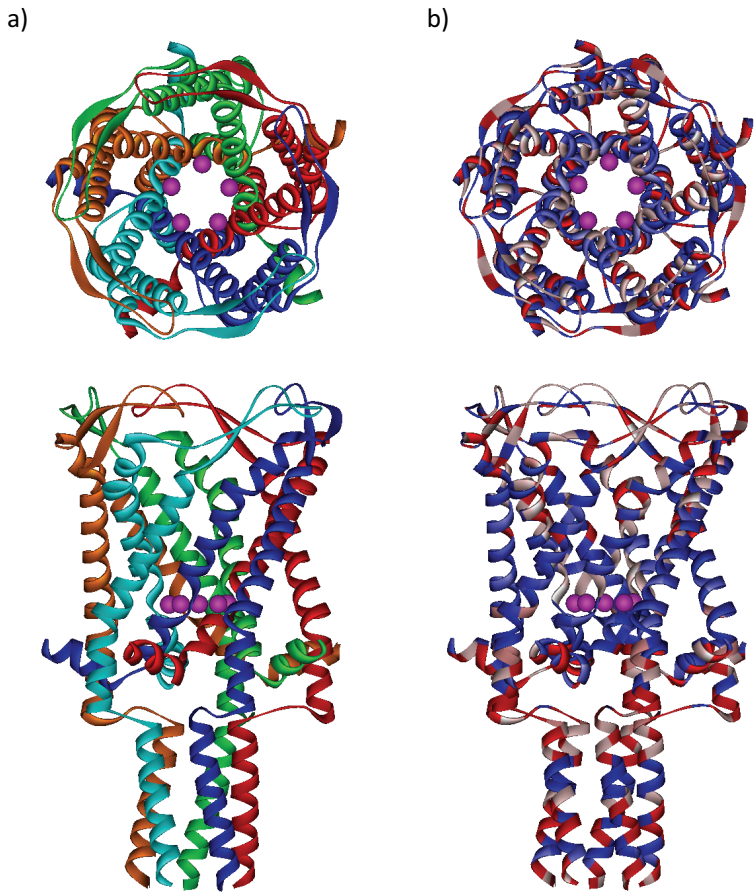

Figure 3.10: Gain of function MscL mutants. a) Top and side view of the V23 point mutation site in the narrowest part of the channel pore as shown by the magenta spheres on each MscL monomer. In this view, each protein monomer is uniquely colored. b) Top and side view of the V23 point mutation site in the narrowest part of the channel pore as shown by the magenta spheres. In this view, protein residues are colored by hydrophobicity, blue being more hydrophobic than red. We clearly see that the transmembrane helices are generally hydrophobic, as is the conducting pore, hence the reason why this point mutation is effective in changing the protein free energy.

and $-0.42\,k_BT$ and $-0.72\,k_BT$ for threonine and aspartic acid respectively. The channel protein is composed of five identical subunits [11], each carrying the point mutation. Thus within the limitations of this estimate, the hydration of the valines in the pore raises the free energy $\sim 3.9\,k_BT$, while hydration of threonine and aspartic acid lower the free energy by $\sim 2.1\,k_BT$ and $\sim 3.6\,k_BT$ respectively. Thus in terms of the change in the change in free energy of gating, from wild type to either of these mutants, we estimate the free energy of the gating transition is lowered by $\sim 6\,k_BT$ for the threonine point mutation, and by $\sim 7.5\,k_BT$ for the aspartic acid mutation. Using our nominal value of the total free energy of gating in the wild type protein of $20\,k_BT$, and change of protein area upon gating of $7\,\text{nm}^2$ we calculate a gating tension of $\sim 2.85\,k_BT/\text{nm}^2$ for the wild type protein, again near expected values for membrane rupture. Using our estimates of the reduction in hydration energy of the threonine and aspartic acid point mutants, the gating tensions are reduced to $\sim 1.98\,k_BT/\text{nm}^2$ and $\sim 1.78\,k_BT/\text{nm}^2$, respectively. While this is a naive estimate, it puts the qualitative mechanism of gating tension reduction by pore point mutation on sound theoretical footing. Additionally, using the estimates of membrane hole nucleation, we can estimate the relative decrease in the rate of hole nucleation, and subsequent membrane failure when using the gain of function mutants. Given that the rate of hole nucleation is proportional to the Arrhenius factor $e^{-\pi\gamma^2/\tau}$, and we now have estimates for the gating tensions in the wild type and mutant channels, the relative decrease in the rate of membrane rupture is given by

$$\frac{k_{\text{wt}}}{k_{\text{mut}}} = e^{\pi\gamma^2\left(\frac{1}{\tau_{\text{mut}}}-\frac{1}{\tau_{\text{wt}}}\right)} \simeq 20, \tag{3.37}$$

meaning that the point mutants, on average, extend the life of the experiment by a factor of twenty! On that high note, let us address one last, less savory experimental reality.

3.4.3 Controlling for Channel Density

At this point we have addressed, to varying levels of detail and accuracy a number of aspects of the mechanics of this experiment, namely: how hard is to gate the channel, and what does that say about how long an experiment can last? Can we simplify what we must know about the dose-response curve? What are reasonable estimates of the permeation through the channel, from molecular dynamics and experiments, and can we use those values to constrain the design principles of the channel as they relate to osmotic and volumetric conductance? How do we turn aspirated vesicle geometry into a useful measurement? In essence, these are all important questions because they relate back to specific parameters in and functional form of the basal model (*i.e.* eqn. 3.35) that will be used during the experiment. However, one parameter has not been adequately commented on, and in fact likely has a large degree of variability. The channel density, N/A, as represented by the channel number N, which appears in all of the dynamical equations so far, is difficult to control. Consider its origin [9]; channels are expressed and grown in bacteria, the protein is purified

[9] Appendices for this chapter discuss in detail the methods of protein purification and reconstitution.

to some concentration that varies from preparation to preparation. The protein is mixed with lipid and detergent with some error, and the final incorporation of the channel into giant unilamellar vesicles relies either on the formation of such vesicles from either a dessicated film or fusion of small unilamellar vesicles with the giant unilamellar vesicles in an uncontrolled manner (see appendices). This is all to say that it is inherently difficult to control N/A in a real experiment from a biochemical perspective.

There are at least two ways to circumvent this problem. First, and certainly more difficult, is that for every preparation of giant unilamellar vesicles with reconstituted MscL, a subset of vesicles could be assayed via electrophysiology to determine the channel concentration from knowledge of the membrane patch size and maximum current through the patch. This seems like an undesirable route for a number of reasons: first, it ties together our already complex experiment with a distinctly different readout of channel function (*i.e.* electrical current), requires independent and equally daunting tasks of measuring patch geometry and size in a visually obscure region of a patch pipette, and has its own challenges for verifying how many channels are present. That said, in principle, electrophysiology could be used as an assay to calibrate the areal density of channels.

An easier and more straightforward way of determining N/A, that does not require the use of a completely separate and laborious experiment, is simply to measure multiple vesicles of different sizes from each preparation of GUVs. Consider that each vesicle of a different size will have a unique evolution of its volume over the course of the experiment, since the pressure, tension and area through which the channels permeate water are unique for a given geometry. Thus, if we perform measurements on multiple vesicles, we essentially have multiple equations and two unknowns: the channel density and the pressure-dependent flow rate. Given that all of the vesicles are coming from the same preparation and have been subjected to the same conditions, we would expect that any variance in the number of channels per vesicle area is small in comparison to mean number of channels per vesicle area. If we take measurements of $\mathrm{d}V/\mathrm{d}t$ from four geometrically distinct vesicles, for instance, this would give us three measures of the channel density and ensemble channel flow rate, allowing us to put a mean and standard deviation on the value of N/A and F_c.

3.5 Speculations

The following two subsections are included as a discussion of other ideas, ways of asking and answering similar questions, and questioning what else might be important for a sound physical understanding of fluid flow at the nanoscopic scale. The first subsection discusses in more depth what role thermal fluctuations might be playing in the conductance properties of the channel. The second section suggests additional classes of experiments and complementary *in vivo* studies for assaying channel flow and the physiological role of osmoregulation.

3.5.1 Possible Effects of Temperature

Clearly, temperature plays an important role in regulating the transitions between the closed and open states of any channel, and in particular this channel, since it adjusts the relative importance of the free energy difference between possible conformations, as seen in eqn. 3.1. Then consider a channel, subject to a membrane tension higher than the gating tension, such that the open-channel probability is essentially unity; this is particularly easy to imagine for the gain-of-function mutants of MscL that gate at lower tensions than wild-type MscL. The pressure drop across the membrane acts to push water and osmolytes from regions of high pressure to regions of low pressure, performing thermodynamic work in the typical PV fashion. Unlike a macroscopic pipe or orifice, where the pressure drop across and volume of the pore results in work with an energy scale much larger than k_BT, as we demonstrate below, the channel pore volume and relevant pressures result in work with an upper bound energy scale on the order of k_BT, suggesting that the pressure driven fluid movement through the pore must compete with fluctuations in fluid flux in the pore produced by thermal fluctuations. Our estimates of the channel volumetric flux using Aristotelian dynamics is flavored with the notion of variability in fluid flow due to thermal fluctuations, because it expressly acknowledges that the driving force is acting in concert with diffusion.

As mentioned earlier, the pore diameter of MscL is approximately 3 nm, and spans a thickness of ~ 2.5 nm, giving the pore a total volume of $\simeq 18\,\mathrm{nm}^3$. The pressure drop across the membrane spans a large range, depending on whether we are considering micropipette aspiration experiments, with pressure gradients on the order of 1/100th of an atmosphere, or pressure gradients experienced by living microbes which can be as high as ~ 3 atmospheres [157]. Given that at any one time the pore contains $\sim 18\,\mathrm{nm}^3$ of fluid volume, this means moving that volume across the membrane corresponds to a change in free energy of $\sim 0.005\,k_BT$ at lower pressures up to $\sim 1\,k_BT$ at higher pressures seen in the real physiological setting. In either case, though especially in the lower pressure scenario, this estimate suggests that fluctuations in the movement of fluid through the pore, caused by temperature, might play an important role in the channel's flow properties. For instance, thermal fluctuations have been theoretically predicted to affect the conductance of other, lower conductance channels [168]. Even the physical state of water in a nanoscopic pore is thought to be variable [169]. Likewise, our own estimates point towards fluctuation playing an important role, where we estimated the diffusive root-mean-square velocity of water through the channel pore was 100 times faster than the drift velocity of water through the pore due to a pressure gradient. To put this fluctuation in more biologically familiar terms, this is querying the processivity of volume movement through the channel. This is analogous to querying the processivity of forward motion of a molecular motor [170, 171], where the free energy difference between motor steps is often small enough that thermal fluctuations cause the motion of the motors to be less than fully rectified, hence effectively slowing down the processive motion of the motors. By analogy, we would expect this fluctuation in fluid movement to cause a generic decrease in the rate of volume flux, though this qualitative prediction certainly does not account for all the effects in play, and awaits experimental

verification.

For purposes of comparison, consider the free energy change of a typical mono-valent ion moving down an electrochemical gradient. A typical transmembrane potential is $\sim 50\,\mathrm{mV}$ [1], which translates into a free energy change for an ion moving from one side of the membrane to the other of $\sim 0.05\,\mathrm{eV} \simeq 2\,k_BT$. Typically, ion channels hold multiple such ions in their pore at any one time, and hence to make the analogy complete, the free energy to move the entire chain of ions through the channel pore, down the electrochemical gradient, is closer to $\sim 20\,k_BT$. This is simply to say that for two classes of channels whose function on the coarsest level is similar, that is, to move 'things' across the membrane, their detailed mechanisms may be quite different. Likewise, the entire interesting and pertinent realm of physics concerned with electro-diffusion and electrochemical flows [172] lies well outside this author's range of expertise, but given that life exists in, and crucially depends on high ionic concentrations, these physics of material transport may yet be an important piece of the nanoscopic fluid flow puzzle.

3.5.2 Interesting Possibilities

While designing, modeling and obtaining preliminary results for this experiment, other interesting ideas for future experiments were generated. We will briefly discuss a few of them here, to keep a record of some possible future directions. The first, and probably simplest extension of this experiment would be to employ fluorescent dyes as an additional readout of material transport across the membrane. For instance, GUVs could be formed that contain ionic calcium at the millimolar level, and after formation could be transferred to a solution containing calcium sensitive dye [173]. Given that the MscL channels are not ion selective [147], the calcium would exit the vesicle and light up the solution around the vesicle. In principle, one could measure the rate of increase of fluorescence, properly corrected for photobleaching, and ascertain the rate at which dye, presumably at a controlled concentration, must have exited the vesicle. Or alternatively, one could use fluorescence correlation spectroscopy to measure the *in situ* change in concentration of dilute dye molecules in the vesicle to get the same generic readout [174, 154].

In the microbial setting, cells that express GFP, or a similar large fluorescent genetic marker, could be loaded with a small organic dye of a different color. Cells could be adhered in a flow chamber where the osmolarity can be quickly and precisely changed. Prior to osmotic down shock, a wild-type cell or cell line expressing MscL would be two colors from the two different markers, and then after down shock, only the protein marker would remain in the cell, hence a large color shift upon hypo-osmotic shock. In a mutant strain missing the genes encoding for mechanosensitive channels, the osmotic down shock should burst the cells allowing both fluorescent markers to escape and hence the mutant cells would go dark under hypo-osmotic shock. In both cases, high speed video microscopy could be used to track the fluorescence changes over time to estimate reaction time of the osmoregulation proteins and rate of passage of the osmolytes.

3.6 Effects of Glass-Bilayer Binding in Electrophysiology

During the course of our research to understand what is known about the flow properties of large pore channels, it became clear that a sound understanding of the state of tension in electrophysiological settings is not known[10]. This section aims for a better understanding of the lateral tension in a bilayer patch found inside an electrophysiological pipette, where nearly all functional measurements of mechanosensitive channels have been made. We will be using an energy formulation to query the state of tension in the membrane, though forces and torques offer another viable solution[175]. To begin, let us tabulate the relevant parameters: the pipette has a certain radius, R_p, typically on the order of a micron, there is a tension-independent interaction energy, γ, between the membrane and the glass pipette, and a pressure gradient, p, across the membrane. For the kinds of tensions and pressures in a bilayer patch, the contribution from bilayer bending is unimportant.

3.6.1 The Zero Pressure Limit

When the pressure gradient is zero, the membrane is flat, and has an initial zero-tension area of πR_p^2. Let us assume that membrane adhered to the pipette is at zero tension, or in other words, has no areal strain. Generally, this is a good assumption for lipids, because the stretch modulus is many times higher than the rupture tension. As the membrane stretches in response to the beneficial binding energy between the membrane and the glass an areal strain develops

$$\phi = \frac{A - A_o}{A_o} \quad \text{or} \quad A = (1+\phi)A_o, \tag{3.38}$$

leading to a new zero-tension area of the patch

$$A_o(\phi) = \frac{\pi R_p^2}{1+\phi}. \tag{3.39}$$

To bind to the glass, the membrane stretches and stores elastic energy of the form

$$G_\phi = \frac{A_o(\phi) K_A}{2}\phi^2, \tag{3.40}$$

where $K_A \simeq 60\, k_B T/\text{nm}^2$) is the elastic stretch modulus [26]. The difference in zero-tension area of the patch before and after adhering to the glass gives a binding energy

$$G_\gamma = -\gamma \pi R_p^2 \left(1 - \frac{1}{1+\phi}\right), \tag{3.41}$$

[10]Thanks goes to Rod MacKinnon and Daniel Schmidt for stimulating discussions on this topic.

where γ is the bilayer-glass adhesion energy per unit area.[11] We minimize $G_\phi + G_\gamma$ with respect to ϕ, to find

$$\phi = \sqrt{1 + \frac{2}{\kappa}} - 1, \tag{3.42}$$

where $\kappa = K_A/\gamma$ is the dimensionless area stretch modulus. The membrane tension is proportional to the areal strain, $\tau = \gamma\kappa\phi$, and hence we find

$$\tau = \gamma\kappa\left(\sqrt{1 + \frac{2}{\kappa}} - 1\right). \tag{3.43}$$

Noting that $\kappa \gg 1$, the resting tension for a membrane patch at zero pressure is $\tau \simeq \gamma$.

3.6.2 Patches Under Pressure

When a pressure gradient is applied across the membrane, we assume the patch shape is described by a section of a sphere, with a radius of curvature R_c and a polar angle θ, restricted by geometry to be

$$\theta = \sin^{-1}\left(\frac{R_p}{R_c}\right), \tag{3.44}$$

as shown in Fig. 3.11. The problem can be stated in a dimensionless fashion, elucidating the important combinations of parameters. Let the change in binding position $\Delta z = \zeta R_p$, noting that $-\frac{1}{2} < \zeta < \frac{1}{2}$, and let the dimensionless curvature $R_p/R_c = \rho$, noting that $0 < \rho < 1$. The area of the curved patch is determined geometrically as

$$A = 2\pi R_c^2(1 - \cos(\theta)) = 2\pi\left(\frac{R_p}{\rho}\right)^2(1 - \sqrt{1-\rho^2}). \tag{3.45}$$

Simultaneously, to create this curved patch, some amount of zero-tension area delaminates from the pipette, and hence the patch has a zero-tension area given by

$$A_o = \pi R_p^2(1 - 2\zeta). \tag{3.46}$$

The zero-tension area is required to calculate the stretch energy in the patch,

$$G_\phi = A_o\frac{K_A}{2}\left(\frac{A - A_o}{A_o}\right)^2. \tag{3.47}$$

The same zero-tension area that delaminates costs adhesion energy of the form

$$G_\gamma = -\gamma 2\pi R_p^2\zeta. \tag{3.48}$$

As the patch curves under pressure, the volume of fluid bounded by the patch increases and couples

[11] Section 3.6.3 uses experimental data to find $\gamma \simeq 0.55\, k_B T/\text{nm}^2$.

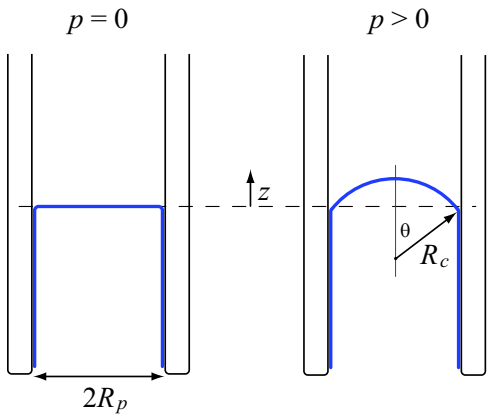

Figure 3.11: Electrophysiological patch geometry. Schematic showing the membrane patch shape at zero (a) and non-zero (b) pressure, with the relevant geometric parameters, in an idealized cylindrical pipette.

to the overall membrane energy. This change in volume is given by

$$\Delta V = \underbrace{\pi R_p^3 \zeta}_{\text{delaminating}} + \underbrace{\frac{\pi}{3}\left(\frac{R_p}{\rho}\right)^3 (1-\cos(\theta))^2(2+\cos(\theta))}_{\text{spherical cap}}, \tag{3.49}$$

and couples energetically to the pressure by $G_p = -p\Delta V$. Already we can see how tension depends on our dimensionless parameters, namely

$$\tau = \gamma\kappa\left(\frac{A}{A_o} - 1\right) = \gamma\kappa\left[2\frac{1-\sqrt{1-\rho^2}}{\rho^2(1-2\zeta)} - 1\right], \tag{3.50}$$

though this is not very useful since we do not have an expression for ζ or ρ as a function of pressure. We can now assemble the free energy

$$\frac{G}{\sigma} = \frac{\kappa}{2(1-2\zeta)}\left[\frac{2}{\rho^2}(1-\sqrt{1-\rho^2}) - (1-2\zeta)\right]^2 - 2\zeta - \epsilon\left[\zeta + \frac{1}{3\rho^3}(1-\sqrt{1-\rho^2})^2(2+\sqrt{1-\rho^2})\right], \tag{3.51}$$

where we define the dimensionless pressure gradient $\epsilon = pR_p/\gamma$ and the energy is normalized by the characteristic energy $\sigma = \pi R_p^2\gamma$. At this point, ρ and ζ are free variables with respect to which the free energy must be simultaneously minimized, by solving

$$\frac{\partial G}{\partial \zeta} = 0 \quad \text{and} \quad \frac{\partial G}{\partial \rho} = 0. \tag{3.52}$$

The first equation can be used to find

$$1 - 2\zeta = \frac{2}{\rho^2}\sqrt{\frac{\kappa(2 - \rho^2 - \sqrt{1-\rho^2})}{\epsilon + \kappa + 2}}, \tag{3.53}$$

which relates ζ and ρ. Upon substitution into the formula for τ, we find a rather (surprisingly) simple result

$$\tau = \gamma\kappa\left(\sqrt{\frac{\epsilon + \kappa + 2}{\kappa}} - 1\right). \tag{3.54}$$

Notice that if we let pressure go to zero ($\epsilon \to 0$), we recover our first result. Additionally, this shows that for a given pressure and pipette radius, stiffer membranes are at higher tensions. If we further assume that membrane area is conserved, that is $\kappa \to \infty$, we find something analogous to the Laplace-Young relation

$$\tau \simeq \gamma(1 + \frac{\epsilon}{2}) = \gamma + \frac{pR_p}{2}. \tag{3.55}$$

One important thing to note is that the radius here is the pipette radius, not the patch radius of curvature. This means that if we know the glass-bilayer interaction energy and pipette radius, we know the tension, without any further measurements on the membrane.

This formulation is insensitive to where the patch is located in the pipette, and hence has translational symmetry along the axis of the pipette, so long as the pipette radius is essentially constant over the delamination length, ζ. The values of the dimensionless delamination are generally bounded to be $|\zeta| < 1/2$, hence this is usually a good assumption.

Further information can be garnered by examining the second of the two energy minimization equations. Solving this equation with the additional knowledge of eqn. 3.53, gives a compact result for the dimensionless curvature

$$\rho = \frac{1}{2}\frac{\epsilon}{\epsilon + 2}\left(1 + \sqrt{\frac{\epsilon + \kappa + 2}{\kappa}}\right), \tag{3.56}$$

and in the limit where membrane area is conserved

$$\rho = \frac{\epsilon}{\epsilon + 2}. \tag{3.57}$$

For a given membrane composition and pipette radius, one can measure how ρ depends on ϵ to determine a value for γ. At first these results, though intuitively pleasing, may seem inconsistent with the Laplace-Young relation, written as

$$\tau = \gamma\frac{\epsilon}{2\rho} \tag{3.58}$$

in dimensionless variables. Upon substitution of eqn. 3.57 into this equation, we recover eqn. 3.55, showing that the Laplace-Young relation still holds — what we have essentially done is filled in the

missing variable of patch curvature as a function of pressure and pipette size.

Notice that for the area conserved model, $0 < \rho < 1$ for all values of ϵ. However, in a membrane with stretch one reaches the (at first) strange conclusion that $\rho > 1$ if $\epsilon > 2\sqrt{2\kappa}$. One can readily derive a rather complicated expression for ζ, where this peculiar property of ρ is accompanied by ζ taking on complex values, as shown by the vertical dashed line in Fig. 3.12c. With area conserved, the delamination is given by

$$1 - 2\zeta = 2\frac{(\epsilon + 2)(\epsilon + 2 - 2\sqrt{\epsilon + 1})}{\epsilon^2}. \tag{3.59}$$

The critical value of dimensionless pressure, where $\epsilon = 2\sqrt{2\kappa}$, indicates a delaminating transition. Physically speaking, above this critical pressure for every unit area of zero-tension membrane that delaminates, costing energy, there is more energy relieved by the subsequent increase in volume above the point of delamination. In other words, above this critical pressure, the membrane will begin to freely slide and rapidly translate up the pipette in an uncontrolled manner.

3.6.3 Determining γ from Patch Curvature

Using a wealth of data[12] that links patch curvature to applied pressure, we examine possible values of the glass-bilayer binding energy, γ, in the limit of a stiff membrane ($\kappa \to \infty$). Better yet, these data also include multiple lipid preparations, and hence we can get an idea of the distribution of this parameter over different lipid types.

Note that we can rewrite eqn. 3.57 in a linear form

$$\rho^{-1} = 2\epsilon^{-1} + 1, \tag{3.60}$$

and with dimensions as

$$R_c = \gamma(2p^{-1}) + R_p. \tag{3.61}$$

During the course of their studies into the intrinsic stimulus of MscL [50], Moe and Blount measured patch tension, and therefore patch curvature. Thus their data can be used to fit eqn. 3.61 for the adhesion energy and the pipette radius R_p. Ideally, if all pipettes and lipid preparations were truly identical, all of the lines associated with a particular lipid would have the same slope, and only the pipette radius would change from one experiment to the next. However, clearly buffer conditions, the type of glass used, the cleanliness of that glass and other variables all effect the actual value of the adhesion energy.

Some lipid types show fairly homogeneous values of the adhesion energy, while others span a factor two or three. Opsahl and Webb [175] reported similar values, also with a wide range of $\gamma = 0.12 - 0.97\, k_BT/\text{nm}^2$. Interestingly, when using the data published in their paper, this theory gives a slightly different result, specifically from their Fig. 3 they calculate $\gamma = 0.63\, k_BT/\text{nm}^2$,

[12] Much thanks to Paul Blount for the kind dissemination of these data.

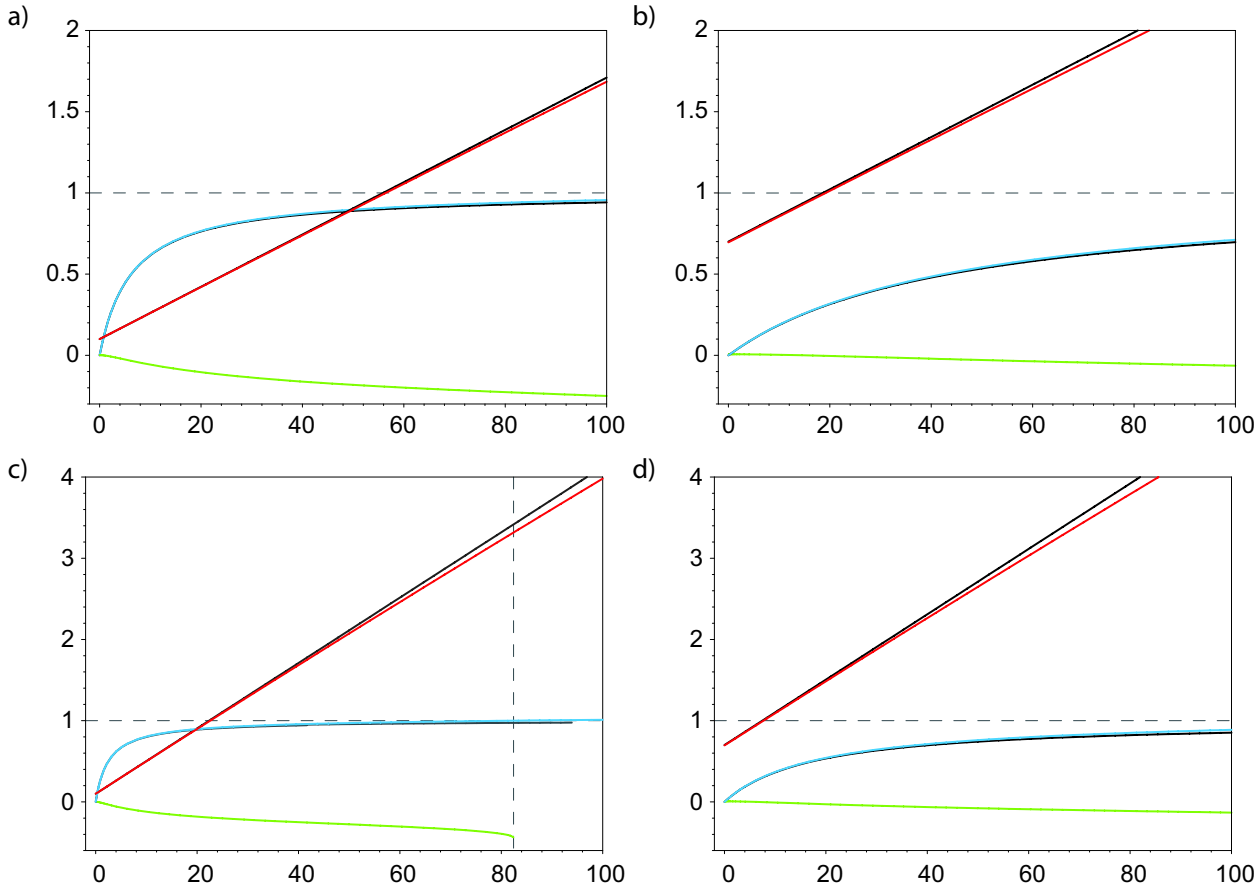

Figure 3.12: Analysis of electrophysiological membrane patch geometry and tension. Analytical results for tension (red) in k_BT/nm^2, dimensionless delamination (green), and dimensionless curvature (blue) as a function of pressure in mmHg for $K_A = 55\,k_BT/\text{nm}^2$, roughly the value for DOPC. See table for other parameter values. The black lines correspond to the tension in the area conserved model, where $\kappa \to \infty$.

Figure:	Parameter:	Value:
3.12a	R_p, γ	$1\,\mu\text{m}$, $0.1\,k_BT/\text{nm}^2$
3.12b	R_p, γ	$1\,\mu\text{m}$, $0.7\,k_BT/\text{nm}^2$
3.12c	R_p, γ	$2.5\,\mu\text{m}$, $0.1\,k_BT/\text{nm}^2$
3.12d	R_p, γ	$2.5\,\mu\text{m}$, $0.7\,k_BT/\text{nm}^2$

whereas we calculate $\gamma = 0.47\,k_BT/\text{nm}^2$; although this could be related to the actual form of the functional fit. These results are summarized in Fig. 3.13

Across all lipid types, the mean bilayer-glass adhesion energy was $0.544 \pm 0.305\,k_BT/\text{nm}^2$. This means that (on average) the lowest state of tension on a patch, which we know is at zero pressure, is $\sim 0.5\,k_BT/\text{nm}^2$ — much higher than the resting tension on most cell membranes ($\sim 0.001 - 0.01\,k_BT/\text{nm}^2$) [13]. Thus, it is likely that inside-out patch electrophysiology has been operating in high a tension regime. Theoretical studies have shown that any channel whose protein-bilayer interface changes upon gating will have some energetic dependence on bilayer tension [68]. This rather high resting tension could effect kinetics of transition, dose-response curves and their parameters, and might cause the appearance or disappearance of entire conformational states in the worst case. It should be noted that in many cases channel function is assayed in whole-cell patch clamping, where there is likely significant interaction between the membrane and cytoskeleton, in which case this theory is invalid. One can speculate further about what intrinsically high patch tension means for the field of channel electrophysiology.

3.7 Concluding Remarks

In many ways this was a chapter of estimates. Using the bacterial mechanosensitive channel MscL as our model volumetric channel, we built a simplified dynamic model of the process of osmotic shock in an attempt to understand and estimate how bilayer and channel properties, as well as molecular transport properties, conspire to regulate volume and surface tension in a cell or vesicle. We explored a number of constitutive models for channel flow to understand how each depends on pore geometry and general physical assumptions, and applied one of the resultant models (diffusive transport) to a range of numerical simulations of the osmotic shock of a spherical bilayer vesicle. Further, we designed in fine detail an experiment capable of measuring the ensemble volumetric flux through such channels via micropipette aspiration of giant unilamellar vesicles, and explored how different mutants of the channel protein might affect to the experiment through numerical simulation of the governing equations. We showed a proof of concept that such an experiment is not only feasible, but will likely work if mutant protein can be reconstituted at sufficient levels. Surely, many detail oriented challenges remain, but we are rapidly approaching a functional measurement that will elucidate the physics, and eventually biology, of nanoscopic flow.

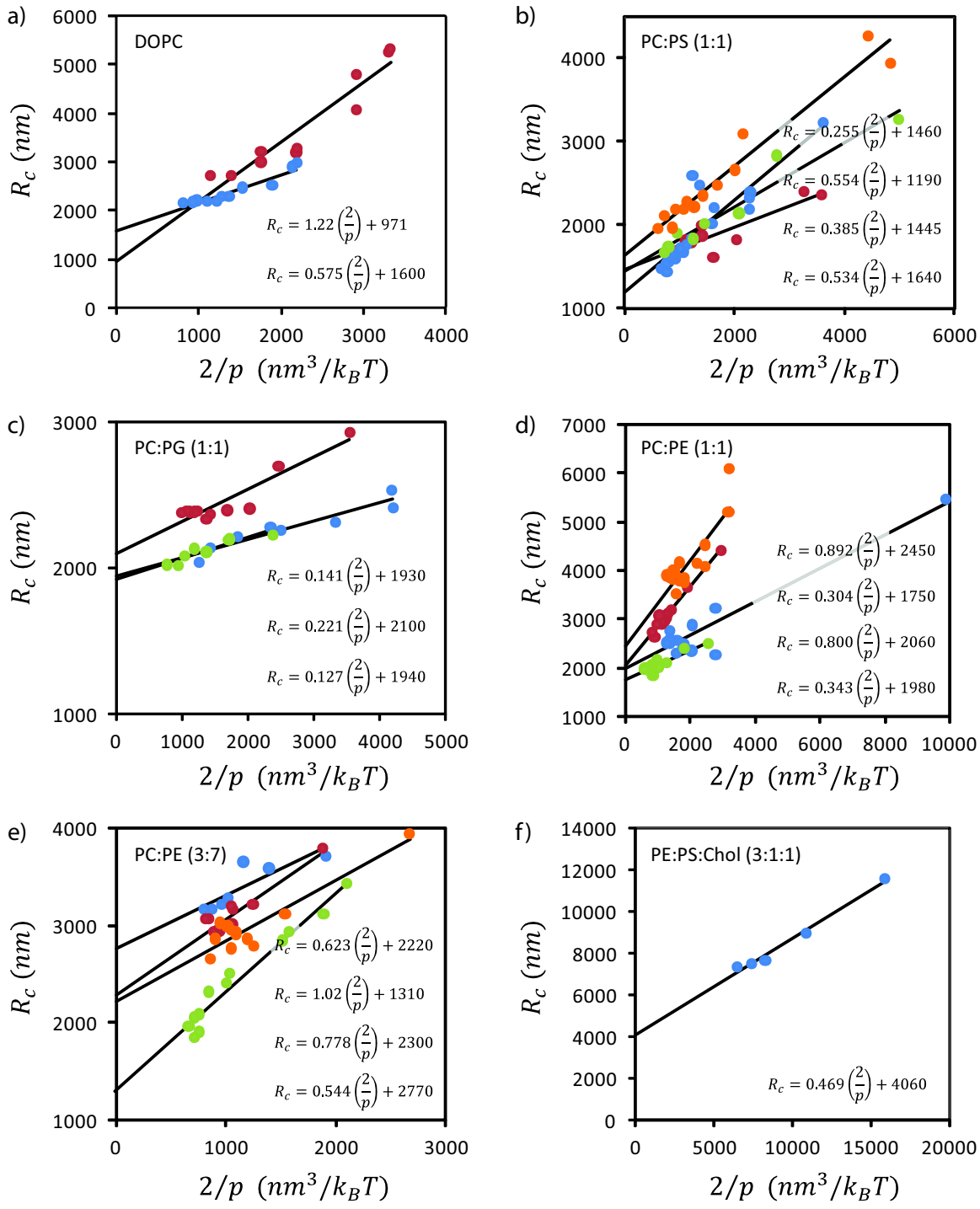

Figure 3.13: Measurements of glass-bilayer adhesion energy in different lipid mixtures. All plots show measurements of patch curvature as a function of applied pressure, which can be fit to eqn. 3.61 to find values of the adhesion energy. The slopes of these lines are the values of γ in k_BT/nm^2 and the intercepts are the pipette radii R_p in nanometers. Clearly, head group charge has an effect on both the magnitude and variation of the adhesion energy. It is also likely that buffer conditions and pipette glass composition affect the values of γ. The lipid compositions are indicated on each plot. Plots (a-e) were made using data kindly provided by P. Blount, and plot (f) uses data from [175].

Chapter 4

Organization and Morphology of Lipid Domains

"Our imagination is stretched to the utmost, not, as in fiction, to imagine things which are not really there, but just to comprehend those things which are there." - Richard Feynman

4.1 Introduction

Cellular membranes are a heterogeneous mix of lipids, proteins and small molecules. Special groupings enriched in saturated lipids and cholesterol form liquid-ordered domains, known as a 'lipid rafts,' serving as platforms for signaling, trafficking and material transport throughout the secretory pathway. Questions remain as to how the cell maintains heterogeneity of a fluid membrane with multiple phases, through time, on a length-scale consistent with the fact that no large-scale phase separation is observed. In the first part of this chapter, we discuss how we have utilized a combination of mechanical modeling and *in vitro* experiments to show that membrane morphology plays a key role in maintaining heterogeneity and organizing domains in a model membrane. We demonstrate that lipid domains can adopt a flat or dimpled morphology, where the latter facilitates a repulsive interaction which slows coalescence and tends to organize domains. These forces, that depend on domain morphology, play an important role in regulating lipid domain size and in the lateral organization of lipids in the membrane.

Lipid composition and morphology can play a key role in regulating a variety of biological processes. For example, viral uptake, plasma membrane tension regulation, and the formation of caveolae all require the creation and control of groups of lipids that adopt specific morphologies. In the second main theme of this chapter, we use a simplified model mixture of lipids and cholesterol to examine the interplay between lipid phase-separation and bilayer morphology. We observe and theoretically analyze three main features of phase-separated giant unilamellar vesicles. First, by tracking the motion of 'dimpled' domains, we measure repulsive, elastic interactions that create short–range translational and orientational order, leading to a stable distribution of domain sizes, and hence maintaining lateral heterogeneity on relatively short length scales and long time scales. Second, we examine the transition to 'budded' domain morphologies, showing that the transition is size-selective, and has two kinetic regimes, as revealed by a calculated phase diagram. Finally, using observations of the interactions between dimpled and budded domains, we build a theoretical framework with an elastic model that maps the free energies and allowed transitions in domain

morphology upon coalescence, to serve as an interpretive tool for understanding the algebra of domain morphology. In all three cases, the two major factors that regulate domain morphology and morphological transitions are the domain size and membrane tension.

This chapter is organized into four main sections. The first section gives the background and motivation behind, as well as in-depth analysis of, our measurements of dilute domain interactions. The second section moves on to analyze the larger set of morphologies that encompass domain budding and interactions between domain buds and dimpled domains. These two sections are followed by a more detailed discussion of domain mechanics and our experimental methods. The last section discusses our experimental efforts to understand the phase separating properties of membrane blebs from living cells.

4.2 Dilute Domain Interactions

The plasma and organelle membranes of cells are composed of a host of different lipids, lipophilic molecules and membrane proteins [176]. Together, they form a heterogeneous layer capable of regulating the flow of materials and signals into and out of the cell. Lipid structure and sterol content play a key role in bilayer organization, where steric interactions and energetically costly mismatch of lipid hydrophobic thickness result in a line tension that induces lateral phase-separation [177], as shown in Fig. 4.1[1]. Saturated lipids and cholesterol are sequestered into liquid-ordered (L_o) domains, often known as 'lipid rafts,' distinct from an unsaturated liquid-disordered (L_d) phase [130, 178, 179]. Domains composed of saturated sphingolipids and cholesterol, with sizes in the range of $\sim 50 - 500\,\text{nm}$, have been implicated in a range of biological processes from lateral protein organization and virus uptake to signaling and plasma-membrane tension regulation [180, 181, 182, 183, 184, 185, 186, 187, 188, 189, 190, 191, 192]. In the biological setting, maintenance of lateral heterogeneity is thought to arise from a combination of lipid recycling and energetic barriers to domain coalescence [193, 194, 195] (potentially provided by transmembrane proteins [196]), ostensibly resulting in a stable distribution of domain sizes. These biological examples serve as a motivation to better understand the biophysical mechanisms that maintain lateral heterogeneity of lipids over time, and pose new challenges to the classical theories of phase-separation and 'domain ripening' (such as Cahn-Hilliard kinetics [197]).

The simplest physical model that describes the evolution of lipid domain size and position predicts that domains diffuse and coalesce, such that the number of domains constantly decreases, while the average domain size constantly increases [197]. Indeed, models of two-dimensional phase separation have been studied in detail for many physical systems [198, 199, 200, 201], and where the phase boundary is unfavorable and characterized by an energy per unit length [138], the domain size grows continuously [197, 202, 203]. However, membranes can adopt three-dimensional morphologies that affect the kinetics of phase separation [204, 205, 206, 207, 208]. In those cases

[1] Appendix D derives in detail the simplest kinetic model of phase separation for a 2D two-component system.

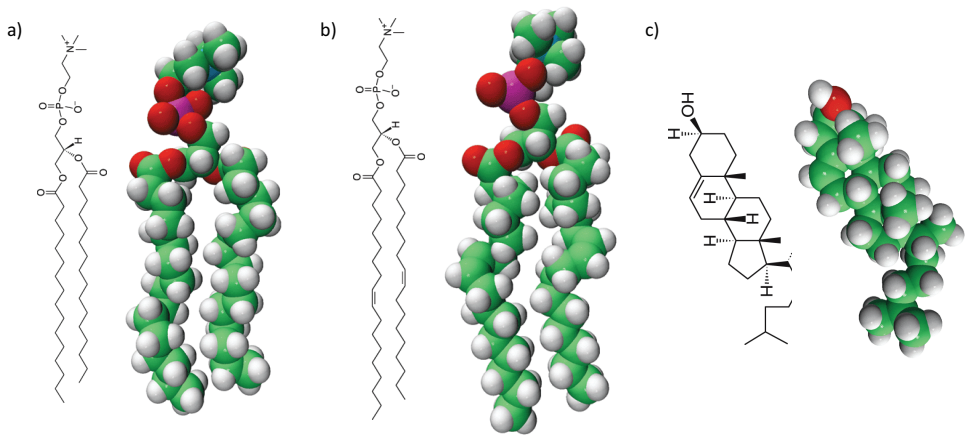

Figure 4.1: Structural differences in amphiphilic lipids. a) Two representations of the chemical structure of the fully saturated lipid DPPC (Avanti Polar Lipids PN: 850355). Both acyl chains are 'straight,' lacking the kinked double bonds that lead to a disordered phase. b) Two representations of the chemical structure of the mono-unsaturated, symmetric acyl chain lipid DOPC (Avanti Polar Lipids PN: 850375). Both acyl chains contain a kinked double bond that leads to a disordered phase. c) Two representations of the chemical structure of the membrane intercalating sterol cholesterol (Avanti Polar Lipids PN: 700000). *In vitro*, liquid ordered domains are enriched in cholesterol and the saturated lipid DPPC. All molecules are oriented with their polar regions up.

where morphology is considered as part of the phase separation model, novel coalescence kinetics emerge [205]. Experimentally, model membranes have shown that nearly complete phase separation on the surface of a giant unilamellar vesicle can be reached in as little as one minute [130]. This seems inconsistent with the fact that on the cell surface, much smaller domains persist on that same time-scale [195] and no large-scale phase separation is observed. With these facts in mind, our central questions are: how can model membranes that have phase-separated maintain their lateral heterogeneity on long time scales and short length scales? Are there membrane-mediated (*i.e.* elastic) forces that inhibit coalescence and spatially organize domains?

We begin to answer these questions by examining the energetics of the membrane using a linear elastic model. A phase-separated membrane is endowed with bending stiffness, membrane tension, an energetic cost at the phase boundary, and domains of a particular size. Membrane bending and tension establish a natural length-scale over which a morphological instability develops that switches domains from a flat to 'dimpled' shape, similar to classical Euler buckling [209] (see Fig. 4.2). The dimpling instability is size-selective and 'turns on' a membrane-mediated interaction that inhibits domain coalescence. This transition is a precursor to budding, and is distinct from transitions that require spontaneous curvature. While variations in membrane composition may change specific parameter values, the mechanical effects we describe are generic. Thus, these systems exhibit shape-dependent coarsening kinetics, that are relevant for a broad class of two-dimensional phase-

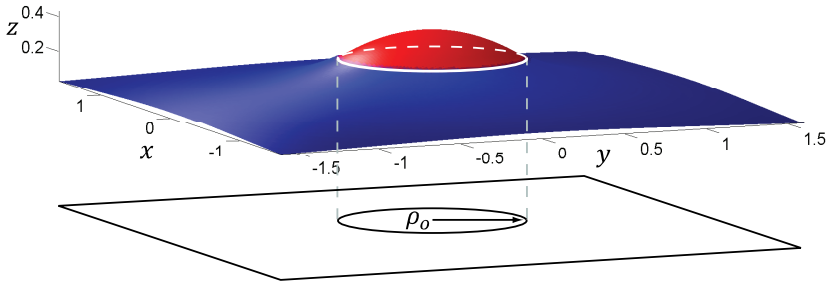

Figure 4.2: Three dimensional rendering of a dimpled lipid domain in dimensionless coordinates. For a domain (shown in red), a competition between bending, membrane tension, and phase boundary line tension results in a morphological transition from a flat to a dimpled state as depicted above. The dimple costs bending energy but relieves line tension by reducing the phase boundary length (shown as a white line around the domain). This morphology facilitates interactions between domains that significantly alter the kinetics of coalescence and lateral lipid organization. The dimensionless projected domain radius is $\rho_o = r_o/\lambda_2$, where r_o is projected radius, and λ_2 is the elastic decay length.

separating systems. The interaction between domains is a mechanical effect, and we use a model treating dimpled domains as curved rigid inclusions to distill the main principles governing this interaction. The confluence of membrane properties required for this morphological change and its attendant forces lies squarely in the biological regime. Experimentally, we use a model mixture of lipids and cholesterol to show that such an interaction exists between dimpled domains and is well approximated by a simple model. We hypothesize that a combination of lipid recycling [193] and elastic interactions could serve as a mechanism for the maintenance of lipid lateral-heterogeneity and organization of domains in cellular membranes.

The first part of this chapter section outlines the energetic contributions to the mechanical model, and predicts the conditions under which domain dimpling occurs. The second section outlines how dimpled domains facilitate an elastic interaction and compares the model interaction to our measurements made in phase-separated giant unilamellar vesicles.

4.2.1 The Elastic Model and Morphological Transitions

The energetics of a lipid domain are dominated by a competition — on one hand the applied membrane tension and bending stiffness both energetically favor a flat domain; on the other hand the phase boundary line tension prefers any domain morphology (in 3D) that reduces the boundary length. We use a continuum mechanical model that couples these effects, relating the energetics of membrane deformation to domain morphology. As we will show, this competition results in a morphological transition from a flat to dimpled domain shape, where two dimpled domains are then capable of interacting elastically.

Lipid domains in a liquid state naturally adopt a circular shape to minimize the phase boundary length [130], allowing us to formulate our continuum mechanical model in polar coordinates. We employ a *Monge* representation, where the membrane mid-plane is described by a height function $h(\mathbf{r})$ in the limit of small membrane deformations (*i.e.* $|\nabla h| < 1$). With this height function, we characterize how membrane tension, bending, spontaneous curvature and line tension all contribute to domain energetics.

Changes in membrane height alter the projected area of the membrane and hence do work against the applied membrane tension, resulting in an increase in energy written as

$$G_{\text{tens}} = \pi\tau \left(\int_0^{r_o} (\nabla h_1)^2 r \mathrm{d}r + \int_{r_o}^{\infty} (\nabla h_2)^2 r \mathrm{d}r \right), \tag{4.1}$$

where τ is the constant membrane tension, r_o is the projected radius of the domain, h_1 is the height function of the domain and h_2 is the height function of the surrounding membrane [57, 32]. Membrane curvature is penalized by the bending stiffness with a bending energy written as [46, 57]

$$G_{\text{bend}} = \pi\kappa_b^{(2)} \left(\sigma \int_0^{r_o} \left(\nabla^2 h_1\right)^2 r \mathrm{d}r + \int_{r_o}^{\infty} \left(\nabla^2 h_2\right)^2 r \mathrm{d}r \right). \tag{4.2}$$

Our model allows the domain and surrounding membrane to have differing stiffnesses, $\kappa_b^{(1)}$ and $\kappa_b^{(2)}$ respectively, characterized by the parameter $\sigma = \kappa_b^{(1)}/\kappa_b^{(2)}$, and from this point on we drop the superscript on $\kappa_b^{(2)}$. Recent experiments suggest that the bending moduli of a cholesterol-rich domain and the surrounding membrane are roughly equal [179, 210], and hence for simplicity, we assume the bending moduli of the two regions are equal (*i.e.* $\sigma = 1$), unless otherwise noted. In addition to bending stiffness, the domain may exhibit a preferred 'spontaneous' curvature due, for instance, to lipid asymmetry [208] or protein binding [211]. The contribution of domain spontaneous curvature can be simplified to a boundary integral, which couples to the overall curvature field by

$$G_{\text{spont}} = -2\pi\sigma\kappa_b c_o \int_0^{r_o} \left(\nabla^2 h_1\right) r \mathrm{d}r = -2\pi\sigma\kappa_b c_o r_o \epsilon, \tag{4.3}$$

where c_o is the spontaneous curvature of the domain and ϵ is the membrane slope at the phase boundary. Further, we assume the saddle-splay curvature moduli are equal in the two regions, yielding no dependence on Gaussian curvature. In principle, this contribution could be accounted for with a boundary term, explored in detail in Section 4.4. The phase boundary line tension is applied to the projected circumference of the domain, as shown in Fig. 4.2, by $G_{\text{line}} = 2\pi r_o \gamma$ where γ is the energy per unit length at the phase boundary.

Finally, a constraint must be imposed that relates the actual domain area, $\mathcal{A}$, to the projected domain radius r_o. The energetic cost to change the area per lipid molecule is high ($\sim 50 - 100\, k_B T/\text{nm}^2$ where $k_B = 1.38 \times 10^{-23}\, J/\text{K}$ and $T = 300\,\text{K}$ [26]), hence we assume the domain area is conserved during any morphological change (see Section 4.4 for details). We impose this

constraint using a Lagrange multiplier, τ_o, with units of tension by

$$G_{\text{area}} = \tau_o \left(\pi \int_0^{r_o} (\nabla h_1)^2 r \mathrm{d}r + \pi r_o^2 - \mathcal{A} \right). \tag{4.4}$$

This results in an effective membrane tension within the domain $\tau_1 = \tau + \tau_o$, which must be negative to induce dimpling. Examining the interplay between bending and membrane tension, we see that two natural length scales emerge - within the domain we define $\lambda_1 = \sqrt{\sigma\kappa_b/\tau_1}$ and outside the domain we define $\lambda_2 = \sqrt{\kappa_b/\tau}$. These length scales allow us to define the relevant dimensionless parameters in this system.

The total free energy of an elastic domain and its surrounding membrane is then the sum of these five terms, $G = G_{\text{tens}} + G_{\text{bend}} + G_{\text{spont}} + G_{\text{line}} + G_{\text{area}}$. Details on all the terms in the free energy can be found in section 4.4. With this free energy in hand, we examine how the morphology of a circular domain evolves as we tune domain size and the elastic properties of the membrane.

The height field and radius can be rescaled by the elastic decay lengths such that the Euler-Lagrange equation for the domain can be written in the parameter-free form $\nabla^2(\nabla^2 + \beta^2)\eta_1 = 0$, while the equation for the surrounding membrane is $\nabla^2(\nabla^2 - 1)\eta_2 = 0$, where the dimensionless variables are defined by $\lambda_2\eta_i = h_i$, $\lambda_2\rho = r$, $\lambda_2\rho_o = r_o$ and $\beta = i\lambda_2/\lambda_1$. Using the same dimensionless notation, the energy from line tension and spontaneous curvature can be written as $G_{\text{line}} = 2\pi\kappa_b\rho_o\chi$ and $G_{\text{spont}} = -2\pi\sigma\kappa_b\epsilon\rho_o\upsilon_o$, with $\upsilon_o = \lambda_2 c_o$ and $\chi = \gamma\lambda_2/\kappa_b$. The dimensionless line tension, χ, is simply a rescaled version of the line tension γ and is one of two key parameters that characterize the morphological transition; the dimensionless domain area, $\alpha = \mathcal{A}/\lambda_2^2$, is the second key parameter.

The admissible solutions for $\eta_1(\rho)$ and $\eta_2(\rho)$ are zeroth order Bessel functions $J_0(\beta\rho)$ and $K_0(\rho)$, respectively, with the boundary conditions $|\nabla\eta_1(0)| = |\nabla\eta_2(\infty)| = 0$ and $|\nabla\eta_1(\rho_o)| = |\nabla\eta_2(\rho_o)| = \epsilon$. The boundary slope, ϵ, is the parameter that indicates the morphology of the domain; $\epsilon = 0$ indicates a flat domain, while $0 < |\epsilon| \lesssim 1$ indicates a dimpled domain. The five contributions to membrane deformation energy yield a relatively simple expression for the total free energy, given by

$$\begin{aligned} G = \pi\kappa_b\rho_o \left[\epsilon^2 \left(\sigma\beta \frac{J_0(\beta\rho_o)}{J_1(\beta\rho_o)} + \frac{K_0(\rho_o)}{K_1(\rho_o)} \right) + 2(\chi - \epsilon\sigma\upsilon_o) \right] \\ -\kappa_b(\sigma\beta^2 + 1)(\pi\rho_o^2 - \alpha). \end{aligned} \tag{4.5}$$

Mechanical equilibrium is enforced by rendering the energy stationary with respect to the unknown parameters ϵ, ρ_o, and β,

$$\frac{\partial G}{\partial \epsilon} = 0, \quad \frac{\partial G}{\partial \rho_o} = 0, \quad \frac{\partial G}{\partial \beta} = 0. \tag{4.6}$$

These equilibrium equations physically correspond to torque balance at the phase boundary, lateral force balance at the phase boundary and domain area conservation, respectively.

Analysis of the equilibrium equations reveals a *second-order* transition at a critical line-tension,

χ_c, as shown in Fig. 4.3. For χ less than this critical value, only the flat, trivial solution with $\epsilon = 0$ exists. At χ_c a non-trivial solution describing buckled or dimpled morphologies emerges. For zero spontaneous curvature, the bifurcation is defined by a transcendental characteristic equation

$$\sigma\beta\frac{J_0(\beta\rho_o)}{J_1(\beta\rho_o)} + \frac{K_0(\rho_o)}{K_1(\rho_o)} = 0, \tag{4.7}$$

with $\beta = \sqrt{(\chi_c/\rho_o - 1)/\sigma}$ and $\rho_o = \sqrt{\alpha/\pi}$. For a given dimensionless domain area, α, this defines the critical line tension required to dimple the domain. In Fig. 4.3a(inset), this relation is used to generate a morphological phase diagram that shows where in the space of dimensionless domain area and line tension we find the discontinuous transition (*i.e.* bifurcation) from a flat domain, to a dimpled domain. Near the morphological transition the boundary slope grows as $|\epsilon| \propto \sqrt{\chi/\chi_c - 1}$, indicating that a dimple rapidly deviates from the flat state. The transition is symmetric, in that both possible dimple curvatures have the same energy, and hence the domain is equally likely to dimple upwards or downwards. In the experimentally relevant limit of small dimensionless domain area, the complexity of eqn. 4.7 is reduced to

$$\chi_c\sqrt{\alpha} = \frac{\gamma_c}{\kappa_b}\sqrt{\mathcal{A}} \simeq 8\sigma\sqrt{\pi}. \tag{4.8}$$

This leads to the conclusion that the dominant parameter governing domain dimpling at zero spontaneous curvature is $\chi\sqrt{\alpha}$. For a small domain, the dimpling transition is directly regulated by domain area, the bending modulus, and line tension, but only weakly depends on applied membrane tension. Intuitively, domains dimple when line tension or domain size increase (subject to small α), as shown in Fig. 4.3a(inset). Likewise, a decrease in bending stiffness, due, for instance, to changes in membrane sterol content [212, 213], can also induce dimpling. The effects of applied membrane tension are weak because the change in projected area upon dimpling does not lead to a significant energy cost relative to the cost of bending and line tension.

If membrane elastic properties are fixed (*i.e.* fixed κ_b, τ and γ), the dimpling-induced interactions 'turn on' only after a critical domain size is achieved. This scenario is encountered when two domains, too small to dimple on their own, diffusively coalesce into a larger domain capable of dimpling and hence interacting. Indeed, such a size-selective coalescence mechanism was observed recently in model membrane vesicles [214]. This constitutes a distinct class of coarsening dynamics, where classical diffusion-limited kinetics are obeyed until the domain size distribution has matured past the critical size for dimpling — then domain coalescence is a relatively slow, interaction-limited process.

For the model domain considered in Fig. 4.3, with area $\alpha = \pi/4$ ($r_o \simeq 250\,\text{nm}$), the critical dimensionless line tension is $\chi_c \simeq 13$, corresponding to a critical line tension of $\gamma_c \simeq 0.65\,k_BT/\text{nm}$ ($1\,k_BT/\text{nm} = 4.14\,\text{pN}$). This value compares well with theoretical estimates of the line tension [138, 215] and falls squarely in the range of values from AFM measurements [177], though it is slightly higher than the value of $\gamma \simeq 0.22\,k_BT/\text{nm}$ measured via shape analysis of fully phase

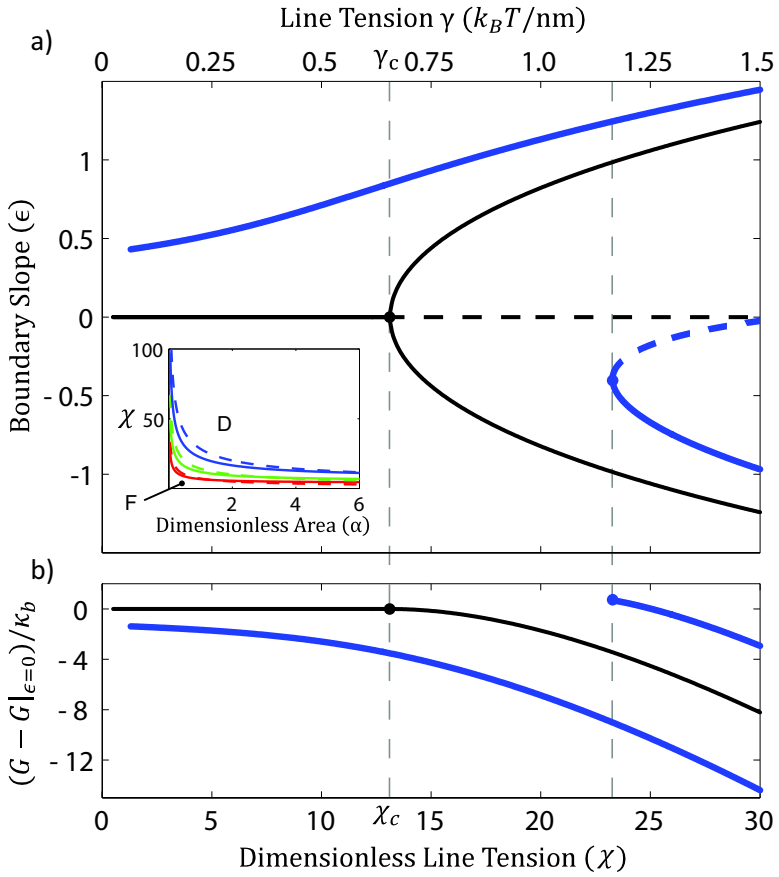

Figure 4.3: Bifurcation diagram for dimpling transition at constant area (dimensionless domain area $\alpha = \pi/4$, bending modulus $\kappa_b = 25\, k_BT$, elastic decay length $\lambda_2 = 500\,\text{nm}$, ratio of bending moduli $\sigma = 1$). Constant line tension and increasing area produces a qualitatively similar graph. a) At zero spontaneous curvature ($\upsilon_o = 0$, thin black line) the bifurcation is symmetric, the upper and lower branches are at the same energy, and the flat domain, $\epsilon = 0$, becomes unstable above the critical point (horizontal black dashed line). With finite spontaneous curvature ($\upsilon_o = 2$, $c_o = (250\,\text{nm})^{-1}$, thick blue line) the lower energy branch (upper) has non-zero boundary slope for all line tensions, asymptoting to the zero spontaneous curvature branch. At a line tension slightly higher than the critical line tension, χ_c, for the zero spontaneous curvature case, a bifurcation yields a higher energy dimple with the opposite curvature as υ_o (indicated by the second vertical dashed line). Inset: Equilibrium phase diagrams for bending moduli ratios of $\sigma = 0.5$(red), $\sigma = 1$(green), and $\sigma = 2$(blue) (the dashed lines are the approximation of eqn. 4.8) showing flat (F) and dimpled (D) domains. b) Energy difference between the flat and dimpled state, normalized by the bending modulus κ_b, for domains with and without spontaneous curvature ($\upsilon_o = 0 \rightarrow$ thin black line; $\upsilon_o = 2 \rightarrow$ thick blue line).

separated vesicles [179] and $\gamma \simeq 0.40\, k_B T/\text{nm}$ measured from micropipette aspiration experiments [216]. In general, measured values of the line tension depend heavily on bilayer composition, spanning a range of $\sim 0.05 - 1.5\, k_B T/\text{nm}$ [179, 216, 177].

Spontaneous curvature does not affect the Euler-Lagrange equations, and hence will not effect the class of equilibrium membrane shapes. However, domains with zero and nonzero spontaneous curvature exhibit qualitatively different behavior. Membranes can be asymmetric with respect to leaflet composition [212, 180, 217], endowing a domain with potentially large spontaneous curvature. The energetic contribution from spontaneous curvature takes the form of an additional line tension depending linearly on the slope taken by the domain boundary, ϵ. This breaks the symmetry of the membrane, giving an energetic preference to a dimple with the same curvature as the spontaneous curvature, and eliminating the trivial $\epsilon = 0$ solution even at small line-tensions. As line tension increases, a bifurcation produces a second, stable, higher-energy dimple of the opposite curvature as v_o. The more energetically stable branch of this transition corresponds to a dimpled state for *all* values of line tension and non-zero values of domain area, as demonstrated in Fig. 4.3a. This predicts that as soon as a domain with finite spontaneous curvature forms, it dimples, regardless of size, and begins to experience interactions with any nearby dimpled domains. It is reasonable to expect that domains with similar composition will have similar spontaneous curvature, and hence form dimples whose curvature has the same sign. As we will show, dimples whose curvature has the same sign tend to interact repulsively. Such a mechanism of coalescence inhibition was observed recently in simulation [208]. This indicates that control of spontaneous curvature via domain composition or protein binding can regulate dimpling and hence domain interaction [218, 217]. Indeed, recent theoretical [219] work shows that lipid asymmetry, leads to precisely these kinds of dimpled domains.

Calculated shapes of dimpled domains induced by line tension and spontaneous curvature are shown in Fig. 4.4a, alongside dimpled domains observed on giant unilamellar vesicles, shown in Fig. 4.4b and d.

4.2.2 Elastic Interactions of Dimpled Domains

Given two domains that have met the criteria for dimpling, the deformation in the membrane surrounding the domains mediates an elastic interaction when they are within a few elastic decay lengths (λ_2) of each other. This equips us to begin addressing how short length-scale and long time-scale membrane heterogeneity might be achieved. As previously stated, free diffusion sets the maximum rate at which a quenched membrane can evolve into a fully phase-separated membrane [197], where this evolution can happen in as little as a minute on the surface of a giant unilamellar vesicle [130]. By comparison, recycling and hence homogenization of cellular membrane is a process that takes place on the time-scale of an hour or more [220]. Our measurements of domain interactions (detailed below and other data shown in section 4.4) estimate the coalescence barrier between dimpled domains at $\sim 5 - 10\, k_B T$. Hence, given the diffusion-limited rate of phase sepa-

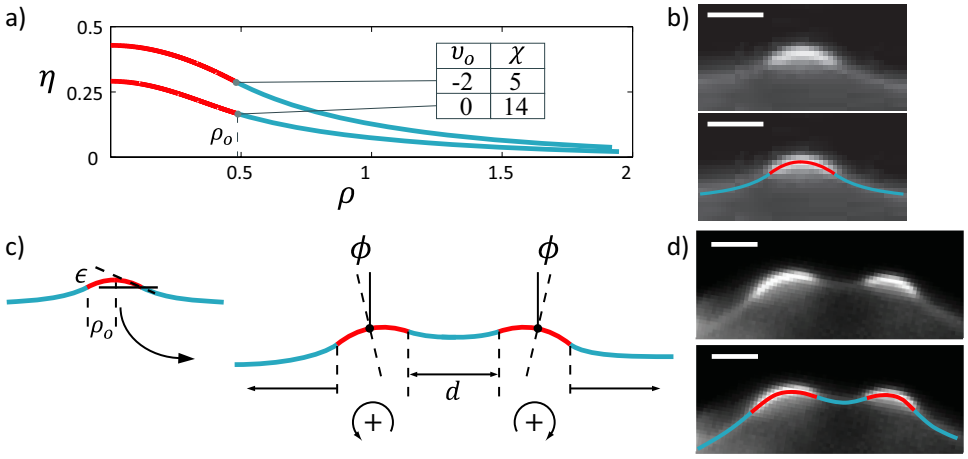

Figure 4.4: Theoretical and experimental dimpled domain shapes. Domains are shown in red, surrounding membrane in blue. a) The dimensionless height profile (η) as a function of dimensionless radius (ρ) for minimum energy dimples with and without spontaneous curvature (dimensionless spontaneous curvature, υ_o, and line tension, χ, are indicated in the legend; dimensionless domain area $\alpha = \pi/4$). b) Epi-fluorescence cross-section of a dimple on the surface of a GUV; the red and blue lines are a guide to the eye. c) 1D model of interaction — dimples maintain shape, but tilt (ϕ) as a function of separation distance (d). Dimples with the same sign of curvature repel, while dimples with opposite sign attract. The single domain shape, with boundary slope ϵ and dimensionless projected radius ρ_o is shown for reference. d) Epi-fluorescence cross-section of two dimpled domains interacting on the surface of a GUV. Scale bars are 3 μm.

ration, interactions slow this process by approximately $e^{-5} \simeq 0.007$ to $e^{-10} \simeq 0.00005$. This makes the time-scale of lipid heterogeneity comparable to the time-scale of membrane recycling and even eukaryotic cell division.

The physical origin of domain interaction is explained by a simple model based on the assumption that the dimpled domain *shape* is constant during interaction, but the domains are free to tilt by an angle ϕ, as shown in Fig. 4.4c. This assumption was, in part, inspired by experimental observations of domain shapes on the surface of giant unilamellar vesicles, as shown, for example, in Fig. 4.4d. The interaction energy is roughly an order of magnitude less than the free energy associated with the morphological transition itself (see Fig. 4.3b), thus interaction does not perturb the domain shape significantly. Only allowing domains to rotate simplifies the interaction between two domains to a change in the boundary conditions in the three regions of interest, shown in blue in Fig. 4.4c. Applying the small gradient approximation, the boundary slope is given by $|\epsilon - \phi|$ in the outer regions and by $|\epsilon + \phi|$ in the inner region. With the single domain boundary slope, ϵ, set by the energy minimization of the previous section (*i.e.* eqn. 4.6), the pairwise energy is minimized at every domain spacing, d, by $\partial G/\partial \phi = 0$ to find the domain tilt angle that minimizes the deformation energy (see Section 4.4 for details). This results in two qualitatively distinct scenarios: two domains whose curvatures have the same sign repel each other, while two domains whose curvatures have the opposite sign attract each other. Scaling arguments can be used to show that the strength of interaction between two dimpled domains increases roughly linearly with their area, so long as they are both larger than some critical area (see Section 4.4 for details). Mathematically, the assumption of rigidly rotating dimpled domains is identical to a previous 2D model of bending-mediated interactions between intramembrane proteins, represented by rigid conical inclusions [117].

Independent of the effects of spontaneous curvature, slight osmolar imbalances and constriction due to the lipid phase boundaries create small pressure gradients across the membrane that tend to orient all dimples on a vesicle in the same direction, resulting in net repulsive interactions between all domains. Transitions between 'upward' and 'downward' dimples are infrequent, due to a large energy barrier. In the simplest case, where the domains are the same size, the tilt angle ϕ monotonically increases as two domains get closer, $\phi(d) \simeq -\epsilon e^{-d}$. Likewise, the interaction energy increases monotonically with decreasing domain separation, $V_{\text{int}}(d) \simeq 2\pi\kappa_b\epsilon^2\rho_o^2 e^{-d}$. To quantitatively compare our interaction model with experiment, we analyzed the thermal motion of small domains on the surface of giant unilamellar vesicles, as described in 'Materials and Methods.' For direct comparison, we fit both the 1D model outlined here and the 2D inclusion model [117] to the measured potential of mean force between domains, as shown in Fig. 4.5. The two models are experimentally indistinguishable, though with a slightly different elastic decay length.

In these experiments, membrane tension was regulated by balancing the internal and external osmolarity, giving us coarse control over the elastic decay length λ_2. Through time, the distance between every domain pair was measured and the net results were used to construct a histogram

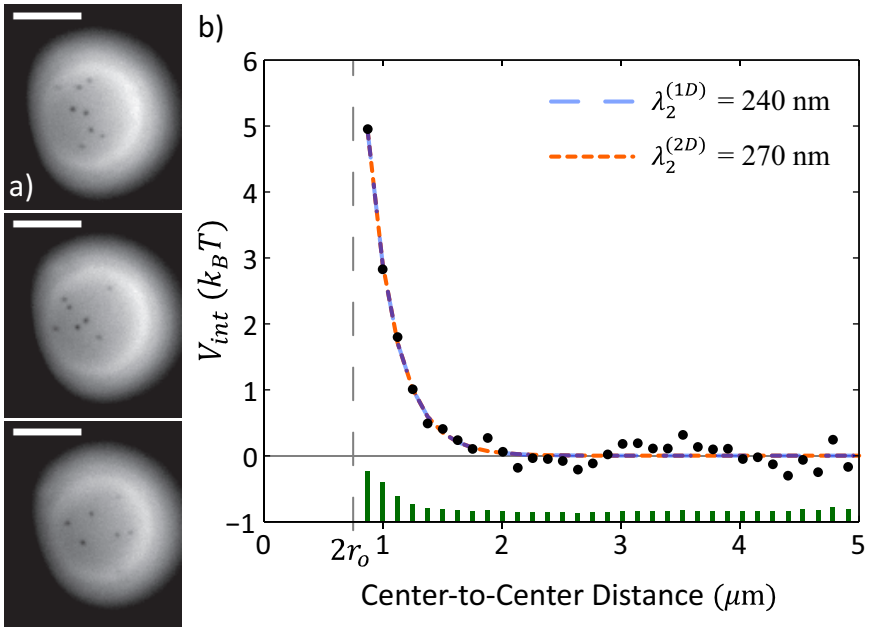

Figure 4.5: Measuring domain interactions on the surface of a vesicle. a) Three images of dilute interacting domains on the surface of the same vesicle (scale bar is 10 μm). b) The repulsive interaction potential (V_{int}) between domains on the surface of the same vesicle as (a). The energy is measured in k_BT and distance is domain center-to-center. The blue dashed line is a fit to the 1D interaction model in this work, $V_{\text{int}}(r) = a_1 e^{-r/\lambda_2^{(1D)}} + a_2$, with elastic decay length $\lambda_2^{(1D)} = 240\,\text{nm}$. The orange dashed line is a fit to the model, $V_{\text{int}}(r) = 2\pi\kappa_b \left[(a_1 a_2)^2 K_0(r/\lambda_2^{(2D)}) + a_2^2 a_3^4 K_2^2(r/\lambda_2^{(2D)})\right] + a_4$, with elastic decay length $\lambda_2^{(2D)} = 270\,\text{nm}$, based on the theory of Weikl *et al* [117]. Both elastic decay lengths indicate a membrane tension of $\sim 4 \times 10^{-4}\, k_BT/\text{nm}^2$. Errors bars are shown in green on the x-axis.

of center-to-center distance probability, the natural logarithm of which is the potential of mean force, as shown in Fig. 4.5b. We selected vesicles that had a low density of approximately equal-sized domains, and thus generally the interactions were described by a repulsive pairwise potential. Though areal density of domains and generic data quality varied in our experiments (see Section 4.4), all data sets exhibit the repulsive core of the elastic interaction. Multi-body interactions occur, though infrequently; their effect can be seen as a small variation in the baseline of Fig. 4.5b, which is not captured by the pairwise interaction model. At high membrane tension, when we would *not* expect dimpled domains, we qualitatively verified that domains coalesce in a rapid manner as compared to our low tension experiments (data not shown). Other recent experiments have also observed repulsive interactions and a correspondingly slower rate of coalescence between domains on low membrane tension vesicles, and a marked increase in coalescence kinetics on the surface of taut vesicles [214].

Our measurement of the pairwise potential allows us to estimate elastic properties of the mem-

brane. The elastic decay length was fit to the 1D and 2D interaction models described above, and found to be $\lambda_2^{(1D)} \simeq 240\,\text{nm}$ and $\lambda_2^{(2D)} \simeq 270\,\text{nm}$, respectively. Taken with a nominal bending modulus of $25\,k_BT$, we estimate the membrane tension to be $\sim 4 \times 10^{-4}\,k_BT/\text{nm}^2$. From the images, we measure the size of the domains at $r_o \simeq 350 - 400\,\text{nm}$, and hence $\rho_o \simeq 1.5$. We estimate the line tension, γ, using eqn. 4.8, based on the fact that the domains *are* dimpled, and find a lower bound of $\gamma \simeq 0.49\,k_BT/\text{nm}$ ($1\,k_BT/\text{nm} = 4.14\,\text{pN}$). This is in good agreement with theoretical estimates and values determined from AFM measurements [177], though somewhat higher than the value of $\gamma \simeq 0.22\,k_BT/\text{nm}$ measured via shape analysis of fully phase separated vesicles [179] and $\gamma \simeq 0.40\,k_BT/\text{nm}$ from micropipette aspiration experiments [216]. Finally, viewing the repulsive core of the interaction as an effective activation barrier to coalescence, a simple Arrhenius argument suggests a decrease in coalescence kinetics by two to three orders of magnitude. Indeed, such a slowing of coalescence was recently observed in a similar model membrane system [214].

4.2.3 Discussion of Dilute Domain Interactions

Comparing biologically relevant domain sizes ($\sim 50 - 500\,\text{nm}$) with the elastic decay length (λ_2), we expect physiologically relevant domains to be small (*i.e.* small α), as presumed in eqn. 4.8. Estimating the elastic decay length requires knowledge of the membrane tension and bending stiffness. We note that *in vitro* experiments of osmotically balanced single and multicomponent vesicles, and measurements of the plasma membrane of unstressed cells suggest membrane tensions of $10^{-4} - 10^{-2}\,k_BT/\text{nm}^2$ [179, 26, 13, 221]. The typical bending modulus of a phosphocholine bilayer is $\sim 10 - 50\,k_BT$, depending on the exact lipid and cholesterol content [26, 222, 223]. Choosing a nominal membrane tension of $10^{-4}\,k_BT/\text{nm}^2$ and nominal bending modulus of $25\,k_BT$ [26, 179] corresponds to an elastic decay length of $\lambda_2 \simeq 500\,\text{nm}$, suggesting that for lipid domains on the order of $50 - 500\,\text{nm}$, small α is an appropriate approximation.

Our experiments on the surface of GUVs have three potentially confounding effects, all due to the spherical curvature of the vesicle. First, the surface metric is not entirely flat with respect to the image plane. Thus, measurements of distance are underestimated the farther they are made from the projected vesicle center. This problem is ameliorated by concentrating on domains which are at the bottom (or top) of the vesicle where the surface is nearly flat and demanding that our tracking software exclude domains that are out of focus; see Section 4.4 for a more detailed explanation. The second potential complication is that we use a flat 2D coordinate system for our theoretical analysis, however domains reside on a curved surface. Given that the domain deformation, and hence energy density, decays exponentially with λ_2, as long as λ_2 is small with respect to the vesicle radius, the energetics that govern morphology converge on an essentially flat surface metric. The final complication is that the circular area of focus creates a fictitious confining potential for the domains, such that the effective measured potential of mean force is the sum of the elastic pairwise potential and a fictitious potential, $V_{\text{eff}} = V_{\text{int}} + V_{\text{fict}}$. The fictitious potential is removed by simulating non-interacting particles in a circle the same size as the radius of focus (see Section

4.4 for details).

The constant tension ensemble used in our theoretical analysis has an experimental range of validity, determined by the excess area available on a thermally fluctuating membrane with conserved volume and total surface area $\mathcal{A}_o$ (*i.e.* a vesicle). In the limit where the morphological transitions use only a small portion ($\Delta\mathcal{A}$) of this excess area, defined by $k_BT/8\pi\kappa_b \gg \Delta\mathcal{A}/\mathcal{A}_o$, the tension is constant. Outside this regime the tension rises exponentially with reduction in excess area, tending to stabilize dimples from fully budding (see section 4.4 for details).

In addition to the elastic mechanism of interaction, described herein, there may be other organizing forces at work in a phase-separated membrane, for instance, those of elastic [138] or entropic [224, 85] origin. However, the putative length scale over which these effects compete with thermal fluctuations (on the order of ten of nanometers) is not accessible to the spatial and temporal resolution of our experiments. Electrostatics may also be at work, in the form of dipole-dipole repulsion due to the net difference in dipole density between the two phases [225, 226, 227], although to first order, symmetry suggests there is a net zero dipole moment per unit volume of bilayer [228]. In our experimental system, the modulator of repulsive interactions is membrane morphology (*i.e.* domain dimpling); if other interactions were a major repulsive effect, we would not expect such forces to depend markedly on large-scale membrane morphology.

4.2.4 Summary of Dilute Domain Interactions

We have shown that lipid domains are subject to a morphological dimpling transition that depends on the bilayer elastic properties and domain size. Dimpling allows two domains in proximity to repulsively interact due to the deformation in the surrounding membrane. Our model makes two key predictions: i) at zero spontaneous curvature the domain size distribution reaches a critical point where coalescence is arrested by repulsive interactions [214], ii) domains with finite spontaneous curvature are always subject to interaction and hence should always coalesce at a rate slower than the diffusion-limited rate [208]. Additionally, the strength of elastic interactions is augmented by increasing line tension or domain area, with an approximately linear scaling. We proposed a simple 1D model of an elastic interaction that mediates dimpled-domain repulsion, and then used a standard ternary membrane system to verify the existence of dimpled domains and their subsequent repulsive interaction. Our model offers a mechanism that works against diffusion-driven coalescence, to maintain fine-scale lateral heterogeneity of lipids over time.

4.3 Dimpled Domain Organization and Budding

Cellular membranes are a complex mixture of lipids, membrane proteins, and small molecules (*e.g.* sterols) [176, 180]. The membrane serves mainly as a chemical barrier and substrate for membrane proteins that are responsible for regulating the movement of materials and information across the membrane. However, there are a host of important tasks that require a change in membrane

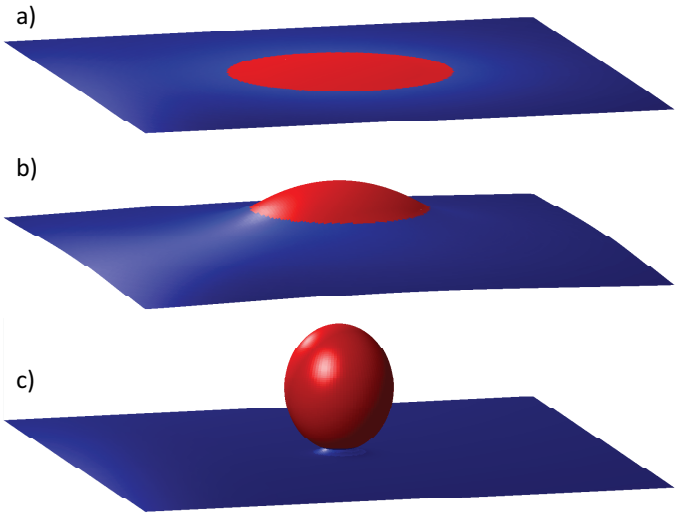

Figure 4.6: Morphologies of a lipid domain. a) A domain (red) lies completely flat when the energy from line tension is small compared to the cost of deformation from bending and membrane tension. b) For domains with a size roughly equal to or less than the elastic decay length, a competition between bending and phase boundary line tension results in a morphological transition from a flat to a dimpled state. This morphology facilitates elastic interactions between domains that slow the kinetics of coalescence significantly. c) Line tension in domains whose size is large compared to the elastic decay length, can cause a transition to a fully budded state.

morphology, such as endo- and exo-cytosis [105, 229], vesicular trafficking from the endoplasmic reticulum and Golgi apparatus to the plasma membrane [230], and the regulation of tension in the plasma membrane [181]. While the role of proteins cannot be ignored in these instances (*e.g.* clathrin, COPI, COPII, caveolin, SNAREs, actin) [231, 232, 233, 234, 218, 235, 236, 237, 238, 239], the lipid composition and bilayer morphology of the membrane play an important part [230, 240, 241, 242, 212, 185, 243]. With that in mind, our goals in this section are to examine how lipids in a model multi-component membrane spatially organize, how this organization relates to membrane morphology, or specifically membrane mechanics, and to examine how transitions in membrane morphology are regulated by bilayer mechanical properties.

In vitro studies have conclusively shown that lipids are capable of lateral self-organization [130, 179, 244], facilitated by the structure of their hydrophobic regions and the presence of intercalated sterols. Saturated lipids and cholesterol are sequestered from the membrane mix to form 'lipid rafts' that serve as platforms for signaling and material transport across the membrane, with sizes ranging from $\sim 50 - 500\,\mathrm{nm}$ [180, 181, 183, 184, 186, 187, 188, 189, 190, 191, 192]. In addition to their unique chemical properties and protein-specific interactions, lipid rafts are mechanical entities in a thermal environment, and as such, our analysis focuses on continuum and statistical mechanics of phase-separated bilayers.

The remainder of this section is organized as follows. The first subsection examines how dimpled domains, which exert repulsive forces on each other, spatially organize themselves into ordered structures as their areal density increases. Specifically, we measure the potential of mean force and orientational order, finding that domains exhibit orientational and translational order on length scales much larger than the domains themselves. The second section studies the transition to a spherical 'budded' morphology [215, 193]. Using a mechanical model that combines effects from bending, line tension and membrane tension, we predict and observe size-selective budding transitions on the surface of giant unilamellar vesicles, and derive a phase diagram for the budding transition. The final section considers the three lipid domain morphologies — flat, dimpled and budded — and constructs a set of transition rules that dictate the resultant morphology resulting from coalescence of two domains.

4.3.1 Spatial Organization of Dimpled Domains

Our analysis begins by viewing the bilayer as a mechanical entity, endowed with a resistance to bending [26], quantified by a bending modulus (κ_b) with units of energy; a resistance to stretch under applied membrane tension (τ) [26], with units of energy per unit area; and in the case where more than one lipid phase is present, an energetic cost at the phase boundary, quantified by an energy per unit length (γ) [245, 138]. For a given domain size, the line tension between the two phases competes with the applied membrane tension and bending stiffness to yield morphologies that reduce the overall elastic free energy. In particular, the bending stiffness and membrane tension both favor a flat domain morphology. Conversely, the line tension prefers any morphology (in three dimensions) that reduces the phase boundary length. A natural length-scale, over which perturbations in the membrane disappear, is established by the bending stiffness and membrane tension, given by $\lambda = \sqrt{\kappa_b/\tau}$. Comparing this 'elastic decay length' with domain size indicates the set of possible domain morphologies. If the domain size is on the order of, or smaller than, the elastic decay length, flat and dimpled morphologies arise; while domains larger than λ generally give rise to the budded morphology [215, 193, 204, 205]. This rule of thumb is based on the fact that bilayer deformations from dimpling are concentrated within a few elastic decay lengths of the phase boundary, while domain budding energetics are governed by basis shapes much larger than λ.

Dimpled domains are characterized by a dome-like shape with finite slope at the boundary between the two lipid phases, as shown in Figs. 4.6 and 4.7(b). In previous work we found a distinct flat-to-dimpled transition, regulated by line tension and domain area [246], where if all the elastic parameters are constant in time, the domain is either flat or dimpled, but cannot make transitions between those states (*i.e.* there is no coexistence regime). Hence, domains below a critical size lie flat, and if all other membrane properties are constant, the only way domains transition from flat to dimpled is by coalescing to form larger domains that are above a critical size. An important

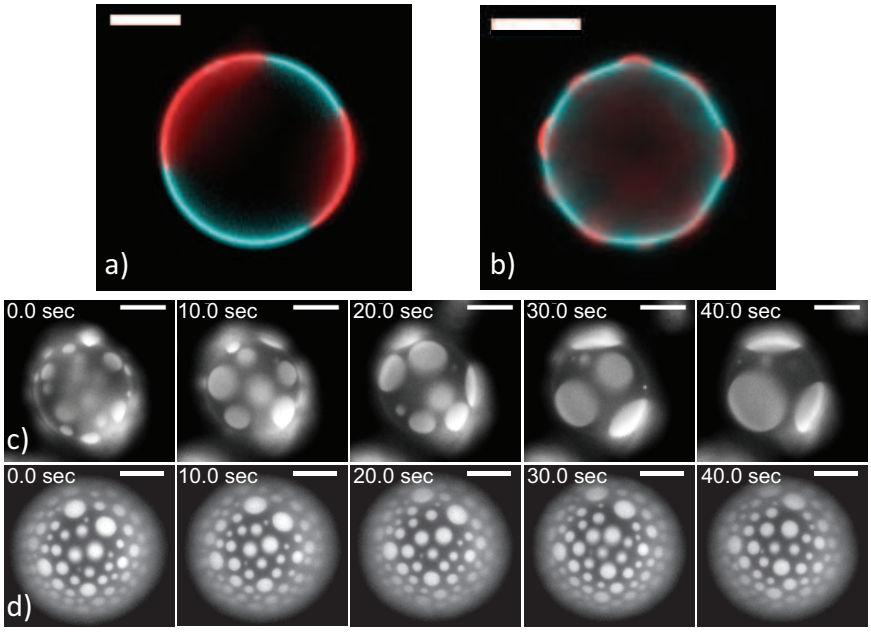

Figure 4.7: Domain morphology and coalescence. a) A nearly fully phase-separated vesicle, showing domains (red) flat with respect to the background curvature of the vesicle (blue). b) At low tension, domains (red) dimple and establish a non-zero boundary slope with respect to the curvature of the vesicle (blue). c) Flat domains on the surface of a vesicle — coalescence is uninhibited by elastic interactions. d) Dimpled domains on the surface of a vesicle - coalescence is inhibited by elastic interactions between the domains, and the domain-size distribution is stable. Directly measuring membrane tension disturbs the domain size evolution, however the magnitude of membrane fluctuations [214, 247] indicates that the tension in (c) is higher than the tension in (d). Scale bars are $10\,\mu$m.

outcome of domain dimpling is the emergence of a membrane-mediated repulsive interaction between domains that tends to inhibit coalescence. Intuitively, the origin of this force is that dimples deform their surrounding membrane, but this deformation decays back to an unperturbed state within a few elastic decay lengths of the phase boundary. Two domains that are within a few elastic decay lengths of each other have overlapping deformed regions, and thus the total elastic free energy depends on the distance between the domains, leading to a net repulsion. A relatively simple mechanical model and previous measurements show that the interaction between two dimpled domains can be approximated by the pair potential $V(r) \propto e^{-r/\lambda}$, where r is the center-to-center separation between the domains [246].

This repulsive interaction arrests coalescence, and hence significantly affects the evolution of domain sizes in a phase-separated membrane. For a simple physical model, in the absence of any interaction, domains would diffuse [248] and coalesce at a rate such that domain size scales as $t^{1/3}$

[197, 202, 203]. This sets the time-scale for full phase separation on a typical giant unilamellar vesicle (GUV) at ~ 1 minute (see Fig. 4.7(c) and [130]). However, viewing repulsive interactions as an energetic barrier to domain growth, and given the measured barrier height of $\sim 5k_BT$ (with $k_B = 1.38\times10^{-23}\,J/\mathrm{K}$ and $T \simeq 300\,\mathrm{K}$) [246], the rate of domain coalescence slows by the Arrhenius factor $e^{-5} = 0.007$. A clear example of the difference in the rate of domain growth, with and without elastic interactions, is shown in Fig. 4.7(d and c), respectively, and [214]. Thus elastic repulsion is a plausible mechanism by which lipid lateral heterogeneity could be maintained on the hour-long time scale required for a cell to recycle (and hence partially homogenize) the plasma membrane [220]. Alternative schemes have been proposed that balance continuous rates of membrane recycling and domain coalescence to yield a stable domain size distribution [193].

We examined the role these elastic interactions play in the spatial organization of lipid domains. Given that all the domains mutually repel each other, as the areal density of domains increases, the arrangement of domains that minimizes the elastic free energy takes on distinctly hexagonal order, so as to maximize the separation between all domains. Indeed, the arrangement of repulsive bodies on a sphere is a well studied problem in physics [249, 250, 251], and a dominant feature of such systems is the emergence of hexagonal and translational order. We measured the strength of this organizing effect by tracking the thermal motion of dimples on the surface of GUVs, and calculating the radial distribution function (see 'Materials and Methods'). For time-courses that have no coalescence events, the vesicle and its domains are in quasistatic equilibrium, thus the negative natural logarithm of the radial distribution function is a measure of the potential of mean force between domains. Our previous theoretical and experimental work showed that the elastic interaction between domains at low areal density is well approximated by a pair potential of the form $V(r) \propto e^{-r/\lambda}$ [246]. As the domain areal density increases, the domains adopt spatial orientations that maximize their mean spacing. This can be understood in terms of the free energy of the entire group of domains. If a domain deviates from this spatial arrangement, the sum of the elastic interaction energy with its neighboring domains increases, providing a mild restoring force to its original position. Thus the potential of mean force develops energy wells, up to $\sim 2\,k_BT$ in depth, that confine domains to a well-defined spacing, as shown in Fig. 4.8(b–f). It should be noted that such a restoring force can arise from the combined *pair* repulsion of the hexagonally-arranged neighboring domains, and does not necessarily mean that there are attractive, non-pairwise interactions.

The mutual repulsion and resulting energetic confinement lead to an effective lattice constant that depends on domain size and packing density. For example, domains may exhibit a well-defined spacing for first, second (Fig. 4.8(b)), third (Fig. 4.8(c–d)), and fourth (Fig. 4.8(e–f)) nearest-neighbors, corresponding to a correlation in the position of domains over a few microns. Interestingly, this means that by forming dimpled domains, the motion of individual lipids can be correlated on length scales up to $\sim 10^4$ times larger than the size of an individual lipid. As indicated by the exponential decay of these 'ringing' potentials (see Fig. 4.8(b–f)), the length scale

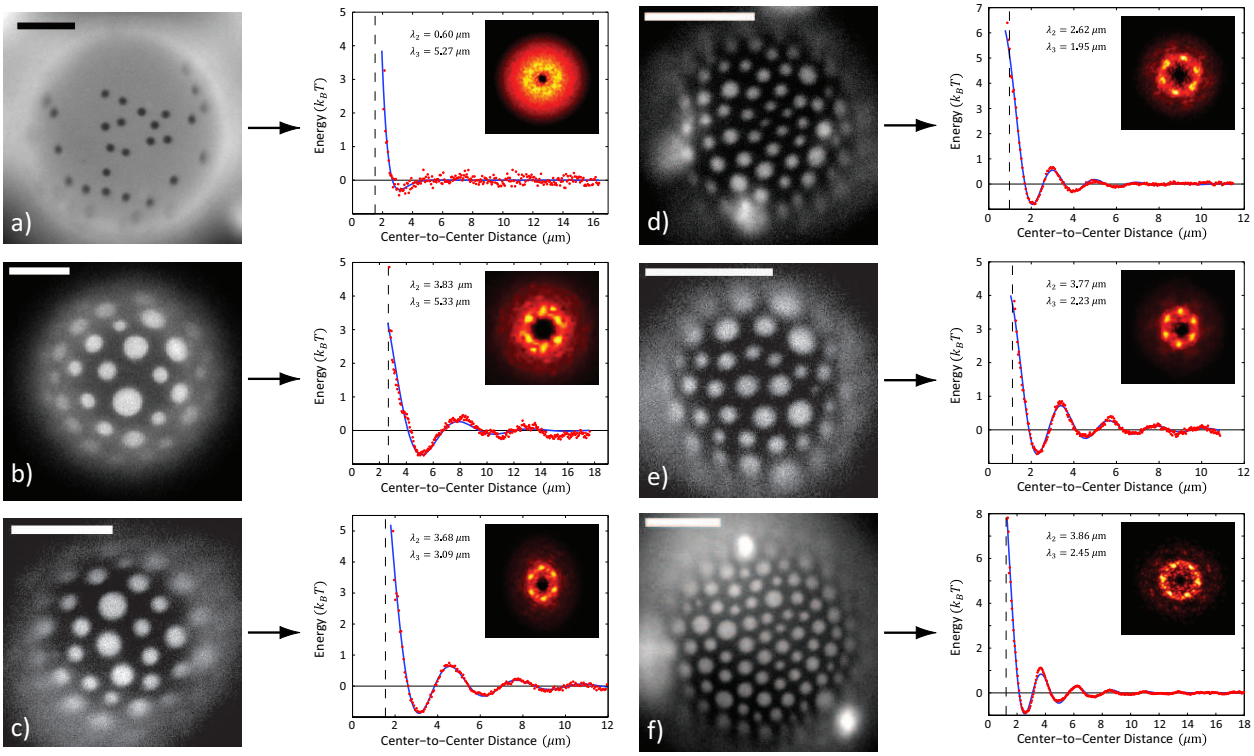

Figure 4.8: Interactions of lipid domains as areal density increases. Left: snapshots of dimples on the surface of GUVs. Right: corresponding potentials of mean force. a) At low areal density, interactions are almost purely repulsive, and there is no translational or orientational order — the domains are in a state analogous to a gas of particles. b–f) At higher areal density, domains 'condense' into a state where each domain is repelled by its neighboring domains, giving rise to energy wells that define a lattice constant and hence translational order. The decay envelope of these 'ringing' potentials indicates the length-scale over which the motion of domains is correlated. In all plots, the blue line indicates the fit to eqn. 4.9, where λ_2 is the order-correlation length and λ_3 is the effective lattice constant. The dashed vertical lines are the approximate minimum center-to-center distance between domains as determined by domain size measurement (a) or one half the lattice constant (b–f). Insets: Time-averaged Fourier transforms, showing that mutually repulsive elastic interactions lead to (thermally smeared) hexagonal order, except in (a) where the density is too low to order the domains. Scale bars are 10 μm.

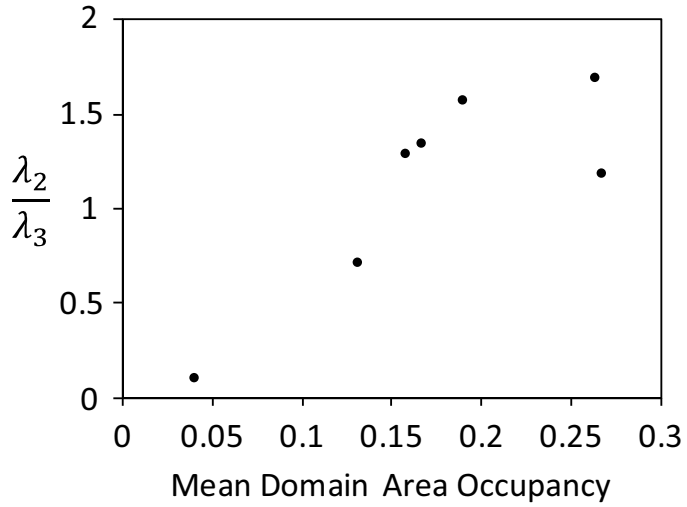

Figure 4.9: Increase in correlated motion of dimpled domains as a function of area occupancy. This plot shows the ratio of the order-correlation length (λ_2) over the lattice constant (λ_3) for the vesicles in Fig. 4.8 (and one additional vesicle) as a function of the total area taken up by the domains divided by the total measurable vesicle area. The ratio λ_2/λ_3 quantifies how many nearest neighbor domains (*i.e.* 1st, 2nd, etc.) exhibit strongly correlated motion.

over which this correlation in motion exists is limited by both the relatively low strength of pair repulsion (relative to k_BT) and the dispersion of domain sizes.

In the picture that emerges, lipid domains exhibit a transition similar to condensation in a liquid–gas system. At the lowest areal densities, the motion of domains is analogous to a 'gas' of particles that occasionally have repulsive pairwise interactions. As the domain areal density increases a 'condensed' phase of domains emerges, identified by its translational and orientational order. As the areal density of dimpled domains increases, the system exhibits three qualitative effects: i) the lattice constant decreases, as it must, to accommodate more domains per unit area; ii) the effective confinement grows stronger because the membrane in between the domains is more severely deformed by the closer packing; iii) hexagonal order clearly emerges, as shown by the characteristic peaks in the time-averaged Fourier transforms of domain positions in Fig. 4.8(b–f)(inset). The time-averaged Fourier transform is the arithmetic mean of the Fourier transforms of domain positions from each image in a data set, with the peaks corresponding to hexagonal order somewhat 'smeared' by the rotational diffusion of the entire group of domains.

To quantify the lattice constant and correlation length of interacting dimpled domains, we added a phenomenological correction term to the previously mentioned pair potential to account for interactions between multiple domains, such that the total potential of mean force has the form

$$V_{\text{fit}}(r) = a_1 e^{-\frac{r}{\lambda_1}} + a_2 e^{-\frac{r}{\lambda_2}} J_0\left(2\pi(r - r_o)/\lambda_3\right), \tag{4.9}$$

where J_0 is the 0^{th}-order Bessel Function of the first kind, and a_1, λ_1, a_2, λ_2, r_o and λ_3 are fit parameters. While this equation offers little insight into the underlying physics of densely interacting domains, the description does an excellent job of capturing the observed features of interactions between multiple dimpled domains, as demonstrated in Fig. 4.8. Using this formula, we extracted the correlation length (λ_2) and lattice constant (λ_3), whose ratio, λ_2/λ_3, is a measure of the translational order in the system, which is shown to increase with domain density. As domain areal density increases, the elastic free energy confines domains to adopt a well-defined mean spacing with hexagonal order. Thus the motion of domains is correlated over multiple layers of neighboring domains, as shown in Fig. 4.9.

The dimpled domains that exhibit this behavior arise in situations where the tension is low and the elastic decay length is longer than the domain size. In the regime where the elastic decay length is short compared to domain size, 'budded' domains emerge as a morphology with distinct transition rules and interactions.

4.3.2 The Budding Transition

Similar to the analysis of domain dimpling; bending, membrane tension, line tension, and domain size all play a role in the transition to a budded domain morphology. Many energetic models have been proposed that describe morphological changes which result in budding and other more complex morphologies [204, 252, 253, 254, 206, 255]. One of the simplest models, and yet most reconcilable with experiment, is the 'spherical' budding model. This model has its foundations in classical 'sessile' droplet wetting theory [256], and posits that the domain is, at all times, a section of a sphere [181, 215]. We will recapitulate this model here, and explore some of its implications for our experiments. This model ignores deformations near the phase boundary, and cannot capture the existence of the dimpled state, but is a reasonable model to employ in the regime where the elastic decay length is smaller than the domain size.

The budding domain is characterized by a wrapping angle θ, where $\theta = 0$ corresponds to a flat domain and $\theta = \pi$ corresponds to the encapsulation of a small volume by a spherical bud, as shown in Fig. 4.6(c) and 4.10(a). The bending energy of a budding domain is calculated as a fraction of the bending energy of a sphere, given by

$$\begin{aligned} G_{\text{bend}} &= 2\kappa_b \int (H - c_o)^2 \, \mathrm{d}\mathcal{A} \\ &= 8\pi\kappa_b \frac{\mathcal{A}}{4\pi R^2} (1 - 2c_o R) + C, \end{aligned} \tag{4.10}$$

where $H = 1/R$ is the mean curvature, R is the radius of curvature of the domain, $8\pi\kappa_b$ is the bending energy of a sphere, $\mathcal{A}$ is the domain area, and c_o is the spontaneous curvature of the domain, which, for simplicity, we assume is zero. A constant energy C, that does not depend on domain shape, is omitted. As the domain becomes more spherical, the areal footprint of the domain shrinks, as shown in Fig. 4.10(a), and work must be done against the applied membrane tension,

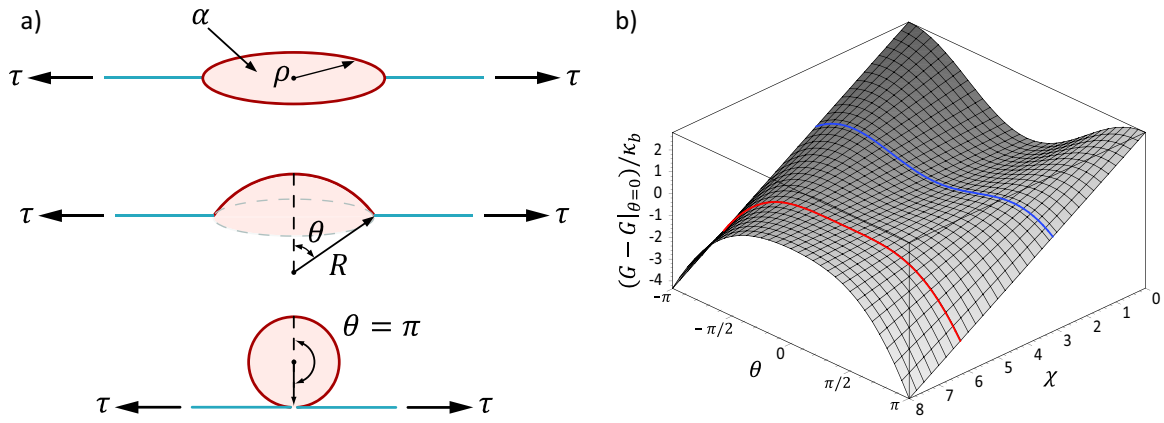

Figure 4.10: Shapes and energies of domain budding. a) A schematic of domain shape going from a flat domain, with area α and flat radius ρ, through a dome shape with wrapping angle θ and radius of curvature R, to a fully budded state, with an applied tension τ. b) The free energy of a budding domain as a function of line tension (χ) and wrapping angle (θ) for domain size $\alpha = 10$. At low line tension (before the blue line), both flat and budded morphologies are stable, but the flat state has a lower elastic free energy and there is an energy barrier between the two stable states. At the blue line, the free energy difference between flat and budded is zero. Between the blue and red lines, both morphologies are stable, but the budded state has a lower elastic free energy. Finally, for line tensions above the red line, the energy barrier disappears and budding is a spontaneous process.

given by

$$G_{\text{tens}} = -\tau\pi(R\sin\theta)^2. \tag{4.11}$$

The driving force for budding is the reduction of phase-boundary line tension, provided by

$$G_{\text{line}} = \gamma 2\pi R\sin\theta. \tag{4.12}$$

Finally, for all reasonable membrane tensions, the domain area is conserved during any change in morphology, and is given by

$$\mathcal{A} = 2\pi R^2(1-\cos\theta). \tag{4.13}$$

This constraint equation links $\mathcal{A}$ and R, allowing us to eliminate R from the total free energy, $G = G_{\text{bend}} + G_{\text{tens}} + G_{\text{line}}$. After some rearrangement, the total free energy can be written in a compact form,

$$G = 4\pi\kappa_b[\ \underbrace{\chi\sqrt{\alpha}\sqrt{\frac{1+\cos\theta}{8\pi}}}_{\text{line tension}} - \underbrace{\alpha\frac{1+\cos\theta}{8\pi}}_{\text{membrane tension}} + \underbrace{1-\cos\theta}_{\text{bending}}\ ], \tag{4.14}$$

where the dimensionless area, $\alpha = \mathcal{A}/\lambda^2$, and dimensionless line tension, $\chi = \gamma\lambda/\kappa_b$, emerge as the regulators of domain budding. The stable morphologies are those found at energy minima, given by $\partial G/\partial\theta = 0$, with only flat ($\theta = 0$) or budded ($\theta = \pi$) morphologies satisfying this equation (in the absence of spontaneous curvature). Figure 4.10(b) shows the free energy of budding as a function of wrapping angle θ and the line tension χ. From this plot, one can readily see that there are two special values of the line tension; the first, shown in blue, is where the free energy difference between the flat and budded states equals zero, but an energy barrier exists between them. The second special value of line tension, shown in red, is where the energy barrier between flat and budded morphologies disappears, and budding becomes a spontaneous process. This graphical analysis primes us to calculate the budding phase diagram. From the solutions for the energy minima, it can be shown that the phase diagram has three regions, as shown in Fig. 4.11: i) for certain values of α and χ both flat and budded domains are stable (coexistence), but flat domains have a lower elastic free energy; ii) in an adjacent region, both morphologies are stable (coexistence), but buds have a lower elastic free energy; iii) in the remaining region only buds are stable (single-phase). The boundary between the regions of the phase diagram that have two stable morphologies (coexistence) versus one stable morphology (single-phase) is given by the inflection point $(\partial^2 G/\partial\theta^2)\big|_{\theta=0} = 0$, which defines the line tension

$$\chi_{\text{bud}} = 8\sqrt{\frac{\pi}{\alpha}} + \sqrt{\frac{\alpha}{\pi}}, \tag{4.15}$$

above which only buds are stable, or alternatively stated, there is no energy barrier to the budding process (see Fig. 4.11). Given that χ is a constant material parameter for constant tension, this equation specifies a size range over which spontaneous domain budding will occur,

$$\frac{\pi}{4}\left(\chi - \sqrt{\chi^2-32}\right)^2 < \alpha < \frac{\pi}{4}\left(\chi + \sqrt{\chi^2-32}\right)^2. \tag{4.16}$$

Thus budding, and in particular spontaneous budding, is a size-selective process that can only occur if $\chi > 4\sqrt{2}$. Membrane tension and line tension can be estimated by measuring size-selective spontaneous budding on the surface of a phase-separated vesicle. In a few instances, we were able to capture the onset of size-selective budding, though as a function of initial conditions and timing, this proves particularly difficult. Sample temperature is a coarse knob that allows us to change the state of tension on the vesicle surface. Though the exact value of the thermal area expansion coefficient for bilayers varies with composition, a good approximate value in the temperature range of interest is $c_{\text{exp}} \simeq 5 \times 10^{-3} K^{-1}$ [257, 258, 259]. In Fig. 4.12(a-c), the temperature is increased slightly (from $\sim 18\,C$ to $\sim 20\,C$, see 'Materials and Methods'), increasing vesicle area by approximately 1% while maintaining the enclosed volume, thus lowering the tension and driving the system into the spontaneous budding regime. The average size of budding domains is $r = 0.93 \pm 0.18\,\mu$m. Using eqn. 4.16, and taking $\kappa_b = 25\,k_BT$ as a nominal value for the bending modulus of a domain [179, 26, 222, 223], we can solve the equations defined by the upper and lower bound to find the line tension and membrane tension. From this analysis, we estimate $\tau \simeq 2.4 \times 10^{-4}\,k_BT/\text{nm}^2$ and $\gamma \simeq 0.45\,k_BT/\text{nm}$. Using the tension and our assumption of bending modulus, we can also calculate the elastic decay length and dimensionless domain size to find $\lambda \simeq 320\,\text{nm}$ and $\alpha \simeq 26$. This membrane tension, which is within the range set by typical free vesicle [179, 26] and unstressed plasma membrane experiments [13, 221], sets the dimensionless domain area larger than one, and hence suggests that the spherical budding model is a good approximation. This estimate of line tension is consistent with previous measurements [179, 216], and quantitatively matches results from our previous work [246].

As a prelude to the calculation of allowed morphological transitions, we note that for the morphology of a domain to move from one region of the phase diagram to another, the domain must either change size via coalescence, or there must be a change in membrane tension which affects both α and χ. On the phase diagram in Fig. 4.11, horizontal lines would correspond to increasing domain area, and the dashed trajectories are increasing membrane tension with fixed domain area. The key fact is that, except within a region very near the phase boundary, the free energy difference between the flat and the fully budded states is much larger than k_BT, as is the energy barrier between those states (*e.g.* Fig. 4.10). Thus, from an equilibrium statistical mechanics perspective, a budding domain can be approximated as a two state system, with the spontaneous budding regime included within the budded state. Thus, it makes sense to impose the thermodynamic requirement that the free energy difference between morphological states be negative for a transition to be allowed, *i.e.* $G|_{\theta=\pi} - G|_{\theta=0} < 0$ if going from flat to budded. This amounts to describing budding with a two-state model where

$$\Delta G_{f\to b} = G|_{\theta=\pi} - G|_{\theta=0} = \pi\kappa_b \left(\rho^2 - 2\chi\rho + 8\right), \tag{4.17}$$

and $\rho = \sqrt{\alpha/\pi}$ is the dimensionless domain radius. Figures 4.12(a–c) and 4.13(b–d) show the two states of budding on the surface of phase-separated vesicles. If we consider ρ, a measure of

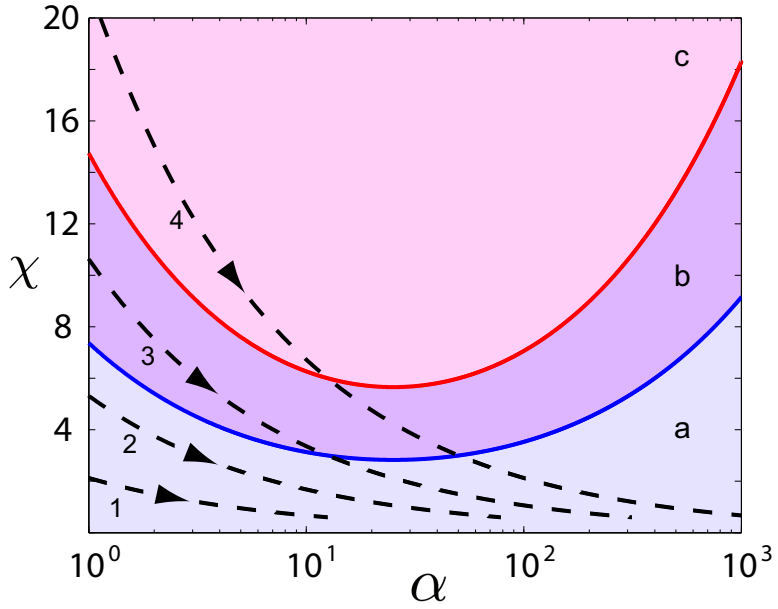

Figure 4.11: Equilibrium phase diagram for domain budding as a function of dimensionless domain area and line tension. In region 'a' flat and budded domains coexist, with flat domains at lower free energy. In region 'b' flat and budded domains coexist, with budded domains at lower free energy. In region 'c' only a single, budded phase is stable. The line separating regions 'a' and 'b' is given by $\chi_{\rm bud}/2$ and between regions 'b' and 'c' by $\chi_{\rm bud}$ (eqn. 4.15). Dashed lines are trajectories of increasing membrane tension (as indicated by the arrows) at constant domain area. In all four trajectories $\gamma = 0.3\,k_BT/\text{nm}$, $\kappa_b = 25\,k_BT$ and tension is varied from $\tau = 10^{-5} - 10^{-2}\,k_BT/\text{nm}^2$; the domain areas are $\mathcal{A}_1 = \pi(100\text{nm})^2$, $\mathcal{A}_2 = \pi(250\text{nm})^2$, $\mathcal{A}_3 = \pi(500\text{nm})^2$, and $\mathcal{A}_4 = \pi(1000\text{nm})^2$.

domain size, as an independent variable, then the single control-parameter χ dictates whether the thermodynamic condition $\Delta G_{f\to b} < 0$ has been met for a particular domain size. If the dimensionless line tension is below the critical value $\chi_c = 2\sqrt{2}$, defined by $\Delta G_{f\to b} = 0$, the budding transition is forbidden for all domain sizes. If $\chi > \chi_c$, budding is allowed, thought not necessarily spontaneous, within the size range given by

$$\rho = \chi \pm \sqrt{\chi^2 - 8}, \tag{4.18}$$

as demonstrated in Fig. 4.12(f). This size range always includes the range specified by eqn. 4.16, because spontaneous budding always has a negative free energy.

4.3.3 The 'Algebra' of Morphology

With an understanding of the conditions under which a domain transitions from flat to dimpled [246], and dimpled to budded, we are in position to calculate the change in free energy when domains of different morphologies coalesce. On a short enough time-scale, coalescence only occurs between two domains at a time, and hence we can think of the coarsening behavior of a phase-separated membrane as many such binary coalescence events happening in succession. The purpose of this section is to begin to build a framework for understanding how domain morphology and coalescence work in concert to affect the morphological evolution of a phase-separated membrane. In particular, we calculate the allowed, resultant morphology when two domains, each of a distinct morphology, coalesce. The change in free energy associated with a change in domain morphology, from flat to dimpled, or dimpled to budded, is much greater than k_BT, and hence, like the budding analysis of the previous section, for a particular transition to be allowed, we demand that the change in free energy be negative. Furthermore, the large reduction in line energy upon coalescence (compared to k_BT) means that, in general, coalescence is irreversible, and hence after each coalescence event the system is presumed to be in a unique quasistatic equilibrium state, with a unique membrane tension. The use of these transitions rules must then be considered in the context of these unique states, that is, transitions involving domains of a particular size that were allowed before a coalescence event might be prohibited afterward, or *vica versa*.

Let us denote transitions that involve flat domains with the letter f, dimpled domains with the letter d, and budded domains with letter b, such that, for instance, a flat domain coalescing with a dimpled domain to yield a budded domain would be denoted by $fd \to b$. There are six possible binary coalescence events: ff, fd, fb, dd, db, and bb; each resulting in a single domain of either f, d or b morphology. Thus at the onset, there are a total of 18 possible morphological transitions, however, not all of them are thermodynamically allowed. Specifically, any domain whose size is greater than the critical size required for dimpling cannot adopt a flat morphology as there is no flat-dimple coexistence, hence only the $ff \to f$ transition can end with an f domain (see Fig. 4.14(a)). This eliminates five of the six possibilities that end with an f domain. The only

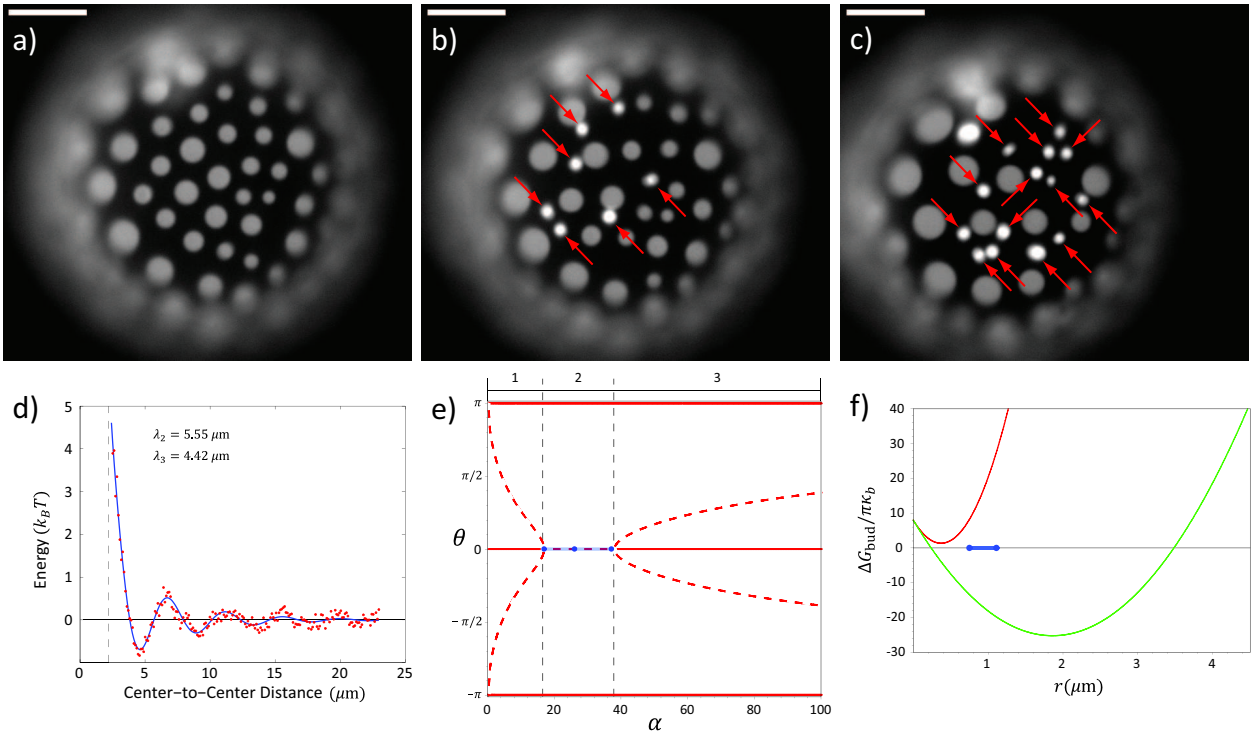

Figure 4.12: Size-selective domain budding. a) Dimples on the surface of a GUV are initially arranged by their repulsive interactions. b) and c) A slight increase in temperature decreases membrane tension, causing smaller domains to spontaneously bud (marked with red arrows) and wander freely on the vesicle surface, while larger domains remain dimpled. The mean size of budding domains is $r \simeq 0.93 \pm 0.18\,\mu$m from which we estimate a line tension of $\gamma \simeq 0.45\,k_BT/$nm. d) Plot of the potential of mean force between the dimpled domains in (a), moments before inducing spontaneous budding. e) Budding stability diagram, showing solutions to $\partial G/\partial\theta = 0$ with $\gamma = 0.45\,k_BT/$nm. Solid red lines are stable solutions at energy minima; dashed red lines are unstable solutions on the energy barriers. Regions 1 and 3 are coexistence regimes, while region 2 is a spontaneous budding regime, only stable at $|\theta| = \pi$. The blue dots indicate domain areas with radii $r \simeq 0.93, 0.93 \pm 0.18\,\mu$m. f) The red curve shows the free energy of budding at $\tau = 1.2 \times 10^{-3}\,k_BT/\text{nm}^2$, which is greater than zero for all domain sizes, and hence all domains would remain flat/dimpled. The green curve shows the free energy of budding at $\tau = 2.4 \times 10^{-4}\,k_BT/\text{nm}^2$. Domains with radius $r \simeq 0.25 - 3.5\,\mu$m have a negative free energy of budding, all other sizes remain flat/dimpled. Most domains within this size range must still overcome an energy barrier to bud, but for a small range of domain sizes ($r \simeq 0.75 - 1.11\,\mu$m), indicated by the blue line segment, budding is a spontaneous process. The energies are calculated using $\kappa_b = 25\,k_BT$ and $\gamma \simeq 0.45 k_BT/$nm. In (a-c) scale bars are $10\,\mu$m.

other transition that can be eliminated immediately is $ff \rightarrow b$, because the coalescence of two flat domains must first go through the dimpled state.

This leaves twelve possible morphological transitions, as shown in Fig. 4.14(a-ℓ). For simplicity we will assume the domains have no spontaneous curvature (though this is straightforward to incorporate [215, 260]). The free energy change associated with each of these twelve transitions is calculated by knowing the free energy change associated with three simpler transitions, namely the $f \rightarrow d$, $f \rightarrow b$, and $ff \rightarrow f$ transitions. Of these, the $f \rightarrow b$ transition free energy was discussed in the previous section, and the $f \rightarrow d$ transition free energy is a complicated function discussed at length in [246], though we note the important fact that $\Delta G_{f\rightarrow d}(\alpha_1+\alpha_2) < \Delta G_{f\rightarrow d}(\alpha_1)+\Delta G_{f\rightarrow d}(\alpha_2)$ if both domains are above the critical size for dimpling, or in words, the free energy of domain dimpling as a function of domain area grows faster than linearly. The scheme we are about to build is a valid frame work for understanding energy based transitions because we know that changes in free energy, when moving along a reaction coordinate, are additive.

The transition of two flat domains coalescing to yield another flat domain is the most fundamental transition, as shown in Fig. 4.14, and can be calculated as the difference in the line tension energy between the initial and final states given by

$$\Delta G_{ff\rightarrow f}(\alpha_1, \alpha_2) = 2\sqrt{\pi}\kappa_b\chi\left[\sqrt{\alpha_1+\alpha_2} - \sqrt{\alpha_1} - \sqrt{\alpha_2}\right], \tag{4.19}$$

where α_1 and α_2 are the dimensionless areas of the two domains and $\Delta G_{ff\rightarrow f}(\alpha_1, \alpha_2) < -k_BT$ for all domain areas of one lipid or more. This situation, depicted by Fig. 4.14(a) and shown experimentally in Fig. 4.7(c), is encountered at high membrane tension, when domains are too small to dimple before and after coalescence.

Using the three basic transitions, we now address the remaining eleven transitions in detail. The next transition we consider is two flat domains, each too small to dimple on their own, coalescing to form a domain large enough to dimple, as depicted in Fig. 4.14(b). The transition free energy is given by

$$\Delta G_{ff\rightarrow d}(\alpha_1, \alpha_2) = \Delta G_{ff\rightarrow f}(\alpha_1, \alpha_2) + \Delta G_{f\rightarrow d}(\alpha_1+\alpha_2), \tag{4.20}$$

and is negative as long as $\alpha_1 + \alpha_2$ is greater than the critical area required for dimpling.

The next transition is a flat and dimpled domain coalescing to form a dimpled domain, as depicted in Fig. 4.14(c). The transition free energy is given by

$$\Delta G_{fd\rightarrow d}(\alpha_1, \alpha_2) = \Delta G_{ff\rightarrow d}(\alpha_1, \alpha_2) - \Delta G_{f\rightarrow d}(\alpha_2). \tag{4.21}$$

No definitive statement about the resultant morphology after coalescence of a flat and dimpled domain can be made, because the free energy of this transition must be compared to the closely related transition of a flat and dimpled domain coalescing to form a budded domain, to determine which has a greater reduction in free energy. This related transition, depicted in Fig. 4.14(h), has

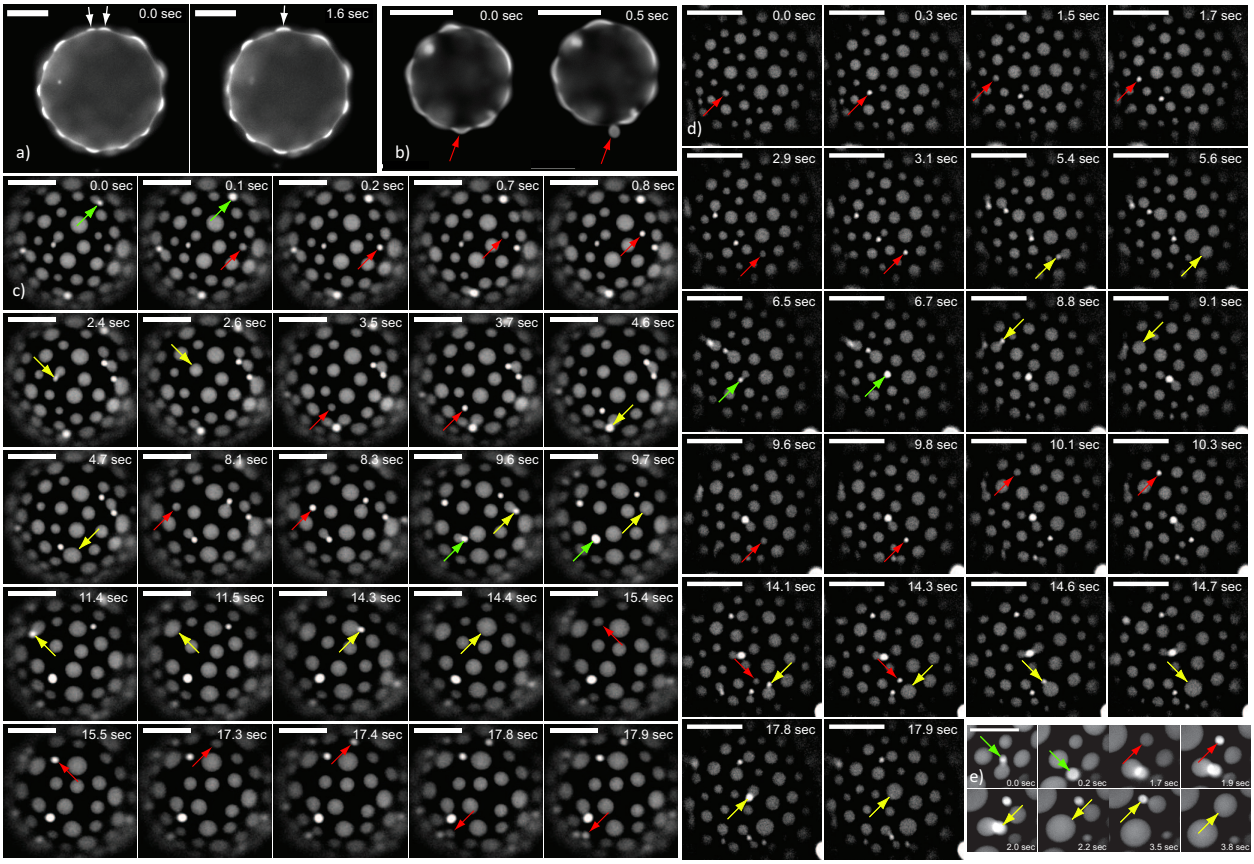

Figure 4.13: Gallery of morphological transitions. a) Two dimpled domains (indicated by the white arrows) interact on the surface of vesicle, eventually coalescing to yield a larger dimpled domain (see Fig. 4.14(d)). b) An equatorial view of a dimple-to-bud transition (indicated by the red arrows). c-e) Time courses of multiple types of morphological transitions. Arrows are color-coded and point to before and after each transition: red arrows indicate a dimple to bud transition, green arrows indicate a bud engulfing a dimple to form a larger bud (see Fig. 4.14(j)), and yellow arrows indicate a bud recombining with a larger dimpled domain (see Fig. 4.14(e)). Using video microscopy, we can put an upper bound on the time scale of the $d \rightarrow b$, $db \rightarrow d$ and $db \rightarrow b$ transitions at $\sim 200 \pm 80$ ms, $\sim 160 \pm 70$ ms and $\sim 210 \pm 70$ ms, respectively. Scale bars are 10 μm.

the transition free energy

$$\Delta G_{fd\to b}(\alpha_1,\alpha_2) = \Delta G_{ff\to f}(\alpha_1,\alpha_2) - \Delta G_{f\to d}(\alpha_2) + \Delta G_{f\to b}(\alpha_1+\alpha_2). \tag{4.22}$$

Which of these two transitions, $fd \to d$ or $fd \to b$, dominates depends on which has a greater reduction in free energy. Comparing eqns. 4.21 and 4.22, asking which transition has the greater reduction in free energy is simply asking whether $\Delta G_{f\to d}(\alpha_1+\alpha_2) > \Delta G_{f\to b}(\alpha_1+\alpha_2)$ or *vica versa*. This energy balance between the $f \to d$ and $f \to b$ transitions determines the outcome of all of the subsequent binary transitions as well, though we will rigorously show this for the remaining cases. Because this energetic comparison crops up so often, we will simply refer to it as the 'bud-dimple energy balance.'

The next transition is two dimpled domains coalescing to yield a dimpled domain, as depicted in Fig. 4.14(d) and shown in Fig. 4.13(a). The transition free energy is given by

$$\Delta G_{dd\to d}(\alpha_1,\alpha_2) = \Delta G_{fd\to d}(\alpha_1,\alpha_2) - \Delta G_{f\to d}(\alpha_2). \tag{4.23}$$

Again, we must consider a closely related transition, namely the coalescence of two dimpled domains yielding a budded domain, as depicted in Fig. 4.14(i), with transition free energy

$$\Delta G_{dd\to b}(\alpha_1,\alpha_2) = \Delta G_{dd\to d}(\alpha_1,\alpha_2) - \Delta G_{f\to d}(\alpha_1+\alpha_2) + \Delta G_{f\to b}(\alpha_1+\alpha_2). \tag{4.24}$$

Comparing these two related transitions, $dd \to d$ and $dd \to b$, we see that the dominant transition is determined by the bud-dimple energy balance.

The next transition is a flat and a budded domain coalescing to form a dimpled domain, as depicted in Fig. 4.14(g). The transition free energy is given by

$$\Delta G_{fb\to d}(\alpha_1,\alpha_2) = \Delta G_{ff\to d}(\alpha_1,\alpha_2) - \Delta G_{f\to b}(\alpha_2). \tag{4.25}$$

The related transition, where a flat and budded domain coalesce to form a budded domain, as depicted in Fig. 4.14(ℓ), has the transition free energy

$$\Delta G_{fb\to b}(\alpha_1,\alpha_2) = \Delta G_{fb\to d}(\alpha_1,\alpha_2) - \Delta G_{f\to d}(\alpha_1+\alpha_2) + \Delta G_{f\to b}(\alpha_1+\alpha_2). \tag{4.26}$$

Comparing these two related transitions, $fb \to d$ and $fb \to b$, we see that the dominant transition is determined by the bud-dimple energy balance.

The next transition is a budded and a dimpled domain coalescing to form a budded domain, as depicted in Fig. 4.14(j) and shown in Fig. 4.13(c–e)(green arrows). The transition free energy is given by

$$\Delta G_{bd\to b}(\alpha_1,\alpha_2) = \Delta G_{fd\to b}(\alpha_1,\alpha_2) - \Delta G_{f\to b}(\alpha_2). \tag{4.27}$$

The related transition, where a budded and dimpled domain coalesce to form a dimpled domain, as

depicted in Fig. 4.14(e), and shown in Fig. 4.13(c–e)(yellow arrows), has the transition free energy

$$\Delta G_{bd\to d}(\alpha_1,\alpha_2) = \Delta G_{bd\to b}(\alpha_1,\alpha_2) - \Delta G_{f\to b}(\alpha_1+\alpha_2) + \Delta G_{f\to d}(\alpha_1+\alpha_2). \tag{4.28}$$

Comparing these two related transitions, $bd \to b$ and $bd \to d$, we see that the dominant transition is determined by the bud-dimple energy balance.

The last set of transitions is when two buds coalesce to form a larger bud, depicted in Fig. 4.14(k), with transition energy

$$\Delta G_{bb\to b}(\alpha_1,\alpha_2) = \Delta G_{fb\to b}(\alpha_1,\alpha_2) - \Delta G_{f\to b}(\alpha_2), \tag{4.29}$$

and when two buds coalesce to form a dimple, depicted in Fig. 4.14(f) with transition energy

$$\Delta G_{bb\to d}(\alpha_1,\alpha_2) = \Delta G_{fb\to d}(\alpha_1,\alpha_2) - \Delta G_{f\to b}(\alpha_2). \tag{4.30}$$

Comparing these two related transitions, $bb \to b$ and $bb \to d$, we see that the dominant transition is determined by the bud-dimple energy balance.

Given the importance of the bud-dimple energy balance in determining the morphology resulting from a coalescence event, we note that if the resulting domain area is outside the range specified by eqn. 4.18, but still larger than the critical size required for dimpling, the dimpled morphology dominates because the free energy change of budding is positive outside that range. Within this size range, selecting the dominant behavior is more subtle, and depends on the resultant domain size, material properties and tension. For this reason, until experimental methods are devised that can track the detailed three dimensional morphology of a phase separated vesicle (*i.e.* the positions and sizes of all domains and the membrane tension), the set of transition rules discussed in this section will remain largely an interpretive tool, useful for understanding the set of possible transitions and resultant morphologies, as well as their underlying physics, but difficult to quantitatively apply to experiment.

We speculate that the kinetics of these coalescence transitions are either relatively fast, when diffusion is the limiting time scale, as might be the case in the transitions shown in Fig. 4.14(a–c,e,g,h,j,ℓ), or relatively slow, limited by elastic interactions (Fig. 4.14(d,i)) or steric hindrance (Fig. 4.14(f,k)). From the viewpoint of coarsening of a two-phase fluid, these transitions represent new coarsening mechanisms that are linked to morphology, and likely have profound effects on the kinetics of phase separation, as demonstrated by the fact that coalescence of dimpled domains is inhibited by an energetic barrier. Additionally, these transitions suggest interesting biological possibilities. For instance, a small volume can be encapsulated at a particular location, as a dimple transitions to a bud. The enclosed volume can then diffuse to other regions of the membrane, and either engulf more volume (see Fig. 4.14(i)) or deposit its contents at the site of another domain (see Fig. 4.14(j)). In fact, both of these scenarios play out in Fig. 4.13(c–e). Furthermore, it is possible

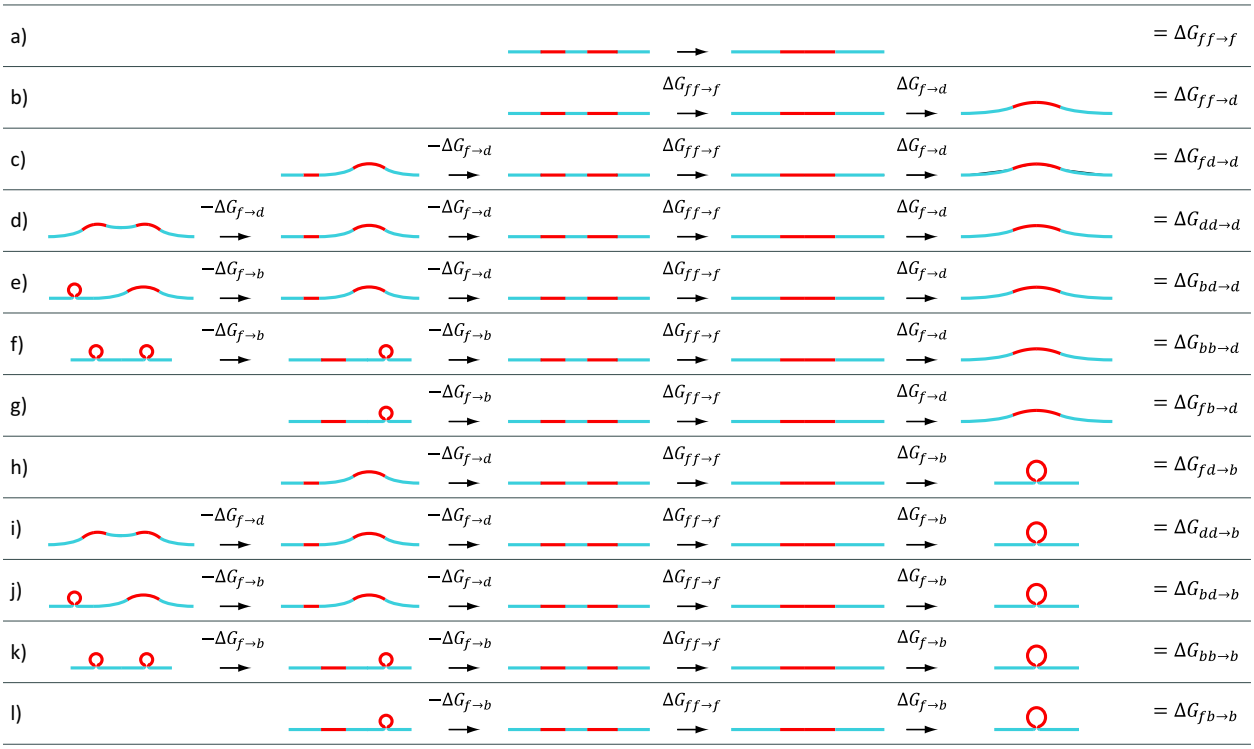

Figure 4.14: Algebra of Morphology. All rows show additive free energies of transition from an initial state on the left to a final state on the right. a) Two flat domains coalesce via diffusion, yielding a flat domain. b) Domains, too small to dimple, coalesce to attain a size capable of dimpling. c) A dimple and a domain too small to dimple coalesce to yield a larger dimpled domain. d) Two interacting dimples coalescence, yielding a larger dimpled domain. e) A dimple and a bud coalesce to yield a larger dimpled domain. f) Two buds coalesce to yield a dimpled domain. g) A flat domain coalesces with a bud, yielding a dimpled domain. h) A flat domain coalesces with a dimpled domain to yield a bud. i) Two interacting dimples coalescence, yielding a bud. j) A bud coalesces with a dimple, yielding a larger budded domain. k) Two budded domains coalesce to form a larger budded domain. l) A flat domain coalesces with a bud to yield a larger budded domain.

that careful control of membrane tension [182] could regulate how large a volume is enclosed, and to which other domains a bud will coalesce and deposit its contents. This has implications for the size-selectivity of endo- and exo-cytosis where membrane invagination and fusion occur, as well as regulation of plasma membrane tension [182].

4.3.4 Discussion of Domain Morphology

The transition free energies calculated in the previous section have the intuitively pleasing feature of being a sum of three simple basis transitions ($f \rightarrow d$, $f \rightarrow b$ and $ff \rightarrow f$) . However, this type of analysis is limited by the fact that it only admits flat, dimpled and budded as valid morphologies. More general theories and computational models can (and have been) constructed that attempt to describe all possible shapes of a domain from precisely flat to fully budded, and other more complex morphologies [205, 252, 253, 206, 199, 208, 261]. Our level of experimental sophistication is commensurate with the simplicity of the analysis employed in the previous section. Conceptually, our model simplifies analysis by reducing domain morphology to one of three classes of shapes, at the cost of excluding other possible morphologies. Though overall an experimental minority, domain-induced tube formation was the most common of these more exotic morphologies. Normally, thin lipid tubes are drawn out by external force [262, 263, 264]. However, in a few instances we observed domains that spontaneously collapse and nucleate a tube that rapidly grows many times longer than its persistence length, as demonstrated in Fig. 4.15. Oddly, the nucleating domain is of one lipid phase, but the tube continues to grow from the other, majority phase by a currently unknown mechanism.

In addition to limiting the class of possible morphologies, our analysis of morphological transitions also employs the simplification that membrane tension is constant during a morphological transition. In reality, our experiments take place on a spherical topology with constrained volume and surface area, such that this approximation has a range of validity. If the membrane area required to complete a morphological transition is small compared to the total vesicle area (see [246] for details) the change in membrane tension will be small. However, morphological transitions that require relatively large areas can result in significant changes to membrane tension, invalidating the constant tension approximation. Although, at times this can be an advantageous feature of our experimental system, for instance, when fairly small changes in vesicle area (on the order of 1%) can reduce the tension enough to cause spontaneous budding, as we showed earlier in this work.

In addition to the limitations mentioned above, our experiments have a number of subtle complications. Notably, the task of measuring the motion and size of lipid domains is complicated by the fact that the spherical curvature of the vesicle slightly distorts measurements of distance and size. Additionally, the motion of domains is confined to lie in a circle defined by a combination of vesicle size and depth of field of the microscope objective. We developed schemes to correct for these issues, as discussed in detail in the supplementary information of our previous work [246].

We take a moment to address some of the finer details of theory and experiment. Our model

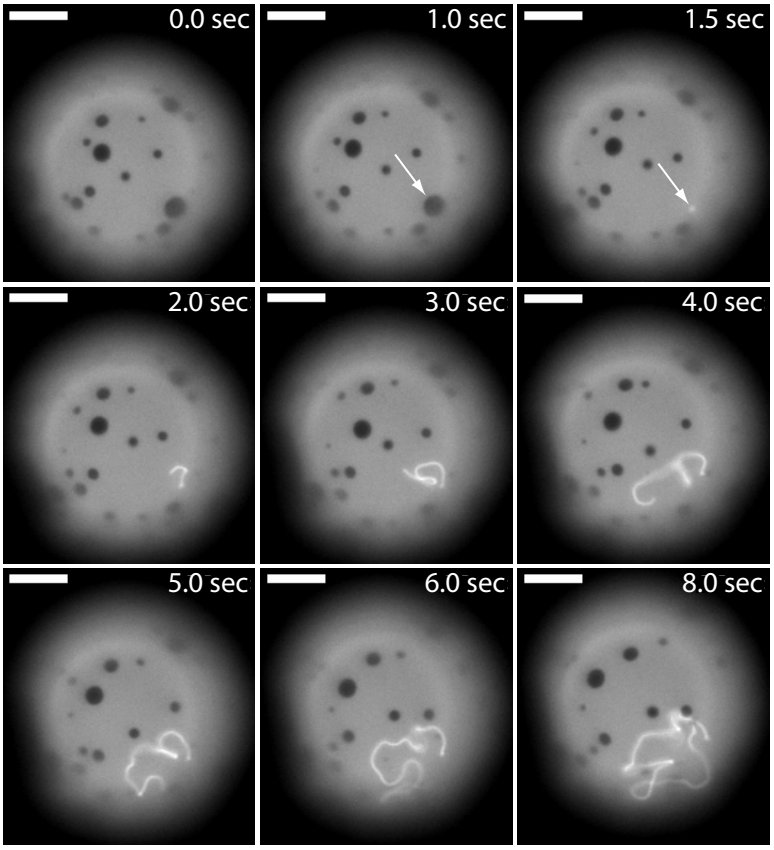

Figure 4.15: Domain-nucleated spontaneous tube formation. A time series of spontaneous tube formation, nucleated from a domain (as indicated by the white arrow). This relatively uncommon morphology is not explained within the context of our simple model. The lipid tube (bright) is many times longer than its persistence length, yet perplexingly, grows from the tube *tip*. With limited optical resolution, we estimate the tube diameter to be $\leq 500\,\mathrm{nm}$. The scale bar is $10\,\mu\mathrm{m}$.

membrane system utilizes neutral saturated and unsaturated lipids, to prevent compounded effects due to lipid charge. Our results indicate that charge is not a major player, simply because membrane tension is the distinction between rapid, flat-domain coalescence and slow, dimpled-domain coalescence, as shown in Fig. 4.7(c and d). We qualitatively observed the movements of dimpled domains in the presence of high salt ($\sim$ 300mM), where the Debye length is on the order of ten nanometers. At low tension the dimpled domains still exhibited significantly slower coalescence kinetics, with an interaction length-scale of order hundreds of nanometers (data not shown). Hence, the dimpled-domain interaction we observe cannot be attributed to a charge-based effect.

4.3.5 Summary of Domain Organization and Morphology

Using a model multi-component membrane, we explored how the interplay between composition and morphology leads to elastic forces that spatially organize domains and significantly impact coalescence kinetics. We expanded upon mechanical models that incorporate bending stiffness, membrane tension, phase boundary line tension, and domain size to show that domains can adopt (at least) three distinct morphologies: flat, dimpled and budded. We showed that dimpled domains exhibit measurable translational and orientational order as a function of increasing domain areal density [249, 250, 251]. Using a spherical budding model, we showed that the transition to a budded state is a domain size selective process, from which one can estimate the membrane tension, line tension, and elastic decay length of a phase separated membrane. Additionally, we found that the large energy scales associated with changes in domain morphology allow us to define morphological transition rules, where domain size and membrane tension are likely the key parameters that regulate the morphological transitions.

In the context of our understanding of the physics of phase separation the elastic forces between dimpled domains that arrest coalescence, and the morphological transitions between flat, dimpled and budded domains, constitute new mechanisms that govern spatial organization of domains and the temporal evolution of domain sizes. For cellular membranes, we speculate that the elastic forces and morphological transitions can be controlled via careful regulation of membrane tension [182], and our work suggests intriguing possibilities for how small volumes can be encapsulated, moved, and released in a phase-separated membrane.

4.4 Detailed Analysis of Theory and Experiment

This section presents all of the theoretical and experiment details relevant to previous two sections. Due to the length of this section, we first provide a summarized version of the materials and methods.

4.4.1 Overview of Materials and Methods

Giant unilamellar vesicles (GUVs) were prepared from a mixture of DOPC (1,2-Dioleoyl-sn-Glycero-3-Phosphocholine), DPPC (1,2-Dipalmitoyl-sn-Glycero-3-Phosphocholine) and cholesterol (Avanti Polar Lipids) (25:55:20/molar) that exhibits liquid-liquid phase coexistence [130]. Fluorescence contrast between the two lipid phases is provided by the rhodamine head-group labeled lipids: DOPE (1,2-Dioleoyl-sn-Glycero-3-Phosphoethanolamine-N- (Lissamine Rhodamine B Sulfonyl)) or DPPE (1,2-Dipalmitoyl-sn-Glycero-3-Phosphoethanolamine-N- (Lissamine Rhodamine B Sulfonyl)), at a molar fraction of ~ 0.005. The leaflet compositions are presumed symmetric and hence $c_o = 0$.

GUVs were formed via electroformation [130, 265]. Briefly, $3 - 4\,\mu$g of lipid in chloroform were deposited on an indium-tin oxide coated slide and dessicated for ~ 2 hrs to remove excess solvent. The film was then hydrated with a 100 mM sucrose solution and heated to ~ 50 C to be above the miscibility transition temperature. An alternating electric field was applied; 10 Hz for 120 minutes, 2 Hz for 50 minutes, at ~ 500 Volts/m over ~ 2 mm. Low membrane tensions were initially achieved by careful osmolar balancing with sucrose (~ 100 mM) inside the vesicles, and glucose ($\sim 100 - 108$ mM) outside. Using a custom built temperature control stage, the *in situ* membrane tension was coarsely controlled by adjusting the temperature a few degrees [258, 259].

Domains were induced by a temperature quench and imaged using standard TRITC epi-fluorescence microscopy at 80x magnification with a cooled (-30 C) CCD camera (Roper Scientific, $6.7 \times 6.7\,\mu$m^2 per pixel, 20 MHz digitization). Images were taken from the top or bottom of a GUV where the surface metric is approximately flat. Data sets contained $\sim 500 - 1500$ frames collected at 10-20 Hz with a varying number of domains (usually > 10). The frame rate was chosen to minimize exposure-time blurring of the domains, while allowing sufficiently large diffusive domain motion. Software was written to track the position of each well-resolved domain and calculate the radial distribution function. The raw radial distribution function was corrected for the fictitious confining potential of the circular geometry. The negative natural logarithm of the radial distribution function is the potential of mean force plus a constant, as shown in Figs. 4.5 and 4.8. Detailed explanations of these concepts can be found in the supplementary information for [246].

Morphological transitions were induced by quenching homogeneous vesicles below the de-mixing temperature and observing those that had many micron-sized domains. Without precise control of membrane tension or the exact initial conditions (*i.e.* the exact number and size distribution of domains) many vesicles had to be sampled to see transitions. Often, a slight increase in temperature ($\sim$ 2C) was used to increase the available membrane area, and hence decrease the membrane tension enough to induce morphological transitions.

Our goal in the following few sections is to add detail to calculations already performed or alluded to earlier in this chapter. We begin by building up the linearized Helfrich functional and examining how spontaneous curvature, line tension and membrane tension affect membrane morphology [215, 181, 204].

4.4.2 Calculating Membrane Curvature and Area

In general, a thin elastic sheet can be described by a surface, $\mathcal{S}(u, v)$, embedded in $\mathbb{R}^3$ and written as a function of the parametric variables (u, v). At each point on this surface, one can calculate the curvature tensor and pointwise contribution to the total area. As we will show in the next few sections, the curvature tensor is used to calculate contributions to the elastic energy from two different modes of bending and the area is used to couple membrane tension, via a particular ensemble, to membrane energetics.

Our first simplifying assumption is that there is some one-to-one height function (*i.e.* no folds) that describes the membrane midplane, $h(\mathbf{r})$, often referred to as a *Monge* representation. Using this representation, the exact area of the membrane is a simple, though non-linear, function of h, given by

$$\mathcal{A} = \int_{\mathcal{S}} \sqrt{1 + (\nabla h)^2}\, \mathrm{d}^2\mathbf{r}. \tag{4.31}$$

In comparison to a completely flat membrane, the increase in actual area due to deformation is given by

$$\Delta\mathcal{A} = \int_{\mathcal{S}} (\sqrt{1 + (\nabla h)^2} - 1)\, \mathrm{d}^2\mathbf{r}, \tag{4.32}$$

which couples to the lateral membrane tension τ by $G_{\text{tens}} = \tau\Delta\mathcal{A}$ in a constant tension ensemble[2]. In the limit where gradients are small, $|\nabla h| \ll 1$, this simplifies to

$$\Delta\mathcal{A} = \frac{1}{2}\int_{\mathcal{S}} (\nabla h)^2\, \mathrm{d}^2\mathbf{r}. \tag{4.33}$$

At every point on the surface $\mathcal{S}$, the matrix of second partial derivatives defines the curvature tensor $\mathcal{C}$, whose eigenvalues are the principal curvatures of the surface at that point, and whose eigenvectors specify the directions of those principal curvatures on the surface, as shown in Fig. 4.16b. Any elastic energy formulation we construct from the curvature tensor should be invariant under rotations, reflections and translations and therefore can be written as a function of the invariants of the curvature tensor, namely the trace, which is the sum of the principal curvatures, and the determinant, which is the product of the principal curvatures. To lowest order, these symmetries dictate that the energy should be linear in the determinant and quadratic in the trace. The determinant's contribution is usually called the Gaussian curvature and will be addressed in subsection 4.4.5. One half the sum of the principal curvatures is called the *mean curvature*, denoted by H, and contributes energy of the form H^2. An intuitively pleasing formulation of the mean curvature is the divergence of the unit normal vector field of the surface [57], as shown in Fig. 4.16a, that is

$$H(\mathbf{r}) = \frac{1}{2}\nabla \cdot \hat{n}(\mathbf{r}), \tag{4.34}$$

[2]See Section 4.5 for an in depth discussion of a variable tension ensemble, applicable to thermal environments.

from which the mean curvature energy is calculated as

$$G_{\text{bend}} = 2\kappa_b \int_{\mathcal{S}} H^2 \sqrt{g}\, \mathrm{d}^2\mathbf{r}, \tag{4.35}$$

where $g = 1 + (\nabla h)^2$ is the surface metric in the Monge representation. The surface $h(x, y)$ can be written as an implicit function $F(x, y, z)$, by

$$h(x, y) = z \;\; \rightarrow \;\; F(x, y, z) = h(x, y) - z = 0, \tag{4.36}$$

from which the unit normal vector is given by

$$\hat{n} = \frac{\nabla F}{\sqrt{(\nabla F)^2}}. \tag{4.37}$$

On the surface defined by h, the unit normal vector field is the gradient normalized by the size of the small piece of area associated with the unit vector at the point $\mathbf{r}$, namely

$$\hat{n} = \frac{(\partial_x h, \partial_y h, -1)}{\sqrt{1 + (\nabla h)^2}}. \tag{4.38}$$

Then the mean curvature becomes a straight-forward, though non-linear, function of h, given by

$$H = \frac{1}{2} \nabla \cdot \left(\frac{\nabla F}{\sqrt{1 + (\nabla h)^2}} \right). \tag{4.39}$$

In situations where the height function is azimuthally symmetric, this can be expanded to

$$H = \frac{1}{2r} \frac{\partial}{\partial r} \left[\frac{r \frac{\partial h}{\partial r}}{\sqrt{1 + \left(\frac{\partial h}{\partial r}\right)^2}} \right]. \tag{4.40}$$

Application of the small gradient approximation yields a linearized curvature of the well-known form

$$H \simeq \frac{1}{2} \nabla^2 h, \tag{4.41}$$

with the linearized metric $g \simeq 1$, such that the integral of the mean curvature elastic energy over the surface is

$$G_{\text{bend}} = 2\kappa_b \int_{\mathcal{S}} H^2 \sqrt{g}\, \mathrm{d}^2\mathbf{r} \simeq \frac{\kappa_b}{2} \int_{\mathcal{S}} \left(\nabla^2 h\right)^2 \mathrm{d}^2\mathbf{r}. \tag{4.42}$$

With azimuthal symmetry this simplifies further to

$$G_{\text{bend}} = \pi \kappa_b \int_{\mathcal{S}} \left(\nabla^2 h\right)^2 r\, \mathrm{d}r, \tag{4.43}$$

and this contribution can now be combined into a linear elastic picture of a stiff membrane under

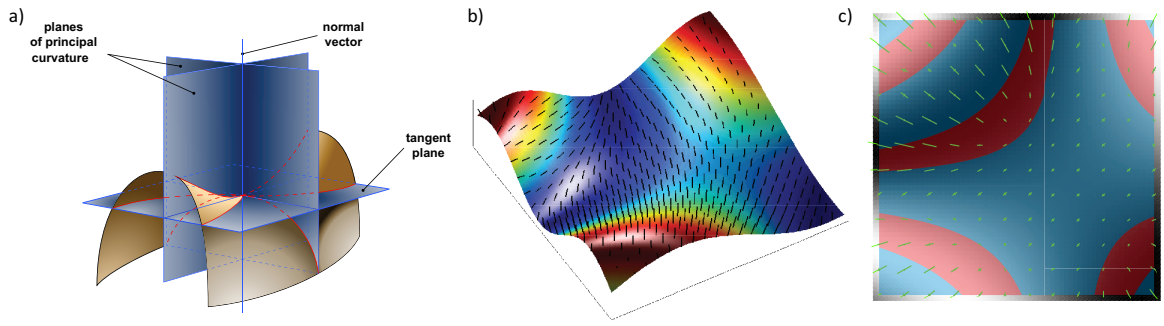

Figure 4.16: Curvature on a Monge surface. a) Illustration showing surface with the tangent plane, normal vector and planes of principal curvature indicated at a saddle point. b) Plot showing a Monge surface with its corresponding unit normal vector field. c) The same surface, now laid flat and shown in gray scale. The small green lines indicate the directions of the principal curvatures, while their lengths indicate the magnitude of the principal curvatures at those points. Zones whose principal curvatures have the same sign are colored in red (positive Gaussian curvature), while zones whose principal curvatures have opposite signs are colored in blue (negative Gaussian curvature). (a) is adapted from an illustration by Eric Gaba under CCL licensor.

lateral tension.

4.4.3 Conservation of Domain Area

Before constructing the full elastic model of a deformed lipid domain and its surrounding membrane, it behooves us to constrain the class of elastic models by discussing certain properties of the domain. In particular, if changes in domain morphology were accompanied by significant changes in domain area, this would require a more complex elastic model. The point of this section is to decisively show that the relevant elastic model conserves domain area during any morphological transition, as posited in earlier sections, though strictly speaking, this need not be true. For instance, if the material parameters were such that the stretch modulus of the domain was very low, while the line tension around the domain was very high, we would expect a large change in domain area. However, as we demonstrate in this section, the material properties of a bilayer favor the conserved area picture, and hence the use of a Lagrange multiplier formulation to impose this area constraint. To see this explicitly, we estimate the area change induced by the line tension for representative values of the relevant bilayer properties.

To be rigorous about this statement, we note that the membrane tension (τ) is linearly related to the areal strain (ϕ) by the area stretch modulus $K_{\mathcal{A}}$ [26],

$$\tau = K_{\mathcal{A}}\phi, \tag{4.44}$$

where

$$\phi = \frac{\mathcal{A} - \mathcal{A}_o}{\mathcal{A}_o} \tag{4.45}$$

and $\mathcal{A}_o$ is the domain area at zero tension. Thus a small change in domain area costs free energy

$$dG_{\text{area}} = \tau(\phi)\mathrm{d}\mathcal{A} = \mathcal{A}_o K_{\mathcal{A}} \phi \mathrm{d}\phi, \tag{4.46}$$

and hence upon integration we find the elastic stretch energy of a domain is

$$G_{\text{area}} = \mathcal{A}_o \frac{K_{\mathcal{A}}}{2} \phi^2. \tag{4.47}$$

For simplicity, let us consider the case where the domain is flat and hence the membrane tension and phase boundary line tension directly compete with each other — this is also the scenario where we would expect the largest potential area change. In this case, the phase boundary is characterized by the circumference

$$\ell = 2\pi r_o = 2\pi \sqrt{\frac{\mathcal{A}_o(1+\phi)}{\pi}} \tag{4.48}$$

where r_o is the projected radius of the domain. This contributes energy of the form

$$G_{\text{line}} = \gamma \ell, \tag{4.49}$$

where γ is the line tension and we assume $\partial\gamma/\partial\phi = 0$. The combined energy, $G_{\text{area}} + G_{\text{line}}$, can be used to solve for the equilibrium value of ϕ by evaluating

$$\frac{\partial}{\partial\phi}(G_{\text{area}} + G_{\text{line}}) = \omega^2\phi^2(1+\phi) - \pi = 0, \tag{4.50}$$

where we introduce the dimensionless parameter $\omega = K_{\mathcal{A}}\sqrt{\mathcal{A}_o}/\gamma$. Using the high estimate of $\gamma = 1.0\,k_BT/\text{nm}$ and low estimate of $K_{\mathcal{A}} = 50\,k_BT/\text{nm}^2$ [26], corresponds to $\omega \gg 1$ for all reasonable domain areas (*i.e.* one lipid or more), and hence the areal strain is

$$\phi \simeq \frac{\sqrt{\pi}}{\omega}, \tag{4.51}$$

resulting in a fractional area change of less than 1% for all reasonable domain areas — thus we work within an approximation in which the domain area is conserved.

4.4.4 The Small Gradient Limit

Using a small gradient approximation is not the most general model for the membrane surface, but it allows us to state our results analytically, and couches domain dimpling as a linearized buckling problem. The line tension at the phase boundary of a domain favors a circular geometry, and hence our model utilizes polar coordinates. Employing a small gradient approximation, valid when

$|\nabla h| \ll 1$, yields a quadratic approximation to the functional which can be solved analytically [57, 29, 32]. With no other approximations, the mean curvature and constant membrane tension give rise to an energy functional of the form

$$G_{\rm el} = G_{\rm tens} + G_{\rm bend} = \frac{1}{2}\int_{\mathcal{S}} \left(\tau(\nabla h)^2 + \kappa_b \left(\nabla^2 h - c_o\right)^2\right) \mathrm{d}^2\mathbf{r} \tag{4.52}$$

where $\mathcal{S}$ is the projected surface of integration, τ is the applied membrane tension, κ_b is the mean curvature bending modulus, and c_o is the spontaneous curvature of the membrane comprising the domain.

However, this only forms part of the complete free energy of a dimpled membrane. In addition to the elastic components, we must conserve area of the domain through the use of a Lagrange multiplier. Further, to have any interesting behavior at all, we impose a penalty at the phase boundary through the use of a line tension, as we did in the estimate of the previous section. Our strategy is to delineate all of the energy sources, posit a set of length-scales that clearly elucidate the important parameters, and solve for the constrained minima in free energy.

To be clear about all of the sources of energy they can be listed as follows: the elastic free energy in the domain region (region 1) is given by

$$G_{\rm el}^{(1)} = \pi \int_0^{r_o} \left[\tau(\nabla h_1)^2 + \kappa_b^{(1)}(\nabla^2 h_1 - c_o)^2\right] r\mathrm{d}r \tag{4.53}$$

while the elastic energy in outer region (region 2) is given by

$$G_{\rm el}^{(2)} = \pi \int_{r_o}^{\infty} \left[\tau(\nabla h_2)^2 + \kappa_b^{(2)}(\nabla^2 h_2)^2\right] r\mathrm{d}r, \tag{4.54}$$

where r_o is the projected domain radius. The subscripts on h and superscripts on κ_b refer to the region of interest. The phase boundary is simply penalized by its length, hence the energy from line tension is given by

$$G_{\rm line} = 2\pi r_o \gamma, \tag{4.55}$$

where γ is the energy per unit length along the phase boundary. Finally, the area constraint is imposed through the use of a Lagrange multiplier, τ_o, written as

$$G_{\rm area} = \tau_o \left(2\pi \int_0^{r_o} \left(1 + \frac{1}{2}(\nabla h_1)^2\right) r\mathrm{d}r - \mathcal{A}\right). \tag{4.56}$$

Our first step is to rearrange the constraint equation to construct what can be thought of as the 'effective' tension in the domain $\tau_1 = \tau + \tau_o$. In particular, we can absorb part of $G_{\rm area}$ into $G_{\rm el}^{(1)}$, resulting in

$$G_{\rm el}^{(1)} = \pi \int_0^{r_o} \left[\tau_1(\nabla h_1)^2 + \kappa_b^{(1)}(\nabla^2 h_1 - c_o)^2\right] r\mathrm{d}r \tag{4.57}$$

and

$$G_{\text{area}} = \tau_o \left(\pi r_o^2 - \mathcal{A}\right). \tag{4.58}$$

Our next step is to non-dimensionalize the free energy, with the understanding that if we are to see dimpling at all, the membrane tension in the domain region must be compressive, in other words, the sum of the external membrane tension and the membrane tension generated by the line tension must be negative. Mathematically this is stated simply as $\tau_1 < 0$; this will turn out to be an important fact when choosing admissible solutions to the Euler-Lagrange equations. To non-dimensionalize the free energy, we first note the two length scales in the problem are

$$\lambda_1 = \sqrt{\frac{\kappa_b^{(1)}}{\tau_1}} \quad \text{and} \quad \lambda_2 = \sqrt{\frac{\kappa_b^{(2)}}{\tau}}, \tag{4.59}$$

and we use these to define the constants

$$\beta = i\frac{\lambda_2}{\lambda_1} \quad \text{and} \quad \sigma = \frac{\kappa_b^{(1)}}{\kappa_b^{(2)}}. \tag{4.60}$$

Given our previous statements, we know that λ_2 and β are both positive and real, while λ_1 is purely imaginary with a positive coefficient when $\tau_1 < 0$. These length-scales give a notion of how quickly the perturbed height functions return to a flat state, where λ_2 is a constant, but λ_1 changes as domain area and line tension are varied. The constant length scale allows us to define the dimensionless variables

$$r = \lambda_2 \rho\,, \quad h_i = \lambda_2 \eta_i\,, \quad r_o = \lambda_2 \rho_o \quad \text{and} \quad \lambda_2 c_o = \upsilon_o. \tag{4.61}$$

With these definitions we can redefine the derivatives as

$$\frac{\partial}{\partial r} = \frac{1}{\lambda_2}\frac{\partial}{\partial \rho} \quad \text{and} \quad \mathrm{d}r = \lambda_2 \mathrm{d}\rho. \tag{4.62}$$

Finally, making all of these substitutions gives the elastic contributions

$$G_{\text{el}}^{(1)} = \pi\sigma\kappa_b^{(2)} \int_0^{\rho_o} \left[-\beta^2(\nabla\eta_1)^2 + (\nabla^2\eta_1 - \upsilon_o)^2\right] \rho \mathrm{d}\rho \tag{4.63}$$

and

$$G_{\text{el}}^{(2)} = \pi\kappa_b^{(2)} \int_{\rho_o}^{\infty} \left[(\nabla\eta_2)^2 + (\nabla^2\eta_2)^2\right] \rho \mathrm{d}\rho, \tag{4.64}$$

also showing that a natural energy scale is $\kappa_b^{(2)}$. The line energy is then written as

$$G_{\text{line}} = 2\pi\kappa_b^{(2)}\rho_o\chi \tag{4.65}$$

with $\chi = \gamma\lambda_2/\kappa_b^{(2)}$ defined as the dimensionless line tension. This is one of two key parameters

used to characterize the phase space of dimple morphology. The remaining contribution from the Lagrange multiplier is then written as

$$G_{\text{area}} = -\kappa_b^{(2)}(\sigma\beta^2 + 1)\left(\pi\rho_o^2 - \alpha\right). \tag{4.66}$$

where the dimensionless area, $\alpha = \mathcal{A}/\lambda_2^2$, is the second key parameter that characterizes the phase space of dimple morphology. The governing differential equations are distinct in each region; in region 1 the Euler-Lagrange equation is

$$\nabla^2(\nabla^2 + \beta^2)\eta_1 = 0, \tag{4.67}$$

while in region 2

$$\nabla^2(\nabla^2 - 1)\eta_2 = 0. \tag{4.68}$$

The solutions to these differential equations, and as we will show in Section 4.4.8, part of the derivation of the elastic free energy, can be found by splitting these fourth-order equations into two simpler, second-order equations. In particular, let us view these differential equations as differential operators acting on η_i

$$\nabla^2(\nabla^2 + c)\eta_i = \mathcal{L}\left[\eta_i\right] = 0 \quad \rightarrow \mathcal{L} = \nabla^2(\nabla^2 + c), \tag{4.69}$$

where c is a constant. To break this down into a set of simpler equations, we call the first differential operator $\mathcal{L}_1 = \nabla^2$ and the second $\mathcal{L}_2 = \nabla^2 + c$, such that $\mathcal{L} = \mathcal{L}_1\mathcal{L}_2$. Each of these simpler operators defines a familiar differential equation: $\mathcal{L}_1\left[\eta_i^{(1)}\right] = 0$ is commonly referred to as the Laplace equation, while $\mathcal{L}_2\left[\eta_i^{(2)}\right] = 0$ is commonly referred to as the Helmholtz equation. The solutions to each equation are unique, as indicated by the superscripts. In polar coordinates, the Laplace equation yields a solution that is the sum of a constant and a natural logarithm, and the Helmholtz equation yields a sum of Bessel functions whose 'kind' depend on the sign of the constant c. For the moment, let us assume that the full solution to the fourth-order equation is the addition of the solutions from each of these second-order equations, that is

$$\eta_i = \eta_i^{(1)} + \eta_i^{(2)}, \tag{4.70}$$

and see what that implies for the operators $\mathcal{L}_i$. The fourth-order equation would then be written as

$$\mathcal{L}\left[\eta_i\right] = \mathcal{L}_1\mathcal{L}_2\left[\eta_i^{(1)} + \eta_i^{(2)}\right] = 0, \tag{4.71}$$

and since the operators $\mathcal{L}_i$ are linear, this can be written as

$$\mathcal{L}_1\mathcal{L}_2\left[\eta_i^{(1)}\right] + \mathcal{L}_1\mathcal{L}_2\left[\eta_i^{(2)}\right] = 0. \tag{4.72}$$

With the trivial fact that $\mathcal{L}_i[0] = 0$, and recalling that the solutions to each second-order equation are unique, this can be simplified to

$$\mathcal{L}_1 \underbrace{\mathcal{L}_2\left[\eta_i^{(1)}\right]}_{\neq 0} + \mathcal{L}_1 \underbrace{\mathcal{L}_2\left[\eta_i^{(2)}\right]}_{=0} = \mathcal{L}_1\mathcal{L}_2\left[\eta_i^{(1)}\right] = 0. \tag{4.73}$$

If the differential operators commute, that is if $[\mathcal{L}_1, \mathcal{L}_2] = 0$, this can be rearranged to

$$\mathcal{L}_1 \underbrace{\mathcal{L}_2\left[\eta_i^{(1)}\right]}_{\neq 0} = \mathcal{L}_2 \underbrace{\mathcal{L}_1\left[\eta_i^{(1)}\right]}_{=0} = 0. \tag{4.74}$$

Indeed, one can show that the operators do commute and hence the full solution to the fourth-order equation is the sum of the solutions from each of the second-order equations. Additionally, the knowledge that the Euler-Lagrange equations can be broken down into commuting operators will prove useful for calculating the elastic energy in Section 4.4.8.

The solutions must meet certain physical boundary conditions; symmetry about $r = 0$ dictates that

$$|\nabla\eta_1(0)| = |\nabla\eta_2(\infty)| = 0, \tag{4.75}$$

while demanding that the membrane be contiguous demands $\eta_1(\rho_o) = \eta_2(\rho_o)$. Finally, as we will show later, the surface cannot have ridges if the bending energy is to be finite, hence

$$|\nabla\eta_1(\rho_o)| = |\nabla\eta_2(\rho_o)| = \epsilon, \tag{4.76}$$

where ϵ is the membrane slope at the phase boundary, which acts as an order parameter for the morphological phase space. Then the general solutions are

$$\eta_1(\rho) = \underbrace{a_1^{(1)} + a_2^{(1)}\ln(\rho)}_{\eta_1^{(1)}} + \underbrace{a_3^{(1)}J_0(\beta\rho) + a_4^{(1)}Y_0(\beta\rho)}_{\eta_1^{(2)}}, \tag{4.77}$$

and

$$\eta_2(\rho) = \underbrace{a_1^{(2)} + a_2^{(2)}\ln(\rho)}_{\eta_2^{(1)}} + \underbrace{a_3^{(2)}K_0(\rho) + a_4^{(2)}I_0(\rho)}_{\eta_2^{(2)}}, \tag{4.78}$$

where J_k and Y_k are k-th order Bessel functions of the first and second kind, respectively, and I_k and K_k are k-th order modified Bessel functions of the first and second kind, respectively. The brackets indicate the contributions from each of the separate differential operators. The constants $a_i^{(j)}$ are set by the boundary conditions and the physical constraint that the area change associated with morphological transitions be finite. Our stated boundary conditions demand that $a_4^{(1)} = a_4^{(2)} = 0$, and to keep the change in the membrane area in both regions bounded we demand $a_2^{(1)} = a_2^{(2)} = 0$. We have a freedom of vertical translation, which we choose to apply to region 2, such that $a_1^{(2)} = 0$.

Applying the slope boundary conditions at the phase boundary gives the final solutions

$$\eta_1(\rho) = -\epsilon \left[\frac{1}{\beta} \frac{J_0(\beta\rho)}{J_1(\beta\rho_o)} - \frac{1}{\beta} \frac{J_0(\beta\rho_o)}{J_1(\beta\rho_o)} + \frac{K_0(\rho_o)}{K_1(\rho_o)} \right] \tag{4.79}$$

and

$$\eta_2(\rho) = -\epsilon \frac{K_0(\rho)}{K_1(\rho_o)}. \tag{4.80}$$

These solutions can be integrated to give closed-form expressions for the elastic energy in the two regions, as shown in Section 4.4.8, where in region 1

$$G_{\text{el}}^{(1)} = \pi\sigma\kappa_b^{(2)}\epsilon^2\rho_o\beta\frac{J_0(\beta\rho_o)}{J_1(\beta\rho_o)} \tag{4.81}$$

and in region 2

$$G_{\text{el}}^{(2)} = \pi\kappa_b^{(2)}\epsilon^2\rho_o\frac{K_0(\rho_o)}{K_1(\rho_o)}. \tag{4.82}$$

The only remaining component of the free energy is the elastic contribution from spontaneous curvature in the domain. If we explicitly write the terms of the bending elastic energy from eqn. 4.63 we find

$$\frac{1}{2}\int(\nabla^2\eta_1 - \upsilon_o)^2\sqrt{g}\mathrm{d}^2\rho = \frac{1}{2}\int(\nabla^2\eta_1)^2\sqrt{g}\mathrm{d}^2\rho - \upsilon_o\int(\nabla^2\eta_1)\sqrt{g}\mathrm{d}^2\rho + \frac{\upsilon_o^2}{2}\underbrace{\int\sqrt{g}\mathrm{d}^2\rho}_{\text{domain area }(\alpha)}, \tag{4.83}$$

where $\sqrt{g}$ is the surface metric, equal to unity in the current approximation. Here, the term proportional to υ_o^2 is conventionally added to the elastic functional so that the interplay between mean curvature and spontaneous curvature is clear, however it is unimportant for determining morphology because the spontaneous curvature does not appear in the governing differential equations (eqn. 4.67 and 4.68), and since the domain area is conserved it does not affect the membrane free energy.

The domain area itself is calculated with the expression for the height field in region 1, namely eqn. 4.79, to give

$$\alpha = 2\pi\int_0^{\rho_o}\sqrt{1+(\nabla\eta_1)^2}\rho\mathrm{d}\rho \simeq 2\pi\int_0^{\rho_o}\left(1+\frac{(\nabla\eta_1)^2}{2}\right)\rho\mathrm{d}\rho, \tag{4.84}$$

and approximated as

$$\alpha = \pi\rho_o^2\left[1+\frac{\epsilon^2}{2}\left(1+\left(\frac{J_0(\beta\rho_o)}{J_1(\beta\rho_o)}\right)^2 - \frac{2}{\beta\rho_o}\frac{J_0(\beta\rho_o)}{J_1(\beta\rho_o)}\right)\right]. \tag{4.85}$$

Let us separate out the term dealing with spontaneous curvature that *does* affect the free energy,

namely

$$G_{\text{spont}} = -2\pi\sigma\kappa_b^{(2)}\upsilon_o \int_0^{\rho_o} \left(\nabla^2\eta_1\right)\rho \mathrm{d}\rho. \tag{4.86}$$

For the case in which we have azimuthal symmetry, the Laplacian can be written as $\nabla^2 = \frac{\partial^2}{\partial\rho^2} + \frac{1}{\rho}\frac{\partial}{\partial\rho}$, and hence we can evaluate this energy by partial integration, where

$$\int_0^{\rho_o} \frac{1}{\rho}\frac{\partial\eta}{\partial\rho}\rho \mathrm{d}\rho = \frac{\partial\eta}{\partial\rho}\rho\Big|_0^{\rho_o} - \int_0^{\rho_o} \frac{\partial^2\eta}{\partial\rho^2}\rho \mathrm{d}\rho. \tag{4.87}$$

Upon rearranging, we see that

$$\int_0^{\rho_o} \left(\nabla^2\eta\right)\rho \mathrm{d}\rho = \frac{\partial\eta}{\partial\rho}\rho|_{\rho=\rho_o} \tag{4.88}$$

and by applying the boundary conditions, we find that the elastic energy from spontaneous curvature is

$$G_{\text{spont}} = -2\pi\sigma\kappa_b^{(2)}\epsilon\rho_o\upsilon_o. \tag{4.89}$$

Finally, with all contributions accounted for, we can assemble the free energy of the system, with contributions

$$G = G_{\text{el}}^{(1)} + G_{\text{el}}^{(2)} + G_{\text{line}} + G_{\text{spont}} + G_{\text{area}}, \tag{4.90}$$

such that the total free energy is

$$G = \pi\kappa_b\rho_o\left[\epsilon^2\left(\sigma\beta\frac{J_0(\beta\rho_o)}{J_1(\beta\rho_o)} + \frac{K_0(\rho_o)}{K_1(\rho_o)}\right) + 2(\chi - \epsilon\sigma\upsilon_o)\right] - \kappa_b(\sigma\beta^2+1)(\pi\rho_o^2 - \alpha), \tag{4.91}$$

with the superscript dropped, $\kappa_b^{(2)} = \kappa_b$. Before searching for the morphological minimizers of this equation, let us address one additional issue.

We demand that the membrane surface be free of ridges, that is, we match the slope of the membrane at the phase boundary ($|\nabla\eta_1(\rho_o)| = |\nabla\eta_2(\rho_o)| = \epsilon$), because a slope mismatch would result in a divergence of the bending energy. This can be shown by direct calculation where the mismatch energy is calculated in a region, $\rho_o \pm \delta/2$, near the phase boundary

$$G_{\text{mismatch}} = \lim_{\delta\to 0}\pi\kappa_b\int_{\rho_o-\delta/2}^{\rho_o+\delta/2}(\nabla^2\eta)^2\rho \mathrm{d}\rho = \lim_{\delta\to 0}\pi\kappa_b\int_{\rho_o-\delta/2}^{\rho_o+\delta/2}\left(\frac{\epsilon_1-\epsilon_2}{\delta}\right)^2\rho \mathrm{d}\rho = \pi\kappa_b(\epsilon_1-\epsilon_2)^2\lim_{\delta\to 0}\frac{\rho_o}{\delta}, \tag{4.92}$$

where the only finite solution occurs when $\epsilon_1 = \epsilon_2$, that is, when the boundary slopes are matched between the domain and the surrounding membrane.

4.4.5 Gaussian Curvature

In line with our calculation of the various elastic energy terms, the following section explicitly calculates the elastic contribution from Gaussian curvature and makes an argument about its relevance to our elastic model. As discussed in the first section, the local curvature tensor is given

by the matrix of partial second derivatives of the surface η, which in Cartesian coordinates takes the form

$$\mathcal{C} = \begin{bmatrix} \frac{\partial^2 \eta}{\partial x^2} & \frac{\partial^2 \eta}{\partial x \partial y} \\ \frac{\partial^2 \eta}{\partial y \partial x} & \frac{\partial^2 \eta}{\partial y^2} \end{bmatrix}. \tag{4.93}$$

The trace of this tensor is the sum of the principal curvatures, while the determinant is the Gaussian curvature [57]. Using the typical polar transformations $\rho = \sqrt{x^2 + y^2}$ and $\theta = \tan^{-1}(y/x)$, the chain rule implies

$$\frac{\partial}{\partial x} = \frac{\partial \rho}{\partial x}\frac{\partial}{\partial \rho} + \frac{\partial \theta}{\partial x}\frac{\partial}{\partial \theta} \tag{4.94}$$

and

$$\frac{\partial}{\partial y} = \frac{\partial \rho}{\partial y}\frac{\partial}{\partial \rho} + \frac{\partial \theta}{\partial y}\frac{\partial}{\partial \theta}, \tag{4.95}$$

and using the equations of the principal curvatures, namely

$$\mathbf{tr}\left[\mathcal{C}\right] = C_1 + C_2 = \frac{\partial^2 \eta}{\partial x^2} + \frac{\partial^2 \eta}{\partial y^2} \tag{4.96}$$

and

$$\mathbf{det}\left[\mathcal{C}\right] = C_1 C_2 = \frac{\partial^2 \eta}{\partial x^2}\frac{\partial^2 \eta}{\partial y^2} - \left(\frac{\partial^2 \eta}{\partial x \partial y}\right)^2, \tag{4.97}$$

it can be shown that the principal curvatures in polar coordinates with azimuthal symmetry are $C_1 = \frac{\partial^2 \eta}{\partial \rho^2}$ and $C_2 = \frac{1}{\rho}\frac{\partial \eta}{\partial \rho}$. Then the Gaussian curvature contributes energy of the form

$$G_{\text{Gauss}} = \kappa_G \int_{\mathcal{S}} (C_1 \cdot C_2) \mathrm{d}^2 \rho. \tag{4.98}$$

Splitting the membrane into the domain and its surrounding region, this is written as

$$G_{\text{Gauss}} \simeq 2\pi \left(\kappa_G^{(1)} \int_0^{\rho_o} \left(\frac{\partial^2 \eta_1}{\partial \rho^2} \cdot \frac{1}{\rho}\frac{\partial \eta_1}{\partial \rho} \right) \rho \mathrm{d}\rho + \kappa_G^{(2)} \int_{\rho_o}^{\infty} \left(\frac{\partial^2 \eta_2}{\partial \rho^2} \cdot \frac{1}{\rho}\frac{\partial \eta_2}{\partial \rho} \right) \rho \mathrm{d}\rho \right) \tag{4.99}$$

where $\kappa_G^{(i)}$ is the saddle-splay (Gaussian bending) modulus in region i. This can be evaluated by partial integration, writing

$$\int_0^{\rho_o} \left(\frac{\partial^2 \eta_1}{\partial \rho^2} \cdot \frac{1}{\rho}\frac{\partial \eta_1}{\partial \rho} \right) \rho \mathrm{d}\rho = \left(\frac{\partial \eta_1}{\partial \rho} \right)^2 \Bigg|_0^{\rho_o} - \int_0^{\rho_o} \left(\frac{\partial^2 \eta_1}{\partial \rho^2} \cdot \frac{\partial \eta_1}{\partial \rho} \right) \mathrm{d}\rho \tag{4.100}$$

which simplifies to

$$2\pi \kappa_G^{(1)} \int_0^{\rho_o} \left(\frac{\partial^2 \eta_1}{\partial \rho^2} \cdot \frac{\partial \eta_1}{\partial \rho} \right) \mathrm{d}\rho = \pi \kappa_G^{(1)} \epsilon^2, \tag{4.101}$$

and likewise

$$2\pi \kappa_G^{(2)} \int_{\rho_o}^{\infty} \left(\frac{\partial^2 \eta_2}{\partial \rho^2} \cdot \frac{\partial \eta_2}{\partial \rho} \right) \mathrm{d}\rho = -\pi \kappa_G^{(2)} \epsilon^2. \tag{4.102}$$

Finally, the contribution from Gaussian curvature is

$$G_{\text{Gauss}} = \pi\epsilon^2(\kappa_G^{(1)} - \kappa_G^{(2)}) = \pi\kappa_b\epsilon^2 \cdot \frac{\kappa_G^{(1)} - \kappa_G^{(2)}}{\kappa_b}. \tag{4.103}$$

For a linear elastic and incompressible bilayer [60, 61], it has been analytically estimated that $\kappa_b \simeq -\kappa_G$ [57], which has been experimentally supported in some lipid mixtures [57, 58], though measurements of κ_G are notoriously difficult due to its topological invariance through the Gauss-Bonnet Theorem. Given that this estimate shows that the magnitude of the Gaussian and mean bending moduli should be equal in each region, and that the mean bending modulus does not vary significantly between regions, we assume the dimensionless difference in the saddle-splay bending modulus between the domain and surrounding membrane is small (*i.e.* $(\kappa_G^{(1)} - \kappa_G^{(2)})/\kappa_b \ll 1$), and hence ignore the contribution from Gaussian curvature altogether. That said, if we take the implications of this estimate for an incompressible bilayer at face value, we can write the energy of eqn. 4.103 as

$$G_{\text{Gauss}} = \pi\kappa_b\epsilon^2(1-\sigma), \tag{4.104}$$

and this term can be added to the total free energy, allowing Gaussian curvature to affect the morphological transition.

4.4.6 Equilibrium Domain Shapes

Having examined the elastic contributions to the free energy and origin of the boundary conditions, the problem statement is then to find minimizers of the total free energy, eqn. 4.91, where we allow ϵ, β, and ρ_o to vary independently. Hence we generate three simultaneous equations

$$\frac{\partial G}{\partial \epsilon} = 0 \qquad \frac{\partial G}{\partial \beta} = 0 \qquad \frac{\partial G}{\partial \rho_o} = 0. \tag{4.105}$$

Physically, the first equation can be interpreted as torque balance at the phase boundary, the second equation as conservation of domain area, and the third equation as lateral force balance at the phase boundary. The first equation can be written as[3]

$$\epsilon\left[\sigma\beta\rho_o\frac{J_0(\beta\rho_o)}{J_1(\beta\rho_o)} + \rho_o\frac{K_0(\rho_o)}{K_1(\rho_o)}\right] = \sigma\rho_o\upsilon_o, \tag{4.106}$$

the second equation is the same as eqn. 4.85

$$\alpha = \pi\rho_o^2\left[1 + \frac{\epsilon^2}{2}\left(1 + \left(\frac{J_0(\beta\rho_o)}{J_1(\beta\rho_o)}\right)^2 - \frac{2}{\beta\rho_o}\frac{J_0(\beta\rho_o)}{J_1(\beta\rho_o)}\right)\right], \tag{4.107}$$

[3]The inclusion of G_{Gauss} adds the term $(1-\sigma)$ in the brackets, modifying the quantitative results slightly.

and the third equation is[4]

$$\frac{\epsilon^2}{2}\left[\rho_o\left(\left(\frac{K_0(\rho_o)}{K_1(\rho_o)}\right)^2-1\right)-\rho_o\sigma\beta^2\left(1+\left(\frac{J_0(\beta\rho_o)}{J_1(\beta\rho_o)}\right)^2\right)\right]=\rho_o(\sigma\beta^2+1)-\chi, \tag{4.108}$$

where we have used the first equation to greatly simplify the third. Specifying a particular dimensionless area, dimensionless line tension, and dimensionless spontaneous curvature we can use these three equations to solve for the boundary slope, Lagrange multiplier, and projected radius that minimize the free energy. Although, it is not that straightforward to find solutions; due to the oscillatory nature of J_k, there are actually multiple, discrete domain shapes that solve these equilibrium equations. Examining eqn. 4.106, we note that possible solutions of this equation, corresponding to discrete domain shapes, are separated by the discrete zeros of $J_1(\beta\rho_o)$. To a good approximation the nth zero of $J_1(\beta\rho_o)$ is given by

$$\beta\rho_o=\frac{\pi}{4}+(n-1)\pi, \tag{4.109}$$

where $n\in[1\ldots\infty]$ is an integer. With this knowledge, we can bound the values of $\beta\rho_o$ for the nth discrete domain shape to

$$\frac{\pi}{4}+(n-1)\pi<\beta\rho_o<\frac{\pi}{4}+n\pi. \tag{4.110}$$

Thus, based on the values of $\beta\rho_o$, we know which discrete shape we are solving for, that is, which n mode shape. As n increases, the bounded values of $\beta\rho_o$ push the elastic energy to ever higher levels, such that from the perspective of shapes that are accessible to thermal fluctuations, only the $n=1$ shape is accessible for all reasonable parameter values. Further, the line tensions required to buckle the domain for $n>1$ are outside the range of reasonable values. To demonstrate these concepts, Fig. 4.17 shows the numerical solutions to the equilibrium equations for $n=1$ and $n=2$. Looking at Fig. 4.17e, one can see that our dimpled solutions are within the bounds of eqn. 4.110 for $n=1$.

Having picked the regime of lowest energy dimpling, we would also like to know where in the space of dimensionless area and line tension the dimpled states lie, that is, where is the phase boundary? We will explore this question in the scenario where $\upsilon_o=0$; in the case where $\upsilon_o\neq 0$, there is no stable flat state and hence no phase boundary for the lowest energy mode.

Approaching the phase boundary from either large domain area or large line tension the boundary slope $\epsilon\to 0$ at some critical value of the membrane parameters, and hence in the above equations we can ignore terms $O(\epsilon^2)$. Not only does this simplify the equations, but precisely *at* the phase boundary, the $O(\epsilon^2)$ terms are identically zero, such that the first equation gives

$$\sigma\beta\frac{J_0(\beta\rho_o)}{J_1(\beta\rho_o)}+\frac{K_0(\rho_o)}{K_1(\rho_o)}=0, \tag{4.111}$$

[4]The inclusion of G_{Gauss} adds the term $2\frac{\sigma-1}{\rho_o}$ in the brackets, modifying the quantitative results slightly.

the second equation gives

$$\rho_o = \sqrt{\frac{\alpha}{\pi}}, \tag{4.112}$$

and the third equation gives

$$\chi = \rho_o(\sigma\beta^2 + 1). \tag{4.113}$$

The first two equations can be solved numerically to find the critical value β_c at the phase boundary as a function of α, and then the critical line tension for dimpling is $\chi_c = (\sigma\beta_c^2 + 1)\sqrt{\alpha/\pi}$. In the regime where the dimensionless domain area is small the relationship between these three equations simplifies to[5]

$$\chi_c \simeq 8\sigma\sqrt{\frac{\pi}{\alpha}}. \tag{4.114}$$

4.4.7 Scaling and the Critical Exponent

Using an approximation similar to how we derived the morphological phase boundary we can also derive the critical exponent of the dimpling transition. This exponent gives us a notion of how 'fast' a domain dimples once the transition has occurred, which is an important shape characteristic of the dimpling transition and will be crucial for understanding how domain interactions scale with domain size and size asymmetry.

It can be shown that the quantity $\beta\rho_o \simeq \beta_c\sqrt{\alpha/\pi}$ after the domain has dimpled, as demonstrated in Fig. 4.17e. This approximation allows us to write the domain area conservation as

$$\alpha \simeq \pi\rho_o^2\left(1 + \delta\frac{\epsilon^2}{2}\right), \tag{4.115}$$

where $\delta = O(1)$ is a constant determined from eqn. 4.85. Using this equation solved for ρ_o and eqn. 4.113 solved for β, we can form a complicated transcendental equation with eqn. 4.111. For small domain area, this transcendental equation can be used to write the boundary slope as

$$|\epsilon| \simeq \sqrt{\frac{2}{\delta}\left(\frac{\chi}{\chi_c} - 1\right)}, \tag{4.116}$$

or using eqn. 4.114 as

$$|\epsilon| \simeq \sqrt{\frac{1}{\delta}\left(\frac{\alpha}{\alpha_c} - 1\right)}, \tag{4.117}$$

with $\alpha_c = 64\pi(\sigma/\chi)^2$. An additional an $O(1)$, numerically-determined and multiplicative constant can be employed to make eqns. 4.116 and 4.117 even more accurate. This calculation shows that the critical exponent is equal to 1/2, whether line tension or domain area is increased, which means that the domains rise rapidly from the flat state once they have gone through the dimpling transition.

[5]The inclusion of G_{Gauss} changes this equation to $\chi_c \simeq 4(\sigma + 1)\sqrt{\pi/\alpha}$.

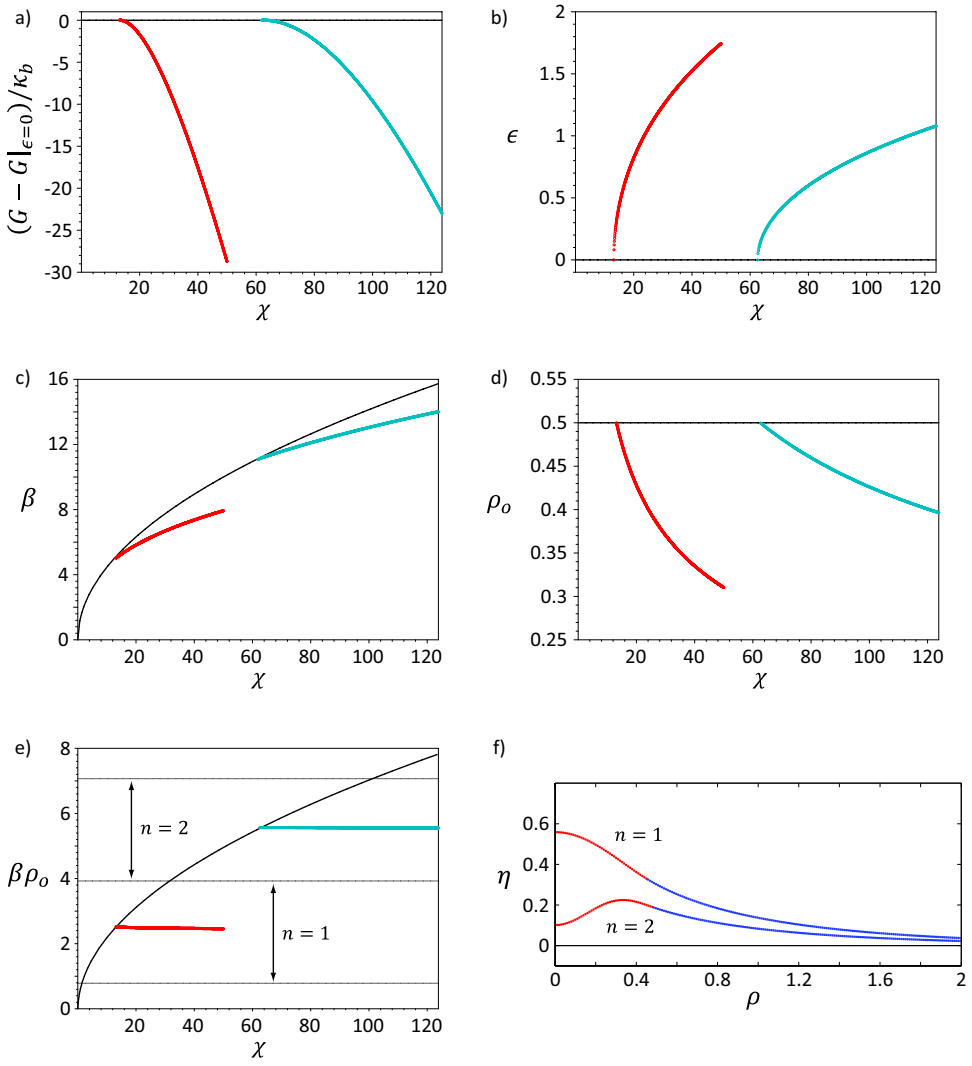

Figure 4.17: Numerical solutions for the equilibrium equations. Plots (a-d) show how morphological parameters vary as χ increases, with $\alpha = \pi/4$ and $\sigma = 1$. The red lines are for $n = 1$, while the blue lines are for $n = 2$, the black lines correspond to the flat state. e) This plot demonstrates that the values of $\beta\rho_o$ are indeed bounded by eqn. 4.110, and that the product $\beta\rho_o$ is approximately constant through the morphological transition. f) This plots shows the domain shapes for the modes ($n = 1$, $\chi \simeq 17$) and ($n = 2$, $\chi \simeq 68$).

4.4.8 Divergence Theorem Solution for the Deformation Energy

We previously made use of the dimensionless functionals

$$G_{\text{el}}^{(1)} = \frac{\kappa_b}{2}\sigma \int_{\mathcal{S}} \left(-\beta^2 (\nabla \eta_1)^2 + \left(\nabla^2 \eta_1\right)^2 \right) \mathrm{d}^2\rho \tag{4.118}$$

and

$$G_{\text{el}}^{(2)} = \frac{\kappa_b}{2} \int_{\mathcal{S}} \left((\nabla \eta_2)^2 + \left(\nabla^2 \eta_2\right)^2 \right) \mathrm{d}^2\rho, \tag{4.119}$$

which describe the contributions to the free energy from bending and membrane tension. Using the resulting Euler-Lagrange equations in the domain region

$$\nabla^2(\nabla^2 + \beta^2)\eta_1 = 0 \tag{4.120}$$

and

$$\nabla^2(\nabla^2 - 1)\eta_2 = 0 \tag{4.121}$$

in the surrounding membrane, we apply the boundary conditions $|\nabla\eta_1(0)| = |\nabla\eta_2(\infty)| = 0$ and $|\nabla\eta_1(\rho_o)| = |\nabla\eta_2(\rho_o)| = \epsilon$. From these differential equations and boundary conditions we found solutions for the membrane shape

$$\eta_1(\rho) = -\epsilon \left[\frac{1}{\beta} \frac{J_0(\beta\rho)}{J_1(\beta\rho_o)} - \frac{1}{\beta} \frac{J_0(\beta\rho_o)}{J_1(\beta\rho_o)} + \frac{K_0(\rho_o)}{K_1(\rho_o)} \right] \quad \text{and} \quad \eta_2(\rho) = -\epsilon \frac{K_0(\rho)}{K_1(\rho_o)}. \tag{4.122}$$

It might appear that the only way to solve for the energy given η_1 and η_2 is to perform a rather tedious integral, when in fact, there is a much more elegant way using the Divergence Theorem, in a way similar to previous calculations [32, 31].

We will perform a series of partial integrations in rapid succession, by rewriting the derivatives in the energy functional. We start by noticing

$$(\nabla\eta)^2 = \nabla \cdot (\eta \nabla \eta) - \eta \nabla^2 \eta. \tag{4.123}$$

The second derivative term is a bit more challenging, we notice that

$$\nabla \cdot (\nabla^2 \eta \nabla \eta) = \nabla^3 \eta \cdot \nabla \eta + (\nabla^2 \eta)^2 \tag{4.124}$$

and

$$\nabla \cdot (\eta \nabla^3 \eta) = \nabla^3 \eta \cdot \nabla \eta + \eta \nabla^4 \eta. \tag{4.125}$$

Subtracting these two equations yields

$$(\nabla^2 \eta)^2 = \eta \nabla^4 \eta + \nabla \cdot (\nabla^2 \eta \nabla \eta - \eta \nabla^3 \eta). \tag{4.126}$$

Let us tackle the functionals for the two regions separately; in region 1

$$-\beta^2(\nabla\eta_1)^2 + (\nabla^2\eta_1)^2 = \nabla\cdot(\nabla^2\eta_1\nabla\eta_1 - \eta_1\nabla^3\eta_1 - \beta^2\eta_1\nabla\eta_1) + \beta^2\eta_1\nabla^2\eta_1 + \eta_1\nabla^4\eta_1, \tag{4.127}$$

which can be rearranged to

$$-\beta^2(\nabla\eta_1)^2 + (\nabla^2\eta_1)^2 = \nabla\cdot(\nabla^2\eta_1\nabla\eta_1 - \eta_1\nabla(\nabla^2+\beta^2)\eta_1) + \eta_1\nabla^2(\nabla^2+\beta^2)\eta_1. \tag{4.128}$$

Then recall that the Euler-Lagrange equations demand $\nabla^2(\nabla^2+\beta^2)\eta_1 = 0$, and further, our condition that the change in area upon dimpling be finite gives $(\nabla^2+\beta^2)\eta_1 = const$, hence this can be simplified to

$$-\beta^2(\nabla\eta_1)^2 + (\nabla^2\eta_1)^2 = \nabla\cdot(\nabla^2\eta_1\nabla\eta_1). \tag{4.129}$$

Upon substitution into the energy functional for region 1 we find

$$G_{\mathrm{el}}^{(1)} = \frac{\kappa_b}{2}\sigma\int_{\mathcal{S}}\left(-\beta^2(\nabla\eta_1)^2 + \left(\nabla^2\eta_1\right)^2\right)\mathrm{d}^2\rho = \frac{\kappa_b}{2}\sigma\int_{\mathcal{S}}\nabla\cdot(\nabla^2\eta_1\nabla\eta_1)\mathrm{d}^2\rho, \tag{4.130}$$

and then using the divergence theorem

$$G_{\mathrm{el}}^{(1)} = \frac{\kappa_b}{2}\sigma\int_{\mathcal{S}}\nabla\cdot(\nabla^2\eta_1\nabla\eta_1)\mathrm{d}^2\rho = \frac{\kappa_b}{2}\sigma\oint_{\partial\mathcal{S}}(\nabla^2\eta_1\nabla\eta_1)\cdot\mathrm{d}\hat{\mathbf{n}}. \tag{4.131}$$

This last expression can be fully evaluated without a particular functional form of η_1, simply by applying azimuthal symmetry and knowing the boundary conditions, namely $\nabla\eta_1(0) = 0\hat{\rho}$ and $\nabla\eta_1(\rho_o) = \epsilon\hat{\rho}$, resulting in

$$G_{\mathrm{el}}^{(1)} = \pi\sigma\kappa_b\rho_o\epsilon(\nabla^2\eta_1)|_{\rho=\rho_o}. \tag{4.132}$$

The second region surrounding the domain is handled in a similar fashion. We write the integrand of the functional as

$$(\nabla\eta_2)^2 + (\nabla^2\eta_2)^2 = \nabla\cdot(\nabla^2\eta_2\nabla\eta_2 - \eta_2\nabla^3\eta_2 + \eta_2\nabla\eta_2) - \eta_2\nabla^2\eta_2 + \eta_2\nabla^4\eta_2, \tag{4.133}$$

which can be reorganized to

$$(\nabla\eta_2)^2 + (\nabla^2\eta_2)^2 = \nabla\cdot(\nabla^2\eta_2\nabla\eta_2 - \eta_2\nabla(\nabla^2-1)\eta_2) + \eta_2\nabla^2(\nabla^2-1)\eta_2. \tag{4.134}$$

In a similar fashion, application of the Euler-Lagrange equation, $\nabla^2(\nabla^2-1)\eta_2 = 0$, and the finite area change condition, $(\nabla^2-1)\eta_2 = const$, yield

$$(\nabla\eta_2)^2 + (\nabla^2\eta_2)^2 = \nabla\cdot(\nabla^2\eta_2\nabla\eta_2). \tag{4.135}$$

With subsequent application of the Divergence Theorem we get a relation similar to region 1,

namely

$$G_{\text{el}}^{(2)} = \frac{\kappa_b}{2}\int_{\mathcal{S}} \nabla\cdot(\nabla^2\eta_2\nabla\eta_2)\mathrm{d}^2\rho = \frac{\kappa_b}{2}\oint_{\partial\mathcal{S}}(\nabla^2\eta_2\nabla\eta_2)\cdot\mathrm{d}\hat{\mathbf{n}}, \tag{4.136}$$

where application of the symmetry and boundary conditions, specifically $\lim_{\rho\to\infty}\rho|\nabla\eta_2| = 0$ and $\nabla\eta_2(\rho_o) = \epsilon\hat{\rho}$, yields

$$G_{\text{el}}^{(2)} = -\pi\kappa_b\rho_o\epsilon(\nabla^2\eta_2)|_{\rho=\rho_o}. \tag{4.137}$$

Now we see that the total elastic free energy is a measure of the curvature change at the boundary between the two regions

$$G_{\text{el}} = \pi\kappa_b\rho_o\epsilon\left[\sigma\left(\nabla^2\eta_1\right) - \left(\nabla^2\eta_2\right)\right]_{\rho=\rho_o}. \tag{4.138}$$

Using the solutions from the Euler-Lagrange equation, we recover the previously stated energy

$$G_{\text{el}} = \pi\kappa_b\rho_o\epsilon^2\left(\sigma\beta\frac{J_0(\beta\rho_o)}{J_1(\beta\rho_o)} + \frac{K_0(\rho_o)}{K_1(\rho_o)}\right). \tag{4.139}$$

4.4.9 Spherical Domain Budding

While the Monge representation of the membrane and domain is useful for understanding certain kinds of domain morphology, it is a model incapable of representing the budded morphology, due to the Monge restriction that the membrane cannot fold over itself. In this section we employ a basis-shape model, where all available domain morphologies are sections of a sphere, while the surrounding membrane is flat, to show that there is a first-order budding transition. Here we will work through the zero spontaneous curvature spherical model.

We characterize the bud by a radius R and wrapping angle θ as shown in Fig. 4.10. A simple geometrical derivation shows that the area of such a domain is

$$\mathcal{A} = 2\pi R^2(1-\cos\theta) \tag{4.140}$$

where $\mathcal{A}$ is the domain area (for consistency, we will use α as the dimensionless area). The energy from line tension is

$$G_{\text{line}} = 2\pi r_o\gamma = 2\pi R\gamma\sin\theta \tag{4.141}$$

where $r_o = R\sin\theta$ is the projected domain boundary. As r_o changes, so does the areal footprint of the domain, and hence work is done against any applied membrane tension, given by

$$G_{\text{tens}} = -\pi\tau r_o^2 = -\pi\tau R^2\sin^2\theta = -\pi\tau R^2(1-\cos\theta)(1+\cos\theta) \tag{4.142}$$

Finally, the mean curvature bending energy is written as a fraction of the bending energy of a sphere

$$G_{\text{bend}} = 8\pi\kappa_b\cdot\frac{\mathcal{A}}{4\pi R^2}(1-2c_oR), \tag{4.143}$$

where c_o is the spontaneous curvature of the domain. All together, this gives the free energy of a

spherical domain

$$G = G_{\text{line}} + G_{\text{tens}} + G_{\text{bend}}. \tag{4.144}$$

We can now use the expression for the area, $\mathcal{A}$, to eliminate R from the free energy. This leaves θ as the only free variable, and shows that this variable characterizes budding; $\theta = 0$ is a flat domain and $\theta = \pi$ is a fully budded domain. Using the relationship between domain area and R we can simplify the mechanical free energy to

$$G = 2\pi R\gamma \sin\theta - \pi\tau R^2 \sin^2\theta + 8\pi\kappa_b \frac{\mathcal{A}}{4\pi R^2}(1 - 2c_o R), \tag{4.145}$$

and further to

$$G = 4\pi\kappa_b \left[\frac{\gamma\sqrt{\mathcal{A}}}{\kappa_b}\sqrt{\frac{1+\cos\theta}{8\pi}} - \frac{\tau\mathcal{A}}{\kappa_b}\frac{1+\cos\theta}{8\pi} + (1-\cos\theta) - c_o\sqrt{\mathcal{A}}\sqrt{\frac{2(1-\cos\theta)}{\pi}} \right]. \tag{4.146}$$

Upon substitution of our previously defined elastic decay length, $\lambda_2 = \sqrt{\kappa_b/\tau}$, we retrieve the familiar dimensionless parameters α and χ as regulators of domain budding, where the mechanical free energy is written as

$$G = 4\pi\kappa_b \left[\chi\sqrt{\alpha}\sqrt{\frac{1+\cos\theta}{8\pi}} - \alpha\frac{1+\cos\theta}{8\pi} + (1-\cos\theta) - \upsilon_o\sqrt{\alpha}\sqrt{\frac{2(1-\cos\theta)}{\pi}} \right]. \tag{4.147}$$

This equation has stable points as defined by the set of equations $\partial G/\partial\theta = 0$ and $\partial^2 G/\partial\theta^2 \geq 0$.

In the symmetric situation where $\upsilon_o = 0$, there are two points (or more accurately, lines) of interest in the phase diagram of domain budding. The most interesting is the transition from a flat-bud coexistence regime with an energy barrier between those states, to a bud-only regime, defined by

$$\left.\frac{\partial^2 G}{\partial\theta^2}\right|_{\theta=0} = 0, \tag{4.148}$$

which yields the relationship

$$\chi_{\text{bud}} = 8\sqrt{\frac{\pi}{\alpha}}\left(1 + \frac{\alpha}{8\pi}\right), \tag{4.149}$$

as shown in Fig. 4.11. Comparing this equation to eqn. 4.114 (with $\sigma = 1$), indicates that the cross-over between dimpling and budding morphologies occurs when $\alpha/8\pi \ll 1$.

The second interesting line in the phase diagram is when it becomes equally favorable to be in either the flat or budded state defined by $G|_{\theta=\pi} = G|_{\theta=0} = 0$, which yields simply $\chi_{\text{bud}}/2$. Figure 4.18 shows the bifurcation diagrams resulting from various scenarios of $\partial G/\partial\theta = 0$ in the spherical budding model, including cases with spontaneous curvature. Note that in the absence of spontaneous curvature only the flat and fully budded states are available, while adding domain spontaneous curvature allows for equilibrium values of θ between flat and fully budded.

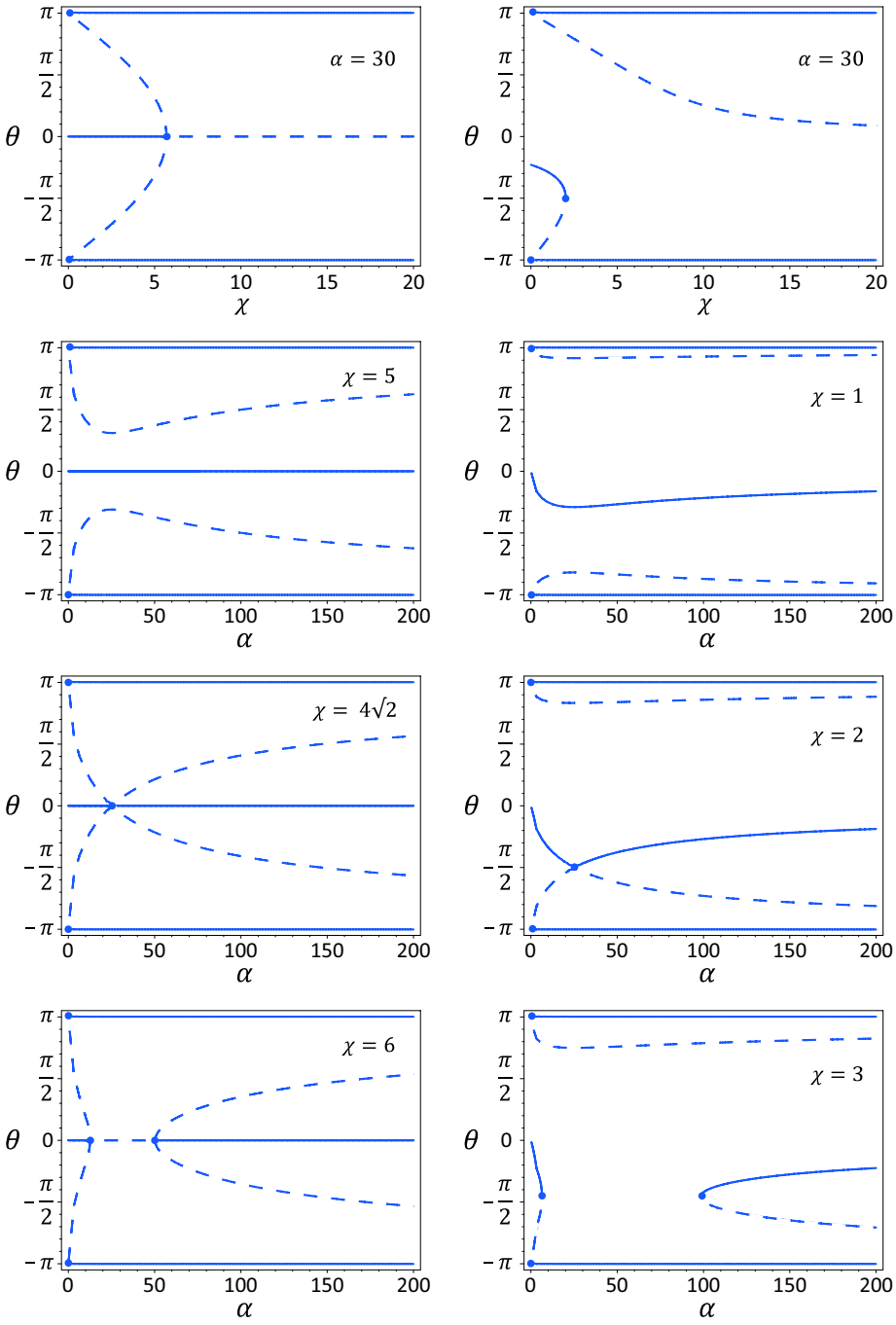

Figure 4.18: Bifurcation diagrams of the spherical budding model. All plots show solutions to $\partial G/\partial\theta = 0$, where θ is the domain wrapping angle, χ is the dimensionless line tension, α is the dimensionless area, and the energy scale is set by $4\pi\kappa_b$. The first column shows diagrams with zero spontaneous curvature ($v_o = 0$), and the second column shows diagrams with a spontaneous curvature of $v_o = 0.5$; all other parameters are noted on the graph. Solid lines indicate stable values, dashed lines indicate unstable values, and dots indicate transitions between stable and unstable solutions.

4.5 Vesicle Tension and Entropy

To keep our mechanical model of membrane morphology tractable and intuitive, certain assumptions were made about the physical state of the membrane. One of our assumptions was that the addition of membrane area due to domain deformation came at a constant cost per unit area, thus setting up a constant tension ensemble. In this section we will examine this assumption in detail, and show that while useful, the constant tension ensemble cannot be blindly employed in all situations. In particular, if the area change connected to a morphological transition (or set of transitions) is too large compared to a reference area, we must consider the membrane tension as a variable, thermally-dependent mechanical attribute of the membrane.

The choice of tension ensemble affects the equilibrium stability of domain morphologies. Our formulation of the equations of mechanical equilibrium shows that the dimpled domain morphology is at an energy extremum, however the use of a Lagrange multiplier turns that extremum into a saddle-point, hence obscuring the exact nature of the shape stability. Some of our preliminary work, using fully non-linear finite element methods, suggests that the dimpled morphology might only be a stable shape if the tension is a monotonically increasing function of the additional area required to deform the membrane. Fortunately, that is precisely the behavior described by a thermally active membrane - a regime of constant tension if domain deformations are small, and a monotonically increasing tension regime if the deformations are large.

For a vesicle with conserved volume and surface area, lateral tension may arise from one of two general sources. At higher tensions, the intrinsic area per lipid increases, corresponding to an areal strain (ϕ) and tension (τ) on the vesicle surface given by $\tau \simeq K_{\mathcal{A}}\phi$, essentially the bilayer equivalent of Hooke's Law. At much lower tensions, this Hookean linear response is not valid; thermal fluctuations of the membrane absorb free area, generating a small, non-linear entropic tension. Our goal in this section is to use a common Fourier space technique to construct a model of this entropic tension [57, 266], namely the equation of state, and determine its implications for the constancy (or lack thereof) of tension on the surface of GUVs with lipid domains that change morphology. This analysis informs the generic mechanical model of the limits of the approximation of the constant tension ensemble. The result of this calculation will also help us form a more accurate model of membrane elasticity and deformation at finite temperature.

To these ends, the following subsections derive the equation of state in rigorous detail, and build intuition for how bending and tension regulate the thermal fluctuations of the membrane. An expression for the contribution to the free energy from a thermally active membrane is derived and a connection is made between the free energy in this thermal ensemble with the zero temperature, constant tension ensemble. Lastly, we try to estimate how changes in domain morphology couple to the thermal fluctuations on a conserved volume and surface area vesicle.

4.5.1 Constructing a Thermal Ensemble

Arguably, one of the most important concepts to discuss when constructing a mechanical model of a membrane is the ensemble in use, which can be loosely defined as the physical or thermodynamic relationship between the patch of membrane of interest and the external physical world. Looking back at eqn. 4.52, we see that the tension, τ, is a material constant, independent of the shape of the membrane itself. This description is a constant tension ensemble, where changes in morphology add area at infinity, by pulling membrane from an external membrane reservoir at a fixed energy cost per unit area. This problem statement is strictly a mechanical model, free from the effects of temperature, or more precisely, it is a statistical mechanical model at $T = 0$. A real membrane at finite temperature is bombarded by various small molecules, (*e.g.* water, ions, and proteins) such that it is never in a flat state. Instead, the membrane undulates in time, with height fluctuations having a specific frequency spectrum that will be derived in this section. These undulations store area that can be surrendered upon application of tension, however the energetic cost of this change in projected unit area is not constant. This constitutes a new kind of tension ensemble, that links the tension in the mechanically deformed membrane region to the variable tension in a thermal membrane reservoir using an equation of state.

The physical reality is that changes in domain morphology (or any change in membrane morphology) and finite temperature bilayer undulations are happening simultaneously on the same patch of membrane, and are energetically coupled together. This coupling combined with only a statistical notion of the fluctuations makes this a difficult scenario to model. One avenue of approach is to construct an entropic tension ensemble as follows. The domain and its attendant mechanical morphologies exist on an infinite patch of membrane at zero temperature, and hence we can model domain morphologies within the framework of standard continuum mechanics. We then construct a thermally active membrane reservoir, with projected area $\mathcal{A}$ and total area $\mathcal{A}_o$, that is able to exchange area with the zero temperature membrane patch, such that the total membrane area in the system is conserved, as shown in Fig. 4.19. By fixing the total area in the system and setting $\mathcal{A}$ and $\mathcal{A}_o$, the equation of state of the reservoir defines the tension in *both* membrane regions. As the zero temperature membrane patch deforms, it pulls area from the thermal membrane reservoir, increasing the tension in both regions according to the non-linear equation of state. This effectively allows us to calculate membrane shapes with a strictly mechanical model, as we have done previously, but couples the continuum mechanics to an accurate representation of a bilayer of finite extent at finite temperature. Additionally, we will show that this analysis clarifies the relevance of the constant tension ensemble. For a system with a large enough thermal reservoir, the ratio $\Delta\mathcal{A}/\mathcal{A}_o \ll 1$, and hence the initial state of tension remains essentially unchanged when the zero temperature membrane changes morphology. If this condition is not met, we must consider the non-linear behavior of the equation of state, and its corresponding effects on the stability of dimpled and budded domain morphologies. The general result is that the non-linear equation of state yields a variable tension that tends to stabilize the dimpled state if enough excess area is

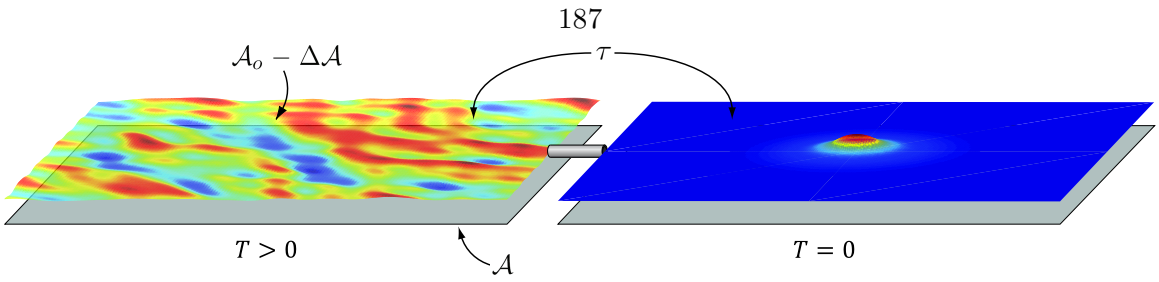

Figure 4.19: Schematic of an ensemble that couples the lateral tension of a zero temperature deformation field to a finite temperature membrane reservoir. The reservoir (left) has a total area $\mathcal{A}_o - \Delta\mathcal{A}$ and a projected area $\mathcal{A}$, where $\Delta\mathcal{A} \in [0 \ldots (\mathcal{A}_o - \mathcal{A})]$. The mechanically deformed region (right - with dimpled domain) has an infinite projected area and an actual area $\Delta\mathcal{A}$ above the projected area, where $\Delta\mathcal{A}$ is the area required to deform the zero temperature membrane from a flat state. The small pipe represents a perfect thermal insulator that permits the flow of lipid from one region to the other, where the total amount of lipid in the ensemble is conserved, resulting in equal tension in both regions. When the zero temperature membrane is flat, the thermal reservoir has a projected area $\mathcal{A}$ and actual area $\mathcal{A}_o$, which, through the equation of state, defines an initial resting tension in both regions.

available.

4.5.2 The Equation of State

We calculate the linearized equation of state in this low tension regime by splitting the reservoir's deformation profile, denoted here as simply h, into planar Fourier modes and using equipartition to calculate the amplitude of each mode. To derive the equation of state, we follow the standard treatment given in [57, 266] with all details shown here for completeness. Recall that the linearized deformation energy is given by

$$G_{\text{el}} = \frac{1}{2}\int_{\mathcal{S}} \left(\tau(\nabla h)^2 + \kappa_b \left(\nabla^2 h\right)^2\right) \mathrm{d}^2\mathbf{r}, \tag{4.150}$$

where $\mathcal{S}$ is the planar projected surface. The projected surface area is $\mathcal{A}$, and we assume for now that we are operating in the entropic tension regime where the area per lipid is conserved. While a two dimensional path integral formulation,

$$Z = \int \mathcal{D}\left[h\right] e^{-\frac{G_{\text{el}}[h]}{k_B T}}, \tag{4.151}$$

which constructs the partition function Z by summing the Boltzmann factors over all possible membrane configurations, is conceptually most straightforward, we will employ a Fourier space approach to calculate the equation of state. For any *Monge* representation of the surface, we can

write the membrane deformation as the Fourier transform

$$h(\mathbf{r}) = \frac{\mathcal{A}}{(2\pi)^2} \int h(\mathbf{q}) e^{-i\mathbf{q}\cdot\mathbf{r}} \, \mathrm{d}^2\mathbf{q}, \tag{4.152}$$

with

$$\mathbf{q} = \frac{2\pi}{\sqrt{\mathcal{A}}} \mathbf{k}, \tag{4.153}$$

where $\mathbf{k} = (n_1, n_2)$ with n_1 and n_2 as integer wave numbers. For a sufficiently large membrane, we are well-justified in using the continuous Fourier Transform, though this approximation breaks down for patches of membrane with area near the area of a single lipid. Then the vector derivatives from the energy functional are

$$\nabla h = \frac{\mathcal{A}}{(2\pi)^2} \int (-i\mathbf{q}) h(\mathbf{q}) e^{-i\mathbf{q}\cdot\mathbf{r}} \, \mathrm{d}^2\mathbf{q}, \tag{4.154}$$

and

$$\nabla^2 h = -\frac{\mathcal{A}}{(2\pi)^2} \int |\mathbf{q}|^2 h(\mathbf{q}) e^{-i\mathbf{q}\cdot\mathbf{r}} \, \mathrm{d}^2\mathbf{q}, \tag{4.155}$$

such that the terms of the deformation functional become

$$(\nabla h)^2 = \frac{\mathcal{A}^2}{(2\pi)^4} \int \int (\mathbf{q}\cdot\mathbf{q}') h(\mathbf{q}) \overline{h(\mathbf{q}')} e^{-i(\mathbf{q}-\mathbf{q}')\cdot\mathbf{r}} \, \mathrm{d}^2\mathbf{q} \mathrm{d}^2\mathbf{q}', \tag{4.156}$$

and

$$(\nabla^2 h)^2 = \frac{\mathcal{A}^2}{(2\pi)^4} \int \int (\mathbf{q}\cdot\mathbf{q}')^2 h(\mathbf{q}) \overline{h(\mathbf{q}')} e^{-i(\mathbf{q}-\mathbf{q}')\cdot\mathbf{r}} \, \mathrm{d}^2\mathbf{q} \mathrm{d}^2\mathbf{q}'. \tag{4.157}$$

Explicitly performing the spatial integrals gives

$$\int (\nabla h)^2 \, \mathrm{d}^2\mathbf{r} = \frac{\mathcal{A}^2}{(2\pi)^4} \int \int \int (\mathbf{q}\cdot\mathbf{q}') h(\mathbf{q}) \overline{h(\mathbf{q}')} e^{-i(\mathbf{q}-\mathbf{q}')\cdot\mathbf{r}} \, \mathrm{d}^2\mathbf{q} \mathrm{d}^2\mathbf{q}' \mathrm{d}^2\mathbf{r}, \tag{4.158}$$

and

$$\int (\nabla^2 h)^2 \, \mathrm{d}^2\mathbf{r} = \frac{\mathcal{A}^2}{(2\pi)^4} \int \int \int (\mathbf{q}\cdot\mathbf{q}')^2 h(\mathbf{q}) \overline{h(\mathbf{q}')} e^{-i(\mathbf{q}-\mathbf{q}')\cdot\mathbf{r}} \, \mathrm{d}^2\mathbf{q} \mathrm{d}^2\mathbf{q}' \mathrm{d}^2\mathbf{r}. \tag{4.159}$$

We recognize that

$$\int e^{-i(\mathbf{q}-\mathbf{q}')\cdot\mathbf{r}} \, \mathrm{d}^2\mathbf{r} = (2\pi)^2 \delta(\mathbf{q}-\mathbf{q}'), \tag{4.160}$$

such that these integrals simplify to

$$\int (\nabla h)^2 \, \mathrm{d}^2\mathbf{r} = \left(\frac{\mathcal{A}}{2\pi}\right)^2 \int |\mathbf{q}|^2 |h(\mathbf{q})|^2 \, \mathrm{d}^2\mathbf{q} \tag{4.161}$$

and

$$\int (\nabla^2 h)^2 \, \mathrm{d}^2\mathbf{r} = \left(\frac{\mathcal{A}}{2\pi}\right)^2 \int |\mathbf{q}|^4 |h(\mathbf{q})|^2 \, \mathrm{d}^2\mathbf{q}. \tag{4.162}$$

The deformation energy can now be written as a sum of independent Fourier modes

$$G_{\text{el}} = \frac{1}{2}\left(\frac{\mathcal{A}}{2\pi}\right)^2 \int_{\frac{\pi}{\sqrt{\mathcal{A}}}}^{\frac{\pi}{\sqrt{a_o}}} |h(\mathbf{q})|^2 \left(\tau|\mathbf{q}|^2 + \kappa_b|\mathbf{q}|^4\right) \, \mathrm{d}^2\mathbf{q}, \tag{4.163}$$

where we integrate from the smallest q vector magnitude, corresponding to the size of the entire projected membrane $\pi/\sqrt{\mathcal{A}}$, to the highest q vector magnitude, corresponding to the lipid intermolecular spacing $\pi/\sqrt{a_o}$, where a_o is the area per lipid.

This free energy can now be used in the canonical partition function to calculate various properties of interest on a fluctuating membrane at equilibrium. The amplitudes of each mode, $|h(\mathbf{q})|$, are degrees of freedom over which we can sum the partition function, however, since they are independent quadratic degrees of freedom, we know that each mode absorbs energy $k_BT/2$ from the thermal reservoir, such that

$$\frac{k_BT}{2} = \left\langle |h(\mathbf{q})|^2 \right\rangle \frac{\mathcal{A}}{2}\left(\tau|\mathbf{q}|^2 + \kappa_b|\mathbf{q}|^4\right), \tag{4.164}$$

and from the definition of the Fourier transform in eqn. 4.152, a factor of $\mathcal{A}/(2\pi)^2$ remains with the integral, and this can be rearranged to

$$\left\langle |h(\mathbf{q})|^2 \right\rangle = \frac{k_BT}{\mathcal{A}\left(\tau|\mathbf{q}|^2 + \kappa_b|\mathbf{q}|^4\right)}. \tag{4.165}$$

Using our previously defined elastic decay length, $\lambda = \sqrt{\kappa_b/\tau}$, this can be recast in a form with fewer effective parameters,

$$\left\langle |h(\mathbf{q})|^2 \right\rangle = \lambda^2 \frac{k_BT}{\tau\mathcal{A}} \frac{1}{\left(\lambda|\mathbf{q}|\right)^2 + \left(\lambda|\mathbf{q}|\right)^4}, \tag{4.166}$$

useful for making scaling arguments. To get a feel for the magnitudes of these fluctuations, we can plug in the minimum and maximum wave vectors to find the maximum and minimum, respectively, root-mean-square height deviations, and find

$$\left[\sqrt{\left\langle |h(\mathbf{q})|^2 \right\rangle}\right]_{|\mathbf{q}|_{\max}} \simeq \frac{a_o}{\pi^2}\left(\frac{k_BT}{\mathcal{A}\kappa_b}\right)^{1/2} \sim 10^{-7}\,\text{nm} \tag{4.167}$$

and

$$\left[\sqrt{\left\langle |h(\mathbf{q})|^2 \right\rangle}\right]_{|\mathbf{q}|_{\min}} \simeq \left[\frac{k_BT}{\pi^2\tau}\left(1 + \frac{(\pi\lambda)^2}{\mathcal{A}}\right)^{-1}\right]^{1/2} \sim 100\,\text{nm}, \tag{4.168}$$

on a vesicle with a 20 μm diameter and resting tension of $10^{-5}\,k_BT/\text{nm}^2$. Thus we see that on small length scales, the membrane is locally very flat. To get an idea of the membrane height gradient over different wavelengths, which helps validate the use of a Monge gauge, we can multiply these

height deviations by their corresponding wave vector magnitude to find

$$|\nabla h|_{\min} \simeq \left[|\mathbf{q}|\sqrt{\langle|h(\mathbf{q})|^2\rangle}\right]_{|\mathbf{q}|_{\max}} \simeq \left(\frac{a_o k_B T}{\pi^2 \mathcal{A}\kappa_b}\right)^{1/2} \sim 10^{-6} \tag{4.169}$$

and

$$|\nabla h|_{\max} \simeq \left[|\mathbf{q}|\sqrt{\langle|h(\mathbf{q})|^2\rangle}\right]_{|\mathbf{q}|_{\min}} \simeq \left[\frac{k_B T}{\tau\mathcal{A}}\left(1+\frac{(\pi\lambda)^2}{\mathcal{A}}\right)^{-1}\right]^{1/2} \sim 0.01. \tag{4.170}$$

These estimates give us two important pieces of information. The estimate of the root-mean-square height fluctuation tells us that in the 'real' physical scenario, on the length scales of domain morphology the thermal fluctuations will be statistically smaller than the height deformations caused by domain morphology. The second estimate shows that the small gradient approximation employed through this section is valid for studying membrane fluctuations.

To better understand the nature of the thermal fluctuations, specifically to build intuition for how the fluctuation modes are regulated, we examine two naturally-arising regimes in more detail. For small $\lambda|\mathbf{q}|$, the quadratic term dominates the denominator to give a log-log power law of the form

$$\ln\left[\left\langle|h(\mathbf{q})|^2\right\rangle \frac{\tau\mathcal{A}}{\lambda^2 k_B T}\right] = -2\ln\left[\lambda|\mathbf{q}|\right], \tag{4.171}$$

while for large $\lambda|\mathbf{q}|$, the quartic term dominates and to give a log-log power law of the form

$$\ln\left[\left\langle|h(\mathbf{q})|^2\right\rangle \frac{\tau\mathcal{A}}{\lambda^2 k_B T}\right] = -4\ln\left[\lambda|\mathbf{q}|\right]. \tag{4.172}$$

Where these two power laws cross is the 'corner' frequency, $\lambda|\mathbf{q}|_c = 1$, as shown in Fig. 4.20a. Frequencies below the corner frequency, having a much higher amplitude, absorb the vast majority of the free area, and hence are almost exclusively regulated by tension. On the other hand, frequencies above the corner frequency correspond to a high degree of curvature but do not absorb significant area, and hence are almost exclusively regulated by bending stiffness.

Moving towards the equation of state of the reservoir, as we have shown in previous sections, the difference between projected and actual area can be written as an integral, and can now also be represented in Fourier-space as

$$\mathcal{A}_o - \mathcal{A} = \frac{1}{2}\int (\nabla h)^2 \,\mathrm{d}^2\mathbf{r} = \frac{1}{2}\left(\frac{\mathcal{A}}{2\pi}\right)^2 \int \left\langle|h(\mathbf{q})|^2\right\rangle |\mathbf{q}|^2 \,\mathrm{d}^2\mathbf{q}, \tag{4.173}$$

where upon replacing the formula for the mean mode variances we find

$$\mathcal{A}_o - \mathcal{A} = \frac{k_B T}{4\pi\kappa_b}\frac{\mathcal{A}}{2\pi}\int \frac{1}{\frac{\tau}{\kappa_b}+|\mathbf{q}|^2}\,\mathrm{d}^2\mathbf{q}. \tag{4.174}$$

By choosing polar coordinates on an isotropic membrane, $\mathrm{d}^2\mathbf{q} = 2\pi q \mathrm{d}q$, this can be written as

$$\frac{\mathcal{A}_o - \mathcal{A}}{\mathcal{A}} = \frac{k_B T}{4\pi\kappa_b} \int_{\frac{\pi}{\sqrt{\mathcal{A}}}}^{\frac{\pi}{\sqrt{a_o}}} \frac{q}{\frac{\tau}{\kappa_b} + q^2} \, \mathrm{d}q. \tag{4.175}$$

The single greatest contribution to the integrand comes from modes at the corner frequency. The result of this integral is the entropic equation of state [266]

$$\frac{\mathcal{A}_o - \mathcal{A}}{\mathcal{A}} = \frac{k_B T}{8\pi\kappa_b} \ln\left[\frac{1 + \frac{\pi^2}{a_o}\frac{\kappa_b}{\tau}}{1 + \frac{\pi^2}{\mathcal{A}}\frac{\kappa_b}{\tau}}\right]. \tag{4.176}$$

This equation of state is the mathematical relationship that, for a given bending modulus, relates a given total membrane area and tension to the observed projected area, or alternately stated, it relates the total membrane area and given projected area to the magnitude of tension on the membrane. This equation of state is the key to deriving the energetic contribution to membrane deformation free energy from the thermal reservoir. Additionally, it is straight forward to include membrane stretch because it corresponds to the relatively simple transformation $\mathcal{A}_o \to \mathcal{A}_o(1 + \tau/K_A)$, such that the equation of state becomes

$$\frac{\mathcal{A}_o}{\mathcal{A}}\left(1 + \frac{\tau}{K_A}\right) - 1 = \frac{k_B T}{8\pi\kappa_b} \ln\left[\frac{1 + \frac{\pi^2}{a_o}\frac{\kappa_b}{\tau}}{1 + \frac{\pi^2}{\mathcal{A}}\frac{\kappa_b}{\tau}}\right], \tag{4.177}$$

and now $\mathcal{A}_o$ is interpreted as the full, zero tension area of the bilayer.

From eqn. 4.176, notice that if $\tau \to \infty$ or $T \to 0$, the right-hand side goes to zero and $\mathcal{A} = \mathcal{A}_o$, confirming that $\mathcal{A}_o$ is the actual area of the membrane, or in other words, the number of lipids multiplied by the equilibrium area per lipid, and implies $\mathcal{A} < \mathcal{A}_o$. Examining the right-hand side of this equation, two reference tensions emerge, between which nearly all tensions of interest lie. From the denominator, the lower bound reference tension is set by $\pi^2\kappa_b/\mathcal{A}_o \sim 10^{-7}\, k_B T/\mathrm{nm}^2 \ll \tau$ for any sufficiently large piece of membrane (*e.g.* vesicle with radius $10\,\mu$m or more). Likewise, from the numerator, the upper bound reference tension is $\pi^2\kappa_b/a_o \sim 400\, k_B T/\mathrm{nm}^2 \gg \tau$ considering that a nominal membrane will rupture at tensions above $\sim 5\, k_B T/\mathrm{nm}^2$. Thus within that range the equation of state can be written as

$$\frac{\mathcal{A}_o - \mathcal{A}}{\mathcal{A}} \simeq \frac{k_B T}{8\pi\kappa_b} \ln\left[\frac{\pi^2\kappa_b}{a_o\tau}\right]. \tag{4.178}$$

This also shows that for sufficiently large patches of membrane, the lower bound wave vector plays almost no role in the equation of state. Likewise, the equation of state is only logarithmically sensitive to any errors in choice of the maximum wave vector. Together, these facts give us confidence that the equation of state is rather robust, and does not depend on the fine details of lipid structure, nor large-scale membrane conformations. Looking back at eqn. 4.176, as tension decreases towards zero, the projected area shrinks to a state where the bending rigidity stabilizes the membrane un-

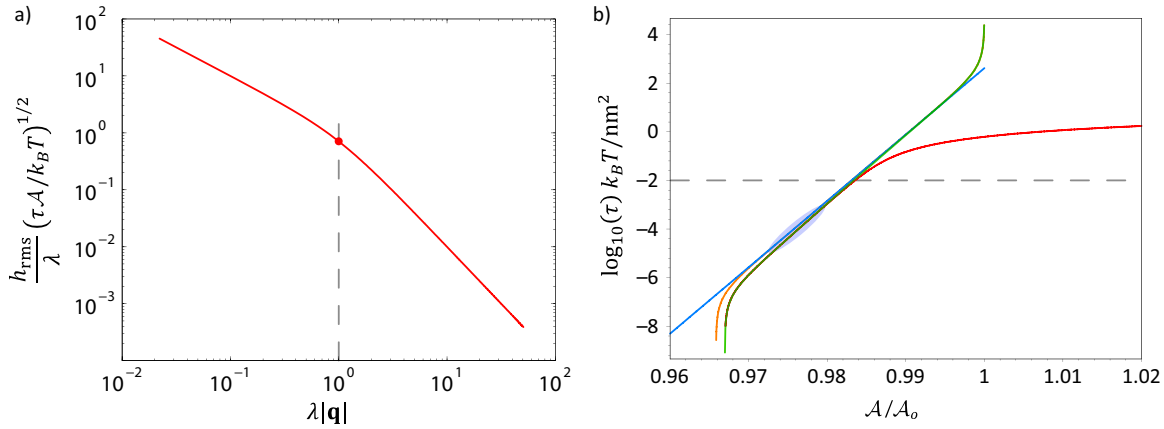

Figure 4.20: Regimes of Entropic Tension. a) Log-log plot of the fluctuation RMS height as a function of the dimensionless wave vector magnitude. The relatively high RMS height of frequencies below the corner frequency is regulated by tension, while the very low RMS height of frequencies greater than the corner frequency is regulated by bending. The circle indicates the corner frequency at which fluctuations switch from being tension regulated to bending regulated. b) Plots of the entropic tension as a function of frame area relative to total, zero tension bilayer area. The green line is the exact formula from eqn. 4.181, while the orange and blue lines are the approximations of eqn. 4.183. The red line is the full entropic and elastic equation of state from eqn. 4.177. The grey ellipse shows the approximate regime of entropic tension in which our experiments reside, known from measurements of the elastic decay length λ. The dashed line shows the tension above which one must account for changes in a_o due to stretch. For all plots the bending modulus is $\kappa_b = 25\,k_BT$, the lipid size is $a_o = 0.6\,\mathrm{nm}^2$, the stretch modulus is $K_\mathcal{A} = 60\,k_BT/\mathrm{nm}^2$, and the nominal vesicle size is $\mathcal{A}_o = 4\pi(10000\,\mathrm{nm})^2$.

dulations. In the limit of zero membrane tension, the difference between the actual and projected areas increases to a degree defined by

$$\left.\frac{\mathcal{A}_o - \mathcal{A}}{\mathcal{A}}\right|_{\tau=0} = \frac{k_B T}{8\pi\kappa_b} \ln\left[\frac{\mathcal{A}}{a_o}\right]. \tag{4.179}$$

The solution to this transcendental equation for $\mathcal{A}$ is the minimum projected area of the membrane, $\mathcal{A}_{\min}$, where with reasonable values for the bending modulus and area per lipid, it is straightforward to show that the maximum entropic areal strain is bounded by

$$0 < \left.\frac{\mathcal{A}_o - \mathcal{A}}{\mathcal{A}}\right|_{\tau=0} \leq 0.05, \tag{4.180}$$

for all reasonable membrane sizes, implying that in many situations we can use $\mathcal{A} \simeq \mathcal{A}_o$ - this will be a useful approximation in calculations that follow. In fact, this upper bound areal strain is not reached until $\mathcal{A}_o/a_o \sim 10^{15}$! The exact entropic equation of state (eqn. 4.176) can be explicitly solved for τ, yielding

$$\tau = \frac{\pi^2\kappa_b}{a_o} \cdot \frac{1 - \frac{a_o}{\mathcal{A}} e^{\left(\frac{\mathcal{A}_o - \mathcal{A}}{\mathcal{A}} \frac{8\pi\kappa_b}{k_B T}\right)}}{e^{\left(\frac{\mathcal{A}_o - \mathcal{A}}{\mathcal{A}} \frac{8\pi\kappa_b}{k_B T}\right)} - 1}. \tag{4.181}$$

This equation of state represents a derivative of the free energy with respect to projected area, namely

$$G_{\text{ent}} = \int_{\mathcal{A}_{\min}}^{\mathcal{A}} \tau(\mathcal{A}')\mathrm{d}\mathcal{A}', \tag{4.182}$$

with κ_b, $\mathcal{A}_o$ and a_o as parameters. The difficulty of this integral is significantly reduced if we realize that in certain strategic locations, we can substitute $\mathcal{A} \to \mathcal{A}_o$, justified by the implications of eqn. 4.179, to get

$$\tau = \frac{\pi^2\kappa_b}{a_o} \cdot \frac{1 - \frac{a_o}{\mathcal{A}_o} e^{\left(\frac{\mathcal{A}_o - \mathcal{A}}{\mathcal{A}_o} \frac{8\pi\kappa_b}{k_B T}\right)}}{e^{\left(\frac{\mathcal{A}_o - \mathcal{A}}{\mathcal{A}_o} \frac{8\pi\kappa_b}{k_B T}\right)} - 1} \simeq \frac{\pi^2\kappa_b}{a_o} e^{-\frac{8\pi\kappa_b}{k_B T} \frac{\mathcal{A}_o - \mathcal{A}}{\mathcal{A}_o}}. \tag{4.183}$$

Integrating this equation gives

$$G_{\text{ent}} = G_o + k_B T \frac{\pi \mathcal{A}_o}{8 a_o} e^{-\frac{8\pi\kappa_b}{k_B T} \frac{\mathcal{A}_o - \mathcal{A}}{\mathcal{A}_o}}, \tag{4.184}$$

with G_o defined by $G_{\text{ent}}|_{\mathcal{A}=\mathcal{A}_{\min}} = 0$. The meaning of this equation is unambiguous; as we increase the frame area from its zero tension resting value of $\mathcal{A}_{\min}$, the free energy exponentially increases because the entropic undulations of the membrane are flattened out. Recalling the arrangement we are using to connect domain morphology to the thermal membrane reservoir, as shown in Fig. 4.19, we interpret changes in morphology as changes in the actual amount of lipid in the thermal reservoir, such that

$$\Delta\mathcal{A} = \frac{1}{2}\int_{\mathcal{S}} (\nabla h)^2 \, \mathrm{d}^2\mathbf{r}, \tag{4.185}$$

where this height function h resides in the zero temperature region. Substituting this into the free energy, we can write the elastic functional as

$$G_{\text{el}} = G_{\text{ent}}|_{\mathcal{A}_o \to \mathcal{A}_o - \Delta\mathcal{A}} + \frac{\kappa_b}{2}\int_{\mathcal{S}} \left(\nabla^2 h\right)^2 \mathrm{d}^2\mathbf{r}, \tag{4.186}$$

or more explicitly as

$$G_{\text{el}} = G_o + k_B T \frac{\pi \mathcal{A}_o}{8a_o} e^{-\frac{8\pi\kappa_b}{\mathcal{A}_o k_B T}\left(\mathcal{A}_o - \mathcal{A} - \frac{1}{2}\int_{\mathcal{S}} (\nabla h)^2 \,\mathrm{d}^2\mathbf{r}\right)} + \frac{\kappa_b}{2}\int_{\mathcal{S}} \left(\nabla^2 h\right)^2 \mathrm{d}^2\mathbf{r}, \tag{4.187}$$

and the variation is still taken with respect to h, as $\frac{\delta G_{\text{el}}}{\delta h} = 0$. This has the pleasing property that if the morphological deformation field is zero, the membrane system returns to the equation of state defined by entropic fluctuations.

We can take this calculation a few steps further by asking: In what regime does the constant tension ensemble match the results of this entropic ensemble? Looking at the first two terms of eqn. 4.187, the regime where tension would be constant is

$$\frac{8\pi\kappa_b}{k_B T}\frac{\Delta\mathcal{A}}{\mathcal{A}_o} \ll 1, \tag{4.188}$$

yielding the approximation to the entropic component of the free energy

$$G_{\text{ent}} \simeq G_o + k_B T \frac{\pi \mathcal{A}_o}{8a_o} e^{-\frac{8\pi\kappa_b}{k_B T}\frac{\mathcal{A}_o - \mathcal{A}}{\mathcal{A}_o}} \left(1 + \frac{8\pi\kappa_b}{k_B T}\frac{\Delta\mathcal{A}}{\mathcal{A}_o}\right). \tag{4.189}$$

Readjusting the zero of the free energy, this can be written as

$$G_{\text{ent}} \simeq G'_o + \underbrace{\frac{\pi^2\kappa_b}{a_o} e^{-\frac{8\pi\kappa_b}{k_B T}\frac{\mathcal{A}_o - \mathcal{A}}{\mathcal{A}_o}}}_{\text{eqn. 4.183 for } \tau} \frac{1}{2}\int_{\mathcal{S}} (\nabla h)^2 \,\mathrm{d}^2\mathbf{r}. \tag{4.190}$$

Taking a nominal bending modulus of $\kappa_b = 25\, k_B T$ and vesicle diameter of $20\,\mu$m, we can use eqn. 4.188 to estimate the area change above which we must consider changes to the entropic reservoir, and find that the tension is approximately constant for the upper bound value of $\Delta\mathcal{A} < 2\,\mu\text{m}^2$. This means that a single domain with flat radius of roughly 800 nm or less can fully bud without changing the resting tension in the membrane significantly. In another estimate, this means that on the vesicle surface ~ 150 domains of area $\alpha = \pi/4$ with $\lambda = 1\,\mu$m, which in real units corresponds to domains with a flat diameter $1\,\mu$m, can dimple to have a boundary slope of $\epsilon = 0.25$ and still maintain an essentially constant frame tension. This is a reasonable estimate which says that the constant tension ensemble is relevant, although depending on the vesicle size and the exact composition of the lipid mixture, the domains may be larger and/or more numerous, and the dimpling process may yield lower values of $\Delta\mathcal{A}$ per domain than the above estimates depending on the values of ϵ. This alludes to a model where it is the total area change of all

domains that couples to the tension of the thermal reservoir; hence for tension to be constant, domains must not only be small, but there must be low enough number of them such that their combined $\Delta\mathcal{A}$ is less than the values suggested by eqn. 4.188.

To put these results in further experimental context, we explore how the entropic tension changes when a domain of area $\mathcal{A}_{\rm D}$, on a GUV with area $\mathcal{A}_o$, changes its morphology from flat to budded. We assume the vesicle is nearly spherical, and hence the volume of the vesicle is $V = \mathcal{A}^{3/2}/3\sqrt{4\pi}$, where $\mathcal{A}$ represents the frame area of the GUV with the flat domain. We assume the domain forms a spherical bud, in which case, it requires volume $V_{\rm D} = \mathcal{A}_{\rm D}^{3/2}/3\sqrt{4\pi}$ to complete this change in morphology. This change in volume corresponds to a change in frame area, such that the new frame area is

$$\mathcal{A}_{\rm n} = \left(\mathcal{A}^{3/2} - \mathcal{A}_{\rm D}^{3/2}\right)^{\frac{2}{3}}. \tag{4.191}$$

Via the phase boundary, the same morphological change isolates a certain amount of lipid from the vesicle, such that

$$\mathcal{A}_o' = \mathcal{A}_o - \mathcal{A}_{\rm D}. \tag{4.192}$$

This effectively causes a change of variable in eqn. 4.181 from

$$\frac{\mathcal{A}_o}{\mathcal{A}} \to \frac{\mathcal{A}_o'}{\mathcal{A}_{\rm n}} = \frac{1 - \frac{\mathcal{A}_{\rm D}}{\mathcal{A}_o}}{\left(\left(\frac{\mathcal{A}}{\mathcal{A}_o}\right)^{3/2} - \left(\frac{\mathcal{A}_{\rm D}}{\mathcal{A}_o}\right)^{3/2}\right)^{\frac{2}{3}}} \simeq \frac{\mathcal{A}_o}{\mathcal{A}}\left(1 - \frac{\mathcal{A}_{\rm D}}{\mathcal{A}_o}\right). \tag{4.193}$$

We can now calculate the tension as a function of the relative frame area ($\mathcal{A}/\mathcal{A}_o$) and the budding domain area relative to the total vesicle area ($\mathcal{A}_{\rm D}/\mathcal{A}_o$), as shown in Fig. 4.21.

The end result of these calculations is that there is a regime in which tension is constant and a regime in which tension rises exponentially as a domain changes morphology. In which regime a vesicles finds itself depends on the number and size distribution of domains on its surface. It is likely that for large vesicles with a low number of small domains, the tension is approximately constant, while for vesicles with larger, more numerous domains the tension cannot be considered constant. In those cases where the tension is exponentially sensitive to domain morphology, it should not have an effect on the actual shape of the dimpled domain because one can always readjust the zero of the free energy about the current state of tension and explore shapes in that region of phase space under the approximation of the constant tension ensemble. Further, we speculate that an exponentially rising tension has the effect of stabilizing dimples against budding; in a sense, complicating the relatively simple phase diagram of the constant tension ensemble, by demanding that we know not only elastic constants of the membrane and domain size, but extrinsic features of the membrane, like the total membrane area.

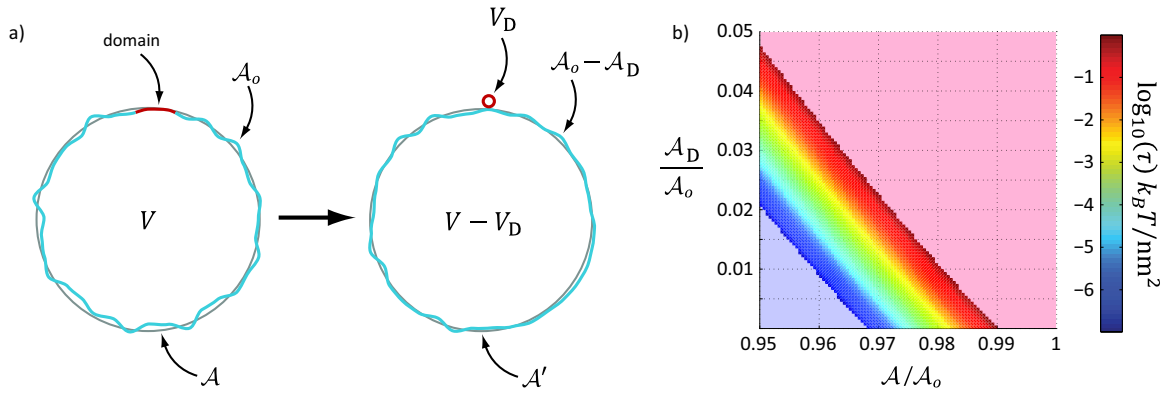

Figure 4.21: Effects of domain budding on entropic tension. a) This schematic shows how the budding of a domain from a large vesicle, conserves total membrane area and enclosed volume, but changes the frame area and actual area available for fluctuations on the vesicle, increasing the entropic tension. b) Plot of the membrane tension upon budding of a domain whose size is a fraction of the total membrane area, $\mathcal{A}_\mathrm{D}/\mathcal{A}_o$, where the initial state had a relative frame area $\mathcal{A}/\mathcal{A}_o$, which specifies an initial state of tension. The light blue area indicates tensions below the minimum tension $\pi^2\kappa_b/\mathcal{A}_o$, whereas the light red region indicates tensions where membrane stretch becomes important.

4.5.3 Simulating Membrane Conformations

In the previous section we showed that the functional, when represented in Fourier space, varied quadratically with each mode amplitude. The symmetry of the energy functional dictates a zero mean amplitude for all modes, $\langle h(\mathbf{q})\rangle = 0$, and hence with knowledge of the mode amplitude variance, we know the probability distribution for detecting a certain mode amplitude with phase θ is

$$P\left(|h(\mathbf{q})|,\theta\right) = \frac{1}{2\pi}\frac{e^{-\frac{|h(\mathbf{q})|^2}{2\langle|h(\mathbf{q})|^2\rangle}}}{\sqrt{2\pi\left\langle|h(\mathbf{q})|^2\right\rangle}}, \tag{4.194}$$

where $\mathcal{A}$ is constrained, given values for $\mathcal{A}_o$, τ and κ_b in the equation of state, and $h(\mathbf{q}) = |h(\mathbf{q})|e^{i\theta}$. Recall that the minimum $|\mathbf{q}| = \pi/\sqrt{\mathcal{A}}$ and the maximum $|\mathbf{q}| = \pi/\sqrt{a_o}$, such that the total number of modes $N = \sqrt{\mathcal{A}/a_o}$. The actual deformation profile can then be written as

$$h(\mathbf{r}) = \sum_{n_1,n_2=1}^{N}\left[a_{(n_1,n_2)}\cos\left(\frac{2\pi}{\sqrt{\mathcal{A}}}(n_1x_1+n_2x_2)\right) + b_{(n_1,n_2)}\sin\left(\frac{2\pi}{\sqrt{\mathcal{A}}}(n_1x_1+n_2x_2)\right)\right] \tag{4.195}$$

where the coefficients are

$$a_{(n_1,n_2)} = 2\Re[h(q_{x_1},q_{x_2})] \tag{4.196}$$

and

$$b_{(n_1,n_2)} = -2\Im[h(q_{x_1},q_{x_2})], \tag{4.197}$$

with $q_{x_1} = 2\pi n_1/\sqrt{\mathcal{A}}$, $q_{x_2} = 2\pi n_2/\sqrt{\mathcal{A}}$, and $|q| = \sqrt{q_{x_1}^2 + q_{x_2}^2}$. The thermal height field in Fig. 4.19 is computed from this scheme.

4.6 The 1D Interaction Potential

As mentioned in our discussion of dilute domain interactions, the 1D interaction potential is an approximation that makes calculations relatively easy by absorbing all the changes that occur during interaction into the boundary conditions of the surrounding membrane. The following subsection will derive the 1D potential in detail and explain the manner in which boundary conditions are imposed. In addition, these ideas permit us to examine how differences in domain size might effect the pairwise interaction potential. We explicitly assume that the shapes of the domains are constant during the interaction; the domains are only allowed to rotate with respect to the flat integration plane. However, the membrane surrounding the domain is allowed to deform in response to this rotation. Casting this into a one-dimensional model allows us to easily find analytical solutions for the interaction potential. In one dimension, there are three regions of membrane to consider: two regions of membrane which extend from the outer domain edges out to infinity on either side and an inner region between the two domains from $-d/2$ to $d/2$, where d is the separation between domain edges.

The elastic energy of the 1D membrane deformation, like the 2D case, is a sum of tension and bending terms. Using Fig. 4.22, let us refer to the blue region to left with the label l, the blue region in between the domains with the label c, and the blue region to the right with the label r. Then, similar to the 2D scenario, in the left region the elastic energy is

$$G_l[\eta_l(x)] = \frac{\kappa_b s}{2\lambda} \int_{-\infty}^{0} \left(\left(\frac{\partial \eta_l}{\partial x_l} \right)^2 + \left(\frac{\partial^2 \eta_l}{\partial x_l^2} \right)^2 \right) \mathrm{d}x_l, \tag{4.198}$$

in the right region

$$G_r[\eta_r(x)] = \frac{\kappa_b s}{2\lambda} \int_{0}^{\infty} \left(\left(\frac{\partial \eta_r}{\partial x_r} \right)^2 + \left(\frac{\partial^2 \eta_r}{\partial x_r^2} \right)^2 \right) \mathrm{d}x_r, \tag{4.199}$$

and in the center region

$$G_c[\eta_c(x)] = \frac{\kappa_b s}{2\lambda} \int_{-\frac{d}{2}}^{\frac{d}{2}} \left(\left(\frac{\partial \eta_c}{\partial x_c} \right)^2 + \left(\frac{\partial^2 \eta_c}{\partial x_c^2} \right)^2 \right) \mathrm{d}x_c. \tag{4.200}$$

Then the total elastic energy is the sum of these three parts. The parameter s is the effective one dimensional length over which the interaction occurs; the exact value is absorbed into the data fitting routine. In Fig. 4.22, s would be the distance the membrane goes 'into' the page. These functionals generate Euler-Lagrange equations identical in form to those in Section 4.17, however

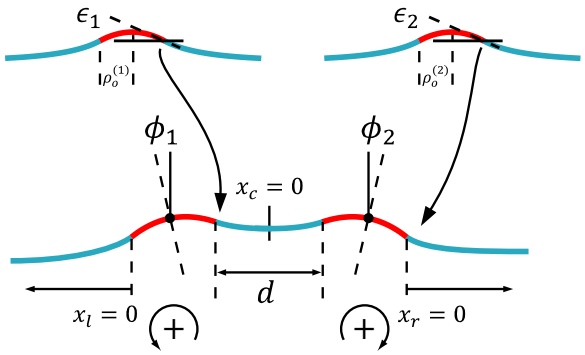

Figure 4.22: A detailed view of the four distinct boundary conditions in the 1D model of interaction between two dimpled domains. If both domains are the same size, then $\epsilon_1 = \epsilon_2$ and $\phi_1 = \phi_2$. The boundary slopes, ϵ_i, are set by the single domain energy minimization described earlier. The inner domain edge separation is d, and the tilt angle sign convention is shown below each angle ϕ_i. The energy is calculated by integrating the membrane shape over the three blue regions, adherent to the boundary conditions.

they are now one dimensional. The solutions are all of the form

$$\eta_i = a_1^{(i)} e^{x_i} + a_2^{(i)} e^{-x_i} + a_3^{(i)} x_i + a_4^{(i)}. \tag{4.201}$$

As we will show, there are two qualitatively different interactions that are distinct realizations of the same four boundary conditions. The results of this analysis are that we explain the domain repulsion in terms of elastic parameters and domain morphology and predict as of yet unobserved attractive interactions for opposite parity domains. Further, we can use results from previous sections to estimate the effects of domain size and size asymmetry.

4.6.1 Interactions of Asymmetric Domains

We refer to domains whose curvature have the same sign as being of the same 'parity', however their size, boundary slope or elastic properties may differ. The parity itself is encoded by the sign of the slope boundary condition, whereas size asymmetry or elastic differences are reflected in the magnitude of the boundary slope and projected domain sizes as demonstrated in the following calculation.

For the outer membrane regions, the boundary conditions are that the membrane be flat far from the domain edges, in particular

$$\left.\frac{\partial \eta_l}{\partial x_l}\right|_{x_l=-\infty} = \left.\frac{\partial \eta_r}{\partial x_r}\right|_{x_r=\infty} = 0, \tag{4.202}$$

that the change in 1D 'area' due to interaction be finite, and we arbitrarily set $x_l(-\infty) = x_r(\infty) = 0$,

which immediately leads to

$$\eta_l = a_1 e^{x_l}, \tag{4.203}$$

for the left-hand side and

$$\eta_r = a_2 e^{-x_r}, \tag{4.204}$$

for the right-hand side. As the domains approach each other, a preferred rotation angle will emerge; applying the small gradient/angle approximation, namely $\tan(\phi_i) \simeq \phi_i$, this boundary slope is

$$\left.\frac{\partial \eta_l}{\partial x_l}\right|_{x_l=0} = \phi_1 - \epsilon_1, \tag{4.205}$$

in the left region and

$$\left.\frac{\partial \eta_r}{\partial x_r}\right|_{x_r=0} = \epsilon_2 - \phi_2, \tag{4.206}$$

in the right region. Taking ϕ_i and s/λ as small allows us to neglect the small contributions to the interaction energy from the change in domain projected area with the rotations ϕ_i. Then the final solutions for the outer regions are

$$\eta_l = (\phi_1 - \epsilon_1)e^{x_l} \quad \text{and} \quad \eta_r = (\phi_2 - \epsilon_2)e^{-x_r}. \tag{4.207}$$

In the inner region ϵ_2 changes sign and the slope boundary conditions read

$$\left.\frac{\partial \eta_c}{\partial x_c}\right|_{x_c=-d/2} = \epsilon_1 + \phi_1 \quad \text{and} \quad \left.\frac{\partial \eta_c}{\partial x_c}\right|_{x_c=d/2} = -(\epsilon_2 + \phi_2). \tag{4.208}$$

Additionally, for the membrane to be contiguous, we must impose the height boundary conditions

$$\eta_c|_{x=-d/2} = \eta_l|_{x_l=0} + 2\rho_o^{(1)}\phi_1 \tag{4.209}$$

on the left side and

$$\eta_c|_{x=d/2} = \eta_r|_{x_r=0} + 2\rho_o^{(2)}\phi_2 \tag{4.210}$$

on the right side, where again we have applied the small angle approximation. Application of these four boundary conditions yields a complicated expression for the membrane shape in between the domains.

The solutions for the membrane shape in the three regions can be integrated in the appropriate elastic functionals, giving a rather complicated expression for the energy as a function of ϕ_1 and ϕ_2. The preferred domain tilt is found by minimizing this energy with respect to the available rotations, $\frac{\partial G}{\partial \phi_i} = 0$, giving

$$\phi_1(d) \simeq -\epsilon_2 e^{-d} \quad \text{and} \quad \phi_2(d) \simeq -\epsilon_1 e^{-d}. \tag{4.211}$$

Substituting the exact equations for $\phi_i(d)$ into $G(d) = G_l + G_c + G_r$ gives the 1D interaction potential in the small gradient limit

$$G(d) = 2\kappa_b\epsilon_1\epsilon_2\frac{s}{\lambda}e^{-d}\left(1 + f(\epsilon_i, \rho_o^{(i)}, d)\right) \simeq 2\kappa_b\epsilon_1\epsilon_2\frac{s}{\lambda}e^{-d}, \tag{4.212}$$

where the function f is

$$f = \frac{\left(\rho_o^{(1)}\epsilon_2 - \rho_o^{(2)}\epsilon_1\right)^2}{\epsilon_1\epsilon_2}\left[4\rho_o^{(1)}\rho_o^{(2)} + e^d\left(d - 2 + 2(\rho_o^{(1)}+1)^2 + 2(\rho_o^{(2)}+1)^2\right)\right]^{-1}. \tag{4.213}$$

Using the relationships for $\rho_o^{(i)}(\alpha_i, \epsilon_i)$ and $\epsilon_i(\alpha_i)$ from eqns. 4.115 and 4.117, respectively, one can show that $f \ll 1$ for all reasonable parameter values.

In processing the experimental data, we made the assumption that the material properties of all domains were identical and their areas were approximately equal, hence $\epsilon_1 = \epsilon_2$, thus the two outer regions of membrane are identical, the inner region is an even function, and $f = 0$. One important feature to notice about this potential is that ϵ_1 and ϵ_2 are multiplicative factors; if both domains have the same parity they will repel, whereas if they have opposite parity they will attract. Size asymmetry is addressed in some detail in the following subsection. The precise fit model used in data analysis was

$$G(r) = a_1 e^{-r/\lambda} + a_2, \tag{4.214}$$

where a_i are fit parameters, and the distance parameter is $r = \lambda(2\rho_o + d)$, where throughout this section we refer to $\lambda_2 = \lambda$. The constant a_2 shifts the zero of the potential which is arbitrarily set when taking the logarithm of the radial distribution function.

Prior to our work, theoretical efforts [117] showed that membrane proteins which deform the membrane midplane exert a repulsive force on each other of the limiting form

$$G(r) \simeq \pi\kappa_b\left[2\epsilon_1\epsilon_2\rho_o^2 K_0(r/\lambda) + (\epsilon_1^2 + \epsilon_2^2)\rho_o^4 K_2^2(r/\lambda)\right] \simeq 2\pi\kappa_b\epsilon_1\epsilon_2\rho_o^2 K_0(r/\lambda). \tag{4.215}$$

Assuming that the dimpled domain shape is constant during interaction, this model maps directly onto the domain interaction scenario with the effective cross-section of interaction having the intuitively pleasing form of projected domain area $s \simeq \lambda\pi\rho_o^2$. This model and the exponential model can be fit to the data, and the two models are visually indistinguishable in their fit quality, though there is a slight change in the measured length-scale of interaction, of about 12%. Fig. 4.23 graphically compares these two models to experimental data.

Additionally, we used fully non-linear, 2D finite element calculations of the elastic interaction of domains to validate these analytical models; the results for an example symmetric interaction are shown in Fig. 4.24.

4.6.2 Effects of Domain Size Asymmetry

Due to the stochastic nature of how domains initially form, there are always slight (or sometimes more than slight) size differences between all the domains on a vesicle's surface. This experimental reality is demonstrated in the domain area histograms of Figs. 4.29, 4.30 and 4.31. In this subsection we derive scaling laws that allow us to comment on how mean domain size and size asymmetry affect the strength of the interaction. We presume that on the surface of a vesicle the domains are sparse enough that pairwise interactions dominate, that is, multi-body interactions are negligible.

We begin by rewriting the exponential interaction as a function of the domain center-to-center distance, $r = \lambda(\rho_o^{(i)} + \rho_o^{(j)} + d_{ij})$, such that we can define the interaction between the ith and jth domains as

$$G_{ij} = 2\kappa_b \epsilon_i \epsilon_j \frac{s_{ij}}{\lambda} e^{\left(\rho_o^{(i)} + \rho_o^{(j)}\right)} e^{-r/\lambda}, \tag{4.216}$$

showing that it is the product of a distance-dependent and size-dependent function; we now examine the size-dependent function, which we will call $\sigma_{ij}(\alpha_i, \alpha_j)$ for ease of notation. To explicitly calculate how domain sizes affect the strength of the interaction, recall from eqn. 4.117 that the boundary slope of each domain can be written as

$$|\epsilon_i| \simeq \sqrt{\frac{1}{\delta}\left(\frac{\alpha_i}{\alpha_c} - 1\right)}, \tag{4.217}$$

where it is important to note that α_c is not a domain-dependent quantity - it is set by the material properties of the membrane, and hence for any interaction to take place between domains, *both* must have an area greater than α_c. For this reason, we define $\alpha_i/\alpha_c = \hat{\alpha}_i$ where $\hat{\alpha}_i > 1$.

To understand the underlying scaling relationship, we must comment on how s_{ij} behaves with changes in α_i and α_j. Clearly, the potential should scale symmetrically with changes in the size of either domain, or in other words $s(\alpha_i + \Delta\alpha, \alpha_j) = s(\alpha_i, \alpha_j + \Delta\alpha)$ if $\alpha_i = \alpha_j$. If we make the approximation that $s/\lambda \simeq \pi\rho_o^2$ in the case of equal domain areas, as indicated by the 2D model [117], then to lowest order, symmetry dictates that $s_{ij}/\lambda \simeq \pi\rho_o^{(i)}\rho_o^{(j)}$. Then using eqn. 4.115 we can relate the boundary slope and domain size to the projected radius by

$$\rho_o^{(i)} = \sqrt{\frac{2\alpha_c}{\pi}\left(\frac{\hat{\alpha}_i}{\hat{\alpha}_i + 1}\right)}. \tag{4.218}$$

After a few algebraic manipulations, we can write

$$\sigma_{ij}(\hat{\alpha}_i, \hat{\alpha}_j) = \frac{4}{\delta}\kappa_b \alpha_c \sqrt{\hat{\alpha}_i \hat{\alpha}_j} \sqrt{\frac{(\hat{\alpha}_i - 1)(\hat{\alpha}_j - 1)}{(\hat{\alpha}_i + 1)(\hat{\alpha}_j + 1)}} e^{\sqrt{\frac{2\alpha_c}{\pi}}\left[\sqrt{\frac{\hat{\alpha}_i}{\hat{\alpha}_i+1}} + \sqrt{\frac{\hat{\alpha}_j}{\hat{\alpha}_j+1}}\right]} \tag{4.219}$$

which characterizes the strength of the pairwise potential given the sizes of the two domains, and material constants. This also gives us the useful scaling relationship that as the average domain

size increases, the strength of the potential scales approximately linearly as

$$\sigma(\hat{\alpha}) = \frac{4}{\delta}\kappa_b\alpha_c\hat{\alpha}\cdot\frac{\hat{\alpha}-1}{\hat{\alpha}+1}\cdot e^{2\sqrt{\frac{2\alpha_c}{\pi}\frac{\hat{\alpha}}{\hat{\alpha}+1}}}, \tag{4.220}$$

thus larger domains should repel each other more strongly than smaller domains. We characterize the difference in domain sizes by writing the mean domain size as

$$\bar{\alpha}_{ij} = \frac{1}{2}(\hat{\alpha}_i + \hat{\alpha}_j), \tag{4.221}$$

and their percent difference as

$$c_{ij} = \frac{\hat{\alpha}_i - \hat{\alpha}_j}{\bar{\alpha}_{ij}}, \tag{4.222}$$

which defines the transformation $\bar{\alpha}_{ij}(1 + c_{ij}/2) = \hat{\alpha}_i$ and $\bar{\alpha}_{ij}(1 - c_{ij}/2) = \hat{\alpha}_j$. We can make these substitutions to find $\sigma_{ij}(\bar{\alpha}_{ij}, c_{ij})$, giving a rather complicated expression for the scaling factor of the potential as a function of the mean size of the two domains and their size difference. Finally, these scaling arguments culminate in Fig. 4.227, where we take the ratio of the scaling factor for some given value of c and $\bar{\alpha}$ and normalize it by the scaling factor at the same $\bar{\alpha}$ but $c = 0$ (*i.e.* $\sigma_{ij}/\sigma_{ij}|_{c=0}$), in essence giving a measure of the relative change in the strength of the potential as size asymmetry increases. This ratio is relatively insensitive to the value α_c, however to be complete, we show plots for two different values of α_c. The result is that the potential remains relatively unchanged within certain bounds of the size asymmetry. The specific values of this bound are set by the mean size $\bar{\alpha}$ and a specified tolerance $p < \sigma_{ij}/\sigma_{ij}|_{c=0} < 1$. Additionally, this analysis shows that for conserved mean domain size, increasing size asymmetry tends to weaken the strength of the interaction, since $\sigma_{ij}/\sigma_{ij}|_{c=0} \leq 1$.

4.6.3 Corrections from Size Asymmetry

With these results, we can begin to connect the distribution of sizes found in a real experiment to the manner in which size asymmetry changes the potential of mean force. Specifically, in this subsection we will derive a correction to the potential of mean force from the width of the distribution of scaling factors σ_{ij}.

For a vesicle with a given number of domains, there are N distinct domain pairs, and hence N distinct pairwise interactions between those domains. The radial distribution function describes the probability of finding two domains a distance r apart from domain center-to-center. As explained in section 4.10.1, the measured potential $V_{\text{eff}}(r)$ is the sum of the potential of mean force, here denoted by $\bar{G}(r)$, and a fictitious potential $V_{\text{fict}}(r)$ that is the same for all domains on a given vesicle. Then the radial distribution function is given by

$$P(r) = \frac{1}{Z}e^{-(\bar{G}(r)+V_{\text{fict}}(r))}, \tag{4.223}$$

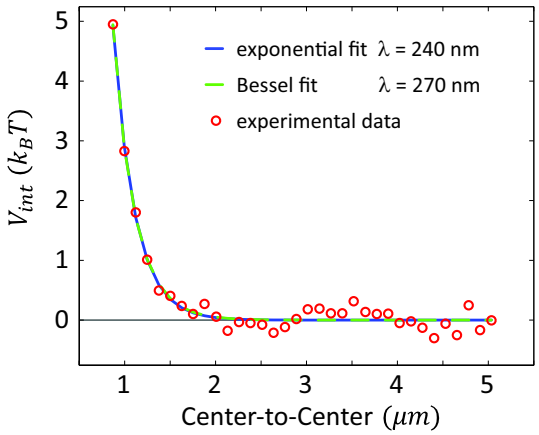

Figure 4.23: Comparison of different interaction models. Using the same data presented in the first section of this chapter, we show graphically that an exponentially repulsive interaction is indistinguishable from a Bessel function repulsion (eqn. 4.215). The only notable difference is that for such excellent alignment of the two models, a slightly different length-scale of interaction must be chosen for each.

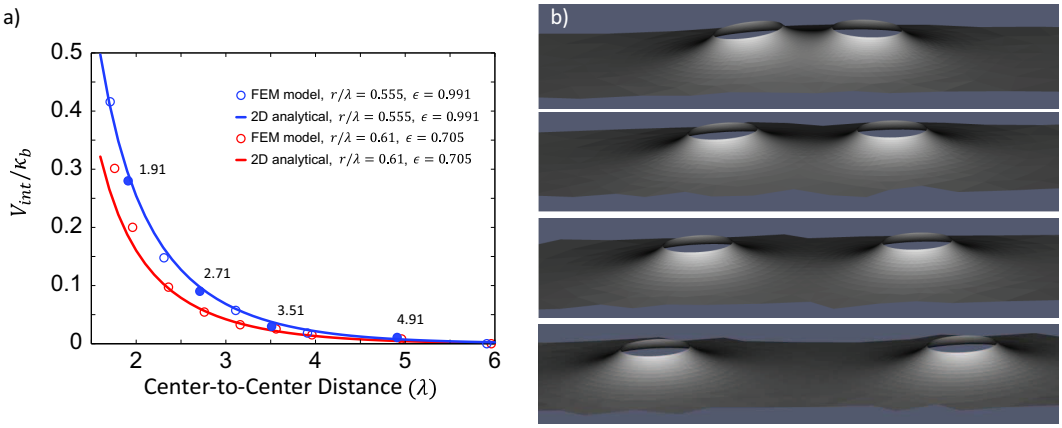

Figure 4.24: Comparison of the 2D interaction model of [117] and fully non-linear finite-element analysis. a) Plots of the interaction potential between symmetric domains as a function of center-to-center distance for two different domain sizes, as indicated in the legend. The fit functions are of eqn. 4.215 with $\epsilon_1 = \epsilon_2$. b) Non-linear finite element solution for the membrane shape with two rigid, interacting domains - the lipid domains are not shown. As the domains get closer, they tilt as predicted by the 1D theory, and the membrane between them becomes ever more deformed. Each of the solid blue data points in (a) correspond to a frame in (b). This figure made in collaboration with and adapted from [267].

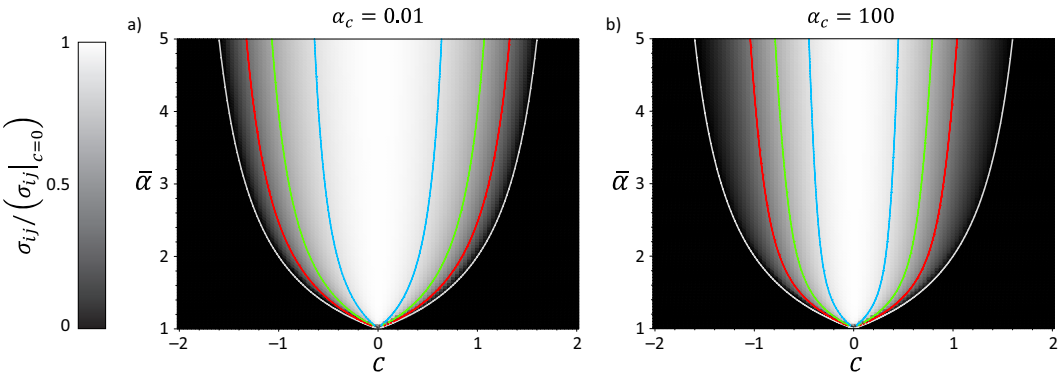

Figure 4.25: Effects of domain size and size asymmetry on the strength of the interaction potential. Plots (a) and (b) are the ratio of the scaling factor σ_{ij} normalized by the scaling factor with the same mean size but zero size asymmetry. The bounded values of c are shown for tolerances of $p = 0.9$ (blue), $p = 0.7$ (green) and $p = 0.5$ (red), with the white line outlining the extent of possible values of c for a given $\bar{\alpha}$. If we demand that the change in the strength of the potential be less than 10%, then the size asymmetry should be between $-1/2 \lesssim c \lesssim 1/2$. Additionally, these plots show that for a given mean size, asymmetry tends to weaken the potential. Plot (a) uses $\alpha_c = 0.01$ while plot (b) uses $\alpha_c = 100$, showing that the bounds of c are fairly insensitive to the value of α_c.

where

$$\bar{Z} = \int_0^{2R_{\text{fict}}} e^{-(\bar{G}(r)+V_{\text{fict}}(r))}\mathrm{d}r, \tag{4.224}$$

R_{fict} is a parameter in the fictitious potential, and the energies are measured in units of k_BT. The fictitious potential is a property of the vesicle and microscope optics only, and hence is the same for all pair interactions. The upper bound of the integral is set by the fact that $\lim_{r\to 2R_{\text{fict}}}[V_{\text{fict}}] = \infty$. On the vesicle surface the same radial distribution function is given by the sum of the radial distribution functions from each pair of domains, that is

$$P(r) = \frac{1}{N}\sum_{ij}\frac{1}{Z_{ij}}e^{-(G_{ij}(r)+V_{\text{fict}}(r))}, \tag{4.225}$$

where

$$Z_{ij} = \int_0^{2R_{\text{fict}}} e^{-(G_{ij}(r)+V_{\text{fict}}(r))}\mathrm{d}r \tag{4.226}$$

and i and j span the set of distinct domain pairs. Equating these two expressions and solving for the measured potential of mean force gives

$$\bar{G}(r) = -\ln\left[\frac{\bar{Z}}{N}\sum_{ij}\frac{1}{Z_{ij}}e^{-G_{ij}}\right] = -\ln\left[\frac{\bar{Z}}{N}\sum_{ij}\frac{1}{Z_{ij}}e^{-\sigma_{ij}e^{-r/\lambda}}\right]. \tag{4.227}$$

The only change in the pairwise potential from one domain pair to another is the value of σ_{ij} and the only intrinsic parameter that changes from one domain to another is the size α. Thus for a given distribution of domain sizes $p(\alpha)$, there is a distribution of the values of σ for domain pairs, $p(\sigma)$, that depends on the joint probability distribution $p(\alpha_1|\alpha_2) \simeq p(\alpha_1)p(\alpha_2)$. Finding the connection between these two distributions is quite complicated, and given the complex functional form of σ_{ij} in eqn. 4.219, we would not be able to analytically solve it. That said, using Monte Carlo methods it is straightforward to generate the appropriate $p(\alpha_1|\alpha_2)$ and corresponding $p(\sigma)$ given a measured $p(\alpha)$.

To derive the relationship between $p(\alpha_1|\alpha_2)$ and $p(\sigma)$, we first note that calculating the moments of $p(\sigma)$ is straightforward, given by

$$\langle \sigma^n \rangle = \int \int p(\alpha_1|\alpha_2)\sigma^n(\alpha_1, \alpha_2)\mathrm{d}\alpha_1\mathrm{d}\alpha_2 \tag{4.228}$$

where the integral spans the appropriate bounds of α_1 and α_2. Then taking the Fourier transform of $p(\sigma)$ we can relate the moments of the distribution to the distribution itself, that is

$$p(k) = \int e^{-2\pi i k\sigma} p(\sigma)\mathrm{d}\sigma = \sum_{n=0}^{\infty} \frac{(-2\pi i k)^n}{n!} \underbrace{\int \sigma^n p(\sigma)\mathrm{d}\sigma}_{=\langle \sigma^n \rangle}. \tag{4.229}$$

Then the inverse Fourier transform gives the distribution $p(\sigma)$, by

$$p(\sigma) = \int e^{2\pi i k\sigma} p(k)\mathrm{d}k = \sum_{n=0}^{\infty} \frac{\langle \sigma^n \rangle}{n!} \int e^{2\pi i k\sigma} (-2\pi i k)^n \mathrm{d}k. \tag{4.230}$$

This method can be used to analytically calculate $p(\sigma)$, however in practice it is likely far easier to generate the distribution via Monte Carlo methods.

Moving forward with eqn. 4.227, let us assume that the sum can be converted to an integral, such that we can write

$$\bar{G}(r) = -\ln \left[\int p(\sigma) \frac{\bar{Z}}{Z(\sigma)} e^{-\sigma e^{-r/\lambda}} \mathrm{d}\sigma \right]. \tag{4.231}$$

To make progress, let us posit the form of $p(\sigma)$ as a Gaussian

$$p(\sigma) = \frac{e^{-\frac{(\sigma-\bar{\sigma})^2}{2a^2}}}{a\sqrt{2\pi}} \tag{4.232}$$

with a standard deviation a much smaller than the mean, which allows us to make the approximation $Z(\sigma) \simeq \bar{Z}$, and take the bounds of the integral to infinity such that the potential of mean force can be written as

$$\bar{G}(r) \simeq -\ln \left[\int_{-\infty}^{\infty} p(\sigma) e^{-\sigma e^{-r/\lambda}} \mathrm{d}\sigma \right]. \tag{4.233}$$

Then examining the integral we find

$$\int_{-\infty}^{\infty} p(\sigma) e^{-\sigma e^{-r/\lambda}} \mathrm{d}\sigma = e^{\left(\frac{a^2}{2} e^{-2r/\lambda} - \bar{\sigma} e^{-r/\lambda}\right)}, \tag{4.234}$$

and finally we can write the potential of mean force as the mean pairwise interaction plus a correction term related to the width of the distribution $p(\sigma)$

$$\bar{G}(r) = \bar{\sigma} e^{-r/\lambda} - \frac{a^2}{2} e^{-2r/\lambda}, \tag{4.235}$$

although this result is only valid if the underlying distribution for σ is Gaussian. In general the correction term can be arbitrarily complex given the possible distributions of $p(\alpha)$, and corresponding distributions of $p(\sigma)$. The key points of this result are that it makes sense to approximate the measured potential as a mean pairwise potential, and it shows that asymmetry, here characterized by a, tends to make the measured potential weaker, a result qualitatively supported by the reduction in the strength and increase in the apparent length scale of the potentials as size asymmetry increases, as shown in Figs. 4.29, 4.30 and 4.31.

4.7 Coarse Control of Membrane Tension and Inducing Phase Separation

As explained earlier in this chapter, there are essentially four main parameters that dictate where in the space of possible morphologies a particular vesicle will find itself: bending stiffness, applied membrane tension, phase boundary line tension and domain size. Of those, the bending stiffness and line tension are dictated by the composition of the membrane, and are not thought to be independent of each other [138]. Considering the difficulty of changing composition *in situ* and the fact that these parameters are not varied independently, we used membrane tension as the 'knob' in our experiment when trying to induce different morphologies. However, control of membrane tension in these experiments is not an exact procedure (as it is, for instance, in micropipette aspiration [26]).

Multi-component GUVs were formed in a 100 mM sucrose solution via heated electroformation ($\sim$ 50 C) to be above the phase separation temperature[6]. The electroformate containing the GUVs was then aliquoted into a number of glucose solutions that were within a few milli-osmolar of the 100mM sucrose solution found inside the vesicles. For instance, the 100 mM sucrose electroformate might be diluted into aliquots of 96, 98, 100, 102, 104, 106, 108, and 110 mM glucose solutions at a dilution of $\sim 1:100$ sucrose:glucose (v/v). A range of sugar dilutions, and hence a range of membrane tensions, is employed because precise control of the osmolar gradients between the inside and outside of the vesicle is not possible. This lack of fine osmolar control is due to measurement

[6] See the protocol in Appendix E.

errors in the sugar concentrations at the millimolar level and more importantly there is evaporation occurring during the electroformation and handling that causes slight variations in sugar concentration. Each of these aliquots would then be examined under epi-fluorescence to determine which had yielded the proper osmolar gradient and membrane tension, as determined by the resulting morphologies (*i.e.* many aliquots have vesicle tensions too high to observe dimpling or budding).

Even with the composition controlled and the tension roughly dictated by the osmolar gradient, individual vesicle composition varies and the thermal history plays a part in the observed phase behavior. Key to observing the described morphologies is a degree of control over the thermal history of any one vesicle. Above the de-mixing transition temperature, the membrane is a homogeneous mix of the three molecular components and hence there are no domains. The precise conditions under which phase separation occurs have some variance from one preparation to another [268, 130], but once the transition has occurred we consistently observe the same types of domain morphologies and qualitative kinetics, as shown in Fig. 4.26. Using a custom built, electronically controlled microscope temperature stage, we were able to dynamically control the temperature of the sample. Our best results occurred when we 'rapidly' decreased the temperature (~ -10 K/min) through the transition temperature, but avoided the formation of a gel phase; the gel phase yields distinctly different morphologies and dynamics, a topic of interest on its own.

4.8 Error Introduced by the Curved Vesicle Surface

Giant unilamellar vesicles are an intrinsically curved surface, whose geometry leads to distortion of distance measurements in the image plane. Measurements of domain interaction are taken at the top or bottom of vesicles where the surface is nearly flat, and hence the measured distance is minimally distorted. However, we can estimate the severity of distance distortion by considering the error introduced by the curvature of the vesicle surface relative to the projected (*i.e.* 2D) image plane. The function $f = \sqrt{R^2 - (x_1^2 + x_2^2)}$ is the hemi-spherical height function specifying the position of the vesicle surface relative to the flat image plane, R is the vesicle radius, and x_i are the Cartesian coordinates in the image plane. The distance between any two points on the vesicle surface is specified by the 'great' circle that connects those two points. This has a particularly simple interpretation in the case of a sphere; the geodesic is a circle that intersects the two points of interest and whose center is common with the sphere. Thus given two domains of interest, whose image plane positions are $(x_1^{(j)}, x_2^{(j)})$, we define their spherical unit vectors by

$$\hat{r}_j = \left[\frac{x_1^{(j)}}{R}, \frac{x_2^{(j)}}{R}, \sqrt{1 - \left(\left(x_1^{(j)}/R \right)^2 + \left(x_2^{(j)}/R \right)^2 \right)} \right], \tag{4.236}$$

with the origin at the sphere's center. The resulting geodesic distance on the vesicle surface is given by

$$l_{\text{act}} = R \cos^{-1}(\hat{r}_1 \cdot \hat{r}_2). \tag{4.237}$$

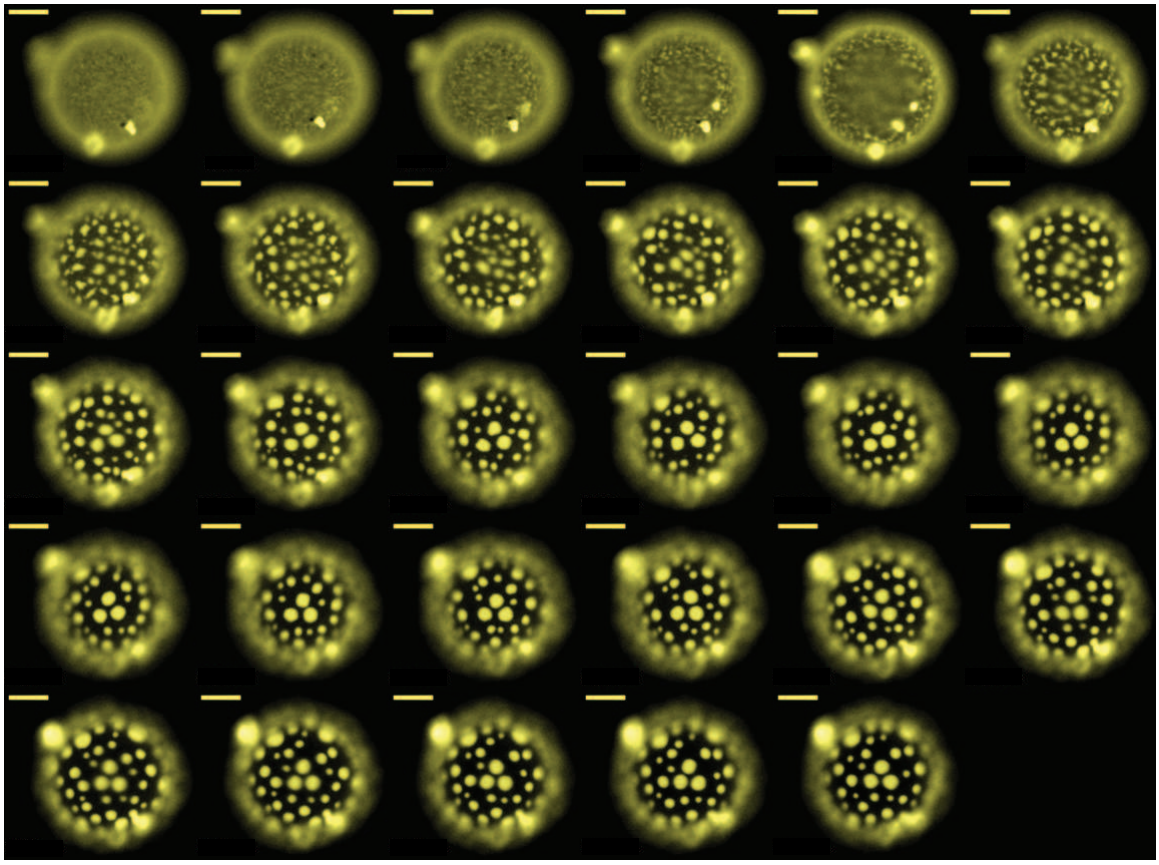

Figure 4.26: Lipid phase separation and domain formation. A multi-component GUV is driven through the de-mixing transition by a reduction in temperature to form discrete domains, via a process analogous to spinodal decomposition. The time between frames is $1.6\,s$. The domains are fluid, circular, and many are of the dimpled morphology. Due to the stochastic nature of their formation, the domains cover a range of sizes; the observed distribution of domain sizes persists (with the occasional coalescence event) on the time-scale of an hour or more, which is much longer than the minute time-scale for full phase separation on a higher tension GUV. The radial distribution function of domains on this vesicle would yield a measure of the potential of mean force between domains. The scale bars are 10μm.

The error in distance measurement between any two points on the vesicle is

$$m = \frac{l_{\text{act}} - l}{l_{\text{act}}}, \tag{4.238}$$

where l is the measured distance (*i.e.* distance in the image plane), with the explicit formula

$$l = \sqrt{(x_1^{(1)} - x_1^{(2)})^2 + (x_2^{(1)} - x_2^{(2)})^2}. \tag{4.239}$$

For the purposes of estimation and formulaic simplicity, we derive a simple formula for the error as measured from the projected vesicle center, where we use the azimuthal symmetry and integrate the error explicitly to find

$$m = 1 - \frac{l/R}{\cos^{-1}\left(\sqrt{1 - \left(\frac{l}{R}\right)^2}\right)} \simeq \frac{1}{6}\left(\frac{l}{R}\right)^2. \tag{4.240}$$

The dimensionless quantity $l/R \in [0 \ldots 1]$ quantifies how far a domain is from the projected vesicle center. The maximum possible error occurs when we measure from the image plane center to a point on the equator of the sphere ($l/R = 1$), resulting in an underestimate of $\sim 36\%$ (exactly $1 - 2/\pi$) in the measured distance. If we demand that at most a 10% error in distance measurement is acceptable, this constrains our measurements to be within a circle of radius $l/R \simeq 0.71$. This calculation gives an estimate of the error in distance measurement, but in reality, the exact error introduced by the surface curvature is a complicated function of the precise positions of each domain relative to the center of the spherical vesicle.

Let us do a sample calculation to make a more concrete connection to our experiments. Given a nominal vesicle size of $R = 15\mu$m, we should be able to measure out to approximately $l = 10.6\,\mu$m from the projected vesicle center with an error in distance measurement of less than 10%. On the surface of the sphere, this maximum allowed l would correspond to a change in the vesicle height of $\sim 4.4\,\mu$m. The depth-of-field of our 20x objective is about $\sim 4\mu$m (a 4x multiplier tube on the camera effectively increases the magnification to 80x without changing the depth-of-field).

Our domain tracking software was written to reject domains which appeared out of focus and/or distorted from a circle, as discussed in section 4.10. Hence, if we ensure that the top (or bottom) of the vesicle is in focus, domains which break our 10% error condition are rejected. The exact numbers will change with different sized vesicles, but due to the fact that a larger vesicle is relatively flat over a larger area, this model calculation shows that for any vesicle $R \gtrsim 15\,\mu$m our software automatically rejects domains that do not meet the error criteria.

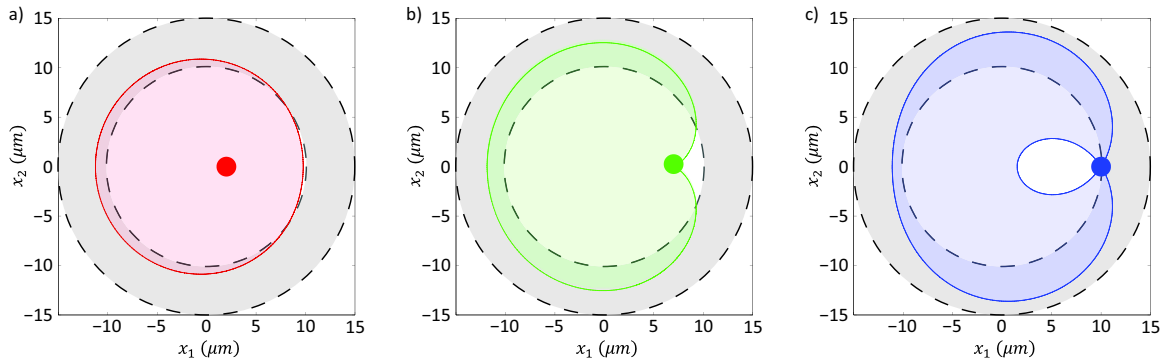

Figure 4.27: Examining spatial regions of acceptable distance measurement error. In all plots, the outer dashed line shows the projected equator of a vesicle with $R = 15\,\mu$m, and the region defined by the inner dashed line is where the depth-of-field of the objective will show domains in focus; the grey region will be out of focus. In all plots, the domain radius is $r = 1\,\mu$m. a) A domain is placed at $x_1 = 2\,\mu$m and $x_2 = 0\,\mu$m; other domains that lie inside the red region have a measured distance error of less than 10%. b) A domain is placed at $x_1 = 7\,\mu$m and $x_2 = 0\,\mu$m; other domains that lie inside the green region have a measured distance error of less than 10%. c) A domain is placed at $x_1 = 10\,\mu$m and $x_2 = 0\,\mu$m; other domains that lie inside the blue region have a measured distance error of less than 10%. In (b) and (c) the smaller white regions indicate regions of measurement error greater than 10%.

4.9 *In vitro* Selection and Representative Data

In this section, we describe: how we chose vesicles for data collection and analysis, some of the common problems with selecting vesicles and collecting data, and the generic quality of collected data.

After the formation of multi-component GUVs, the raw solution of vesicles is diluted in an osmolar-balanced glucose solution to roughly regulate the membrane tension, as discussed in Section 4.7. A viewing chamber is created using two #1 cover-slips with an O-ring between them, loaded with $\sim 135\,\mu$l of the osmolar balanced vesicle solution. Small density gradients between the glucose outside and sucrose inside the vesicles sediment them toward the bottom of the chamber, where the dilution ratio is adjusted such that there is a single, sparse layer of vesicles (*i.e.* no stacked vesicles). In all the data shown here, the vesicles were close to the glass substrate (roughly within a vesicle radius), but had a small z-displacement between the substrate and the lower focal plane of the vesicle, indicating that the vesicles were not resting directly on the substrate. At approximately 1 cm in diameter, the viewing chamber is small enough that we can scan the entire chamber, examining hundreds of vesicles relatively quickly.

Within a single field of view we look for vesicles that meet the following criteria:

- Vesicle size needs to be large enough that we can clearly resolve domains, given the optical limits of the microscope, and large enough that there is an appreciable area of the vesicle at the top or bottom where we can approximate the surface as flat (see Section 4.8). This usually corresponds to vesicles with a radius greater than $\sim 10\,\mu$m.

- Vesicles need to be 'clean', by which we mean the vesicle itself does not have any obvious tubes, protrusions, or internal structures attached to it, nor should it have other vesicles nearby obstructing the view of the image plane or excessively polluting the image with light from outside the image plane.

- While we have recorded vesicles with domains of a wide distribution of sizes, we prefer vesicles whose domain sizes are in a narrower range, usually with a standard deviation half the mean size. In cases where we want to observe many closely interacting domains, or disperse domains, the interaction potentials tend to be less noisy the narrower the distribution of domain sizes. See the following paragraphs and Section 4.6.2 for more discussion of domain size asymmetry.

- Slight thermally-driven fluid flows in the chamber can cause vesicles to drift in the image plane, and beyond a certain drift speed ($\sim 10\,\mu\text{m}/s$) it becomes impractical to follow even the best vesicles that meet the above criteria. That said, most vesicles are quite stationary in the image plane, with drift speeds of only a few microns per minute.

Figure 4.28 shows a typical microscope view from which vesicles would be chosen for data collection, and subsequent analysis.

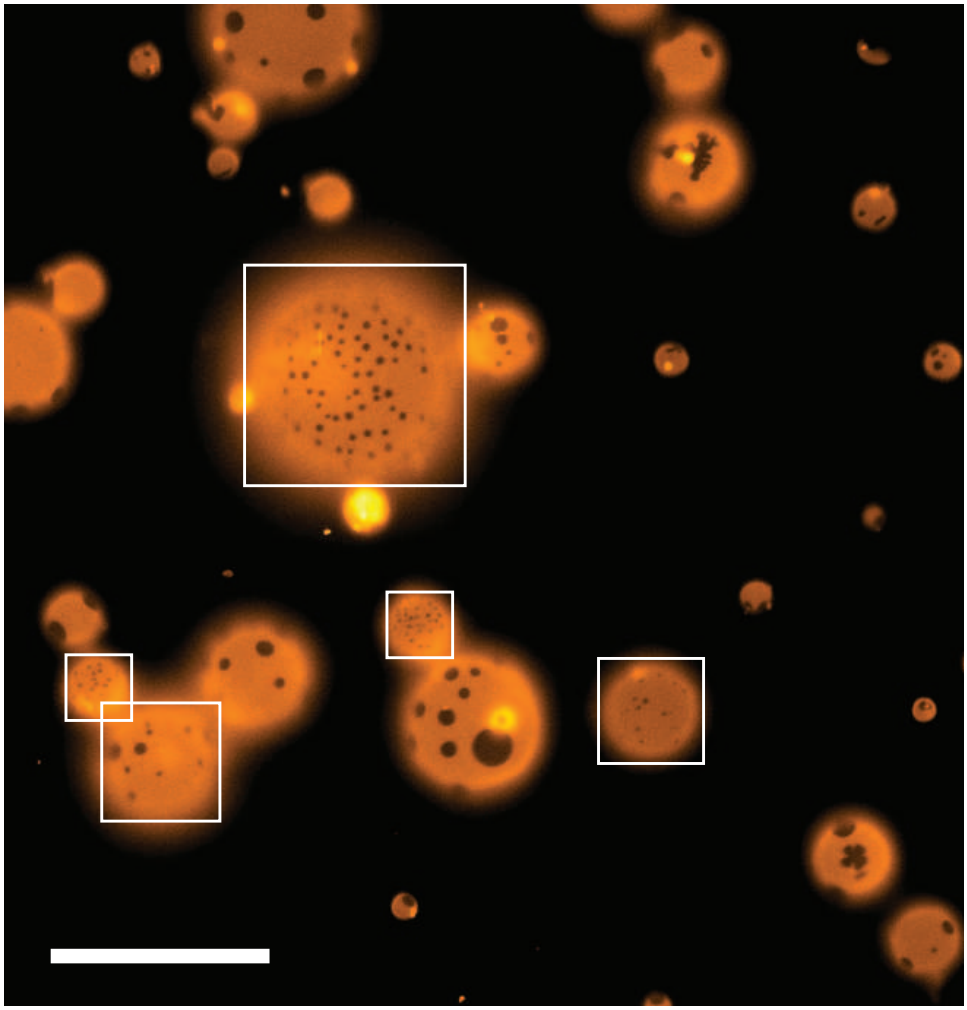

Figure 4.28: A typical view of phase-separated GUVs in the TRITC fluorescence channel. This field of view is at 20X magnification, though most measurements were taken at 80X. This particular combination of field of view and membrane compositions shows dark domains in a light surrounding membrane. The white squares outline vesicles from which data would likely be collected. The scale bar is 50 μm.

Rather than offer our own subjective interpretation of data quality, we present a subset of the 29 total data sets that have a relatively low areal density of domains, showing the range from very poor data sets up to what we consider very good data sets. We classify a good data set solely in terms of the noise characteristics of the interaction potential. Data sets with low noise, whose potentials are relatively smooth, have well-resolved features and are considered to be of the highest quality. Generally, the noise is related to the chosen spatial resolution of the potential; increased spatial resolution decreases the number of events in each bin of the histogram and hence lowers the signal to noise ratio. Higher levels of noise in the interaction potential also arise from a vesicle whose domains have a widely varying size distribution, as demonstrated in Fig. 4.31. The qualitative explanation of the correlation between increasing width of the domain area distribution and increasing noise in the measured potentials is as follows: if all domains are the same size, then the pairwise potential describing the interaction between each unique domain pair has the same scaling factor (*i.e.* eqn. 4.219), and hence each measurement of a pairwise distance is essentially sampling from the same underlying distribution, thus the signal to noise ratio is high. On the other hand, if all the domains are different sizes, the scaling factors of the potentials associated with each unique domain pair are different, hence each measurement of a pairwise distance is sampling from the distribution describing only that pair's interaction. All those measurements, describing distinct pairwise interactions, are then combined to form the potential of mean force, however, being made up of a large number of slightly different pairwise potentials, the potential of mean force has lower signal to noise.

The only degree of subjectivity that we will add is a classification system where data sets will be put into one of three categories according to the quality of their interaction potentials: good (Fig. 4.29), fair (Fig. 4.30) and poor (Fig. 4.31). In the following figures we give two examples of each type of data set, and state how many data sets fall within each classification. For each data set we show a plot of the raw, uncorrected histogram of domain positions, the raw and corrected potentials resulting from that histogram, a histogram of the number of domains found in each frame, and a histogram of the identified domain areas. A clear correlation exists between vesicles whose domains have a wide size distribution and interaction potentials with higher noise, as demonstrated in the figures.

4.10 Domain Tracking and Data Analysis

Having established that we can measure distances between domains in the image plane to within a reasonable error tolerance, we are in a good position to begin transforming images into quantitative data. After a suitable vesicle has been chosen, images are collected in the form of 16 bit TIFF stack image files. Each stack contains ~ 500 to 1500 frames collected at a rate such that diffusion allows the domains to explore their local configuration space during the course of the video — a typical time scale is 50 – 200 ms between frames. If the domain density is approximately constant

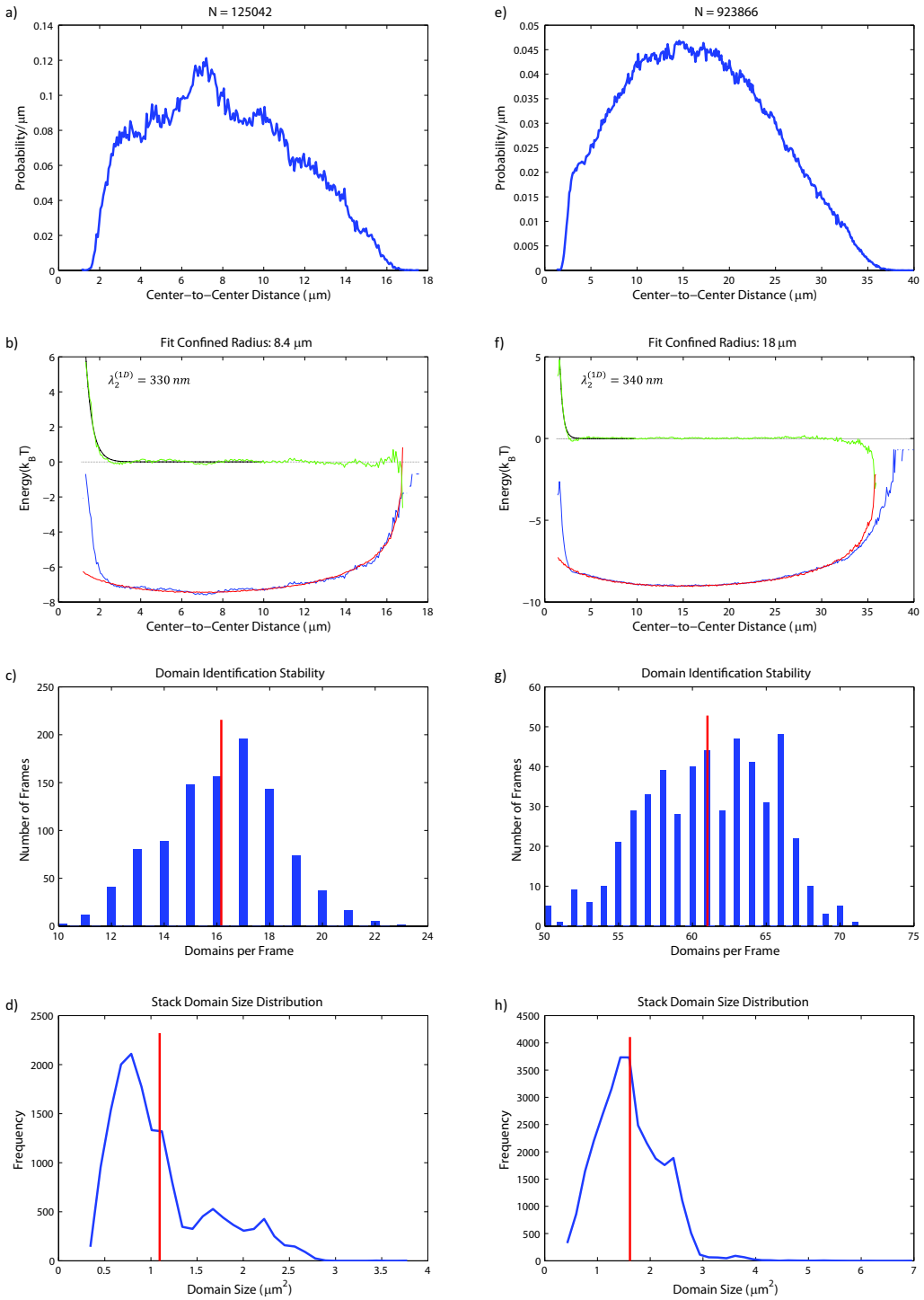

Figure 4.29: Representative 'good' quality domain interaction data. Each column represents a unique 'good' quality data set, in total 12 of 29 data sets. Plots (a) and (e) show the raw distribution of domain distances, where N is the total number of unique distances measured. Plots (b) and (f) show the raw (blue), fictitious (red), and corrected (green) potential of mean force. The black line is a fit to eqn. 4.214, with the length scale indicated on the graph, corresponding to $\tau \simeq 2 \times 10^{-4}\, k_B T/\mathrm{nm}^2$ with $\kappa_b = 25\, k_B T$. Plots (c) and (g) are histograms of the number of domains identified in each frame. Plots (d) and (h) are the distribution of domain areas throughout the stack. In (c), (d), (g) and (h) the red line is the mean.

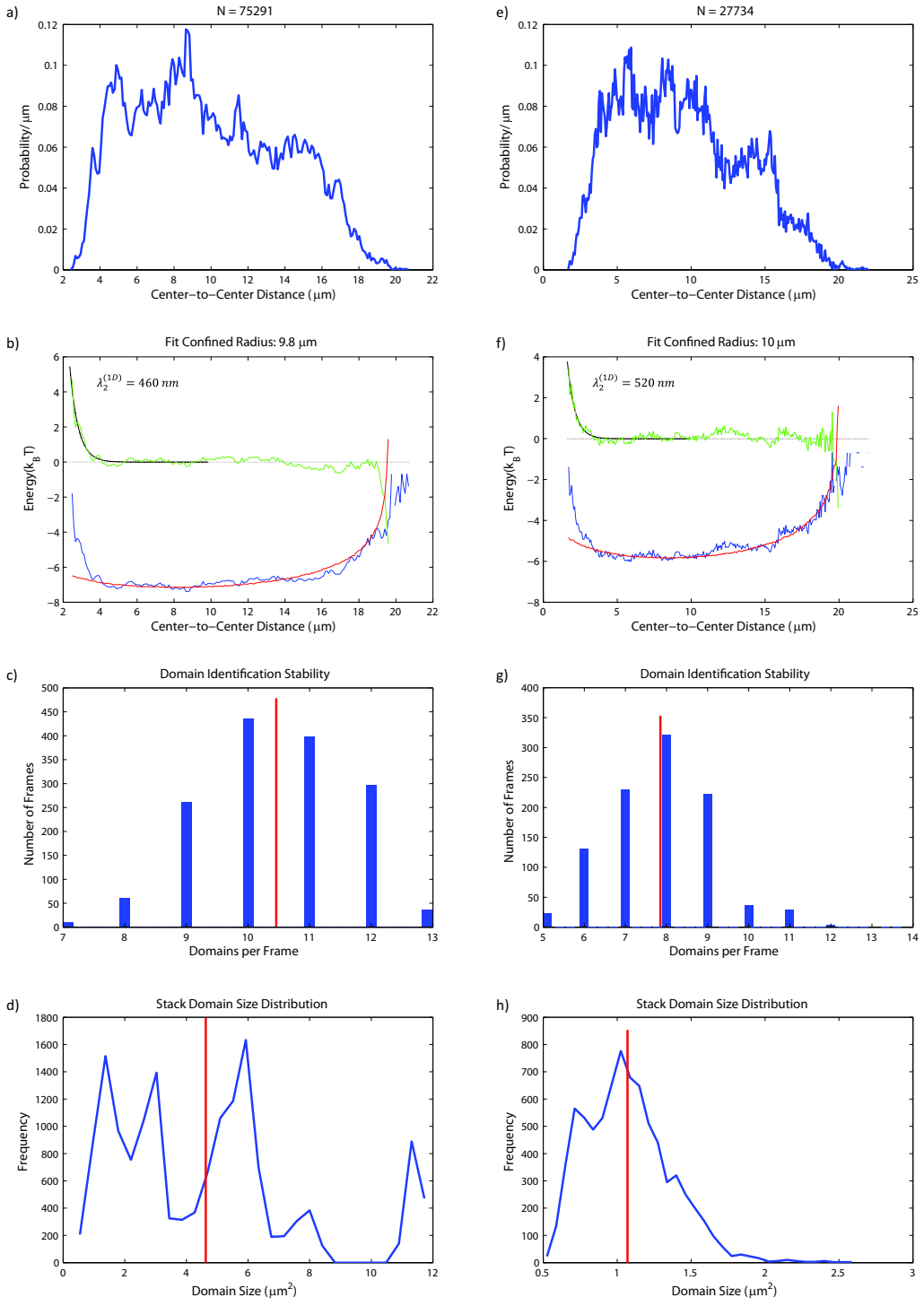

Figure 4.30: Representative 'fair' quality domain interaction data. Each column represents a unique 'fair' quality data set, in total 6 of 29 data sets. Plots (a) and (e) show the raw distribution of domain distances, where N is the total number of unique distances measured. Plots (b) and (f) show the raw (blue), fictitious (red), and corrected (green) potential of mean force. The black line is a fit to eqn. 4.214, with the length scale indicated on the graph, corresponding to $\tau \simeq 1 \times 10^{-4}\, k_B T/\mathrm{nm}^2$ with $\kappa_b = 25\, k_B T$. Plots (c) and (g) are histograms of the number of domains identified in each frame. Plots (d) and (h) are the distribution of domain areas throughout the stack. In (c), (d), (g) and (h) the red line is the mean.

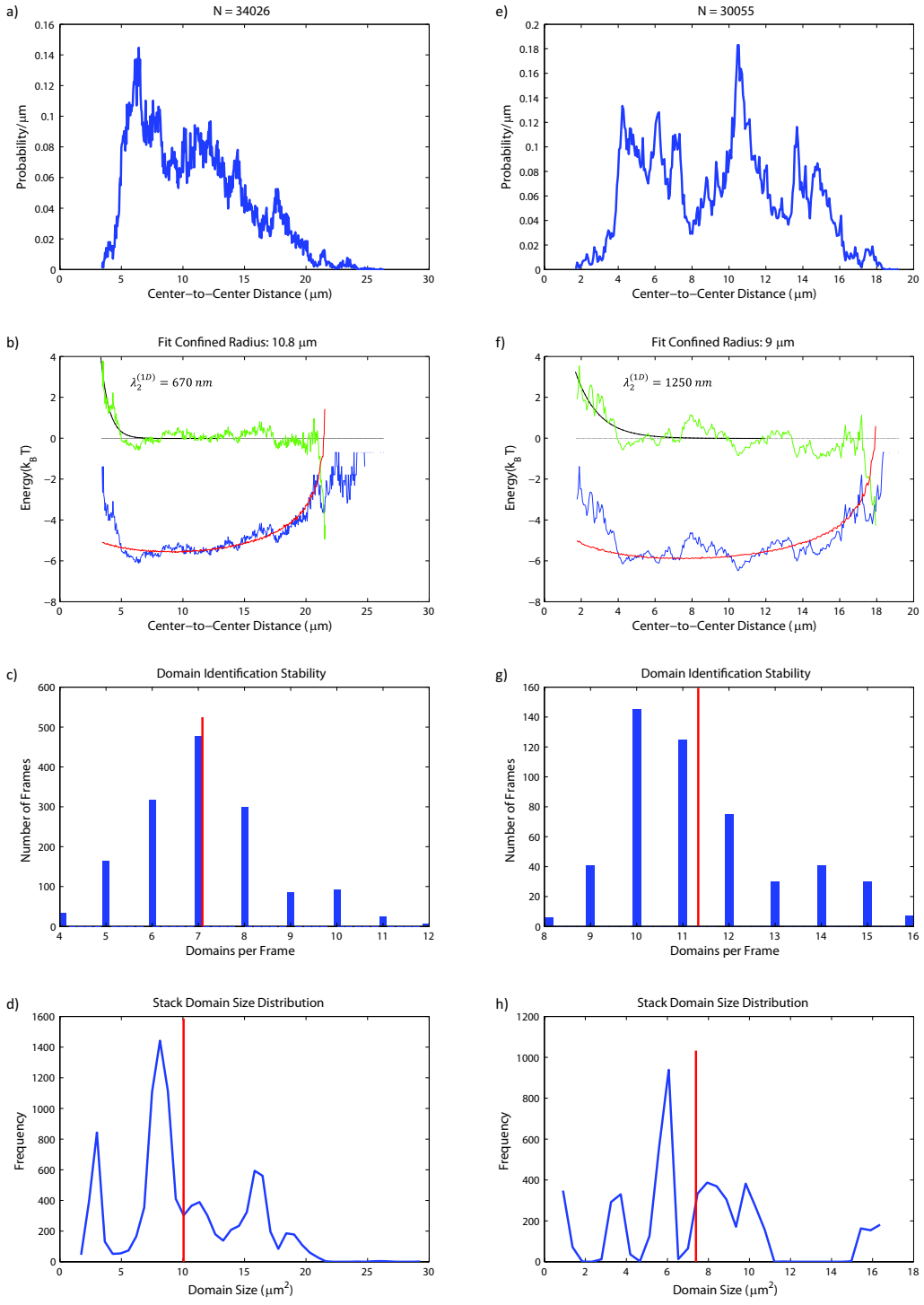

Figure 4.31: Representative 'poor' quality domain interaction data. Each column represents a unique 'poor' quality data set, in total 11 of 29 data sets. Plots (a) and (e) show the raw distribution of domain distances, where N is the total number of unique distances measured. Plots (b) and (f) show the raw (blue), fictitious (red), and corrected (green) potential of mean force. The black line is a fit to eqn. 4.214, with the length scale indicated on the graph, corresponding to $\tau \simeq 4 \times 10^{-5}\, k_B T/\mathrm{nm}^2$ with $\kappa_b = 25\, k_B T$. Plots (c) and (g) are histograms of the number of domains identified in each frame. Plots (d) and (h) are the distribution of domain areas throughout the stack. In (c), (d), (g) and (h) the red line is the mean.

during the stack collection, then the system is in quasistatic equilibrium, and time ordering of the frames is not necessary. Thus any software that identifies domains need only calculate the distances between domains in each frame, and combine data from all frames to construct a radial distribution function for the entire stack - tracking domains through time gives no additional information for the purposes of our measurement.

Regarding the 'nuts-and-bolts' level of image processing required to construct the radial distribution function, each image progresses through three phases of processing: i) background removal and contrast adjustment, ii) edge detection and brightness filtering, and iii) morphological selection. Each of these phases has a number of parameters that may be tuned to best fit a particular data set. The rest of this section discusses each phase in some detail.

It is often easier to process data sets where the vesicles are stationary and closely cropped to the total image size. We wrote a separate piece of software that translates a vesicle to be stationary in time - many data sets require such alignment.

Background removal and contrast adjustment are not required to process a stack, however, they help compensate for brightness changes due to photo-bleaching, and can enhance contrast between a domain and its background, thereby making edges easier to find. For each data set, we employ one of two methods. The first method, which is more manual but generally yields better results, is outlined in Fig. 4.32. The second method is more automated, using so-called 'adaptive' contrast adjustment, briefly:

- a square tile size of $n \times n$ pixels is chosen such that the tile fully encompasses a domain and its local background
- the image is divided into regions of that tile size and the contrast in each region is enhanced according to standard histogram equalization
- each tile is then bilinearly interpolated with the neighboring tiles to prevent fictitious edges

In regions of the image where no domain is present, the adaptive contrast adjustment enhances the noise, but such regions neither pass the brightness nor morphological criteria. The tile size is the only user-specified parameter in this stage of domain tracking. The contrast-adjusted image from either method is then passed onto the second stage of the algorithm — edge detection and brightness filtering.

The well-known and robust *Canny* edge detection algorithm [269], as implemented in MatLab©, is used to find domain edges in the contrast-adjusted images, whether the domains are bright in a dark background or dark in a bright background. The edge detection algorithm requires three user-specified parameters to find edges, however those parameters need little tuning between data sets. Our software only examines 'connected' objects as potential domains, thus if an edge is found it must topologically make a circle to be examined further. Once the edge detection has found a topologically circular element, it examines that element to determine if it has the correct general

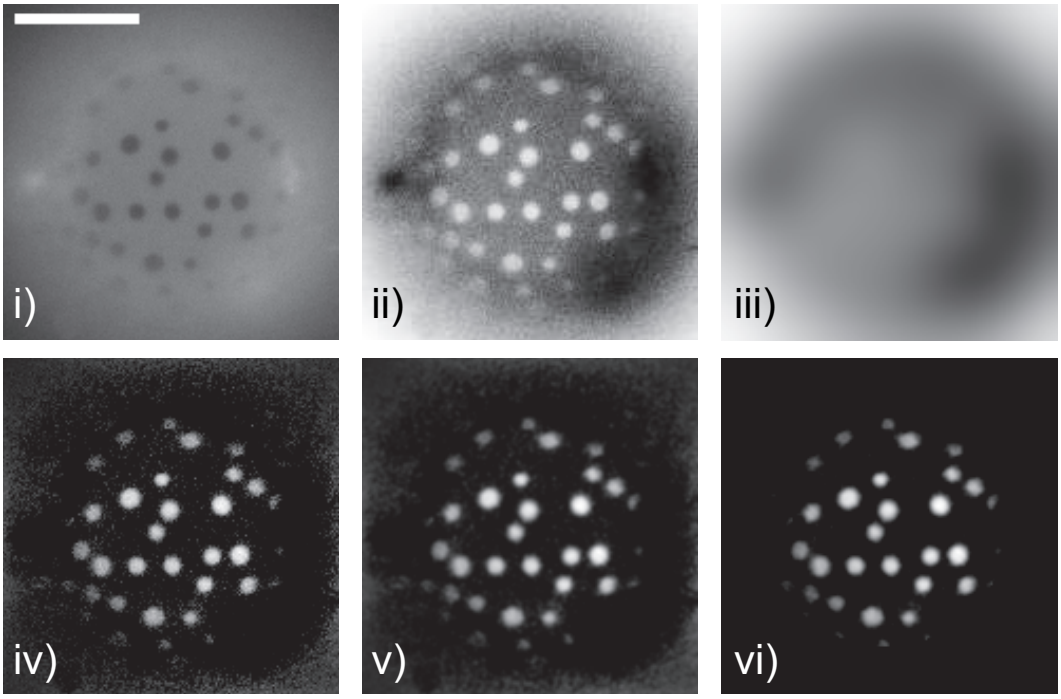

Figure 4.32: Example of manual background removal and contrast adjustment. i) The raw fluorescence image; in this case dark domains in a light background, but the method also applies to reverse contrast vesicles. ii) Inverted (i) and contrast maximized by 0.5% histogram thresholding. iii) Gaussian blur of (ii) using a 30 pixel radius. iv) Subtraction of (iii) from (ii), essentially removing background and increasing the signal-to-noise of the domains. v) Gaussian blur of (iv) using a 1 pixel radius - this decreases high frequency noise that can trigger the edge detection algorithm without sacrificing spatial resolution. vi) Finally, spatially irrelevant intensities are removed and the stack contrast is adjusted. The scale bar is 20 μm.

brightness features — for instance, a light domain in a dark background should be brighter at its center than in the transition zone at the domain edge. The user specifies a cut-off for the ratio of the edge-to-center brightness, thereby allowing the edge detection algorithm to be promiscuous in what edges it detects and connects into circles. Those circular elements are then checked against the relevant edge-to-center brightness cut-off; only connected objects that meet the criterion are queried in the next stage for their morphological properties.

Once topologically circular objects have been found that meet the brightness criterion, they must also have roughly the correct shape, namely a circle. There are many ways to measure how much a given shape deviates from a circle; our software uses the dimensionless measure of the square of the perimeter length divided by the area, $\ell^2_{\text{perim}}/4\pi A$. Using this measure a perfect circle has a value of 1, and higher values correspond to less circular objects. The user specifies a cut-off above which the object is rejected. There are two main reasons why a domain might appear acircular. First, it could be that the domain is in focus but is near the vesicle equator, and hence lies in a region where its projection is elliptical and thus our distance measurement error is too high. Second, it could be that the domain is partially out of focus, such that the point-spread-function of the microscope warps the shape into something acircular. These domains would not have a well-defined center, and hence might also break our error tolerance criterion. For domains near the equatorial regions of the vesicle, these effects often occur simultaneously. The final morphological criterion is that any putative domain must lie within a certain reasonable size range, the minimum and maximum of which is specified by the user. For instance, a putative domain with an area of only a few pixels or an area approaching the size of the entire vesicle would likely be rejected for being too small or too large, respectively.

Any object that has passed through these three stages is then considered a well-resolved domain. Each domain's center is then identified by a simple first-moment calculation, and the centers are used to calculate the pairwise distances in each image. The pairwise distance data from the entire stack is then combined and binned into a probability distribution for the separation of two domains. The natural logarithm of that probability distribution is then the potential of mean force between domain pairs. Figure 4.33 shows a screen-shot of the program after a data set has been processed.

4.10.1 The Fictitious Confining Potential

Extracting the interaction energy from the statistical distribution of distances between domains is not entirely straightforward. As we have just shown, we can reasonably assume that the surface is flat in our measurements, and hence the actual distances we measure are not severely distorted. However, there is also an effect coming from the circular geometry of our measurement. More specifically, all of the domains the software detects are confined to lie in a circle of some effective radius (R_{fict}), smaller than the radius of the vesicle (R). This means that any two domains we detect will be maximally separated by $2R_{\text{fict}}$. When making a histogram of the pairwise distance data, we never detect two domains farther apart than this distance, and thus it appears there is a

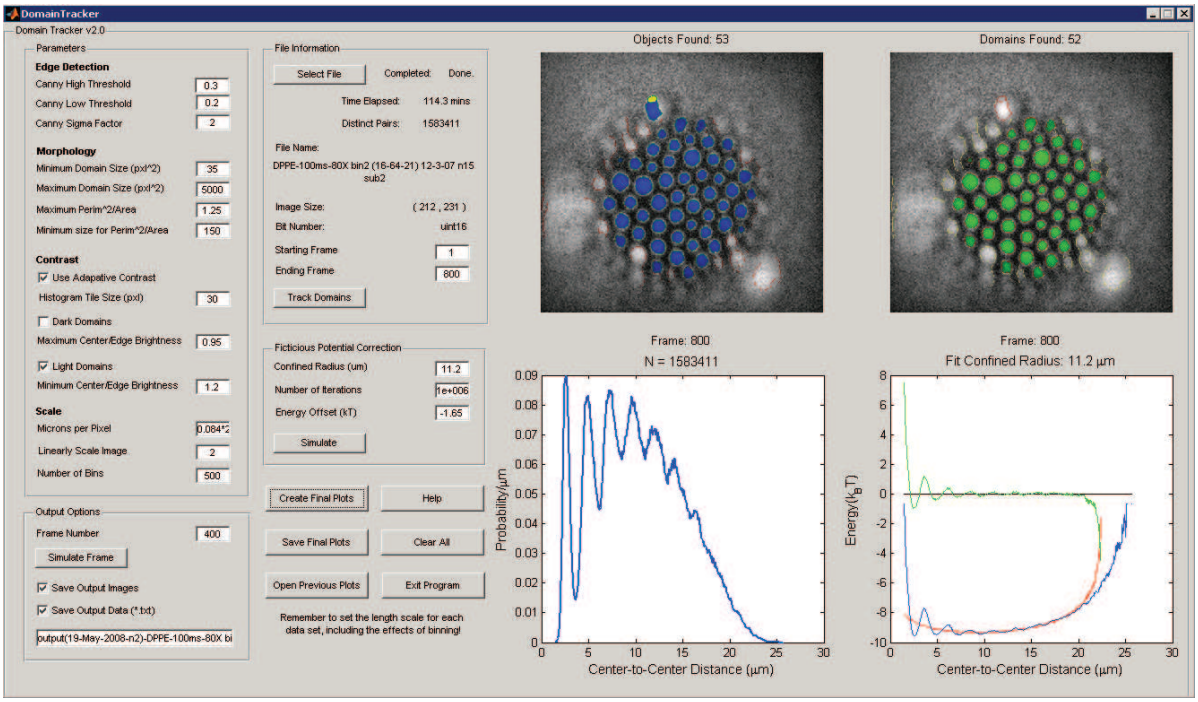

Figure 4.33: Screen shot of the domain tracking software. Parameters for contrast adjustment, edge detection, brightness, and morphological criteria are entered on the left. The top left graph shows connected-edge objects that have met the brightness criterion in blue (failed in yellow). The top right graph shows in green the subset of blue objects which have also met the morphological criteria. The lower left graph is the radial distribution function for the entire stack. The lower right graph is the natural logarithm of that probability distribution (in blue), the simulated fictitious potential (in red), and their difference — the potential of mean force (in green).

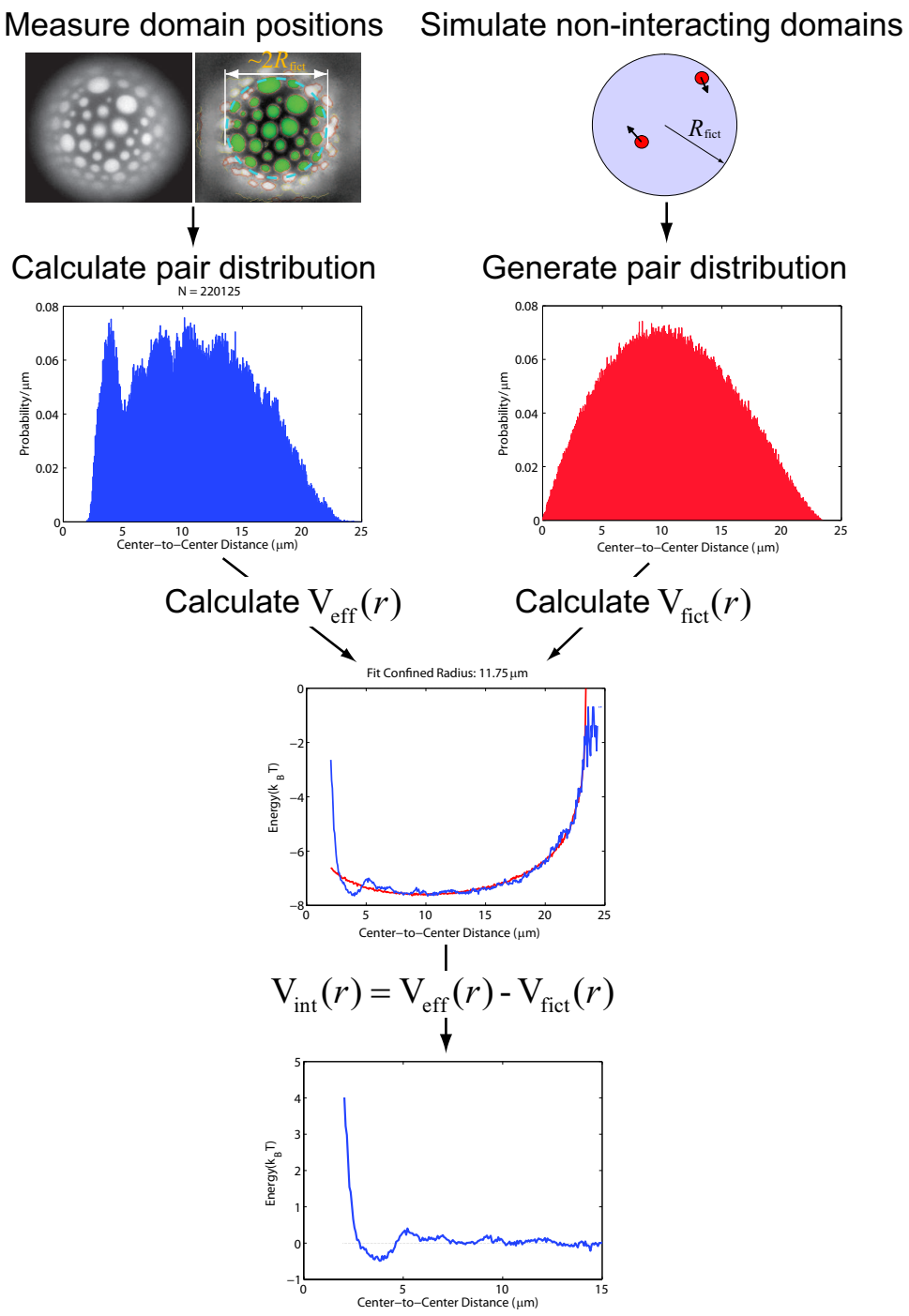

Figure 4.34: Flow diagram explaining how the fictitious potential is removed from measured data. The positions of well-resolved domains are measured, the radial distribution function is generated, and the effective potential between the domains is calculated as the blue line. Simultaneously, the radial distribution function for two non-interacting domains in a user-defined circle of radius R_{fict} is generated, and the corresponding fictitious potential is calculated as the red line. Subtracting the fictitious potential from the effective potential leaves only the potential of mean force, $V_{\mathrm{int}}(r)$. Intervals of r with very low statistics are excluded.

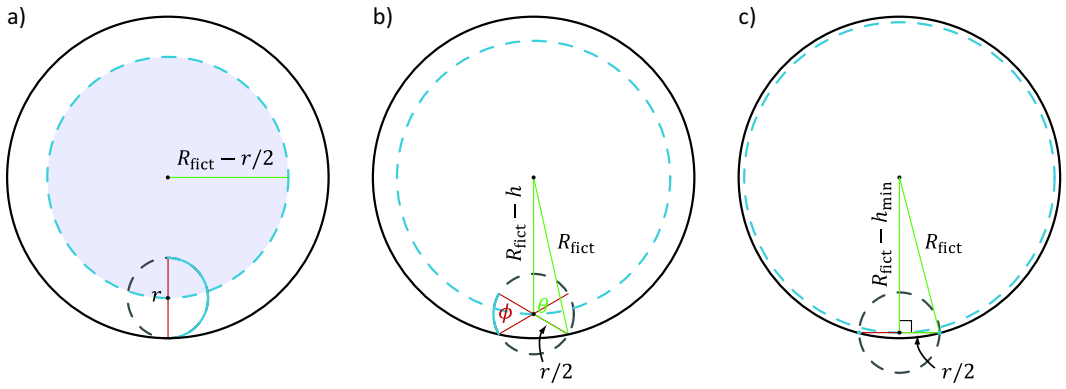

Figure 4.35: Geometric relationships for the analytical calculation of the fictitious potential. a) This schematic shows the first contribution to the density of states, $P_1(r)$. Two points separated by a distance r, as shown by the red line, sweep out π radians for every point in the gray region, contributing a statistical weight proportional to the product of the area of the gray region and the length of the solid blue line. b) This schematic shows the second contribution to the density of states, $P_2(r)$. If the points lie outside of the gray region in (a), the density of states for a given value of h is proportional to the product of the length of the dashed blue line and the solid blue line. Then all such contributions for $h \in [h_{\text{min}} \ldots r/2]$ must be summed. c) This schematic shows the geometric origin of the minimum height, h_{min}, as a function of the separation r.

strong confining potential keeping all domains within $2R_{\text{fict}}$ of each other. The actual interaction energy we measure is the sum of this fictitious confining potential, $V_{\text{fict}}(r)$, and the real interaction potential, $V_{\text{int}}(r)$,

$$V_{\text{eff}}(r) = V_{\text{int}}(r) + V_{\text{fict}}(r). \tag{4.241}$$

The fictitious confining potential can be easily simulated via Monte Carlo methods. Given a circle of radius R_{fict}, we generate a uniform distribution of points within the circle and calculate the radial distribution function as shown in the upper right of Fig. 4.34. The negative natural logarithm of this distribution is $V_{\text{fict}}(r)$. All that remains is to pick a proper R_{fict} for a given data set; that is, to isolate the correct interaction potential there is one fit parameter for each data set. An example of processed data is shown in Fig. 4.34.

4.10.2 The Geometric Derivation

Given certain constraints of our analysis software, it is often quicker to generate the fictitious potential via Monte Carlo methods, though in this section we will show a geometric derivation that leads to a closed form expression for the fictitious potential. A key result is that the fictitious potential for any value of R_{fict} is simply a scaled version of the same underlying function.

As we have shown previously, the measured potential of mean force is the sum of the interaction potential and the fictitious potential, which, in terms of the underlying probability distributions

can be written as

$$V_{\text{eff}}(r) = -\ln\left[P_{\text{int}}(r)\cdot P_{\text{fict}}(r)\right], \tag{4.242}$$

where the distribution $P_{\text{fict}}(r)$ is somehow related to the geometry of the space available to two non-interacting domains, essentially 'counting' up the number of states with a separation r. This geometric relationship can be found exactly for a circle as follows. First, consider two points a distance r apart connected by a line segment, whose center lies at some position inside the circle defined by $(R_{\text{fict}} - r/2)$ as shown in Fig. 4.35a. For every point inside this region we can rotate the line segment about its center point to find the density of states with separation r, where the rotation is restricted to π radians to avoid double counting. We refer to this contribution to $P_{\text{fict}}(r)$ as

$$P_1(r) = \underbrace{\pi\frac{r}{2}}_{\text{rotation}}\cdot\underbrace{\pi\left(R-\frac{r}{2}\right)^2}_{\text{region area}}. \tag{4.243}$$

For those states with separation r whose connecting line segment has its center outside the region defined by $(R_{\text{fict}} - r/2)$ not all rotations of the line segment are available. Referring to Fig. 4.35b, the rotation of the line segment is now defined by the angle ϕ, which depends on the distance, h, from the outer circle, R_{fict}. Determining this angle is then only a matter of geometry, where using the law of cosines and the fact that $\phi = 2\theta - \pi$, one finds

$$\phi(\bar{r},\bar{h}) = 2\cos^{-1}\left[\frac{(1-\bar{h})^2 + (\bar{r}/2)^2 - 1}{\bar{r}(1-\bar{h})}\right] - \pi, \tag{4.244}$$

where for ease of notation we now define $\bar{r} = r/R_{\text{fict}}$ and $\bar{h} = h/R_{\text{fict}}$. Then for each value of h the density of states with rotation ϕ and separation r is simply the product of $r/2$, the angle ϕ, and the circumference of the circle defined by $(R_{\text{fict}} - h)$, as shown by the dashed blue line in Fig. 4.35b. Summing these contributions for all available values of h we find the second contribution to $P_{\text{fict}}(r)$,

$$P_2(r) = \int_{h_{\min}(r)}^{\frac{r}{2}} \underbrace{2\pi(R_{\text{fict}}-h)}_{\text{circumference}}\underbrace{\frac{r}{2}\phi(r,h)}_{\text{rotation}}\,\mathrm{d}h. \tag{4.245}$$

For a given value of r there is some value of h below which there are no available states, or in other words $\phi = 0$, as shown in Fig. 4.35c. This value can be found by solving $\phi = 0$ for $\bar{h}$ giving

$$\bar{h}_{\min} = 1 - \sqrt{1-\left(\frac{\bar{r}}{2}\right)^2}. \tag{4.246}$$

Then the total density of states for a separation $\bar{r}$ is given by the sum

$$P_{\text{fict}}(\bar{r}) = \frac{1}{a}(P_1(\bar{r}) + P_2(\bar{r})) = \frac{\pi R_{\text{fict}}^3}{a}\left[\pi\frac{\bar{r}}{2}\left(1-\frac{\bar{r}}{2}\right)^2 + \int_{\bar{h}_{\min}}^{\frac{\bar{r}}{2}}(1-\bar{h})\bar{r}\phi(\bar{r},\bar{h})\mathrm{d}\bar{h}\right], \tag{4.247}$$

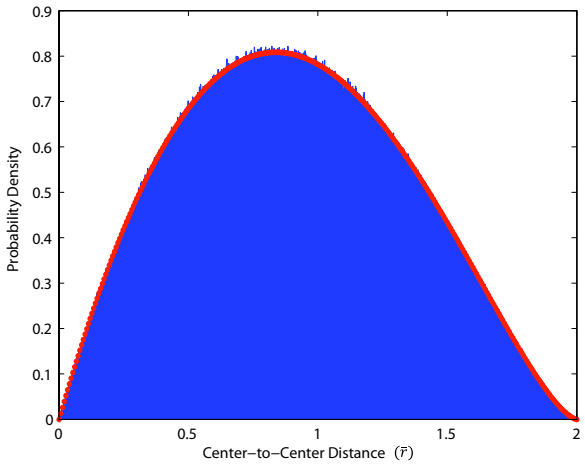

Figure 4.36: Comparison of the fictitious radial distribution function from analytical and Monte Carlo methods. The fictitious radial distribution function generated by Monte Carlo methods is shown in the blue histogram, while the distribution calculated from $P_{\text{fict}}(\bar{r})$ is shown by the orange points, both plotted as a function of the point separation $\bar{r}$.

where a is a normalization constant defined by

$$a = \pi R_{\text{fict}}^3 \int_0^2 \left[\pi \frac{\bar{r}}{2} \left(1 - \frac{\bar{r}}{2}\right)^2 + \int_{\bar{h}_{\min}}^{\frac{\bar{r}}{2}} (1 - \bar{h}) \bar{r} \phi(\bar{r}, \bar{h}) \mathrm{d}\bar{h} \right] \mathrm{d}\bar{r}. \tag{4.248}$$

Then finally, the properly normalized distribution is

$$P_{\text{fict}}(\bar{r}) = \nu \left[\pi \frac{\bar{r}}{2} \left(1 - \frac{\bar{r}}{2}\right)^2 + \int_{\bar{h}_{\min}}^{\frac{\bar{r}}{2}} (1 - \bar{h}) \bar{r} \phi(\bar{r}, \bar{h}) \mathrm{d}\bar{h} \right] \tag{4.249}$$

where $\nu \simeq 2.4675$ and $P_{\text{fict}}(r) = P_{\text{fict}}(\bar{r})/R_{\text{fict}}$. Fig. 4.36 compares this analytical result to the fictitious radial distribution function generated by Monte Carlo methods, showing excellent agreement between the two methods. Additionally, this analytical result shows that the fictitious radial distribution function for any value of R_{fict}, is simply a scaled version of $P_{\text{fict}}(\bar{r})$.

4.11 Plasma Membrane Domains

This section briefly outlines our efforts to understand the phase separating properties, and domain morphologies, of native membranes from RAW macrophages. A number of recent studies have shown that certain kinds of eukaryotic cells can be coaxed into blebbing large unilamellar vesicles or membrane appendages from their plasma membrane [245, 270, 271]. While the process itself is fatal to the cell, it presents an interesting bridge between *in vitro* and *in vivo* systems. These giant plasma membrane vesicles (GPMV) contain a representative mix of the actual lipids and proteins

found in the plasma membrane, and hence are of great interest as an arena in which to explore lipid phase properties and bilayer morphology from real cells.

4.11.1 Experimental Methods

A detailed list of reagents and the blebbing protocol are found in Appendix F, however we will discuss some experimental details here. Our group had (and has) an active branch of research to understand the membrane biophysics of phagocytosis in RAW macrophages. Conveniently, we figured these cells probably have a large amount of extra membrane, considering that phagocytosis requires large degrees of membrane invagination, and therefore would they make good candidate cells to form giant plasma membrane vesicles. This turned out to be a good hunch, and after honing an experimental protocol, we can reliably produce large GPMVs from macrophages that are grown under standard mammalian cell culture conditions to $\sim 50\%$ confluency. Blebbing of the plasma membrane is induced by a change of media, from their normal Dulbecco Modified Eagle Medium (DMEM[7]) to a simple phosphate–buffered saline (PBS[8]) solution with addition of 10% glucose (w/w), the addition of $\sim$ 5% dimethylsulfoxide (DMSO[9]) (v/v)[10] is also required. As a weakly amphiphilic solvent, DMSO is used to solubilize the lipophilic dyes used to visual the different phases in the GPMVs. We use a number of different fluorescent small molecules to label the two membrane phases, however the clearest labeling occurs with two different sets of dyes. In one set of experiments, the liquid ordered domains are labeled with the green fluorescent lipid DPPE-NBD[11] and the liquid disordered phase is labeled with the red fluorescent lipid DOPE-Rhodamine[12]. This gave excellent fluorescence contrast, and indicated that the two phases were indeed liquid ordered and liquid disordered. This is somewhat surprising considering that the plasma membrane is a complex and varied mixture of lipids and proteins. Although, it should be noted that if other phases exist that are characterized by properties other than their acyl chain order, the aforementioned probes might be insensitive to the presence of such lipid phases. The second set of probes again uses DOPE-Rhodamine to label the liquid disordered phase, but uses a non-polar blue fluorescent small molecule, perylene[13], to label the liquid ordered phase. Examples of GPMV labeling with both sets of probes are shown in Fig. 4.37.

4.11.2 Plasma Membrane Domain Interactions

Like the *in vitro* phase separating vesicles we have already discussed, we observed that domains in distinct GPMVs had qualitatively different kinetics. Unlike the *in vitro* experiments, we do not

[7] Invitrogen PN: 12430
[8] Invitrogen PN: 10010031
[9] Sigma Aldrich PN: D8418
[10] The experiment also works with either acetone or ethanol at approximately the same fractions, however our best results are with DMSO.
[11] Avanti Polar Lipids PN: 810144C
[12] Avanti Polar Lipids PN: 810150C
[13] Sigma Aldrich PN: 77341

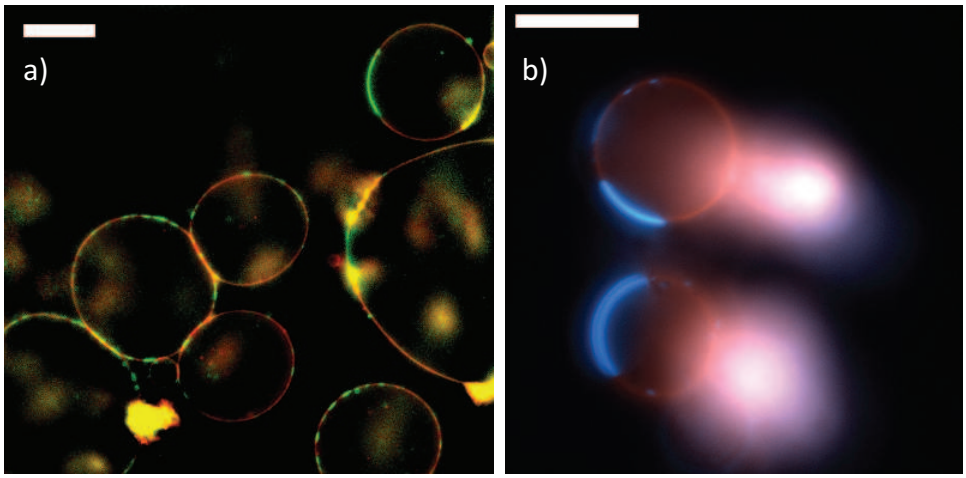

Figure 4.37: Labeling giant plasma membrane vesicles. a) A background subtracted equatorial view of giant plasma membrane vesicles from RAW macrophages. The liquid ordered phase is labeled with green fluorescent lipid, and the liquid disordered phase is labeled with red fluorescent lipid. b) Epi-fluorescence view of two giant plasma membrane vesicles. The liquid ordered phase is labeled with a blue fluorescent non-polar small molecule, while the liquid disordered phase is labeled with red fluorescent lipid. In both images, the diffuse intensity comes from fluorescent label inside the cells, that is out of the focal plane. Scale bars are 10 μm.

have direct control over the osmotic environment inside the vesicle, and hence control of membrane tension was difficult at best. We also have no control of the lipid composition of the GPMVs, more specifically, the degree of spontaneous curvature in the membrane is unknown. In a number of instances we observed the volume of GMPVs changing over the time scale of minutes (data not shown), indicating that there was some amount of exchange of osmolytes with the external aqueous environment. In Fig. 4.38 we show a group of six GPMVs, each on different cells but all originally in the same field of view, where a temperature quench initiated the formation of lipid domains, hence their phase separation is approximately synchronized. Over the course of a few minutes, domains in two of the GPMVs rapidly coalesce such that there are only a few ($\sim$ 2) domains left, indicating a lack of the kind of coalescence inhibiting interactions we measured in the *in vitro* system. On the other hand, four other GPMVs in this same field of view experience arrested coalescence on the same time scale, indicating that the domains on their surface might be interacting. To quantitative whether the same kinds of interaction we observed *in vitro* were present in this system, we measured the thermal motion of the domains in the arrested coalescence setting, and calculated the potential of mean force, as shown for instance in Fig. 4.39. Interestingly, it seems that domains in GPMVs that exhibit arrested coalescence indeed have an interaction very similar to the repulsive interaction observed *in vitro*, despite the fact that this membrane has a complex mixture of lipids and proteins. In general, with no control of membrane composition or tension, it is difficult to known which GPMVs will exhibit coalescence inhibition, and only a few data sets

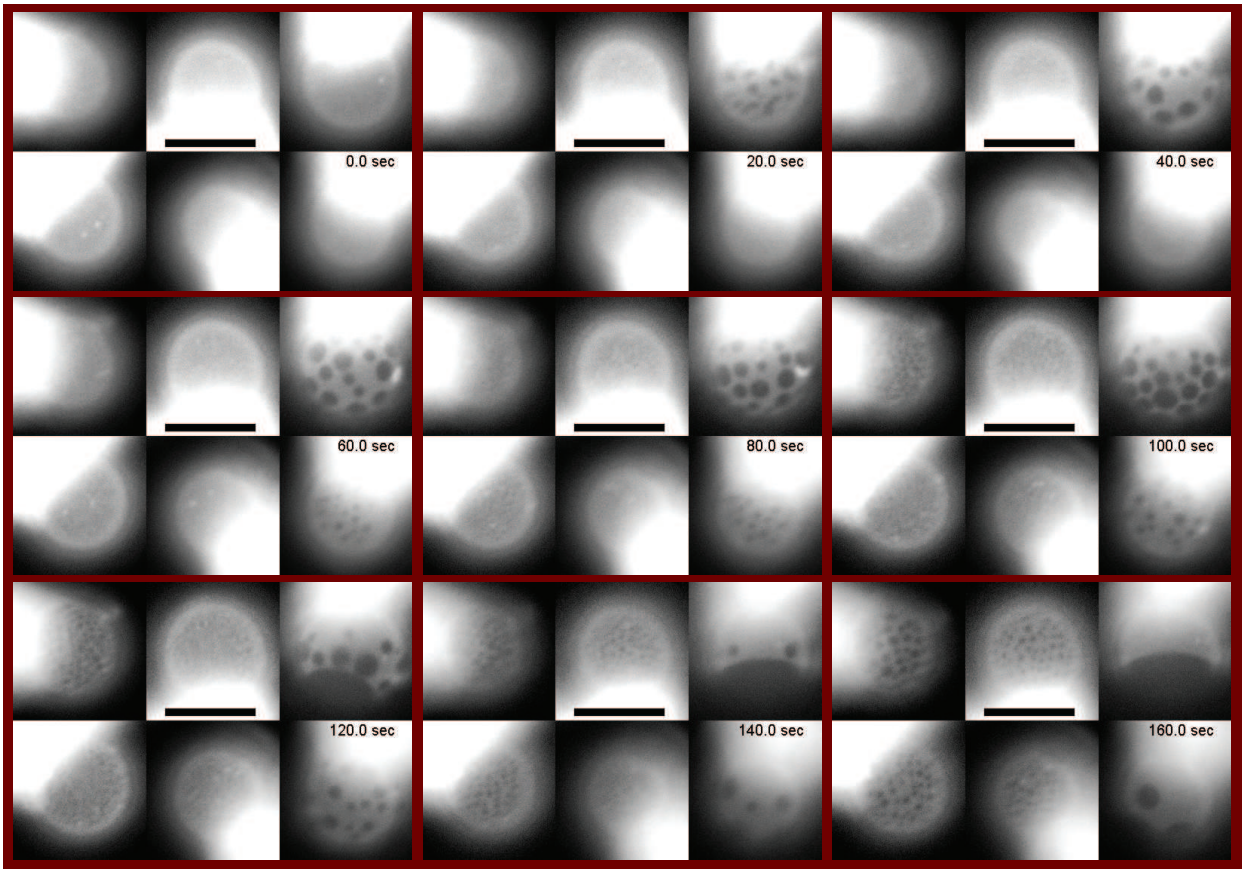

Figure 4.38: Kinetics of domain coalescence in GPMVs. Each pane shows six GPMVs, each from a different cell, but all are located in the same field of view, and were temperature quenched at the same time. Each frame is 20 s apart; each pane has a time stamp in the lower right. The left hand four GMPVs in each pane exhibit arrested coalescence as compared to the two right hand GPMVs, which nearly completely phase separate over the course of ~ 3 minutes. In the last pane (lower right), the difference is clearly visible as each of the four left hand vesicles have a distribution of domains that are small in comparison to the vesicle, as compared to the domains in the right hand vesicles whose length scale is comparable to the size of the vesicle itself. The saturated bright regions are the parent cell, which contains a high concentration of fluorescent label. Scale bars are 10 μm.

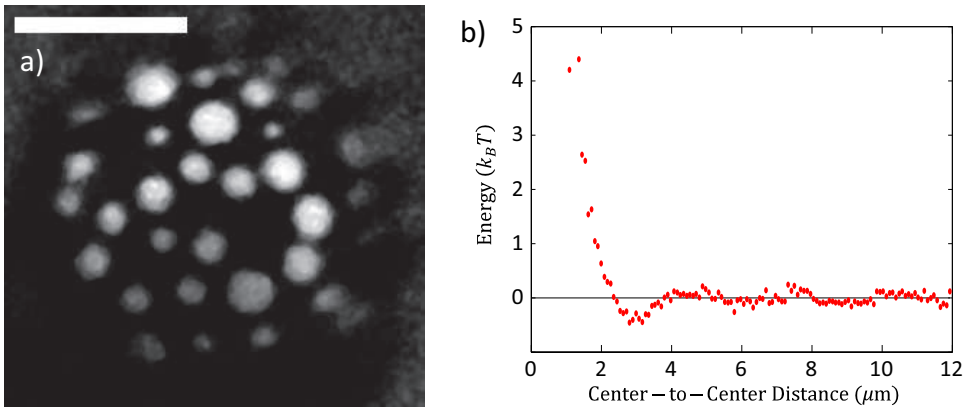

Figure 4.39: Domains repulsively interacting on the surface of a GPMV. a) Background subtracted image of a GMPV with interacting domains. Using precisely the same methods as the *in vitro* experiments, the interactions of domains on the surface the GPMV in (a) were measured, and are shown to be of a similar repulsive nature as the *in vitro* system, as shown in (b), where the length scale of interaction is $\lambda_2 \simeq 140\,\text{nm}$. If we assume the same bending stiffness as the *in vitro* bilayer ($\kappa_b = 25\,k_BT$), the length scale of interaction can be used to estimate the tension, and is found to be $\tau \simeq 1 \times 10^{-3}\,k_BT/\text{nm}^2$, a value about twice that of the *in vitro* measurements. Scale bar is $10\,\mu\text{m}$.

were taken. However, on those GPMVs that did exhibit coalescence inhibition, the domains appear to be of the dimpled morphology. Further, it appears that, similar to the *in vitro* system, these interactions can stabilize the domain size distribution even when the domains are densely packed, as demonstrated in Fig. 4.40. These results are a good start, but much work remains to properly characterize the mechanics of GPMVs, their resulting phase properties, and the attendant bilayer morphologies. Likewise, as an experimental bridge between *in vitro* and *in vivo* systems, we need to devise ways to create a more controlled experiment, ideally with the ability to measure bilayer mechanical properties, like tension and spontaneous curvature, and even biochemical techniques to quantitate the protein and lipid composition of GPMVs.

4.12 Concluding Remarks

This chapter examined in detail the biophysical nature of lipid domain morphology and resulting interactions. Among the main insights, we found that: i) depending on mechanical properties, domains can take on a (at least) three morphologies, termed 'flat', 'dimpled' and 'budded', ii) for a single domain, transitions between these morphological states are determined by the bilayer mechanical properties and domain size, and in the case of dimpled domains, the morphological transition turns on a membrane mediated elastic interaction that tends to inhibit domain coalescence and spatially organizes the domains, iii) upon coalescence, transitions between these morphologies

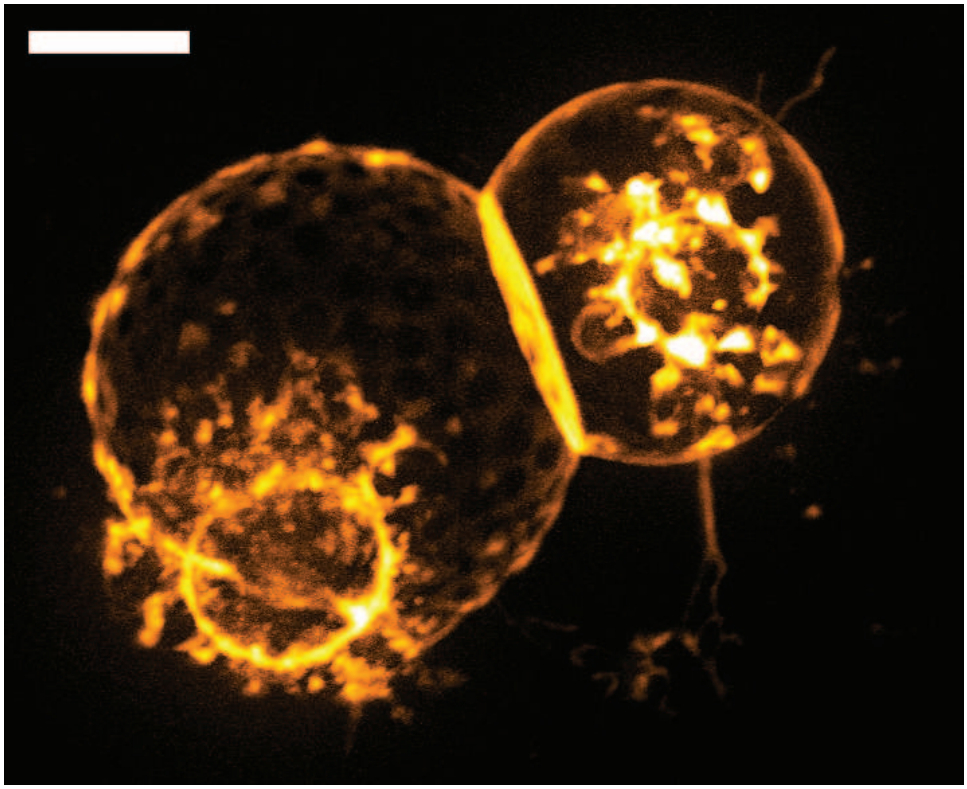

Figure 4.40: Dense domains on the surface of a GPMV. Two cells each with an attached GPMV are shown. The GPMV on the left has many domains on its surface (dark circles) whose repulsive interactions stabilize the domain size distribution. The GPMV on the right has a more dilute set of domains (dark circles) that are more difficult to see. The aspherical intensities are the parents cells. Scale bar is 10 μm.

should obey certain rules derived from an analysis of the mechanical free energy.

A number of directions of further research are available. On the modeling front, there are both analytical and non-linear numerical efforts underway to better understand the full phase diagram of the three domain morphologies discussed in this chapter, in part to better understand the nature of transitions between the morphologies, and in part to understand their mechanical stability. Additionally, stochastic simulations have been started that will be used to better understand the expected coalescence kinetics in a phase separated giant unilamellar vesicle under different physical conditions, where the interactions between domains are taken into account. On the experimental front, new model systems should be developed to better control membrane mechanical properties during an experiment. For instance, it might be possible to use free floating planar bilayers to better control the state of tension as well as ameliorate issues from the curved geometry of giant unilamellar vesicles. Additionally, it would be interesting to test our predictions about the difference in qualitative behavior of dimpled domain interactions in the presence and absence of spontaneous curvature. Notably, in the giant unilamellar vesicle system, lysolipids and/or specific proteins could be introduced into the aqueous phase outside the vesicle, that preferentially segregate into the domains, imbuing them with spontaneous curvature and hence changing their morphological properties. Finally, it would be helpful to conduct precise kinetic measurements of domain coalescence to further bolster our understanding of these phase-separated systems, as well as test predictions from analytical theory and stochastic simulations of the connection between various mechanical properties and the resulting phase separation.

4.13 Acknowledgments

We would like to thank Patricia Bassereau, Ben Freund, Kerwyn Huang, Greg Huber, Sarah Keller, Udo Seifert and Pierre Sens for stimulating discussion and comments, and Jenny Hsaio for help with experiments.

Chapter 5

Membrane Adhesion by Homophilic Protein Binding

"Some laws are unwritten, but they are better established than all written ones." – Seneca

5.1 Introduction

For many organisms and cell types it is crucial that they stick together. Clearly for multi-cellular organisms, cellular adhesion is a simple mechanism (conceptually) by which cells make direct physical contact, allowing cell-to-cell transfer of materials and signals, and in many cases the formation of connective tissues [272]. One common theme uniting the varied morphologies of epithelia in higher organisms is that these structures rely on the adhesion of adjacent cells, as shown in Fig. 5.1. Even organisms classically considered as single cells participate in cell adhesion, sometimes with members of their own species, such as in biofilms [273, 274], and sometimes in a non-obligatory manner with very different species [275], and in all these cases, at some scale there are molecules mediating this adhesion. In this chapter, we will narrow our view down to a single homophilic membrane adhesion protein known as 'L1.' Using an approximate analytical model and results from preliminary experiments, we will discuss how one can understand the biophysics of homophilic binding using giant unilamellar vesicle shape as a mechanical read out of adhesion.

5.2 Physiology of L1 Binding

The protein L1 is a transmembrane, immunoglobulin superfamily (IgSF) member known to mediate homophilic and heterophilic adhesion events in neuronal cell growth [276, 277, 278]. Composed of six Ig-like domains followed by five fibronectin domains, a transmembrane domain and a short, but well-conserved, intracellular domain, L1 interacts with various distinct binding partners and plays important roles in neural development as well as in the adult nervous system; including neurite outgrowth, neuronal migration and survival, and synapse organization [279, 280]. Mutants of L1 have been found to cause mental retardation, hydrocephalus, impairment of sensorimotor control, abnormal cerebellar development, and other pathological phenotypes [281, 282].

Evidence shows that the first four Ig domains of L1 form a horseshoe-shaped structure [283], believed to be critical in L1 homophilic adhesion. Based on homolog studies, two models, the domain-swapped dimer model and the domain-swapped multimer 'zipper' model, have been pro-

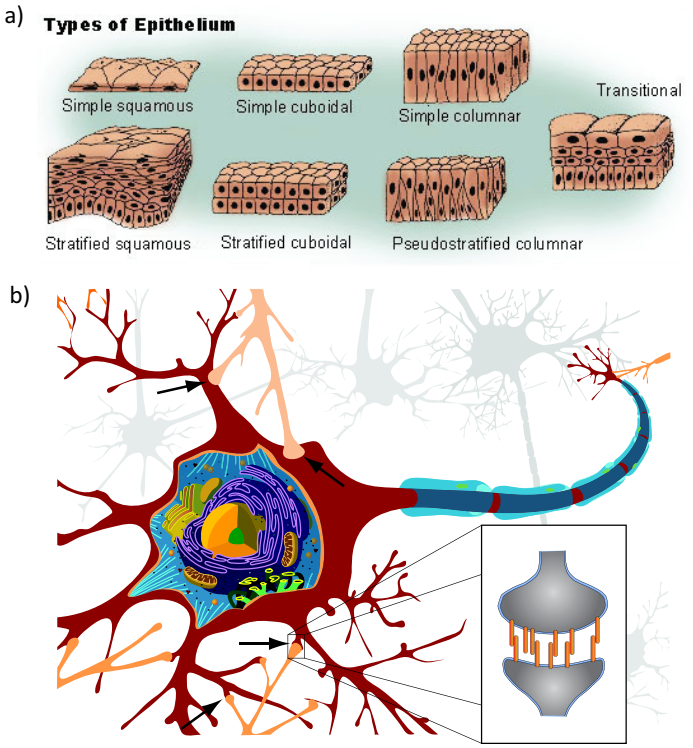

Figure 5.1: Representations of different adhered cell morphologies in epithelia. a) A gallery of the varied kinds of adhered cell morphologies found in the tissues of higher multi-cellular organisms. b) Depiction of a nerve cell with synapses shown by the black arrows. In a zoomed view, the synapses are schematically shown being held together by the homophilic binding of membrane-anchored proteins. Image (a) is in the public domain under federal licensor and (b) is modified from an image originally under Creative Commons licensor.

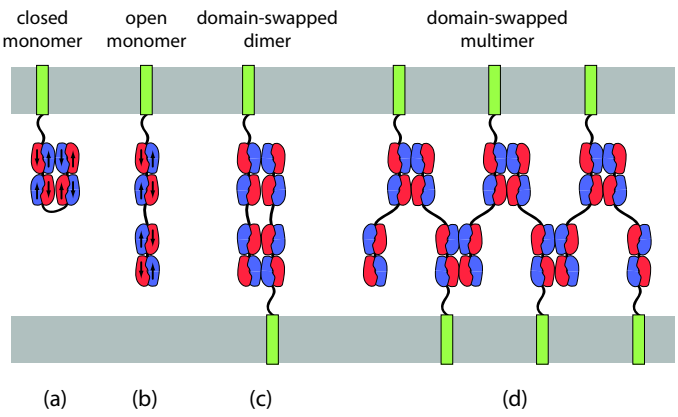

Figure 5.2: Proposed models for the homophilic adhesion interaction of L1. This cartoon shows the approximate domain structure of the homophilic binding protein L1 in two different mechanisms of homophilic adhesion. a) The closed monomer conformation of a single L1 protein. b) The open monomer conformation, now able to engage in homophilic binding. c) The domain-swapped dimer configuration for the homophilic binding of two L1 proteins in a *trans* configuration. d) The domain-swapped multimer configuration (aka the 'zipper' model) of the homophilic binding of multiple L1 proteins. The gray region represents the bilayer, and the green regions of the proteins are the transmembrane anchoring domains.

posed to explain this homophilic interaction [276, 284]. The proposed mechanism of homophilic binding is shown in Fig. 5.2, though no direct observation has yet been obtained to support either model.

Overarching the discussion that will follow, there are three basic questions we would like to answer:

1) What is the per subunit binding energy of L1?

2) Is binding between distinct L1 proteins cooperative (or anti-cooperative) in any way?

3) Are the known disease phenotypes related to homophilic binding energy differences? If so, do they bind generically weaker, stronger or does it depend on disease genotype?

The basic plan to answer these questions is to create giant unilamellar vesicles that, after suitable preparation, contain a controlled density of L1. From there, a number of vesicle geometries can be used to relate vesicle shape, bending stiffness of the bilayer, and the vesicle area and enclosed volume to the adhesion strength between L1 proteins. The first, and arguably the simplest, geometric configuration we will explore theoretically is the azimuthally symmetric binding of giant unilamellar vesicles to a glass substrate, coated with a known density of L1 binding protein. The bound shape

of the vesicle, in particular the shape of the toroidal bilayer transition zone, between the spherical vesicle and binding patch, acts as a reporter of adhesion strength. The second case we will explore in some detail is a variation on this setup, where an optical tweezer is used to pull a membrane tether, whose force extension curve can report on the adhesion strength.

5.3 The Adhered Vesicle Shape

The shape of an adhered vesicle depends heavily on its mechanical properties as well as the strength of adhesion. In particular, the fluidity of the bilayer translates into the simplification that we need not consider shear stresses in our mechanical model. Bending stiffness is the key intrinsic attribute of the bilayer that resists changes in shape from a sphere, while the various constraints (discussed below) extrinsically affect vesicle shape. Our model assumes azimuthal symmetry which greatly simplifies the problem and will allow us to state nearly all our results in closed form.

In terms of our physical intuition, it would be incorrect to consider this problem as 'simply' a problem of finding shapes that are extrema of the vesicle surface area. Such analysis does describe the adhered shapes of typical thin liquid films, like soap bubbles composed of mixtures of water and amphiphilic molecules (*e.g.* detergents) as shown in Fig. 5.3 and discussed in an excellent book by Isenberg [285]. However vesicles have a unique constraint that distinguishes their mechanics from the mechanics of typical thin liquid films. Like bubbles, vesicles do have a conserved volume enclosed by the two dimensional fluid, however, unlike bubbles, the total area of a vesicle is a conserved quantity for the tensions we consider here. This difference is due to the detailed molecular architecture of these two materials. Whereas the thickness of a typical liquid film can change to expose more or less surface area and hence regulate the surface energy by changing the number of amphiphilic molecules at the material interface, the alignment of amphiphilic lipids into a bilayer means that the number of molecules at the interface is fixed. This is in some sense unfortunate — our analysis would be much simpler, and microscopy more informative, were it not the case. Another key difference is that, although not strictly zero[1], the bending stiffness of thin liquid films is not a major determinant of shape, whereas the bending stiffness of a bilayer affects vesicle shape in a way that makes our proposed measurement possible.

In addition to azimuthal symmetry, we will also assume that the vesicle contour is described by three basis shapes: an upper spherical section with circular contour, a lower toroidal dish with circular contour, and a flat, circular adhesion zone. While one can construct models that describe shapes beyond those described by this basis set [252, 286, 287], this formulation has two advantages, in addition to being relatively simple in a mathematical sense. First, given that homophilic binding is adhesive, and hence corresponds to a reduction in free energy, we expect the equilibrium shapes of adhered vesicles (*i.e.* those near the shape free energy minimum) will not have tubes, necks or buds, as these shapes unnecessarily use area that could be adhered. The second reason is that in a

[1]For instance, bending stiffness due to surface area differences between the two film-air interfaces of a bubble.

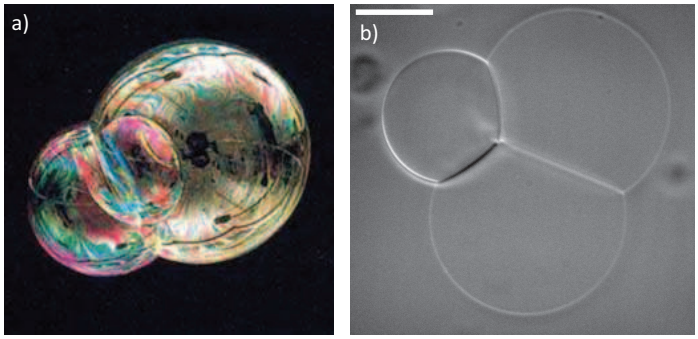

Figure 5.3: Similar appearance different physics. The free floating, adhered soap bubbles in (a) look very similar to the free floating, adhered vesicle 'bubbles' in (b). While both conserve volume of the enclosed regions, and adhesion between those bubbles drives them to adopt their overall shapes, a critical difference exists between these physical scenarios in that soap bubbles (a) do not have conserved area, but vesicles (b) do. The scale bar in (b) is 20 μm.

real experiment it is difficult to reliably measure more than two radii of curvature on the adhered vesicle, and in fact, two radii of curvature — one for the spherical region and one for the toroidal region — encode the necessary information to extract the adhesion strength from shape analysis.

Free of constraints, the azimuthally symmetric adhered shape is specified by five parameters: the radius of curvature (R_1) and angle (θ_1) of the spherical section, the principal radius of curvature (R_2) and angle (θ_2) of the toroidal region, and the radius of the adhesion contact zone (R_3), all schematically shown in Fig. 5.4.

5.3.1 Shape Constraints

If our model is to describe a physically reasonable shape, certain shape constraints must be imposed. In particular, we will demand that the shape is free of holes or rips and that our surface is smooth all over, that is, it does not have ridges or points (so-called C_1 continuity). Physically speaking, the first constraint is reasonable because we know that holes in lipid bilayers are severely energetically discouraged via a hydrophobic line tension [165][2]. The second constraint is physically reasonable because any material with a finite bending stiffness (like lipid bilayers) will have infinite bending energy density on ridges and points.

Imposing these constraints relates the shape parameters shown in Fig. 5.4. The condition that the surface lack ridges requires

$$\tan(\theta_1) = -\tan(\theta_2), \tag{5.1}$$

which can be recast as

$$\theta_2 = \pi - \theta_1, \tag{5.2}$$

[2]With an interesting and notable exception of very small vesicles composed of charged lipid species, that form polyhedra structures with stable pores [288].

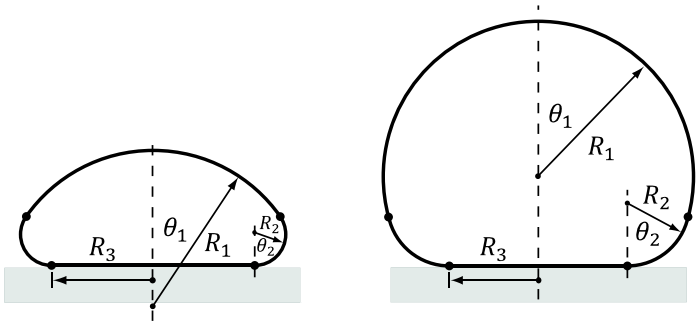

Figure 5.4: Schematic of the parameters needed to construct the basis shape model of vesicle adhesion. While the fundamental parameters required do not change from one vesicle to another, the observed vesicle shape can be very different - in this case the vesicles have a significant difference in their surface area to volume ratio. The small black dots demarcate where one basis shape ends and another begins. The gray regions on the bottom represent an adhesive glass substrate.

implying that $\theta_1 \in [0 \dots \pi]$. Further imposing that the surface be continuous gives

$$R_1 \sin(\theta_1) = R_3 + R_2 \sin(\theta_2), \tag{5.3}$$

which is further simplified to

$$R_3 = \sin(\theta_1)(R_1 - R_2) = R_2 \sin(\theta_1)(\alpha - 1), \tag{5.4}$$

with $\alpha = R_1/R_2$. These two relations effectively eliminate θ_2 and R_3 from our equations, leaving only the variables R_1, R_2, and θ_1.

5.3.2 Calculating Surface Area

When we attempt to minimize the free energy in a few sections it will only be meaningful if certain extrinsic constraints are imposed. In particular, for a given equilibrium shape, the area of the lipid bilayer is conserved. By extrinsic we mean that we must now introduce the total vesicle area (A_o) as a new parameter related to vesicle geometry; we will calculate the area for each basis shape and then sum those contributions to find the total vesicle area [57].

The spherical section has an area given by

$$A_1 = 2\pi R_1^2 \int_0^{\theta_1} \sin(\theta_1) \mathrm{d}\theta_1 = 2\pi R_1^2 (1 - \cos(\theta_1)). \tag{5.5}$$

The area of the toroidal section is a bit more complicated. To calculate this contribution, we first rotate the toroidal section by $\pi/2$ and write the function describing this surface as

$$z(r) = R_3 + \sqrt{R_2^2 - r^2}. \tag{5.6}$$

The area can then be written as

$$A_2 = 2\pi \int_{R_2\cos(\theta_2)}^{R_2} z(r)\sqrt{1+\dot{z}(r)^2}\mathrm{d}r, \tag{5.7}$$

which can be evaluated as

$$A_2 = 2\pi R_2 R_3 \left(\theta_2 + \frac{R_2}{R_3}(1-\cos(\theta_2))\right). \tag{5.8}$$

As a quick sanity check, letting $R_3 \to 0$ and $\theta_2 \to \pi$, should give the area of a sphere with radius R_2, and indeed it does. This can be re-written as

$$A_2 = 2\pi R_2^2 \left(\sin(\theta_1)(\alpha-1)(\pi-\theta_1) + 1 + \cos(\theta_1)\right). \tag{5.9}$$

The final, and easiest piece, is the adhesion zone, whose area is

$$A_3 = \pi R_3^2 = \pi R_2^2(\alpha-1)^2\sin^2(\theta_1), \tag{5.10}$$

such that the total area is

$$A_o = A(R_1, R_2, \theta_1) = A_1 + A_2 + A_3. \tag{5.11}$$

5.3.3 Calculating Volume

As with the vesicle area, any attempt to minimize the equilibrium free energy must also conserve volume[3]. This is physically reasonable because: i) the nominal membrane tensions are low compared to the bilayer rupture tension and hence no spontaneous holes open in the membrane to exchange volume; ii) osmotic pressure across the membrane is balanced (given a brief equilibration time), and hence no net volume permeates across the membrane; and iii) the water enclosed by the vesicle is essentially incompressible.

The volume of the spherical section is given by

$$V_1 = \pi \int_0^{R_1(1-\cos(\theta_1))} r_1(z)^2\mathrm{d}z \tag{5.12}$$

with

$$r_1(z) = \sqrt{2zR_1 - z^2}. \tag{5.13}$$

This integral can be simplified to

$$V_1 = \frac{\pi}{3}R_1^3(1-\cos(\theta_1))^2\left(2+\cos(\theta_1)\right). \tag{5.14}$$

[3]To be precise, we note that the volume and area only need be conserved on time scales appropriate for vesicle shape to reach equilibrium. The slow removal of volume or surface area, relative to the shape equilibration time, scale does not affect these results.

The volume in the toroidal section is given by a similar function

$$V_2 = \pi \int_0^{R_2(1-\cos(\theta_2))} r_2(z)^2 \mathrm{d}z \tag{5.15}$$

with

$$r_2(z) = R_3 + \sqrt{2zR_2 - z^2}. \tag{5.16}$$

This can be solved analytically to give

$$V_2 = \pi R_2^3 \left[\left(\frac{R_3}{R_2} \right)^2 (1 - \cos(\theta_2)) + \frac{R_3}{R_2}(\theta_2 - \sin(\theta_2)\cos(\theta_2)) + \frac{1}{3}(2 + \cos(\theta_2)^3) - \cos(\theta_2) \right], \tag{5.17}$$

and re-written as

$$\begin{aligned} V_2 = \pi R_2^3 \big[&(\alpha - 1)^2 \sin^2(\theta_1)(1 + \cos(\theta_1)) + \sin(\theta_1)(\alpha - 1)(\pi - \theta_1 + \sin(\theta_1)\cos(\theta_1)) \\ &+ \frac{1}{3}(2 - \cos^3(\theta_1)) + \cos(\theta_1) \Big]. \end{aligned} \tag{5.18}$$

A quick sanity check shows that if we let $\theta_1 \to 0$, we recover the volume of a sphere with radius R_2. Then the volume constraint equation is

$$V_o = V(R_1, R_2, \theta_1) = V_1 + V_2. \tag{5.19}$$

5.3.4 Protein Conservation and Surface Energy

The final conserved quantity is the number of L1 proteins in the vesicle as a whole. We presume that due to membrane fluidity, diffusion, and the energetic benefit of homophilic binding there will be a difference in L1 density between the adhered and non-adhered zones. To conserve the number of proteins, we impose the conservation equation

$$A_o \rho_1 = \rho_2 (A_o - \pi R_3^2) + \rho_3 \pi R_3^2, \tag{5.20}$$

where ρ_1 is the areal density of L1 in the free floating vesicle, ρ_2 is the density in the unadhered zone, and ρ_3 is the density in the adhered zone. Quantitating the protein density in the two regions is necessary for calculating both the binding energy per protein and the degree of cooperativity between proteins.

In the absence of a direct readout of protein density in the membrane, we must rely on fluorescent protein reporters, where L1 is fused to GFP[4]. The ratio of fluorescence intensities in the adhered and non-adhered zones is the ratio of the protein density in the two regions[5]. This ratio-metric measurement still leaves an undetermined constant necessary to actually calculate the protein

[4]The Bjorkman Lab at Caltech, with whom we collaborate, has produced such fusions.

[5]With the background properly subtracted.

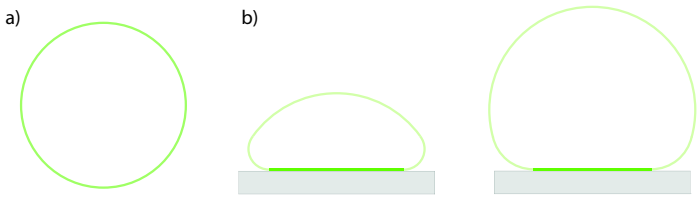

Figure 5.5: Schematic of L1-GFP fluorescence intensity differences for bound and unbound vesicles. a) The fluorescence intensity of a free floating vesicle is greater than the fluorescence intensity of the unadhered zone of an adhered vesicle (b), but less than the fluorescence intensity of the adhered zone of the vesicle. Measurements of the fluorescence of free floating and adhered vesicles can be used to calculate the constant of proportionality between fluorescence intensity and actual protein concentration, f.

density in the two regions. For the moment, let us ignore the effects of photo-bleaching; then the integrated fluorescent protein intensity (I_{p}) during a set exposure time t_{exp} from a bilayer patch of area A has the relationship

$$I_{\mathrm{p}} = Af\rho t_{\mathrm{exp}}, \tag{5.21}$$

where f is the rate of intensity counts coming from each labeled protein. The constant f depends on everything from sample preparation to the optical properties of the microscope, fluorescence lamp and camera in use, and hence needs to be determined uniquely for each experiment. However, in concept it is fairly easy to measure this number. As we will discuss later in this chapter, we have a degree of control over the density of L1 in the membrane. If all of the L1 is labeled and we know the density of L1, then the fluorescent intensity of a free floating vesicle allows us to calculate the constant f. Figure 5.5 shows a schematic of what the fluorescence intensity of a free floating and adhered vesicle might look like. While entropy plays a role in the distribution of proteins between the two regions, as we will explore below, the fact that the free energy of binding is favorable means that the proteins will be enriched in the adhesion zone. The degree of enrichment depends on the strength of adhesion, the total number of proteins, the size of the adhesion zone, and the possibly the steric constraints of densely packed L1 binders.

For a large adhesion zone, where fluctuations in the number of binding partners is small in comparison to the mean, the enthalpy of binding can be written as an ensemble quantity given by

$$G_{\mathrm{bind}} = -\pi R_3^2(\gamma\rho_3 + c\rho_3^2), \tag{5.22}$$

where γ is the homophilic binding energy per L1 oligomer. The quadratic term is a simple way to account for possible cooperative effects, similar to how a Virial expansion is written [111]. If the coefficient c is a positive, then the interactions between multiple L1 proteins are cooperative; if c is negative then there is anti-cooperativity between L1 proteins. A single measurement of vesicle shape is not enough to determine γ and c, multiple vesicle measurements will be needed. Determining c

is slightly confounded by the fact that there is a chemical potential penalty to increasing the L1 density in the adhesion zone, due to the loss of configurational entropy. Presumably, this imparts a generic anti-cooperativity to adhesion, since the creation of a concentration gradient, in this case between the adhered and non-adhered zones, costs free energy.

The configurational entropy is relatively straight-forward to calculate. Let A_{L1} denote the effective area of a single L1 protein projected on the bilayer (*i.e.* the steric area), then the total number of sites on a vesicle is

$$N_1 = A_o/A_{\mathrm{L1}} \tag{5.23}$$

while the number of sites in the unadhered and adhered zones, respectively, is

$$N_2 = (A_o - \pi R_3^2)/A_{\mathrm{L1}} \tag{5.24}$$

and

$$N_3 = \pi R_3^2/A_{\mathrm{L1}}, \tag{5.25}$$

with the obvious condition $N_1 = N_2 + N_3$. Then the number of indistinguishable proteins in each zone is

$$M_2 = \rho_2(A_o - \pi R_3^2) \tag{5.26}$$

and

$$M_3 = \rho_3 \pi R_3^2. \tag{5.27}$$

The configurational entropy of the free floating vesicle is given by

$$S_o = k \ln \left[\frac{(N_2 + N_3)!}{(M_2 + M_3)!(N_2 + N_3 - M_2 - M_3)!} \right], \tag{5.28}$$

whereas the entropy of the bound state is given by

$$S_b = k \ln \left[\frac{N_2! N_3!}{M_2! M_3! (N_2 - M_2)! (N_3 - M_3)!} \right]. \tag{5.29}$$

The entropic component of the free energy is then

$$G_k = -T(S_b - S_o). \tag{5.30}$$

What this means is that once the protein density in the two regions has been measured, and the vesicle area calculated, we can calculate the free energy cost of the loss of configurational entropy of the L1 proteins. This free energy penalty directly competes with the enthalpic benefit of homophilic binding. Hence if we know how many proteins are in the adhered zone (from our measurement of protein density), the binding energy between the bilayer and the substrate per unit area (from shape analysis), and the configurational entropy cost to create the adhesion zone, we can solve for

the binding energy per L1 oligomer.

Before finishing our discussion of configurational entropy, we should be able to put an upper bound on the importance of this effect. For instance, from measurements of the spacing of L1 tight binding in liposomes [284], $A_{\mathrm{L1}} \simeq 100\,\mathrm{nm}^2$, and then consider a vesicle whose area is $A_o = 4\pi(10\,\mu\mathrm{m})^2$, such that the maximum number of potential, configurational sites is $\sim 10^7$. The maximum initial configurational entropy,S_o, occurs if half of those sites are occupied. To get an upper bound on the change in configurational entropy, let us assume the unrealistic scenario where one third of the total vesicle area is adhered to the substrate, and all possible sites in that region are filled. This gives an upper bound because filling all sites in the adhesion zone corresponds to the greatest reduction in configurational entropy. This is unrealistic because not all sites will be filled in such a region, and having a full third of the vesicle area adhered is a relatively large adhesion zone (*e.g.* see the most deformed shape in Fig. 5.6). This estimate indicates that going from the free floating vesicle to the adhered vesicle state raises the free energy per protein by $\sim 0.5\,k_BT$, independent of vesicle size (A_o) and protein area (A_{L1}). Again, this is an upper bound, and more precise estimates can be made with exact figures of protein density and vesicle shape from experiment. This estimate indicates that protein entropy will be an unimportant effect the binding energy per oligomer is much larger than this entropic contribution; whether that is true remains to be seen [105].

5.3.5 Vesicle Bending Energy

The only source of membrane elastic energy in this problem comes from the mean curvature bending of the bilayer. From the Gauss-Bonnet Theorem, as discussed in Chapter 4, we know that Gaussian curvature does not contribute to the free energy budget because the vesicle topology (genus) remains fixed throughout the adhesion process.

The spherical section of the vesicle contains a fraction of the total bending energy of a sphere, written as

$$G_b^{(1)} = 8\pi\kappa_b \frac{A_1}{4\pi R_1^2} = 4\pi\kappa_b(1-\cos(\theta_1)). \tag{5.31}$$

The toroidal section is more difficult — to tackle this region we will use a combination of cylindrical coordinates and the parametric equations that define a torus. First, we generically write the curvature energy in cylindrical coordinates as

$$G_b^{(2)} = (2\pi)(2\kappa_b)\int_{\mathcal{S}} H^2\sqrt{g}\,r\mathrm{d}r, \tag{5.32}$$

where $\sqrt{g}$ is the surface metric, and we have already made use of the azimuthal symmetry. Using the parametric equations for a torus, the boundary of the toroidal region is given by

$$r(\theta_2) = R_3 + R_2\sin(\theta_2), \tag{5.33}$$

with the coordinate transformation written as

$$\mathrm{d}r = \frac{\partial r}{\partial \theta_2}\mathrm{d}\theta_2 = R_2\cos(\theta_2)\mathrm{d}\theta_2. \tag{5.34}$$

The surface metric in cylindrical coordinates is written as

$$g = 1 + \left(\frac{\partial z}{\partial r}\right)^2, \tag{5.35}$$

with

$$z = R_2 - \sqrt{R_2^2 - (r - R_3)^2} = R_2(1 - \cos(\theta_2)). \tag{5.36}$$

Then the surface metric in toroidal coordinates is

$$g = 1 + \left(\frac{\partial z}{\partial \theta_2}\frac{\partial \theta_2}{\partial r}\right)^2 = [\cos(\theta_2)]^{-2}. \tag{5.37}$$

The mean curvature of a torus can been calculated [289], and when translated into our notation gives

$$H = -\frac{1}{2R_2}\cdot\frac{R_3 + 2R_2\sin(\theta_2)}{R_3 + R_2\sin(\theta_2)}. \tag{5.38}$$

Using a dummy variable, θ, the integrand has a pleasingly simple form, given by

$$H^2\sqrt{g}|J|r = \frac{1}{4}\frac{(\beta + 2\sin(\theta))^2}{\beta + \sin(\theta)}, \tag{5.39}$$

with $\beta = R_3/R_2 = (1+\alpha)\sin(\theta_1)$. The mean curvature energy is then given by

$$G_b^{(2)} = 4\pi\kappa_b\int_0^{\theta_2} H^2\sqrt{g}\, r|J|\mathrm{d}\theta, \tag{5.40}$$

which has the relatively simple closed form

$$G_b^{(2)} = 2\pi\kappa_b\left[2(1-\cos(\theta_2)) + \frac{\beta^2}{\sqrt{\beta^2-1}}\tan^{-1}\left[\frac{\sin(\theta_2)\sqrt{\beta^2-1}}{\sin(\theta_2) + \beta(1+\cos(\theta_2))}\right]\right], \tag{5.41}$$

which can be written as a function of θ_1 as

$$G_b^{(2)} = 2\pi\kappa_b\left[2(1+\cos(\theta_1)) + \frac{\beta^2}{\sqrt{\beta^2-1}}\tan^{-1}\left[\frac{\sin(\theta_1)\sqrt{\beta^2-1}}{\sin(\theta_1) + \beta(1-\cos(\theta_1))}\right]\right]. \tag{5.42}$$

As a check, letting $\beta \to 0$ and $\theta_1 \to 0$ turns the torus into a sphere of radius R_2 giving the expected bending energy $G_b^{(2)} = 8\pi\kappa_b$. Being a flat disc, the adhesion zone has zero bending energy for all values of R_3, and hence the total bending energy is the sum of the bending energy in the spherical and toroidal regions.

5.4 Free Energy of Adhesion

With basis shapes chosen, shape and extrinsic constraints applied, and mechanical sources of energy calculated, we are now in a position to calculate the equilibrium shape of an adhered vesicle. The general prescription is to minimize the free energy subject to the area and volume constraints, however, application of those constraints may take on multiple forms. The first method one might employ is to use Lagrange multipliers to impose the constraints, which would require functional minimization over five independent variables — the radii R_1 and R_2, the angle θ_1 and the Lagrange multipliers for area and volume, that is the tension and pressure, respectively. We will employ an alternate method, where we treat the membrane area and the enclosed volume as linear elastic media. This requires knowledge of the area stretch modulus of the membrane ($K_A = O(100)\, k_BT/\text{nm}^2$ [26]) and bulk modulus of water ($K_V = 520\, k_BT/\text{nm}^3$ [155]), but advantageously does not require two more optimization variables. Then sum of all the contributions to the free energy is

$$G = G_b^{(1)} + G_b^{(2)} - \pi R_3^2 \rho_3 \gamma + A_o \frac{K_A}{2} \left(\frac{A - A_o}{A_o} \right)^2 + V_o \frac{K_V}{2} \left(\frac{V - V_o}{V_o} \right)^2, \tag{5.43}$$

where the bending modulus of the membrane is nominally $\kappa_b = 20\, k_BT$ [26]. This free energy is now minimized with respect to the two radii of curvature and solid angle, generating the three equations

$$\frac{\partial G}{\partial R_1} = 0 \ , \ \frac{\partial G}{\partial R_2} = 0 \text{ and } \frac{\partial G}{\partial \theta_1} = 0, \tag{5.44}$$

which must be solved simultaneously. Given the minimized values of the three shape parameters, our use of an elastic penalty makes calculating the membrane tension and pressure gradient straightforward, where the tension on the membrane is

$$\tau = K_A \left(\frac{A - A_o}{A_o} \right) \tag{5.45}$$

and the pressure gradient across the membrane is

$$p = -K_V \left(\frac{V - V_o}{V_o} \right). \tag{5.46}$$

Measuring these two quantities is less straightforward in practice, because measurements from microscopy give us A and V via measurements of R_1, R_2 and θ_1, *not* precisely A_o and V_o as we would like. However, this is not a serious issue considering that the fractional change in area and volume due to adhesion will be very small, and knowing the pressure and tension are not required to perform the shape analysis.

We have ignored the effects of configurational entropy, although, it is in a sense encompassed in the parameter γ, since any oligomeric binding energy we measure is the sum of the enthalpic and entropic free energy contributions [105]. The configurational entropy imparts a chemical potential

that penalizes proteins which enter the adhesion zone, however, for a given protein density this simply means there is some 'effective' binding energy, which we will assume is the same as γ. That said, recall in Section 5.3.4 we explicitly discussed how to handle the contribution from configurational entropy. With the protein density of the free floating vesicle specified, we could also minimize the free energy of the adhered vesicle shape treating the ratio of the densities of the protein in the two regions as a free variable, hence adding a fourth minimization equation. In the numerical simulations that follow, we chose not to implement this because it does not change the class of available shapes. Although, in future theoretical work it could be added as a useful tool for estimating desired, nominal protein densities in an experiment for a given L1 oligomeric binding energy.

5.4.1 Connection to Experiment

A typical experiment is, in some sense, precisely the opposite of searching for the shapes that minimize the free energy. In an experiment, an image or images of an adhered vesicle give a measure of R_1, R_2, R_3, θ_1, and θ_2, thus allowing us to calculate V and A, as well as the bending energy of each region (to within a constant), as prescribed by the formulas that incorporate these shape parameters. The assumption is that this measured shape is the result of mechanical equilibrium. Hence, upon measuring vesicle shape, the only 'free' parameters in our energy functional are the bending modulus (κ_b) and the adhesion energy ($\gamma\rho_3$ or γ depending on whether one takes into account configurational entropy). As we stated earlier, the adhesion energy has an entropic component, making it difficult to tease out the exact oligomeric binding energy in the absence of measurements of the protein density in the adhered and unadhered zones. If one calibrates the phL1-GFP fluorescence, as discussed earlier, and calculates the density and hence number of proteins in the adhesion zone, then only the bending modulus and the enthalpic oligomeric binding energy are free parameters. Looking back at eqn. 5.43, since both $E_b^{(1)}$ and $E_b^{(1)}$ have a pre-factor of κ_b, from any one measurement of vesicle shape we can only determine the ratio of the bending energy to the adhesion energy. If, however, a vesicle is imaged at different reduced volumes this changes the shape parameters in such a way that we can untangle κ_b from γ. Thus to properly calibrate the results, either multiple vesicles, or multiple shapes from the same vesicle must be measured, from which one can determine the bending modulus and the adhesion strength uniquely.

5.5 Simulating Adhered Vesicle Shape

In our numerical simulations, whose results are qualitatively discussed below, we explored the effects of changing different material and extrinsic parameters on vesicle shape. In most cases that follow, we adopt a scheme where an area, A_o, is chosen in accordance with vesicles in the size range of microns, and the corresponding volume is slightly less than a sphere with the same area. One key

parameter we use to characterize vesicle shape is the reduced volume, s, defined by

$$V_o = s \cdot \frac{A_o^{3/2}}{6\sqrt{\pi}}, \tag{5.47}$$

where this parameter falls in the range $0 < s < 1$. In the following figures, we simulate how the shape, tension, pressure, and overall energy vary as we adjust either: i) the reduced volume for fixed vesicle area with bending moduli of $\kappa_b = 5\,k_BT$ as in Fig. 5.6, $\kappa_b = 20\,k_BT$ as in Fig. 5.7, or $\kappa_b = 80\,k_BT$ as in Fig. 5.8; or ii) the vesicle area and hence overall vesicle size for fixed reduced volumes of $s = 0.8$ as in Fig. 5.9, and $s = 0.93$ as in Fig. 5.10.

After spending arduous hours writing, troubleshooting and stabilizing a numerical MatLab© routine, we explored how reduced volume, vesicle size, bending stiffness, and adhesion strength affect the vesicle shape. Many of these effects are complementary, that is, changing one parameter is similar to inversely changing another. Likewise, distinct regions of parameter space may yield very similar shapes, which we refer to as 'limiting shapes.' One can understand this with a simple thought experiment. Consider what happens if either the adhesion strength is very high or the bending modulus is very low. In either case the toroidal transition zone shrinks leaving only the circular adhesion zone and spherical vesicle above it. This type of shape is only determined by the vesicle area and enclosed volume. This is an important conclusion because it means that if we cannot experimentally distinguish the adhered vesicle shape from the limiting shape with the same surface area and volume, we learn nothing about adhesion. Hence, as we discuss below, it behooves us to use either relatively stiff membranes or a relatively low density of phL1 proteins in the membrane.

Increasing the bending modulus generically increases all radii of curvature subject to the constraints, however its effect becomes more pronounced at lower reduced volumes. Naturally, this is because as reduced volume grows close to one ($s = 1$), we approach the limiting shape of a sphere, with little freedom for changes in shape. As the reduced volume of a relatively stiff bilayer decreases, the shape remains more spherical. At relatively low bending modulus, we approach the class of limiting shapes.

Reduced volume is the most sensitive knob we have to turn, and luckily it can be adjusted relatively easily in experiment, where an adhered vesicle can have volume added or removed by osmotic conditioning. As the reduced volume approaches one, we reach the limiting shape of a sphere. However, as we decrease from $s = 1$, a range distorted shapes become available to the vesicle. Depending on the bending modulus and adhesion strength these shapes may remain rather spherical or approach the limiting shape. For low adhesion strength and/or high bending modulus the spherical shapes are preferred. For lower reduced volume with high adhesion strength and/or low bending modulus we approach the limiting shape.

We also explored the effect of overall vesicle size, by fixing the reduced volume and adjusting the total surface area. Related to our comments above, for fixed bending modulus and adhesion

strength, smaller vesicles are more spherical and larger vesicles approach the limiting shape, as shown in Figs. 5.9 and 5.10.

Lastly, augmenting adhesion strength has a very similar effect to decreasing bending modulus. While varying adhesion strength, we explored how the shape changes for a fixed volume, surface area and bending modulus. This seems to be the least sensitive parameter with many shapes close to the class of limiting shapes.

5.5.1 Note on Linearity of Tension and Pressure

Additional results showed that when volume and surface area are fixed increasing adhesion strength linearly increases both tension and pressure. The fluidity of the membrane allows surface energy, created by adhesion, to be directly and uniformally translated into an increase in membrane tension. In the scenario of fixed volume and surface area, where we are approaching the limiting shape, the adhesion zone size is approximately independent of adhesion strength. Thus linearly increasing adhesion strength means linearly increasing membrane tension. The corresponding linear increase in pressure is merely a reflection of the fact that given a fixed volume and surface area, and approaching the geometrically limited shape, the radius of curvature is also independent of adhesion strength. In such situations, where the free energy of bending is small in comparison to the work done by changes in area and volume, increasing adhesion strength is related to increasing pressure via the membrane tension through the Laplace-Young relation

$$p = 2\frac{\tau}{R_1}. \tag{5.48}$$

This relationship only holds true in regimes where the bending energy is small in comparison to the surface ($\tau(A - A_o)$) and volumetric ($-p(V - V_o)$) energies. In our numerical analysis, we verified that this independently derivable law holds true in such regimes, as shown in all the subsequent figures by the blue dashed lines in the plots of vesicle pressure.

5.6 Tether-Based Assay of Vesicle Adhesion

In addition to passively measuring the mechanical properties of adhered vesicles, that is, by simply looking at the adhered shape of a vesicle, we can also design experiments that allow us to apply well-controlled forces that deform the vesicle in such a way that we can measure its mechanical properties. The tethered vesicle shape is such a case, where in the simplest model we presume there are two vesicle regions: i) a large spherical section defined by radius R_1 and angle θ_1, ii) a thin tubule region defined by R_2 and L. As shown in Fig. 5.11, a force F is applied to the tube's end to distort the shape. In this section we derive the constrained volume and area of this geometry, and minimize the energy to better understand its force–extension properties.

It should be noted that much work has been done, both theoretically [264, 263] and experimentally [182, 290, 262], to understand the shape and force extension properties of membrane tubes.

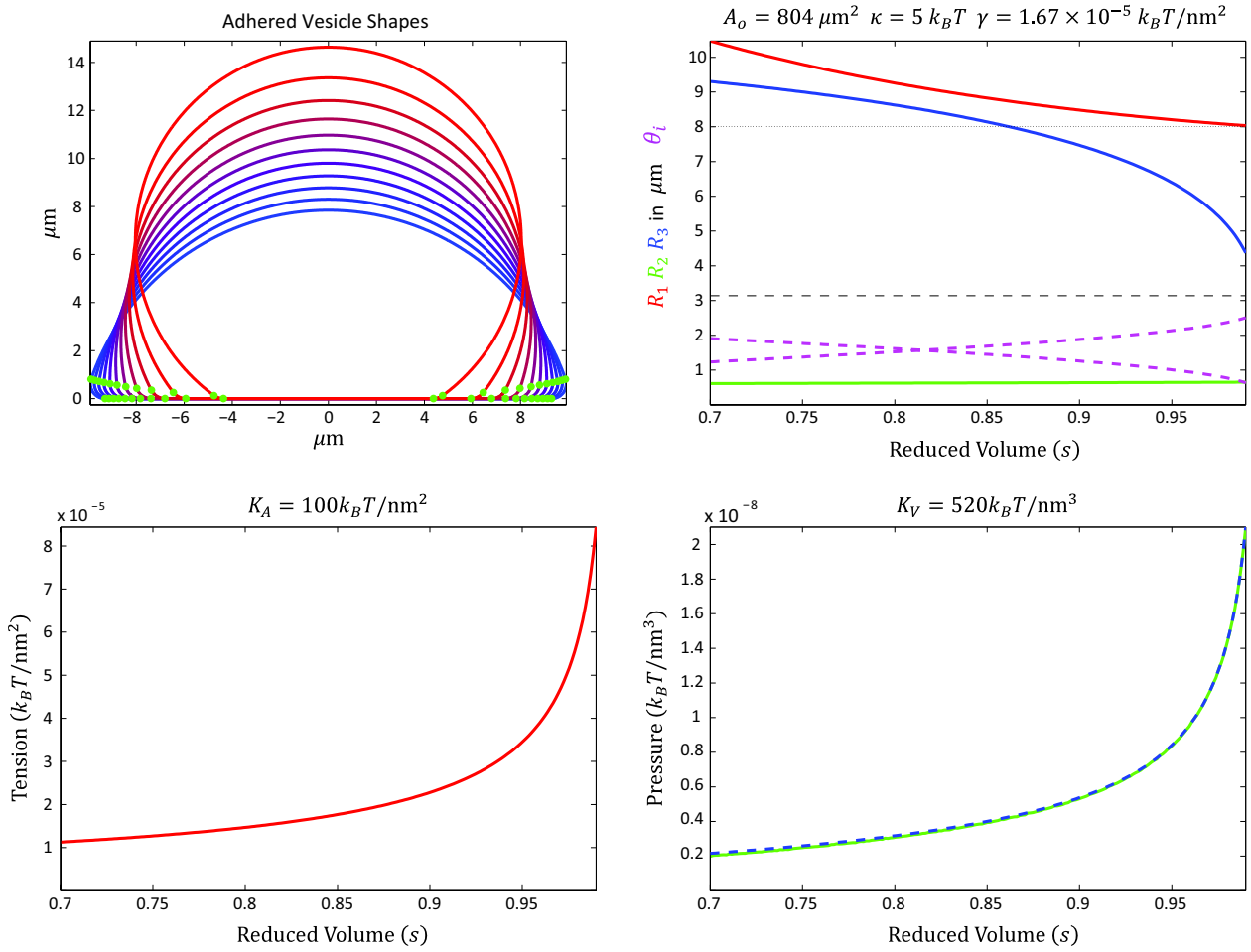

Figure 5.6: Simulations of adhered vesicle shape for fixed area with effects of decreasing the reduced volume on shape, tension, and pressure with $\kappa_b = 5\,k_BT$. The green dots in the upper-left plot demarcate the basis functions. The blue dashed line in the lower right plot is the approximate result from the Laplace-Young relation in eqn. 5.48.

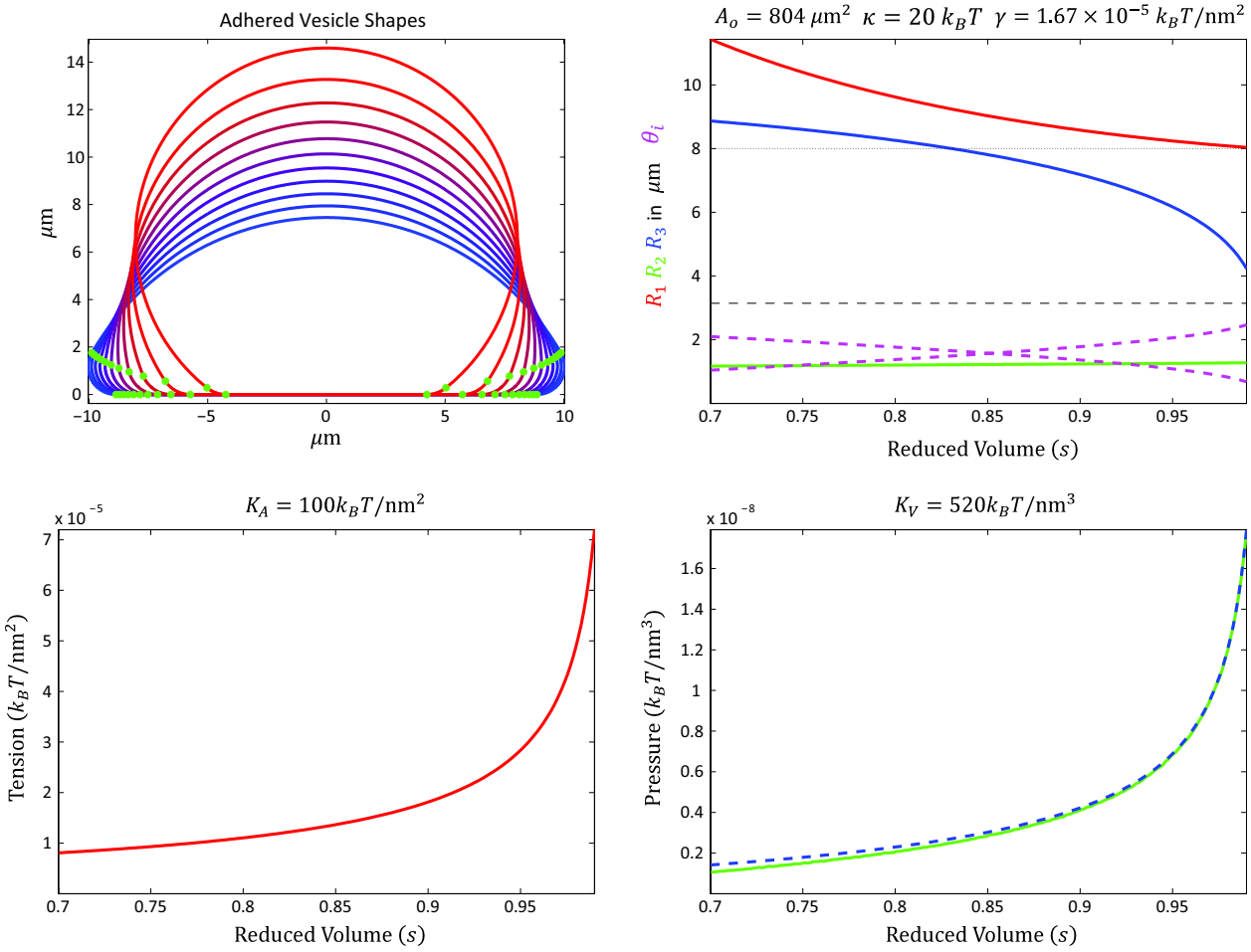

Figure 5.7: Simulations of adhered vesicle shape for fixed area with effects of decreasing the reduced volume on shape, tension, and pressure with $\kappa_b = 5\,k_BT$. The green dots in the upper-left plot demarcate the basis functions. The blue dashed line in the lower right plot is the approximate result from the Laplace-Young relation in eqn. 5.48.

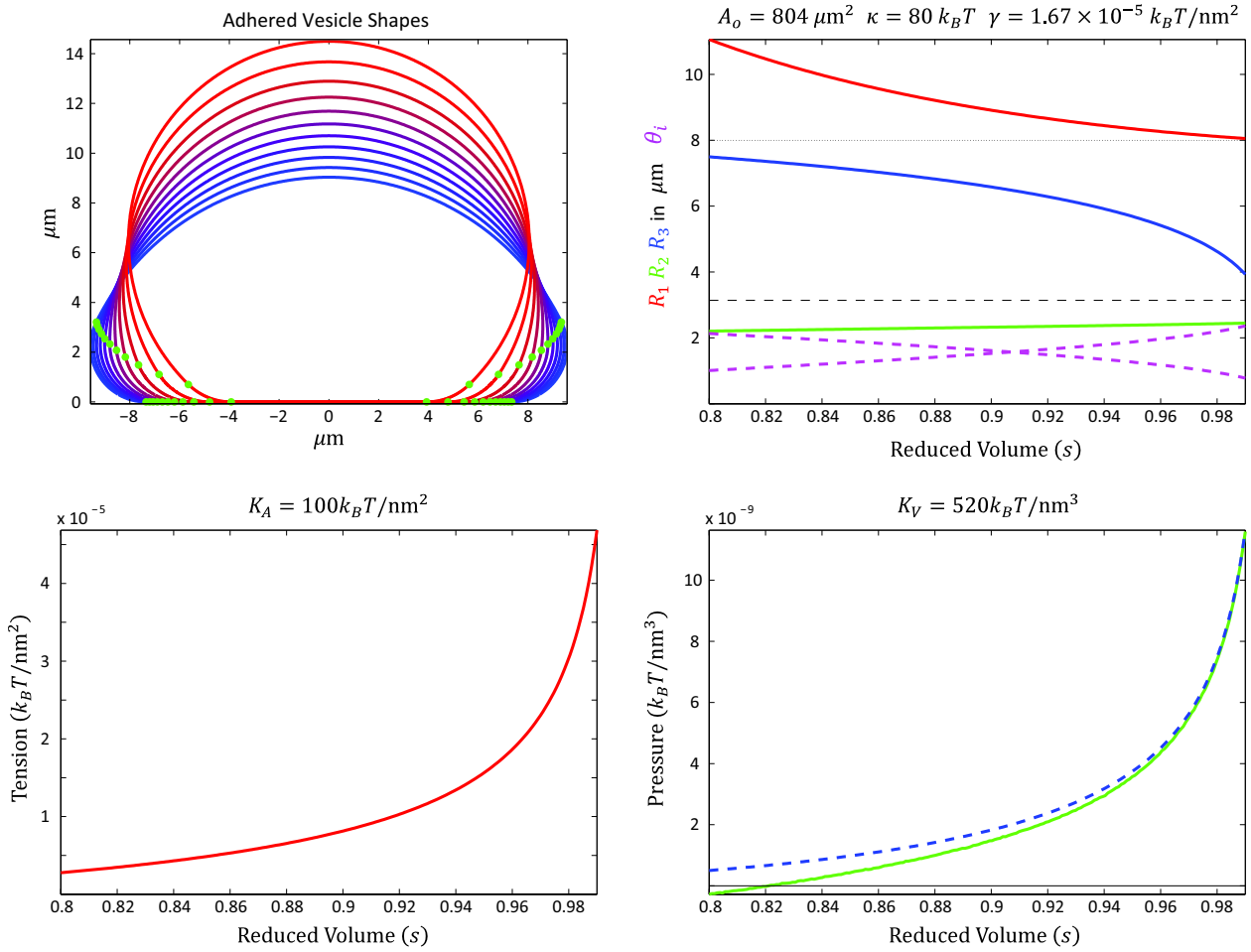

Figure 5.8: Simulations of adhered vesicle shape for fixed area with effects of decreasing the reduced volume on shape, tension, and pressure with $\kappa_b = 5\,k_BT$. The green dots in the upper-left plot demarcate the basis functions. The blue dashed line in the lower right plot is the approximate result from the Laplace-Young relation in eqn. 5.48.

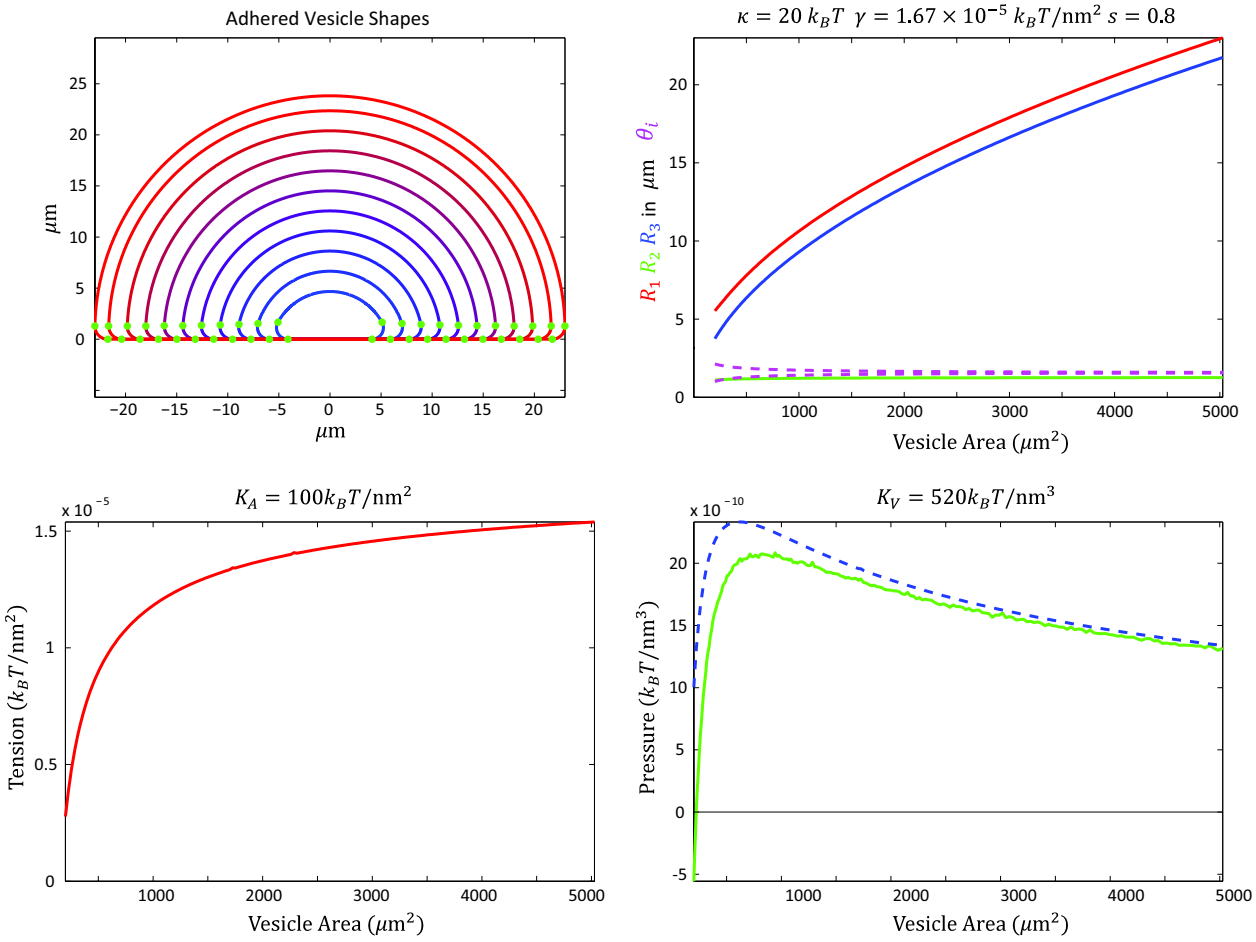

Figure 5.9: Simulations of adhered vesicle shape for fixed reduced volume with effects of increasing total vesicle area, and hence overall vesicle size, on shape, tension, and pressure with $s = 0.8$ and $\kappa_b = 20\, k_B T$. The green dots in the upper-left plot demarcate the basis functions. The blue dashed line in the lower right plot is the approximate result from the Laplace-Young relation in eqn. 5.48.

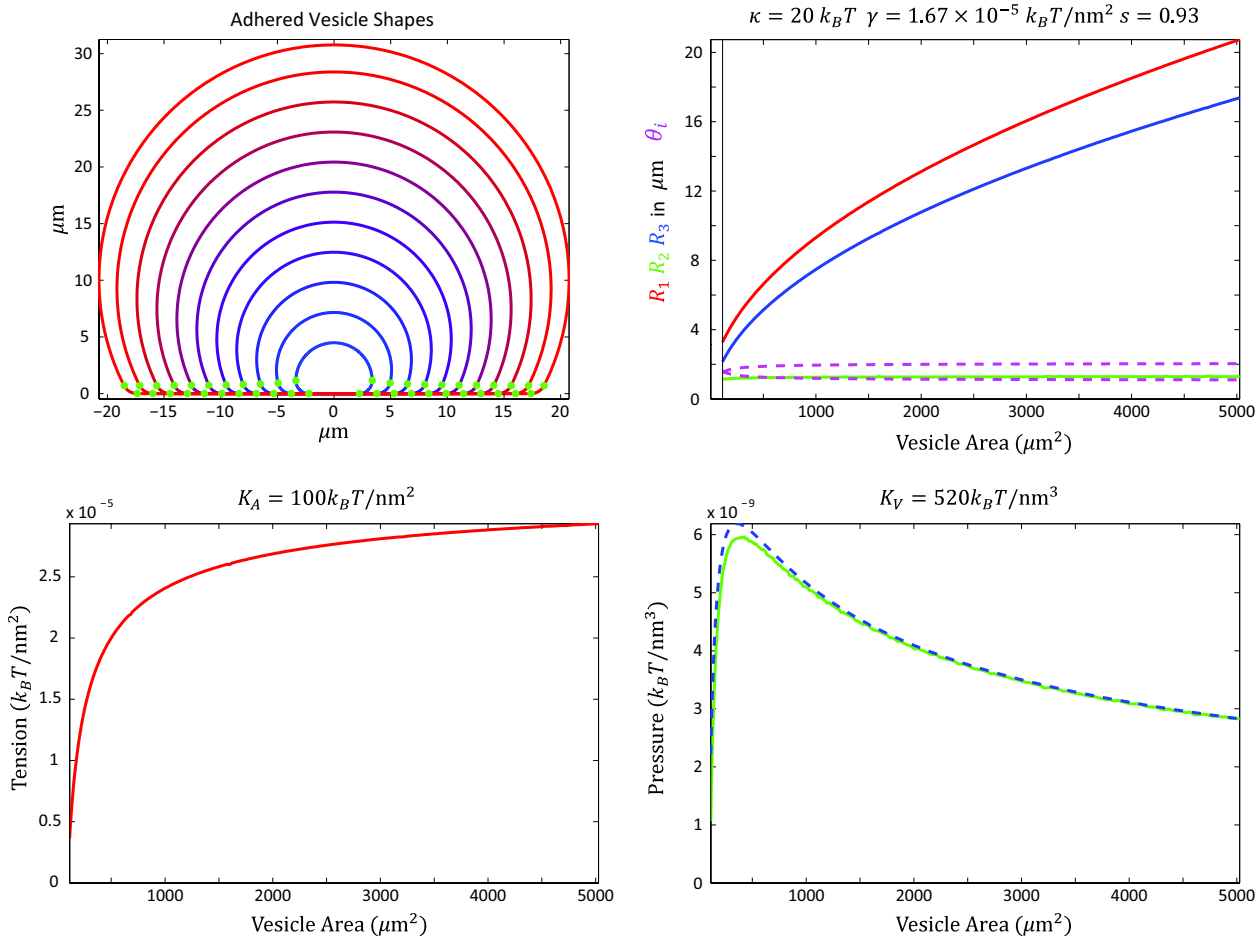

Figure 5.10: Simulations of adhered vesicle shape for fixed reduced volume with effects of increasing total vesicle area, and hence overall vesicle size, on shape, tension, and pressure with $s = 0.93$ and $\kappa_b = 20\, k_B T$. The green dots in the upper-left plot demarcate the basis functions. The blue dashed line in the lower right plot is the approximate result from the Laplace-Young relation in eqn. 5.48.

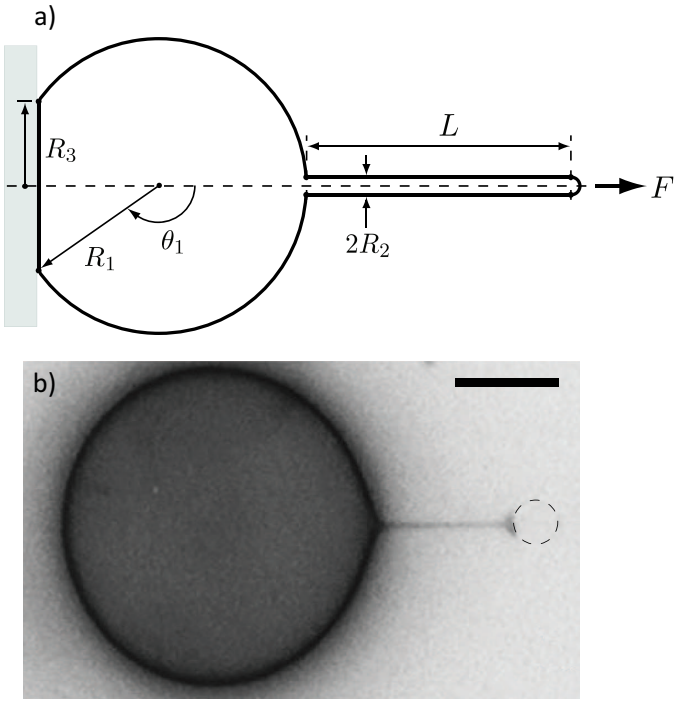

Figure 5.11: Schematic of the parameters needed to construct the basis shape model of tethered vesicle adhesion. a) A diagram showing the geometric parameters that characterize the shape of an adhered vesicle with a membrane tubule. A known force F is applied to the tether end via an optical tweezer, and the force extension properties of the tether can, in certain regimes, give a readout of the adhesion strength. The small black dots demarcate where one basis shape ends and another begins. b) A phase contrast image of membrane tether being pulled from a GUV by a bead in an optical trap, as outlined by the dashed line. The scale bar is $10\,\mu$m. This image adapted from [262].

As we will see later, one of the generic features that arises in a system with fixed surface area and volume is that for large tube lengths, as compared to their diameter, the force–extension properties are linear and do not encode specific information about substrate adhesion.

5.6.1 Tethered Vesicle Area

Calculating vesicle area is relatively simple compared to the previous geometry. Using eqn. 5.5, we know the area of the spherical region is

$$A_1 = 2\pi R_1^2(1 - \cos(\theta_1)) - \pi R_2^2, \tag{5.49}$$

while the area of the of the tether region is

$$A_2 = 2\pi R_2 L + 2\pi R_2^2. \tag{5.50}$$

Finally, the area of the adhesion zone is

$$A_3 = \pi R_3^2 = \pi R_1^2 \sin^2(\theta_1). \tag{5.51}$$

Together, these form the area constraint equation

$$A_o = A(R_1, R_2, \theta_1, L) = A_1 + A_2 + A_3. \tag{5.52}$$

5.6.2 Tethered Vesicle Volume

Likewise, calculating vesicle volume is relatively simple compared to the previous geometry. Using eqn. 5.14, we can write the volume in the spherical region as

$$V_1 = \frac{\pi}{3} R_1^3 (1 - \cos(\theta_1))^2 (2 + \cos(\theta_1)) - \frac{\pi}{3} R_1^3 (1 - \sqrt{1 - (R_2/R_1)^2})^2 (2 + \sqrt{1 - (R_2/R_1)^2}), \tag{5.53}$$

where the angle $\sin^{-1}(R_2/R_1)$ is used to remove double counted volume. In the tether region, the volume is given by

$$V_2 = \pi R_2^2 L + \frac{2}{3} \pi R_2^3. \tag{5.54}$$

Then the volume constraint is given by

$$V_o = V(R_1, R_2, \theta_1, L) = V_1 + V_2. \tag{5.55}$$

5.6.3 Bending Energy of a Tethered Vesicle

The bending energy of the spherical and tether region are relatively easy to calculate in the geometry. We already calculated the bending energy of the spherical region in eqn. 5.31, giving us

$$G_b^{(1)} = 8\pi\kappa_b \frac{A_1}{4\pi R_1^2} = 4\pi\kappa_b (1 - \cos(\theta_1)) - 2\pi\kappa_b \left(\frac{R_2}{R_1}\right)^2 \tag{5.56}$$

The bending energy in the tether region is then

$$G_b^{(2)} = 2\kappa_b H^2 A_2 = 2\kappa_b \left[\frac{2\pi R_2 L}{(2R_2)^2} + 2\pi\right], \tag{5.57}$$

which simplifies to

$$G_b^{(2)} = 4\pi\kappa_b \left[\frac{L}{4R_2} + 1\right]. \tag{5.58}$$

The bending energy of the hemispherical cap of the tube is constant and hence does not affect the vesicle shape.

5.6.4 Free Energy of Tethered Vesicle Adhesion

As force is applied to the membrane tether, an increase in tether length does work against the force lowering the free energy. Thus, this geometry has one new energetic term connected to the externally applied force,

$$G_F = -F\left[\, R_1[(1-\cos(\theta_1)) - (1-\sqrt{1-(R_2/R_1)^2})] + L + R_2 \,\right] \tag{5.59}$$

where F is the applied force and the term in brackets is simply the distance from the substrate to the tether tip. As we did earlier, we treat the membrane and enclosed volume as linear elastic media, and apply the surface area and volume constraints using an elastic penalty, yielding the total free energy of a tethered vesicle as

$$G = G_b^{(1)} + G_b^{(2)} + G_F - \pi R_3^2 \rho_3 \gamma + A_o \frac{K_A}{2}\left(\frac{A-A_o}{A_o}\right)^2 + V_o \frac{K_V}{2}\left(\frac{V-V_o}{V_o}\right)^2. \tag{5.60}$$

Given the set of relevant parameters, namely κ_b, F and γ, this energy is minimized with respect to the four shape variables R_1, θ_1, R_2 and L, using the system of equations defined by the partial derivatives of G. Again, we have neglected the specific contribution from configurational entropy, however it does not affect the class of possible vesicle shapes.

Numerical solutions for the geometric parameters, and the resulting vesicle shapes, are shown in Fig. 5.13. Initially, as force increases and the tether elongates, the majority of the area required to elongate the tether is coming from delamination of membrane in the adhesion zone, and hence this initially nonlinear rise in the force encodes information about the adhesion strength, as shown in Fig. 5.12. At relatively high forces, the tether is very thin and many times longer than the spherical vesicle diameter. For tethers much longer than they are wide, that is $L/R_2 \gg 1$ and consequently $R_1/R_2 \gg 1$, one finds that the tether length is proportional to the force and is independent of the adhesion strength. To see this, consider that the free energy in eqn. 5.60 can be written in a simplified form if $R_1/R_2 \gg 1$. Then examining the equilibrium equation for L, that is $\partial G/\partial L = 0$, results in an equation that has no dependence on R_1 and R_2, and the force extension relationship is given by

$$L = F \cdot \frac{A_o - (36\pi)^{\frac{1}{3}} V_o^{\frac{2}{3}}}{4\pi^2 \kappa_b}, \tag{5.61}$$

which clearly has no dependence on the adhesion strength, γ. Thus it is only the low force regime that reports on adhesion properties.

5.6.5 Connection with Experiments

As with the previous geometry, the experiment provides values for geometric parameters of the vesicle, namely R_1, R_3, θ_1, L, and in this geometry measurements of the pulling force F as measured by the optical trap. Before the bead is attached to the membrane, we have the same adhered

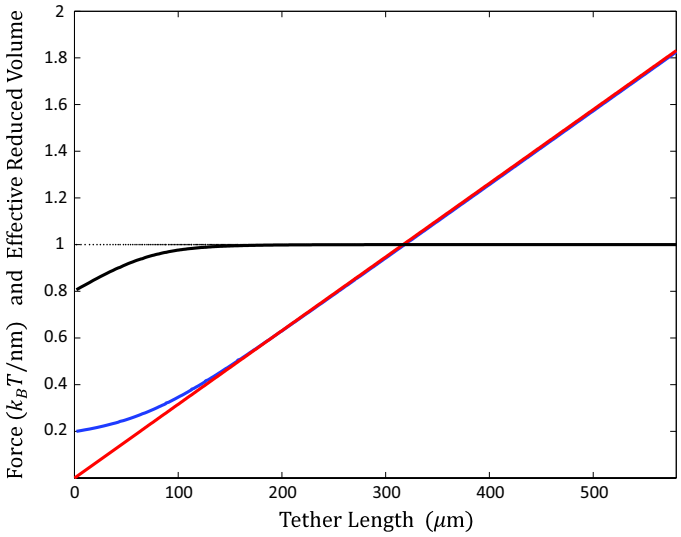

Figure 5.12: Force extension properties of a tether pulled from an adhered vesicle with reduced volume $s = 0.8$. The blue shows the numerical simulation of force extension. At sufficiently high force the tube is very long in comparison to its diameter and the force-extension is linear (red), hence the tether behaves like a spring. The effective reduced volume, shown in black, is defined as the reduced volume of the spherical region without the tether. Pulling a tether removes both volume and area, but with a scaling such that the vesicle itself approaches a sphere (*i.e.* $s = 1$). It is the (brief) nonlinear portion of the force extension curve that encodes information about the adhesion strength. $1\,k_BT/\text{nm} = 4.14\,\text{pN}$.

vesicle geometry that we explored in the previous section, and it is straightforward to measure the conserved vesicle volume and surface area in that geometry. By measuring the R_1, R_3, θ_1 and L, and knowing the surface area and volume, we can calculate the value of R_2 for all values of F. It is difficult to directly measure R_2 because membrane tubes are often quite thin and hence difficult to resolve optically and measure accurately under the microscope [262]. With all the shape parameters known, we can minimize the shape energetics with respect to the material parameters κ_b and γ as we discussed in Section 5.4.1. Additionally, as we discussed earlier, multiple vesicle measurements need to be performed to tease apart the contributions to the nonlinear part of the force extension curve from bending stiffness and adhesion.

5.7 Experimental Setup

In the following few subsections we will discuss some progress that has been made in forming giant unilamellar vesicles with incorporated L1 protein. This work progressed first by examining whether we could achieve vesicle-vesicle adhesion, and has recently moved on to confocal microscopy experiments of vesicles on adhered glass substrates, in correspondence with our theoretical analysis.

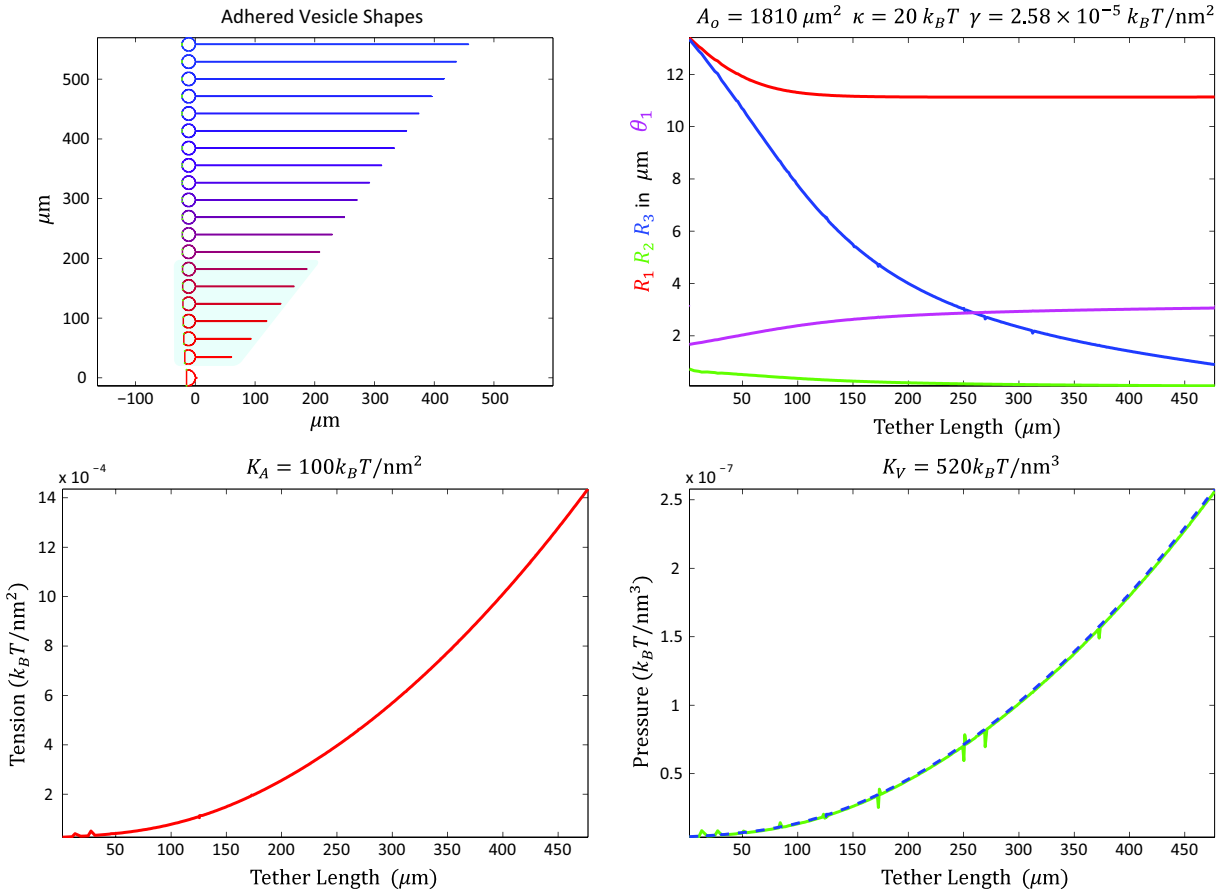

Figure 5.13: Effects of increasing tether force on vesicle shape, tension, and pressure with $s = 0.8$ and $\kappa_b = 20\,k_BT$. In the upper-left plot, the green dots demarcate the adhesion zone and light blue region is the approximate range of vesicle shapes whose force extension properties encode information about adhesion. The blue dashed line in the lower right is the result from the Laplace-Young relation of eqn. 5.48.

The experimental setup will be discussed in some detail, along with certain challenges and future directions.

5.7.1 Controls and Vesicle-Vesicle Binding

Lipid head groups can be tailored to take advantage of a number of molecular interactions, and in particular certain phospholipids have been made with coordinated Ni^{+2}, such that a poly-histidine purification epitope will bind tightly, though reversibly, by chelation to the lipid head group, in a way chemically identical to standard poly-histidine affinity chromatography [291]. The lipids themselves are hydrophobically anchored in the bilayer, hence this gives us a method for securing proteins to a bilayer at a known concentration. In short, as the experimentalists, we control the exact composition of the bilayer, and in particular we used a standard DOPC phospholipid bilayer[6] and 'dope' it with a small mole fraction (0.5%) of the Ni^{+2} containing lipid DOGS-NTA[7], to whose head group the epitope will bind. Truncation mutants of the wild type L1 were made that lack the transmembrane and cytosolic domains, but have an added poly-histidine epitope (we call this form of the protein 'phL1')[8].

Throughout this thesis, we have discussed experiments that make use of giant unilamellar vesicles, formed by electroformation [265], as discussed in detail in Appendix E. The GUVs in this experiment are formed with a molar mixture of 99:0.5:0.5 (DOPC:DOGS-NTA:DOPE-Rhodamine[9]), such that the GUVs are easy to form, are fluorescently labeled, and have a surface to which phL1 will adsorb. The structure of the acyl chains of all three of these lipids, and hence their hydrophobic properties, are identical, thus we neither expect nor observe any lipid immiscibility [130].

After formation, GUVs were split into control and adhesion groups. No phL1 was added to the control group, and phL1 was added at a concentration of $\sim 25\mu$g/ml to the adhesion group, and left to incubate at room temperature for one hour. This protein concentration leads to nearly complete coverage of the glass substrate (data not shown). Figure 5.14 shows images of unadhered vesicles in the control group, and adhered vesicles in both bright field and fluorescence in the adhesion group. The density of vesicles in the control was kept relatively high to ensure that vesicles were in direct contact. The density of vesicles in the adhesion group can be adjusted such that either most vesicles are unadhered and free floating, vesicles occasionally adhere to one another to form groups of two, or at the highest density vesicles form large, adhered multi-vesicle aggregates, as shown in Fig. 5.15.

With a good handle on how to form doped vesicles, adhere the phL1 to the vesicles, and control its density, we began to look for ways realize our experimental setup, where the deformation shape of an azimuthally symmetric vesicle adhered to a substrate could serve as a reporter of adhesion properties.

[6] Avanti Polar Lipids, Inc. PN: 850375C

[7] Avanti Polar Lipids, Inc. PN: 790404C

[8] Thanks goes to Fan Yang and the Bjorkman Lab at Caltech for constructing these mutants.

[9] This head group labeled fluorescent lipid is also available from Avanti Polar Lipids, PN: 810150C.

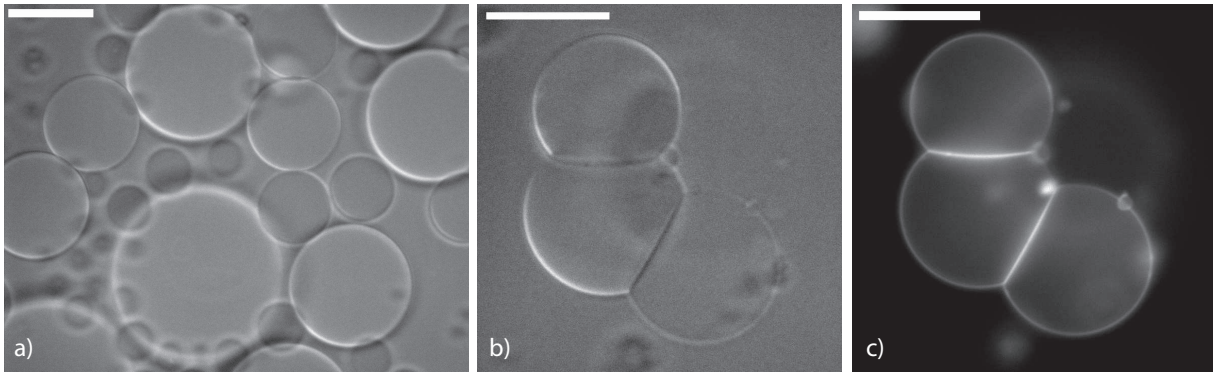

Figure 5.14: Control and adhesion vesicle groups. a) This bright field image shows the control group of GUVs, composed of a mixture of DOPC, DOGS-NTA and DOPE-Rhodamine, with no phL1 introduced. Though the vesicles are at high density, they remain separate as indicated by their perfectly spherical shape. b) Vesicles with the same composition as those in (a), except these have been incubated with phL1 for one hour at room temperature, and adhesion between vesicles is ubiquitous, in contrast to the control group. c) The same set of adhered vesicles as in (b), except viewed in epi-fluorescence. The scale bars are 20 μm.

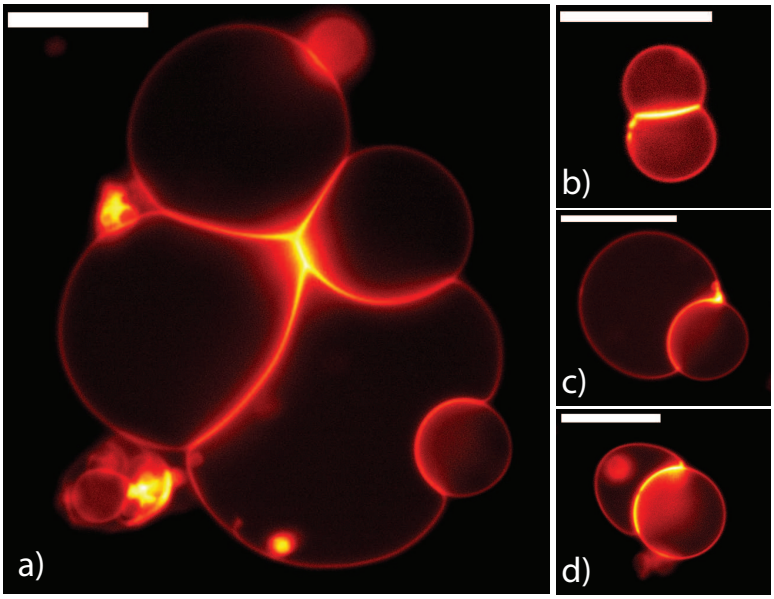

Figure 5.15: Adhered vesicles at varying density. a) This fluorescent picture shows a collection of adhered vesicles when the overall vesicle density is high. b–d) Examples of two adhering vesicles that have different surface area to volume ratios. Notice in (b) the vesicles are roughly the same size and have the same surface area to volume ratio, and hence have roughly symmetric adhered shapes, whereas in (c) and (d) one vesicle is spherical and hence incapable of deforming, while the other vesicle severely deforms upon adhesion. The scale bars are 20 μm.

5.7.2 Azimuthally Symmetric Vesicle Adhesion

Having shown that we can control the density of L1 in a bilayer through the use of lipids with coordinated Ni^{+2}, we set out to produce the substrate-adhered vesicle geometry, as described earlier. Again, the poly-histidine epitope on the otherwise wild type protein, comes in handy. Recently, protein microarrays have made use of professionally fabricated substrates that link coordinated ions, specifically Cu^{+2}, such that poly-histidine epitopes tightly bind to the coated glass substrate[10]. The phL1 is incubated in Tris-buffered saline solution (TBS) with the glass substrate for approximately one hour at room temperature. The substrate is then washed with the same buffering solution that does not contain phL1, to remove any unadhered protein. Vesicles that have been separately incubated with phL1 are then introduced into the chamber and allowed to settle to the bottom, where they will adhere.

For the first round of experiments, confocal microscopy was used to image the adhered vesicle shape, as shown in Fig. 5.16. These first experiments present us with some encouragement and a number of challenges. Vesicle adhesion to the glass substrate, forming shapes that report on the properties of adhesion, is certainly possible. That said, at least two challenges still remain. First, we need to titrate the concentration of phL1 incubated with the substrate, so that the density is high enough that vesicles adhere, but low enough that their shape deviates from the limiting shape, discussed in Section 5.5. Second, we need to ensure that the substrate directly under the vesicle is clean and free of small adhered vesicles that will block formation of a circular adhesion zone. Figure 5.16a, for instance, shows an adhered vesicle whose adhesion zone is disturbed by smaller vesicles, such that the adhesion zone is slightly acircular. In Fig. 5.16b, the azimuthal projection of the adhesion zone is distorted by the acircularity of the adhesion zone.

5.7.3 Possible Extensions and Complications

Once the issues in the previous section have been addressed, there are new directions to be taken and complications to be considered. One potential complication is that it may be that phL1 proteins that engage in homophilic adhesion do so in groups or patches. Hence there would be no reason to expect the adhesion zone to be perfectly circular. This would present a problem for shape analysis since one of key assumptions is azimuthal symmetry. On a related note, while the author has no precise thoughts on this topic, future bearers of this torch should consider whether by additional measurements or new experiments more detailed information about the structure of the bound oligomeric state of L1 can be gleaned from mechanical analysis of membrane shape; conceptually this is akin to the kinds of bounds that have been explored for structural rearrangements during the gating of ion channels [68].

There are at least four other experimental directions to pursue. First, the experiment could be

[10]We purchased Cu^{+2} coated glass substrates from Microsurfaces, Inc., Minneapolis, Minnesota; http://proteinslides.com/HisTAG.html). Their web site contains numerous scholarly references and useful technical data on this product.

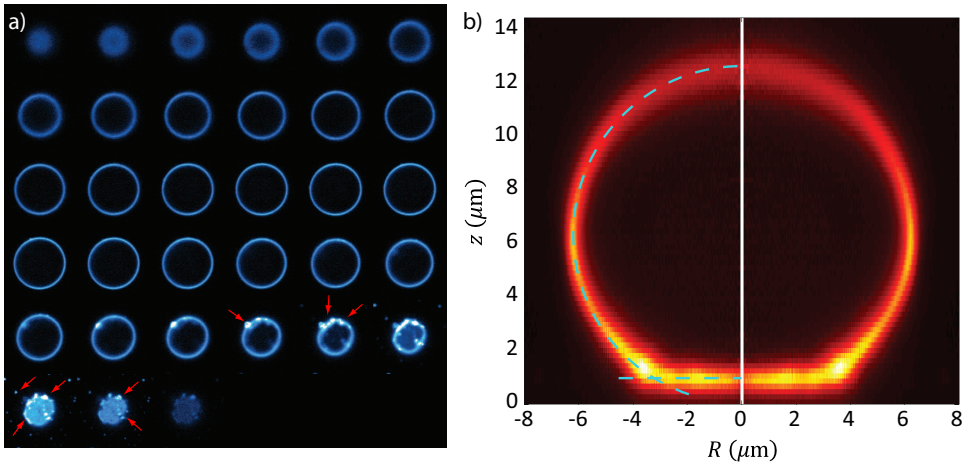

Figure 5.16: Vesicle adhered to a glass substrate. a) This montage shows consecutive confocal microscopy slices through a vesicle adhered to a glass substrate, starting from the spherical top down past the flat adhesion zone. Notice in the last few frames that small vesicles can be seen on the glass substrate that interfere with the formation of a circular adhesion zone, some of which are shown by the small red arrows. b) Images from the same vesicle in (a) are processed to form this side view of the adhered vesicle. Again, the adhesion zone shows intensity aberrations from the small vesicles that disturb it. The circular dashed line indicates the spherical portion of the vesicle, while the flat dashed line indicates the flat adhesion zone. The vertical white line is a 'blind' region in image processing.

performed in a flow chamber, where external osmolarity could be adjusted and hence the internal volume of the vesicle could be controlled. This would give an easy knob to adjust the vesicle shape and perform multiple measurements on the same vesicle. One could also perform the experiment hysteretically to ensure that adhesion shapes accurately portray the underlying mechanics. Additionally, this makes it easy to wash out the unadhered phL1 and free floating small vesicles that might otherwise adhere to the substrate. Second, while confocal microscopy is a way to gather three dimensional vesicle shape data, the resolution in z, which is essential for reconstructing an accurate shape, is lower than the $x-y$ resolution. Additionally, data from confocal microscopy must be post-processed to form the vesicle side view that is necessary for shape analysis (see Fig. 5.16). Both of these issues could be remedied if the vesicle were rotated after substrate adhesion, such that the $z-y$ or $z-x$ plane became the $x-y$ plane. This has the effect of putting a side view of the vesicle, necessary for shape analysis, into the image plane, hence increasing spatial resolution and reducing the required post processing. In fact, we are in the initial stages of doing precisely that; we cut small pieces of the substrate glass and orient them perpendicular to the image plane. Using a micropipette, we pick up the vesicle and put it in contact with the vertical substrate, to encourage adhesion. As of yet, no useful data have yet come from these experiments. The third direction is an assay similar to the tether-based shape analysis assay discussed here, that uses micropipettes and vesicle aspiration instead of beads and optical tweezers, to actively deform the adhered vesicle, and use deformed shape as a reporter of adhesion properties [292]. If the aforementioned version of the experiment that has the vesicle equator aligned with the image plane can be made to work, it is straightforward to employ his micropipette aspiration technique to measurements of membrane adhesion. Finally, all of these experimental techniques can, and where applicable, should be employed to better understand the properties of homophilic adhesion in the mutated forms of L1 that are associated with the aforementioned disease phenotypes.

5.8 Concluding Remarks

This chapter derived in detail basis shape models for vesicle adhesion that will be used as a tool for studying the biophysical properties of protein-mediated adhesion. We outlined a few questions that motivate this research, and while much work remains before they are adequately answered, we have made encouraging progress on both the experimental and theoretical fronts. Contingent upon working out the experimental kinks, this author looks forward to seeing if this system can be applied to other proteins or other systems of membrane adhesion. On a broader note, rarely do we as biophysicists get a chance to make a conceptually straightforward measurement that might inform us as to the roots of such a broad range of issues in human health.

Appendix A

Detailed Derivation of Bilayer Thickness Deformation

This section performs in detail the calculation of the thickness deformation of a bilayer and the resulting deformation free energy; these results were used and/or alluded to in Chapters 1 and 2.

Rescaling the radial coordinate and the deformation profile by the elastic decay length of the system

$$\lambda = \left(\frac{\kappa_b l^2}{K_A}\right)^{\frac{1}{4}}, \tag{A.1}$$

and translating the deformation profile by the tension-induced thinning

$$u(r) \to u(r) - \chi, \tag{A.2}$$

we can non-dimensionalize the energy functional to read

$$G = \pi\kappa_b \int_{\rho_o}^{\infty} \left(u^2 + (\nabla^2 u)^2\right) r\mathrm{d}r \tag{A.3}$$

yielding the parameter-free governing differential equation

$$(\nabla^4 + 1)u = 0. \tag{A.4}$$

We think of this differential equation as a linear operator, $\mathcal{L} = \nabla^4 + 1$, such that

$$\mathcal{L}[u] = 0. \tag{A.5}$$

In reality $\mathcal{L}$ is actually the multiplication of two other linear operators

$$\mathcal{L}_\pm = \nabla^2 \pm i, \tag{A.6}$$

where these operators obey the commutation rule $[\mathcal{L}_+, \mathcal{L}_-] = 0$, such that

$$\mathcal{L}_+\mathcal{L}_- = \mathcal{L}_-\mathcal{L}_+ = \nabla^4 + 1. \tag{A.7}$$

Since the equation is linear, the independent solutions for $\mathcal{L}_\pm$ are added to find the full solution.

To show this, assume there is a solution for $\mathcal{L}_{\pm}[u] = 0$, say $u(r) = u_+(r) + u_-(r)$, such that

$$\mathcal{L}_+[u_+] = 0 \tag{A.8}$$

and

$$\mathcal{L}_-[u_-] = 0, \tag{A.9}$$

then

$$\mathcal{L}[u] = \mathcal{L}_+\mathcal{L}_-\left[u_+ + u_-\right] = \mathcal{L}_- \underbrace{\mathcal{L}_+[u_+]}_{=0} + \mathcal{L}_+ \underbrace{\mathcal{L}_-[u_-]}_{=0} = 0. \tag{A.10}$$

The differential equations defined by $\mathcal{L}_{\pm}$ are known as the 'Complex Bessel Equations.' The roots of the secular equations, n, generated by $\mathcal{L}_{\pm}$ will be complex, and the solutions are given by $J_0(nr)$ and $K_0(nr)$, as one can verify by substitution. $\mathcal{L}_+$ generates the secular equations

$$J_0(nr) \rightarrow n^2 - i = 0 \rightarrow n = \pm k \tag{A.11}$$

$$K_0(nr) \rightarrow n^2 + i = 0 \rightarrow n = \pm ik \tag{A.12}$$

while $\mathcal{L}_-$ generates the secular equations

$$J_0(nr) \rightarrow n^2 + i = 0 \rightarrow n = \pm ik \tag{A.13}$$

$$K_0(nr) \rightarrow n^2 - i = 0 \rightarrow n = \pm k, \tag{A.14}$$

with $k = \sqrt{i}$, for what is initially a total of eight solutions. Immediately we can make use of the fact that $J_0(kr) = J_0(-kr)$ to reduce the solution set to

$$J_0(nr) \rightarrow n^2 - i = 0 \rightarrow n = k \tag{A.15}$$

$$K_0(nr) \rightarrow n^2 + i = 0 \rightarrow n = \pm ik \tag{A.16}$$

and

$$J_0(nr) \rightarrow n^2 + i = 0 \rightarrow n = ik \tag{A.17}$$

$$K_0(nr) \rightarrow n^2 - i = 0 \rightarrow n = \pm k. \tag{A.18}$$

One can also show that

$$J_0(kr) = \frac{i}{\pi}\left(K_0(ikr) - K_0(-ikr)\right) \tag{A.19}$$

$$J_0(ikr) = \frac{i}{\pi}\left(K_0(kr) - K_0(-kr)\right), \tag{A.20}$$

for $r > 0$ and any k. Since, the solution already contains $J_0(kr)$ and $J_0(ikr)$, we can use these

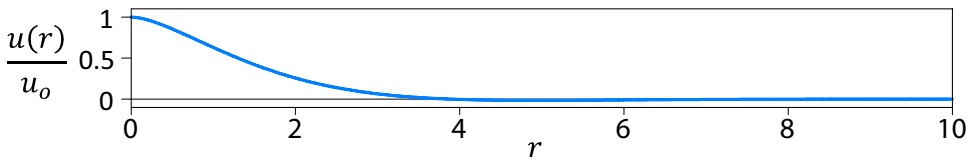

Figure A.1: The normalized deformation profile $u(r)/u_o$ that solves $\mathcal{L}[u] = \mathcal{L}_+\mathcal{L}_-[u] = 0$, with the stated boundary conditions at $r = R$.

relationships to write the general solution as only a function of K_0,

$$u(r) = c_1 K_0(kr) + c_2 K_0(-kr) + c_3 K_0(ikr) + c_4 K_0(-ikr), \tag{A.21}$$

or

$$u(r) = c_1 K_0(kr) + c_2 K_0(-kr) + c_3 K_0(-\bar{k}r) + c_4 K_0(\bar{k}r), \tag{A.22}$$

where $-ik = \bar{k}$ and the coefficients, c_j, are complex. Now we are prepared to apply the four boundary conditions

$$\lim_{r\to\infty} u(r) = 0 \tag{A.23}$$

$$\lim_{r\to R} u(r) = u_o \tag{A.24}$$

$$\lim_{r\to\infty} \partial_r u(r) = 0 \tag{A.25}$$

$$\lim_{r\to R} \partial_r u(r) = 0, \tag{A.26}$$

that generate four equations which can be solved simultaneously to find

$$c_1 = -u_o \frac{\bar{k}K_1(\bar{k}R)}{kK_1(kR)K_0(\bar{k}R) - \bar{k}K_1(\bar{k}R)K_0(kR)} \tag{A.27}$$

$$c_2 = 0 \tag{A.28}$$

$$c_3 = 0 \tag{A.29}$$

$$c_4 = u_o \frac{kK_1(kR)}{kK_1(kR)K_0(\bar{k}R) - \bar{k}K_1(\bar{k}R)K_0(kR)} \tag{A.30}$$

A plot of this function with $R = 0$ is shown in Fig. A.1.

The last thing we will do is solve for the energy. We will take the elegant route of calculating the energy by partial integration and conversion to a boundary integral. Recall the energy functional has the form

$$L[u] = u^2 + (\nabla^2 u)^2 \tag{A.31}$$

yielding the differential equation

$$\nabla^4 u + u = 0. \tag{A.32}$$

We can re-write the functional using the chain rule as

$$\nabla(\nabla^2 u \nabla u) = \nabla^3 u \cdot \nabla u + (\nabla^2 u)^2 \tag{A.33}$$

and

$$\nabla \cdot (u \nabla^3 u) = \nabla^3 u \cdot \nabla u + u \nabla^4 u. \tag{A.34}$$

Subtracting these two equations yields

$$(\nabla^2 u)^2 = u \nabla^4 u + \nabla \cdot (\nabla^2 u \nabla u - u \nabla^3 u), \tag{A.35}$$

allowing us to write the functional as

$$u^2 + (\nabla^2 u)^2 = u \underbrace{(u + \nabla^4 u)}_{=0} + \nabla \cdot (\nabla^2 u \nabla u - u \nabla^3 u) \tag{A.36}$$

$$u^2 + (\nabla^2 u)^2 = \nabla \cdot (\nabla^2 u \nabla u - u \nabla^3 u), \tag{A.37}$$

where we have made use of the Euler-Lagrange equation to eliminate the first term. Then using the Divergence Theorem, the integral for the energy can be written

$$G = \frac{\kappa}{2} \int_S \left(u^2 + (\nabla^2 u)^2\right) \mathrm{d}^2 r = \frac{\kappa}{2} \oint_{\partial S} \left(\nabla^2 u \nabla u - u \nabla^3 u\right) \cdot \mathrm{d}\hat{\mathbf{n}}. \tag{A.38}$$

Due to the azimuthal symmetry, the integrand is constant on the contour defined by ∂S, both at $r = R$ and $r \to \infty$, and the unit normal to the contour always points in the $\hat{r}$ direction, hence this integral is reduced to

$$G = \pi \kappa_b \hat{r} \cdot \left[\lim_{r \to \infty} r \left(\nabla^2 u \nabla u - u \nabla^3 u\right) - \left(r \left(\nabla^2 u \nabla u - u \nabla^3 u\right)\right)\big|_{r=R} \right]. \tag{A.39}$$

To handle the term that goes to infinity we examine the solution to find that

$$\lim_{r \to \infty} u(r) = c_1 \sqrt{\frac{\pi}{2kr}} e^{-kr} + c_4 \sqrt{\frac{\pi}{2\bar{k}r}} e^{-\bar{k}r}. \tag{A.40}$$

The exponential asymptotic behavior guarantees that u and all of its derivatives go to zero faster than the growth of any polynomial, hence

$$\lim_{r \to \infty} r \left(\nabla^2 u \nabla u - u \nabla^3 u\right) \cdot \hat{r} = 0, \tag{A.41}$$

reducing the energy to

$$G = -\pi \kappa_b R \hat{r} \cdot \left(\nabla^2 u \nabla u - u \nabla^3 u\right)\big|_{r=R}. \tag{A.42}$$

Using the boundary conditions $\partial_r u(R) = 0$ and $u(r) = u_o$ this further simplifies to

$$G = \pi \kappa_b u_o R \left(\hat{r} \cdot \nabla^3 u \right) \big|_{r=R} . \tag{A.43}$$

The gradient of the Laplacian of u can be written out explicitly along the $\hat{r}$ coordinate with knowledge of the differential operators in cylindrical coordinates

$$\nabla^2 = \partial_r^2 + \frac{1}{r} \partial_r \tag{A.44}$$

and

$$\nabla = \hat{r} \partial_r \tag{A.45}$$

such that

$$\nabla^3 = \nabla \nabla^2 = \hat{r} \left[\partial_r^3 + \frac{1}{r} \partial_r^2 - \frac{1}{r^2} \partial_r \right] . \tag{A.46}$$

Then explicitly, the energy is

$$G = \pi \kappa_b u_o R \cdot \left[\partial_r^3 u + \frac{1}{r} \partial_r^2 u \right] \Bigg|_{r=R} , \tag{A.47}$$

where again we have made use of $\partial_r u(R) = 0$. The solution for u can be written

$$u(r) = c_1 K_0(kr) + c_4 K_0(\bar{k} r), \tag{A.48}$$

yielding a relatively simple expression for the energy

$$G = 2\pi \kappa_b u_o^2 R \frac{i K_1(kR) K_1(\bar{k} R)}{k K_1(kR) K_0(\bar{k} R) - \bar{k} K_1(\bar{k} R) K_0(kR)} \tag{A.49}$$

Finally, an accurate and even simpler form can be written for the physiologically relevant cases where $R > 1$ via series expansion

$$G \simeq \pi \kappa_b u_o^2 \left(1 + \sqrt{2} R \right) . \tag{A.50}$$

Putting the dimensions back into this equation the energy becomes

$$G \simeq \pi \kappa_b \left(\frac{u_o}{\lambda} \right)^2 \left(1 + \sqrt{2} \frac{R}{\lambda} \right) . \tag{A.51}$$

A comparison of the energy in eqns. A.49 and A.50 is shown in Fig. A.2.

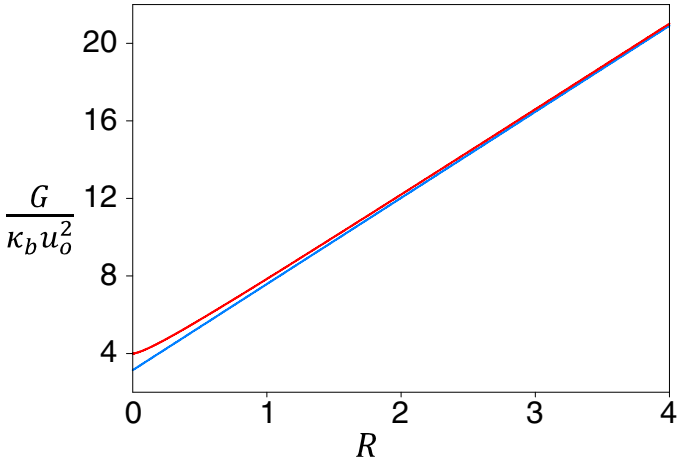

Figure A.2: Plots comparing the energy of thickness deformation as a function of channel radius. The normalized energy is plotted as a function of the dimensionless protein radius. The red line is the exact result from the Bessel function solution in eqn. A.49, and the blue line is the linear approximation from eqn. A.50.

MscL Expression, Purification and Reconstitution (with DOPC or Azolectin)

MscL STRAINS

Strain Name:	Tag / Selection	Description:
WT – 6His	6-His / Amp	Wt Ec MscL
V23D – 6His *	6-His / Amp	GoF Ec MscL
V23T – 6His	6-His / Amp	Severe GoF Ec MscL

(wt MscL - 14.96 kDa, MscL-6HIS – 15.78 kDa)
*toxic at purification levels

BUFFERS

LB (~2 L) and LB + Amp (5 mL – made fresh)

Component	Amount to Add	Final Concentration
Ampicillin (Sigma A9393)	4 mg	0.05 mg/mL (in LB)
ddH_20	1 mL	
64 uL aliquots for 5 mL LB		
Ampicillin (Sigma A9393)	16 mg	0.2 mg/mL (in LB)
ddH_20	1 mL	
64 uL aliquots for 5mL LB		

IPTG (Syringe filter with 0.2 μm pore size)

Component	Amount to Add	Final Concentration
IPTG (Sigma I5502)	1 g	1 M (245 mg/mL)
ddH_20	4196 μL	n/a

20x MscL Buffer: need 1 L per prep

Component	Amount to Add	Final Concentration
NaCl	116.88 g	2 M
Tris-HCl (Sigma T5941)	72.84 g	600 mM
ddH_20	1L	n/a

pH to 7.42, where upon dilution to 1X will be pH ~7.3.

Lysis Buffer: need 30 mL per prep
Notes: pH to 7.2-7.3 w/ HCl before adding protease inhibitor, DNase, lysozyme

Component	Amount to Add	Final Concentration
20x MscL Buffer	1.5 mL	1x
Complete EDTA-free protease inhibitor (Roche 11873580001)	1 tablet	n/a
DNase I (Sigma DN25)	30 mg	1 mg/mL
Lysozyme (Sigma L6876)	30 mg	1 mg/mL
ddH_20	28.5 mL	n/a

Elution Buffers:
Note: pH to 7.2-7.3 w/ HCl after adding imidazole; see **Lipid Preparation**

Component	Final Concentration
20x MscL Buffer	1x
n-Octyl-β-D-glucopyranoside (βOG) (A.G. Scientific O-1036)	1% by mass

Lipid (DOPC – Avanti 850375C) (Azolectin – Sigma P7443)	1:50 lipid:OG molar ratio; ~0.54 mg/mL of typical 800 g/mol lipid
4 M imidazole (Sigma I5513 or I0125)	10 mM / 100 mM / 500 mM
ddH_20	n/a

To make fresh Elution and Extraction buffers in the aforementioned amounts:

1) Blow out and evaporate two glass vials. Put 37 mg of desired lipid in each (assuming MW 800 per lipid), and evaporate the solvent in an inert gas stream until no chloroform remains (~30 mins).
2) To each dried lipid film add 20 ml of 1x MscL Buffer and 1.85 g of OG, tumble mix and sonicate until all lipid has been solubilized (may require additional OG).
3) In 4 x 10mL Falcon tubes and 1 x 50 mL Falcon tube prepare:

Buffer:	Lipid Soln:	DDH_2O:	20X MscL Buffer:	4M Imidazole:	Total Volume:
Bead Wash (BW)	1.5 mL	3.237 mL	250 μL	13 μL (10mM)	5 mL
Low Elution (L)	3 mL	6.475 mL	500 μL	25 μL (10mM)	10 mL
Med Elution (M)	3 mL	6.25 mL	500 μL	250 μL (100mM)	10 mL
High Elution (H)	3 mL	5.25 mL	500 μL	1.25 mL (500mM)	10 mL
Extraction (E)	9 mL	19.425 mL	1.5 mL	75 μL (10mM)	30 mL

   a. Add an additional 1.0 g (~3%) OG to the extraction buffer above.

4) Use NaOH and HCl to pH all buffers to 7.3 (this will take some time).
5) These are now your elution and extraction buffers, necessary for 1ml of beads in column.

Dialysis Buffer: pH 7.2-7.3, 4L per prep

Component	Amount to Add	Final Concentration
20x MscL Buffer	200 mL	1x
SM-2 Absorbent BioBeads (BioRad 152-8920)	~2 g	n/a
ddH_20	3800 mL	n/a

2x Gel Loading Buffer: 10 mL*

Component	Amount to Add	Final Concentration
1M TRIS HCl (pH 6.8) (Sigma T5941)	1.6 mL	160 mM
β – mercaptoethanol** (Sigma M6250)	1 mL	10% (w/w)
SDS (electrophoresis grade) (BioRad 161-0301)	0.2 g	2 % (w/v)
Bromophenol blue (Sigma B-0126)	5 mg	0.05% (w/w)
Glycerol (Sigma G6279)	4 mL	40 % (v/v)
ddH_20	3.4 mL	n/a

* ~180 μL + ~20 μL βME aliquots freshly combined (~ 20 lanes)

** **Gel Loading Buffer** can be stored at RT, βME is added immediately before use.

Gel Running Buffer (for 1-2 gels)

Component	Amount to Add	Final Concentration
10x Gel Running Buffer (BioRad 161-0732)	100 mL	1x

ddH_20	900 mL	n/a

Dessication Buffer (10 mL)

Component	Amount to Add	Final Concentration
MOPS (Sigma M1254)	21 mg	10 mM (pH 7.3)
Ethylene Glycol (Sigma 102466)	1 mL	10% v/v
ddH_20	9 mL	n/a

Rehydration Buffer / **Recording Buffer** (50 mL) (~430 mOsm)

Component	Amount to Add	Final Concentration
KCl	756 mg	200 mM
$MgCl_2$	24 mg	5 mM
HEPES (Sigma H3375)	119 mg	10 mM (pH 7.3)
ddH_20	50 mL	n/a

Lipid Preparation:

Only use syringes made of steel, Teflon and glass.

Removing oxidized lipids from lyophilized lipid stock:

1. Blow out and evaporate a Teflon-capped glass vial.
2. Put ~150% of desired lipid in the glass vial.
3. Fill the vial with two lipid volumes of acetone, and vortex for 30 seconds. Let this sit for 5 minutes.
4. Pour off the free acetone, and repeat step 3, pour off the free acetone.
5. Dry the lipid in an Argon or N_2 stream for at least 30 minutes – there should be no scent of acetone.
6. Seal and store the dry lipids under Argon or N_2 at -20 C – OR – emulsify the lipids in pure chloroform and seal and store under Argon or N_2 at -20 C.

Drying Emulsified Lipids:

1. Blow out and evaporate a Teflon-capped glass vial.
2. Deposit desired amount of emulsified lipid in the glass vial.
3. Run Argon or N_2 over lipid while rotating and 'heating' the tilted vial with your hand. This does not require a heavy stream of gas.
4. Once all visible liquid has evaporated, leave the vial in the gas stream for ~30 minutes. There should not be any detectable scent of chloroform.
5. Lipid can be stored dry if under Argon or N_2 at -20C.

<u>Days 1 and 2: Growing up Cells</u>

Use over expression strain from Rees lab: BL21 Gold(DE3) cells for wt protein.
Grow GoF mutants on plates first at high Amp (0.4 mg/ml) for 24 hrs, scrape and inoculate culture.

1. Grow a 5 mL starter growth in LB + 62.5 μL Amp (4 mg/mL stock) for 11 hrs.
3. Inoculate 2 x 1L LB no Amp cultures with 5 mL starter culture.
4. Grow to OD_{600} 2; induce each 1L culture with 1 mL 1 M IPTG (=1 mM final concentration) , then grow 3-4 more hours. Will grow slowly after induction.
5. Put in cold room ~30 min, spin 8500 rcf 10 min, scrape pellet out and store in cold room/freeze. Yields ~ 8 g cells.

<u>Day 3: Cell Lysis and Centrifugation</u>

1. Resuspend 8 g pellet in 30 mL **Lysis Buffer** in 50 mL falcon tube (sets the correct liquid level for Rees Lab tip sonicator).
2. Tumble mix in cold room 30 min.
3. Lyse cells via tip sonication: place falcon tube in 0.5 L bottle full of ice + water; use high power tip (short stubby one, not long thin one); cycle is 3 s on / 9 s off, for a total of 4 min; use max power (level 100). Follow tuning instructions on wall! The light tan lysate becomes a more translucent liquid after sonication.
4. Ultracentrifuge: Add **Lysis Buffer** w/cells so that volume in centrifuge tube is 90% full if there is not enough volume; balance to within 0.01 g; spin 40,000 rpm w / Ti-45 rotor (~186000 rcf), 1 hr 10 min, 4° C. Should result in 1) clear supernatant*, 2) dark gel-like pellet, 3) grey-brown opaque pellet below gel-like pellet.
   * Take 20ul of this supernatant for SDS gel analysis.
5. Carefully pour off supernatant and store at 4C until SDS gel analysis shows protein is in pellet.
6. Scrape the pellet onto the end of glass piston homogenizer and add 30 mL **Extraction Buffer**, homogenize by slowly pushing the piston up and down ~ 20 times – avoid creating foam. Make sure all of the material is homogenized.
7. Tumble mix homogenate in falcon tube in cold room overnight (~12 hrs).

Day 4: Ni-NTA Column Purification (6xHIS tag chelating columns)

1. Spin homogenate at 15000 rcf 10 min, store supernatant at 4°C until column is ready, discard pellet.
2. Prepare column:
   Spin 2 mL bead stock solution (QIAGEN 30410) (1 mL beads) for 2 min at 1000 rcf, pipette off supernatant, carefully so as not to lose any beads!, add 2 mL Low Imidazole **Elution Buffer**, vortex, spin, pipette off supernatant and repeat.
   Add homogenate, vortex to resuspend beads, tumble mix in cold room at for 2 hours.
3. Gravity column (BioRad 7311550) (do not allow the column to run dry!)
   Carefully pour bead + homogenate mixture into column and collect into 50 mL falcon tube.
   Run 10 column volumes (~10 mL) Low Imidazole **Elution Buffer -** use this to get the rest of the beads out of the original tube before pouring it over the column.
   Add 10 column volumes Medium Imidazole **Elution Buffer**, collect 10 1 mL fractions in eppendorfs (~46 drops); repeat for High Imidazole **Elution Buffer**
   Recommended flow rate: 1ml/min Binding capacity ~1uMol (@20KDa)
4. Take 20ul samples from each of the first four fractions of the medium and high imidazole fractions for SDS gel analysis. Immediately snap freeze all medium and high fractions and store at -80C so as not to precipitate the protein. Fractions can be kept indefinitely at -80C.

Day 4-5: Protein Gels, Bradford assay, Dialysis

1. Protein Gels:
   Use 4-15% Tris-HCl linear gradient gels, precast, from BioRad (ReadyGel 161-1104):
   Make sure to expose bottom of gel by cutting along black line with razor blade. Set up gel apparatus and fill with ~0.5 L of 1x **Gel Running Buffer** (BioRad 161-0732)**.** Gently pull out the comb while under running buffer so as to fill lanes with buffer.

   Lane Sample Prep:
   All lanes contain 20 μL.

   11 μL of each sample + 11 μL 2x **Gel Loading Buffer**. Heat at 95C for 5 mins with cover on top, then spin down tubes to pull down condensate. Run 20 μL on the gel per lane.

At the same ratio, prepare 22 μL of Mass Standard (MS), load 20 μL on the gel, which contains 5 μg/band of the following: Lysozyme (14.7 kD), Carbonic Anhydrase (29 kD), and Bovine Serum Albumin (~66 kD).

In one lane, run the white-light visible protein ladder (GE Healthcare RPN756E or BioRad 161-0734) - Dilute by a factor of 2 and load 20 μL.

In another lane, run the UV visible protein ladder (Sigma S8445) – Dilute by a factor of 2 and load 10 μL.

Run gel for ~1 hr at ~160 VDC, 500 mA. Check every 15 minutes to make sure lanes do not overrun. The blue dye should reach the bottom of the gel.

Carefully remove gel from plastic casing (tears easily), using green gel removal tool.

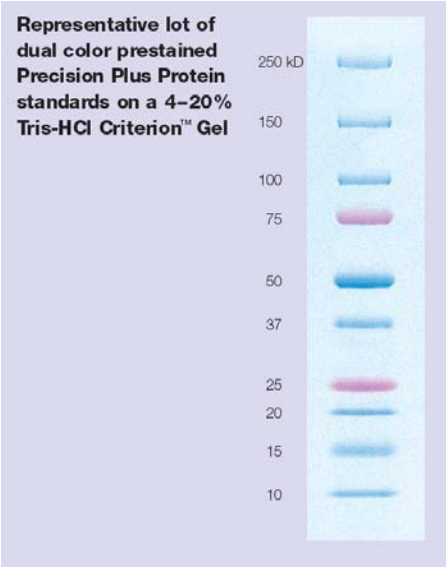

BioRad 161-0734

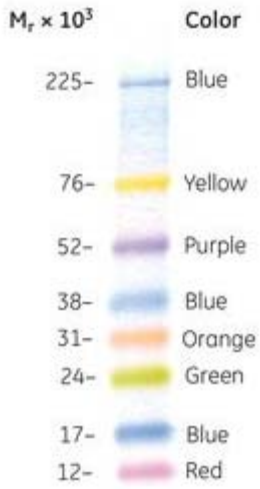

GE Healthcare RPN756E

Calibration Gel

Lane 1: 10ul 0.5X Protein Ladder
Lane 2: 10ul 2X Loading Buffer + 10ul 0.0005 mg/ml Lysozyme MS (5ng / band)
Lane 3: 10ul 2X Loading Buffer + 10ul 0.005 mg/ml Lysozyme MS (50ng / band)
Lane 4: 10ul 2X Loading Buffer + 10ul 0.05 mg/ml Lysozyme MS(500ng / band)
Lane 5: 10ul 2X Loading Buffer + 10ul 0.5 mg/ml Lysozyme MS (5ug / band)
Lane 6: 10ul 1X Protein Ladder

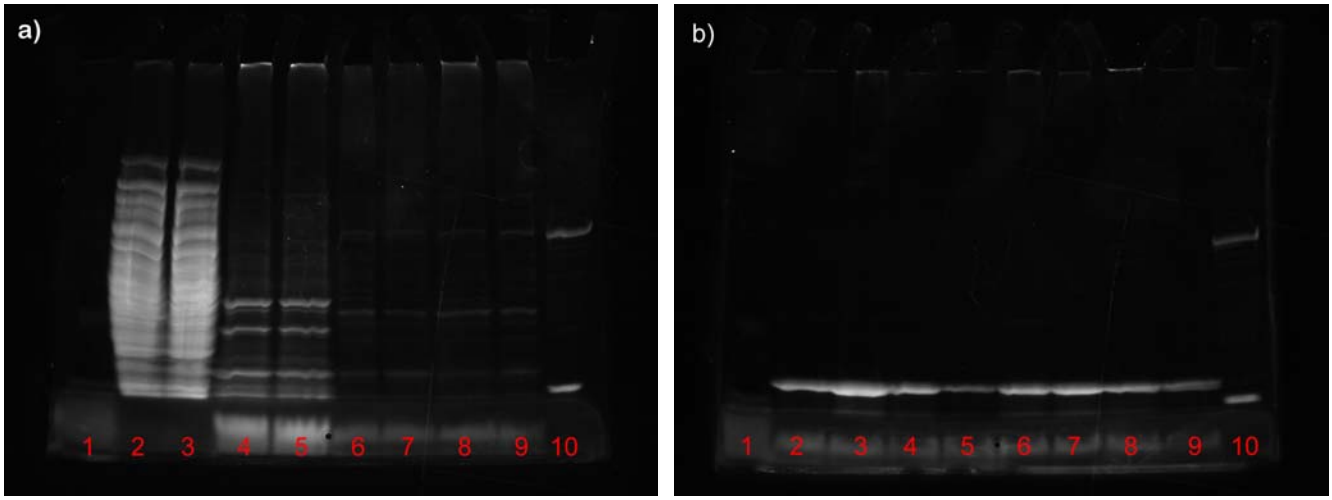

Figure 1: Protein gels from the MscL purification prep. In both gels the protein ladder in lane 1 is not visible in fluorescence staining, and the lack of BSA purity is evident in the lane 10 protein standard by the presence of superfluous bands near the main BSA band. a) Gel #1: Notice the huge reduction in protein going from the ultra-spin (lanes 2 and 3) to the first column purification step (lanes 4 and 5). The medium imidazole fractions (6-9) have even less protein per fraction. Lane 10 is the BSA / Lysozyme mass standard. b) Gel #2: Lanes 2-5 and 6-9 are the high imidazole fractions from the DOPC and Azolectin preparations, respectively. Notice that we have pure 16KDa MscL monomers. Other very faint bands appear, which are most probably some combination of contaminating protein and higher oligomers of MscL. Lane 10 is the BSA / Lysozyme mass standard.

Gel Staining:

1. Dilute SYPRO Red© stock solution 1:5000 (12 uL / 60 mL Gel Stain) in a solution of ddH_2O with 10% Glacial Acetic Acid (v/v). Use approximately 60ml of staining solution per gel – the gels may be combined into one dish.
2. Cover the dish with aluminum foil to prevent signal damage from light. Stir slowly for ~60 minutes (longer is fine) to stain gel.
3. Destain for ~5 mins in same volume of ddH_2O with 10% Glacial Acetic Acid (v/v).
4. Image the gel using UV trans-illumination; band quantitation is performed using custom written MatLab© software and the protein concentration standards.

2. Dialysis:

Desired ratios: 60 μg protein to 10 mg lipid all in 1ml (1:20000 molar ratio protein:lipid).

1. Dry 10 mg lipid in glass vial.
2. Calculate appropriate amount of High Imidazole fraction to meet ratios (call it 'X').
3. Add 'X' of High Imidazole fraction to the dried lipid.
4. To dried lipid, add 1 - X mL **Dialysis buffer**.
5. Slowly add OG detergent so that the minimal amount is used until all lipid is dissolved and solution has gone clear. Add ~ 2mg detergent at a time and bath-sonicate to maximally dissolve lipid.
6. Rinse the dialysis membrane with ddH_20 inside and out allowing the membrane to soak for ~15 minutes at 4 C in a suitable size beaker.
7. Rinse the dialysis membrane with **Dialysis Buffer** twice.
8. Using fine-tipped pipettes (VWR 14670-327 PIPET TRANS EX FT STERL) gently add all 1 mL of dialysis sample and put membrane holding device in 4 L of **Dialysis Buffer** at 4 C with a gentle stirring action.
9. Add ~ 2g of BioBeads SM-2 (BioRad 152-8920) to 4L **Dialysis Buffer.**

10. Allow to sit (at least) overnight, or until the solution becomes cloudy (up to one week). DOPC becomes very cloudy. Azolectin becomes translucent / 'smoky'.
11. One can also add beads in 1X Dialysis buffer directly to the lipid and protein emulsified mixture, and stir in original glass vial gently overnight. The solution should begin to go cloudy within minutes of bead addition. This method is much faster than full dialysis.
12. In either case, the dialysate may be aliquoted and snap frozen for later use.

Day 6: Post Dialysis and Lipid Film Deposition

1. Carefully remove all of the cloudy liquid from dialysis.
2. Put all 1ml of this liquid + 9 mL of 1x **MscI Buffer** into a 10 mL Ti-70.1 ultracentrifuge tube.
3. Balance the tubes to within 0.01 g and run for 15 minutes at 70000 rpm and 4 C.
4. A milky white, lipid + protein pellet will form. This pellet is very delicate.
5. Carefully pour off the supernatant and discard. Resuspend the pellet in 2x the pellet volume of **Dessication Buffer.** This resuspended pellet may be snap frozen for later use.
6. Onto a clean, dry glass slide deposit 5 μL of this solution and vacuum desiccate for ~12 hours.
7. Once desiccated, deposit enough **Rehydration Buffer** to complete cover the desiccate, and allow to sit in a 100% relative humidity environment for ~12 hours or until lipid forms vesicles.

Recharging the NTA Resin

Handling
Ni-NTA matrices are stable under a wide variety of conditions and need not be refrigerated, except to inhibit growth of microorganisms for long-term storage. After use they should be washed for 30 minutes with 0.5M NaOH. Ni-NTA matrices should be stored in 30% ethanol to inhibit microbial growth. The matrix can be stored for up to one week in any of the denaturing buffers.

Reuse of Ni-NTA Resin
The reuse of Ni-NTA resin depends on the nature of the sample and should only be performed with identical recombinant proteins. Based on the experience of Hoffmann-La Roche Ltd. (Basel, Switzerland), who have purified more than 100 different proteins on Ni-NTA resin, we recommend a maximum of 5 runs per column. If the Ni-NTA Agarose changes from light blue to brownish-gray, the following regeneration procedure is recommended.

Procedure:
1. Wash the column with 2 volumes of Regeneration Buffer (6 M GuHCl, 0.2 M acetic acid).
2. Wash the column with 5 volumes of H_2O.
3. Wash the column with 3 volumes of 2% SDS.
4. Wash the column with 1 volume of 25% EtOH.
5. Wash the column with 1 volume of 50% EtOH.
6. Wash the column with 1 volume of 75% EtOH.
7. Wash the column with 5 volumes of 100% EtOH.
8. Wash the column with 1 volume of 75% EtOH.
9. Wash the column with 1 volume of 50% EtOH.
10. Wash the column with 1 volume of 25% EtOH.
11. Wash the column with 1 volume of H_2O.
12. Wash the column with 5 volumes of 100 mM EDTA, pH 8.0.
13. Wash the column with H_2O.
14. Recharge the column with 2 volumes of 100 mM $NiSO_4$.
15. Wash the column with 2 volumes of H_2O.
16. Wash the column with 2 volumes of Regeneration Buffer.
17. Equilibrate with 2 volumes of a suitable buffer (e.g., Buffer A or B).

1-24-09
Grew 5 mL starter cultures in LB + 0.2mg/ml Amp
Used starter cultures for lawns on 10cm plates (11ml media /plate)
Plate growth: 0.05 mg/ml 0.2 mg/ml 0.4 mg/ml Amp for each strain (WT, V23T, V23D) (9 plates total)

1 plate worth scraped cells per 1L media. Grew WT in 0.2 mg/ml Amp and both mutants at 0.4 mg/ml Amp.

Innoc. Liquid cultures at 3:30pm

Amp Conc:	Strain:	6:10pm	7:10pm	9:00pm
0.2 mg/ml	WT #1	0.881	2.09 (induced)	
0.2 mg/ml	WT #2	1.322	2.156 (induced)	
0.4 mg/ml	V23D #1	0.165	0.596	2.073 (induced)
0.4 mg/ml	V23D #2	0.127	0.458	1.85 (induced)
0.4 mg/ml	V23T #1	0.402	0.999	2.283 (induced)
0.4 mg/ml	V23T #2	0.425	1.115	2.341 (induced)

All gels below:
Lane 1: Mass Standard
Lane 2: First High Fraction
Lane 3: Second High Fraction
Lane 4: Third High Fraction
Lane 5: First Medium Fraction
Lane 6: Second Medium Fraction
Lane 7: Third Medium Fraction
Lane 8: Low Fraction
Lane 9: White-light Ladder
Lane 10: UV Sigma Ladder

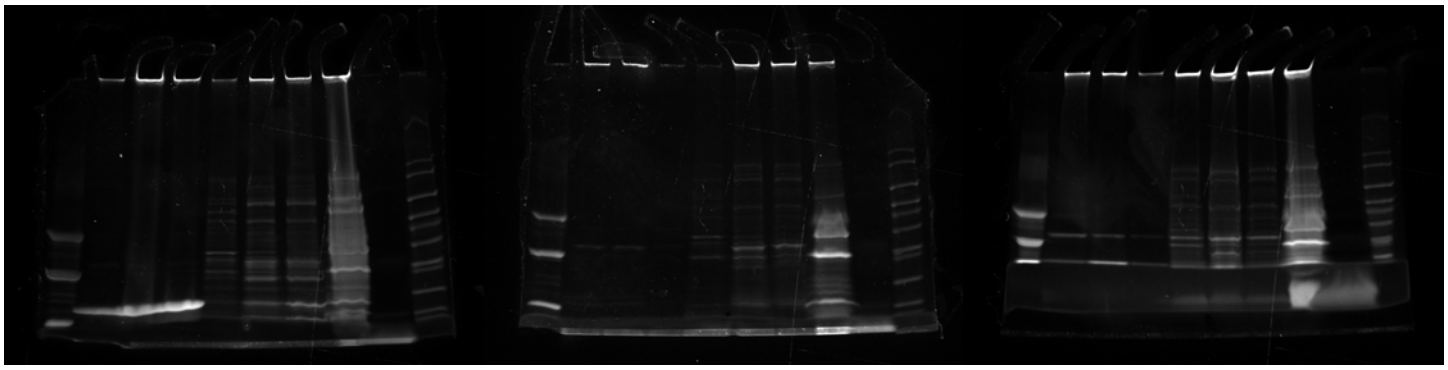

WT V23D V23T

Strain:	Fraction H1:	Fraction H2:	Fraction H3:
WT	0.9 mg/mL	2 mg/mL	2.6 mg/mL
V23D	~50 μg/mL	~50 μg/mL	n/a
V23T	140 μg/mL	425 μg/mL	100 μg/mL

Appendix C

Micropipette Preparation Protocol

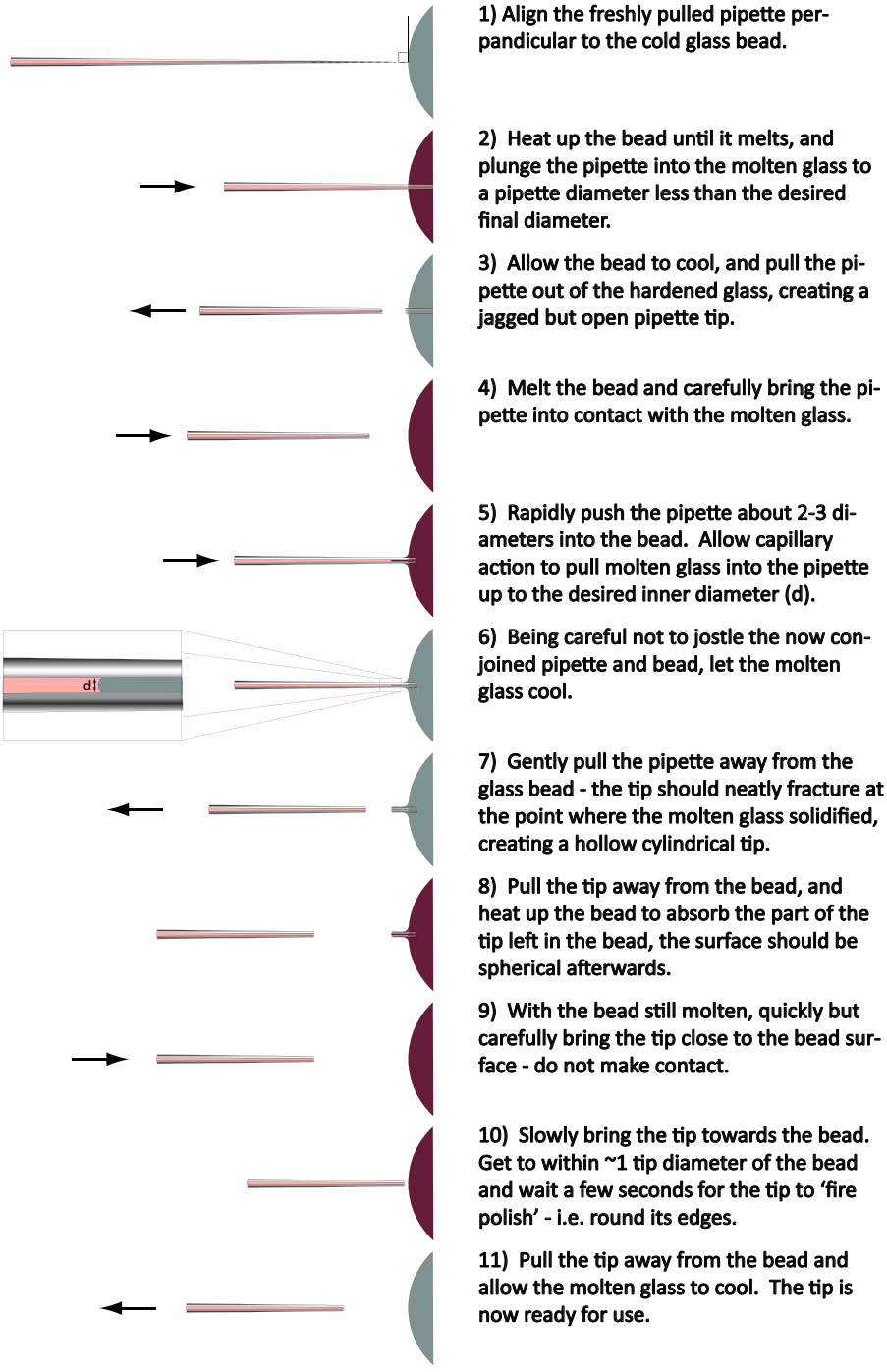

Figure C.1: Flow chart, with instructions, showing in detail how to form a vesicle aspiration pipette. Prior to the steps shown here, the pipette is pulled from stock boro-silicate glass tube (Kimble Glass, Inc. PN: 46485) using a Flaming-Brown Pipette Puller (Sutter Instruments Inc.) in a single pulling step to create a long tapered tip. After these steps, the tube is carefully filled with the appropriate, filtered (0.2 μm) chamber solution, using a MicroFil needle (World Precision Instruments, Inc. PN: MF34G-5), and is ready for use.

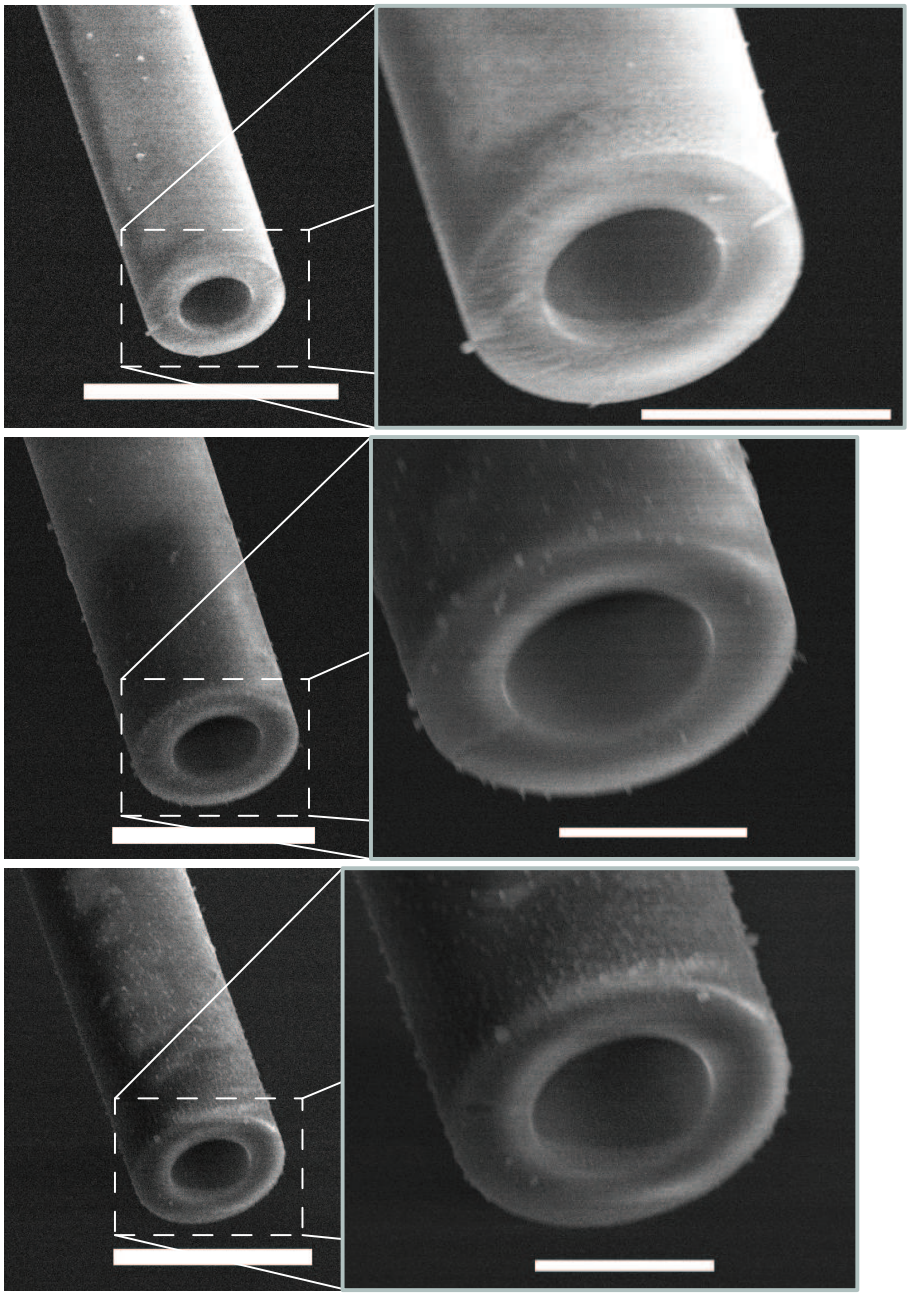

Figure C.2: Electron micrographs showing detailed view of well-formed micropipette tips. With the exception of some small dust particles, these tips show the desired cylindrical shape of a micropipette tip, onto which an aspirated vesicle will (hopefully) seal well, allowing for an accurate pressure reading and low leakage. The scale bars on the left are 10 μm and on the right are 4 μm.

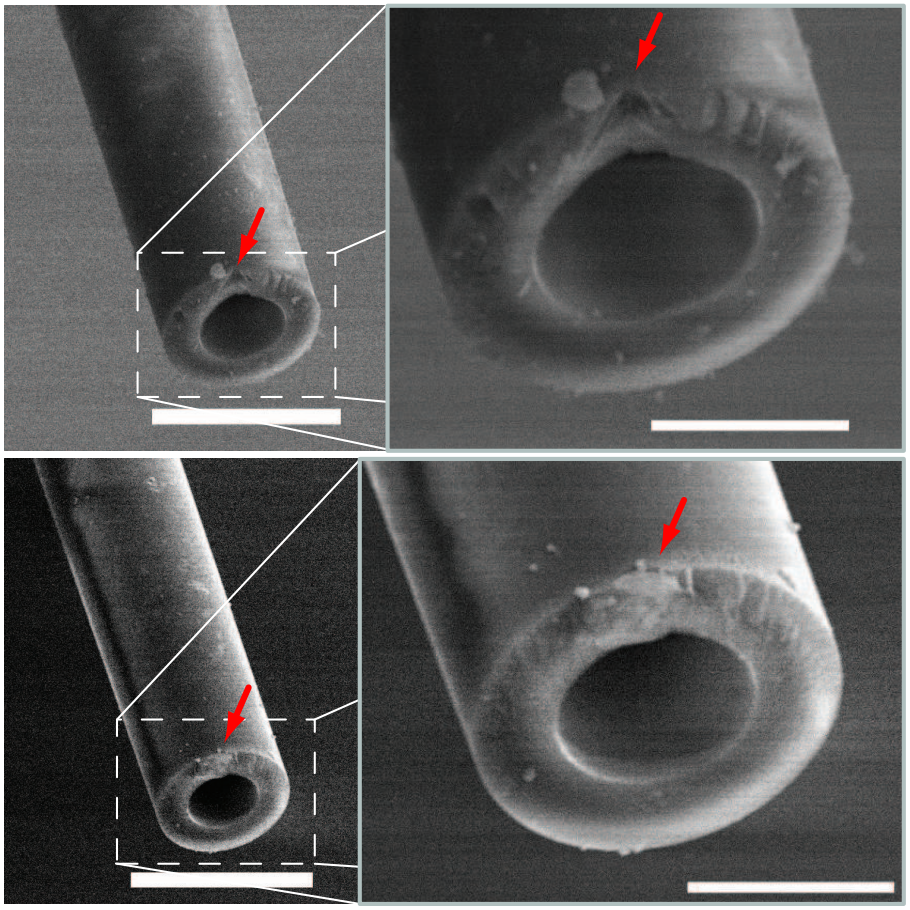

Figure C.3: Electron micrographs showing detailed views of malformed micropipette tips. In both cases, major imperfections in the tip, as denoted by the red arrows, are caused by poor breakage during steps 6 and 7 in Fig. C.1, and poor fire-polishing. These kinds of imperfections will lead to poor sealing upon aspiration, and hence inaccurate pressure readings. Additionally, aspirated vesicles will be distorted by fluid leakage. The scale bars on the left are 10 μm and on the right are 4 μm.

Appendix D

Basics of 2D Phase Separation

D.1 Background

A great many systems, both physical and abstract, have constituents with specific energetic interactions. When a system of such interacting particles is subject to fluctuations of a well-defined spectrum (*e.g.* an exponential distribution of energy, like Boltzmann statistics) the system attempts to maximize the degree of *disorder* in a way that is proportional to the magnitude of these fluctuations (*i.e.* the temperature). This is, of course, the notion of entropy, and the origin of the energetic term $-TS$ in thermodynamic potentials. Simultaneously, each particle in the system is trying to minimize its energy of interaction with neighboring particles, setting up a competition between the entropy of mixing and the enthalpic benefit of having certain preferred neighbors, though in some sense both are manifestations of the system's desire to maximize entropy. This competition leads to a temperature-dependent phase transition. Parts of this derivation, and excellent discussion of the background as well as more advanced methods can be found in [197, 111].

In the case explored below, this is a so-called 'order-disorder' transition, closely related to a 'second-order' transition. Effectively, this means that below a certain critical temperature (or critical value of some other parameter in the system) particles in the system will organize themselves such that enthalpy is minimized. Most often, the specific interactions are such that like-likes-like, hence particles organize spatially by similar type to form unique phases. This is the basic physical mechanism behind lipid phase separation model (and presumably biological) membranes, where the enthalpic component of interaction derives from the hydrophobic mismatch between lipids that prefer the liquid ordered (L_o) phase and those that prefer the liquid disordered (L_d phase.

The purpose of this appendix is both to understand some aspects of this entropy-enthalpy competition and subsequently the kinetics of phase separation in a simple 2D system.

D.2 Derivation of the Cahn-Hilliard Equation

For the purposes of this discussion, let us assume we are modeling a 2D binary fluid composed of A and B particles in the limit where diffusion is the major transport mechanism (as opposed to hydrodynamics or other more complex mechanisms). Let us define the order-parameter field ϕ such that $\phi = 1$ is a phase completely made of A particles, and $\phi = -1$ is a phase completely made of B

particles, with a linear interpolation between those two phases. We assume the interactions of AA and BB are favorable relative to the $AB = BA$ interaction. If a particle A and a particle B are interacting, this means there is an unfavorable energy associated with a gradient in the field $\nabla\phi$. Obviously, the direction of that gradient does not matter (*i.e.* we have rotational symmetry) and we want energy and its derivatives to be well-defined, thus gradients in the field must be energetically penalized by $|\nabla\phi|^2$ to obey that symmetry.

Many entire text books have been written on the theory of phase transitions, hence we will not dwell on that topic here. We assume that due to the inter-molecular interactions, and interactions with any external fields there is a potential energy landscape, $V(\phi, T)$, that has a temperature dependent transition from a random, high temperature phase, to an ordered, low temperature phase. In the Landau formalism, this can be approximated by a potential of the form

$$V(\phi, T) = c_1(T)\phi^2 + c_2(T)\phi^4, \tag{D.1}$$

where the coefficients c_i are connected to the precise Hamiltonian of the system, but are unimportant for our analysis. Clearly, when $(\partial^2 V/\partial\phi^2)|_{\phi=0} = 0$, or in other words when c_1 switches sign, something interesting happens — the one minimum at $\phi = 0$ vanishes, and yields a state with two distinct minima at non-zero field values — this is the phase transition. With no loss of generality, we rewrite this potential as

$$V = \frac{1}{4}(a - (b\phi)^2)^2. \tag{D.2}$$

The stable phases, given by $\partial V/\partial\phi = 0$, are

$$\phi^* = \pm\frac{\sqrt{a}}{b}, \tag{D.3}$$

with the clear interpretation that real values of ϕ^* are always stable (*i.e.* $a > 0$); the energy barrier between those fixed points is at $\phi = 0$. Thus the interpretation is that values of $a > 0$ correspond to systems whose temperature is below the phase transition temperature, and values of $a < 0$ correspond to an entropy dominated system.

We combine this potential with the boundary penalty to form an energy functional for the entire field ϕ in space and time

$$F[\phi(\bar{x}, t)] = \int \left[\frac{1}{4}(a - (b\phi)^2)^2 + \frac{\gamma}{2}|\nabla\phi|^2\right] \mathrm{d}\bar{a} \tag{D.4}$$

where γ is a constant that penalizes phase boundaries, akin to the line tension, though with units of tension, since the phase boundary exists over some area, not simply along a line. The microscopic origins of γ are in the interactions between the A and B particles. If ϕ is understood as a measure of particle number, and F is the energy of a particular configuration of ϕ, then the variation in F with respect to ϕ is quantifying how the energy changes when particles change position, or in other

words, it defines the chemical potential of the system

$$\frac{\delta F}{\delta \phi} = \mu. \tag{D.5}$$

From that one simple idea, a quick series of steps bring us to the Cahn-Hilliard equation. All we need to do is remember that Fick's First Law states that the flux of particles in a system is proportional to the gradient of the chemical potential

$$\bar{J} = -D\nabla\mu, \tag{D.6}$$

where D is the diffusion coefficient of the particles. We assume that the system cannot create, destroy or switch particles types (as we have currently set things up), which means this flux must obey a continuity equation

$$\frac{\partial \phi}{\partial t} + \nabla \cdot \bar{J} = 0, \tag{D.7}$$

or

$$\frac{\partial \phi}{\partial t} = D\nabla^2\mu. \tag{D.8}$$

To finish off the derivation we need only calculate the chemical potential

$$\mu = \frac{\delta F}{\delta \phi} = (b^4\phi^3 - ab^2\phi) - \gamma\nabla^2\phi. \tag{D.9}$$

Finally

$$\frac{\partial \phi}{\partial t} = D\nabla^2\left[(b^4\phi^3 - ab^2\phi) - \gamma\nabla^2\phi\right], \tag{D.10}$$

where D is playing the role of an effective diffusion coefficient, and in the next section we will extract out a natural length and time scale, such that there is only one free parameter in the Cahn-Hilliard equation.

D.2.1 Deriving a Natural Length and Time Scale

Let us make the assumption that this system has a natural length scale λ and natural time scale τ, such that $t = \tau\hat{t}$ and $\bar{x} = \lambda\hat{x}$. Then the differentials can be rewritten

$$\frac{\partial}{\partial t} = \frac{1}{\tau}\frac{\partial}{\partial \hat{t}} \tag{D.11}$$

and

$$\nabla^n = \frac{1}{\lambda^n}\nabla^n_{\hat{x}}. \tag{D.12}$$

Then the Cahn-Hilliard equation can be written (leaving the subscript off ∇)

$$\frac{\partial \phi}{\partial \hat{t}} = \nabla^2\left[\frac{D\tau ab^2}{\lambda^2}(\alpha^2\phi^3 - \phi) - \frac{D\tau\gamma}{\lambda^4}\nabla^2\phi\right] \tag{D.13}$$

with $\alpha = b/\sqrt{a}$. This leaves us with two equations and two unknowns, hence we find

$$\tau = \frac{\gamma}{a^2 b^4 D} \tag{D.14}$$

and

$$\lambda = \frac{1}{b}\sqrt{\frac{\gamma}{a}}. \tag{D.15}$$

The Cahn-Hilliard equation is now

$$\frac{\partial \phi}{\partial \hat{t}} = \nabla^2 \left[\alpha^2 \phi^3 - \phi - \nabla^2 \phi\right]. \tag{D.16}$$

Already we notice two things; first, we retrieve the well-known result that the length scale diverges at the phase transition (*i.e.* $\lim \lambda_{a\to 0} = \infty$). Second, we see that the nonlinearity in the PDE is strongest near the phase transition (*i.e.* $\lim \alpha_{a\to 0} = \infty$).

For a given initial condition, $\phi(\hat{x}, 0)$, this equation can be numerically solved, however to make analytic headway, we will employ the so-called 'strong-segregation' limit. This simply means that we are far from the phase transition where particles A and B strongly seek their own kind, such that $\alpha \ll 1$. Hence the Cahn-Hilliard equation is written in a linearized form

$$\frac{\partial \phi}{\partial \hat{t}} = -\nabla^2 \left[\phi + \nabla^2 \phi\right]. \tag{D.17}$$

The next section will use this linearized equation to derive wavelength-dependent dynamics and the general linearized solution.

D.3 Kinetics in Fourier Space

Given the orthonormality and completeness relations, we know that we can represent ϕ by its Fourier Transform

$$\phi(\hat{x}, \hat{t}) = \int A_k(\hat{t}) e^{-i\bar{k}\cdot\hat{x}} \mathrm{d}\bar{k}. \tag{D.18}$$

We can also represent derivatives in space and time using the Fourier Transform, such that

$$\frac{\partial \phi}{\partial \hat{t}} = \int \dot{A}_k(\hat{t}) e^{-i\bar{k}\cdot\hat{x}} \mathrm{d}\bar{k} \tag{D.19}$$

and for $n = 2, 4$ the gradient of ϕ can be written as

$$\nabla^n \phi = \int A_k(\hat{t})(-i)^n (\bar{k}\cdot\bar{k})^{n/2} e^{-i\bar{k}\cdot\hat{x}} \mathrm{d}\bar{k} = \int A_k(\hat{t}) i^n |k|^n e^{-i\bar{k}\cdot\hat{x}} \mathrm{d}\bar{k}. \tag{D.20}$$

Using these two relations, we can write an *independent* dynamic equation for the evolution of each Fourier component

$$\dot{A}_k = (|k|^2 - |k|^4) A_k. \tag{D.21}$$

This is the classic 'spinodal decomposition' result, stating that instabilities with wavelengths near $|k| = 1/\sqrt{2}$ grow fastest, and that all wavelengths with $|k| > 1$ are exponentially damped, while all wavelengths with $0 < |k| < 1$ grow exponentially. Physically this results in a rapid evolution of features on a certain length scale, followed by a long-time evolution of long-wavelength features, as shown in Fig. D.1a. Interestingly, the dynamics show a kind of 'scale-invariance', whereby evolution of the system in time is equivalent to increasing the spatial scaling, as shown in Fig. D.1b.

Lastly, the general solution for the linearized equation is found by solving the dynamics for each wave vector

$$A_k(\hat{t}) = A_k(0)e^{(|k|^2-|k|^4)\hat{t}}. \tag{D.22}$$

The initial condition, $\phi(\hat{x}, 0)$, specifies the initial conditions for each wavelength

$$A_k(0) = \frac{1}{2\pi}\int \phi(\hat{x}, 0)e^{i\bar{k}\cdot\hat{x}}\mathrm{d}\hat{x}, \tag{D.23}$$

such that the general solution is written

$$\phi(\hat{x}, \hat{t}) = \int A_k(0)e^{(|k|^2-|k|^4)\hat{t}}e^{-i\bar{k}\cdot\hat{x}}\mathrm{d}\bar{k}. \tag{D.24}$$

Phrased differently, if we use a δ-function, then

$$A_k(0) = \frac{1}{2\pi}\int \delta(\hat{x} - \hat{x}')e^{i\bar{k}\cdot\hat{x}}\mathrm{d}\hat{x}, \tag{D.25}$$

and

$$A_k(0) = \frac{1}{2\pi}e^{i\bar{k}\cdot\hat{x}'}. \tag{D.26}$$

Substituting this into the general linearized solution gives the Green's Function

$$G(\hat{x}, \hat{x}', \hat{t}) = \frac{1}{2\pi}\int e^{(|k|^2-|k|^4)\hat{t}}e^{-i\bar{k}\cdot(\hat{x}-\hat{x}')}\mathrm{d}\bar{k}, \tag{D.27}$$

and the general solution

$$\phi(\hat{x}, \hat{t}) = \int G(\hat{x}, \hat{x}', \hat{t})\phi(\hat{x}', 0)\mathrm{d}\hat{x}'. \tag{D.28}$$

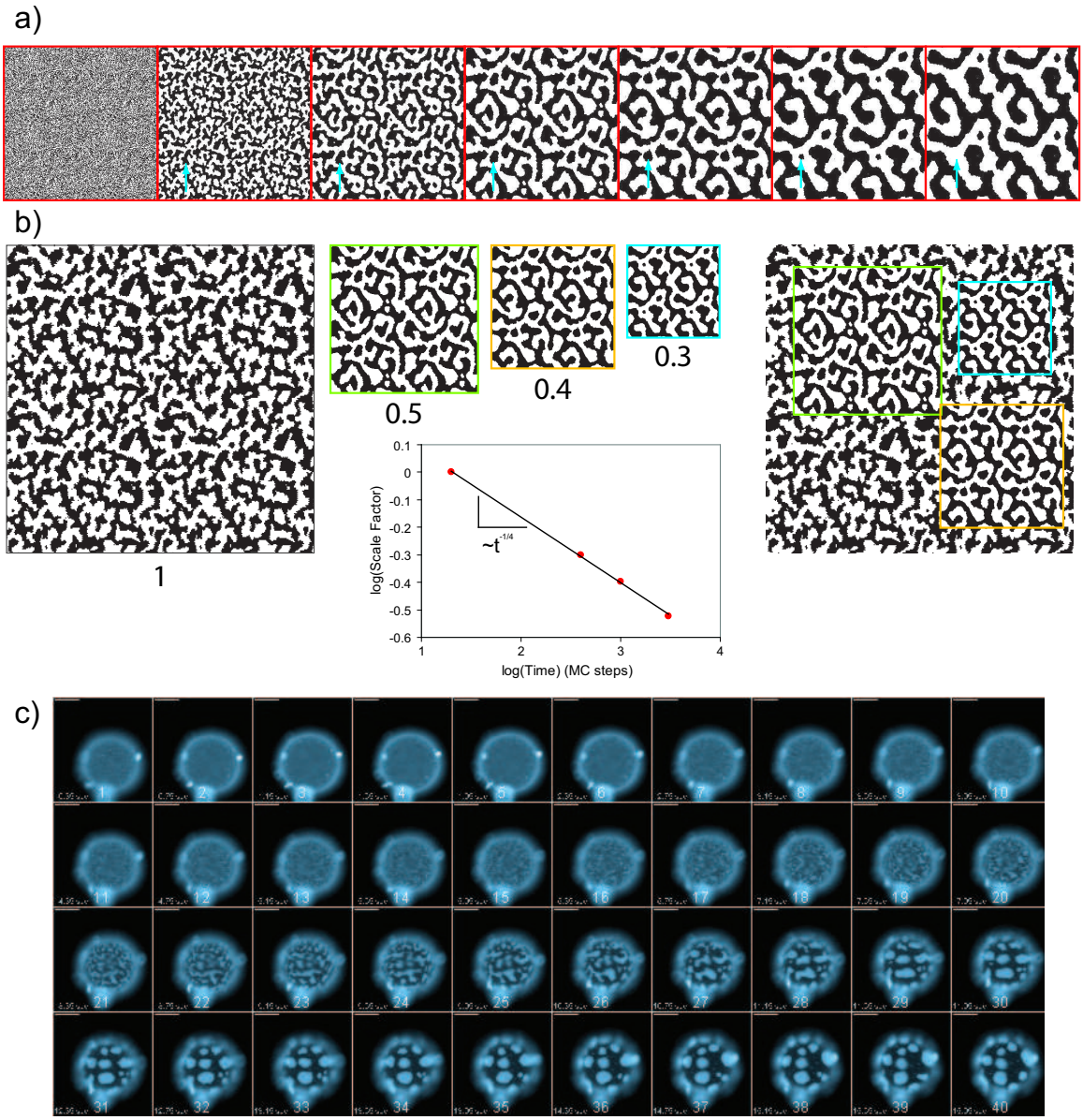

Figure D.1: Phase kinetics in simulation and experiment. a) Progression of phase separation in a diffuse Monte Carlo simulation in two dimensions with A (white) and B (black) particles at $\langle\phi\rangle = 0$, that is, equal mounts of A and B particles. The frames correspond to pre-quench, 20, 100, 400, 1000, 3000, and 5000 Monte Carlo steps, respectively. Notice short wavelengths disappear quickly, and long wavelengths evolve slowly. Ostwald ripening is also visible during the simulation, as small domains 'evaporate' and join larger domains, shown by the small blue arrows. b) A qualitative demonstration of scale invariance showing the similarity between frames 20, 400, 1000, and 3000. The scale factors are listed below each frame, and a plot of scale factor vs. time shows a power law relationship with an exponent $\simeq -1/4$. To demonstrate the scale invariance, the three scaled images are then embedded in the original image, showing they are almost indistinguishable. The scaled images are color coded for clarity. c) Phase separation on a spherical lipid vesicle of the mixture explore in chap. 4. See the video on YouTube at http://www.youtube.com/watch?v=kDsFP67_ZSE.

Appendix E

Electroformation of Giant Unilamellar Vesicles

Materials

- Ethanol, DI water and Kimwipes for cleaning
- 5–10 μl glass syringe (Hamilton Co.)
- 200 μl pipette (with wide mouth tips)
- two Eppendorf tubes (1.7 ml)
- vacuum desiccator
- One of the following:
  · nitrile O-ring (9.25 mm ID x 1.78 mm radius)
  · vacuum grease required
  · $\sim 134\,\mu$l fill volume
  or
  · Grace Biolabs FW9-2.0 FastWell
  · no grease required
  · $\sim 96\,\mu$l fill volume
- appropriate buffer
  · low salt (< 10mM)
  · DDI H_2O, sugars (sucrose and glucose) and other anionic compounds work up to ~ 500mM.
- desired lipid or lipid mixture; concentration such that there are ~ 100 bilayers for a typical lipid film deposition (typically 2 mg/ml seems to work well)

Notes on cleanliness

The strength of bilayers, their elastic properties, as well as their phase separating properties (with multiple lipid species) are all quite sensitive to contaminants. Hence, everything in the procedure is made of metal (steel or copper), Teflon or glass. Polyethylene pipette tips and Eppendorf tubes can only be used in aqueous conditions, not during stages that use solvents. Adhesives, cleaning agents, and other surfactants often lead to anomalous behavior.

Preparation

- Clean the chamber with ethanol and DI water using Kimwipes, alternating the water and ethanol at least twice to make sure any grease or sugars are removed from the slides
- Make sure the ITO slides in the chamber are firmly in place and the copper conductor gasket is in contact at the top and bottom of each slide, check the resistance from BNC to slide, it should be no more than $\sim 50\,\Omega$
- Using the $10\,\mu$l glass syringe apply a $2-3\,\mu$l (@ 2 mg/ml conc.) droplet of the lipid/chloroform solution in the center of the ITO slide on the shorter side of the chamber. The layer should appear greenish under white light reflection (corresponding to ~ 100 bilayers thick).
- We find that film deposition is one of the most crucial steps depositing a uniform green(ish) film is key to high yield electroformation.
- Quickly (within a minute) place the whole chamber in the vacuum desiccator, desiccate for ~ 2 hrs. This removes excess solvent (chloroform) from the lipid film.
- Meanwhile, clean the nitrile O-ring or FastWell using a Kimwipe and ethanol. If using an O-ring, use a Que-tip or grease slide to apply a thin layer of vacuum grease to one side of the O-ring.
- Remove the chamber from the desiccator and place the O-ring (greased side down) or FastWell approximately in the center of the short side of the chamber, directly over the greenish film.
- Using the 200μl pipette, place the appropriate fill volume (see **Materials**) of buffer solution in the O-ring or FastWell.
- Secure the top half of the chamber onto the bottom using the alignment pins, ensure there are no bubbles (very small bubbles are okay).
- Carefully bring the chamber over to the microscope and position over objective (20X is fine).

Procedure

- Place the chamber on the microscope stage, lipid coated side down.
- Secure the chamber with the spring clips on the microscope stage.
- *Carefully* attach the BNC connector to the chamber.
- Set the voltage amplitude between 1V and 4V, never exceed 5V as this will damage the ITO coating. Set the driving frequency to $\sim$ 10Hz. One can vary the amplitude and frequency to suit the lipid/buffer composition (vesicles have been formed with frequencies as low as 2Hz and as high as 20Hz and 1–4 V).

- Our general formation recipe is 120 minutes, 1V, 10Hz; 60 minutes,1V, 2Hz
- Note: multicomponent membranes need to be formed at higher temperatures ($\sim$ 50 C). A special chamber, shown below, is used to simultaneously heat and electroform.
- Wait and watch as vesicles begin to form over the course of 2–3 hours. Blistering of the lipid layer should be noticeable within a few minutes.
- When the formation is done, turn off the equipment and remove chamber from microscope. Using a wide-mouth tip, pipette out the $\sim 100\,\mu$l of the solution from the chamber into the Eppendorf tube already filled with $\sim$ 1ml desired buffer. *Slowly* mix this solution in the centrifuge tube. Depending on the yield, a 10:1 dilution of this solution may be in order. The vesicles are now ready! They are good for $\sim$ 24 hours.

Tension in the membrane

Regulating the internal and external osmolarity is the key to having tense or floppy vesicles. My experiments usually require floppy vesicles which requires careful control of the difference in osmolarity between the inside and outside of the vesicle. If the vesicles are too floppy, protrusions, tubes, buds and other nasties form. I usually form vesicles with 100 mM sucrose inside and 102–108 mM glucose outside. Additionally, this will cause the vesicles to sediment upon viewing.

Lipid Storage

Many lipids can be oxidized, and hence ruined if exposed to improper conditions. All lipids should be stored in Teflon capped, glass vials, under argon at -20C. When you are about to use a lipid mixture, wait until it has reached room temperature before opening this will prevent water condensation inside the vial from damaging the lipid. Labeled lipids should have minimum exposure to light. The shelf-life of a properly stored lipid is about a year.

Chamber Construction

ITO slides can be purchased from Sigma-Aldrich ($\sim$ 400$ per 10, AN: 578274) and the rest of the materials are widely available. The body of the formation chambers are made of machined Teflon. Teflon tape is used to hold on copper gasket to the ITO slide. Occasionally, lab quality masking tape is used. A function generator or computer controlled DAQ card (we use LabView) are suitable for applying the AC electric field. Technical drawings of the simpler room temperature and heated electroformation chambers are shown in Fig. E.1 and E.2. The latter figure also shows the dimensions of the custom build temperature control stage using during various experiments.

Photo-Induced Phase Effects A number of studies [130, 268] and our experience with phase separating membranes indicates that fluorescence visualization of a labeled, multi-component bilayer affects the phase transition temperature. The observational consensus is that, upon fluorescent

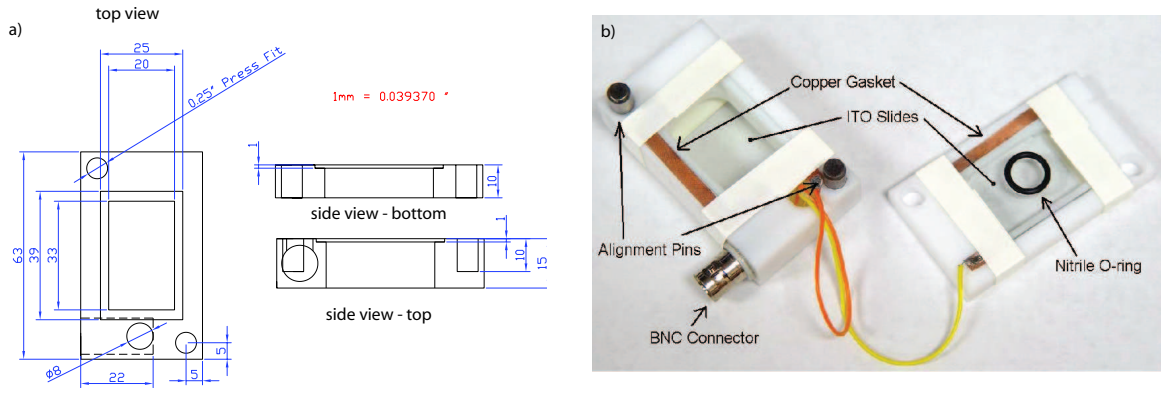

Figure E.1: Simple electroformation chamber. a) Technical drawing of small electroformation chamber with dimensions in millimeters. The preferred construction material is Teflon. b) Photograph of the assembled, functional electroformation chamber with annotations.

viewing, labeled membranes shift to a higher demixing transition temperature, nominally by about $\sim 5C$. Our hypothesis, which is supported by a number of papers in the photochemistry literature [293, 294], as well as our, albeit preliminary, NMR experiments, is that the double bond in the acyl chain of the thinner mono-unsaturated lipid, in our case DOPC, undergoes a *cis-trans* isomerization, photo-catalyzed by the presence of the labeled lipid. This has the effect of slightly thinning these lipids (as shown schematically in Fig. E.3), hence creating a greater hydrophobic mismatch between the two lipid phases and thus raising the transition temperature [177]. One set of relatively simple experiments that could bolster this idea, is to make ternary lipid vesicles from different mixtures of the *cis*[1] and *trans*[2] forms of the unsaturated lipid, and verify that increasing molar fraction of the *trans* lipid increases the transition temperature. Coupled with a detailed carbon NMR study of the changes in lipid structure upon fluorescence viewing, we are poised to answer the nagging issue of photo-induced effects in model membranes systems.

[1] Avanti Polar Lipids PN: 850375
[2] Avanti Polar Lipids PN: 850376

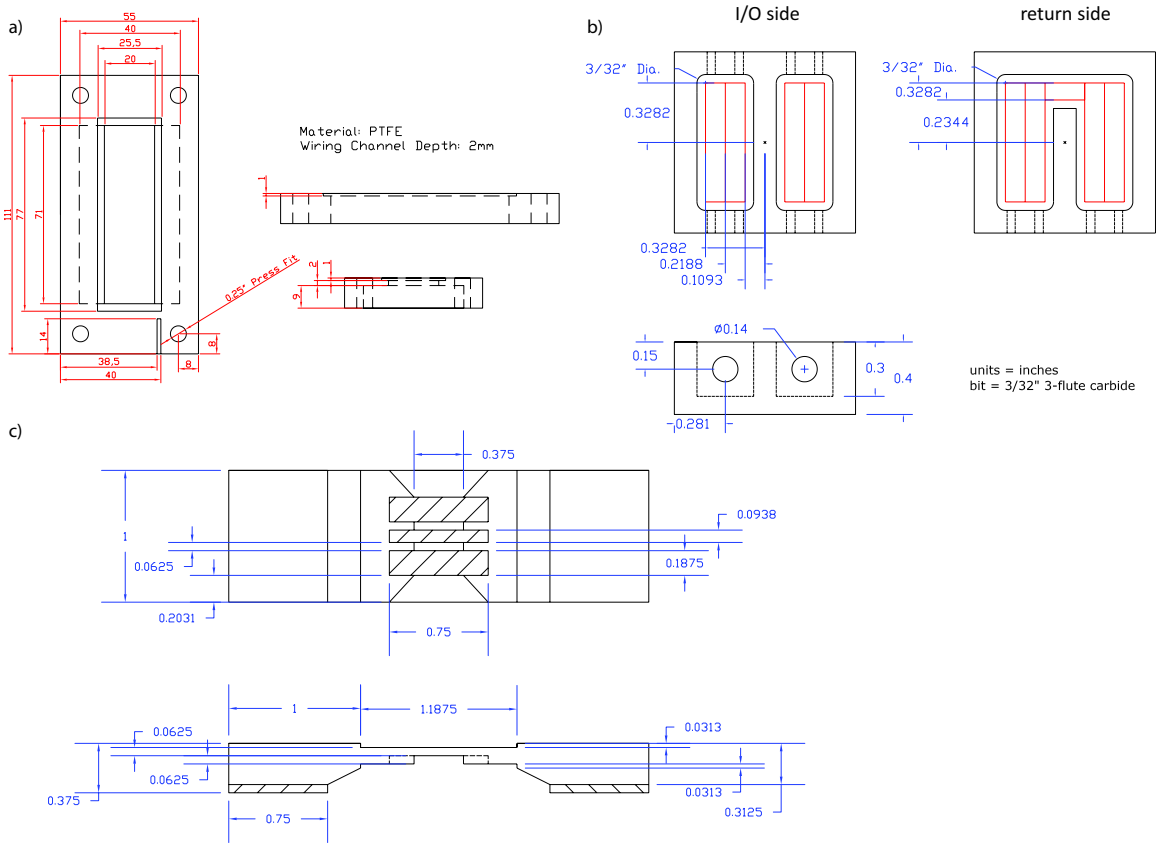

Figure E.2: Heated electroformation chamber and temperature stage. a) Technical drawing of the heated electroformation chamber used in forming multicomponent vesicles, with dimensions are in millimeters. The preferred material is Teflon. b) Technical drawing of the water heat exchanger for the temperature control stage, with dimensions in millimeters. The material is 6061 aluminum. c) Technical drawing of the temperature control led viewing chamber used in a variety of experiments, with dimensions in millimeters. The material is 304 stainless steel.

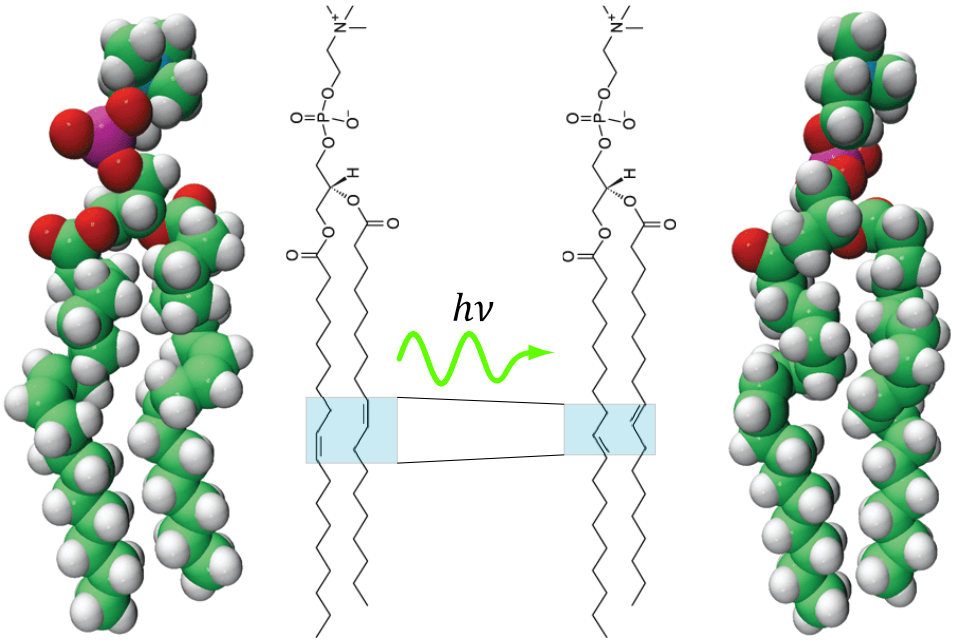

Figure E.3: Photoisomerization of lipids. This schematic shows the photo-induced structural changes in a mono-unsaturated lipid from a *cis* configuration to a *trans* configuration upon exposure to green incident light. This isomerization process has the effect of taking the thinner disordered phase, and further thinning it, hence raising the phase transition temperature. Part of our hypothesis is that this process is photo-catalyzed by the presence of the rhodamine head group labeled lipids used for visualization.

Appendix F

Protocol for Giant Plasma Membrane Vesicles

Cell type: NIH 3T3 Fibroblast or RAW Macrophage

Reagents and Dyes

- Vesiculation Buffer
  · 200 μg/ml DOPE-Rhodamine (Avanti Polar Lipids) (TRITC)
  · 50 μg/ml Naphthopyrene (or Perylene) (Sigma-Aldrich) (CFP) in Ethanol, Acetone or DMSO (preferred)
  · Remove chloroform with argon stream, then resuspend in solvent.

- GPMV Buffer ($\sim$ 315 mOsm) [100 ml]
  · 2 mM $CaCl_2$ (0.022g)
  · 10 mM HEPES (pH 7.4) (0.238g)
  · 150 mM $NaCl$ (0.878g)

- GPMV Reagent ($\sim$ 342 mOsm) [100 ml]
  · 2 mM $CaCl_2$ (0.022g)
  · 10 mM HEPES (pH 7.4) (0.238g)
  · 150 mM $NaCl$ (0.878g)
  · 25 mM formaldehyde (0.075g) in solution (Sigma PN: 5016), Specific gravity 1.08, m/m $HCHO$ 37.5%)
  · 2 mM DTT (0.031g)

- PBS/G
  · PBS +10 mM Glucose

- (Pre-Bleb) Cholesterol Depletion and Repletion Reagent (30x)
  · DME (3ml)
  · M-βCD (1.18g) ($\sim$ 300 mM)
  · (Repletion) (58mg) ($\sim$ 50 mM)
  · Incubate in full media for 15-30 min at 37C.

- (Post-Bleb) Cholesterol Depletion and Repletion Reagent (30x)
  · PBS/G (3ml)

· M-βCD (1.18g) ($\sim$ 300 mM)
· (Repletion) (58mg) ($\sim$ 50 mM)

- Osmotic Up-shock Reagent
  · PBS/G (20ml)
  · Sucrose (2.74g) ($\sim$ 400 mM / $\sim$ 440 mOsm)

Cell Culture

NIH 3T3 or RAW macrophage cells are grown to confluency in DMEM with Penn/Strep and FBS, then passaged and plated at a density of $\sim 5 \times 10^4$ cells per square centimeter in a four-well chamber (Nalgene-NUNC) with 2 cm^2 of area per well and a #1.5 borosilicate glass coverslip bottom. The cells are then incubated at 37C in phenol–red free media for 2.5 hours and subsequently rinsed in PBS plus 10 mM glucose (PBS/G) before addition of solvent/dye solution to induce formation of cell-attached GPMVs as described below.

Procedure

- Cell-attached
  · GPMVs are prepared by addition of 1–5% vol/vol of Vesiculation Buffer to adherent NIH 3T3 or RAW macrophage cells in four-well chambers. Cells are incubated for $\sim$ 15 minutes before imaging.

- Cell-free
  · Cells are grown to confluency in a 25 cm^2 tissue-culture flask and washed twice with GPMV Buffer ($\sim$ 2 ml). Then $\sim$ 1.5 ml of freshly prepared GPMV Reagent is added to the flask and incubated for 1 hour at 37C with slow shaking (60 cycles per minutes). After incubation, GPMVs that have detached from cells are gently decanted ($\sim$ 1 ml) into a 15 ml conical tube. The conical tube is put on ice for $\sim$ 30 minutes. Using a wide-mouth pipette tip, the lower $\sim$ 20% of liquid is removed from the conical tube.

  · Depending on the GPMV yield, 1-5% vol/vol of Vesiculation Buffer is added and allowed to incubate with the vesicles at 37C.

- Imaging
  · Free GPMVs are aliquoted into 60 μl samples and osmolarity is sampled in increments of $\sim$ 2 mOsm by addition of low glucose solution ($<$ 25 mM) or high glucose solution ($>$ 350 mM). Each aliquoted is viewed in a 47μl Grace-Biolabs FW-9. DOPE-Rhodamine is viewed

in TRITC and Perylene or Naphthopyrene in CFP. Images can be taken using either confocal or standard epi-fluorescence microscopy.

- Short Protocol[1]
  · Grow cells to 50% confluency in phenol–red free media.
  · Remove media, and replace with equal volume of PBS/G buffer.
  · Add $\sim$ 5% (v/v) dying solution, and slowly stir to make sure the solution is properly mixed.
  · Incubate the cells at 37C for 30 minutes, they are now ready for imaging.

[1] After experimenting with the more complicated protocol above [245], we developed a much easier protocol for cell attached GPMVs, that uses only a few steps. All the data in Chapter 4 was collected with this short protocol.

References

[1] R. Phillips, J. Kondev, and J. A. Theriot. *Physical Biology of the Cell.* Garland Science, 1st edition, 2008.

[2] D. E. Clapham, L. W. Runnels, and C. Strubing. The TRP ion channel family. *Nat Rev Neurosci* 2:387–96, 2001.

[3] P. H. Barry and J. W. Lynch. Ligand-gated channels. *IEEE Trans Nanobioscience* 4:70–80, 2005.

[4] F. Sachs. Mechanical transduction by membrane ion channels: a mini review. *Mol Cell Biochem* 104:57–60, 1991.

[5] A. Kloda and B. Martinac. Molecular identification of a mechanosensitive channel in archaea. *Biophys J* 80:229–40, 2001.

[6] P. G. Gillespie and R. G. Walker. Molecular basis of mechanosensory transduction. *Nature* 413:194–202, 2001.

[7] G. L. Fain. *Sensory Transduction.* Sinauer Associates, 2003.

[8] A. Katsumi, A. W. Orr, E. Tzima, and M. A. Schwartz. Integrins in mechanotransduction. *J Biol Chem* 279:12001–4, 2004.

[9] S. M. Nauli and J. Zhou. Polycystins and mechanosensation in renal and nodal cilia. *Bioessays* 26:844–56, 2004.

[10] S. I. Sukharev, P. Blount, B. Martinac, and C. Kung. Mechanosensitive channels of *Escherichia coli*: the Mscl gene, protein, and activities. *Annu Rev Physiol* 59:633–57, 1997.

[11] G. Chang, R. H. Spencer, A. T. Lee, M. T. Barclay, and D. C. Rees. Structure of the Mscl homolog from *Mycobacterium tuberculosis*: a gated mechanosensitive ion channel. *Science* 282:2220–6, 1998.

[12] C. D. Pivetti, M. R. Yen, S. Miller, W. Busch, Y. H. Tseng, I. R. Booth, and Jr. Saier, M. H. Two families of mechanosensitive channel proteins. *Microbiol Mol Biol Rev* 67:66–85, 2003.

[13] C. E. Morris and U. Homann. Cell surface area regulation and membrane tension. *J Membr Biol* 179:79–102, 2001.

[14] Y. Kamada, U. S. Jung, J. Piotrowski, and D. E. Levin. The protein kinase C-activated MAP kinase pathway of *Saccharomyces cerevisiae* mediates a novel aspect of the heat shock response. *Genes Dev* 9:1559–71, 1995.

[15] M. Christensen and K. Strange. Developmental regulation of a novel outwardly rectifying mechanosensitive anion channel in *Caenorhabditis elegans*. *J Biol Chem* 276:45024–30, 2001.

[16] A. Duggan, J. Garcia-Anoveros, and D. P. Corey. Insect mechanoreception: what a long, strange TRP it's been. *Curr Biol* 10:R384–7, 2000.

[17] E. S. Haswell and E. M. Meyerowitz. Mscs-like proteins control plastid size and shape in *Arabidopsis thaliana*. *Curr Biol* 16:1–11, 2006.

[18] R. B. Bass, P. Strop, M. Barclay, and D. C. Rees. Crystal structure of *escherichia coli* Mscs, a voltage-modulated and mechanosensitive channel. *Science* 298:1582–7, 2002.

[19] E. Perozo, D. M. Cortes, P. Sompornpisut, A. Kloda, and B. Martinac. Open channel structure of Mscl and the gating mechanism of mechanosensitive channels. *Nature* 418:942–8, 2002.

[20] E. Perozo and D. C. Rees. Structure and mechanism in prokaryotic mechanosensitive channels. *Curr Opin Struct Biol* 13:432–42, 2003.

[21] S. I. Sukharev, W. J. Sigurdson, C. Kung, and F. Sachs. Energetic and spatial parameters for gating of the bacterial large conductance mechanosensitive channel, Mscl. *J Gen Physiol* 113:525–40, 1999.

[22] E. Perozo, A. Kloda, D. M. Cortes, and B. Martinac. Physical principles underlying the transduction of bilayer deformation forces during mechanosensitive channel gating. *Nat Struct Biol* 9:696–703, 2002.

[23] C. S. Chiang, A. Anishkin, and S. Sukharev. Gating of the large mechanosensitive channel *in situ*: estimation of the spatial scale of the transition from channel population responses. *Biophys J* 86:2846–61, 2004.

[24] B. Akitake, A. Anishkin, and S. Sukharev. The "dashpot" mechanism of stretch-dependent gating in Mscs. *J Gen Physiol* 125:143–54, 2005.

[25] M. Goulian, O. N. Mesquita, D. K. Fygenson, C. Nielsen, O. S. Andersen, and A. Libchaber. Gramicidin channel kinetics under tension. *Biophys J* 74:328–37, 1998.

[26] W. Rawicz, K. C. Olbrich, T. McIntosh, D. Needham, and E. Evans. Effect of chain length and unsaturation on elasticity of lipid bilayers. *Biophys J* 79:328–39, 2000.

[27] B. Martinac and O. P. Hamill. Gramicidin A channels switch between stretch activation and stretch inactivation depending on bilayer thickness. *Proc Natl Acad Sci U S A* 99:4308–12, 2002.

[28] M. O. Jensen and O. G. Mouritsen. Lipids do influence protein function: the hydrophobic matching hypothesis revisited. *Biochim Biophys Acta* 1666:205–26, 2004.

[29] H. W. Huang. Deformation free energy of bilayer membrane and its effect on gramicidin channel lifetime. *Biophys J* 50(6):1061–70, 1986.

[30] N. Dan and S. A. Safran. Effect of lipid characteristics on the structure of transmembrane proteins. *Biophys J* 75:1410–4, 1998.

[31] C. Nielsen, M. Goulian, and O. S. Andersen. Energetics of inclusion-induced bilayer deformations. *Biophys J* 74:1966–83, 1998.

[32] P. Wiggins and R. Phillips. Membrane-protein interactions in mechanosensitive channels. *Biophys J* 88:880–902, 2005.

[33] K. Yoshimura, A. Batiza, M. Schroeder, P. Blount, and C. Kung. Hydrophilicity of a single residue within Mscl correlates with increased channel mechanosensitivity. *Biophys J* 77:1960–72, 1999.

[34] A. Anishkin, C. S. Chiang, and S. Sukharev. Gain-of-function mutations reveal expanded intermediate states and a sequential action of two gates in Mscl. *J Gen Physiol* 125:155–70, 2005.

[35] J. Gullingsrud, D. Kosztin, and K. Schulten. Structural determinants of Mscl gating studied by molecular dynamics simulations. *Biophys J* 80:2074–81, 2001.

[36] J. Gullingsrud and K. Schulten. Gating of Mscl studied by steered molecular dynamics. *Biophys J* 85:2087–99, 2003.

[37] D. E. Elmore and D. A. Dougherty. Molecular dynamics simulations of wild-type and mutant forms of the *Mycobacterium tuberculosis* Mscl channel. *Biophys J* 81:1345–59, 2001.

[38] D. E. Elmore and D. A. Dougherty. Investigating lipid composition effects on the mechanosensitive channel of large conductance (Mscl) using molecular dynamics simulations. *Biophys J* 85:1512–24, 2003.

[39] M. K. Doeven, J. H. Folgering, V. Krasnikov, E. R. Geertsma, G. van den Bogaart, and B. Poolman. Distribution, lateral mobility and function of membrane proteins incorporated into giant unilamellar vesicles. *Biophys J* 88:1134–42, 2005.

[40] Y. Gambin, R. Lopez-Esparza, M. Reffay, E. Sierecki, N. S. Gov, M. Genest, R. S. Hodges, and W. Urbach. Lateral mobility of proteins in liquid membranes revisited. *Proc Natl Acad Sci U S A* 103:2098–102, 2006.

[41] G. Guigas and M. Weiss. Size-dependent diffusion of membrane inclusions. *Biophys J* 91:2393–8, 2006.

[42] N. Kahya, D. Scherfeld, K. Bacia, B. Poolman, and P. Schwille. Probing lipid mobility of raft-exhibiting model membranes by fluorescence correlation spectroscopy. *J Biol Chem* 278:28109–15, 2003.

[43] G. Shapovalov and H. A. Lester. Gating transitions in bacterial ion channels measured at 3 microsecond resolution. *J Gen Physiol* 124:151–61, 2004.

[44] T. A. Harroun, W. T. Heller, T. M. Weiss, L. Yang, and H. W. Huang. Theoretical analysis of hydrophobic matching and membrane-mediated interactions in lipid bilayers containing gramicidin. *Biophys J* 76:3176–85, 1999.

[45] R. S. Cantor. Lipid composition and the lateral pressure profile in bilayers. *Biophys J* 76:2625–39, 1999.

[46] W. Helfrich. Elastic properties of lipid bilayers: theory and possible experiments. *Z Naturforsch [C]* 28:693–703, 1973.

[47] P. Wiggins and R. Phillips. Analytic models for mechanotransduction: gating a mechanosensitive channel. *Proc Natl Acad Sci U S A* 101:4071–6, 2004.

[48] E. Perozo, A. Kloda, D. M. Cortes, and B. Martinac. Site-directed spin-labeling analysis of reconstituted Mscl in the closed state. *J Gen Physiol* 118:193–206, 2001.

[49] S. Sukharev, M. Betanzos, C. S. Chiang, and H. R. Guy. The gating mechanism of the large mechanosensitive channel Mscl. *Nature* 409:720–4, 2001.

[50] P. Moe and P. Blount. Assessment of potential stimuli for mechano-dependent gating of Mscl: effects of pressure, tension, and lipid headgroups. *Biochemistry* 44:12239–44, 2005.

[51] G. Niggemann, M. Kummrow, and W. Helfrich. The bending rigidity of phosphatidylcholine bilayers: Dependences on experimental method, sample cell sealing and temperature. *J Phys II France* 5:413–425, 1995.

[52] A. M. Powl, J. M. East, and A. G. Lee. Lipid-protein interactions studied by introduction of a tryptophan residue: the mechanosensitive channel Mscl. *Biochemistry* 42:14306–17, 2003.

[53] E. Evans, V. Heinrich, F. Ludwig, and W. Rawicz. Dynamic tension spectroscopy and strength of biomembranes. *Biophys J* 85:2342–50, 2003.

[54] M. S. Turner and P. Sens. Gating-by-tilt of mechanically sensitive membrane channels. *Phys Rev Lett* 93:118103, 2004.

[55] R. H. Spencer and D. C. Rees. The alpha-helix and the organization and gating of channels. *Annu Rev Biophys Biomol Struct* 31:207–33, 2002.

[56] H. Aranda-Espinoza, A. Berman, N. Dan, P. Pincus, and S. Safran. Interaction between inclusions embedded in membranes. *Biophys J* 71:648–56, 1996.

[57] D. Boal. *Mechanics of the Cell*. Cambridge University Press, 1st edition, 2002.

[58] D. Marsh. Elastic curvature constants of lipid monolayers and bilayers. *Chem Phys Lipids* 144:146–59, 2006.

[59] H. von Grunberg and J. Zanghellini. Phospholipid de-mixing and the birth of a lipid droplet. *Arxiv*, 2009.

[60] R. E. Tosh and P. J. Collings. High pressure volumetric measurements in dipalmitoylphosphatidylcholine bilayers. *Biochim Biophys Acta* 859:10–4, 1986.

[61] H. Seemann and R. Winter. Volumetric properties, compressibilities and volume fluctuations in phospholipid-cholesterol bilayers. *Zeitschrift fur physikalische Chemie* 217:831–846, 2003.

[62] V. S. Markin and F. Sachs. Thermodynamics of mechanosensitivity. *Phys Biol* 1:110–24, 2004.

[63] A. G. Lee. Lipid-protein interactions in biological membranes: a structural perspective. *Biochim Biophys Acta* 1612:1–40, 2003.

[64] A. G. Lee. How lipids and proteins interact in a membrane: a molecular approach. *Mol Biosyst* 1:203–12, 2005.

[65] R. Finn. Capillary surface interfaces. *Notices of AMS* 46:770–781, 1999.

[66] C. X. Gu, P. F. Juranka, and C. E. Morris. Stretch-activation and stretch-inactivation of Shaker-IR, a voltage-gated K+ channel. *Biophys J*, 80(6):2678–93, 2001.

[67] B. Calabrese, I. V. Tabarean, P. Juranka, and C. E. Morris. Mechanosensitivity of N-type calcium channel currents. *Biophys J* 83:2560–74, 2002.

[68] D. Reeves, T. Ursell, P. Sens, J. Kondev, and R. Phillips. Membrane mechanics as a probe of ion-channel gating mechanisms. *Phys Rev E* 78:041901, 2008.

[69] N. Levina, S. Totemeyer, N. R. Stokes, P. Louis, M. A. Jones, and I. R. Booth. Protection of *Escherichia coli* cells against extreme turgor by activation of Mscs and Mscl mechanosensitive channels: identification of genes required for Mscs activity. *Embo J* 18:1730–7, 1999.

[70] Y. Li, P. C. Moe, S. Chandrasekaran, I. R. Booth, and P. Blount. Ionic regulation of Msck, a mechanosensitive channel from *Eescherichia coli*. *Embo J* 21:5323–30, 2002.

[71] F. Maingret, M. Fosset, F. Lesage, M. Lazdunski, and E. Honore. TRAAK is a mammalian neuronal mechano-gated K+ channel. *J Biol Chem* 274:1381–7, 1999.

[72] F. Maingret, A. J. Patel, F. Lesage, M. Lazdunski, and E. Honore. Lysophospholipids open the two-pore domain mechano-gated K+ channels TREK-1 and TRAAK. *J Biol Chem* 275:10128–33, 2000.

[73] N. P. Franks and E. Honore. The TREK K2P channels and their role in general anaesthesia and neuroprotection. *Trends Pharmacol Sci* 25:601–8, 2004.

[74] I. Lauritzen, J. Chemin, E. Honore, M. Jodar, N. Guy, M. Lazdunski, and A. Jane Patel. Cross-talk between the mechano-gated K2P channel TREK-1 and the actin cytoskeleton. *EMBO Rep* 6:642–8, 2005.

[75] C. C. Cruickshank, R. F. Minchin, A. C. Le Dain, and B. Martinac. Estimation of the pore size of the large-conductance mechanosensitive ion channel of *Escherichia coli*. *Biophys J* 73:1925–31, 1997.

[76] B. Hille. Pharmacological modifications of the sodium channels of frog nerve. *J Gen Physiol* 51:199–219, 1968.

[77] A. G. Lee. How lipids affect the activities of integral membrane proteins. *Biochim Biophys Acta* 1666:62–87, 2004.

[78] Y. Jiang, A. Lee, J. Chen, M. Cadene, B. T. Chait, and R. MacKinnon. The open pore conformation of potassium channels. *Nature* 417:523–6, 2002.

[79] J. A. Lundbaek, P. Birn, S. E. Tape, G. E. Toombes, R. Sogaard, 2nd Koeppe, R. E., S. M. Gruner, A. J. Hansen, and O. S. Andersen. Capsaicin regulates voltage-dependent sodium channels by altering lipid bilayer elasticity. *Mol Pharmacol* 68:680–9, 2005.

[80] T. M. Suchyna, S. E. Tape, 2nd Koeppe, R. E., O. S. Andersen, F. Sachs, and P. A. Gottlieb. Bilayer-dependent inhibition of mechanosensitive channels by neuroactive peptide enantiomers. *Nature* 430:235–40, 2004.

[81] O. S. Andersen and R. E. Koeppe Ii. Bilayer thickness and membrane protein function: An energetic perspective. *Annu Rev Biophys Biomol Struct* 36:107-130, 2007.

[82] D. Schmidt and R. MacKinnon. Voltage-dependent K+ channel gating and voltage sensor toxin sensitivity depend on the mechanical state of the lipid membrane. *Proc Natl Acad Sci U S A* 105:19276–81, 2008.

[83] C. E. Morris and P. F. Juranka. Nav channel mechanosensitivity: activation and inactivation accelerate reversibly with stretch. *Biophys J* 93:822–33, 2007.

[84] T. Chou, K. S. Kim, and G. Oster. Statistical thermodynamics of membrane bending-mediated protein-protein attractions. *Biophys J* 80:1075–87, 2001.

[85] M. Goulian, P. Pincus, and R. Bruinsma. Long-range forces in heterogeneous fluid membranes. *Europhys Lett* 22:145–150, 1993.

[86] N. Dan, P. Pincus, and S. Safran. Membrane-induced interactions between inclusions. *Langmuir* 9:2768–2771, 1993.

[87] T. Ursell, K. C. Huang, E. Peterson, and R. Phillips. Cooperative gating and spatial organization of membrane proteins through elastic interactions. *PLoS Comput Biol* 3(5):e81, 2007.

[88] R. L. Goforth, A. K. Chi, D. V. Greathouse, L. L. Providence, 2nd Koeppe, R. E., and O. S. Andersen. Hydrophobic coupling of lipid bilayer energetics to channel function. *J Gen Physiol* 121:477–93, 2003.

[89] M. L. Molina, F. N. Barrera, A. M. Fernandez, J. A. Poveda, M. L. Renart, J. A. Encinar, G. Riquelme, and J. M. Gonzalez-Ros. Clustering and coupled gating modulate the activity in Kcsa, a potassium channel model. *J Biol Chem* 281:18837–48, 2006.

[90] A. V. Botelho, T. Huber, T. P. Sakmar, and M. F. Brown. Curvature and hydrophobic forces drive oligomerization and modulate activity of rhodopsin in membranes. *Biophys J* 91:4464–4477, 2006.

[91] K. Mitra, I. Ubarretxena-Belandia, T. Taguchi, G. Warren, and D. M. Engelman. Modulation of the bilayer thickness of exocytic pathway membranes by membrane proteins rather than cholesterol. *Proc Natl Acad Sci U S A* 101:4083–8, 2004.

[92] J. M. Park and T. C. Lubensky. Interactions between membrane inclusions on fluctuating membranes. *J Phys I France* 6:1217–1235, 1996.

[93] T. Sintes and A. Baumgartner. Protein attraction in membranes induced by lipid fluctuations. *Biophys J* 73:2251–9, 1997.

[94] S. Takamori, M. Holt, K. Stenius, E. A. Lemke, M. Gronborg, D. Riedel, H. Urlaub, S. Schenck, B. Brugger, P. Ringler, S. A. Muller, B. Rammner, F. Grater, J. S. Hub, B. L. De Groot, G. Mieskes, Y. Moriyama, J. Klingauf, H. Grubmuller, J. Heuser, F. Wieland, and R. Jahn. Molecular anatomy of a trafficking organelle. *Cell* 127:831–46, 2006.

[95] A. D. Dupuy and D. M. Engelman. Protein area occupancy at the center of the red blood cell membrane. *Proc Natl Acad Sci U S A* 105:2848–52, 2008.

[96] S. B. Zimmerman and A. P. Minton. Macromolecular crowding: biochemical, biophysical, and physiological consequences. *Annu Rev Biophys Biomol Struct* 22:27–65, 1993.

[97] R. J. Ellis. Macromolecular crowding: obvious but under-appreciated. *Trends Biochem Sci* 26:597–604, 2001.

[98] K. Yoshimura, T. Nomura, and M. Sokabe. Loss-of-function mutations at the rim of the funnel of mechanosensitive channel Mscl. *Biophys J* 86:2113–20, 2004.

[99] R. Phillips, T. Ursell, P. Wiggins, and P. Sens. Emerging roles for lipids in shaping membrane-protein function. *Nature* 459:379–385, 2009.

[100] O. G. Mouritsen and M. Bloom. Models of lipid-protein interactions in membranes. *Annu Rev Biophys Biomol Struct* 22:145–71, 1993.

[101] D. Bray, M. D. Levin, and C. J. Morton-Firth. Receptor clustering as a cellular mechanism to control sensitivity. *Nature* 393:85–8, 1998.

[102] V. Sourjik. Receptor clustering and signal processing in *E. coli* chemotaxis. *Trends Microbiol* 12:569–76, 2004.

[103] K. A. Gibbs, D. D. Isaac, J. Xu, R. W. Hendrix, T. J. Silhavy, and J. A. Theriot. Complex spatial distribution and dynamics of an abundant *Escherichia coli* outer membrane protein, Lamb. *Mol Microbiol* 53:1771–83, 2004.

[104] A. D. Douglass and R. D. Vale. Single-molecule microscopy reveals plasma membrane microdomains created by protein-protein networks that exclude or trap signaling molecules in T cells. *Cell* 121:937–50, 2005.

[105] H. Gao, W. Shi, and L. B. Freund. Mechanics of receptor-mediated endocytosis. *Proc Natl Acad Sci U S A* 102:9469–74, 2005.

[106] D. M. Engelman. Membranes are more mosaic than fluid. *Nature* 438:578–80, 2005.

[107] G. Brannigan and F. L. Brown. Contributions of Gaussian curvature and nonconstant lipid volume to protein deformation of lipid bilayers. *Biophys J* 92:864–76, 2007.

[108] U. Schmidt, G. Guigas, and M. Weiss. Cluster formation of transmembrane proteins due to hydrophobic mismatching. *Phys Rev Lett* 101:128104, 2008.

[109] G. Guigas and M. Weiss. Influence of hydrophobic mismatching on membrane protein diffusion. *Biophys J* 95:L25–7, 2008.

[110] G. B. Arfken and H. J. Weber. *Mathematical Methods for Physicists*. Harcourt Academic Press, 5th edition, 2001.

[111] R. Pathria. *Statistical Mechanics*. Butterworth-Heinemann, 2nd edition, 1996.

[112] N. R. Stokes, H. D. Murray, C. Subramaniam, R. L. Gourse, P. Louis, W. Bartlett, S. Miller, and I. R. Booth. A role for mechanosensitive channels in survival of stationary phase: regulation of channel expression by RpoS. *Proc Natl Acad Sci U S A*, 100(26):15959–64, 2003.

[113] J. B. Fournier. Microscopic membrane elasticity and interactions among membrane inclusions: interplay between the shape, dilation, tilt and tilt-difference modes. *Eur Phys J B* 11:261–272, 1999.

[114] P. G. Dommersnes and J. B. Fournier. N-body study of anisotropic membrane inclusions: Membrane mediated interactions and ordered aggregation. *Eur Phys J B* 12:9–12, 1999.

[115] D. Bartolo and J. B. Fournier. Elastic interaction between "hard" or "soft" pointwise inclusions on biological membranes. *Eur Phys J E* 11:141–6, 2003.

[116] A. R. Evans, M. S. Turner, and P. Sens. Interactions between proteins bound to biomembranes. *Phys Rev E* 67:041907, 2003.

[117] T. R. Weikl, M. M. Kozlov, and W. Helfrich. Interaction of conical membrane inclusions: Effect of lateral tension. *Phys Rev E* 57:6988–6995, 1998.

[118] D. P. Siegel and M. M. Kozlov. The Gaussian curvature elastic modulus of n-monomethylated dioleoylphosphatidylethanolamine: relevance to membrane fusion and lipid phase behavior. *Biophys J* 87:366–74, 2004.

[119] J. R. Elliott, D. Needham, J. P. Dilger, and D. A. Haydon. The effects of bilayer thickness and tension on gramicidin single-channel lifetime. *Biochim Biophys Acta* 735:95–103, 1983.

[120] A. Karlin and M. H. Akabas. Substituted-cysteine accessibility method. *Methods Enzymol* 293:123–45, 1998.

[121] G. Wilson and A. Karlin. Acetylcholine receptor channel structure in the resting, open, and desensitized states probed with the substituted-cysteine-accessibility method. *Proc Natl Acad Sci U S A* 98:1241–8, 2001.

[122] H. Hastrup, N. Sen, and J. A. Javitch. The human dopamine transporter forms a tetramer in the plasma membrane: cross-linking of a cysteine in the fourth transmembrane segment is sensitive to cocaine analogs. *J Biol Chem* 278:45045–8, 2003.

[123] M. Bogdanov, W. Zhang, J. Xie, and W. Dowhan. Transmembrane protein topology mapping by the substituted cysteine accessibility method (SCAM(tm)): application to lipid-specific membrane protein topogenesis. *Methods* 36:148–71, 2005.

[124] T. Haselgrubler, A. Amerstorfer, H. Schindler, and H. J. Gruber. Synthesis and applications of a new poly(ethylene glycol) derivative for the crosslinking of amines with thiols. *Bioconjug Chem* 6:242–8, 1995.

[125] R. O. Blaustein, P. A. Cole, C. Williams, and C. Miller. Tethered blockers as molecular 'tape measures' for a voltage-gated K+ channel. *Nat Struct Biol* 7:309–11, 2000.

[126] S. I. Sukharev, M. J. Schroeder, and D. R. McCaslin. Stoichiometry of the large conductance bacterial mechanosensitive channel of *E. coli*. A biochemical study. *J Membr Biol* 171:183–93, 1999.

[127] J. A. Lundbaek and O. S. Andersen. Spring constants for channel-induced lipid bilayer deformations. Estimates using gramicidin channels. *Biophys J* 76:889–95, 1999.

[128] M. B. Partenskii, G. V. Miloshevsky, and P. C. Jordan. Stabilization of ion channels due to membrane-mediated elastic interaction. *J Chem Phys* 118:10306–10312, 2003.

[129] M. L. Skoge, R. G. Endres, and N. S. Wingreen. Receptor-receptor coupling in bacterial chemotaxis: evidence for strongly coupled clusters. *Biophys J* 90:4317–26, 2006.

[130] S. L. Veatch and S. L. Keller. Separation of liquid phases in giant vesicles of ternary mixtures of phospholipids and cholesterol. *Biophys J* 85:3074–83, 2003.

[131] A. P. Minton. The influence of macromolecular crowding and macromolecular confinement on biochemical reactions in physiological media. *J Biol Chem* 276:10577–80, 2001.

[132] D. Homouz, M. Perham, A. Samiotakis, M. S. Cheung, and P. Wittung-Stafshede. Crowded, cell-like environment induces shape changes in aspherical protein. *Proc Natl Acad Sci U S A* 105:11754–9, 2008.

[133] H. X. Zhou. Crowding effects of membrane proteins. *J Phys Chem B* 113:ASAP, 2009.

[134] Y. L. Rezus and H. J. Bakker. Observation of immobilized water molecules around hydrophobic groups. *Phys Rev Lett* 99:148301, 2007.

[135] M. Khanpour and G. Parsafar. New equations of state for hard disk fluid by asymptotic expansion method. *Fluid Phase Equilibria* 262:157–160, 2007.

[136] H. I. Petrache, S. W. Dodd, and M. F. Brown. Area per lipid and acyl length distributions in fluid phosphatidylcholines determined by (2)H NMR spectroscopy. *Biophys J* 79:3172–92, 2000.

[137] L. Onsager. The effects of shape on the interaction of colloidal particles. *Ann N Y Acad Sci* 51:627 – 659, 1949.

[138] P. I. Kuzmin, S. A. Akimov, Y. A. Chizmadzhev, J. Zimmerberg, and F. S. Cohen. Line tension and interaction energies of membrane rafts calculated from lipid splay and tilt. *Biophys J* 88:1120–33, 2005.

[139] C. M. Khursigara, X. Wu, P. Zhang, J. Lefman, and S. Subramaniam. Role of Hamp domains in chemotaxis signaling by bacterial chemoreceptors. *Proc Natl Acad Sci U S A* 105:16555–60, 2008.

[140] K. Olbrich, W. Rawicz, D. Needham, and E. Evans. Water permeability and mechanical strength of polyunsaturated lipid bilayers. *Biophys J* 79:321–7, 2000.

[141] J. M. Wood. Osmosensing by bacteria. *Sci STKE* 2006(357):pe43, 2006.

[142] M. L. Zeidel, S. V. Ambudkar, B. L. Smith, and P. Agre. Reconstitution of functional water channels in liposomes containing purified red cell Chip28 protein. *Biochemistry* 31:7436–40, 1992.

[143] P. Agre. The aquaporin water channels. *Proc Am Thorac Soc*, 3:5–13, 2006.

[144] S. Karlgren, N. Pettersson, B. Nordlander, J. C. Mathai, J. L. Brodsky, M. L. Zeidel, R. M. Bill, and S. Hohmann. Conditional osmotic stress in yeast: a system to study transport through aquaglyceroporins and osmostress signaling. *J Biol Chem* 280:7186–93, 2005.

[145] M. Borgnia, S. Nielsen, A. Engel, and P. Agre. Cellular and molecular biology of the aquaporin water channels. *Annu Rev Biochem* 68:425–58, 1999.

[146] M. Betanzos, C. S. Chiang, H. R. Guy, and S. Sukharev. A large iris-like expansion of a mechanosensitive channel protein induced by membrane tension. *Nat Struct Biol* 9:704–10, 2002.

[147] B. Martinac, M. Buechner, A. H. Delcour, J. Adler, and C. Kung. Pressure-sensitive ion channel in *Escherichia coli*. *Proc Natl Acad Sci U S A* 84:2297–301, 1987.

[148] M. Schleyer, R. Schmid, and E. P. Bakker. Transient, specific and extremely rapid release of osmolytes from growing cells of *Escherichia coli* K-12 exposed to hypoosmotic shock. *Arch Microbiol* 160:424–31, 1993.

[149] C. Berrier, A. Coulombe, I. Szabo, M. Zoratti, and A. Ghazi. Gadolinium ion inhibits loss of metabolites induced by osmotic shock and large stretch-activated channels in bacteria. *Eur J Biochem* 206:559–65, 1992.

[150] E. Evans and W. Rawicz. Entropy-driven tension and bending elasticity in condensed-fluid membranes. *Phys Rev Lett* 64:2094–2097, 1990.

[151] S. I. Sukharev, P. Blount, B. Martinac, F. R. Blattner, and C. Kung. A large-conductance mechanosensitive channel in *E. coli* encoded by Mscl alone. *Nature* 368:265–8, 1994.

[152] S. B. Long, E. B. Campbell, and R. Mackinnon. Crystal structure of a mammalian voltage-dependent Shaker family K+ channel. *Science* 309:897–903, 2005.

[153] S. Steinbacker, R. Bass, P. Strop, and D. C. Rees. *Structures of the Prokaryotic Mechanosensitive Channels MscS and MscL*, volume 58 of *Current Topics in Membranes*. Elsevier Inc., 2007.

[154] G. van den Bogaart, V. Krasnikov, and B. Poolman. Dual-color fluorescence-burst analysis to probe protein efflux through the mechanosensitive channel Mscl. *Biophys J* 92:1233–40, 2007.

[155] *CRC Handbook of Chemistry and Physics*. CRC Press LLC, 88th edition, 2007.

[156] R. Fettiplace and D. A. Haydon. Water permeability of lipid membranes. *Physiol Rev* 60:510–50, 1980.

[157] J. B. Stock, B. Rauch, and S. Roseman. Periplasmic space in *Salmonella typhimurium* and *Escherichia coli*. *J Biol Chem* 252:7850–61, 1977.

[158] J. Happel and H. Brenner. *Low Reynolds Number Hydrodynamics*. Springer, 1st edition, 1973.

[159] R. Brown. Minimum energy theorem for flow of dry granules through apertures. *Nature* 191:458–461, 1961.

[160] H. M. Jaeger and S. R. Nagel. Physics of the granular state. *Science* 255:1523–1531, 1992.

[161] J. FLores, G. Solovey, and S. Gil. Flow of sand and a variable mass Atwood machine. *Am J Phys* 71:715–720, 2003.

[162] D. Hirshfeld, Y. Radzyner, and D. Rapaport. Molecular dynamics studies of granular flow through an aperture. *Phys Rev E* 56:4404–4415, 1997.

[163] F. Zhu, E. Tajkhorshid, and K. Schulten. Pressure-induced water transport in membrane channels studied by molecular dynamics. *Biophys J* 83:154–60, 2002.

[164] I. R. Booth, M. D. Edwards, S. Black, U. Schumann, W. Bartlett, T. Rasmussen, A. Rasmussen, and S. Miller. Physiological analysis of bacterial mechanosensitive channels. *Methods Enzymol* 428:47–61, 2007.

[165] D. V. Zhelev and D. Needham. Tension-stabilized pores in giant vesicles: determination of pore size and pore line tension. *Biochim Biophys Acta* 1147:89–104, 1993.

[166] J. Kyte and R. F. Doolittle. A simple method for displaying the hydropathic character of a protein. *J Mol Biol* 157:105–32, 1982.

[167] S. H. White and W. C. Wimley. Membrane protein folding and stability: physical principles. *Annu Rev Biophys Biomol Struct* 28:319–65, 1999.

[168] I. Kosztin and K. Schulten. Fluctuation-driven molecular transport through an asymmetric membrane channel. *Phys Rev Lett* 93:238102, 2004.

[169] O. Beckstein and M. S. Sansom. Liquid-vapor oscillations of water in hydrophobic nanopores. *Proc Natl Acad Sci U S A* 100:7063–8, 2003.

[170] A. Yildiz, J. N. Forkey, S. A. McKinney, T. Ha, Y. E. Goldman, and P. R. Selvin. Myosin V walks hand-over-hand: single fluorophore imaging with 1.5-nm localization. *Science* 300:2061–5, 2003.

[171] A. Yildiz, M. Tomishige, R. D. Vale, and P. R. Selvin. Kinesin walks hand-over-hand. *Science* 303:676–8, 2004.

[172] T. Squires and M. Bazant. Breaking symmetries in induced-charge electro-osmosis and electrophoresis. *J Fluid Mech* 560:65–101, 2006.

[173] B. J. Baker, E. K. Kosmidis, D. Vucinic, C. X. Falk, L. B. Cohen, M. Djurisic, and D. Zecevic. Imaging brain activity with voltage- and calcium-sensitive dyes. *Cell Mol Neurobiol* 25:245–82, 2005.

[174] M. A. Medina and P. Schwille. Fluorescence correlation spectroscopy for the detection and study of single molecules in biology. *Bioessays* 24:758–64, 2002.

[175] L. R. Opsahl and W. W. Webb. Lipid-glass adhesion in giga-sealed patch-clamped membranes. *Biophys J* 66:75–9, 1994.

[176] S. J. Singer and G. L. Nicolson. The fluid mosaic model of the structure of cell membranes. *Science* 175:720–31, 1972.

[177] A. J. Garcia-Saez, S. Chiantia, and P. Schwille. Effect of line tension on the lateral organization of lipid membranes. *J Biol Chem* 282:33537–33544, 2007.

[178] K. Bacia, P. Schwille, and T. Kurzchalia. Sterol structure determines the separation of phases and the curvature of the liquid-ordered phase in model membranes. *Proc Natl Acad Sci U S A* 102:3272–7, 2005.

[179] T. Baumgart, S. T. Hess, and W. W. Webb. Imaging coexisting fluid domains in biomembrane models coupling curvature and line tension. *Nature* 425:821–4, 2003.

[180] K. Simons and E. Ikonen. Functional rafts in cell membranes. *Nature* 387:569–72, 1997.

[181] P. Sens and M. S. Turner. Budded membrane microdomains as tension regulators. *Phys Rev E* 73:031918, 2006.

[182] D. Raucher and M. P. Sheetz. Characteristics of a membrane reservoir buffering membrane tension. *Biophys J* 77:1992–2002, 1999.

[183] K. Simons and W. L. Vaz. Model systems, lipid rafts, and cell membranes. *Annu Rev Biophys Biomol Struct* 33:269–95, 2004.

[184] A. Schlegel, D. Volonte, J. A. Engelman, F. Galbiati, P. Mehta, X. L. Zhang, P. E. Scherer, and M. P. Lisanti. Crowded little caves: structure and function of caveolae. *Cell Signal* 10:457–63, 1998.

[185] G. van Meer and H. Sprong. Membrane lipids and vesicular traffic. *Curr Opin Cell Biol* 16:373–8, 2004.

[186] N. Chazal and D. Gerlier. Virus entry, assembly, budding, and membrane rafts. *Microbiol Mol Biol Rev* 67:226–37, 2003.

[187] S. Mayor and M. Rao. Rafts: scale-dependent, active lipid organization at the cell surface. *Traffic* 5:231–40, 2004.

[188] C. Dietrich, L. A. Bagatolli, Z. N. Volovyk, N. L. Thompson, M. Levi, K. Jacobson, and E. Gratton. Lipid rafts reconstituted in model membranes. *Biophys J* 80:1417–28, 2001.

[189] H. Park, Y. M. Go, P. L. St John, M. C. Maland, M. P. Lisanti, D. R. Abrahamson, and H. Jo. Plasma membrane cholesterol is a key molecule in shear stress-dependent activation of extracellular signal-regulated kinase. *J Biol Chem* 273:32304–11, 1998.

[190] J. B. Helms and C. Zurzolo. Lipids as targeting signals: lipid rafts and intracellular trafficking. *Traffic* 5:247–54, 2004.

[191] H. A. Lucero and P. W. Robbins. Lipid rafts-protein association and the regulation of protein activity. *Arch Biochem Biophys* 426:208–24, 2004.

[192] K. Gaus, E. Gratton, E. P. Kable, A. S. Jones, I. Gelissen, L. Kritharides, and W. Jessup. Visualizing lipid structure and raft domains in living cells with two-photon microscopy. *Proc Natl Acad Sci U S A* 100:15554–9, 2003.

[193] M. S. Turner, P. Sens, and N. D. Socci. Nonequilibrium raftlike membrane domains under continuous recycling. *Phys Rev Lett* 95:168301, 2005.

[194] L. A. Gheber and M. Edidin. A model for membrane patchiness: lateral diffusion in the presence of barriers and vesicle traffic. *Biophys J* 77:3163–75, 1999.

[195] C. Dietrich, B. Yang, T. Fujiwara, A. Kusumi, and K. Jacobson. Relationship of lipid rafts to transient confinement zones detected by single particle tracking. *Biophys J* 82:274–84, 2002.

[196] K. Murase, T. Fujiwara, Y. Umemura, K. Suzuki, R. Iino, H. Yamashita, M. Saito, H. Murakoshi, K. Ritchie, and A. Kusumi. Ultrafine membrane compartments for molecular diffusion as revealed by single molecule techniques. *Biophys J* 86:4075–93, 2004.

[197] A. J. Bray. Theory of phase-ordering kinetics. *Adv Phys* 51:481–587, 2002.

[198] C. Sagui and R. C. Desai. Ostwald ripening in systems with competing interactions. *Phys Rev Lett* 74:1119–1122, 1995.

[199] M. Laradji and P. B. Sunil Kumar. Dynamics of domain growth in self-assembled fluid vesicles. *Phys Rev Lett* 93:198105, 2004.

[200] M. Seul and D. Andelman. Domain shapes and patterns: The phenomenology of modulated phases. *Science* 267:476–483, 1995.

[201] C. Sagui and R. C. Desai. Kinetics of phase separation in two-dimensional systems with competing interactions. *Phys Rev E* 49:2225–2244, 1994.

[202] M. Seul, N. Y. Morgan, and C. Sire. Domain coarsening in a two-dimensional binary mixture: Growth dynamics and spatial correlations. *Phys Rev Lett* 73:2284–2287, 1994.

[203] L. Foret. A simple mechanism of raft formation in two-component fluid membranes. *Europhys Lett* 71:508–514, 2005.

[204] J. L. Harden, F. C. Mackintosh, and P. D. Olmsted. Budding and domain shape transformations in mixed lipid films and bilayer membranes. *Phys Rev E* 72:011903, 2005.

[205] T. Taniguchi. Shape deformation and phase separation dynamics of two-component vesicles. *Phys Rev Lett* 76:4444–4447, 1996.

[206] W. T. Gozdz and G. Gompper. Shape transformations of two-component membranes under weak tension. *Europhys Lett* 55:587–593, 2001.

[207] R. Reigada, J. Buceta, and K. Lindenberg. Nonequilibrium patterns and shape fluctuations in reactive membranes. *Phys Rev E* 71:051906, 2005.

[208] M. Laradji and P. B. Kumar. Anomalously slow domain growth in fluid membranes with asymmetric transbilayer lipid distribution. *Phys Rev E*, 73:040901, 2006.

[209] L. B. Freund and S. Suresh. *Thin Film Materials: Stress, Defect Formation and Surface Evolution.* Cambridge University Press, Cambridge, UK, 2004.

[210] R. Parthasarathy, C. H. Yu, and J. T. Groves. Curvature-modulated phase separation in lipid bilayer membranes. *Langmuir* 22:5095–9, 2006.

[211] K. Farsad and P. De Camilli. Mechanisms of membrane deformation. *Curr Opin Cell Biol* 15:372–81, 2003.

[212] K. Simons and E. Ikonen. How cells handle cholesterol. *Science* 290:1721–6, 2000.

[213] Y. Lange, J. Ye, and T. L. Steck. How cholesterol homeostasis is regulated by plasma membrane cholesterol in excess of phospholipids. *Proc Natl Acad Sci U S A* 101:11664–7, 2004.

[214] M. Yanagisawa, M. Imai, T. Masui, S. Komura, and T. Ohta. Growth dynamics of domains in ternary fluid vesicles. *Biophys J* 92:115–25, 2007.

[215] R. Lipowsky. Budding of membranes induced by intramembrane domains. *J Phys II France* 2:1925–1840, 1992.

[216] A. Tian, C. Johnson, W. Wang, and T. Baumgart. Line tension at fluid membrane domain boundaries measured by micropipette aspiration. *Phys Rev Lett* 98:208102, 2007.

[217] W. Wang, L. Yang, and H. W. Huang. Evidence of cholesterol accumulated in high curvature regions: implication to the curvature elastic energy for lipid mixtures. *Biophys J* 92:2819–30, 2007.

[218] H. T. McMahon and J. L. Gallop. Membrane curvature and mechanisms of dynamic cell membrane remodelling. *Nature* 438:590–6, 2005.

[219] K. C. Huang, R. Mukhopadhyay, and N. S. Wingreen. A curvature-mediated mechanism for localization of lipids to bacterial poles. *PLoS Comput Biol* 2(11):e151, 2006.

[220] S. H. Hansen, K. Sandvig, and B. van Deurs. Internalization efficiency of the transferrin receptor. *Exp Cell Res* 199:19–28, 1992.

[221] G. Popescu, T. Ikeda, K. Goda, C. A. Best-Popescu, M. Laposata, S. Manley, R. R. Dasari, K. Badizadegan, and M. S. Feld. Optical measurement of cell membrane tension. *Phys Rev Lett* 97:218101, 2006.

[222] Z. Chen and R. P. Rand. The influence of cholesterol on phospholipid membrane curvature and bending elasticity. *Biophys J* 73:267–76, 1997.

[223] J. Henriksen, A. C. Rowat, and J. H. Ipsen. Vesicle fluctuation analysis of the effects of sterols on membrane bending rigidity. *Eur Biophys J* 33:732–41, 2004.

[224] D. S. Dean and M. Manghi. Fluctuation-induced interactions between domains in membranes. *Phys Rev E* 74:021916, 2006.

[225] D. Andelman, F. Brochard, and J. F. Joanny. Phase transitions in Langmuir monolayers of polar molecules. *J Chem Phys* 86:3673–3681, 1987.

[226] H. M. McConnell. Theory of hexagonal and stripe phases in monolayers. *Proc Natl Acad Sci U S A* 86:3452–3455, 1989.

[227] J. Liu, S. Qi, J. T. Groves, and A. K. Chakraborty. Phase segregation on different length scales in a model cell membrane system. *J Phys Chem B* 109:19960–9, 2005.

[228] J. Wohlert and O. Edholm. The range and shielding of dipole-dipole interactions in phospholipid bilayers. *Biophys J* 87:2433–45, 2004.

[229] F. R. Maxfield and T. E. McGraw. Endocytic recycling. *Nat Rev Mol Cell Biol* 5:121–32, 2004.

[230] T. D. Pollard, W. C. Earnshaw, J. Lippincott-Schwartz, and G. Johnson. *Cell Biology*. Saunders, 2nd edition, 2007.

[231] A. F. Quest, L. Leyton, and M. Parraga. Caveolins, caveolae, and lipid rafts in cellular transport, signaling, and disease. *Biochem Cell Biol* 82:129–44, 2004.

[232] L. Hinrichsen, A. Meyerholz, S. Groos, and E. J. Ungewickell. Bending a membrane: how clathrin affects budding. *Proc Natl Acad Sci U S A* 103:8715–20, 2006.

[233] H. Cai, K. Reinisch, and S. Ferro-Novick. Coats, tethers, Rabs, and SNARES work together to mediate the intracellular destination of a transport vesicle. *Dev Cell* 12:671–82, 2007.

[234] M. Fix, T. J. Melia, J. K. Jaiswal, J. Z. Rappoport, D. You, T. H. Sollner, J. E. Rothman, and S. M. Simon. Imaging single membrane fusion events mediated by SNARE proteins. *Proc Natl Acad Sci U S A* 101:7311–6, 2004.

[235] B. Antonny. Membrane deformation by protein coats. *Curr Opin Cell Biol* 18:386–94, 2006.

[236] J. S. Bonifacino and B. S. Glick. The mechanisms of vesicle budding and fusion. *Cell* 116:153–66, 2004.

[237] C. J. Merrifield, D. Perrais, and D. Zenisek. Coupling between clathrin-coated-pit invagination, cortactin recruitment, and membrane scission observed in live cells. *Cell* 121:593–606, 2005.

[238] K. Tsujita, S. Suetsugu, N. Sasaki, M. Furutani, T. Oikawa, and T. Takenawa. Coordination between the actin cytoskeleton and membrane deformation by a novel membrane tubulation domain of PCH proteins is involved in endocytosis. *J Cell Biol* 172:269–79, 2006.

[239] D. Yarar, C. M. Waterman-Storer, and S. L. Schmid. A dynamic actin cytoskeleton functions at multiple stages of clathrin-mediated endocytosis. *Mol Biol Cell* 16:964–75, 2005.

[240] S. Mukherjee, T. T. Soe, and F. R. Maxfield. Endocytic sorting of lipid analogues differing solely in the chemistry of their hydrophobic tails. *J Cell Biol* 144:1271–84, 1999.

[241] S. Mukherjee and F. R. Maxfield. Role of membrane organization and membrane domains in endocytic lipid trafficking. *Traffic* 1:203–11, 2000.

[242] T. Harder, P. Scheiffele, P. Verkade, and K. Simons. Lipid domain structure of the plasma membrane revealed by patching of membrane components. *J Cell Biol* 141:929–42, 1998.

[243] K. D'Hondt, A. Heese-Peck, and H. Riezman. Protein and lipid requirements for endocytosis. *Annu Rev Genet* 34:255–295, 2000.

[244] E. J. Shimshock and H. McConnell. Later phase separations in binary mixtures of cholesterol and phospholipids. *Biochem Biophys Res Commun* 53:446–451, 1973.

[245] T. Baumgart, A. T. Hammond, P. Sengupta, S. T. Hess, D. A. Holowka, B. A. Baird, and W. W. Webb. Large-scale fluid/fluid phase separation of proteins and lipids in giant plasma membrane vesicles. *Proc Natl Acad Sci U S A* 104:3165–70, 2007.

[246] T. S. Ursell, W. S. Klug, and R. Phillips. Morphology and interactions between lipid domains. *submitted to PNAS*, 2009.

[247] J. Pecreaux, H. G. Dobereiner, J. Prost, J. F. Joanny, and P. Bassereau. Refined contour analysis of giant unilamellar vesicles. *Eur Phys J E* 13:277–90, 2004.

[248] P. Cicuta, S. L. Keller, and S. L. Veatch. Diffusion of liquid domains in lipid bilayer membranes. *J Phys Chem B* 111:3328–31, 2007.

[249] A. R. Bausch, M. J. Bowick, A. Cacciuto, A. D. Dinsmore, M. F. Hsu, D. R. Nelson, M. G. Nikolaides, A. Travesset, and D. A. Weitz. Grain boundary scars and spherical crystallography. *Science* 299:1716–8, 2003.

[250] M. Bowick, A. Cacciuto, D. R. Nelson, and A. Travesset. Crystalline order on a sphere and the generalized Thomson problem. *Phys Rev Lett* 89:185502, 2002.

[251] T. Erber and G. Hockney. Complex systems: Equilibrium configurations of n equal charges on a sphere ($2 < n < 112$). volume 98 of *Advances in Chemical Physics*. John Wiley and Sons, Inc., 1997.

[252] U. Seifert, K. Berndl, and R. Lipowsky. Shape transformations of vesicles: Phase diagram for spontaneous- curvature and bilayer-coupling models. *Phys Rev A* 44:1182–1202, 1991.

[253] F. Julicher and R. Lipowsky. Shape transformations of vesicles with intramembrane domains. *Phys Rev E* 53:2670–2683, 1996.

[254] P. Sens and M. S. Turner. Theoretical model for the formation of caveolae and similar membrane invaginations. *Biophys J* 86:2049–57, 2004.

[255] J. M. Allain and M. Ben Amar. Budding and fission of a multiphase vesicle. *Eur Phys J E* 20:409–20, 2006.

[256] B. Widom. Line tension and the shape of a sessile drop. *J Phys Chem* 99:2803–2806, 1995.

[257] E. Evans and D. Needham. Giant vesicle bilayers composed of mixtures of lipids, cholesterol and polypeptides. Thermomechanical and (mutual) adherence properties. *Faraday Discuss Chem Soc* 81:267–80, 1986.

[258] D. Needham and E. Evans. Physical properties of surfactant bilayer membranes: thermal transitions, elasticity, rigidity, cohesion and colloidal interactions. *J Phys Chem* 91:4219–4228, 1987.

[259] J. Kas and E. Sackmann. Shape transitions and shape stability of giant phospholipid vesicles in pure water induced by area-to-volume changes. *Biophys J* 60:825–44, 1991.

[260] T. Kohyama, D. M. Kroll, and G. Gompper. Budding of crystalline domains in fluid membranes. *Phys Rev E* 68:061905, 2003.

[261] B. Hong, F. Qiu, H. Zhang, and Y. Yang. Budding dynamics of individual domains in multicomponent membranes simulated by n-varied dissipative particle dynamics. *J Phys Chem B* 111:5837–5849, 2007.

[262] G. Koster, A. Cacciuto, I. Derenyi, D. Frenkel, and M. Dogterom. Force barriers for membrane tube formation. *Phys Rev Lett* 94:068101, 2005.

[263] I. Derenyi, F. Julicher, and J. Prost. Formation and interaction of membrane tubes. *Phys Rev Lett* 88:238101, 2002.

[264] T. R. Powers, G. Huber, and R. E. Goldstein. Fluid-membrane tethers: minimal surfaces and elastic boundary layers. *Phys Rev E* 65:041901, 2002.

[265] M. I. Angelova, S. Soleau, P. Meleard, J. F. Faucon, and P. Bothorel. Preparation of giant vesicles by external AC electric fields. Kinetics and applications. *Progr Colloid Polym Sci* 89:127–131, 1992.

[266] W. Helfrich and R. M. Servuss. Undulations, steric interactions and cohesion of fluid membranes. *Il Nuovo Cimento* 3:137–151, 1984.

[267] L. Ma. Finite element modeling of shell structures in cell biology: Applications for cell membranes and viral capsids. *PhD Dissertation, UCLA*, 2009.

[268] J. T. Buboltz, C. Bwalya, K. Williams, and M. Schutzer. High resolution mapping of phase behavior in a ternary lipid mixture: Do lipid-raft phase boundaries depend on sample-prep procedure? *Langmuir* 23:11968–11971, 2007.

[269] J. Canny. A computational approach to edge detection. *IEEE Transactions on Pattern Analysis and Machine Intelligence*, PAMI-8:679–698, 1986.

[270] P. Sengupta, A. Hammond, D. Holowka, and B. Baird. Structural determinants for partitioning of lipids and proteins between coexisting fluid phases in giant plasma membrane vesicles. *Biochim Biophys Acta* 1778:20–32, 2008.

[271] S. L. Veatch, P. Cicuta, P. Sengupta, A. Honerkamp-Smith, D. Holowka, and B. Baird. Critical fluctuations in plasma membrane vesicles. *ACS Chem Biol* 3:287–93, 2008.

[272] B. M. Gumbiner. Cell adhesion: the molecular basis of tissue architecture and morphogenesis. *Cell* 84:345–57, 1996.

[273] J. W. Costerton, P. S. Stewart, and E. P. Greenberg. Bacterial biofilms: a common cause of persistent infections. *Science* 284:1318–22, 1999.

[274] L. Hall-Stoodley, J. W. Costerton, and P. Stoodley. Bacterial biofilms: from the natural environment to infectious diseases. *Nat Rev Microbiol* 2:95–108, 2004.

[275] G. Wanner, K. Vogl, and J. Overmann. Ultrastructural characterization of the prokaryotic symbiosis in "chlorochromatium aggregatum". *J Bacteriol* 190:3721–30, 2008.

[276] X. D. Su, L. N. Gastinel, D. E. Vaughn, I. Faye, P. Poon, and P. J. Bjorkman. Crystal structure of Hemolin: a horseshoe shape with implications for homophilic adhesion. *Science* 281:991–5, 1998.

[277] F. S. Walsh and P. Doherty. Neural cell adhesion molecules of the immunoglobulin superfamily: role in axon growth and guidance. *Annu Rev Cell Dev Biol* 13:425–56, 1997.

[278] C. Chothia and E. Y. Jones. The molecular structure of cell adhesion molecules. *Annu Rev Biochem* 66:823–62, 1997.

[279] D. Kiryushko, V. Berezin, and E. Bock. Regulators of neurite outgrowth: role of cell adhesion molecules. *Ann N Y Acad Sci* 1014:140–54, 2004.

[280] P. F. Maness and M. Schachner. Neural recognition molecules of the immunoglobulin superfamily: signaling transducers of axon guidance and neuronal migration. *Nat Neurosci* 10:19–26, 2007.

[281] E. De Angelis, J. MacFarlane, J. S. Du, G. Yeo, R. Hicks, F. G. Rathjen, S. Kenwrick, and T. Brummendorf. Pathological missense mutations of neural cell adhesion molecule L1 affect homophilic and heterophilic binding activities. *Embo J* 18:4744–53, 1999.

[282] S. Kenwrick, A. Watkins, and E. De Angelis. Neural cell recognition molecule L1: relating biological complexity to human disease mutations. *Hum Mol Genet* 9:879–86, 2000.

[283] G. Schurmann, J. Haspel, M. Grumet, and H. P. Erickson. Cell adhesion molecule L1 in folded (horseshoe) and extended conformations. *Mol Biol Cell* 12:1765–73, 2001.

[284] Y. He, G. J. Jensen, and P. J. Bjorkman. Cryo-electron tomography of homophilic adhesion mediated by the neural cell adhesion molecule L1. *Structure* 17:460–71, 2009.

[285] C. Isenberg. *The Science of Soap Films and Soap Bubbles*. Dover Publications, 1st edition, 1992.

[286] F. Julicher and U. Seifert. Shape equations for axisymmetric vesicles: A clarification. *Phys Rev E* 49:4728–4731, 1994.

[287] H. G. Dobereiner, E. Evans, M. Kraus, U. Seifert, and W. Wortis. Mapping vesicle shapes into the phase diagram: A comparison of experiment and theory. *Phys Rev E* 55:4458–4474, 1997.

[288] M. Dubois, B. Deme, T. Gulik-Krzywicki, J. C. Dedieu, C. Vautrin, S. Desert, E. Perez, and T. Zemb. Self-assembly of regular hollow icosahedra in salt-free catanionic solutions. *Nature* 411:672–5, 2001.

[289] A. Gray. *Modern Differential Geometry of Curves and Surfaces with Mathematica*. CRC Press, Boca Raton, 2nd edition, 1997.

[290] A. Roux, D. Cuvelier, P. Nassoy, J. Prost, P. Bassereau, and B. Goud. Role of curvature and phase transition in lipid sorting and fission of membrane tubules. *Embo J* 24:1537–45, 2005.

[291] V. Gaberc-Porekar and V. Menart. Perspectives of immobilized-metal affinity chromatography. *J Biochem Biophys Methods* 49:335–60, 2001.

[292] V. Heinrich and C. Ounkomol. Force versus axial deflection of pipette-aspirated closed membranes. *Biophys J* 93:363–72, 2007.

[293] B. Loffeld and H. Keweloh. cis/trans isomerization of unsaturated fatty acids as possible control mechanism of membrane fluidity in *Pseudomonas putida* P8. *Lipids* 31:811–5, 1996.

[294] K. Yasuhara, Y. Sasaki, and J. Kikuchi. A photo-responsive cholesterol capable of inducing a morphological transformation of the liquid-ordered microdomain in lipid bilayers. *Colloid Polym Sci* 286:1675–1680, 2008.